

FLOW OF EMULSIONS THROUGH POROUS MEDIA

Ph.D. THESIS

by

PARTHA KUNDU



**DEPARTMENT OF CHEMICAL ENGINEERING
INDIAN INSTITUTE OF TECHNOLOGY ROORKEE
ROORKEE-247667 (INDIA)
JANUARY, 2016**

FLOW OF EMULSIONS THROUGH POROUS MEDIA

A THESIS

*Submitted in partial fulfilment of the
requirements for the award of the degree
of*

DOCTOR OF PHILOSOPHY

in

CHEMICAL ENGINEERING

by

PARTHA KUNDU



**DEPARTMENT OF CHEMICAL ENGINEERING
INDIAN INSTITUTE OF TECHNOLOGY ROORKEE
ROORKEE-247667 (INDIA)
JANUARY, 2016**



**©INDIAN INSTITUTE OF TECHNOLOGY ROORKEE, ROORKEE-2016
ALL RIGHTS RESERVED**



INDIAN INSTITUTE OF TECHNOLOGY ROORKEE ROORKEE

CANDIDATE'S DECLARATION

I hereby certify that the work which is being presented in this thesis entitled “FLOW OF EMULSIONS THROUGH POROUS MEDIA” in partial fulfilment of the requirement for the award of the Degree of Doctor of Philosophy and submitted in the Department of Chemical Engineering of the Indian Institute of Technology Roorkee, Roorkee is an authentic record of my own work carried out during a period from July, 2011 to January, 2016 under the supervision of Dr. Vimal Kumar, Assistant Professor, Department of Chemical Engineering, Indian Institute of Technology Roorkee and Dr. Indra Mani Mishra, Professor (Ret.), Department of Chemical Engineering, Indian Institute of Technology Roorkee.

The matter presented in the thesis has not been submitted by me for the award of any other degree of this or any other Institute.

(PARTHA KUNDU)

This is to certify that the above statement made by the candidate is correct to the best of our knowledge.

(Vimal Kumar)
Supervisor

(Indra Mani Mishra)
Supervisor

Dated:

ABSTRACT

Fluid transport in porous media has been an area of intense research due to its importance in a number of chemical and allied industries. Modeling flow through porous media at the engineering scale usually employs semi empirical equations which assume the medium to be a continuum. Only limited work is available on flow of emulsion (oil and water in different proportions) through porous media. Detailed experimentation is, therefore, needed to understand the single- and multi-phase (emulsion) flow phenomena through porous media.

The dissertation reports on the preparation of oil-in-water (o/w) and water in oil (w/o) emulsions, and their stability and rheology. An in-depth study was carried out for flow of Newtonian and non-Newtonian (emulsion) fluids through porous media. Computational study of the single phase fluid flow through an isotropic porous media was carried out using viscous, Reynolds averaging Navier-Stokes (RANS) and large eddy simulation (LES) approaches.

The mathematical and statistical approach was adopted to study the formation and stability of o/w emulsion with an integrated hybrid genetic algorithm (GA) coupled with feed-forward back-propagation artificial neural network (BPANN) and response surface methodology (RSM) based on Box-Behnken design (BBD). The hybrid GA model was found to be useful in the optimization of process parameters. The optimum condition predicted by the hybrid GA was 0.913 of emulsion stability index, ESI_{24} , with 4.70% error for 50% (v/v) o/w emulsion, 2% (w/v) surfactant, 5691 revolutions per minute (rpm) of stirring for 5 min time.

The rheological behavior of o/w and w/o emulsions with varying internal phase concentrations (10–80%) and an anionic surfactant, i.e. sodium dodecyl benzene sulfonate (SDBS) varying in concentration from 0.5 to 2 w/v %, at different temperatures (25–50 °C) was studied. A controlled stress rotational viscometer is used with shear rates ranging from 1 to 100 s⁻¹. The emulsions exhibited typical shear thinning behavior and described well by the power law relationship between shear stress and shear rate. Different viscosity models have been tested and fitted with the experimental rheological data using rigorous-linear/non-linear regression analysis. The Herschel-Bulkley model described the rheological data significantly well. It was observed that the emulsion viscosity and pseudoplasticity increased with an increase in oil concentration. The Herschel-Bulkley and power law models better represented the emulsion rheological behavior as compared to the Casson models.

The rise in nonlinearity in Darcy law to describe the evolution of inertial effects in a porous medium has been investigated experimentally. The demarcation limit of the various flow regimes (pre-Darcy, Darcy, transition and non-Darcy) is highlighted, which enabled accurate determination of permeability (K) and form drag coefficient (F_D) for different types

of porous media. It is observed that the flow changes from weak inertial regime to quadratic Forchheimer regime at critical Re in between 5 to 10 and the microscopic inertial effect is the governing factor which leads to the transition from the Darcy to non-Darcy flow regimes. The detailed microscopic pore hydrodynamics in the form of flow streamlines and velocity contours is observed over the Darcy and non-Darcy flow regimes, i.e. $0.02 \leq Re_D \leq 30$.

Further, emulsion (o/w) flow behaviour is investigated for different oil volume fractions (10-80% v/v) and porous media, such as packed bed with four different sizes of glass beads. The rheological properties of emulsions flowing through the porous media have been studied on the basis of shear stress ($\bar{\tau}_w$) versus shear rate ($\delta u_w/R_h$) relationship. It is observed that the emulsion volume fraction significantly influences the porous bed pressure drop. Pressure drop data ($d\langle\bar{P}\rangle/dL$) across the porous bed for all sets of o/w emulsions increases with an increase in emulsion volume fraction, increases with a decrease in particle diameter (glass beads) and an increase in medium porosity. An increase in shear stress and volume fraction during percolation of emulsions through the porous bed is observed. Further, it is found that the effective viscosity of the emulsion for porous bed of different particle diameter decreases with an increase in shear rate and resistance factor (RF) for different porous bed increases with an increase in emulsion volume fraction and decreases with an increase in emulsion injection rate. The pressure drop across the core holder increased with emulsion injection flow rate for all three different sand pack core holders (S-A, S-B, and S-C) studied in the present work. Pressure drop also increases with an increase in emulsion volume fraction due to the increase in emulsion viscosity. It is seen that the permeability ratio across the core holder decreases with an increase in pore volume (PV) of emulsion injected. The Permeability reduction behaviour of porous media is investigated by observing the change in pressure drop across the core holder as a function of number of pore volume of emulsion injected. The permeability reduction across the core holder decreased largely with an increase in emulsion volume fraction and also with an increase in the number of pore volume injected.

The laminar flow and turbulent characteristics of flow through an isotropic porous media was studied assuming it to be a *representative elementary volume* (REV) and comprising an array of square or circular cylinders. Both porous media porosity (ϕ) and Reynolds number based on particle diameter (Re_p), were varied over a wide range. Viscous, Low Re k- ϵ turbulence, standard k- ϵ turbulence, pseudo-direct numerical simulations (DNS), and large eddy simulation (LES) approaches were used in these studies. The turbulent parameters predicted using low Re k- ϵ -LB turbulent model were found to be in good agreement with the LES as compared to that with v2f model and the predictions of the pressure gradient were found to be in good agreement with the Forchheimer-extended Darcy law. The low Re-k- ϵ -LB model was found to be valid only for flows with $Re_p > 300$.

ACKNOWLEDGMENT

My profound appreciation goes to God almighty and my parents who has helped me tremendously in all my academic endeavors. I will also like to thank, very profoundly, my supervisor Professor Indra Mani Mishra and Dr. Vimal Kumar for their guidance, wisdom, relentless help, and endless patience, and have thoroughly enjoyed working with them throughout my PhD. I have learned a great deal from Professor Mishra and Dr. Kumar, not least about the subject of my PhD, but also about research methodology, and as such I am indebted to her for raising the quality of my research and the standard of my technical writing.

I am also very thankful to Prof. Basheshwer Prasad, Dr. Krishna M. Singh and Prof. Shishir Sinha for their invaluable help and suggestions and for serving on the research examining committee. I am also thankful to Dr. Vimal Chandra Srivastava for continuous support and encouraging words.

I am profoundly thankful to all the faculty members of the Chemical Engineering Department at IIT Roorkee, and in particular Prof. Chandrajit Balomajumder Professor and Head, Department of Chemical Engineering, Indian Institute of Technology, Roorkee, India who is a constant source of motivation. I would even remain thankful to Prof. Indra Deo Mall, Prof. Shri Chand, Prof. Vijay Kumar Agarwal, Prof. Bikash Mohanty, and Dr. Parsenjit Mondal for their kind help and suggestion toward the successful completion of my PhD journey. I also like to extend my gratitude to all the other respectful faculty members of Chemical Engineering Department, IIT Roorkee, who, from behind the curtain, furnished me with their valuable assistance towards my lessons during my PhD. I wish to acknowledge all the staff of the Department of Chemical Engineering for their help and assistance during my work.

During the five years of my study at Indian Institute of Technology, Roorkee, I have came across many respectful and kind persons, who had helped me a lot in doing and finishing my PhD degree, and they would remain evergreen in my memory. It is their kind help and untiring effort that had resulted in successful completion of my PhD, today.

I would like to express my gratitude to Dr. Jyoti Sharma, Dr. Shilpi Verma, Dr. Krunal Gangawane, Dr. Praveen Kumar for their encouragement, extensive discussion and constant help. I am also thankful to my dear friends Mr. Anil Verma, Mr. Nitin Naresh Pandhare, Mr. Nelamber Bariha, Mr. Vijay Verma, Mr. Soumitra Maiti, Mr. Ravikant Gupta, Mr. Deepak Sahu, Mr. Ambrish Maurya, Mr. Krishnakant Dhakar, Mr. Vikash, Mr. Varun Paul and juniors for their moral support. I am greatly indebted to all my colleagues and friends beyond words. They have been always there for me with their suggestions, moral

support and hand of help for everything I needed. Deep appreciation is given to my lab mate for their help in the laboratory.

My sincere thanks to Mr. Ayodhya Prasad Singh, Mr. Arvind Kumar, Mr. Suresh Saini, Mr. Satyapal, Mr. Tara Chand, Mr. R. Bhatnagar, Mr. Akka and Mr. Arvind for helping me during my research work. I am also thankful to the Head, Institute Instrumentation Centre (IIC) and Institute Computer Center of IIT Roorkee for providing me necessary facilities for my research work.

The financial assistance in the form of fellowship provided by Ministry of Human Resource Department (MHRD), Government of India is highly appreciated. I also like to appreciate financial support of Indian Institute of Chemical Engineers (IChE) who provided funds under the R&D project grant IIC-734-CHD.

I also like to express a profound gratitude to my parents, Mr. Deb Dutta Kundu & Mrs. Pratima Kundu for their continuous support. Same gratitude goes to my sibling Mrs. Baby Roza, My Brother in law Mr. Sudip Roza and my little niece Bidisha and Sudeepa for all their help and encouragement. The unfailing supports from the above people have been very instrumental in the completion of my PhD journey. I deeply thankful to my late grandfather Mr. Kalipada Kundu and my late grandmother Mrs. Binapani Kundu for their divine blessings.

My deepest gratitude goes also to my family for their indefatigable love and support throughout my life. To all of them I dedicate this thesis.

Above all, I thank 'Almighty' with whose beatitude, I could reach this far.

(PARTHA KUNDU)

JANUARY, 2016

CONTENTS

CANDIDATE’S DECLARATION	i
ABSTRACT	iii
ACKNOWLEDGEMENTS	v
CONTENTS	vii
LIST OF TABLES	xiii
LIST OF FIGURES	xv
NOMENCLATURE	xxv
CHAPTER 1: INTRODUCTION	
1.1 GENERAL	1
1.2 SURFACTANT AND ITS ROLE AS AN EMULSIFYING AGENT	4
1.3 STABILITY OF EMULSIONS	7
1.3.1 Sedimentation	8
1.3.2 Flocculation	8
1.3.2.1 London-Van Der Waals interactions	9
1.3.2.2 Electrical double-layer interactions	9
1.3.3 Coalescence	11
1.3.4 Ostwald ripening or Disproportionation	12
1.4 INDUSTRIAL APPLICATION OF EMULSIONS	13
1.5 FLUID FLOW THROUGH POROUS MEDIA	15
1.6 EMULSIONS FLOW THROUGH POROUS MEDIA	18
1.7 MOTIVATION	20
1.8 OBJECTIVES	22
1.9 THESIS ORGANIZATION	23
CHAPTER 2: LITERATURE REVIEW	
2.1 STABILITY OF EMULSION	25
2.2 RHEOLOGY OF EMULSION	26

2.2.1	Factors Influencing Emulsion Rheology	31
2.3	POROUS MEDIA FLOW	33
2.3.1	Incompressible Single Phase Fluid Flow Through Porous Media	38
2.3.2	Non-Newtonian Fluid Flow Through Packed Bed and Porous Media	40
2.3.3	Emulsion Flow Through Porous Media	40
2.4	FLUID FLOW MODELLING	49
2.5	OVERVIEW OF LITERATURE REVIEW	52
CHAPTER 3: MATERIALS AND METHODS		
3.1	EXPERIMENTAL DETAILS FOR EMULSION PREPARATION	53
3.1.1	Chemicals	53
3.1.2	Preparation of Emulsion	53
3.2	EMULSION CHARACTERIZATION	55
3.2.1	Emulsion Stability Measurements	55
3.2.2	Droplet Size Measurement	56
3.2.3	Zeta Potential and Electrophoretic Mobility Measurements	56
3.2.4	Surface Tension (SFT) and Interfacial Tension (IFT) Measurement of Emulsions	56
3.2.5	Microscopy of O/W Emulsions	57
3.2.6	Rheological Measurements	57
3.2.7	Error Estimation	58
3.3	EXPERIMENTAL DESIGN AND EMULSIFICATION PROCESS MODELING	59
3.3.1	Response Surface Methodology (RSM)	59
3.3.2	Artificial Neural Network (ANN)	60
3.3.2.1	ANN model development	61
3.3.2.2	Network training	62
3.3.3	Genetic Algorithm (GA)	63
3.3.4	Integrated Modeling	64
3.4	POROUS MEDIA	64
3.4.1	Glass Beads as Porous Packing Materials	64
3.4.2	Sand-pack Core Holder Details and Sand-pack Preparation	65

CHAPTER 4: STABILITY AND RHEOLOGICAL BEHAVIOUR OF OIL-IN-WATER (O/W) EMULSIONS

4.1	STATISTICAL MODELLING OF EMULSION FORMULATION AND STABILITY AND OPTIMIZATION OF PROCESS PARAMETERS	71
4.1.1	RSM Modeling	71
4.1.2	BP-ANN Modeling	77
4.1.3	Multi Objective Hybrid GA Optimization Model	83
4.1.4	Process Parametric Interactions	86
4.1.5	Validation of Hybrid GA and RSM-BBD Models	89
4.2	EMULSION STABILITY	92
4.2.1	Effect of Volume Fraction on Emulsion Stability	92
4.2.1.1	<i>Droplet size distribution (DSD) of emulsions</i>	92
4.2.1.2	<i>Electrophoretic characteristics of emulsions</i>	95
4.2.1.3	<i>Surface tension of emulsions</i>	96
4.2.2	Effect of pH on Emulsion Stability	96
4.2.2.1	<i>Droplets size distributions (DSD) of emulsions</i>	98
4.2.2.2	<i>Electrophoretic characteristics of emulsions</i>	101
4.3	RHEOLOGICAL BEHAVIOR OF O/W EMULSION	102
4.3.1	Steady Shear Rate Analysis	102
4.3.2	Modeling of Emulsion Flow Behavior	103
4.3.3	Effect of Temperature on Emulsion Rheology	109
4.3.4	Modelling of Temperature Dependency on Emulsion Rheology	113
4.3.5	Effect of Volume Fraction on O/W Emulsion Rheology	114
4.3.6	Effect of Surfactant Concentration on O/W Emulsion Rheology	118
4.3.7	Effect of pH on Rheological Behavior Under Steady Shear Flow	121
4.3.8	Scaling Analysis of Rheological Response of Emulsions	125
4.3.9	Electro-viscous effect on emulsion rheology	126
4.4	VISCOELASTIC BEHAVIOUR OF EMULSIONS	129
4.4.1	Rheological Behavior of O/W Emulsion Under Dynamic Oscillatory	130

Shear Flow	
4.4.2 Modeling The Dynamic Viscoelastic Behavior of O/W Emulsions	132
4.4.3 Cox–Merz Rule	136
4.4.4 Time-Dependent Flow Behavior of O/W Emulsions	138
4.4.5 Effect of Temperature on Steady and Dynamic (Viscoelastic) Rheological Behavior of O/W Emulsions	139

CHAPTER 5: FLUID FLOW THROUGH POROUS MEDIA

5.1 NEWTONIAN FLUID FLOW THROUGH POROUS MEDIA	145
5.1.1 Pressure Drop-Velocity Relationship	145
5.1.2 Various Flow Regimes in Porous Media	149
5.1.3 Pressure Gradient-Flow Rate Behavior	152
5.2.4 Variation of Medium Permeability at Different Pore Flow Regimes	156
5.2 FLOW OF EMULSIONS THROUGH POROUS MEDIA	159
5.2.1 Emulsion Flow Modeling	159
5.2.2 Pressure Drop in Packed Bed of Different Porous Media for o/w Emulsion Flow	161
5.2.3 Modified Friction Factor-Reynolds Number Relation for Flow through Porous Media	161
5.2.4 Rheological Behavior of Emulsions through Porous Media	164
5.2.5 Quantification of Emulsion Flow Resistance Factor in Porous Media	172
5.2.6 Emulsion Flow through Sand Pack Core Holder	172
5.2.6.1 <i>Pressure drop-flow rate relation of emulsion flow</i>	172
5.2.6.2 <i>Permeability reduction</i>	176

CHAPTER 6: MODELING OF FLUID FLOW THROUGH AN ISOTROPIC POROUS MEDIA

6.1 GENERAL	179
6.2 GOVERNING EQUATIONS FOR POROUS MEDIA FLOW MODELING	180
6.2.1 Laminar Flow Model	180
6.2.2 Turbulence models	180

6.2.2.1	<i>Reynolds averaged Navier–Stokes (RANS) turbulence models</i>	180
6.2.2.2	<i>Standard $k-\varepsilon$ turbulence model</i>	180
6.2.2.3	<i>Low $Re-k-\varepsilon$ turbulence model</i>	181
6.2.3	Large eddy simulation (LES) modeling approach	182
6.3	SIMULATION FRAMEWORK AND GRID TOPOLOGY	183
6.3.1	Computational Domain	183
6.3.2	Grid Topology	185
6.4	NUMERICAL APPROACH AND BOUNDARY CONDITIONS	188
6.4.1	Numerical Approach	188
6.4.2	Boundary conditions for the computational domain	188
6.4.2.1	<i>Array of square cylinders</i>	188
6.4.2.2	<i>Array of circular cylinders</i>	189
6.5	MICROSCOPIC LAMINAR PORE SCALE FLOW SIMULATION	190
6.6	TURBULENT FLOW MODELING IN POROUS MEDIA	195
6.6.1	Microscopic Streamlines and Velocity Field	195
6.6.2	Macroscopic Turbulent Kinetic Energy and Dissipation Rate	200
6.6.3	Comparison of Turbulence Model	206
6.6.4	Direct Numerical Simulations (DNS)	210
6.6.5	Computation of Macroscopic Pressure Gradient	211
6.6.6	Macroscopic Turbulence Modeling	216
6.7	FLOW THROUGH ISOTROPIC ARRAY OF CIRCULAR CYLINDERS	217
6.7.1	Spanwise Microscopic Turbulent Flow Fields	217
6.7.2	Solid fluid interactions and 3D flow structures	223
6.7.3	Mean flow statistics	227
6.7.4	Computation of macroscopic turbulent kinetic energy and dissipation rate	229
6.7.5	Computation of pressure drop across the REV	232
6.7.6	Computation of permeability and Darcy-Forchheimer correlation for porous REV	234
6.7.7	Effect of Medium Morphology on Porous Media Flow	239

CHAPTER 7: CONCLUSIONS AND RECOMMENDATIONS

7.1	CONCLUSIONS	243
7.1.1	Emulsion Formation, Stability and Characterizations	243
7.1.2	Effect of Oil Volume Fraction, Surfactant Concentration, pH and Temperature on Emulsion Rheology	244
7.1.3	Newtonian Fluid Flow through Porous Media	245
7.1.4	Emulsion Flow through Porous Media	246
7.1.5	Modeling of Fluid Flow through an Isotropic Porous Media	247
7.1.5.1	Array of square cylinder	247
7.1.5.2	Array of circular cylinder	247
7.2	RECOMMENDATIONS	248
	REFERENCES	249
	APPENDIX A	275
	APPENDIX B	281
	AUTHORS BIODATA	289

LIST OF TABLES

Table No.	Title	Page No.
Table 1.1	Classification of Surfactants on the basis of HLB	6
Table 1.2	Examples of Emulsions in the Petroleum Industry (Schramm, 1992)	14
Table 2.1	Overview of studies related to emulsion stability.	27
Table 2.2	Various viscosity models for emulsions.	32
Table 2.3	A literature overview of study regarding emulsion rheology.	34
Table 2.4	Representative studies of non-Newtonian fluid through porous media and packed	41
Table 2.5	Model equations for the prediction of bed friction factor proposed by various investigators	44
Table 3.1	Physico-chemical properties of sodium dodecyl benzene sulphonate (SDBS). (Source: Kundu et al., 2013)	54
Table 3.2	Properties of light petroleum oil.	54
Table 3.3	Different types o/w emulsions used in the study.	55
Table 3.4	Details of viscosity measuring system (Rheometer).	58
Table 3.5	Levels and code of independent process variables chosen for BBD.	60
Table 3.6	Porous bed and particles details.	65
Table 3.7	Physical properties of core holder packing materials.	66
Table 4.1	A 3 ⁴ Box Behnken design (BBD) Matrix with the experimental and predicted responses of emulsion stability (ESI_{24}).	72
Table 4.2	Analysis of variances (ANOVA) results for the RSM-BBD model.	75
Table 4.3	Selection of adequate model for optimization of emulsion stability process parameters.	76
Table 4.4	Determination of optimum number of neurons for hidden layer in BP-ANN.	78
Table 4.5	Network weights and biases for BP-ANN model.	82
Table 4.6	Criteria of hybrid GA simulation leading to the optimal solution.	83
Table 4.7	Comparative results of confirmatory experiments for model validation.	91
Table 4.8	Effect of pH on modified capillary number ($N_{Ca,m}$) and drops deformation (D_m) in the emulsions.	99

Table 4.9	Power law model fitting parameters for o/w emulsions at different temperature.	105
Table 4.10	Casson model fitting parameters for o/w emulsions at different temperatures.	106
Table 4.11	Herschel-Bulkley (HB) model fitting parameters for o/w emulsions at different temperatures.	107
Table 4.12	Arrhenius model parameters for temperature dependency on apparent viscosity of different sets of o/w emulsions.	112
Table 4.13	Parameters from master-curve for power law equation fitting into master curve at various temperatures ($^{\circ}\text{C}$).	113
Table 4.14	Various model fitting parameters of o/w emulsions at different surfactant concentrations.	120
Table 4.15	Flow parameters of o/w emulsions determined by power law and Sisko model.	122
Table 4.16	Flow parameters of o/w emulsions determined by Cross and Carreau model.	124
Table 4.17	Dynamic shear parameters of power-law functions describing storage and loss moduli of o/w emulsions at different pH and temperature.	135
Table 4.18	Arrhenius model temperature dependency parameters of o/w emulsions.	143
Table 5.1	Coefficient of different types of flow correlation equations between the pressure gradient and velocity in porous bed with various particle diameters.	148
Table 5.2	Flow regimes boundaries of different porous media for incompressible Newtonian fluid.	153
Table 5.3	Parameters of Forchheimer equation for different porous media.	156
Table 5.4	Variation of C_f given by Eq. (5.39-5.42) for different emulsion volume fraction.	163
Table 5.5	Statistical comparison (MRQE) of various model predictions (Eq. 5.39-5.42) and experimental results.	166
Table 5.6	Statistical comparison (MRQE) of various model predictions for o/w emulsions as test fluid.	167
Table 6.1	Computed permeability, K for different porosity at $Re_D = 10$.	235

LIST OF FIGURES

Fig. No.	Title	Page No.
Fig. 1.1	(a) Oil-in-water (o/w), (b) water-in-oil (w/o) and (iii) multiple emulsions.	2
Fig. 1.2	Classification of emulsions based on dispersed phase droplet size.	3
Fig. 1.3	Schematic representation of different Winsor phases (for Winsor IV, a bicontinuous micro-emulsion is also a possible structure). Light gray indicates the oil phase and blue water phase, and the light green indicates the microemulsion (Source: Paul and Moulik, 2001).	3
Fig. 1.4	Schematic representation of the Gibbs-Marangoni effect acting on two approaching droplets during emulsification: (a) droplets insufficiently covered approaching; surfactants dispersed in the water phase are less numerous where the film is thinner, and (b) droplets are not covered uniformly by the surfactants, inducing an interfacial tension gradient (bent arrows) responsible for the thin film.	6
Fig. 1.5	Theories of electrical double layer.	7
Fig. 1.6	Schematic representation of several types of instability in o/w emulsions.	11
Fig. 1.7	Porous medium of randomly arranged polydispersed spheres through which flows a fluid of density ρ and dynamic viscosity η over cross-section area A . Further parameters are explained in the text.	16
Fig. 1.8	Microscopic, mesoscopic and macroscopic flow patterns within porous media according to Tsotsas (Tsotsas, 1992). Flow profiles are given qualitatively.	17
Fig. 1.9	Parameters influencing the emulsion flow through porous medium	19
Fig. 2.1	Schematic diagram of the structure of droplets in emulsions within in a range of 0 to 1 volume fractions (Mason, 1999).	31
Fig. 2.2	Emulsion blockage mechanism (Jamin effect).	45
Fig. 2.3	Schematic representation of porous medium with the hierarchy of various characteristic length scales and position vector (Ω_S and Ω_F are the solid and fluid phases, respectively).	51

Fig. 3.1	Schematic diagram of lab scale experimental setup for emulsification.	55
Fig. 3.2	Mechanism of an artificial neuron.	61
Fig. 3.3	Design of the stainless-steel sand-pack core holder.	67
Fig. 3.4	Schematic diagram of experimental set-up.	69
Fig. 4.1	Experimental results and Predicted responses of emulsion stability analysis.	74
Fig. 4.2	Pattern of optimized ANN architecture (4-24-1).	79
Fig. 4.3	The performance of the BP-ANN model (4-26-1) in the training phase showing performance value (MSE- 0.014751) after 6 epochs.	80
Fig. 4.4	Regression plot showing regression coefficient of experimental data and BP-ANN (4-24-1) model simulated values.	81
Fig. 4.5	Algorithm for hybrid GA (GA coupled with BP-ANN and RSM-BBD) to optimize the emulsion stability process parameters.	84
Fig. 4.6	Hybrid GA model simulated Fitness function plot. Best and average fitness values show a gradual convergence towards the optimum value of 1.0952 after 100 generations.	85
Fig. 4.7	Single factor plot showing the effect of (a) oil concentration; (b) surfactant concentration; (c) stirring time; and (d) stirring speed on emulsion stability (ESI_{24}).	87
Fig. 4.8	3D response surface plot showing the effect of oil concentration and surfactant concentration on emulsion stability index (ESI_{24}).	88
Fig. 4.9	2D contour plot showing the variation of emulsion stability index (ESI_{24}) with oil concentration and surfactant concentration.	88
Fig. 4.10	2D contour plot showing the combine effect of stirring time and stirring speed on emulsion stability index (ESI_{24}).	89
Fig. 4.11	3D response surface plot showing the effect of oil concentration and stirring time on emulsion stability index (ESI_{24}).	90
Fig. 4.12	2D contour plot showing the combined effect of stirring time and oil concentration on emulsion stability index (ESI_{24}).	90

Fig. 4.13a	Variation of creaming index (CI) with time for different o/w emulsions. Set 5 (—●—); set 4(—▼—); set 3(—■—); set 2(—◆—); set 1(—▲—).	93
Fig. 4.13b	Variation of emulsification index (EI) with time for different o/w emulsions Set 5 (—●—); set 4(—▼—); set 3(—■—); set 2(—◆—); set 1(—▲—).	93
Fig. 4.14	Photomicrographs of freshly prepared oil-in-water emulsions at 40X.	94
Fig. 4.15	Droplet size distribution of o/w emulsions. Set 5 (—●—); set 4(—▼—); set 3(—■—); set 2(—◆—); set 1(—▲—).	94
Fig. 4.16	Zeta potential and electrophoretic mobility of emulsions with oil volume fraction (Zeta potential —●—; Mobility —▲—.)	95
Fig. 4.17	Variation of surface tension of emulsions with oil volume fraction.	96
Fig. 4.18	Influence of pH on o/w emulsion stability (a) Emulsification stability index (EI) plot (b) Creaming index (CI) plot. pH: 12 —■—; 10 —●—; 8 —▲—; 6 —▶—; 4 —◀—; 2 —▶—	97
Fig. 4.19	Evolution of droplet size distribution (DSD) of o/w emulsions with pH.	100
Fig. 4.20	Zeta potential and electrophoretic mobility of o/w emulsions with different system pH.	102
Fig. 4.21a	Rheograms (shear rate vs shear stress plots) of different o/w emulsions. Set 5 (—■—); set 4(—●—); set 3(—▲—); set 2(—▼—); set 1(—◆—)	103
Fig. 4.21b	Shear rate vs apparent viscosity of different o/w emulsions. Set 5 (—■—); set 4(—●—); set 3(—▲—); set 2(—▼—); set 1(—◆—)	104
Fig. 4.22	Effect of temperature on flow behavior index (n) of o/w emulsions. Set 5 (—■—); set 4(—●—); set 3(—▲—); set 2(—▼—); set 1(—◆—)	108
Fig. 4.23	Effect of temperature on flow consistency index (K) of o/w emulsions. Set 5 (—■—); set 4(—●—); set 3(—▲—); set 2(—▼—); set 1(—◆—)	109

Fig. 4.24	Effect of temperature on the rheograms of o/w emulsion. 25 °C (—■—); 30 °C (—●—); 40 °C (—▲—); 50 °C (—◆—).	111
Fig. 4.25	Arrhenius plot for apparent viscosity of different o/w emulsions. Set 5 (—●—); set 4(—▼—); set 3(—■—); set 2(—◆—); set 1(—▲—).	112
Fig. 4.26	Shift factor plot for master curve for different o/w emulsions. Set 5 (—●—); set 4(—▼—); set 3(—■—); set 2(—◆—); set 1(—▲—).	114
Fig. 4.27	Master-curve showing superimposition on (a) shear stress– temperature (b) emulsion apparent viscosity–temperature with shear rate for different o/w emulsions at different temperature ($T_{ref} = 30$ °C). Set 5 (—●—); set 4(—▼—); set 3(—■—); set 2(—◆—); set 1(—▲—).	115
Fig. 4.28	Variation of emulsions apparent viscosity with internal phase (oil) volume fraction with temperature as a parameter at different shear rates. 25 °C (—●—); 30 °C (—▼—); 40 °C (—■—); 50 °C (—◆—).	116
Fig. 4.29	Parity Plot of predicted viscosity with experimental viscosity of o/w emulsions at $\dot{\gamma} = 40 \text{ s}^{-1}$.	117
Fig. 4.30	Effect of surfactant concentration on the rheograms of o/w emulsions. Surf. Conc. (wt %): 0.5% (—■—); 1% (—●—); 2% (—▲—).	119
Fig. 4.31	Evolution of steady-state rheograms of o/w emulsion for different pH: (a) Shear stress-shear rate plot (b) Apparent viscosity-shear rate plot. pH: 12 —■—; 10 —●—; 8 —▲—; 6 —▼—; 4 —◆—; 2 —◆—; surf 1 wt% —◆—.	123
Fig. 4.32	(a) Relative viscosity (η_r) as a function of particle Reynolds number ($N_{Re,p}$) and (b) pH-Reduced master flow curve and evolution of the shift factor for 30% (v/v) oil-in-water emulsions with 1 wt% surfactant concentration. pH: 12 —■—; 10 —●—; 8 —▲—; 6 —▼—; 4 —◆—; 2 —◆—	127
Fig. 4.33	The dynamic oscillation spectra of o/w emulsions at different emulsion pH. G'' —□—; G' —■—; η^* —●—	131

- Fig. 4.34 Evolution of phase angle ($\tan\delta$) as a function of angular frequency at different pH. 133
 pH: 12 —■—; 10 —●—; 8 —▲—; 6 —▼—; 4 —◆—; 2 —→—
- Fig. 4.35 Influence of pH on the steady-state viscosity at 0.01 s^{-1} , the plateau modulus (G_p^0) and with cross over moduli (G_c) of o/w emulsion. 134
 $\eta_{a(0.01)}$ —■—; G_p^0 —◆—; G_c —◇—.
- Fig. 4.36 Comparison of dynamic oscillatory and steady-state shear viscosities (Cox–Merz rule) of all the o/w emulsions at different pH. η_a —■—; η^* —●—. 137
- Fig. 4.37 Time dependent behavior ($\eta - t$ plot) of o/w emulsions at different pH. 138
- Fig. 4.38 Rheogram of o/w emulsions at different temperature. 139
 20°C —■—; 30°C —●—; 40°C —▲—; 50°C —▼—.
- Fig. 4.39 Effect of temperature on evolution of droplet size distribution (DSD) of o/w emulsions. 140
- Fig. 4.40 Influence of temperature on the dynamic oscillatory mechanical spectra of o/w emulsions. (a) G' versus ω plot ; (b) G'' versus ω plot ; (c) η^* versus ω plot. 142
 (20°C —■—; 30°C —●—; 40°C —▲—; 50°C —▼—.)
- Fig. 5.1 Relationship between the Pressure gradient per unit length versus average velocity across the porous bed with different particle sizes. 146
 Porous media (d_p (mm) = 2.5 —▲—; 3.2 —●—; 5 —■—; Mix —▼—)
- Fig. 5.2 Reduced pressure drop (RPD) plot for flow regime demarcation of different types of porous media: pre-Darcy (■); transition to Darcy (◆); Darcy (■); weak inertia(□); non-Darcy Forchheimer regime (■). 150
- Fig. 5.3 Friction factor-Reynolds number plots for Newtonian fluid flow through different types of porous media. Kozney-Carman (-----); Ergun (-----) equation. 154

Fig. 5.4	Permeability based modified friction factor versus Reynolds number plot for different porous media.	157
Fig. 5.5	Variation of reciprocal of normalized permeability of different porous media with Re_p .	158
Fig. 5.6	Relationship between the Pressure gradient per unit length versus average velocity across the porous bed for different emulsion volume fraction. Emulsion vol. fr. (v/v) = 10% ; 30% ■; 50% ▲; 70% ▼; 80% ◀ .	162
Fig. 5.7	Modified friction factor-Reynolds number plot and model compression for o/w emulsion flowing through PM-1at different volume fraction.	165
Fig. 5.8	Modified friction factor-Reynolds number plot different emulsion volume fraction. Emulsion vol. fr. (v/v) =10% ●; 30% ■; 50% ◀; 70% ▲; 80% ▼ .	168
Fig. 5.9	f_m vs Re_M plot for different particle diameter (50% o/w emulsion). PM ■; PM2 ●; PM3 ▲; PM4◊	169
Fig. 5.10	Rheological behavior of emulsions in different type of porous media. Emulsion vol. fr. (v/v)= 10% ■; 30% ●; 50% ▲; 70% ▼; 80% ◀ .	170
Fig. 5.11	Effective viscosity of emulsions with volume fraction at different shear rates in porous media. Emulsion vol. fr. (v/v) = 10% ■; 30% ●; 50% ▲; 70% ▼; 80% ◀ .	171
Fig. 5.12	RF versus injected flow rate of emulsion with different volume fraction in porous media. Emulsion vol. fr. (v/v)= 10% ■; 30% ●; 50% ▲; 70% ▼; 80% ◀ .	173
Fig. 5.13	Effect of emulsion volume fraction on the RF for different porous media (Emulsion flow rate $5 \times 10^{-6} \text{ m}^3/\text{s}$). PM1 ■; PM2●; PM3▲;PM◊	174
Fig. 5.14	Relationship between the Pressure gradient per unit length versus injection flow rate across the sand pack core holder for o/w emulsions and water. Emulsion vol. fr. (v/v)= 10% ●; 30% ▲; 50% ▼; 70% ◀; water ■	175
Fig. 5.15	Plot of pressure gradient per unit length versus injection flow rate for 30 % O/W emulsions. Porous media: S-1 ■S-B ●S-C ▲	176

Fig. 5.16	Permeability reduction of different porous media versus number of pore volume of emulsion injected at different emulsion quality (Flow rate= 15 ml/min). Emulsion Vol. fr. (v/v): 10% ■; 30% ●; 30% ▲; 50% ◆	177
Fig. 5.17	Variation of emulsion volume fraction on permeability reduction of porous media as a function of different pore volume of emulsion injected. No. of PV injected: PV-1 ■ PV-5 ● PV-50 ▲	178
Fig. 6.1	Conceptual porous media flow domain for numerical computations (a) periodic array of square cylinder, and (b) representative enetry volume (REV) for array of square cylinders.	184
Fig. 6.2	Conceptual porous media flow domain for numerical computations (a) periodic array of circular cylinder, and (b) representative enetry volume (REV) for array of circular cylinders.	186
Fig. 6.3	(a) Grid topology of REV of array of (a) square cylinders, and (b) 3D porous representative elementary volume (REV) of circular cylinders.	187
Fig. 6.4	Plot of dimensionless pressure gradient (DPG) versus Re_P for different isotropic porous media (Experimental (-■-); Simulation (-●-); Kozney-Carman (Δ); Ergun (∇); Zhavoronkov (\triangleleft)).	192
Fig. 6.5	Evolution of Streamlines for the case (three REV) of $\phi = 0.3478$ wih different Re_P .	193
Fig. 6.6	Contours of velocity magnitude for the case (three REV) of $\phi = 0.3478$ wih different Re_P .	194
Fig. 6.7(a)	Streamline contours in porous media at porosity (ϕ) = 0.84 and 0.64.	196
Fig. 6.7(b)	Streamline contours in porous media at porosity (ϕ) = 0.5 and 0.3.	197
Fig. 6.8(a)	Velocity contours in porous media at porosity (ϕ) = 0.84 and 0.64.	198
Fig. 6.8(b)	Velocity contours in porous media at porosity (ϕ) = 0.5 and 0.3.	199
Fig. 6.9	Variation in normalized $\langle k \rangle^f$ with Re_D for different porosities (ϕ) (0.84 —●—; 0.64 ⋯○⋯, 0.5 ---▼---; 0.3 -·Δ-·.)	201
Fig. 6.10	Variation in normalized $\langle e \rangle^f$ with Re_D for different porosities (ϕ) (0.84 —●—; 0.64 ⋯○⋯; 0.5 ---▼---; 0.3 -·Δ-·.)	201

Fig.6.11	Turbulent kinetic energy and dissipation rate contours in porous media at differfent porosities: (a) $\phi = 0.84$, (b) $\phi = 0.64$, (c) $\phi = 0.50$, and (d) $\phi = 0.30$.	202
Fig. 6.12	Variation of normalized macroscopic turbulent kinetic energy with Re_D at porosity, ($\phi = 0.84$): Low-Re $k-\varepsilon-LB$ model (present work) $\text{---}\bullet\text{---}$; LES (Kuwahara et al., 2006) $\cdots\nabla\cdots$; v2f (Kazerooni and Hannani, 2009) $\text{---}\blacksquare\text{---}$.	207
Fig. 6.13	Variation of normalized macroscopic turbulent kinetic energy with Re_D at porosity, ($\phi = 0.64$): Low-Re $k-\varepsilon-LB$ model (present work) $\text{---}\bullet\text{---}$; LES (Kuwahara et al., 2006) $\cdots\nabla\cdots$; v2f (Kazerooni and Hannani, 2009) $\text{---}\blacksquare\text{---}$.	207
Fig. 6.14	Variation of normalized macroscopic turbulent kinetic energy with Re_D at porosity, ($\phi = 0.5$): Low-Re $k-\varepsilon-LB$ model (present work) $\text{---}\bullet\text{---}$; LES (Kuwahara et al., 2006) $\cdots\nabla\cdots$; v2f (Kazerooni and Hannani, 2009) $\text{---}\blacksquare\text{---}$.	208
Fig. 6.15	Variation of normalized macroscopic turbulent kinetic energy with Re_D at porosity ($\phi = 0.3$): Low-Re $k-\varepsilon-LB$ model (present work) $\text{---}\bullet\text{---}$; LES (Kuwahara et al., 2006) $\cdots\nabla\cdots$; v2f (Kazerooni and Hannani, 2009) $\text{---}\blacksquare\text{---}$.	208
Fig. 6.16	Normalized macroscopic turbulent kinetic energy versus $(1 - \phi)/\phi^{1/2}$ (Low-Re $k-\varepsilon-LB$ model (present work) $\text{---}\bullet\text{---}$; LES (Kuwahara et al., 2006) $\cdots\nabla\cdots$; v2f (Kazerooni and Hannani, 2009) $\text{---}\blacksquare\text{---}$.)	209
Fig. 6.17	Normalized macroscopic dissipation rate versus $(1 - \phi)/\phi^{1/2}$ (Low-Re $k-\varepsilon-LB$ model (present work) \bullet ; v2f [27] ∇ .)	209
Fig. 6.18	Comparison of different turbulence model at $Re_D=100$ (Low-Re $k-\varepsilon-LB$ model (present work) $\cdots\nabla\cdots$; DNS (present work) $\text{---}\bullet\text{---}$; LES (Kuwahara et al., 2006) $\text{---}\blacksquare\text{---}$.)	210
Fig. 6.19	Pressure contour in porous media at $Re_D = 40000$.	212
Fig. 6.20	Macroscopic pressure gradient versus Re_D for different porosities ($\phi = 0.84$ $\text{---}\bullet\text{---}$; 0.64 $\text{---}\nabla\text{---}$; 0.5 $\text{---}\blacksquare\text{---}$; 0.3 $\text{---}\blacklozenge\text{---}$).	213

Fig. 6.21	Macroscopic pressure gradient versus $(1 - \phi)/\phi^3$ for Forchheimer drag (—) (Low-Re $k-\varepsilon$ -LB model (present work) —▼—; LES (Kuwahara et al., 2006) —●—; v2f (Kazerooni and Hannani, 2009) —○—.)	214
Fig. 6.22	Dimensionless macroscopic pressure gradient versus $(1 - \phi)/\phi$ fitted with Eq. (6.18).	215
Fig. 6.23	Friction factor (f) versus Re_{deq} for different porosity (ϕ) ($\phi = 0.84$ —◆—; 0.64 —■—; 0.5 —▲—; 0.3 —●—).	215
Fig. 6.24	Plot for the determination of constant c_k using simulation data for different porosity and Re_D ($\phi = 0.84$ —○—; 0.64 —□—; 0.5 —△—; 0.3 —◇—).	217
Fig.6.25(a)	Contours of pressure, velocity and turbulent kinetic energy from RANS simulations at $\phi = 0.8$.	219
Fig.6.25(b)	Contours of pressure, velocity and turbulent kinetic energy from LES computations at $\phi = 0.8$.	220
Fig.6.25(c)	Contours of pressure, velocity and turbulent kinetic energy from RANS simulations at $\phi = 0.3$.	221
Fig.6.25(d)	Contours of pressure, velocity and turbulent kinetic energy from LES computations at $\phi = 0.3$.	222
Fig. 6.26	3D pore flow iso-contours of computed velocity magnitude for different porosities at $Re_D=10000$ from (a) RANS simulation and (b) LES.	224
Fig. 6.27	3D perspective view of mean velocity iso-surfaces of different porous enclosers for LES computations at $Re_D=10000$ (ϕ : (a) 0.8; (b) 0.6; (c) 0.5; (d) 0.4; (e) 0.3).	226
Fig. 6.28	Comparison of normalized streamwise mean velocity—profiles predicted using different turbulence models at centerlines in x- and y- directions, respectively. LES (—); low $Re-k-\varepsilon$ (—); Std. $k-\varepsilon$ (—).	228
Fig. 6.29	Normalized turbulent kinetic energy versus Re_D at different porosities (i.e. $\phi = 0.3, 0.4, 0.5, 0.6, \text{ and } 0.8$) using various turbulence models. LES (—▲—); Low $Re k-\varepsilon$ (—■—); Std $k-\varepsilon$ (—●—).	230

Fig.6.30(a)	Normalized turbulent kinetic energy versus $(1-\phi)/\phi^{1/2}$ using different turbulence models. LES (-▲-); Low Re $k-\varepsilon$ (-■-); Std $k-\varepsilon$ (-●-).	231
Fig.6.30(b)	Normalized energy dissipation versus $(1-\phi)/\phi^{1/2}$ using different turbulence models. LES (-▲-); Low Re $k-\varepsilon$ (-■-); Std $k-\varepsilon$ (-●-).	231
Fig. 6.31	Dimensionless macroscopic pressure gradient versus (a) Re_D , (LES (-▲-); Low Re $k-\varepsilon$ (-■-); Std $k-\varepsilon$ (-●-).) and (b) $(1-\phi)/\phi^3$ (LES (-▲-); Low Re $k-\varepsilon$ (-□-); Std $k-\varepsilon$ (-○-)).	233
Fig. 6.32	Streamlines in porous REV at $Re_D = 10$ at different porosities ($\phi = 0.8, 0.6$ and 0.4 from top to bottom diagonally).	235
Fig.6.33(a)	Numerically computed permeability for the porous REV fitted to Kozeny-Carmen equation.	238
Fig.6.33(b)	Numerically computed permeability as a function of porosity fitted to the proposed correlation (Eq. 6.55).	238
Fig. 6.34	Darcy-Forchheimer plot in terms of modified friction factor and $Re_{\sqrt{K}}$ for different turbulence models. LES (—); Low Re $k-\varepsilon$ (- - -); Std. $k-\varepsilon$ (.....).	239
Fig. 6.35	Simulated microscopic results of different porous matrix at $Re_D=40000$.	241
Fig. 6.36	Normalized $k_\phi - \varepsilon_\phi$ plot for different media morphology. (Filled legend: 3D circular cylinder[present study]; Unfilled legend: 2D square cylinder [21].)	242

NOMENCLATURE

ABBREVIATIONS

ANOVA	analysis of variance
AS	amplitude sweep
BPANN	back-propagation artificial neural network
BBD	Box–Behnken design
CI	creaming index
CV	coefficient of variation
CFL	Courant–Friedrichs–Lewy
DSD	Droplet size distribution
<i>DPG</i>	dimensionless pressure gradient
<i>ESI</i> ₂₄ , EI	emulsification index
<i>FS</i>	frequency sweep
GA	genetic algorithm
IFT	Interfacial tension
LVR	linear viscoelastic range
LES	Large eddy simulation
M.R.Q.E	mean relative quadratic error
MSE	Mean of square error
<i>REV</i>	representative elementary volumes
RANS	Reynolds average navier stokes
RF	resistance factor
RSM	and response surface methodology
RPD	Relative percent deviation
SSE	Sum of square error
<i>SFT</i>	<i>Surface tension</i>
<i>SEE</i>	standard error of estimate
<i>PRESS</i>	predicted residual sums of squares

SYMBOLS

A, b_1, b_2	constant in eq. (5.17, 5.18)
a_T	shift factor
A', B'	Model constant in eq. (5.37)
$C_{1\epsilon}, C_{2\epsilon}, C_{3\epsilon}$	turbulence model dimensionless constants
C_k	characteristic constant of porous media (eq. 6.47)

C_i	molar concentration of an ion in the solutions phase
C_s	Smagorinsky coefficient
C_t	Tortuosity factor
D	Diameter of square and circular cylinder
\hat{D}	diffusion coefficient of a droplet
D_m	deformation of the droplets
D_t	Column diameter (m)
d_{43}	volume weighted diameter (μm)
E_η	activation energy
G'	storage modulus (Pa)
G''	loss modulus (Pa)
G_p^0	plateau modulus (Pa)
G_C	cross over moduli (Pa)
G^*	complex modulus (Pa)
H	center to center vertical distance between two circular cylinders (m)
K	porous medium permeability (m^2)
$K_M, K_V, K_p, C_1, C_2, C_3$	Model constant eq. (4.13)
k	turbulent kinetic energy (m^2/s^2)
K^*	Modified permeability (m^2)
kT	thermal energy
$\langle k \rangle^f$	intrinsic volume average turbulent kinetic energy (m^2/s^2)
K''	modified consistency coefficient
K_0	initial permeability of porous media (m^2)
F	Faraday constant in eq. (1.5)
f	Friction factor $\left(= \frac{-d\langle p \rangle^f / dx}{(\rho u_D^2 / 2d_{eq})} \right)$
f_{K-C}	friction factor in Kozney-Carman eq. (5.12)
f_{Er}	friction factor in Ergun eq. (5.13)
$f_{\sqrt{K}}$	Permeability based friction factor in eq. (5.15)
f_1, f_2, f_μ	low Re - k - ε damping functions
f_m^*	Modified friction factor
L	center to center horizontal distance between two circular cylinders (m)
l_e	The tortuous path of the channel
n''	flow behavior index
n	flow behavior index
$N_{Ca,m}$	modified capillary number
N_{Ca}	capillary number
N_{Pe}	Peclet number
$N_{Re,p}$	particle Reynolds number
$\langle p \rangle^f$	volume average pressure gradient (Pa)
$\Delta P/L$	pressure gradient across the length L
ΔP	Pressure drop
$\Delta P_{emulsion}$	Pressure drop for emulsion flowing through porous bed

ΔP_{water}	Pressure drop for water flowing through porous bed
P and P_0	vapor pressure of the liquid droplet and the bulk liquid
p_1, p_2, p_3, p_4	Model constant on eq. (4.15)
P_L	Laplace pressure
q	volumetric flow rate through capillary
R^2	regression co-efficient
R	droplet radius
Re_p^*	Modified Reynolds number
Re_p'	Reynolds number in Ergun eq.
$Re_{\sqrt{K}}$	modified Reynolds number
Re_D	Reynolds number based on particle diameter
Re_p	Particle Reynolds number
Re_H	Reynolds number based on the center-to-center distance H
$Re_{D_{eq}}$	Equivalent Reynolds number based on Darcy velocity $\left(= \frac{u_D d_{eq}}{\nu} \right)$
R_h	Hydraulic radius
Re_y	turbulent Reynolds number based on y ($y\sqrt{k}/\nu$)
Re_T	turbulent Reynolds number ($k/\nu\epsilon$)
r_1, r_2	principal radii of the curvature in eq. (2.1)
\bar{S}_{ij}	filtered strain rate tensor
$\langle u \rangle^f$	intrinsic volume average velocity (m/s)
u_i, u_j	velocity vector in x and y directions (m/s)
u_D	Darcy velocity (m/s)
U_∞	free stream velocity (m/s)
\bar{u}	average fluid velocity (m/s)
V_f	fluid volume inside the porous media (m^3)
Y_M	Model constant eq. (4.12)
W_j^i	weight connection from neuron i to neuron j

GREEK SYMBOLS

β	Forchheimer coefficient (Eq. 6.56)
β_j	bias of neuron j
ϕ	medium porosity
θ	concentration of droplets
α_1, α_2	constant in eq. (5.4)
Δ	characteristic sub-grid length scale given
Λ, m	constant in eq. (5.5)
Ω, ω	characteristic coefficients of particles eq. (5.7, 5.8)
μ	fluid viscosity (kg/m.s)
ρ	fluid density (kg/m^3)
τ_w	Shear stress in porous bed
ν	kinematic viscosity (m^2/s)
ϵ	dissipation rate of k (m^3/s^2)
$\langle \epsilon \rangle^f$	intrinsic volume average turbulent kinetic energy dissipation

	rate (m^3/s^2)
$\sigma_k \sigma_\varepsilon$	turbulent Prandtl numbers for k and ε
κ	Kolmogorov scale
μ_t	turbulent (or eddy) viscosity ($\text{kg}/\text{m}\cdot\text{s}$)
μ_{eff}	effective viscosity of emulsion
σ_{ij}	stress tensor
τ_{ij}	subgrid- scale stress
Ψ	dimensionless pressure gradient
ζ	Zeta potential
κ^{-1}	Debye length (nm)
τ_y	yield stress
τ	Shear stress
Λ	Model constant eq. (4.13)
$\dot{\gamma}$	Shear rate (s^{-1})
η_c	viscosity of continuous phase
η_{em}	viscosity of emulsion
η_r	relative viscosity (i.e. η_{em}/η_c)
η_d	dispersed-phase viscosity
η^*	complex viscosity
ρ_c	continuous-phase density
ρ_d	dispersed-phase density
σ	interfacial tension
δ	phase angle shift
ω	frequency ($\text{rad}\cdot\text{s}^{-1}$)
ω^*	cross-over frequency
$(\tan\delta)$	phase angle
Ω_j	activation function at the j^{th} neuron
α_0	Constant in eq. (3.10)
α_{ii}	the linear interaction effect between the input factor X_i and X_j ,
α_{ij}	quadratic effect of input factor X_i and X_j ,
Π	response function
ε_r	dielectric constant of the solution
ε_0	permittivity of vacuum
γ	interfacial tension

SPECIAL SYMBOLS

$\langle \rangle$	volume average
$\langle \rangle^f$	intrinsic average

CHAPTER 1

INTRODUCTION

1.1 GENERAL

An emulsion is defined as a mixture of two immiscible liquids, where droplets of one liquid are encapsulated within the other liquid. The encapsulated phase is called the internal or dispersed phase, whereas the outer phase is called the external or continuous phase (Kundu et al. 2013). When an emulsion is prepared with oil and water, it may either be oil-in water (o/w) or water-in-oil (w/o) emulsion. The o/w emulsions are formed in the presence of emulsifying agents, which are more soluble in water, whereas emulsifying agents which are more soluble in oil are used for the preparation of w/o emulsions (Bancroft, 1913). Emulsions do not form spontaneously and are unstable. For the formation of an emulsion, an external source of energy, such as stirring, shaking and heating is required. An emulsifying agent, also emulsifier or surfactant, is used to increase the stability of emulsion systems. The emulsifying agents get adsorbed on the interface and change the characteristics to make the emulsion more stable. The stability of an emulsion system can be enhanced (for days, months, or even years) by the method of preparation or by adding other substances, such as co-surfactants, electrolytes, polymers, or particles.

Emulsions are classified based on compositions of water/oil, emulsification methods, emulsion preparation using emulsifying agent, particle sizes. Typically, in produced oil fields emulsions are classified into three broad groups:

- Water-in-oil (w/o)
- Oil-in-water (o/w)
- Multiple or complex emulsions
 - Water-in-oil-in-water (w/o/w)
 - Oil-in-water-in-oil (o/w/o)

In case of w/o emulsions water droplets are dispersed in a continuous oil phase, while in o/w emulsions oil droplets are dispersed in a continuous water phase. Fig. 1.1 shows both w/o as well as o/w emulsions systems. Multiple or complex emulsions are comprised of tiny droplets suspended in bigger droplets that are dispersed in a continuous phase (Fig. 1.1c), e.g. in case of w/o/w emulsion system water droplets are suspended in larger oil droplets that, in turn, are suspended in a continuous water phase. Multiple emulsion systems can be either w/o/w (water-in-oil-in-water) or o/w/o (oil-in-water-in-oil) dispersions. Higher multiplicities

are also possible, e.g. o/w/o/w or w/o/w/o systems. However, as multiple emulsions have a variety of phases and interfaces, they appear even more unstable than common emulsions (Myers, 2006; Morais et al., 2009; Schmidts et al., 2009, 2010).

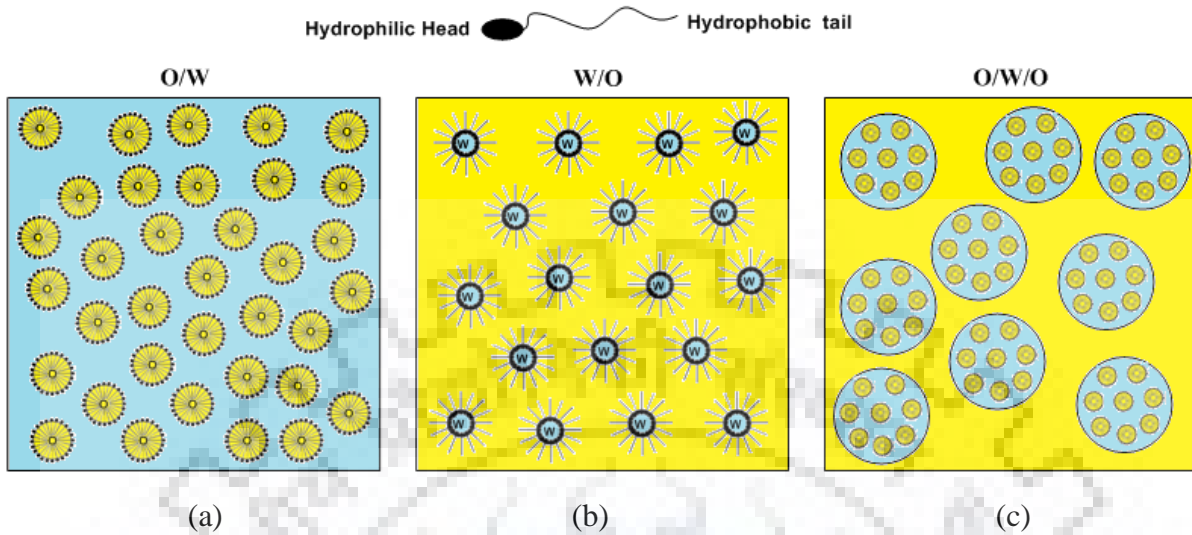


Fig. 1.1: (a) Oil-in-water (o/w), (b) water-in-oil (w/o) and (iii) multiple emulsions.

Based on the droplet size of the dispersed phase in continuous phase, an emulsion is referred to either as a macro- or micro- or nano-emulsion. The macro-emulsion is a kinetically stable system with uniformly dispersed droplets of size greater than $0.5 \mu\text{m}$, whereas the micro-emulsion is a thermodynamically stable system with dispersed droplet size ranging from 0.01 to $0.1 \mu\text{m}$ (Schramm, 1922; Schubert and Armbruster, 1992). The micro-emulsions are transparent in appearance, while macro-emulsions are milky-white or opaque. Further, for the preparation of micro-emulsions, high concentration of surfactants is required. In macroemulsions interfacial energy reduces due to droplets coalescence, and hence two phases separate with time. However, with a proper stabilization mechanism droplet coalescence can be reduced. The type of emulsions in produced oil fields belongs to macroemulsions.

Microemulsions are thermodynamically stable and can be formed without use of any external energy input. The microemulsions have an approximate radius between 20 nm to low (2 nm). The micro-emulsions are either transparent or semitransparent. The color is blue-white for particles ranging $0.1\text{-}1 \mu\text{m}$, gray for $0.05\text{-}0.1 \mu\text{m}$ and transparent for emulsions with particle size $< 0.05 \mu\text{m}$. Microemulsions are also described with the help of Winsor regime (or Winsor phase diagram). According to Winsor (1948), there are four possible types of equilibria for a water-oil-surfactant (and co-surfactant) system. The schematic and composite representations of various Winsor regimes are shown in Figure 1.3.

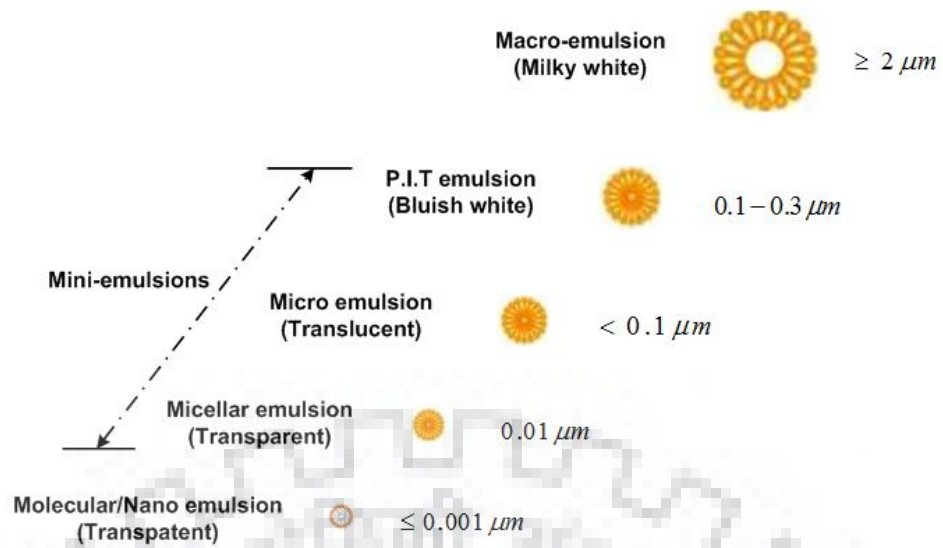


Fig. 1.2: Classification of emulsions based on dispersed phase droplet size.

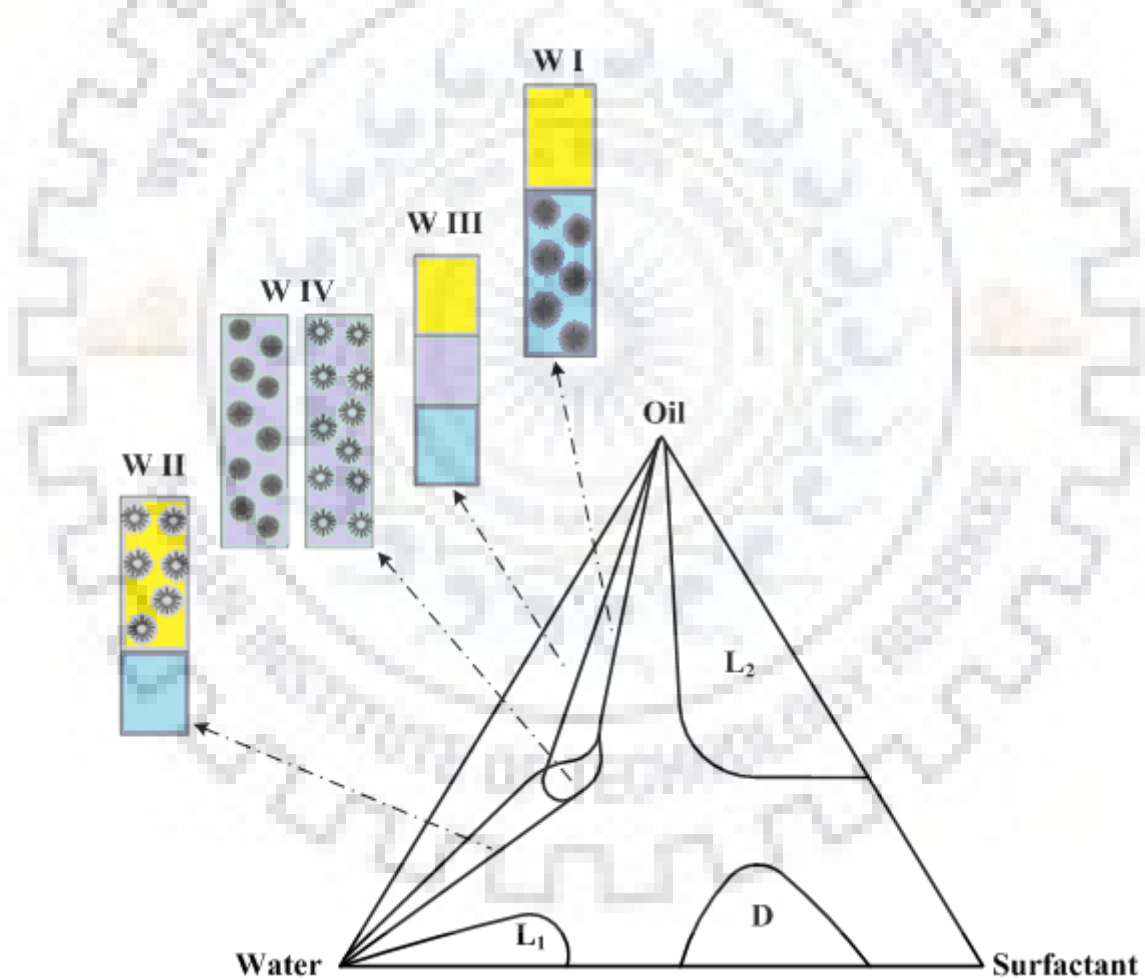


Fig. 1.3: Schematic representation of different Winsor phases. Light gray and blue colors indicate the oil and water phase, respectively, while microemulsion is indicated by light green (Source: Paul and Moulik, 2001).

The various Winsor regimes (Pan et al., 2010) are described as follows:

- (i) Winsor I: the microemulsion coexists with an oil-rich region (top phase).
- (ii) Winsor II; the microemulsion coexists with an water-rich region (bottom phase).
- (iii) Winsor III: the microemulsion coexists with both oil- (top) as well as water- (bottom) rich regions.
- (iv) Winsor IV: there is no phase coexistence and only the microemulsified phase is observed, or a bicontinuous microemulsion.

Microemulsions can be spontaneously formed, have good solubilizing characteristics and low interfacial tension, therefore are used in number of industrial applications, such as pharmaceuticals, food processing, cosmetics, cleaning technology, or soil remediation. However, for the formation of microemulsions large amount of surfactant is required, which is one of the disadvantages.

Further, dispersed phase with a droplet size varying from 10 to 100 nm in continuous phase are referred to as nanoemulsions, mini-emulsions, or ultrafine emulsions. In appearance nanoemulsions are transparent or translucent, due to very small droplet size (Tadros et al., 2004; Solans et al., 2005). They are highly stable as compared to macro- and micro-emulsions. Due to very small droplet sizes, and thus Brownian motion, the diffusion rates in nanoemulsions is higher as compared to sedimentation (or creaming) rates, and therefore they are very stable. They are thermo-dynamically unstable, i.e they are non-equilibrium systems, and have high kinetic stability. For the formation of nanoemulsions very high energy input is required. The destabilization mechanism in nanoemulsions is mainly driven by the Ostwald ripening or molecular diffusion, which is due to the difference in solubility between the small and larger droplets and the polydispersity. Depending on the method of preparation and their droplet size, nanoemulsions can remain stable for several hours, days, or even years (Solans et al., 2005).

1.2 SURFACTANT AND ITS ROLE AS AN EMULSIFYING AGENT

Surfactant, derived from the term *surface-active agent*, which has the property to get adsorb onto the dispersed and continuous phases interfaces and significantly alter the interfacial free energy of those interfaces (fluid/fluid or fluid/gas interfaces). Surfactants usually reduce the interfacial free energy at the interface of the emulsion droplet, prevent re-coalescence and facilitate droplet break-up (Bancroft, 1912; Finkle et al., 1923; Walstra, 1993). Surface-active or emulsifying agents have a characteristic molecular structure, which is also termed as *amphipathic* structure. These structure consist of lyophilic (has strong

attraction for the solvent) and lyophobic (has little or no attraction for the solvent) groups. In case of aqueous media, the molecular structure is termed as *amphiphilic* structure, and the terms lyophobic or lyophilic groups are replaced with *hydrophobic* or *hydrophilic* groups, respectively. The hydrophilic and hydrophobic groups of an emulsifying agent are also commonly referred as *head* and *tails*, respectively. The nature of *hydrophobic* or *hydrophilic* groups of surfactants can be very different (Eastoe, 2005). In a surfactant the hydrophilic group can be small or a large polymeric chain, charged or neutral; whereas the hydrophobic group is usually a single or double, straight or branched hydrocarbon chain, may contain aromatic group(s) or may also contain a fluorocarbon or a siloxane. When a surface active agent is dissolved in a solvent, the presence of lyophobic group causes a distortion of the solvent liquid structure, increasing the free energy of the system. This means water molecule requires more work to be done than a surfactant molecule. The surfactant, therefore, concentrates at the surface. However, the lyophilic group present in a surfactant prevents it from being expelled completely as a separate phase from the solvent. The surfactants are classified based on the type of hydrophilic group, as follow:

- (i) *Anionic*: the head moiety bears a negative charge;
- (ii) *Cationic*: the head moiety bears a positive charge;
- (iii) *Nonionic*: the head moiety bears no apparent charge;
- (iv) *Zwitterionic*: the head moiety bears both positive and negative charges.

The surfactant molecules get adsorbed at the droplet interface and replace the oil and water molecules from the original interface. Therefore, the presence of surface active agent at the droplet interface increases the interaction between the dispersed and the continuous phase molecules, which results into the reduction in interfacial tension across the interface (Rosen, 1989). Therefore, the surfactant concentration significantly influences the interfacial tension, either it may increase or it may decrease, and hence affects the droplet size and droplet size distribution. Surfactant concentration also affects the coalescence process in an emulsification process, i.e. if the concentration of surfactant is too low, the droplets will coalesce if they move towards each other (Wang et al., 2004). The prevention or reduction in coalescence in the droplets in an emulsion system is due to the Gibbs-Marangoni effect, and is described in Fig. 1.4 (Pichot et al., 2010).

The emulsions are also classified based on the presence of surfactant, as it alters the emulsion characteristics. Bancroft described the ability of a surfactant for the stabilization of o/w or w/o emulsion systems, whether it is soluble in oil or water. According to the Bancroft rule “oil soluble surfactant tends to stabilise w/o emulsion, while water soluble surfactant tends to stabilise o/w emulsion”.

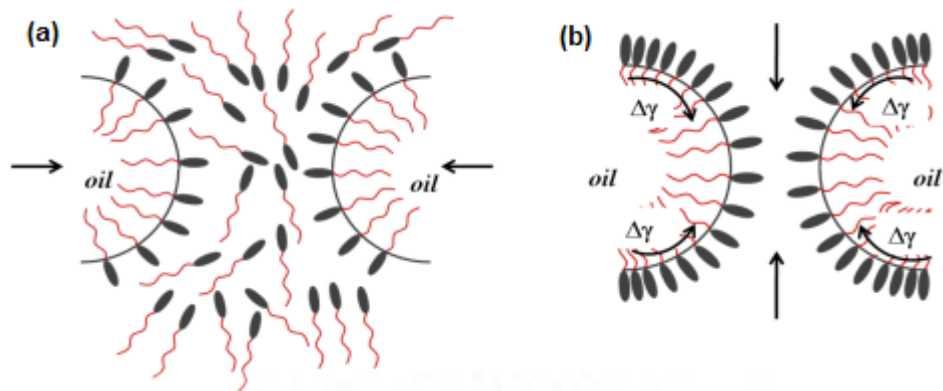


Fig. 1.4: Schematic representation of the Gibbs-Marangoni effect acting on two approaching droplets during emulsification: (a) insufficiently covered droplets approaching to each other; surfactants dispersed in the water phase and the film is thin, and (b) droplets are not covered uniformly by the surfactants, inducing an interfacial tension gradient (bent arrows) responsible for the thin film.

The selection of surfactant is complicated due to the variable composition of both oil and water phases. Generally, it is determined experimentally which surfactant is suitable for a given system. The surfactants are classified according to their HLB values and ability to stabilize an emulsion system (Godwin, 2004; Griffin, 1949), and are depicted in Table 1.1. Sometimes, surfactants are mixed together to obtain the right HLB value for a given system, typically by considering Bancroft rule. The lower limit of HLB value (i.e. 0) describes a completely lipophilic/hydrophobic molecule, while a higher HLB value (i.e. 20 or more than that) describes a hydrophilic/lipophobic.

Table 1.1: Classification of Surfactants on the basis of HLB

Types	HLB range
lipid soluble	<10
water soluble	>10
anti foaming agent	4 to 8
w/o emulsifier	7 to 11
o/w emulsifier	12 to 18+
wetting agent	11 to 14
Detergent	12 to 15
Solubiliser	16 to 20

1.3 STABILITY OF EMULSIONS

In the absolute sense an emulsion is never stable, as the surface free energy is set by the interface between phases. When two droplets coalesce together, there is a net reduction in interfacial area and hence the surface free energy. Therefore, the coalescence of droplets is a thermodynamically spontaneous process, whereas, the reverse process requires energy, and is, therefore, not a spontaneous process. An emulsifying agent is used to stabilize the emulsion by getting adsorbed on the liquid-liquid interface, i.e. film between two phases. This results into the reduction of the interfacial tension between two liquid phases and thus decreases the coalescence rate of the dispersed liquid droplets by forming mechanical, steric and/or electrical barriers around them (Gaonkar and Borwankar, 1991; Pichot et al., 2012). In emulsion studies, an emulsion is considered stable, if it is resistant to physical changes over a practical length of time. Different emulsions exhibit different types of instability. The emulsion stability may be categorized in a number of ways that reflect the different mechanisms involved i.e. creaming or sedimentation, flocculation, coalescence and Ostwald ripening, and are shown schematically in Fig. 1.5.

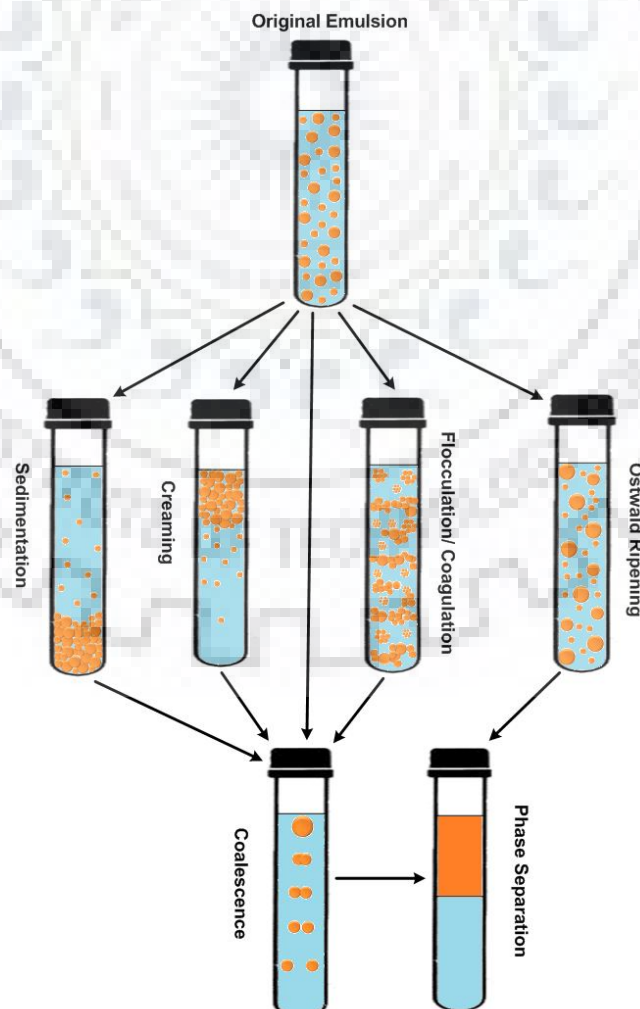


Fig. 1.5: Schematic representation of several types of instability in o/w emulsions.

1.3.1 Sedimentation

Sedimentation, the first phenomenon that relates to emulsion stability, is characterized by the formation of a droplet concentration gradient within the emulsion, while there is no change in the droplet size distribution (DSD). This can result in a, usually random, close-packed array of droplets at one end of the system. The droplet concentration gradient is caused by external forces acting on the system (gravitational, centrifugal and electrostatic). In the "Creaming" process a concentrated layer is formed at the top of the emulsion due to the collection of droplets. The rate of sedimentation for non deformable, non interacting spheres of radius r_p in a liquid of viscosity η_0 can be given by Stokes' law (1851), by equating the gravitational force with the opposing hydrodynamic force. In applying Stokes' law, the assumption is introduced that the spherical particles do not interact during settling:

$$\frac{4}{3} \pi r_p^3 \Delta \rho g = 6 \pi \eta_0 r_p v \quad (1.1)$$

where v is the sedimentation rate and $\Delta \rho$ is the difference between the particle and the bulk liquid densities. Thus,

$$v = \frac{2 \Delta \rho g r_p^2}{9 \eta_0} \quad (1.2)$$

If other external, e.g. centrifugal forces are working on the system, the acceleration induced by this force must be substituted for g . Eq. 1.2 is thus only valid for very dilute emulsions. Most emulsions also show a wide variation in droplet size resulting in different sedimentation rates. In almost all practical cases the sedimentation rate v must be decreased to enhance the stability of the emulsion. The application of Eq. 1.2 however, depends on the validity of Stokes' law for the emulsion being considered. A liquid droplet moving within a second liquid phase may have an internal circulation imparted to it. Rybczynski (1911) treated this problem theoretically, resulting in an equation for the sedimentation rate in which the viscosity of the dispersed phase (η) appears:

$$v = \frac{2 \Delta \rho g r_p^2}{3 \eta_0} \frac{\eta_0 + \eta}{3 \eta_0 + 2 \eta} \quad (1.3)$$

1.3.2 Flocculation

The emulsion stability is strongly affected by the droplet flocculation and is usually considered as an instability phenomenon for emulsion systems. In an emulsion system the creaming rate is influenced by the formation of droplet flocs (Pinfield et al., 1997; Robins, 2000; Shields et al., 2001). In the emulsion, it is characteristic of the flocculation process that no change in the size of the primary droplets occurs, although large aggregates of droplets are

formed. The identity of individual droplets is retained within the aggregates. The flocculation process results from the existence of attractive forces between the droplets. In cases where these net attractive forces are relatively weak, reversible flocculation may be achieved. It can be shown that for a given system, a critical droplet number concentration exists, below which the emulsion is stable with respect to flocculation (Ash and Ash, 2008). For strongly interacting droplets this critical droplet concentration is so low as to be practically insignificant. For systems which are thermodynamically unstable, flocculation can be effectively prevented if a large enough free energy barrier exists between the dispersed (deflocculated) state and the flocculated state. The emulsion is then stable in a kinetic sense. The London-Van Der Waals forces, due to the electrical double-layer interactions, are the net interactive forces between the droplets.

In addition, steric interaction may be caused by the emulsifying agents adsorbed in the interface between the two liquid phases. Depending on the composition of the final product, flocculation can be controlled by several methods. The rate and extent of flocculation can be controlled by regulating the colloidal interactions (steric, electrostatic, hydrophobic, etc.) between droplets.

1.3.2.1 London-Van Der Waals interactions

There exist two general approaches for the calculation of the interaction-energy between condensed phases. The first, de Boer (1936) and Hamaker (1937) assume pairwise additivity of the forces between the molecules. The other more general approach, initiated by Lifshitz (1955), considers the interactions in terms of macroscopic properties of the media.

Hamaker (1937) calculated the interaction energy by integrating the attractive energy for two infinitesimal volume elements dV_1 and dV_2 separated by a distance r , over the total volumes V_1 and V_2 of the two particles:

$$\Psi = -\frac{\lambda q^2}{r^6} \int_{V_1} dV_1 \int_{V_2} dV_2 \quad (1.4)$$

where λ is the London-Van Der Waals constant, determined by polarisability of the atoms, and q is the number of atoms per unit volume. Hamaker assumed that the parameter λ does not depend on the inter-atomic distance r . For large values of r this assumption is not valid and the attractive interaction is then called retarded.

1.3.2.2 Electrical double-layer interactions

Emulsion droplets can possess an electrical surface charge due to adsorption of ions such as anionic surfactants. The electrical surface charge is compensated by a distribution of counter-ions in a diffuse layer around the particles. When two droplets, carrying such a layer, come close to each other, repulsion results from an overlapping of these diffuse layers. Due

to the gradient in electrical charges at the interface, one side of the interface acquires a net charge of a particular sign and the other side acquires a net charge of opposite sign, which results into a potential across the interface and is referred as the electrical double layer. Helmholtz proposed a theory about the distribution of these neutralizing charges in the solution. It was proposed that the electrical potential should fall rapidly to zero within a very short distance from charged surface. However, since thermal agitation must diffuse some of the counter-ions throughout the solution, the model was inadmissible. Gouy and Chapman reported that at first the concentration of counter-ions fall rapidly with distance from charged surface and then more and more gradually with distance (Hunter, 1989). Their model was adequate for planar charged surfaces with low charge densities; however it was inadequate for surfaces with high charge densities. Thereafter Stern modified this by dividing the solution of double layer into a layer of strongly held counter-ions in a manner corresponding to Langmuir type adsorption and a diffuse layer of counter-ions. The modified model suggested that the electrical potential decrease rapidly in the fixed portion (Stern Layer) while in diffuse portion it decreases more gradually. In the Stern layer, the fixed counter-ions may even change the sign of potential resulting from the charged surface. A schematic description of electrical double layer is shown in Fig. 1.6.

The mathematical analysis of the diffuse portion of the electrical double layer yields the concept of Debye length or the effective thickness ($1/\kappa$) of that layer. The effective thickness is defined as the distance from the charged surface into the solution where most of the electrical interactions with the surface can be considered to occur. The effective thickness is given by:

$$\frac{1}{\kappa} = \left(\frac{\epsilon_r \epsilon_0 RT}{4\pi F^2 \sum_i C_i Z_i^2} \right)^{1/2} \quad (1.5)$$

where, ϵ_r ($= \epsilon/\epsilon_0$) is relative static permittivity or dielectric constant of the solution, ϵ_0 is the permittivity of vacuum, R is the gas constant, T is the absolute temperature, F is the Faraday constant, C_i is the molar concentration of an ion in the solutions phase.

An emulsion system is also characterized in terms of zeta or electrokinetic potential which is also associated with the electrical double layer, and is defined as the potential of a charged particle calculated from electrokinetic phenomena (electro-osmosis, electrophoresis, sedimentation potential). It is also referred as the potential of the charged surface at the plane of shear between the particle and the surrounding solution as the particle and the solution move with respect to each other.

1.3.3 Coalescence

Coalescence is an increase in the droplets size by joining two droplets which may eventually result in the separation of the oil and aqueous phases. This process is irreversible unless the process is disrupted by an energy input (i.e. homogenization) and significantly influences the droplet size distribution. Due to coalescence, the emulsion is completely separated into two immiscible bulk liquids. Coalescence occurred due to rupture of thin-liquid film and hence has major role in the removal of the thin liquid film between the two phases. Thus, the forces to be considered during coalescence are the forces acting within thin-liquid-film systems. When droplets approach each other, first they may be deformed and the droplets surface may get flattened (van den Tempel, 1961; Walstra, 2003; Sanfeld and Steinchen, 2008). Due to deformation, the contact surface between droplets increases and the coalescence between droplets may take place. Therefore, in the prediction of coalescence the rate of thin film rupture is an important parameter (Borwankar et al., 1992; Marrucci, 1969).

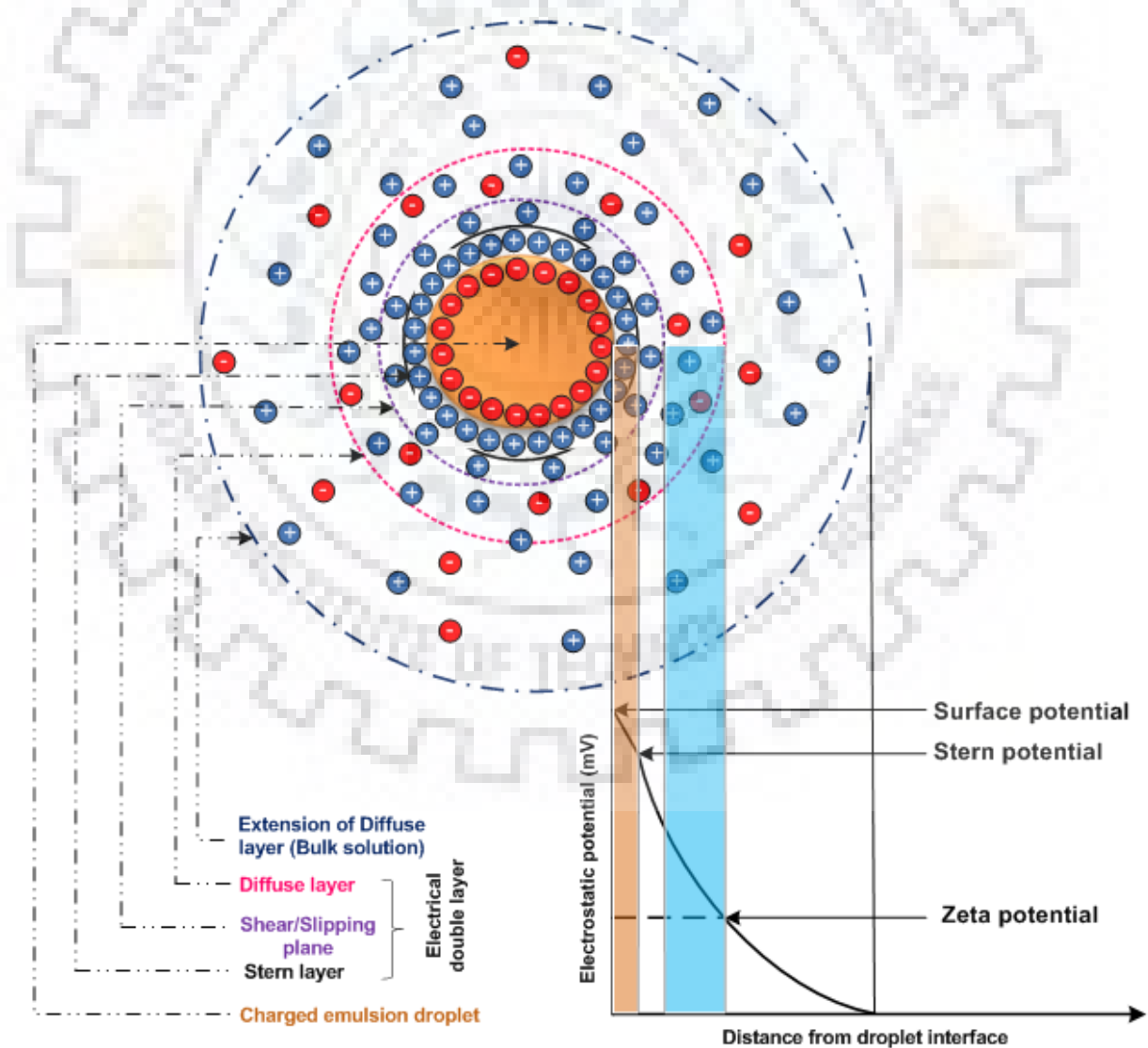


Fig. 1.6: The concept of electrical double layer.

The droplets are surrounded by surfactant molecules and form a layer, also referred as *interfacial membrane*, which protects them from rupture. In an emulsion system, the coalescence between droplets depends on (a) the hydrodynamic and colloidal interactions between the droplets, and (b) the continuous phase, and (c) the properties of an emulsifying agent used for the preparation of an emulsion. The thin film rupture mechanisms are very complex and almost unique for different emulsion systems (McClements, 2004). The following two aspects need to be considered for understanding the film rupture phenomena.

- a. the nature of the forces acting across the film, and
- b. kinetic aspects of local fluctuations in the film thickness.

The coalescence between droplets can be prevented by reducing (i) droplets contact, and (ii) thin film rupture (Kabalnov, 1998). The presence of an emulsifying agent in the thin film significantly affect (prevent or enhance) the droplet coalescence. The charged (positive or negative) emulsifiers in the thin film induce electrostatic attraction or repulsion between the droplets, which tends to enhance or reduce droplet contact. Therefore, an emulsifying or surface active agent (or surfactant) plays an important role in preventing contact between droplets and reducing interfacial tension at the droplet interface. An emulsifying agent form a thin protective interfacial film on the droplets interface and may provide strong electrostatic repulsive or attractive forces between droplets.

1.3.4 Ostwald ripening or Disproportionation

The *Ostwald ripening*, in an emulsion system, is the process of mass transport of soluble dispersed phase through the continuous phase resulted into gradual growth of larger droplets at the expense of smaller ones (Kabalnov and Shchukin, 1992; Taylor, 1995; Dickinson, 2009). If the two phases of an emulsion are mutually miscible to some extent, the average diameter of the emulsion can increase. If the initial emulsion system is truly monodisperse no effect of this slight solubility will arise. However, in polydisperse systems there is formation of larger droplets at the expense of smaller ones. This so called Ostwald ripening arises as a consequence of the Kelvin effect, i.e. the growth of the particles' solubility in media with decrease in their size.

Ostwald ripening depends on the diffusion of molecules in the disperse phase through the continuous phase from smaller to larger droplets. The pressure of dispersed material is greater for smaller droplets than larger droplets and is given by the Laplace equation:

$$P = \frac{2\gamma}{r} \quad (1.6)$$

where P is the Laplace pressure, γ is the interfacial tension at the interface and r is the droplet radius. This pressure difference between small and large droplets is the driving force for diffusion. However, the diffusion rate depends on the solubility of the dispersed phase in the continuous phase. The higher the disperse phase volume, the greater is its relative vapor pressure (and thus the solubility), as described by the Kelvin equation:

$$\ln[P_0/P] = \frac{2\gamma V_m}{rRT} \quad (1.7)$$

where P and P_0 are the vapor pressure of the liquid droplet and the bulk liquid, respectively, and V is the molar volume of the disperse phase. The diffusion rate is also affected by the viscosity of the continuous phase, as given by the Stokes-Einstein equation:

$$D = \frac{k_b T}{6\pi\eta r} \quad (1.8)$$

where D is the diffusion coefficient of a droplet and η is the continuous phase viscosity. For larger the droplets size, the Ostwald ripening process gets slowed down, however, coalescence and flocculation of droplets are more likely to occur.

1.4. INDUSTRIAL APPLICATION OF EMULSIONS

Emulsions are widely used in various industrial applications and processes, such as foods, cosmetics, pharmaceuticals, and agricultural industries. In many of the applications the stability of the emulsion is of importance. In other applications in which emulsions occur, the flow properties are an important factor. Reservoir engineering deals with the flow of fluids and fluid mixtures through porous media since the advent of oil production, particularly in oil recovery processes. In produced oil fields, from petroleum recovery to processing, emulsions are encountered at all stages, e.g. drilling fluid, oil production from pores, and oil transportation.

Emulsions are of great importance in enhanced oil recovery (EOR) techniques. The use of emulsions is critical and fundamental to the oil recovery process. Oil production occurs in three major stages:

- (a) In the first stage the oil is produced by just pumping it out of the production well.
- (b) After this stage, the oil has to be forced to the production well by injecting water in the oil field. This so-called water flooding results in a higher recovery, but still most of the crude oil (in some cases 65% to 70%) is left in the reservoir.
- (c) The final tertiary stage can be further classified into two groups as recovery by:
 - (i) thermal processes (in-situ combustion, steam injection, wet combustion, etc.,)
 - and

- (ii) chemical flooding processes (caustic flooding, surfactant flooding, micellar-polymer flooding, CO₂ flooding etc.)

After the water flooding, the residual oil is trapped in the pores of the rocks of reservoir and believed to be in the form of discontinuous oil ganglia or blobs. The two forces working on these oil ganglia are the viscous and the capillary forces, and the ratio of these two forces as expressed Capillary number, $N_{Ca} = u\eta/\gamma$ (where u is the fluid velocity, η is the viscosity of the continuous phase and γ the interfacial tension between the oil droplet and the continuous phase) determines the microscopic displacement efficiency. At the end of the water flooding process N_{Ca} is as low as 10^{-6} . The Capillary number has to be increased to 10^{-3} to 10^{-2} to further recover additional oil by a chemical flooding process. In a produced oil field the Capillary number can be increased by decreasing the interfacial tension at the oil/water interface. The occurrence of different type of desirable and undesirable emulsions, in petroleum industry, is shown in Table 1.2.

Table 1.2: Typical emulsions in the petroleum industry (Schramm, 1992)

Occurrence	Typical emulsion types
Undesirable emulsions	
Well-head emulsions	W/O
Fuel oil emulsions (marine)	W/O
Oil sand floatation process, froth	W/O or O/W
Oil sand floatation process, dilution froth	O/W/O
Oil spill mousse emulsions	W/O
Tanker bilge emulsions	O/W
Desirable emulsions	
Heavy oil pipeline emulsion	O/W
Oil sand floatation process slurry	O/W
Emulsion drilling fluid, oil-emulsion mud	O/W
Emulsion drilling fluid, oil-base mud	W/O
Asphalt emulsion	O/W
EOR in-situ emulsions	O/W

In an oil field, an emulsion may be desirable in production and transportation process while it may be undesirable during processing at refinery. Further, from oil recovery process to wellhead a desirable emulsion (oil dispersed in water) created may be changed to an undesirable form of emulsion (water dispersed in oil). The emulsion obtained at the well head may have to be broken and converted into a new emulsion, which is suitable for transportation by pipeline to a refinery. The emulsion form of the crude oil has to be broken and water should be separated; otherwise the presence of water in the crude oil would cause problems during the refining processes. During transportation of heavy oil over larger distances, it is made to flow through pipelines by creating emulsions with water, which

reduce viscosity. The heavy oil is dispersed in water to create an emulsion for transportation through pipelines, which is very stable and less viscous as compared to the original crude oil during transportation and at the end of pipeline the emulsion form of heavy oil is then broken.

1.5 FLUID FLOW THROUGH POROUS MEDIA

According to Darcy (1856), a porous medium is “system ensembles of a solid matrix with its void space filled with fluids”. The voids are generally interconnected so as to allow fluid to flow through the porous medium. The solid matrix may either be rigid or deformable, and either consolidated or unconsolidated, with its structure being either ordered or disordered (Bear, 1972). The analysis of fluid flowing through porous media has applications in a number of industries such as chemical, mechanical, nuclear, petroleum, geological, environmental and especially in engineering systems based on fluidized bed combustion, enhanced oil reservoir recovery, combustion in an inert porous matrix, underground percolation of chemical waste and chemical catalytic reactors, etc. (Sahimi and Stauffer, 1991).

Generally, a close relationship exists between the pore structure of a porous medium and many of its macroscopic properties (porosity, permeability, and macroscopic homogeneity). Pore structure parameters describe the pore size, shape and connectivity between different pores, and represent the average behavior of a sample containing many pores. The porosity is defined as the ratio of relative fractional volume of the void space to the total volume while permeability refers to the conductivity of a porous medium with respect to fluid flow (Durst et al., 1990). A porous medium is macroscopically homogeneous when all samples of a size compared to the size of the medium have the same macroscopic properties such as porosity and permeability. Most natural porous media however contain areas with a spatial variability in the morphology, such as packing structure and particle size, and are thus macroscopically heterogeneous. Those media, which are homogeneous on a macroscopic scale, often show heterogeneity on a smaller scale.

Darcy (Darcy, 1856) was the first to study flows through porous media, setting up the famous Darcy Law for laminar Newtonian fluid flow through packed beds as follows:

$$Q \propto A.K \frac{\Delta P}{L} \quad (1.9)$$

with volumetric flow rate (Q) dependent on the packing cross-sectional area (A), packing length (L), pressure drop over the packing length (ΔP), and packing permeability (K). The parameter ‘K’ correlates with packing characteristics, such as particles size and shape,

particle size distribution (PSD) and the packed bed porosity (ϵ) (Fig. 1.7). Packing parameters, as introduced above, include the packing porosity, which is defined as the ratio of void volume to total packing volume. This parameter is widely used within porous media flow analysis. The volumetric flow rate (Q) is often expressed in terms of superficial fluid velocity based on an empty column cross-section (V_s). Fluid properties affecting porous media flow are fluid density (ρ) and dynamic viscosity (η).

In case of generalized non-Newtonian fluids the dynamic fluid viscosity is a function of shear rate ($\dot{\gamma}$), as given by $\eta = f(\dot{\gamma})$. It has to be noted that viscosities of non-Newtonian fluids used within integral equations relating the volumetric flow rate to packing and fluid parameters, such as Darcy's Law, are based upon averaged shear rates. Laminar flow through porous media, with packed beds of spheres randomly distributed being one example, are characterized by a well-balanced composition of domains dominated by shear and elongational flow, partially even periodically recurring. Porous media made of spheres can be either built up randomly or in the case of monodispersed spheres, structured packings such as cubically arranged or hexagonal-close packings (HCP) can be realized.

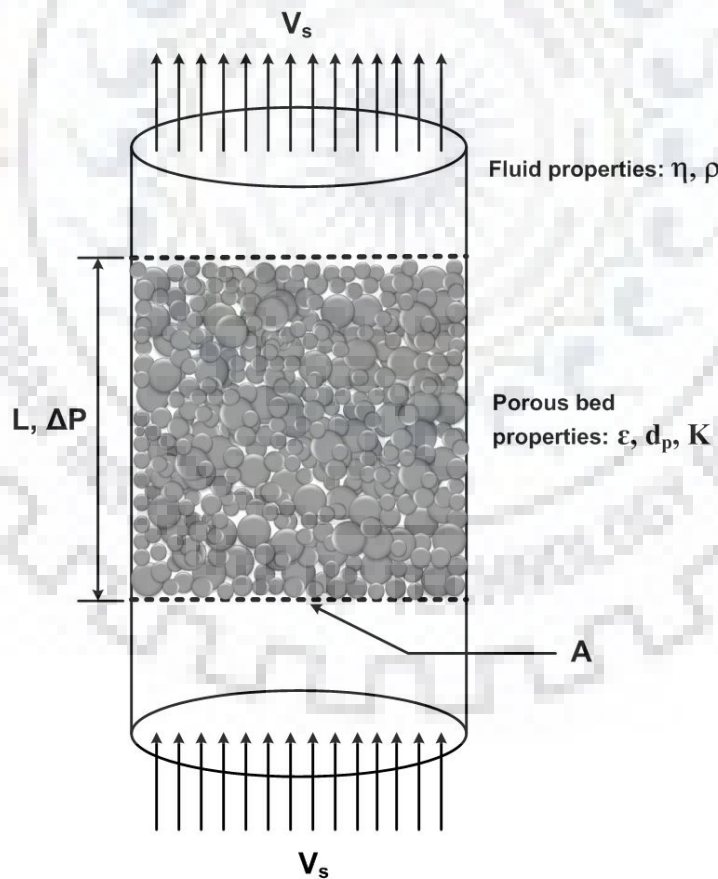


Fig. 1.7: Porous medium of randomly arranged polydispersed spheres through which flows a fluid of density ρ and dynamic viscosity η over cross-section area A . Further parameters are explained in the text.

According to Tsotsas (Tsotsas, 1992), flow patterns through porous media can be categorized into (i) microscopic, (ii) mesoscopic, and (iii) macroscopic, depending on the length scale considered. As depicted in Figure 1.8 on the left (A), microscopic flow denotes the flow between individual spheres, which do not necessarily have to be regularly arranged as shown. Even in laminar flow, individual profiles at any cross-section depend strongly on the Reynolds number, not only quantitatively but also qualitatively due to the formation of jet-like flow with higher – still laminar – Reynolds-numbers as opposed to the flow pattern shown. Mesoscopic flow is due to bypass channels possibly forming within the porous media. This can be observed in improperly fixed packing's or in the case of dense packings, which partially rearrange under flow conditions forming areas with even lower porosity and likewise allowing for bypass channels to form. With less resistance to the flow in such bypass areas, flow rates within them are higher.

The macroscopic flow profile over the whole porous medium cross-section depicted on the right of Fig. 1.8 (C) shows a somewhat unexpected flow profile compared to pipe flow in which highest flow rates occur along the centerline. In porous media flow, high flow rates close to the wall stem from a variation of porosity over the cross-section.

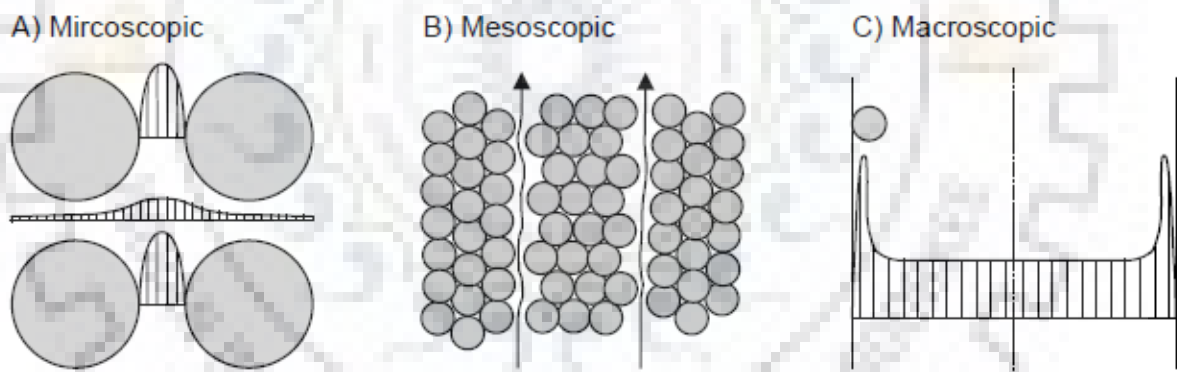


Fig. 1.8: Microscopic, mesoscopic and macroscopic flow patterns within porous media according to Tsotsas (Tsotsas, 1992). Flow profiles are given qualitatively.

Flow through such packing's can be expressed in terms of dimensionless numbers including the particle Reynolds-number (Re_p), the friction coefficient and the packing porosity. Packing parameters comprise mean sphere diameter, packing porosity, and packing length. Fluid density and fluid dynamic viscosity function account for the fluid behavior. Pressure drop and volumetric flow rate account for the process parameters.

1.6 EMULSIONS FLOW THROUGH POROUS MEDIA

The emulsion flow through porous media is encountered in the produced oil fields (for recovering heavy oil from oil reservoirs) and chemical industries (processes involving two immiscible liquids). During heavy oil recovery from underground reservoirs, emulsions may either form naturally during simultaneous flow of oil and water in porous rock formations, or emulsion formation may be promoted by injection of external chemical flooding, or reservoirs are flooded with externally generated emulsions (Kokal et al., 1992). The fluid flow behavior is complicated as it involves a complex and unstable fluid flow through an extremely tortuous path (porous rock formations). For understanding and solving problems encountered during flow of an emulsion through porous media the nature and properties of an emulsion system, characteristics of porous media and the basic mechanisms involved for simple fluid flow through porous media are important.

The flow of an emulsion (o/w or w/o) system through porous media is a more complicated process, due to the complex nature of both an emulsion system as well as the porous medium. In an emulsion system the major challenge is whether to consider it as a homogeneous or heterogeneous fluid. When the droplets size is very small as compared to the flow channel, the continuum model approach is used for understanding the physics of flow. Both the fluids are considered similar and they are assigned with equivalent homogeneous properties. However, practically the droplet sizes of emulsion systems are comparable to pore sizes. Therefore, in real situations the emulsions cannot be treated as a pseudo-single-phase fluid.

While dealing with flow of an emulsion system, it is important to consider the similarities or differences with the simultaneous oil and water flow through the porous medium. In case of simultaneous flow of oil and water, both fluids flow separately and continuously through the flow channels. However, in case of o/w emulsion flow through pores, oil is dispersed in the water in the form of tiny droplets, which may be of similar sizes of pore sizes, and both phases occupy the flow channels in a porous medium. Further, in an emulsion flow system the relative permeabilities to oil and water are quite different for the same water saturations.

In process oil fields, oil droplets (also referred as ganglia) get trapped at pore throats during normal flow of oil and water by the snap-off process of oil filament (Mohanty et al., 1987). However, during the o/w emulsion flow through rock formations the mechanism of straining capture is responsible for trapping of oil droplets at the pore throat, even though it is smaller than the oil droplets. Therefore, for an emulsion system to behave like an effective blocking agent the droplet size of the dispersed phase should be slightly bigger than the pore

throat size. Though, the constrictions of pore throat should not be very large. When an o/w emulsion is formed (or injected) in the pores, the permeable zones get flooded with the emulsions, which restrict the fluid flow in the more permeable zones. Therefore, the water (and emulsion) gets displaced into the less permeable zones and thus the sweep efficiency gets improved effectively. Sweep efficiency is defined as the displacement of oil volume from the reservoir by the injected fluid.

The emulsion flow through porous media is influenced by large number of variables. Typically, they are categorized based on the characteristics of emulsion and porous media, as summarized in Fig. 1.9. Emulsion characteristics such as quality, stability, drop size and drop size distribution, emulsifying agent properties, and dispersed and continuous phase viscosities. Emulsion quality is defined as the dispersed phase volume fraction (or percent) in and emulsion systems significantly influence the rheological behavior of the emulsion. Drop size in relation to pore throat size influence the flow through porous media, and it depends on oil type, brine composition, pH, interfacial properties, emulsifying agents, flow velocity, and nature of porous material.

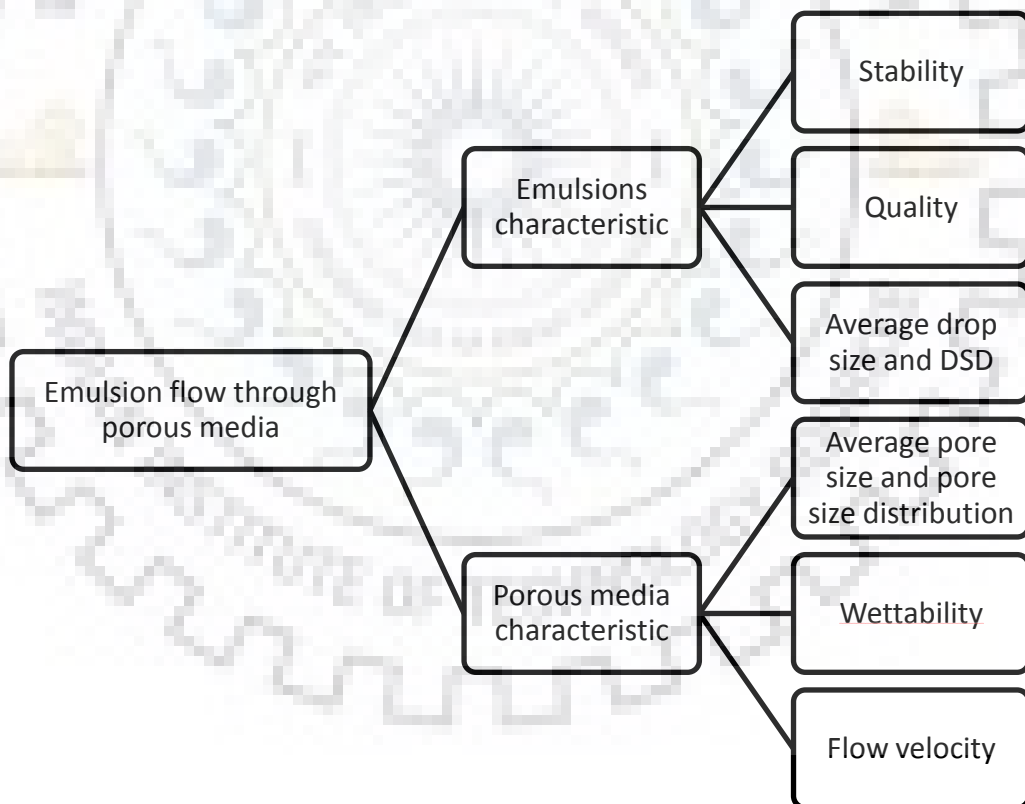


Fig: 1.9 Parameters influencing the emulsion flow through porous medium

The emulsion flow through porous media is also affected by the characteristics of a porous medium, such as pore size and pore size distribution and wettability and fluid velocity through pores. The wettability controls the fluid distribution and flow location inside a reservoir, and directly influences relative permeability, capillary pressure, secondary and

tertiary recovery performances, irreducible water saturations and residual oil saturations (Craig 1971; Mohanty et al., 1987). The flow rate through porous medium influences the shear rate and for high-quality non-Newtonian emulsions it directly influences their rheology. The capture and breakup rates of oil droplets through the rock can be determined using flow velocity. Theoretically, the w/o emulsions flow in oil-wet media should be similar to the o/w emulsions flow in water-wet porous media. Hence, similar observation, or discussion in the preceding section for o/w can also be applied to the flow of w/o emulsions.

1.7 MOTIVATION

Recently, with the advancement of soft computing, various artificial intelligence-based modeling studies have been proposed in a number of real-life engineering problems. However, research articles related to modeling and optimization of emulsification process using robust expert system with sophisticated artificial intelligence are scarce. From the detailed literature carried out, it was found that no study has so far reported on the implementation of an integrated RSM coupled resilient hybrid ANN-GA modeling and optimization approach for the formation of oil-in-water (o/w) emulsions and the prediction of emulsion stability. Therefore, a new adaptive modeling framework is considered as an interesting field of investigation to assess the stability of o/w emulsions and the optimization of process parameters by combining the advantages of RSM, ANN and GA methodologies.

The emulsion flow dynamics are of considerable importance from both theoretical and practical point of view. The o/w emulsions are usually characterized by a complex rheological behavior due to the collective interactions of surface charge, droplet size distribution, phase volume fraction, continuous-phase ionic strength, dispersed-phase viscosity, and the chemical structure of the emulsifier (Sanchez et al., 1998). In emulsion systems, three major properties of the continuous phase are important: (i) the viscosity of the medium which is influenced by the additives (emulsifiers and thickeners) for preventing the sedimentation or creaming to maintain the right consistency for application; (ii) the chemical composition, such as polarity and pH, which affect the electrostatic charge interaction among the droplets; and the ionic nature and concentration of the electrolyte in the system. Besides, the emulsion viscosity can be affected by surfactant concentration, dispersed phase volume fraction and temperature, etc. These effects can be altered by varying the pH of the emulsion which plays a significant role in enhanced oil recovery (EOR) mechanism, flow through porous media and ASP (alkaline-surfactant-polymer) flooding. The emulsion viscosity is an important parameter to meliorate the o/w mobility ratio and adjust the water intake profile,

which also makes an impact on the effectiveness of flooding (Zhang et al., 2005; Strand et al., 2014). An alkaline chemical such as sodium hydroxide or sodium carbonate can be added to the injected water inside the reservoirs in order to alter the pH (Shiran and Skauge, 2013; Strand et al., 2014). Simultaneously, temperature significantly influences the viscosity of the emulsion during the thermal processes for the recovery of water flooding residual oil. Most of the existing emulsion viscosity models are based on the fact that the overall viscosity of the emulsion depends on the viscosity of the continuous phase, and are usually reported in terms of relative viscosity, η_r , (the ratio of the viscosity of the emulsion to that of the continuous phase). The viscosity of o/w emulsions is strongly influenced by the volume fractions of the oil and water phases, and temperature (Krieger and Dougherty, 1959) and electrostatic interactions. However, experimental data on the effect of temperature and pH (electro-viscous effect) on viscosity of o/w emulsion systems are scarce. Therefore, the study of the effect of the pH and temperature on rheology of o/w emulsion is important. Also, for understanding and predicting the rheology of an emulsion system, it is essential to correlate their flow characteristics to the inter-particle interactions.

Fluid transport in porous media has been an area of intense research due to its importance in number of areas in chemical engineering and in enhanced oil recovery (EOR). Modeling flow in packed beds and porous media at the engineering scale usually employs semi empirical equations, such as the Ergun equation, Darcy's law, or the Carman-Kozeny equation. These empirical approaches are backed by years of experimental validation, and are known to work well for single-phase flow of Newtonian fluids. Most of the researchers studied on non-Newtonian fluid (polymeric solutions, oil-water dispersion) flow through a section of pipe and packed bed. Flow of emulsions through porous media has attracted few researchers. Physics of emulsion flow through porous media is quite complex and interesting as they are non-Newtonian fluids. Therefore, a detail experiment study with model validation is necessary to understand the single phase and multiphase (emulsion) flow phenomena flowing through porous media.

In a porous media, voids are generally interconnected so as to allow fluid to flow through porous space. The solid matrix may either be rigid or deformable, and either consolidated or unconsolidated, with its structure being either ordered or disordered. Reservoir engineering deals with the flow of fluids and fluid mixtures through porous media since the advent of oil production, particularly in oil recovery processes. Various flow regimes are encountered during the fluid transport in porous media, based on the pore Reynolds number, Re_D : (a) Darcy or creeping flow regime ($Re_D < 1$); (b) Forchheimer flow regime ($1 < Re_D < 150$); (c) post-Forchheimer flow regime (unsteady laminar flow, $150 < Re_D < 300$); and (d) fully

turbulent flow regime ($Re_D > 300$). Such flows can be analyzed by modeling the topology of the porous medium and resolving the microscopic flow equation in the fluid phase. The range of pore-size is large, and can vary over 8-order magnitude spanning Angstrom (ultra-micro-pores) to centimeters (pebbles) or even larger. The conditions encountered in different applications are broad enough to cover a large range of Reynolds numbers. Due to lack of geometric information to model each and every pore, such systems are difficult to simulate with full geometric details. Despite the fact that it might be possible to describe some of these systems in an almost exact representation or a meaningful statistical approximation of the geometry, the computational effort required to solve the flow field in such geometries is still formidable. This motivates further research in the development of porous media approximation, representing the system composed of macroscopic homogenous pores with uniform properties.

1.8 RESEARCH OBJECTIVE

On overall basis, the objective of the PhD thesis is to pursue and describe the studies on stability and rheology of oil-in-water emulsions, and finally emulsion flow through porous media in an effective way and to find an application in enhanced oil recovery (EOR) as an alternative. Emulsion flow through porous media is the core element of this thesis. The specific objectives of the present work are as follows:

1. To characterize the hydrocarbon petroleum oil.
2. To prepare, characterize and carry out the stability analysis of oil-in-water (o/w) emulsions through measurement of the droplet size distribution (DSD), Zeta potential, electrophoretic mobility, surface tension (SFT) and interfacial tension (IFT).
3. To study the influence of parameters, such as pH, oil and water volume fraction, surfactant concentration and temperature on the rheological characteristics of emulsions.
4. To carry out experiments on the flow of single phase incompressible Newtonian and multiphase emulsion flow through porous media and to study the effect of particle size, flow rate etc.
5. To carry out computational fluid dynamics (CFD) modeling and simulation of fluid flow through structured porous media, consisting of an array of square and circular cylinders.

1.9 ORGANIZATION OF THE THESIS

Base on the motivations and objectives, the thesis has been organized into seven sections or chapters as follows:

Chapter 1 introduces the theme of the thesis, which provides a summary of the background, and motivation of this thesis. The objectives and the thesis organization are also provided.

Chapter 2 presents the detailed but critical literature review on incompressible single phase Newtonian and non-Newtonian fluid flow through porous media, and emulsion rheology.

Chapter 3 deals with the experimental methodology; the materials/reagents used and the experimental and analytical methods used/applied for the experimentation.

Chapter 4 presents the results and discussion of the experiments on emulsion stability, emulsion characterization and rheological behavior of o/w emulsion. Effect of phase volume fraction, pH, temperature and shear rate on the steady and dynamic rheological behavior of emulsions are discussed.

Chapter 5 presents the single phase and emulsion transport phenomena through porous media for both Newtonian and non-Newtonian fluids.

Chapter 6 presents the computational modeling of single phase fluid flow through an structured porous media, i.e. an array of square/circular cylinders, with detailed modeling approach.

Chapter 7 states the overall conclusions drawn from the experimental work and possible recommendations for future research.

CHAPTER 2

LITERATURE REVIEW

The emulsion flow through porous media has found important application in left over (enhanced) oil recovery from reservoirs. In recent years, an extensive effort has been made to understand the various, and different, aspects of fluid flow of fluids through porous media. Both, emulsion systems and normal fluid flow through porous medium are complicated process, due to inherent complexities associated with them. There are number of variables associated in the description of both emulsion systems and porous media. An emulsion flow (oil-in-water or water-in-oil) through porous media make it further complicated process. An emulsion can be considered as a homogeneous fluid if droplets size is very small as compared to the pore size of a porous media. In such cases, a continuum approach can be taken for emulsion flow through porous media and it can be considered as fluid having equivalent homogenous macroscopic properties. However, in reality the size of the dispersed phase droplets are in comparison to the pore structure or the magnitude of the droplets size is not very different. Therefore, the homogeneous fluid assumption for emulsion would be inappropriate.

In case of an oil-in-water (o/w) emulsion flow system, oil droplets are dispersed in water (continuous medium) and have comparable size as of pore structures. As oil is dispersed in water, both oil and water occupy the same flow channels. Further, for same water saturation, oil and water have different wettabilities in the porous medium, and the relative permeabilities for both oil and water flows through porous channels are different in case of emulsion flow (Schramm, 1992). Also, in case of normal fluid flow systems, both oil and water phases flow separately, due to the density differences.

2.1 STABILITY OF EMULSION

An emulsion system is prepared by dispersing a fluid into a continuous phase in the presence of an emulsifying agent (or surfactant). The stability of an emulsion depends entirely on the composition of dispersed and continuous phases, emulsifying agent and the energy required in the formation of an emulsion. The break-up of a droplet during the formation of an emulsion is opposed by the Laplace pressure (P_L). Laplace pressure is

defined as the difference in pressure between the concave and convex sides of the droplet interface, and is given by (Lucassen-Reynders, 1996; Tcholakova et al., 2004):

$$P_L = \gamma \left(\frac{1}{r_1} + \frac{1}{r_2} \right) \quad (2.1)$$

where r_1 and r_2 are the principal radii of the curvature and γ is the interfacial tension. An external stress is required for the deformation of a drop, which involves a very large pressure gradient. In a fluid system, the stress can be either due to a velocity gradients (shear stress) or differences in pressure arising from the inertial effects (Schubert and Engel, 2004). For the deformation and breakup of droplets, energy is needed to be dissipated in the liquid. It can be seen from Eq (2.1), that the magnitude of the interfacial tension dictates the quantity of energy required for droplets deformation, and hence droplets break-up. The addition of a suitable surfactant in sufficient amount reduces the interfacial tension, which also prevents the immediate re-coalescence of the newly formed droplets (Dokic et al., 1990). A number of researchers investigated the stability aspect of emulsions at different process conditions.

2.2 RHEOLOGY OF EMULSION

Rheology (*rheo* "flow" and *logia* "study of") is the science of deformation and flow of matter under influence of an applied shear stress (Reiner, 1960). In an emulsion flow system the important properties of emulsions are their flow properties, or their rheological behavior. The understanding of rheology of an emulsion system has been of great interest for both fundamental scientific knowledge and industrial applications (Barnes, 1994; Tadros, 1994). Furthermore, the fluid rheology and morphology of the medium affect the flow behavior in porous medium. Many applications of flow in porous media involve Newtonian fluids, in which the viscosity is independent of shear rate. Any fluid that does not obey Newton's law of viscosity is a non-Newtonian fluid. The rheological behavior of an emulsion can be either Newtonian or non-Newtonian depending upon its composition. At low to moderate values of dispersed phase concentration, emulsions generally exhibit Newtonian behavior. In the high concentration range, emulsions behave as shear-thinning fluids (Pal et al., 1992; Ahuja and Singh, 2009). The rheological properties of dilute, semi-dilute and highly concentrated emulsions have been reviewed in many studies (Choi and Schowalter, 1975; Aomari *et al.*, 1998; Medhi et al., 2011; Singh, 2013). Investigations revealed that increasing an emulsion concentration in excess of a critical value could considerably modify its structural and rheological properties (Fig. 2.2). This includes the yield stress appearance and a marked change in viscosity (Mason, 1996; Mason *et al.*, 1999).

Table 2.1: Overview of studies related to emulsion stability.

Author	Study investigated	Remarks
Shinoda and Saito (1969)	The stability of o/w emulsions at different temperatures and HLB of emulsifiers.	The size of droplets is very small, however droplets were less stable towards coalescence close to the phase inversion temperature (PIT).
Avranas et al. (1988)	Developed an empirical correlation between demulsification rate and zeta potential as a function of surfactant concentration for dilute o/w emulsions of octane and iso-octane.	The presence of micelles between adjacent droplets would favour desorption of surfactants and reduce emulsion stability.
Stalidis et al. (1990)	The effect of sodium dodecyl sulfate (SDS) on the stability of o/w emulsions stabilized with Tween 80, a non-ionic surfactant, at concentrations above and below the critical micelle concentration (CMC).	The stability of emulsions prepared with a mixture of Tween 80 and SDS was higher as compared to the stability of the emulsions prepared with SDS alone. This was probably due to the solubilization of SDS into the micelles of Tween 80.
Velev et al. (1994)	The emulsion stability of xylene (oil)-in-water emulsions stabilized with a non-ionic surfactant mixture (Tween 20 and Span 20) at different pH and the electrolyte concentrations.	The surfactant film thickness and the emulsion stability decreases with an increase in the electrolyte concentration.
Ahmad et al. (1996)	The stability of palm o/w emulsions with reference to the type and concentration of oil and emulsifiers.	Emulsions having different emulsifiers with the same HLB values had varying stability as indicated by the relative volume of the emulsion.
Gullapalli and Sheth (1999)	The stability of mineral oil (hydrocarbon)-water emulsions and olive oil (triglycerides)-water emulsions at an optimum HLB value with different emulsifier blends,	The structural similarity of the emulsifier mixture to the dispersed phase is more critical than the resultant HLB of the mixture for obtaining stable emulsions.

Author	Study investigated	Remarks
Song et al. (2000)	Stability of water in diesel by varying HLB of the surfactants (blends of Span 80 and Tween 80),	The stability of the emulsion system was maximum at a HLB value of 6.
Orafidiya and Oladimeji (2002)	The required HLB values of stable emulsions prepared for different essential oils with emulsifier blends using droplet size analysis and turbidimetric method.	An increase in the mean oil droplet diameter results in a significant shift of +0.2 to +0.4 in the optimum HLB values.
Chen and Tao (2005)	The effect of sorbitan monooleate (emulsifier) concentration, oil to water ratio, stirring intensity, temperature and time of agitation on the stability of emulsions of commercial diesel in water.	The optimum values for the maximum emulsion stability were reported for o/w ratio equal to 1:1, surfactant concentration of 0.5% by volume, stirring intensity of 2500 rpm, and the stirring time of 15 min at a temperature of 30°C.
Hempoonsert et al. (2010)	The aggregation characteristics and floc morphology of oil droplets was studied at different pH and temperatures in relation to effectiveness of destabilization of o/w emulsions, and quantified the ability of flocs to capture and separate oil.	Temperature had a significant effect on the aggregation number of flocs and droplets size, while floc size and aggregation number are significantly affected by pH.
Kundu et al. (2013)	The effect of an anionic surfactant (sodium dodecyl benzene sulphonate, SDBS) to oil ratio, various electrolytes and temperature on the o/w emulsion stability using phase inversion temperature (PIT) method.	The PIT was found to decrease with an increase in surfactant to oil ratio. The narrowing of the DSD was observed with an increase in surfactant to oil ratio from 0.1 to 0.7 (w/w), and the initial average size of the droplets decreased from 26 to 14 µm.
Korac et al. (2014)	The colloidal structure, physical stability and formulation approach of the fast inverted o/w emulsions alternatively SWOP (Switch Oil Phase) emulsions.	The samples of w/o emulsions were less stable as compared to the o/w emulsions and SWOP.

Author	Study investigated	Remarks
Karbachi et al. (2014)	Studied the stability and kinetics of coalescence using a technique for tracking the process in the bulk phase. This technique was applied on various w/o systems at different mixing rates and emulsifying agent concentration for predicting coalescence rate.	Developed a new semi-quantitative approach for estimating coalescence rate between drops, in concentrated emulsions. The colour intensity is affected by change in droplets size at the time of subsequent drop coalescence between drops in concentrated emulsions. The received light intensity also reflects the coalescence between droplets in the concentrated emulsions.
Sanatkaran et al. (2014)	Studied the physical properties (interfacial tension and droplet size distribution) of mixed binary surfactant of different co-surfactant systems for stabilization of highly concentrated emulsions.	The stability of the emulsions is mainly determined by degree of synergism between the surfactant and co-surfactant, which is also depend on the structure of the co-surfactant. Span structure is more sensitive towards stability as compared to the (oil soluble) Tween structure (water soluble).
Ghosh et al. 2015	The impact of cooling rate and mixing on the long-term kinetic stability of wax-stabilized w/o emulsions was investigated. Four cooling/mixing protocols were investigated: cooling from 45 °C to either 25 °C or 4 °C with/without stirring and two cooling rates – slow (1 °C/min) and fast (5 °C/min).	The long-term stability of the present wax-stabilized W/O emulsions was highly-dependent on the concerted role of interfacial and network wax crystallization, with the combination of stirring and quench-cooling providing the highest kinetic stability.

Author	Study investigated	Remarks
Leonardi et al. (2015)	Formation and destabilization in bulk of silicone/vegetable oil, Janus emulsions stabilized by Tween 80, also examined the role of interfacial equilibria/relative volumes of the two oils (silicone/vegetable oil) in emulsion drops.	The emulsions showed rapid creaming irrespective of the preparation method, but a few days storage did not significantly change the drop size in the creamed layer, nor was separation of the oils detected. The energy difference between a Janus and an engulfed drop becomes zero at a critical surfactant concentration which gives the silicone oil/aqueous solution interfacial tension equal to the sum of the remaining interfacial tensions. At this point the energy difference between the Janus drop and separate drops was maximal and gradually reduced with increasing surfactant concentration.
Schulz et al. (2016)	The emulsifier properties of aq. mixture of sodium oleate (NaOl)-hexadecyltrimethylammonium bromide (HTAB) using different proportions of the surfactants for the o/w and w/o emulsions formation. The behaviour of the emulsions in contact with a petrous substrate also studied in order to evaluate their possible use in pavement production.	A very stable and concentrated o/w emulsions is formed with a mixture of 0.75 mole fraction of HTAB without considering the solvent formed. It has a narrow unimodal size distribution with smaller droplets which were destroyed via heterocoagulation by quartzite sand. These mixtures have high potential applicability in the asphalt emulsification for pavement production or sand fixation.

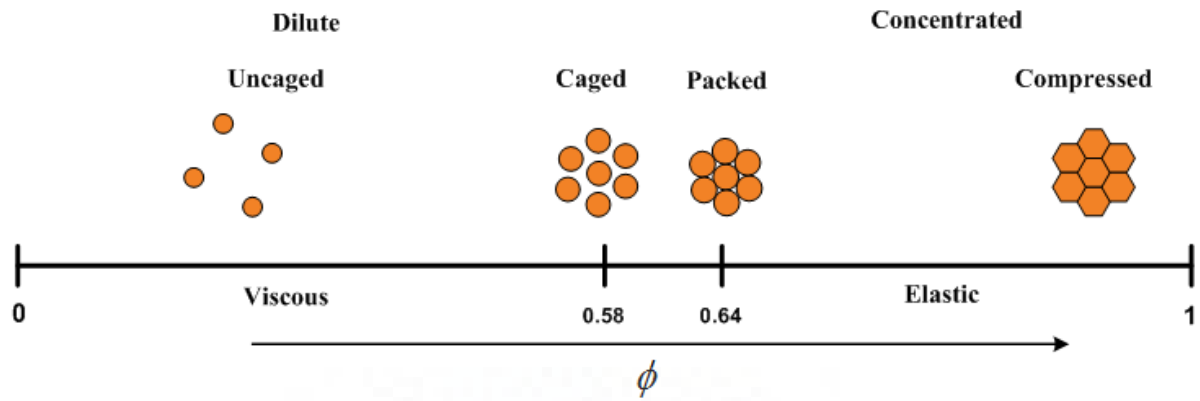


Fig. 2.1: Structure of droplets in emulsions within in a range of 0 to 1 volume fractions (Source: Mason, 1999).

2.2.1 Factors Influencing Emulsion Rheology

For the shear-thinning liquids, emulsions can be described by apparent shear viscosity η , which is similar to that of pure fluids. From Newton's law, η is the proportionality coefficient (or ratio) between shear stress (τ_{ij}) and rate of strain (or shear rate, $\dot{\gamma}_{ij}$), $\eta = \tau_{ij} / \dot{\gamma}_{ij}$. The rheology of emulsions is also influenced by various factors associated with emulsions, such as (Sherman, 1968; Tadros, 1994):

- i. the continuous phase viscosity,
- ii. the dispersed phase volume fraction and viscosity,
- iii. pH and electrolyte concentration ,
- iv. the average droplet size and droplet size distribution (DSD),
- v. shear rate,
- vi. the surfactant concentration and nature, and
- vii. temperature

Various viscosity models used for emulsions and their special features are given in Table 4.1. The earliest model given by Einstein (Einstein, 1906) is dependent on the dispersed phase volume fraction ($< 2\%$). Most of the existing emulsion viscosity models are based on the fact that the overall viscosity of the emulsion depends on the viscosity of the continuous phase, and are usually reported in terms of relative viscosity, η_r (the ratio of the viscosity of the emulsion to that of the continuous phase). The viscosity of o/w emulsions is strongly influenced by the volume fractions of the oil and water phases, and temperature (Krieger and Dougherty, 1959). However, experimental data on the effect of temperature on viscosity of o/w emulsion systems are scarce. Ronningsen (Ronningsen, 1995) developed a correlation for estimation of η_r for stable water-in-crude oil emulsions.

Table 2.2: Various viscosity models for emulsions.

Authors	Models	Remarks
Einstein (1906)	$\eta_r = 1 + 2.5\phi$	Valid only upto 2% volume fraction of dispersed phase.
Taylor (1932)	$\eta_r = \left[1 + 2.5\phi \left(\frac{\eta_d + 0.4\eta_c}{\eta_d + \eta_c} \right) \right]$	Incorporated the effect of viscosity of continuous and dispersed phases of w/o emulsions.
Guth and Simha (1936)	$\eta_r = 1 + 2.5\phi + 14.1\phi^2$	Considered a wide range of dispersed phase concentration and the interaction between droplets.
Richardson (1950, 1953)	$\ln \eta_r = k\phi$	Taken into account the non-Newtonian behavior of the emulsions and non-linear relationship between η_r on ϕ .
Mooney (1951)	$\ln \eta_a = (2.5\phi / 1 - a_M \phi)$ with $1.35 < a_M < 1.91$.	The non-Newtonian behavior of the emulsions was predicted by exponential relationship.
Brinkman (1952)	$\eta_r = (1 - \phi)^{-2.5}$	Valid for higher concentration of dispersed phase.
Becher (1965)	$\eta_r = (1 + a_1\phi + a_2\phi^2 + a_3\phi^3)$	Considered a wide range of dispersed phase concentration and the interaction between droplets.
Krieger and Dougherty (1959)	For high concentration: $\eta_r = \left[1 - \left(\frac{\phi}{\phi_m} \right) \right]^{- \eta \phi_m}$ For low concentration: $\eta_r = \lim_{\phi \rightarrow 0} \left[1 - \left(\frac{\phi}{\phi_m} \right) \right]^{- \eta \phi_m} = 1 + \eta \phi$	Considered the maximum packing concentration of the dispersed phase (ϕ_m).
Pal and Rhodes (1985)	$\eta_r = \left[1 + \frac{1.342\phi/(\phi)_{\eta_r=100}}{1.194 - \phi/(\phi)_{\eta_r=100}} \right]^{2.226}$	An empirical correlation for relative viscosity of o/w and w/o emulsions as a function of normalized dispersed phase concentration, which is valid only for $\phi/(\phi)_{\mu_r=100} < 1$.
Ronningsen (1995)	$\ln \eta_r = k_1 + k_2T + k_3\phi + k_4T\phi$ For shear rate: $30 \leq \dot{\gamma} \leq 500 \text{ s}^{-1}$ Temperature: $5 \leq T \leq 40 \text{ }^\circ\text{C}$, and Volume fraction: $0 \leq \phi \leq 60$.	Considered the effect of volume fraction of crude w/o emulsions and temperature. Correlation cannot be used for fluids other than the experimental oils.
Phan-Thien and Pham (1997)	$\eta_r^{2/5} \left(\frac{2\eta_r + 5\mu}{2 + 5\mu} \right)^{3/5} = \left(\frac{1}{1 - \phi} \right)$	For concentrated emulsions using effective medium averaging approach. Only applicable for low capillary

		numbers (N_c).
Pal (1998)	<p>For concentrated emulsions: $\phi_m^{0.5} [1 - \eta_r^{-1/ \eta \phi_m}] = A_0 + A_1 \log_{10}(N_{re,p}) + A_2 [\log_{10}(N_{re,p})]^2$</p> <p>For dilute emulsions: $\phi_m^{0.5} [1 - \eta_r^{-1/ \eta }] = A_0 + A_1 \log_{10}(N_{re,p})$</p>	Valid for mono-dispersed emulsions, with similar phase densities and low interfacial tension based on mineral o/w and kerosene o/w emulsions neglecting the Brownian movement of droplets.
Farah et al. (2005)	<p>For $T > WAT$: $\ln(\ln(\nu + 0.7)) = k_1 + k_2 \phi + k_3 \ln(T) + k_4 \phi \ln(T)$</p> <p>For $T < WAT$: $\ln(\ln(\nu + 0.7)) = k'_1 + k'_2 \phi + k'_3 \ln(T) + k'_4 \phi \ln(T)$</p>	Valid for w/o emulsions. Correlated the crude oil emulsions viscosity of at different concentrations of dispersed phase and temperatures (above and below WAT).
Dan and Jing (2006)	$\eta_r = (1 - K_e \phi)^{-2.5}$	Valid for dispersed phase concentration varying from 0.1 to 0.5.

Rheological behaviour of emulsions has been studied by various researchers periodically which is shown in Table 2.3.

2.3 POROUS MEDIA FLOW

Darcy's law is the fundamental for fluid flow through porous media. For sufficiently “low Reynolds numbers” and single-phase fluid flow through porous media, Darcy established a linear relationship between the seepage velocity and the pressure gradient as (Darcy, 1856):

$$\bar{u}_D = -\frac{\bar{K}_{ij}}{\mu} \frac{\partial \bar{P}}{\partial x_j} \quad (2.2)$$

In the equation 2.2, non-linearity appears as the Reynolds number is gradually increased. This deviation from the Darcy's law is because of the increase in inertial forces (Chauveteau and Thirriot, 1967). However, differentiating between the linear laminar flow and the onset of non-linear flow regimes (non-Darcy) is still not clearly defined. The transition depends strongly on the pore geometry and the Reynolds number collectively, and it cannot be defined independently in a simple way from the flow parameters (Skjetne and Auriault, 1999). Various researchers proposed that the possible reasons for this deviation from the Darcy's law may be the viscous boundary layer formation (Whitaker, 1966), non-homogeneity of the porous medium which causes higher local fluid velocity (McFarland and Dranchuk, 1976), microscopic inertial forces manifested in the interstitial drag force (Ma and Ruth, 1993), the interstitial pore space curvature (Hayes et al., 1995), macro-roughness of the pores (Hlushkou and Tallarek, 2006), kinetic energy losses in the constrictions and the restrictions,

Table 2.3 Literature overview on emulsion rheology

Authors	Parameter studied	Remarks
Pal (1992)	Studied the rheological behavior of o/w emulsions prepared from concentrated non-ionic surfactant solutions (Triton X-100). Based on aqueous phase the surfactant concentration was varied up to 38.2% wt., while concentration of oil was varied from 0 to 70% vol.	Highly flocculated nature of emulsions was observed and emulsions exhibited high degree of non-Newtonian, shear-thinning type. Also, significant yield stress was observed even at low oil concentration.
Pal (1993)	Investigated the effect of concentration of surfactant on the rheological properties of w/o macro-emulsions. The surfactant and water concentrations were varied from 1 to 50 wt.% based on the oil phase and 0 to 75 vol.%, respectively.	Highly flocculated nature of emulsions was observed at high surfactant concentrations. Emulsions exhibited non-Newtonian yield-pseudoplastic behavior. The emulsions apparent and relative viscosities increased with an increase in surfactant concentration, for a given water concentration. However, relative viscosity was not influenced by surfactant concentration at higher shear stresses.
Otsubo and Prud'homme (1994)	Investigated the effect of DSD on flow behaviour of o/w emulsions at three different volume fractions ($\phi = 0.5, 0.63$ and 0.8). The effect of internal and external phase volume fraction and drop size on emulsion viscosity was studied by performing steady-state shear experiments.	Emulsion having higher volume fraction exhibit elasticity due to the deformation of droplets. The emulsions also show dilatant behaviour because of the elastic responses of interfaces during the collision of the drops.
Mason et al. (1995, 1996)	Experimentally studied the effect of volume fraction and droplet size on bulk elasticity and yield transition of concentrated monodisperse emulsions.	The surface elasticity of surfactant significantly influences the emulsion viscosity.
Liu et al. (1996)	Studied the anomalous viscoelastic behaviour of concentrated emulsions and proposed a model predicting the contribution of complex dynamic shear modulus.	The model yields an anomalous contribution to the complex dynamic shear modulus that varies as the square root of frequency.
Pal (1997)	For o/w and w/o emulsions, reported the effect of droplet size and droplet size distribution (DSD) on the steady and oscillatory behaviour.	The viscosity and storage modulus of fine emulsions were greater than corresponding coarse emulsions. Fine emulsions exhibited more shear-thinning behaviour as compared to course emulsions.

Authors	Parameter studied	Remarks
Lee et al. (1997)	The bulk rheological behaviour and morphology of w/o emulsions was experimentally studied for steady and dynamic shear flow.	During the shear rate sweep, the flocculation–deflocculation transition was observed, which results in instant dilatancy of viscosity near the critical shear rate ($\dot{\gamma} \approx 10^2 \text{ s}^{-1}$). Also, with an increase in volume fraction of dispersed phase, the rheological property is predominated by the secondary morphological effects by the flocculated state.
Guerrero et al. (1998)	Studied the influence of composition (sucrose palmitate and oil concentrations, 60-80 wt.%) and temperature on linear viscoelasticity properties of highly concentrated o/w emulsions; and also reported relationship in linear viscoelasticity functions, DSD and stability.	The linear viscoelastic properties of concentrated emulsions depend on the DSD, as well as on the consistency of the thin film of the continuous phase located among the droplets.
Bower et al. (1999)	Experimentally studied the rheology and microstructure of concentrated o/w emulsions stabilized by macromolecular and low-molecular-weight emulsifiers.	Concentrated emulsions appear to fall into a general rheological class of behavior characterized by a strain softening damping factor and a "plateau" relaxation spectrum. Although concentrated emulsions have high viscoelasticity at small strain deformations, and also strain soften to give an essentially viscous fluid at large strain deformation.
Jansen et al (2001)	A new scaling parameter for the viscosity of surfactant stabilized emulsions was proposed, which is also referred as the depletion flow number, (Fl_d), (ratio between the viscous energy needed to separate the droplets and the depletion energy that opposes this separation.)	A master plot between relative emulsion viscosity and Fl_d was reported. An overlap of data for systems with different components and surfactants but with similar volume fraction and viscosity ratio was observed. Almost all viscosity data for surfactant stabilized emulsions could be accurately predicted using a simple empirical model.

Authors	Parameter studied	Remarks
Romero et al. (2002)	Investigated the effect of mean droplet diameter and distribution, bitumen concentration, ethylene oxide chain length, presence of electrolytes, and storage temperature on the dynamic shear rheology of concentrated bitumen in water emulsions. The surfactant used for the preparation of o/w emulsion was nonyl phenol ethoxylated.	A viscoelastic behavior was observed for the emulsion, for bitumen concentration higher than 60% (v/v). An increase in shear modulus was observed with a decrease in mean droplet diameter at a constant bitumen concentration, or with an increase in bitumen concentration at a constant mean droplet diameter.
Dagreu et al. (2005)	Developed a statistical model for describing the linear viscoelastic properties of o/w emulsions.	The statistical mechanical approach gives a much better description of the viscoelastic behaviour of emulsion samples than purely hydrodynamic models.
Saiki et al. (2007)	Investigated the effect of droplet deformability on SDS-stabilized polydimethylsiloxane (PDMS) emulsions rheology for a wide range of volume fraction ($\phi=0.01-0.72$).	The droplet deformability dependent shear thinning behavior increases with the volume fraction.
Torres et al. (2007)	Studied the preparation and characterization of solid particle stabilized o/w (hexane-in-water) emulsion using oscillatory rheology.	Based on rheological study, criteria were set to distinguish between physically stable and unstable emulsions. An emulsion is considered (a) stable if $G' > G''$ and both G' and G'' are independent on frequency, and emulsion exhibit gel-like properties; (b) physically unstable if $G'' > G'$ and both G'' and G' are dependent on frequency, and emulsion behaves like a dilute solution.
Santos et al. (2011)	Investigated the rheology of concentrated o/w emulsions stabilized by mixtures of ethoxylated surfactants and normal alcohols.	The droplet size had a direct impact on emulsion stability and apparent viscosity.
Shu et al. (2013)	Studied linear and nonlinear viscoelasticity of w and paraffin oil emulsion at different w/o phase volume ratio with the SAOS (small amplitude oscillatory shear) and LAOS (large amplitude oscillatory shear) methods.	The emulsions changed from liquid-like state to solid-like state as the w/o volume ratio increased to 0.3. The droplet elasticity significantly contributes to the nonlinear viscoelasticity of the emulsions.

Authors	Parameter studied	Remarks
Haj-shafiei et al. (2013)	The isothermal rheological properties of w/o emulsions was studied at different continuous phase wax solidification and water fractions (10–50 wt.%).	W/O emulsion rheology is significantly influenced by water cut and continuous phase wax solidification, though this greatly depends on the emulsion aging. The yield stress of freshly-prepared emulsions also increased with water cut and time. The effects of the wax crystals on rheology became more evident with the formation of a more developed network and/or interfacially-bound crystals over time.
Sun et al. (2014)	Investigated, the viscoelastic and yield behaviours of waxy crude oil and water-in-waxy crude oil emulsion gel.	The rheological behaviour is dramatically changed due to the existence and deformation of the dispersed water droplets in combination with the precipitation of wax crystals and also the formation of a structure with wax crystals and water droplets. The emulsion gels show different yield behaviors from the gelled waxy crude oil. First, the yield process shows that the emulsion gel becomes more ductile with increasing water cut, compared to the brittle-fracture-like yielding of the waxy crude oil gel. Second, the yield stresses of both crude oil and emulsion gels increase monotonically with an increase in precipitated wax and water cut, while the yield strains show different trends.
Liu et al. (2016)	Studied the influence of drop sizes on the rheology behaviour of w/o emulsions.	With change in shear rates, the rheological behaviour of concentrated emulsions changes qualitatively from Newtonian to non-Newtonian flow. In Newtonian flow regime, higher viscosity was observed for smaller drop size, and further increase in viscosity was observed at high dispersed phase volume fractions. In non-Newtonian flow regime, shear thinning behaviour was observed for emulsions and it becomes stronger for smaller drop sizes.

the singularity of streamline patterns and/or the non-periodicity of the micro scale flow, and variation in integral viscous dissipation due to a deformation of streamline patterns (Panfilov and Fourar, 2006). Due to such factors, several flow regimes depending on the local fluid velocity were observed during the percolation of liquid through the porous space in the porous media. Chauveteau and Thirriot (1967) and Skjetne et al., (1999) classified the flow regimes for geometrically simple and complex porous media. For geometrically simple porous media, the flow regimes are characterized as: i) Darcy, ii) Weak inertia, iii) strong inertia, and iv) turbulence. For geometrically complex media, the flow regimes are characterized as: i) Darcy, ii) Weak inertia, iii) Transition from weak to strong inertia, iv) Strong inertia, v) Transition from strong inertia to turbulence, and vi) Turbulence.

The Darcy and non-Darcy flow regimes have significant importance in the production oil fields as well as in processing. Flow regimes are key parameters in reservoir engineering both in understanding the flow behavior in the reservoirs as well as the in the prediction of production performances (Krishnamoorthy et al., 2011; Selvaraju and Pushpavanam, 2009; Swernath et al., 2010; Thirupathi et al., 2007). Typically, in gas wells nearly turbulent flows are attained when the fluids converge at the wellbore, which resulted into non-Darcy flow regimes (Macini et al., 2011). Therefore, the classical Darcy's law cannot be used for pressure drop estimation around the wellbore, and it also leads inaccurate evaluation of the production performances. Therefore, it is necessary to investigate the limit of Darcy regimes and pinpoint the onset of non-Darcy flow regime to fully developed non-Darcy flow regime. Most of the reported works describe the pressure drop-friction factor relationship for relatively higher Reynolds numbers. There is lack of experimental data for fluid flow (single phase or emulsions) through porous media validating of Darcy's law, the breakdown of Darcy law and the non-Darcy flow. At low flow rates, the existing experimental data are scarce to test the validity of the Darcy's law. Even the pre-Darcy flow regime has been overlooked due to lack of experimental data.

2.3.1 Incompressible Single Phase Fluid Flow Through Porous Media

A pioneering semi-empirical correlation was derived by Darcy (1856) for single phase fluid transport through packed beds. Carman and Kozeny (1937) reported an expression for pressure drop under viscous flow regimes. Further, an expression for change in pressure drop under turbulent flow regime was derived by Burke and Plummer in 1928. Thereafter, Ergun (1952) proposed a popular semi-empirical equation covering all flow types and conditions and packing materials by combining the Carman-Kozeny equation for laminar flow with the

Burke-Plummer equation for the turbulent flow. The Kozeny equation was further modified by Dullien et al. (1976) assuming pores with periodic step changes in their diameter. The Blake-Kozeny equation was further generalized by MacDonald et al. (1991) for different spherical particles sizes. The Ergun equation was modified in cylindrical coordinated system to represent the pressure drop in the packed bed Bey and Eigenberger (1997).

Soni et al. (1978) experimentally studied the water flow through an unconsolidated porous media (sands and glass beads) for a broad range of flow velocities, including Darcy and non-Darcy flow regimes. Dybbs and Edwards (1984) performed experiments in fixed beds of arranged spheres and cylinders, and concluded that the inertial regime initiates for an interstitial Reynolds number of particle Re_i somewhere between 1 and 10. Fand et al. (1987), Liu and Masliyah, (1996) experimentally reported the departures from Darcy's law at low flow rates.

The complex departures from Darcy's law at low gas velocities was experimentally reported by Meyer and Krause (1998) for various pressure ranges in consolidated rock samples. Seguin et al. (1998a, 1998b) studied laminar and turbulent flow regimes in porous media by electrochemical technique using platinum cathode as an electrochemical probes. Chhabra and Srinivas (1991), Srinivas and Chhabra (1992) and Tiu et al. (1997), Comiti et al. (2000) Chhabra et al. (2001), were studied creep or Darcy flow regimes for both Newtonian as well as non-Newtonian fluids with different types of particles (spheres, cylinders, plates and polyhedorns). They characterized the Darcy flow regimes in terms of the particle Reynolds number (Re_p), interstitial Reynolds number (Re_i) and modified Reynolds number (Re_m). Wen et al. (2003) adopted a generalized approach for pressure drop predictions in packed beds based on different packing geometry.

Moutsopoulos and Tsihrintzis (2005) analytical studied transient and fully-developed turbulent flows through confined porous media. It was reported that inertial terms in the microscale (the non-linear terms) are dominant for relatively small times. However, the inertial terms were insignificant for larger times as the disturbance spread through the entire medium, and therefore the pressure gradient becomes low. In order to estimate the coefficients of non-Darcy flow, Sidiropoulou et al. (2007) assessed the validity of various empirical relations.

Cheng et al. (2008) used quadratic and power law, formulations in terms of seepage Reynolds numbers for correlating the experimental results covering Darcy to non-Darcy flows through porous media. Moutsopoulos et al. (2009) experimentally investigated the hydraulic behavior of inertial flows in porous media and observed that both the Forchheimer and power law equations (Izbash equations) offer good descriptions of the flow process. A

discontinuity was observed in the velocity–hydraulic gradient curve for moderate values of the Reynolds number.

Recently, Li and Ma (2011) experimentally studied the frictional pressure drops for fluid flow through porous beds comprised of non-spherical particles as porous media and examined the applicability of the Ergun equation for the assessment of flow resistance. Pamuk and Özdemir (2012) studied experimentally the oscillatory and steady flows of water through two different porous media consisting of mono-sized stainless steel balls. They concluded that for the same range of Reynolds number, the permeability and inertial coefficient of oscillating flows are greater than those of steady flows. Sedghi-Asl et al. (2014) performed laboratory experiments to investigate the effect of high flow velocities through granular materials. The experimental data was fitted with widely used non-Darcy equations and verified the well-known non-Darcy relationship. Bagci et al. (2014) characterized the flow regimes for fluid flow through a porous media of two different spherical particles (1 and 3mm).

2.3.2 Non-Newtonian Fluid Flow through Packed Bed and Porous Media

An extensive literature is available for flow of a variety of non-Newtonian fluids through packed beds with uniform or different porous media. In the present work, an extensive literature is carried out and studied after 90's are summarized in Table 2.4.

2.3.3 Emulsion Flow through Porous Media

McAuliffe (1973) proposed the concept of permeability reduction in a porous medium by using dilute emulsions as mobility control agents for oil recovery processes. They also studied the transient permeability behavior for a single droplet of an oil emulsion flowing through a pore throat smaller than the droplet (Fig. 2.2). From Fig. 2.2 it can be seen that the radius of curvature of the droplet is bigger at the trailing edge and smaller at the leading edge in the pore throat, which results into the lower capillary pressure at the leading edge as compared to the trailing edge of the droplet. Therefore, to move the droplet through the pore throat a certain amount of pressure is required. The pressure required to move the droplet through the constriction is referred as the Laplacian differential pressure, and is given by:

$$\Delta P = 2\sigma \left[\frac{1}{r_1} - \frac{1}{r_2} \right] \quad 2.2$$

where ΔP is the Laplacian differential pressure, r_1 and r_2 are the radii of curvature at the trailing and leading edges of the droplet, respectively, and σ is the interfacial tension. The emulsion droplet plugs the pore throat, if the actual pressure difference across the pore is less than that predicted by Eq. 2.2.

Table 2.4: Representative studies of non-Newtonian fluid through porous media and packed bed

Authors	Type of fluid used	Parameter studied	Remarks
Flew and Sellin, (1993)	polyacrylamide (PAA) solutions	Explored the extensional flow behavior of PAA solutions at different dilutions, similar to those used in oil fields (as viscosifying agents), in different flow geometries including hexagonal-rod arrays and glass-bead packs as regular porous media.	PAA solutions developed extensional viscosity values many times those generated, for the same strain rate, under simple shear flow.
Rodriguez (1993)	Poly ethylene oxide (PEO) solutions	The molecular mechanism for viscosity enhancement was studied for PEO solutions flow through porous media.	A substantial increase in flow resistance was observed and the mechanism for increase in flow resistance was related to the formation of transient networks of polymer molecules in the flow field.
Rao and Chhabra, (1993)	Aq. solutions of CMC and a low molecular weight synthetic polymer (Alcomer 120).	Reported pressure loss measurements for laminar flow of inelastic polymer solutions through packed beds comprised of uniform size spheres as well as mixtures of two different sizes. The significance of wall effects was demonstrated by using a range of column to particle diameter ratios (5.8 to 20).	The wall correction for Newtonian fluids is also applicable for flow of power law fluids in packed beds. The applicability of mean of hydraulic radii of individual particles was experimentally confirmed to characterize a bed of mixed size spheres.
Vorwerk and Brunn (1994)	Surfactant solution of Cl 6TMA-Br (hexadecyltrimethylammonium bromide) and polymer solution of HPG (hydroxypropyl guar).	Studied the effect of shear for the flow through a porous medium (packed bed of spheres) of cationic surfactant solutions and polymeric solutions.	An analogous behavior for surfactant solutions was observed in porous medium flow, where friction coefficient suddenly decreases at constant hydraulic radius, irrespective of packed bed details. For the polymeric solution flow through porous medium, the onset of increased resistance coincides with onset point for drag reduction. Viscoelasticity in porous media flow contribute the shear wave, which causes possible disturbances in fluid.

Authors	Type of fluid used	Parameter studied	Remarks
Sabiri and Comiti (1995)	Aq. solution of carboximethylcellulose (CMC) sodium salt	Proposed an empirical model for pressure drop calculations for non-Newtonian purely viscous fluid flow through packed beds of different structures by taking into account the structural parameters of the porous medium (tortuosity, dynamic specific surface area and porosity).	Satisfactorily predicted the pressure drop values by incorporating tortuosity and dynamic specific surface area in pressure drop correlation, over a large range of Reynolds number for non-Newtonian purely viscous fluid flow through porous media.
Helmreich et al. (1995)	Xanthan solution	Investigated the polysaccharide xanthan solution flow through porous media (glass bead packs).	The flow resistance increases with an increase in xanthan concentration. The onset of increased non-viscous resistance occurs at particular stress levels, at which viscous flows (shear stress) are dominated by elastic effects (first normal stress differences) and viscometric flows.
Sabiri and Comiti (1997)	Aq. solution of CMC, xanthan, and natrosol	Experimentally validated the model proposed by Sabiri and Comiti (1995) for packed beds comprised of spherical and non-spherical particles over a wide range of Reynolds numbers, even when important wall effects exist.	The model was successfully tested for different non-Newtonian fluids, which can be used for predicting pressure gradients for flow through fixed beds over a large range of Reynolds number, without internal porosity.
Tiu et al. (2001)	Aq. solution of Separan AP30 (polyacrylamide)	Studied flow of viscoelastic polymer solutions through packed beds of mixed size spheres and uniform size spheres and cylinders for creeping flow.	The hydraulic radius or equivalent diameter was estimated based on surface-mean particle diameter for mixed beds, which allows the fitting of pressure drop data, for non-Newtonian fluids, well for existing correlations. In case of viscoelastic polymer solutions the excess pressure losses were well correlated with the Weissenberg number.
Basu (2001)	CMC	Experimentally studied non-Newtonian fluid flow through packed bed for different column to packing particle diameter ratio to study the wall effect.	With an increase in CMC concentration and flow rate the pressure drop increases.

Authors	Type of fluid used	Parameter studied	Remarks
Dolejs et al. (2002)	Polymer solutions (Bogar fluid, Separan AP-45, Polyox)	Using corresponding relations for consistency variables proposed an approach, based on modified Rabinowitsch–Mooney equation, for the calculation of pressure drop for viscoelastic fluid flow through fixed beds of particles.	Suggested an approach for the solution of momentum transfer in viscoelastic fluid–particle bed interaction systems.
Yilmaz et al. (2009)	polyacrylamide solution	Experimentally studied the Newtonian and non-Newtonian fluid flows through porous media (Berea Sandstone core) and compared as pressure losses, flow rates and permeability coefficients.	The characteristic of the flow curve for the polyacrylamide solutions were nonlinear in nature, whereas it was linear for Newtonian fluids.
Kaur et al. (2011)	CMC solution and Polyacrylamide (PAA) solution	Experimentally studied the pressure drop-flow rate behaviour of Newtonian (water), non-Newtonian viscoinelastic (CMC in water) and viscoelastic (PAA in water) fluids flowing through packed bed and compared the pressure drop behaviour with existing models.	The phenomenon of drag reduction and drag enhancement (under creeping flow limits) were observed for viscoinelastic and viscoelastic fluids
Dimitrios et al. (2015)	HPAM polymer, 3 630S	Studied the influence of wettability on polymer flow behavior through porous media was investigated through a series of synthetic polymer floods conducted in water- and oil-wet Bentheim and Berea sandstone cores.	In presence of residual oil, the oil-wet cores display the lowest degree of polymer retention (Berea) and the lowest inaccessible pore volume (IPV) (Bentheim). The largest wettability impact on the polymer flow behavior in porous media appears to be for the Berea formation; polymer retention in oil-wet cores decreases 90% and IPV 52% compared to the corresponding amounts for the water-wet ones.

CMC - carboxymethylcellulose sodium salt

Over a decade various researches proposed the relation between bed friction factor and modified Reynolds number based on their studies which is summarized in Table 2.5.

Table 2.5: Model equations for the prediction of bed friction factor proposed by various investigators.

Authors	Model equation	Modified Reynolds number
Christopher and Middleman (1965)	$f = \frac{1}{\text{Re}}$ $f = \frac{\Delta P D_p \varepsilon^3 \rho_f}{L G^2 (1 - \varepsilon)}$	$\text{Re} = \frac{D_p G^{2-n} \rho^{n-1}}{150 H (1 - \varepsilon)}$ $H = \frac{\mu^*}{12} \left(9 + \frac{3}{n}\right)^n (150 K \varepsilon)^{(1-n)/2}$
Kemblowski and michniewicz , 1979	$f_{BK} = \frac{180}{\text{Re}_{BK}^*}$ $f_{BK} = \frac{D_p}{\rho v_0^2} \left(\frac{\Delta P}{L}\right) \frac{\varepsilon^3}{1 - \varepsilon}$	$\text{Re}_{BK}^* = \frac{v_0^{2-n} D_p^n \rho}{\mu^* (1 - \varepsilon)^n} \left(\frac{4n}{3n+1}\right)^n \left(\frac{15\sqrt{2}}{\varepsilon^2}\right)^{1-n}$
Kumar and Upadhyay (1981)	$f_m = \frac{150}{N_{\text{Re}'}} + 1.75$ $f_m = \frac{\Delta P}{L} \frac{D_p \varepsilon^3}{\rho v_0^2 (1 - \varepsilon)}$	$N_{\text{Re}'} = \frac{D_p v_0 \rho}{\mu_{\text{eff}} (1 - \varepsilon)}$ $\mu_{\text{eff}} = \mu^* \left(\frac{8v_0}{D_e \varepsilon}\right)^{n-1}; D_e = \text{eq. particle dia} = \frac{2\varepsilon D_p}{3(1 - \varepsilon)}$
Al Fariss (1989)	$f^* - f_0^* = \frac{150}{\text{Re}^*}$ $f^* = \left(\frac{\Delta P}{L}\right) \frac{D_p \varepsilon^3}{v_0^2 \rho (1 - \varepsilon)}$ $f_0^* = \left(\frac{25}{2}\right) \frac{\tau_0 \varepsilon^2}{v_0^2 \rho}$	$\text{Re}^* = \frac{D_p v_0^{2-n} \rho}{\mu_{\text{eff}} (1 - \varepsilon)}$ $\mu_{\text{eff}} = \frac{\mu^*}{4} \left(3 + \frac{1}{n}\right)^n \left[\frac{D_p \varepsilon^2}{3(1 - \varepsilon)}\right]^{1-n}$
Al-Fariss (1990)	$f^* = \frac{150}{\text{Re}^*}$	$\text{Re}^* = \frac{D_p v_0^{2-n} \rho}{\mu_{\text{eff}} (1 - \varepsilon)}$ $\mu_{\text{eff}} = \frac{\mu^*}{12} \left(9 + \frac{3}{n}\right)^n (150 K \varepsilon)^{(1-n)/2}$
Rao and Chhabra (1993)	$f_{BK} = \frac{150}{\text{Re}_{BK}^*}$ $f_{BK} = \frac{D_p}{\rho v_0^2} \left(\frac{\Delta P}{L}\right) \frac{\varepsilon^3}{1 - \varepsilon} \times \frac{1}{M}$	$\text{Re}_{BK}^* = \frac{v_0^{2-n} D_p^n \rho}{\mu^* (1 - \varepsilon)^n} \left(\frac{4n}{3n+1}\right)^n \left(\frac{15\sqrt{2}}{\varepsilon^2}\right)^{1-n} \times \frac{1}{M^n}$ $M = \left[1 + \frac{2D_p}{3D_c (1 - \varepsilon)}\right]$
Al Fariss (1994)	$f^* = \frac{C^*}{\text{Re}_e^*}$ $C^* = 150 \text{ or } 180$	$\text{Re}_e^* = \frac{12 \rho v_0^2}{(2\mu^* D_p \varepsilon^3 v_0^n / \varphi) + \tau_0 \varepsilon^2}$ $\varphi = 6 \left[\frac{\varepsilon n}{3n+1}\right]^n \left(\frac{D_p \varepsilon}{3(1 - \varepsilon)}\right)^{n-1} (1 - \varepsilon)$

<p>Hayes et al. (1996)</p>	$f = \frac{A_1}{\text{Re}_M} + B_1$ $f = \left(-\frac{\Delta P}{L} \right) \frac{1}{\rho \left(\frac{v_0}{\varepsilon} \right)^2} \left(\frac{d\varepsilon}{1-\varepsilon} \right)$	$\text{Re}_M = \frac{\rho(v_0/\varepsilon)^{2-n}}{\mu^*} \left(\frac{d\varepsilon}{1-\varepsilon} \right)^n$ $A_1 = \frac{6((2+4n)/n)^n}{\left\{ (1-\varepsilon)^{2/3} [1-(1-\varepsilon)^{2/3}] [1-(1-\varepsilon)^{1/3}] / \varepsilon^2 \right\}^n}$ $B_1 = \left(\frac{\varepsilon}{1-(1-\varepsilon)^{2/3}} \right)^2$
<p>Hayes et al. (1996)</p>	$f = \frac{A_2}{\text{Re}_M} + B_2$ $f = \left(-\frac{\Delta P}{L} \right) \frac{1}{\rho \left(\frac{v_0}{\varepsilon} \right)^2} \left(\frac{d\varepsilon}{1-\varepsilon} \right)$	$\text{Re}_M = \frac{\rho(v_0/\varepsilon)^{2-n}}{\mu^*} \left(\frac{d\varepsilon}{1-\varepsilon} \right)^n$ $A_2 = 2C_i \left(\frac{3n+1}{n} \right)^n 3^{n+1}$ $B_1 = 1.75$
<p>Sabiri and Comiti (1997)</p>	$f_{pore} = \frac{16\alpha}{\text{Re}_{pore}} + 0.194\beta$ $f_{pore} = \frac{2\Delta P \varepsilon^3}{\rho_f v_0^2 L \tau^3 (1-\varepsilon) a_{vd}}$	$\text{Re}_{pore} = \frac{\rho_f \varepsilon^{2n-2} (\tau v_0)^{2-n}}{2^{n-3} \mu^* [(3n+1)/4n]^n (1-\varepsilon)^n a_{vd}^n}$

Emulsions with different droplet sizes were injected into consolidated Berea sandstone under a constant pressure. A drastic reduction in water permeability of the sandstone (i.e., sometimes by up to 90%) was observed, with the larger reductions for larger droplets to initial permeability ratios. Further, it was observed that the rate and amount of permeability reduction decreases with an increase injection pressure. This behavior was referred as “pseudo” non-Newtonian, although the rheology of the dilute, bulk emulsion was found to be Newtonian.

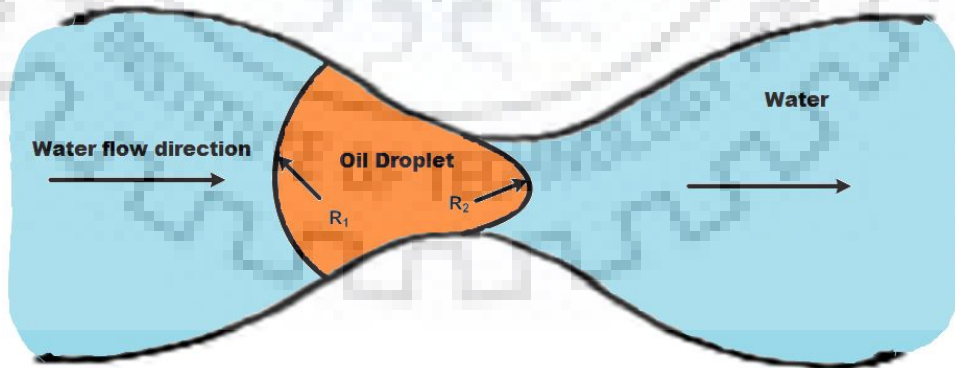


Fig. 2.2: Emulsion blockage mechanism (Jamin effect).

Devereux, (1974) developed a model for flow of a stable emulsion through a porous solid, over a wide range of parameters. It was assumed that there is a linear relationship between fluid element velocities and driving force acting on an individual fluid element. Also, the contribution of compression and gravitational components was neglected. The contact angle

hysteresis and variation due to pore size were considered in defining the capillarity force. For emulsion flow through a porous media under constant pressure, saturated with continuous phase of the emulsion, invaded regions were reported.

Basu et al., (1996; 2000) performed experiments on bitumen film rupture and displacement on model surfaces (glass plate) for understanding the real mechanism of oil film rupture and the displacement of oil by water on sand grain.

Cartmill and Dickey (1979) experimentally studied the oil migration mechanism through reservoir sand stones for a stable crude oil-in-water emulsions flow with different permeability zones and also reported large permeability reductions. It was found that at the junction between two different permeability zones a considerable amount of oil drops were retained, with maximum retention at the front portion of the low permeability zone.

Flow mechanism of dilute, stable emulsions in a porous media was studied by Soo and Radke (1984) in a fine grained porous media. They also investigated the transient permeabilities, drop and pore size distributions and droplet concentrations of inlet and effluent streams for constant volumetric flow rate. It was reported that when emulsions are introduced into porous media, permeability decreases and drops are retained in the pores. The droplet blocked the pores of throat sizes smaller than it, and also captured on pore walls and in crevices. The larger the droplet size higher is its capture probability. When all capture sites were occupied, a steady state was reached and local flow diverts to contiguous large channels.

Thomas and Ali (1989) investigated the crude oil-in-water and water-in-crude oil emulsions flow through porous media consisting of Berea sandstone cores, Ottawa sand and glass bead packs. It was reported that the mobility of an emulsion is strongly dependent on emulsion quality and rheology and drop size distribution (DSD), for a given pore size distribution. Further, in pore entrainment of emulsion drops was reported, however, drops can be mobilized by increase in pressure gradients.

A new correlation for non-Newtonian flow through porous media was developed by Al-Fariss (1989) for wax containing oils, which exhibit Herschel-Bulkley flow behavior. A modified form of Blake-Koseny equation was used to describe non-Newtonian fluid flow through porous media. The fluids used were solution of paraffinic wax in oil and Saudi crude oil. The pressure drop was measured through a packed bed of glass beads by changing the flow rate over a wide range of temperatures. It was observed that, with an increase in temperature there is a decrease in yield stress until it vanishes off. Further, the yield stress increases with an increase in the wax-concentration and the crude oils viscosities decrease with an increase in shear rates at constant temperature.

The electrostatic repulsion and emulsion stability influences the permeability reduction caused during the emulsion flow through porous medium was investigated by Hofman and Stein (1991). Two different emulsions, stabilized by Na oleate and Aerosol OT were studied. The permeability reduction effected by a stable (Na oleate-stabilized) emulsion depends both on the droplet diameter and on the flow velocity of emulsion. The pronounced permeability reduction was reported for a larger emulsion droplet size and low velocity. Stable emulsions reduce the permeability of a porous media, and emulsions with low interfacial tension affects permeability more efficiently. It is due to a self reinforcing effect of easy adjustment of a droplet with the shape of the solid wall near a pore throat, and easy coagulation followed by coalescence.

Al-Fariss (1994) further investigated the flow of o/w and w/o macroemulsion through porous media. A new model was developed to describe the emulsion flow through porous media that uses both capillary and core flow data. Results are presented in the form of modified friction factor and modified Reynolds number correlation. Newtonian behavior was observed for emulsion of 10, 20, 30 and 40% oil content. When the oil concentration was increased above 40%-60% oil, the emulsion behaved as non-Newtonian fluids (pseudo plastic) which was fitted by power law model. Finally, when oil concentration was increased above 60% (70%, 80%, 90%) oil, the non-Newtonian behavior becomes significant. Data were fitted to Hershel-Bulkley model. At high concentration of oil, the droplets reach the most crowded packing, then as further increase in the internal phase, the droplets begin to flatten and non-Newtonian behavior becomes remarkable. At this situation a yield stress was observed as a minimum stress needed to deform the fluid.

Soma et al. (1995) experimentally study the flow of dilute, sub-micron emulsions through porous media for pH and ionic strength varying from 3.4 – 9.6 and 5×10^{-4} to 10^{-1} (M), respectively. In this study the average diameter of the droplets used was the order of 0.4 μm , which was considerably smaller than the mean pore diameter. It was reported that the permeability of a porous medium can be substantially reduced even when the drop size is much smaller than the pore size. The droplets are captured mainly by interception, a mechanism primarily dictated by electrostatic interactions. The permeability was unaffected and there was no deposition at high pH and low ionic strengths. Soma and Papadopoulos (1997) further evaluate the effect of the cationic surfactant cetyl trimethyl ammonium bromide (CTAB) on the transport of emulsions in a model porous medium.

Romero et al. (2011) developed a network model by assuming emulsion flow as an effective single phase fluids flow by incorporating empirical data from single capillary tube results. The behavior of emulsion flow through sandstone samples was captured qualitatively

by the proposed model. A parametric analysis was also conducted to study the effect of dispersed phase droplet size and permeability on the flow response to emulsion flooding in porous media. The predictions of network model were qualitatively compared with equivalent results obtained with experimental results in terms of mobility reduction, which was related to emulsion injection. Mineral oil (Shell Tivela 460) was used as the dispersed phase and its concentration was used as 10% for the preparation of the o/w emulsion. A solution of 70% glycerin and 30% distilled water was used as continuous phase and the surfactant used was Sodium dodecyl sulfate (SDS). The porous media was comprised of two sandstone cores, from Botucatu (Brazil).

Arhuoma et al. (2009) experimentally determined the viscosities of w/o emulsions in a porous media (i.e. three different sandpacks) for volume fractions varied from 6.78% and 33.48%. It was reported that emulsion quality is a significant parameter while DSD did not have a significant impact on the viscosity of the w/o emulsions. It was reported that the emulsion viscosity decreases with an increase in flow rate due to shear-thinning behavior. For emulsions with high emulsion quality the degree of reduction was higher as compared with lower quality emulsions. For low-permeability porous media the reduction was stronger due to high shear rate in lower-permeability porous media for the same flow rate.

The mechanisms for pore-scale flow and the relative phase permeabilities (RPPs) for two-phase flow in a pore network were experimentally reported by Khasanov et al. (2011). The conditions for forming and destroying emulsions in water-in-oil systems were determined seep through porous structures. The model described the nonlinear properties of non-stabilized w/o emulsions, which allowed the consideration of the relaxation time in determining the permeability for immiscible displacement processes.

Guillen et al. (2012) visualized recovery results in a semi-transparent porous medium to understand how pore-level mobility control leads to microscopic flow diversion and consequently reduced residual oil saturation. The improved macroscopic reservoir sweep was illustrated by emulsion injection. It was observed that the emulsion flooding affects the oil displacement by a water phase in a multi-scale manner. In the pore level, pore blockage by the dispersed phase diverts the flow path, which leads to change in the residual oil saturation. The mobilization of residual oil after slugs of o/w emulsion was visualized experimentally in a transparent porous media. The average mobility of the water phase affects the pore blockage and lead to more uniform sweep fronts.

A dynamic capillary network model was developed which uses experimentally determined pore-level constitutive relationships between flow rate and pressure drop in constricted capillaries by Nogueira et al. (2013). The emulsion was described as a Newtonian

single phase which contains a low concentration of dispersed drops. The effect of dispersed phase droplet size and capillary number on the flow response was studied in both emulsion as well as alternating water/emulsion flooding. It was reported that the emulsion flooding changes the continuous-phase mobility, and consequently flow paths in the porous media. The transient flow behavior of emulsion flow through porous media was described qualitatively to prove the capillary driven mobility control mechanism.

Baldygin et al. (2014) developed a new emulsion (o/w) core flooding experimental setup with unconsolidated sand packs as a porous medium. Two different strategies for emulsion flooding was demonstrated, direct injection of emulsion and water flooding followed by emulsion flooding. They found that the emulsion worked effectively as a substitute fluid after the water flooding. Comparison between these two runs suggested that the emulsion flooding was effective in terms of the time needed for the oil to be recovered from the porous media, whereas second strategy was effective in terms of the emulsion used for the oil recovery process.

The capillary trapping of the drops in porous media as a function of drop to pore size ratio and capillary number was investigated experimentally by Moradi et al. (2014). The influence of emulsion flow on pressure drop oscillation was also reported. It was reported that the oil drops can block the pore throats and divert the water flow toward unswept areas. The blockage phenomena caused by emulsion injection can be effective even when emulsion was displaced with water without any additives. The blockage mechanism was associated with the pressure drop oscillation, which speculated the collective effects of drops passage through pore-throats. Pressure drop data revealed the dependency of the blockage mechanism on the capillary number. It was also reported that the blockage-release mechanism of the trapped drops would occur at the higher capillary number. The pore-scale dynamics was depends on local capillary number and emulsion drop sizes. The critical capillary number, below which emulsion works as a mobility control agent increases with an increase in drop size to pore-throat size ratio.

Furthermore, Chakrabarti et al. (2006), De et al. (2010), Kaushik et al. (2012) Balakhrisna et al. (2010) extensively studied two phase/multiphase flow (oil-water) in various pipe cross-section relevant to petroleum process industries.

2.4 FLUID FLOW MODELLING

Various flow regimes are encountered during the fluid transport in porous media, based on the pore Reynolds number, Re_p , (Pedras and De Lemos, 2001):

- (a) Darcy or creeping flow regime ($Re_p < 1$)
- (b) Forchheimer flow regime ($1 < Re_p < 150$)

- (c) post-Forchheimer flow regime (unsteady laminar flow, $150 < Re_p < 300$) and
- (d) fully turbulent flow regime ($Re_p > 300$).

Such flows can be analyzed by modeling the topology of the porous medium and resolving the microscopic flow equation in the fluid phase. The range of pore-size is large, and can vary over 8- order magnitude spanning Angstrom (ultra-micro-pores) to centimeters (pebbles) or even larger (Kaviany, 1991). The conditions encountered in different applications are broad enough to cover a large range of Reynolds numbers. Due to lack of geometric information to model each and every pore, such systems are difficult to simulate with full geometric details. Despite the fact that it might be possible to describe some of these systems in an almost exact representation or a meaningful statistical approximation of the geometry, the computational effort required to solve the flow field in such geometries is still formidable (Teruel and Rizwan-uddin, 2009). This motivates further research in the development of porous media approximation, representing the system composed of macroscopic homogenous pores with uniform properties.

The porous media present a complex structural configurations. The pore scale flow inside a porous medium is characterized by a wide range of length scales, as shown in Fig. 1. The smallest scales, l_F and l_S , represent the average pore size and particle diameters of the pore-like structures, while the largest scale is the characteristic macroscopic porous length L . In such cases, it is difficult to impose boundary conditions across the control volume. The geometric complexity of such porous matrix causes problems in simulating the detailed flow field inside each individual porous structure. The common practice is therefore, to smooth out the local complexity of the actual phenomena by concentrating on the mass and momentum conservation principles while treating the porous medium as a continuum. This approach allows one to define fluid quantities at every point, irrespective of whether it corresponds to the fluid or the solid phase. The local volume-averaging theory (VAT) has been widely used in the study of porous media flow since its introduction by Whitaker (1996). This technique considers only the macroscopic flow behaviour (Liu et al., 1994, Liu and Masliyha, 1996). Therefore, a small control volume ΔV of radius r has been considered in a fluid-saturated porous medium in the present study (Fig. 1) and the governing equations (Navier-Stokes equations) have been averaged over ΔV for the volume averaged unknowns. A general assumption is that length scales are well separated, i.e. $l_S \sim l_F \ll r \ll L$. Therefore, volume-averaged quantities result vary smoothly and are free of small scale fluctuations (Whitaker, 1999).

The volume averaging theory (VAT) is usually applied to treat the momentum equations of flows in porous media (Nield and Bejan, 2006). Vafai and Tien (1981) Du

Plessis and Masliyah (1988, 1991) derived the general equations for fluid flow through porous media using the volume-averaging technique. This technique is a rigorous mathematical procedure for deriving the governing mass, momentum and energy equations in porous media. Since flows become turbulent in porous media when the pore Reynolds number is larger than a few hundred (Dybbs and Edwards, 1984), the two equations based $k-\varepsilon$ turbulence models have been used to represent the turbulence characteristics in the porous media (Nakayama and Kuwahara, 1999; Pedras, and de Lemos, 2001; Pinson et al., 2006). Lee and Howell (1987) proposed an elaborated version of the general (porous medium) turbulence transport equations, by including a turbulence eddy diffusivity in the viscous diffusion term of the general momentum equation. However, the general momentum equation was not time averaged, therefore, their model neglects an additional contribution of the Reynolds stresses.

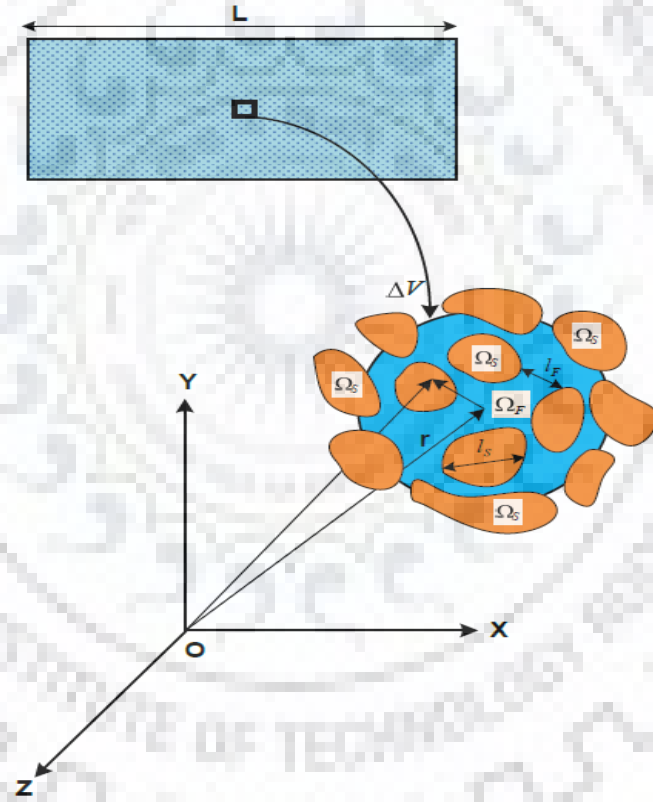


Fig. 2.3: Schematic representation of porous medium with the hierarchy of various characteristic length scales and position vector (Ω_S and Ω_F are the solid and fluid phases, respectively).

Travkin et al. (1993) developed the turbulence model for highly porous media along with statistical and numerical methodologies. Masuoka and Takatsu (1996) derived a zero-equation turbulence model using the local volume-averaging technique. They modeled the effective eddy diffusivity as the algebraic sum of the eddy diffusivities estimated from two

types of vortices- the pseudo vortex and the interstitial vortex. Antohe and Lage (1997) derived the two-equation turbulence model for incompressible flow within a fluid saturated rigid porous medium by time-averaging the general (macroscopic) transport equations and closing the model with the classical eddy diffusivity concept and the Kolmogorov-Prandtl relation. Kuwahara et al. (2006) used large eddy simulations (LES) and compared their results with the conventional two equation model for turbulent flow through a porous media comprising of periodic array of square cylinders. It has been reported that the Darcy–Forchheimer equation could be satisfactorily used to provide pressure losses. Teruel and Rizwanuddin (2009) formulated a new k - ε model by conjugating the spatial- and time fluctuations in to a single quantity. The space–time fluctuation in this model was treated as a unique quantity and a transport-diffusion equation has been derived for the entire kinetic energy filtered in the averaging process of the momentum equation. For rigid and isotropic porous media this approach leads to a natural construction of k and ε equations, where all the kinetic energy filtered during averaging process was modeled. The methodology was further extended to understand the macroscopic turbulence behaviour at high Re in the porous REV (a 2D arrangement of staggered square rods). Drouin et al (2013) proposed a macroscopic turbulence model, based on a two-scale analysis, and a calibration methodology for flows in stratified porous media with constant porosity. They considered clusters of flat plates and circular pipes as the stratified porous medium.

2.5 OVERVIEW OF LITERATURE REVIEW

The literature review illustrates studied related to emulsion formation and stability, emulsion rheology and porous media flow. For emulsion formation and stability, various researchers studied effect of different parameters on emulsion stability. There is very limited study is available for emulsion formation and optimization of processes parameters influencing the emulsification process. The study was focused on:

- For emulsion rheology, study related to viscoelasticity, effect of temperature and electro-viscous effect on emulsion rheology were limited.
- For porous media flow, most of study reported the flow of different polymeric and surfactant solution (non-Newtonian fluids) through porous media/packed or fixed bed. Study related to emulsion flow through porous media is also limited.

Therefore, a detailed study including stability and formation of emulsions, rheological behaviour of emulsion and flow modeling and emulsion flow behaviour through porous media have been studied.

CHAPTER 3

MATERIALS AND METHODS

In this chapter, the materials and methods have been described which were used during the preparation and characterization of oil-in-water (o/w) emulsion system. The chapter has been divided into several sections, i.e., Experimental details for emulsion preparation, Petroleum oil and emulsion characterization, Experimental design and process modeling and Emulsion flow experimental set up. The section 3.2 deals with the materials, experimental procedures and the methods of analysis adopted to collect the experimental data and data analysis.

3.1 EXPERIMENTAL DETAILS FOR EMULSION PREPARATION

3.1.1 Chemicals

Deionized water was used throughout the experiments in the present work for the preparation of oil-in-water (o/w) emulsions. The chemicals used in the experimental work were procured from different sources: NaOH (RFCL, New Delhi), anhydrate Na_2SO_4 (Rankem, New Delhi), sodium dodecyl benzene sulfonate, SDBS (Himedia, Mumbai), NaCl (SRL, Mumbai), Na_2CO_3 (NICE, Cochin), and were used as received. SDBS was used as a surfactant and its physico-chemical properties are shown in Table 3.1. Light petroleum oil was procured from the Indian Oil Corporation Ltd (IOCL) for preparing o/w emulsions. The petroleum oil was characterized by ASTM standards. The detail for various ASTM standards used for the characterization of petroleum oil is reported in ANNEXURE A. Table 3.2 shows the physico-chemical characteristics of oil.

3.1.2 Preparation of Emulsion

Emulsions were prepared by rigorous shearing of known amounts of the continuous and dispersed phases in the presence of 1 % (w/v) of an anionic surfactant, sodium dodecyl benzene sulfonate, (SDBS) at room temperature, which is water soluble. Emulsions were prepared by dissolving the surfactant in water and then by a slow addition of oil while stirring the mixture vigorously.

Table 3.1: Physico-chemical properties of sodium dodecyl benzene sulphonate (SDBS).

(Source: Kundu et al., 2013)


Characteristics	
Type	Anionic surfactant
Molecular Formula	$\text{CH}_3(\text{CH}_2)_{11}\text{C}_6\text{H}_4\text{SO}_3\text{Na}$
Molecular weight	348.48
Critical micelle concentration (CMC) in water	1.20×10^{-3} mM
Equilibrium partition constant (K_p)	$29.3 \text{ dm}^3/\text{mol}$
Structural Formula	
Appearance	White or pale yellow powder
Apparent density (g/ml)	0.18
Minimum assay (%)	20.0
Moisture content (%)	5.0

Table 3.2: Properties of light petroleum oil.

Property	Values	Standard method used
Kinematic viscosity at 30 °C	5.81 St	ASTM D88
Dynamic Viscosity at 30 °C	0.4772 Pa.s	-
Specific gravity 30 °C	0.8213	ASTM D1298
Water content	3 - 4 %	ASTM D95
Pour point	(-) 18 °C	ASTM D97
Cloud point	(-) 3 ± 1 °C	ASTM D2500
Flash point	54 ± 1 °C	ASTM D93
Fire point	58 ± 2 °C	ASTM D92
Aniline point	73 ± 2 °C	ASTM D611

All o/w emulsions were prepared by an agent-in-water method (Sherman, 1968) using a high shear mixer at different stirring rates (RPM), oil and surfactant concentration and time. The

high shear mixer consisted a rotor-stator assembly (six pass) which was designed and fabricated indigenously in the workshop. The schematic diagram of the experimental set-up for emulsification is shown in Fig. 3.1. A series of different types of o/w emulsions were prepared by varying oil-water volume ratios, as shown in Table 3.3. All emulsions were allowed to age for 24 hours at room temperature (30°C) for attaining a stable physico-chemical structure prior to the commencement of the viscosity measurements. For the effect of surfactant concentration on emulsion rheology, the surfactant concentration was varied from 0.5% to 2% (w/v).

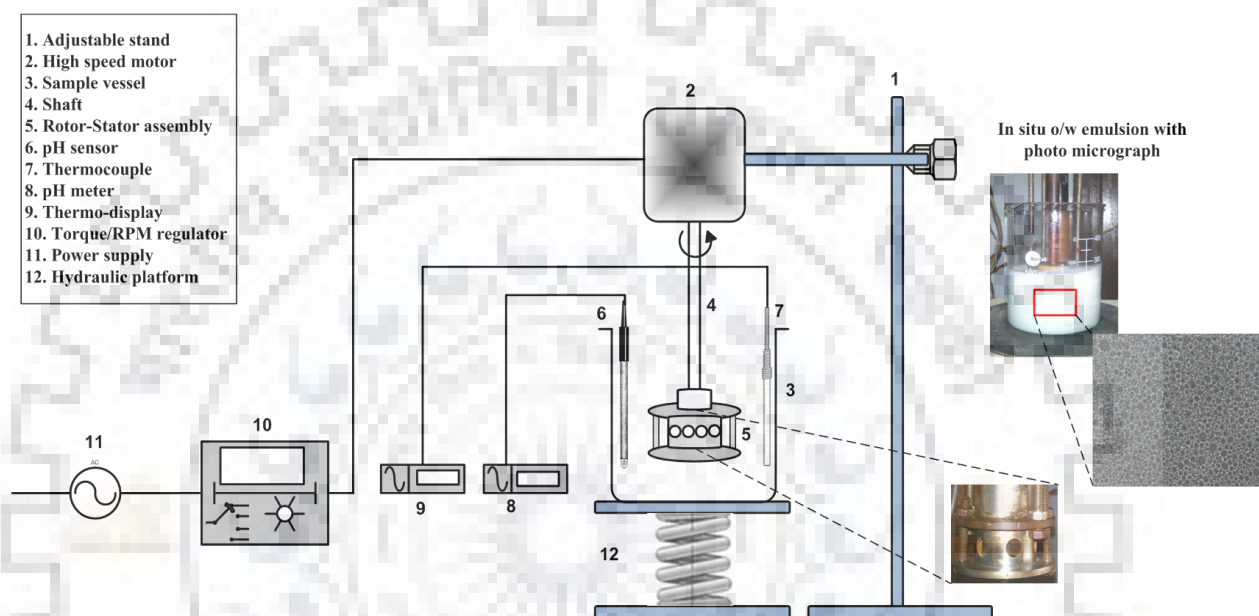


Fig. 3.1: Schematic diagram of lab scale experimental setup for emulsification.

Table 3.3: Different types o/w emulsions used in the study.

Emulsions set	Oil : water volume ratio	Type of emulsion
Set 1	10:90	Dilute
Set 2	30:70	Semi-dilute/Moderately concentrated
Set 3	50:50	Concentrated
Set 4	70:30	Highly concentrated
Set 5	80:20	Highly concentrated

3.2 EMULSION CHARACTERIZATION

3.2.1 Emulsion Stability Measurements

The relative volume method was used to estimate the stability of emulsions using two indices, namely the “creaming index (*CI*)” and “emulsification index (*EI*)”. The freshly prepared emulsion was immediately transferred into a graduated cylinder (150 ml, Borosilicate), sealed with a stopper and then stored for 72 h at 30°C. After storage, the

emulsions were separated into a thin “creamed” layer at the top and a turbid “serum” layer at the bottom. The initial volume of the emulsions (V_0), the volume of the serum layer (V_S) and the final volume of the emulsion (cream) layer (V_E) were measured over a period of time. The extent of creaming of emulsions was estimated by a creaming index (CI) as given by

$$CI(\%) = \frac{V_S}{V_0} \times 100 \quad (3.1)$$

The emulsification index (EI) is given as

$$EI(\%) = \frac{V_E}{V_0} \times 100 \quad (3.2)$$

Both CI and EI provide indirect information about the extent of droplet aggregation and coalescence in an emulsion. Higher CI indicates more aggregation, larger the droplets faster the creaming (Perrechil and Cunha, 2010; Lovaglio et al., 2011). Higher EI indicates the higher stability of the emulsion.

3.2.2 Droplet Size Measurement

Mean droplet size and droplet size distribution (DSD) of the emulsion phase were determined by the dynamic light scattering (DLS) technique at room temperature (25 °C) using a Malvern Zetasizer (Malvern Nano ZS 90, UK). Each sample of the emulsion was analyzed three times and the average of three values is presented here. The average droplet size was characterized by volume weighted diameter (d_{43}) as defined by the following equation:

$$d_{43} = \frac{\sum_i n_i d_i^4}{\sum_i n_i d_i^3} \quad (3.3)$$

where, n_i is the number of droplets and d_i is the droplet diameter.

3.2.3 Zeta Potential and Electrophoretic Mobility Measurements

Zeta potential and electrophoretic mobility of the emulsions were measured by a Zetasizer (Malvern Nano ZS 90, UK) using Laser Doppler micro-electrophoresis (LDME) technique at 25 °C. All experimental measurements were made in triplicate and the average values were used for further analysis.

3.2.4 Surface Tension (SFT) and Interfacial Tension (IFT) Measurement of Emulsions

The SFT and IFT of emulsions were measured by using a Tensiometer (Dataphysics, Germany) at atmospheric pressure and room temperature with Du Noüy ring method (du

Noüy, 1925). The ring was made of platinum-iridium. For each measurement, the platinum-iridium ring was thoroughly cleaned and flame-dried (red hot). All SFT measurements were done in triplicate and the mean values are reported. The standard deviation of the measurements did not exceed ± 0.1 mN/m.

3.2.5 Microscopy of O/W Emulsions

Photomicrographs of all sets of o/w emulsion samples were taken with a Nikon (Eclipse, LV100, Japan) polarizing microscope equipped with a digital camera connected to a computer. The small quantity of a freshly prepared o/w emulsion sample was carefully placed on a glass slide and illuminated with transmitted light (50W halogen light source) from the bottom.

3.2.6 Rheological Measurements

The rheological measurement of o/w emulsions was carried out using a controlled-stress rheometer (Physica MCR 100, Anton Paar, Germany), which was equipped with an EC motor (electronically commutated synchronous motor). The rheological measurements were made under both controlled stress (CS) and controlled strain (CR) modes. A cone and plate sensor was used to make shear stress/shear rate rotation tests. A Peltier cylinder temperature system TEK150P was used for the precise temperature control of the sample compartment. The temperature of the sample compartment was controlled using a water bath/circulator Viscotherm VT2 Temperature Controller System (TCS) (Anton Paar, Germany). The details of the measuring system are given in Table 3.4.

Both steady shear and oscillatory measurements were performed. The steady shear viscosity measurements have been carefully performed for all emulsion samples over a shear rate range of 10^{-3} – 10^3 s^{-1} . In steady rate sweep measurement equilibrium time was set as 10s for each single data point ensuring viscosity data acquired under steady state conditions. At higher shear rates ($\dot{\gamma} \geq 10^2$) time required to reach the equilibrium is less as compared to low shear rates ($\dot{\gamma} \leq 10^0$). Thus, for better reproducibility of the viscosity data point 10 s was set as an equilibrium time within the shear rate range of 10^{-3} – 10^3 s^{-1} . During steady shear flow experiments, the shear rate was applied to the emulsion samples as a step function (stepped flow) with step time of 10 s and the shear rate was increased logarithmically. The resulting viscosity measurements were done when the sample has reached equilibrium, ensuring the steady shear flow and giving a single viscosity data point at a particular shear rate. Oscillatory measurements were made to study the viscoelastic behavior of the emulsions.

Initially, amplitude sweeps (*AS*) were performed to establish the linear viscoelastic range of emulsion samples. Then frequency sweeps (*FS*) were performed within the range of the angular frequency (ω) $1-10^2 \text{ s}^{-1}$ to characterize the viscoelastic behavior of the emulsion. Triplicate sample runs were taken. For each steady and oscillatory measurement, fresh sample was used. The plate and cone section of the rheometer was thoroughly cleaned with Millipore water and acetone between each measurement of different emulsion samples.

All rheological measurements were carried out with fresh emulsions immediately after preparation. Emulsion samples were gently and carefully mixed before measurements to avoid phase separation and air entrapment, and results are shown as average value and mean percent deviation (lower than 10%).

Table 3.4: Details of viscosity measuring system (Rheometer).

Measuring geometry	Dimensions
Measuring system (Standard: ISO 3219)	Cone and plate : CP50-1/Ti
Cone diameter	49.95 mm
Plate diameter	60 mm
Cone angle	0.998°
Cone Truncation	51.0 μm
Cone concentricity	$\pm 5.0 \mu\text{m}$
Cone parallelity	$\pm 4.0 \mu\text{m}$
Measuring cell	TEK 150P-C
Temperature controller	Peltier

3.2.7 Error Estimation

Non-linear regression analysis was carried out for the rheological data and the analysis of variance (*ANOVA*), at alpha level (sensitivity of regression) of 0.05, was performed to establish the influence of different variables. The best fit to the model was selected on the basis of correlation coefficient (R^2), χ^2 , standard error of estimate (*SEE*) and predicted residual sums of squares (*PRESS*). All the regression factors were defined as follows (Allen, 1974; Tarpey, 2000):

$$R^2 = 1 - \frac{SSE}{SST} \quad (3.4)$$

$$SEE(\sigma_{est}) = \sqrt{\frac{\sum (Y - Y')^2}{n}} \quad (3.5)$$

where, Y is the experimental value, Y' is the calculated value for the fitted data point, and n is the number of observations.

$$\text{PRESS} = \sum_{i=1}^n (Y_i - \widehat{Y}_{i,-i})^2 \quad (3.6)$$

where, Y_i is the i^{th} value of the experimental data to be predicted, $\widehat{Y}_{i,-i}$ is the predicted value of Y_i . The statistical analysis was performed within 95% of confidence level.

3.3 EXPERIMENTAL DESIGN AND EMULSIFICATION PROCESS MODELING

3.3.1 Response Surface Methodology (RSM)

Box-Behnken design (BBD) is a class of rotatable or nearly rotatable second-order design based on three-level factorial design (Box and Behnken, 1960). It is a spherical design with all points lying on a sphere of radius $\sqrt{2}$, and no points at the vertices of the cube region created by the upper and lower limits for each variable (Kundu and Mishra, 2013). This could be advantageous when the points on the corners of the cube represent factor-level combinations that are prohibitively expensive or impossible to test because of physical constraints (Box and Behnken, 1957). The number of experiments (N) required for the development of BBD model is defined as:

$$N = 2k(k-1) + N_c \quad (3.7)$$

where k is the number of factors and N_c is the number of central points. In the present work, the three levels, four factors (oil concentration, surfactant concentration, mixing speed and mixing time) BBD model was chosen. Factors were designated as $\xi_1, \xi_2, \xi_3, \xi_4$ and prescribed into three levels, and successively coded, which was necessary due to the randomization of the experiments. The factor levels were coded as -1 (low), 0 (central point or middle) and 1 (high) (Montgomery, 2004). Three raw experimental data were applied to transform a real value (ξ_i) into a coded value (X_i) according to the following equation:

$$X_i = \left(\frac{\xi_i - \xi_i^0}{\Delta \xi_i} \right); \quad i=1,2,3,4 \quad (3.8)$$

where, X_i is the coded value of an independent variable; ξ_i is the actual value of an independent variable; ξ_i^0 is the actual value of an independent variable at the center point; and $\Delta \xi_i$ is the step change value of an independent variable. The process factors and factor levels of the emulsion stability are shown in Table 3.5.

Table 3.5: Levels and code of independent process variables chosen for BBD.

Variables	Factor	Coded Levels ($\hat{\alpha}$)		
		-1	0	1
Oil Concentration (v/v %)	A	10	30	50
Surfactant Concentration (w/v %)	B	0.1	1.05	2
Stirring Speed (rpm)	C	2000	4000	6000
Stirring Time (min)	D	5	12.5	20

The relationship between the response (Y) and input process parameters (X_k) is described as:

$$Y = \Pi(X_1, X_2, \dots, X_k) + \varepsilon \quad (3.9)$$

where Π is the real response function and ε is the residual error to describe the differentiation that can be included by the function Π . Data from the BBD were analyzed by multiple regressions to fit the following quadratic polynomial model:

$$Y = \alpha_0 + \sum_{i=1}^k \alpha_i \cdot X_i + \sum_{i=1}^k \alpha_{ii} \cdot X_{ii}^2 + \sum_{i < j}^k \sum_j^k \alpha_{ij} \cdot X_i \cdot X_j + \dots + \varepsilon \quad (3.10)$$

where, α_0 is the constant, α_i the slope or linear effect of the input factor X_i , α_{ii} the linear interaction effect between the input factor X_i and X_j , α_{ij} is the quadratic effect of input factor X_i and X_j , and ε is the statistical error (Montgomery, 2004).

The experimental design matrix, data analysis and optimization procedure were performed using the Design Expert[®] (V7.1.6, StatEase Inc., Minneapolis, USA) statistical package.

3.3.2 Artificial Neural Network (ANN)

A typical computational neural network consists of three layers such as input, hidden and output layers. Each layer comprises several operating neurons, which are related with each other by parallel connections. The strength of these interconnections is determined by the weight associated with them. For every ANN, the input layers constitute independent variables and the output layers constitute dependent variables. The hidden layers with multiple neurons exist between input and output layers as an interface to fully interconnect input and output layers. The pattern of hidden layer to be applied in the hierarchical network can be either multiple layers or a single layer. Each neuron sums all of the inputs that it receives and converts the sum into an output value based on a predefined activation, or transfer function (Soleimani et al., 2013). The connection between neurons in separate layers

is defined in terms of weights and biases as shown in Fig. 3.2. If W_j^i represents the weight connection from neuron i to neuron j , x_i is the input at neuron i , β_j is the bias of neuron j , then the activation at the j^{th} neuron (Ω_j) is given by

$$\Omega_j = \left(\sum_i W_j^i x_i \right) + \beta_j \quad (3.11)$$

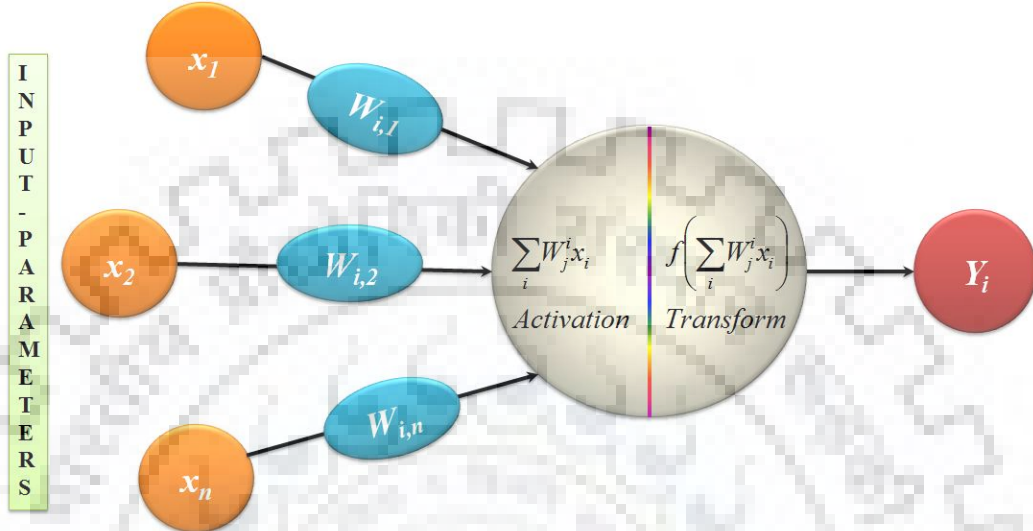


Fig. 3.2: Mechanism of an artificial neuron.

3.3.2.1 ANN model development

The universal approximation theory suggests that a network with a single hidden layer and with a sufficiently large number of neurons can interpret any input-output structure effectively (Prinderre et al., 1998; Pareek et al. 2002). Therefore, a single layer of hidden-neurons was used. The use of raw experimental data as the input causes convergence problem. Therefore, the data pre-processing is carried out and the data is normalized through min-max normalization technique using ‘PREMNMX’ function to make it in a range of $[-1, 1]$. This makes the neural network training more efficient. At the end of each algorithm, the outputs are denormalized back into the original data format to obtain the desired results.

The feed-forward network with error back-propagation algorithm (BP-ANN) was used for the development of the network. The input variables to feed forward neural network were same as those for BBD under RSM. ESI_{24} was taken as the experimental response or output variable. An optimum number of neurons were selected on the basis of MSE and SSE.

The optimized network parameters were determined on the basis of the MSE, SSE, R^2 and/or RPD obtained from a trial and error method, according to the following equations (Prinderre et al., 1998; Pareek et al., 2002):

$$MSE = \frac{\sum_{i=1}^{i=N} (y_{i,pred} - y_{i,exp})^2}{N} \quad (3.12)$$

$$SSE = \sum_{i=1}^n (y_{i,exp} - y_{m,exp})^2 \quad (3.13)$$

$$R^2 = 1 - \frac{\sum_{i=1}^N (y_{i,pred} - y_{i,exp})^2}{\sum_{i=1}^N (y_{i,exp} - y_{m,exp})^2} \quad (3.14)$$

$$RPD = \frac{100}{N} \sum_{i=1}^n \frac{|(y_{i,pred} - y_{i,exp})|}{|y_{i,exp}|} \quad (3.15)$$

where N is the number of data points, $y_{i,pred}$ is the network prediction, $y_{i,exp}$ is the experimental response, $y_{m,exp}$ is the average of the actual values, and i is the index of the data. The network having minimum MSE and maximum R^2 was selected as the best ANN model.

Sigmoid function was used for pattern recognition and to model the pattern (network), in which four parameters interact and determine the optimum stability. Hyperbolic tangent sigmoid function takes input from the entire domain of real numbers ($-\infty$ to $+\infty$) and returns an output between -1 and $+1$, which is differentiable, and neurons can only use a differentiable function. Thus, hyperbolic tangent sigmoid transfer function, $f(x)$, was used for hidden layer activation function:

$$f(x) = \tan sig(x) = \frac{2}{1 + e^{-2x}} - 1 \quad (3.16)$$

Linear function was used to predict the output, which is differentiable. Therefore, the output layer activation function was assumed to be a linear transfer function, i.e. $f(x) = x$.

3.3.2.2 Network training

The developed network was trained for function approximation using experimental data and resilient back-propagation (BP) algorithm as the underlying training framework. BP-ANN has the advantages of fast response and high learning accuracy (Soleimani et al., 2013). The superiority of a network function approach depends on the network architecture and parameters, number of data sets and the problem complexity (Maier and Dandy, 1998; Setoodeh et. al., 2012). Each neuron in the hidden layer is connected to each one in the input layer and also to each one in the output layer. Each of these connections has a distinct weight and bias (Fig. 3.2). All ANNs were trained by using the BP faster algorithm using standard numerical optimization (nonlinear regression) technique. In training the present network, a computational sequence was followed for the prediction of dependent variables from input to hidden layers and then from hidden to the output layer. The error value (computed from the

actual and predicted values of the dependent variables) was propagated backward (from output to hidden layers and then from hidden to input layer) in such a way that the new values of weights and the biases at the output and hidden layers could be established. During successive forward and backward computations with input–output data pairs, the resulting weights and the biases could be weighted in such a way that it can predict the correct values of output from an input data set. Levenberg–Marquardt (TRAINLM) algorithm was adopted for training the network. “Back-propagation trainlm (BP TRAINLM)” is a unique high performance algorithm that can converge from one to two orders of magnitude faster than the traditional BP algorithms (gradient descent, and gradient descent with momentum) (Hagan and Menhaj, 1994; Setoodeh et. al., 2012). The prime goal of training was to minimize MSE by searching for a set of connection weights and biases that caused the ANN to produce outputs, which were in the close proximity of target values. To assess the generalization of the selected BP-ANN model, it was run on a series of experimental data for different conditions. In order to study the effect of number of the data sets, the ANN was also trained, verified and tested with 120 data sets. The criteria for MSE, RPD and R^2 were used to assess the predictability of the ANN model. The ANN model was developed to the desired level of precision. It was used in the following section for finding the optimal process conditions resulting in the maximum possible emulsion stability.

3.3.3 Genetic Algorithm (GA)

GA is essentially an iterative, population based, parallel global search algorithm that is widely used for solving optimization and approximation problems in a high dimensional space (Goldberg, 1989; Fogel, 1994). GA was constructed according to the following sequence of operations: encoding, fitness evaluation, selection, and genetic operations (reproduction, crossover and mutation) for each generation. A population of individuals was maintained at each generation in which each individual represents a possible solution to the problem. A fitness (or objective) function was used to determine the fitness of each candidate solution and the individuals with higher fitness values were selected. These individuals form pairs called parents. The selection policy employed herein is a combination of the rotating roulette wheel strategy and the elite strategy. The elite strategy can force the best surviving chromosomes of the current generation in the next generation. The selected chromosomes were undergoing genetic transformation by genetic operators such as crossover and mutation. Crossover is the main operator used for reproduction and it randomly combines two parent chromosomes to create two new individuals, called ‘off spring’. The mutation operator randomly selects one individual from the parent population and changes its internal

representation, and puts it in the child population (Izadifar and Zolghadri, 2007). The individual process parameters (A, B, C, and D) were selected as the parent chromosomes for GA, which were undergoing genetic simulations. For initializing the GA simulation, BP-ANN network generated data were employed as initial population. The GA repeatedly modified a population of individual solutions. At each step, the GA selected individuals at random from the current population to be parents and used them to produce children for the next generation. Over successive generations, the population evolved toward an optimal solution. GA was used to determine the maximum emulsion stability at optimized conditions. In the present study, the optimization toolbox (GAOT) in MATLAB 7.6[®] (Mathworks Inc, Natick, US) for genetic algorithm (GA) interface was used to search the optimal conditions.

3.3.4 Integrated Modeling

An integrated modeling approach was followed to effectively optimize the process parameters for emulsion stability under multi-response consideration. The proposed approach integrates BBD method, BP-ANN and GA optimization concepts. BBD used an orthogonal array to statistically arrange the experimental programme and reduce the number of experiments. The optimized data from BBD were applied for the generation of BP-ANN network. This network was effectively trained and tested by additional 120 experiments to map the relationship between the input control process parameters and the output responses. BBD model equation was used as a fitness function and BP-ANN data were employed as the initial population for GA to search for the optimal initial process parameter settings. Finally, confirmatory experiments were performed for the optimal process parameter settings.

3.4 POROUS MEDIA

3.4.1 Glass Beads as Porous Packing Materials

The porous bed was made up of glass column packed with uniform size spherical glass beads. A porous bed core holder was fabricated by a plexi glass column of 37 mm of diameter and 200 mm of length. Details of the porous bed and the particles used are given in Table 3.6. A calming section (100 mm) below the test section and an exit section (100 mm) above the test section were provided to avoid the entrance and exit effects. Each section was joined together through flanges made from the acrylic sheet and PVC gasket to avoid any leakage. Core holder was packed with spherical glass beads to measure the pressure loss for flow through porous beds of spherical particles.

The porosity (bed voidage) of the bed was estimated by measuring the volume of water needed to fill the void space for a known weight of packing in a tube of the same diameter as

the packed bed. The average of triplicate measurements which were within $\pm 2\%$ of the mean value, were used in the calculations. The average values of the porosities were: 0.4174, 0.3696, 0.3478 and 0.3913 and details are shown in Table 3.6.

Table 3.6: Porous bed and particles details.

Porous bed characteristics	Dimensions			
Bed diameter D_C , (mm)	37			
Bed height L , (mm)	200			
Porous bed	PM-1	PM-2	PM-3	PM-4
Diameter of particle, D_p (mm)	2.5	3.5	5.0	3.25
Bed type	Homogeneous, Isotropic	Homogeneous, Isotropic	Homogeneous, Isotropic	Mixed, Non-isotropic
Sphericity of glass beads, ϕ_s	1	1	1	1
Bed porosity, ϕ	0.4174	0.3696	0.3478	0.3913
Bulk density of bed (kg/m^3)	2423.1	2422.0	2323.3	2371.3
Characteristic coefficients of particles				
Ω	71.26	55.21	49.55	96.67
ω	1.199	0.615	0.580	1.038

After characterizing the porous bed, emulsion flow experiments were performed with the same experimental set up. Glass beads were cleaned to reproducibly renew their surface. Glass beads were soaked for 24 hr in concentrated chromic acid, followed by washing with distilled water in several times. Next, the beads were dried at 100 °C followed by acetone rinsed, and again air dried to hot air oven drying at 100°C for 2-3 hr. Dry beads were then stored in sealed polyethylene containers for subsequent experiments.

All experimental and predicted values were compared in terms of mean relative quadratic error (M.R.Q.E) which is defined as below:

$$M.R.Q.E = \left[\frac{\sum \left(\frac{\text{Experimental value} - \text{predicted value}}{\text{Experimental value}} \right)^2}{(\text{Number of experimental value} - 1)} \right]^{\frac{1}{2}} \quad (3.17)$$

The lower value of M.R.Q.E. indicates a better fit of the experimental data to the model prediction.

3.4.2 Sand-pack Core Holder Details and Sand-pack Preparation

Fig. 3.3 shows the sand-pack core holder used for all emulsion flow tests. The core holder was segmented into different parts i.e., middle core section of which contains the porous media, upper and lower end caps, two distributors and two synthetic rubber O-rings.

The core holder was made of a stainless-steel pipe section with an internal diameter (ID) of 45 mm, wall thickness of 15 mm and a total length of 186 mm. The distributors were equipped with a very fine screen to prevent sand production, and the O-rings offered a tight seal on both ends. Three major steps involved in preparing each porous medium included seizing the sand, packing the core holder, and determining properties of the porous medium.

First, the silica sand was classified into three categories, namely, S-A, S-B, and S-C, each having different particle size range: 180-212, 250-355, and 425-500 μm , respectively. The sieving process was done using a mechanical sieve shaker (Metrex, India) with different sieves sizing from 150 μm to 500 μm . Sieved sand particles were first washed by tap water in repeated manner. Then it was rinsed with distilled water in several times. Next the sand was treated with concentrated hydrochloric acid (12N HCl) and soaked for 24 hr. The sand was then decanted from the acid solution and rinsed several times with distilled water until the wash solution become clear. Finally, sand particles were dried in the hot air-oven at 100 °C and dried sand particles were stored in sealed polyethylene containers for use in experiments.

The porous bed was prepared to pack the core holder with fresh dried clean sand particles at the ambient temperature of 30 °C. The core holder was packed with sand particles by "tap-and-fill" method. The porous bed was compacted with a packing rod.

When the bed is fully packed, the porous medium fills the space between the two screens at the ends of the test section. The pore volume of the dry porous medium is then filled with liquid supplied from a burette to determine the porosity as the ratio of the required volume of liquid divided by the total volume of the bed. The same procedure is repeated several times for each medium and the mean value taken to represent the porosity of the medium. The properties of the packing materials and of the investigated fluids are given in Table 3.7. For each test, fresh sand was packed into the core holder to ensure the same wettability of particles for all tests.

Table 3.7: Physical properties of core holder packing materials.

Sand particle	Particle size range, μm	Mean particle diameter, μm	Porosity (ϕ)	Pore volume PV (ml)	Permeability (10^{-11}m^2)	Bulk density (ρ_b) kg/m^3
S-A	180-212	196	0.429	90	3.717	1573
S-B	250-355	303	0.444	96	6.002	1519
S-C	425-500	463	0.445	98	9.690	1505

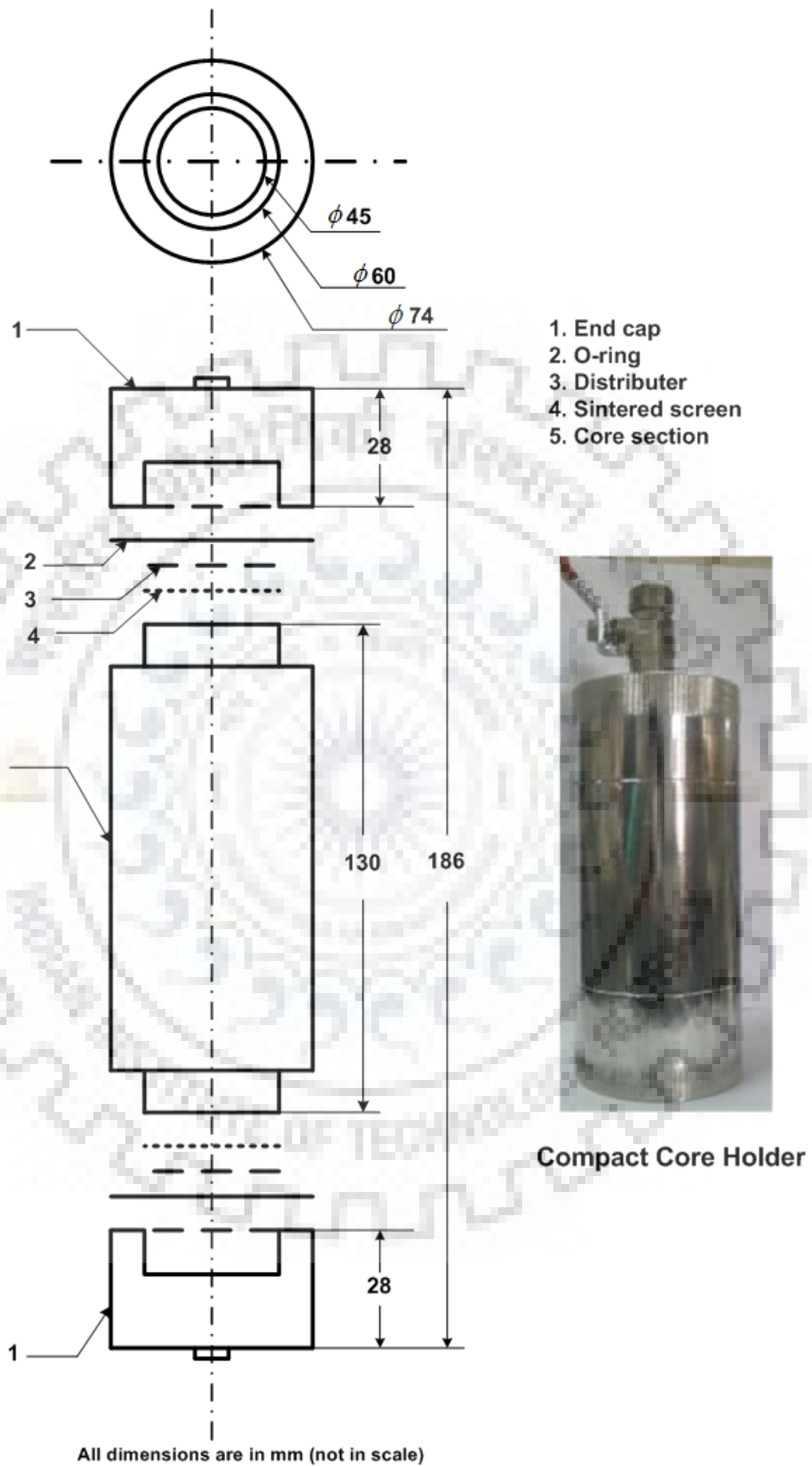


Fig. 3.3: Design of the stainless-steel sand-pack core holder.

3.5 FLOW EXPERIMENTAL SET UP AND PROCEDURES

The plexi glass column was tightly packed by conventional tap filling method. Three kinds of mean uniform particle sizes (i.e. 2.5 mm, 3.5 mm, and 5 mm) and mixed particle (combination of all three particles) mixture were selected to examine the flow characteristics under incompressible Newtonian laminar flow conditions. Thereafter non-Newtonian emulsion was passed through the porous media. A schematic diagram of the experimental set-up is shown in Fig. 3.4. Distilled water was used as the incompressible test liquid which was circulated through the porous bed using a peristaltic pump by pumping water from a reservoir situated above the porous bed section. Water flows from the bottom to the top to ensure the absence of any dead volume and channeling of the flow through the porous bed. A pair of pressure tap was drilled just above and below the porous bed. Pressure drop across the bed for different flow rate was measured using U-tube manometers with carbon tetrachloride (CCl₄) and mercury (Hg) as the manometric fluid.

For sand-pack core holder similar experimental set up (Fig. 3.3) was used and plexi glass column was replaced by stainless steel sand-pack test section. After measuring the physical characteristics of sand-pack core holder, the distilled water was first circulated through the core holder in all the runs to saturate the core with water so as to replicate a water wet core condition. Then core was equilibrated by flashing 30 pore volume of water at the same ionic strength and pH as that of the experiment to be performed. After equilibration, emulsions were started injecting into the core at constant flow rate using a peristaltic pump. The flow rate is maintained till the steady and constant pressure drop attained across the core holder. The pressure differential across the porous bed was measured by manometer. Samples were collected both inlet and outlet section to analyzed the drop size distribution. Once a constant pressure differential is obtained, flow rate is increased in next steps and flow rate maintained till a steady pressure is obtained. At each flow rate steps, samples were collected periodically to observe the droplet size distribution in relation to the original sample. Prior to running the experiment, care must be taken to ensure that all the pipe connections are fitted properly to prevent any fluid leaks and pressure losses.

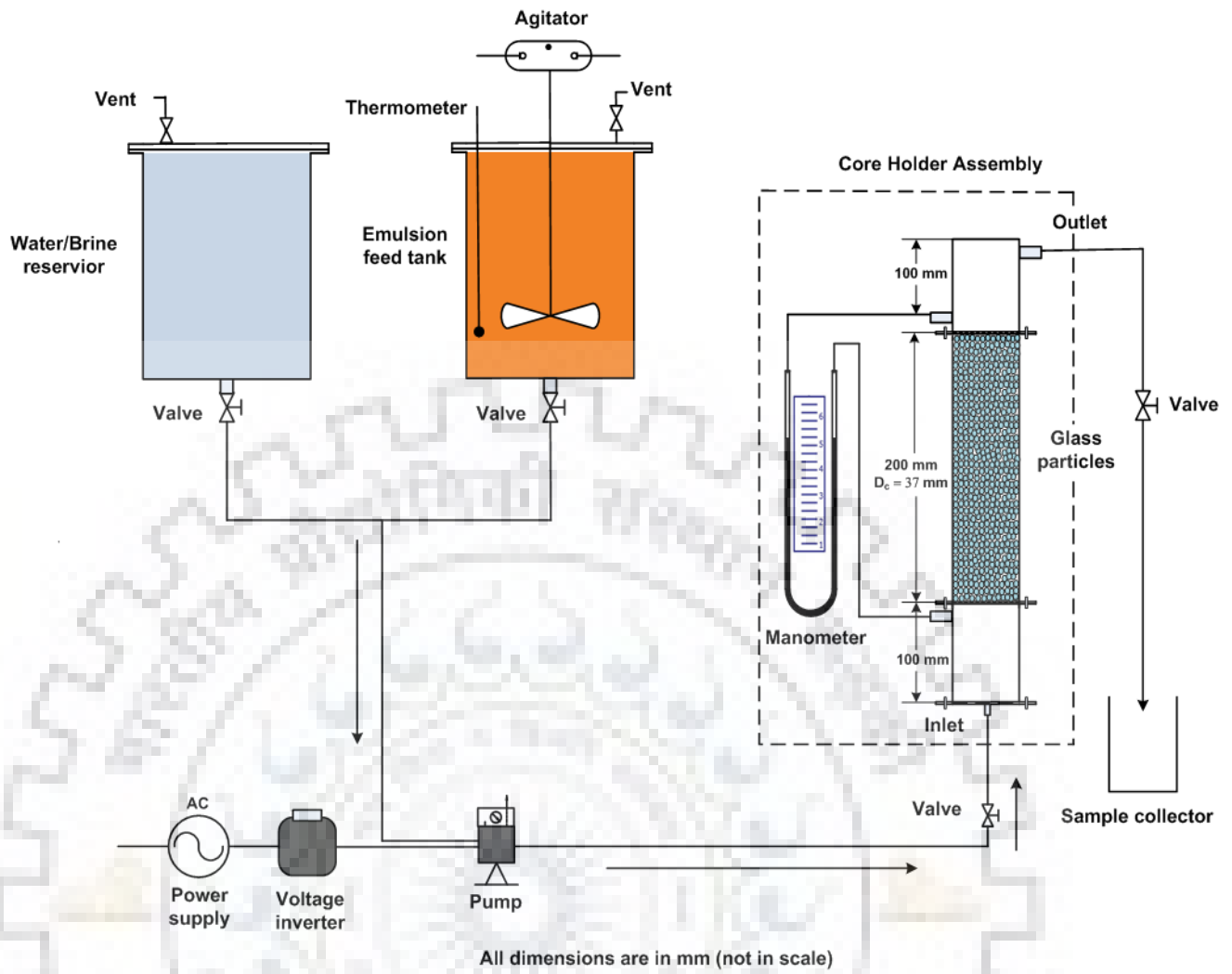


Fig. 3.4: Schematic diagram of experimental set-up.

CHAPTER 4

STABILITY AND RHEOLOGICAL BEHAVIOUR OF OIL-IN-WATER (O/W) EMULSIONS

In this chapter, the formation and stability of oil-in-water emulsion was studied using mathematical and statistical approach. An integrated hybrid genetic algorithm (GA) coupled with feed-forward back-propagation artificial neural network (BPANN) and response surface methodology (RSM) based on Box–Behnken design (BBD) was adopted for optimization of input parameters. A detailed experimental finding for emulsion stability and rheological behavior of emulsions are discussed. The input parameters considered for the optimization of emulsion stability were oil concentration, surfactant concentration, stirring speed and stirring time and the output parameter was relative emulsion volume expressed as emulsion stability index (ESI_{24}). Sections 4.2 and 4.3 are dedicated to statistical modeling of emulsion formation and stability and rheology of emulsions is reported in section 4.4.

4.1 STATISTICAL MODELLING OF EMULSION FORMULATION AND STABILITY AND OPTIMIZATION OF PROCESS PARAMETERS

A synchronized approach has been adopted in the present work. The significant parameters influencing the emulsification process and emulsion stability were identified and experiments were designed according to four levels of BBD matrix under RSM to find out the actual response (ESI_{24}). Based on statistical analysis (analysis of variance (ANOVA)), a model was developed for predicting maximum emulsion stability and the model predictions were then compared with the actual experimental response. Thereafter optimization of process parameters was done using a newly developed hybrid ANN-GA framework assisted by RSM-BBD.

4.1.1 RSM Modeling

A three level-four factor BBD was employed to determine the simple and combined effects of four operating variables on the emulsion stability. The variation in emulsion stability (ESI_{24}) under different conditions is presented in Table 4.1. Linear and second order polynomials were fitted to the experimental data to obtain the regression equations. The sequential F-test, lack-of-fit test and other adequacy measures were used in selecting the best model.

Table 4.1: A 3^4 Box Behnken design (BBD) Matrix with the experimental and predicted responses of emulsion stability (ESI_{24}).

Standard run order	A: Oil Conc. (v/v %)	B: Surfactant Conc. (w/v %)	C: Stirring Speed (rpm)	D: Stirring Time (min)	Response (Y), ESI_{24}		Error, ϵ
					$Y_{experimental}$	$Y_{predicted}$	
1	-1	-1	0	0	0.121	0.126	-0.005
2	1	-1	0	0	0.072	0.133	-0.061
3	-1	1	0	0	0.196	0.157	0.040
4	1	1	0	0	0.781	0.797	-0.016
5	0	0	-1	-1	0.372	0.326	0.046
6	0	0	1	-1	0.382	0.450	-0.068
7	0	0	-1	1	0.466	0.419	0.047
8	0	0	1	1	0.069	0.136	-0.067
9	-1	0	0	-1	0.120	0.083	0.037
10	1	0	0	-1	0.704	0.665	0.039
11	-1	0	0	1	0.168	0.232	-0.063
12	1	0	0	1	0.235	0.296	-0.061
13	0	-1	-1	0	0.162	0.183	-0.021
14	0	1	-1	0	0.475	0.530	-0.055
15	0	-1	1	0	0.132	0.104	0.029
16	0	1	1	0	0.450	0.451	-0.001
17	-1	0	-1	0	0.144	0.203	-0.059
18	1	0	-1	0	0.570	0.527	0.043
19	-1	0	1	0	0.175	0.124	0.051
20	1	0	1	0	0.504	0.447	0.056
21	0	-1	0	-1	0.165	0.192	-0.027
22	0	1	0	-1	0.512	0.539	-0.027
23	0	-1	0	1	0.168	0.082	0.086
24	0	1	0	1	0.488	0.429	0.059
25	0	0	0	0	0.481	0.476	0.005
26	0	0	0	0	0.489	0.476	0.005
27	0	0	0	0	0.466	0.476	-0.010
28	0	0	0	0	0.468	0.476	-0.008
29	0	0	0	0	0.475	0.476	-0.001

Statistical testing of various models was performed with the analysis of variance (ANOVA) to investigate and predict the desired model and to identify the significant factors. The ANOVA results are shown in Table 4.2. The $F_{Statistics}$ and p values were used in the analysis to test the significance level of the regression model and also for each coefficient, which indicated the interaction effects between each independent variable. The F-value of 27.8 implies that the model is significant. There is only a 0.01% chance that an “F-value” could be large due to noise. If $p > F$ -value is less than 0.05, the model is considered to be statistically significant. From Table 5, it can be seen that the coded parameters A, B, C, D, A^2 , B^2 , C^2 , D^2 and AB, AD, CD are significant parameters, i.e. $(p > F) < 0.05$. The higher value of correlation coefficient (R^2) showed the desirability of the model to describe the relationship between variables. The value of R^2 was 0.9474 indicated that only 5.26% of the total variation could not be explained by the empirical model. Further, $Adj-R^2$ and coefficient of variation (CV) were estimated to check the model adequacy. A higher $adj-R^2$ demonstrated that non-significant terms were not included in the model. Generally, a low CV shows that the variation in the mean value is low and that a satisfactory and adequate response model can be developed. For the present model, $Adj R^2$ was 0.9133 and CV was 16.92. The high $Adj R^2$ (nearer to 1.0) and the low CV values for the proposed model indicated the precision and reliability of the experimental runs. Adequate precision (Adeq) measures the signal-to-noise ratio (S/N); with a ratio greater than 4 being desirable. For the proposed model, Adeq was ~ 19, i.e. a very good S/N ratio (Table 4.2). The comparison between predicted and actual values for the response variables also indicated that the proposed quadratic regression models were suitable to determine optimum formulation for preparing o/w emulsions with maximum physical stability, as shown in Fig. 4.1.

The adequate model for the emulsion stability was selected by Fisher’s F-value and the probability value ($p < 0.05$) along with a correlation coefficient (R^2). The linear, 2FI and quadratic models were suggested by the analysis of data reported in Table 4.3. However, a higher order model was selected. The fit summary statistics (Table 4.3) indicated that the quadratic model is statistically highly significant ($R^2 = 0.9497$). Fig. 5 confirmed the adequacy of the model in predicting the precise values. The following polynomial model for the stability of the o/w emulsion was used to correlate the dependent and independent variables (in terms of coded factors) within confidence interval, $CI > 95\%$:

$$Y = (ESI_{24})^{1.04} = 0.48 + 0.16A + 0.17B - 0.040C - 0.055D - 0.082A^2 - 0.091B^2 - 0.068C^2 - 0.075D^2 + 0.16AB - 0.13AD - 0.10CD \quad (4.1)$$

Model equation in terms of actual factors (units):

$$\begin{aligned}
 (ESI_{24})^{1.04} = & -0.9661 + 0.0225 \text{ Oil Concentration} + 0.1435 \text{ Surfactant Concentration} \\
 & + 2.0196 \times 10^{-04} \text{ Stirring Speed} + 0.079 \text{ Stirring Time} \\
 & - 2.0581 \times 10^{-04} (\text{Oil Concentration})^2 - 0.1003 (\text{Surfactant Concentration})^2 \\
 & - 1.712 \times 10^{-08} (\text{Stirring Speed})^2 - 1.332 \times 10^{-03} (\text{Stirring Time})^2 \\
 & + 8.325 \times 10^{-03} (\text{Oil Concentration} \times \text{Surfactant Concentration}) \\
 & - 8.636 \times 10^{-04} (\text{Oil Concentration} \times \text{Stirring Time}) \\
 & - 6.793 \times 10^{-06} (\text{Stirring Speed} \times \text{Stirring Time})
 \end{aligned} \tag{4.2}$$

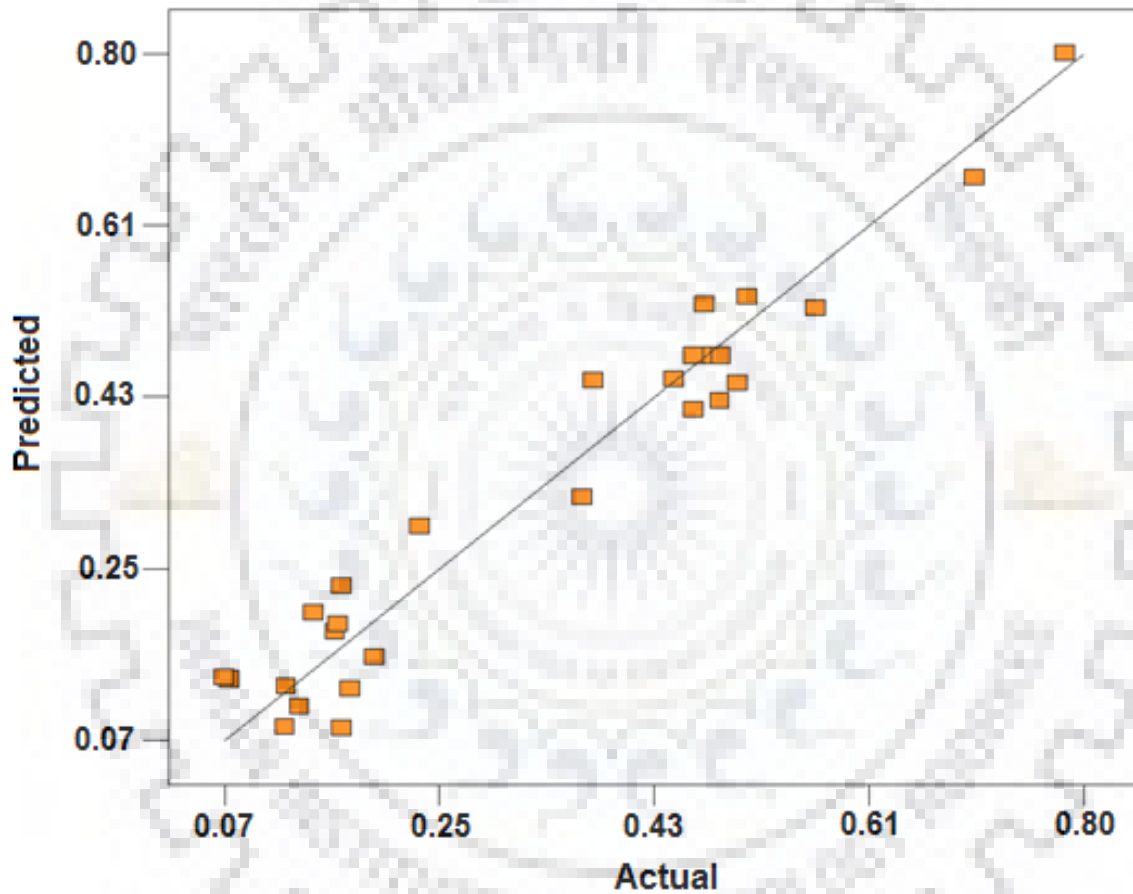


Fig. 4.1: Experimental results and Predicted responses of emulsion stability analysis.

Table 4.2: Analysis of variances (ANOVA) results for the RSM-BBD model.

Source	Sum of Squares	DF	Mean Square	F Value	Prob> F	Remark
Model	1.0447	11	0.0950	27.8299	< 0.0001	Highly significant
A- oil concentration	0.3140	1	0.3140	92.0193	< 0.0001	Highly significant
B- Surfactant concentration	0.3609	1	0.3609	105.7660	< 0.0001	Highly significant
C- stirring speed	0.0190	1	0.0190	5.5729	0.0304	Significant
D- Stirring time	0.0364	1	0.0364	10.6541	0.0046	Significant
A ²	0.0440	1	0.0440	12.8820	0.0023	Highly significant
B ²	0.0532	1	0.0532	15.5823	0.0010	Highly significant
C ²	0.0304	1	0.0304	8.9134	0.0083	Significant
D ²	0.0364	1	0.0364	10.6655	0.0046	Significant
AB	0.1001	1	0.1001	29.3233	< 0.0001	Highly significant
AD	0.0671	1	0.0671	19.6686	0.0004	Highly significant
CD	0.0415	1	0.0415	12.1694	0.0028	Highly significant
Residual	0.0580	17	0.0034	-	-	-
Pure Error	0.0004	4	0.0001	-	-	-
Cor Total	1.1027	28	-	-	-	-
Model statistics						
R ²	0.9474		Adeq Precision	19.010		
Adj R ²	0.9133		PRESS	0.23		
Pre R ²	0.7870		C.V.	16.920		
Std. Dev.	0.058					

Table 4.3: Selection of adequate model for optimization of emulsion stability process parameters.

Source	Sum of Squares	DF	Mean Square	F Value	Prob> F	Remark
Sequential Model Sum of Squares						
Mean	3.4548	1	3.4548	-	-	-
Linear	0.7303	4	0.1826	11.7679	< 0.0001	Suggested
2FI	0.2112	6	0.0352	3.9333	0.0109	Suggested
Quadratic	0.1056	4	0.0264	6.6638	0.0032	Suggested
Cubic	0.0489	8	0.0061	5.5761	0.0253	Not recommended
Residual	0.0066	6	0.0011	-	-	-
Total	4.5575	29	0.1572	-	-	-
Model Summary Statistics						
Source	Std. Dev.	R^2	Adj. R^2	Pre R^2	PRESS	Remark
Linear	0.1246	0.6623	0.6060	0.5094	0.5410	-
2FI	0.0946	0.8539	0.7727	0.6902	0.3416	-
Quadratic	0.0630	0.9497	0.8994	0.7116	0.3180	Suggested
Cubic	0.0331	0.9940	0.9722	0.1883	0.8950	Not recommended

4.1.2 BP-ANN Modeling

A total of 120 experimental data sets were used to feed the ANN structure (Appendix B, Table B1). These experimental data sets were apportioned into training (60 % of data sets), validation (20 %) and testing (20 %) subsets that contained 72, 30, and 18 experimental data sets, respectively, to improve the accuracy of the model by eliminating the errors. In the present study, 4 neurons in the input layer, 24 neurons in the hidden layers and 1 neuron in the output layer (Fig. 4.2), were used. Thus, the ANN architecture is 4-24-1. A fully connected three-layer BP-ANN with the input, hidden, and output layers is shown in Fig. 4.2.

In order to determine the optimum number of hidden neurons, a series of computations were performed, in which the number of neurons were varied from 1 to 30. An optimum number of neurons present in the hidden layer which ensure that there is no over-fitting of the experimental data were selected on the basis of MSE and SSE as shown in Table 4.4. A total of 24 neurons were used in the hidden layer.

The variation of MSE of training, validation and testing data set with respect to the epoch (i.e. the number of cycles the network is presented with a new input pattern) is shown in Fig. 4.3. The MSE decreases very rapidly in the beginning, and the reduction rate slows down with an increase in the number of epochs, finally reaching a saturation point. The validation data set was used to stop the training process in early stopping criteria for providing better generalization. Fig. 4.3 shows that the validation error (MSE) is minimum at epoch 6. Therefore, the training was stopped at this point and the weights and biases were used to model ESI_{24} . The associated network weights and biases were used for generating BP-ANN model, which were further used in GA is shown in Table 4.5.

The correlation coefficient between the target (experimental value) and output (ANN output) of training, validation and testing is shown in Fig. 4.4. The ANN training was done for 1000 iterations for the best fit values using a feed forward scaled conjugate algorithm and the resilient BP algorithm which reduced the training iterations significantly. The training data indicate a very good fit ($R=0.9975$). However, a global regression correlation coefficient value (R) of 0.8123 was obtained (Fig. 4.4) between the ANN-simulated output values and the actual experimental values, signifying the model with not very good predictive power. Scattered data points indicate that non-linear parametric relationships are involved in the formation of these emulsions. The regression correlation coefficient of 0.9975 for training and 0.8123 for the overall model (Fig. 4.4) between the ANN-simulated output and the actual experimental data were obtained. These regression values concluded that there is satisfactory agreement between the experimental data points and the proposed model fit.

Table 4.4: Determination of optimum number of neurons for hidden layer in BP-ANN.

No. of neurons in the hidden layer	SSE*	MSE**	RPD***
1	1.4139	0.0196	42.4
2	0.8025	0.0111	41.9
3	0.8402	0.0117	44.7
4	0.3538	0.0049	26.6
5	0.3449	0.0048	32.6
6	0.5720	0.0079	33.1
7	1.0723	0.0149	41.7
8	0.5046	0.0070	30.9
9	0.9160	0.0127	42.0
10	0.4129	0.0057	27.6
11	0.8332	0.0116	39.2
12	0.8715	0.0121	17.3
13	0.6131	0.0085	31.9
14	1.1280	0.0157	30.1
15	0.3483	0.0048	19.8
16	0.4762	0.0066	29.9
17	0.2542	0.0035	22.8
18	0.4960	0.0069	35.5
19	0.6590	0.0092	36.5
20	0.4226	0.0059	28.1
21	0.1962	0.0027	16.6
22	0.8983	0.0125	35.6
23	0.3565	0.0050	20.9
24	0.1372	0.0019	11.7
25	0.6761	0.0094	31.3
26	2.5050	0.0348	64.1
27	0.4019	0.0056	17.4
28	1.7419	0.0242	60.3
29	0.3679	0.0051	31.1
30	0.8353	0.0116	22.8

*SSE = Sum of square error; ** MSE = Mean of square error; ***RPD = Relative percent deviation.

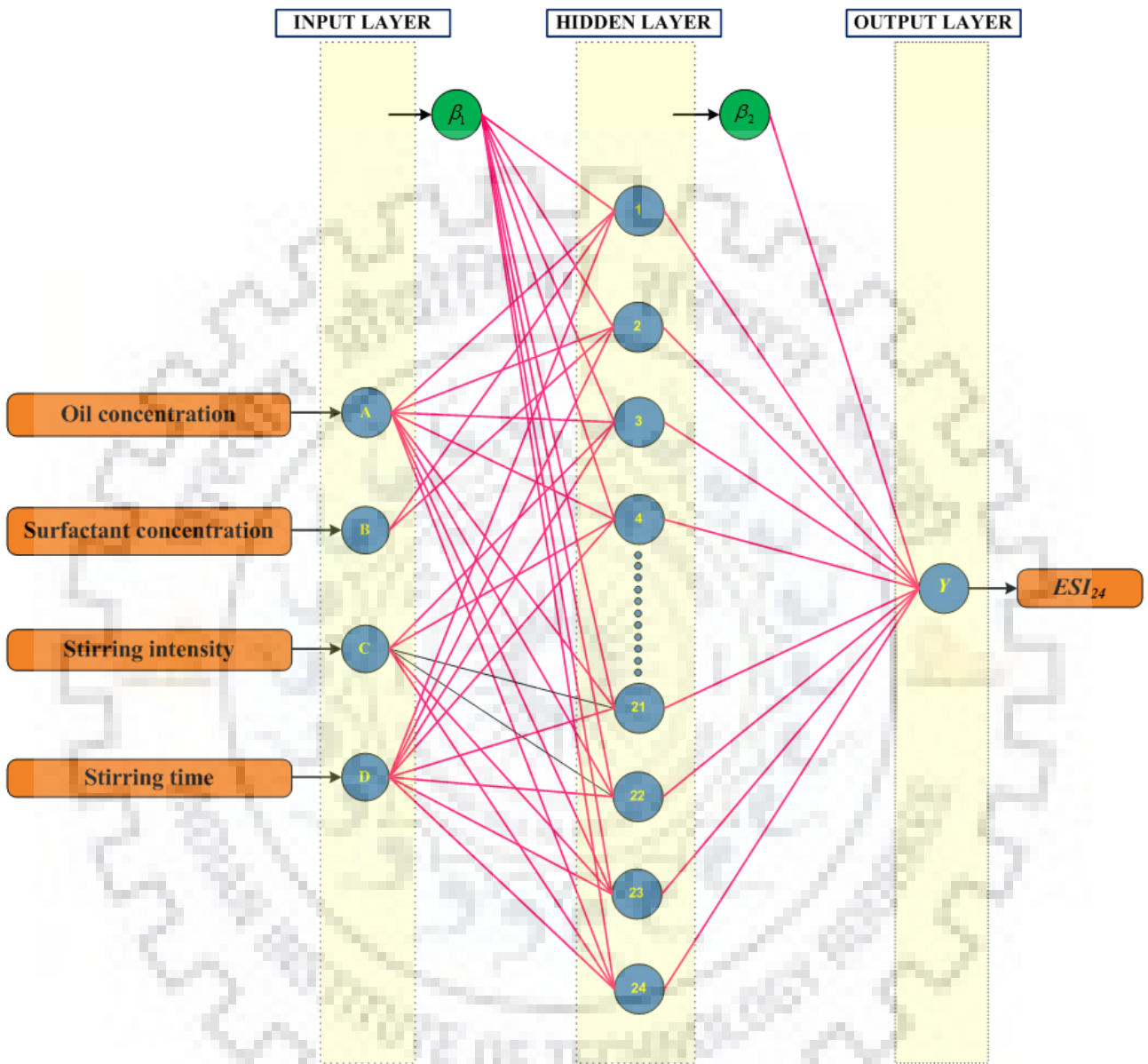


Fig. 4.2: Pattern of optimized ANN architecture (4-24-1).

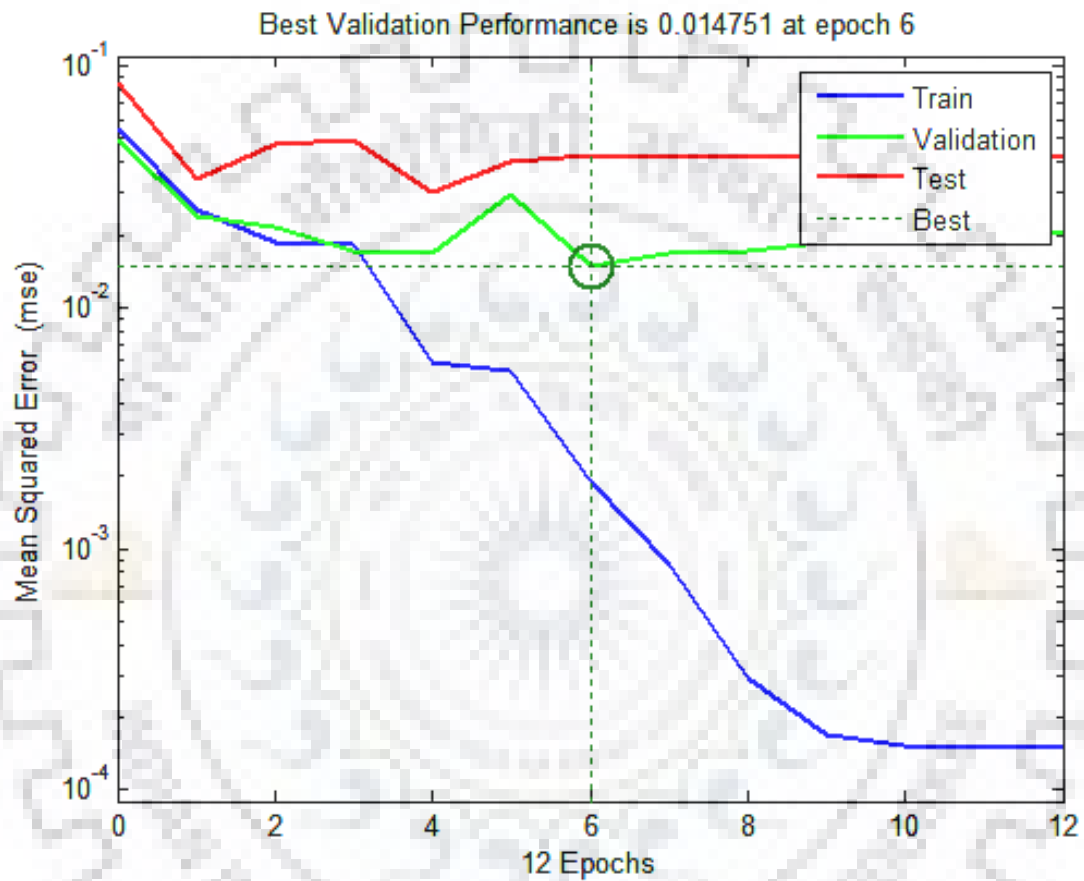


Fig. 4.3: The performance of the BP-ANN model (4-26-1) in the training phase showing performance value (MSE- 0.014751) after 6 epochs.

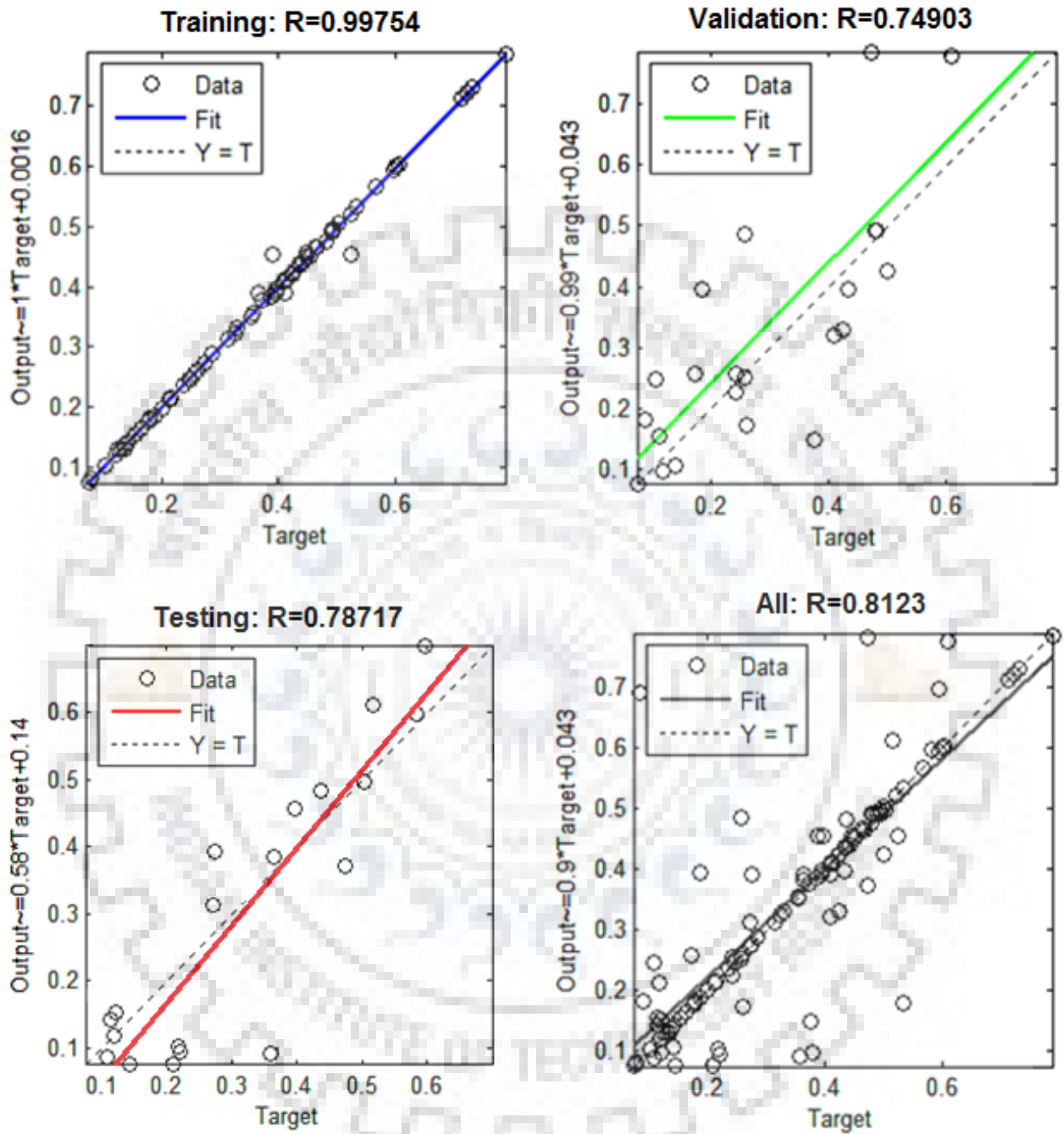


Fig. 4.4: Regression plot showing regression coefficient of experimental data and BP-ANN (4-24-1) model simulated values.

Table 4.5: Network weights and biases for BP-ANN model.

Neuron no.	Weights from input layers to hidden layers				Bias to hidden layers	Weights from hidden layers to output layers	Bias to output layers
	A:	B:	C:	D:			
	Oil Concentration	Surfactant Concentration	Stirring Speed	Stirring Time			
1	-1.1257	2.1398	3.7060	0.8470	2.2442	0.2841	
2	2.2821	1.2000	-1.5587	-0.6192	-2.8097	0.6445	
3	2.3110	0.3994	1.1309	-1.7821	-2.8616	1.0125	
4	-1.7211	-0.7713	1.5979	-2.5585	1.9393	-0.2174	
5	0.8582	0.4652	-3.3252	0.7471	-1.4605	0.0559	
6	1.9062	-0.2080	-2.8216	-2.2559	-1.9145	-0.9933	
7	0.9966	-0.1734	-2.4875	-1.9653	-1.2082	1.4229	
8	0.5570	-2.1592	2.3924	0.9110	1.7392	-0.0234	
9	1.9111	0.6332	-1.9769	1.4253	0.5915	0.0685	
10	-1.9962	0.6479	1.0797	0.1140	1.7175	0.8235	
11	-0.6826	2.7577	-0.3466	1.7228	-1.1971	0.3846	
12	0.1628	1.8386	1.1104	-2.6044	0.0965	0.1558	
13	-1.9451	-3.0334	-0.8859	-1.4257	0.0700	0.3855	1.0235
14	0.4749	0.9029	-2.1286	-2.2904	0.5862	0.1146	
15	0.8540	-1.7570	-2.6914	0.9351	-0.3475	0.2085	
16	-1.0599	-2.8120	2.0560	-1.0711	-1.7215	-0.8983	
17	0.0172	-2.8595	0.0241	-0.4856	-1.3963	0.3112	
18	-2.3689	-2.4126	1.0343	0.8641	-1.4886	-0.8574	
19	0.4027	-1.6645	0.6760	2.4744	1.6631	0.7024	
20	2.2570	0.8435	-2.0088	0.8680	2.1602	-0.2165	
21	-1.4654	-0.5637	1.9730	-1.6874	-2.2184	0.3447	
22	-3.3087	-1.6882	0.9718	0.8884	-2.5184	0.8774	
23	-2.6290	-0.3691	-1.9320	0.8932	-2.6429	-0.7018	
24	2.3235	-1.8168	0.5767	0.0854	2.6037	1.3169	

4.1.3 Multi Objective Hybrid GA Optimization Model

A hybrid multi objective optimization approach was adopted for optimizing emulsion stability process parameters. Fig. 4.5 illustrates the flow chart for the operation of the proposed hybrid GA to optimize the proposed problem. The RSM regression model, Eq. (4.1), was taken as the optimization objective function or fitness function and the BP-ANN network data were used as an initial population. The minimum and maximum process parameter values of the experimental design were used to define the GA optimization constraints as follows:

$$\left. \begin{array}{l} 10 \leq A \leq 50 \\ 0.1 \leq B \leq 2 \\ 2000 \leq C \leq 6000 \\ 5 \leq D \leq 20 \end{array} \right\} \quad (4.3)$$

Before proceeding for the optimization of the emulsion stability parameters, the GA parameters, i.e. numbers of generations (N_g), cross-over rate (C_r) and mutation fraction (M_f) were selected by trial and error. These values were taken as the optimum simulation criteria of hybrid GA algorithm for the development of the hybrid GA model, as shown in Table 4.6. The weighted average change in the fitness function value over 200 generations was used as the criteria for stopping the algorithm.

Table 4.6: Criteria of hybrid GA simulation leading to the optimal solution.

Parameters	Function type / values
Population size	72
Scaling function	Rank
Selection Function	Roulette wheel
Crossover Function	Heuristic
Crossover rate (C_r)	0.8
Mutation Function	Adaptive feasible
Direction for migration	Forward
Migration fraction (M_f)	0.2
Generation (N_g)	100

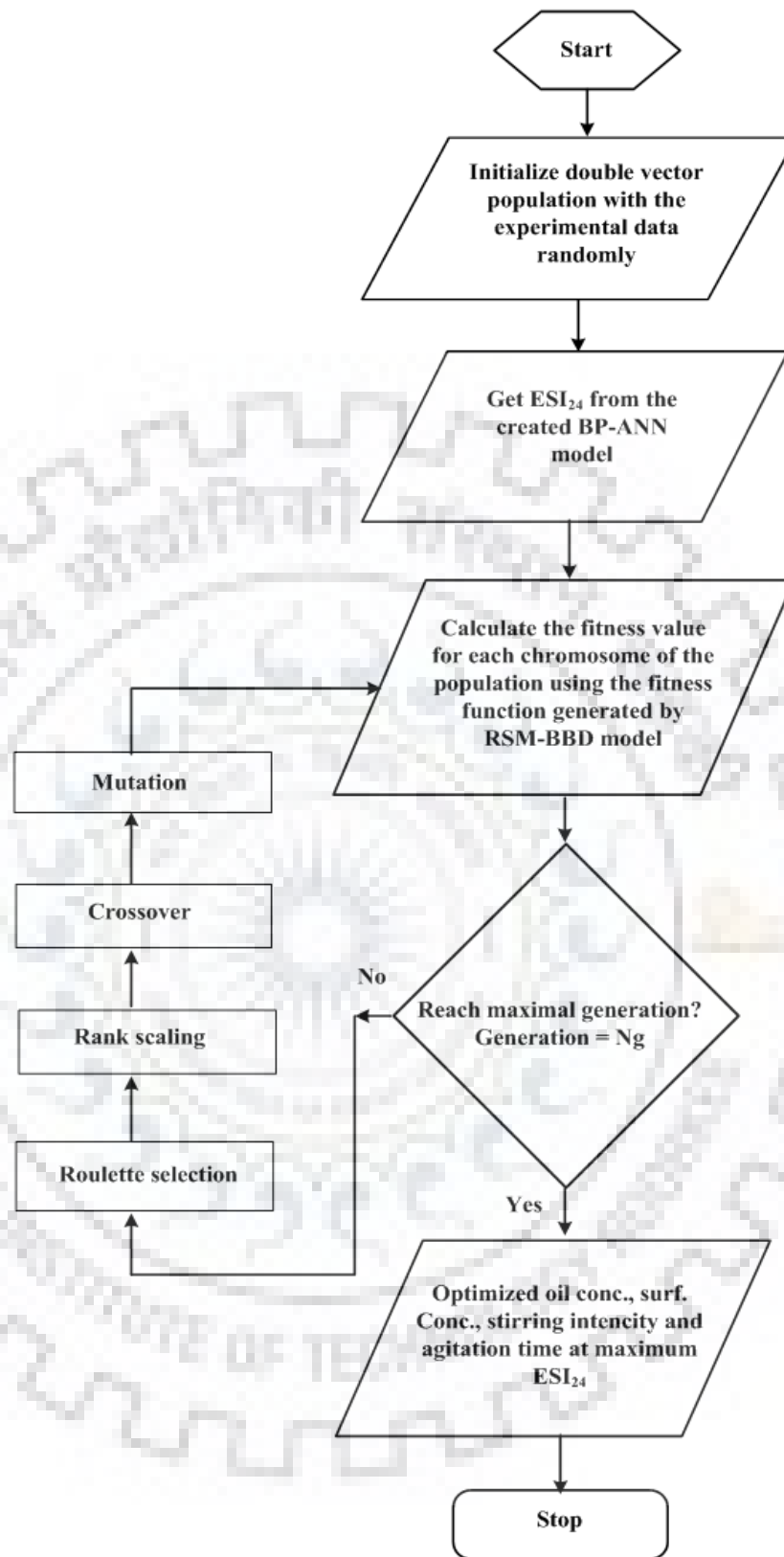


Fig. 4.5: Algorithm for hybrid GA (GA coupled with BP-ANN and RSM-BBD) to optimize the emulsion stability process parameters.

In the present study, 29 experimental data sets were used for the RSM-BBD model, and 120 experimental data sets were used for the Hybrid ANN-GA model. These models were compared and validated by performing confirmatory experiments (in triplicate) at the predicted optimal parametric conditions. The deviation between the predicted results from the hybrid GA and the BBD models and the averaged values of the experimental data are also shown in Table 4.7. It was observed that the optimal process parameter values, which lead to the maximum ESI_{24} value of 0.913, were: 50% (v/v) oil concentration, 2% (w/v) surfactant concentration, 5691 rpm stirring speed and 5 min stirring time. The optimal solution was obtained at the 100th generation. The best fitness value of the hybrid GA model, 1.0952 and the mean fitness value of 1.1324 are comparable (Fig. 4.6). This indicates the potential of the hybrid GA model to converge rapidly in a few generations. This signifies that copying an individual according to its fitness leads to a higher probability of it contributing a better offspring (having a higher fitness) in the next generation.

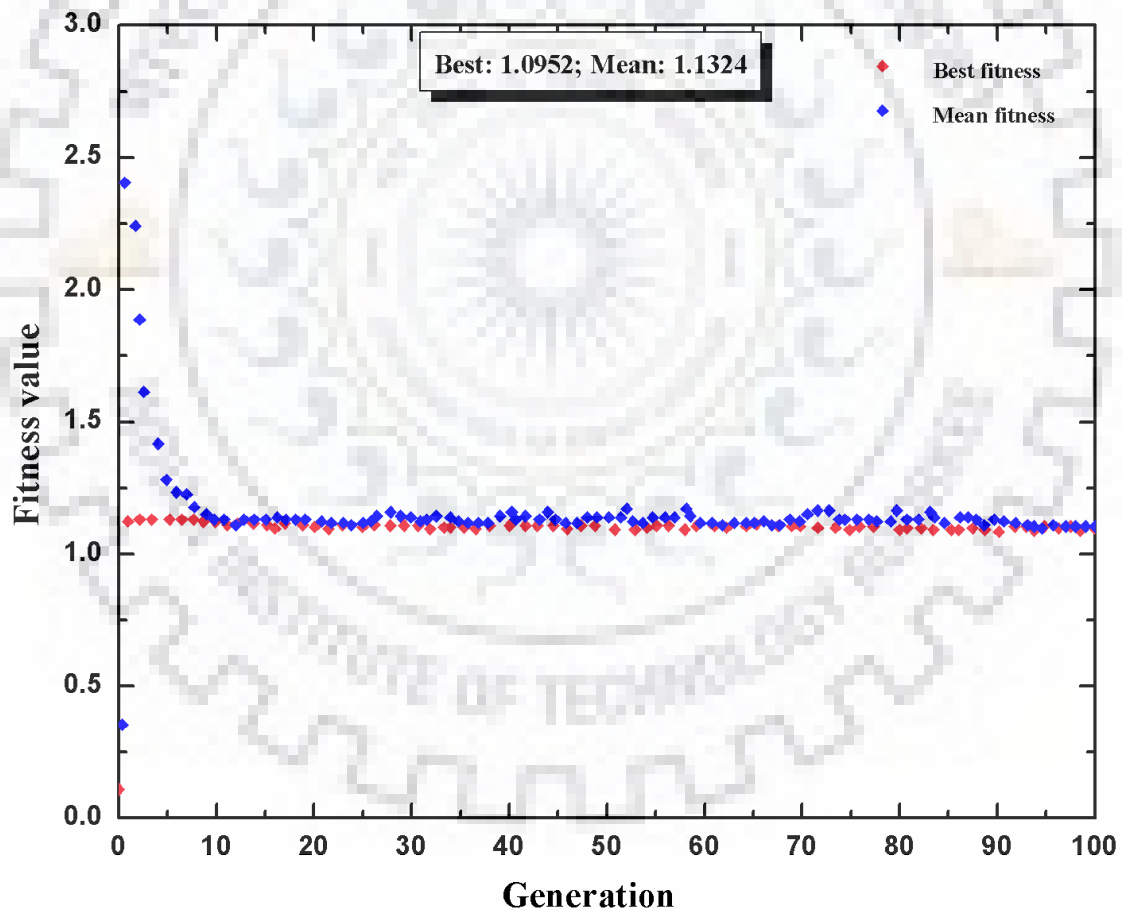


Fig. 4.6: Hybrid GA model simulated Fitness function plot. Best and average fitness values show a gradual convergence towards the optimum value of 1.0952 after 100 generations.

4.1.4 Process Parametric Interactions

The ANOVA results (Table 4.2) predicted that the response (ESI_{24}) was affected by the oil and surfactant concentrations, stirring speed and stirring time ($p < 0.05$). It also showed that the mutual interactions among all the parameters were also significant ($p < 0.05$). The effect of oil and surfactant concentrations were highly significant ($p < 0.0001$) as compared to stirring speed and time.

Fig. 4.7 shows the effect of a single parameter on the emulsion stability at the optimized conditions. From Fig. 4.7(b), it was observed that as the surfactant concentration increases from 0.1 to 1.2 % (w/v), the ESI_{24} increases sharply from 0.10 to 0.7 and thereafter, the increase in ESI_{24} slows down. ESI_{24} increases steadily with an increase in oil concentration (Fig. 4.7a). ESI_{24} increases with an increase in the stirring speed, reaches a maxima at ~4000-5000 rpm and then decreases (Fig. 4.7c). Further, the maximum ESI_{24} was attained at the stirring time of 5-8 min. ESI_{24} decreases with an increase in the stirring time beyond 8 min (Fig. 4.7d).

The mutual interactions of oil and surfactant concentration, stirring speed and time with ESI_{24} were found to be very significant ($p < 0.05$), as shown in Table 4.2. Fig. 4.8-4.9 show the 3D and 2D surface plots for ESI_{24} of emulsions as a function of oil and surfactant concentrations. It was observed that at low oil concentrations (<30 % (v/v)) and low surfactant concentrations (<1 % (w/v)), the ESI_{24} is in the range of 0.10-0.25, which indicated that the emulsion is unstable and highly flocculating in nature. At low surfactant concentrations, the emulsion is unstable, mainly because of agglomeration of the oil droplets. In the oil concentration range of 10-25 vol%, an increase in the surfactant concentration from 0.8 to 2 wt% has little effect on ESI_{24} ($ESI_{24} \sim 0.30$). At high surfactant and low oil concentrations, the emulsion destabilization occurs probably because of the rapid coalescence. ESI_{24} increased significantly from ~ 0.40 to 0.65 as the oil concentration increased from 30% to 40% (v/v) with an increase in surfactant concentration. The most desirable stable region (ESI_{24} in the range of 0.66-0.86) was observed with oil concentration in the range of 40-50% (v/v) and surfactant concentration in the range of 1-2% (w/v) (Fig.4.8-4.9). As the dispersed phase concentration (oil phase) increases in the continuous phase, more oil droplets were formed and an external layer of surfactant film was formed at the interface, increasing the steric repulsion potential between the oil droplets and reducing the rate of creaming over the storage time. The stability of emulsions is affected by the thickness of the interface layer as the surfactant concentration changes.

For the emulsification process, stirring time and speed play an important role. Emulsification proceeds with an increase in the interfacial area between the immiscible phases because of rupturing of the larger droplets into smaller ones, when the intensity and the duration of the mechanical energy dissipation were varied. Effective rupturing of larger oil droplets can occur

with an increase in the local dissipation energy in the droplets breakdown zone. This can be achieved by increasing the circulation through the mixing zone (Graillat et al., 1990). For this purpose, a high shear, six pass rotar-stator mixer was used for the preparation of the emulsions. Fig. 4.10 shows the variation of ESI_{24} as a function of stirring speed and time. Emulsion stability increases with an increase in stirring speed, which in turn reduced the radii of the oil droplets. Optimum ESI_{24} of 0.86 was obtained at a stirring speed of ~ 5000 rpm and for a stirring time of ~ 7 min. Fig. 4.7(d), shows that the ESI_{24} reaches a maxima at around ~ 5000 rpm and thereafter, it decreases. At a higher stirring speed (> 5000 rpm), the emulsifier gets detached from the oil-water interface. A range of 2500-5000 rpm for stirring speed and 5-12 min of stirring time helps in the formation of stable emulsions with ESI_{24} in the range of 0.70-0.86. If the stirring time increases beyond 14 min, the ESI_{24} decreases rapidly with an increase in rpm. It was observed that for longer stirring time, low stirring speed improves the emulsion stability and that the stirring speed has no effect on the ESI_{24} , if the time of stirring is more than 17 min.

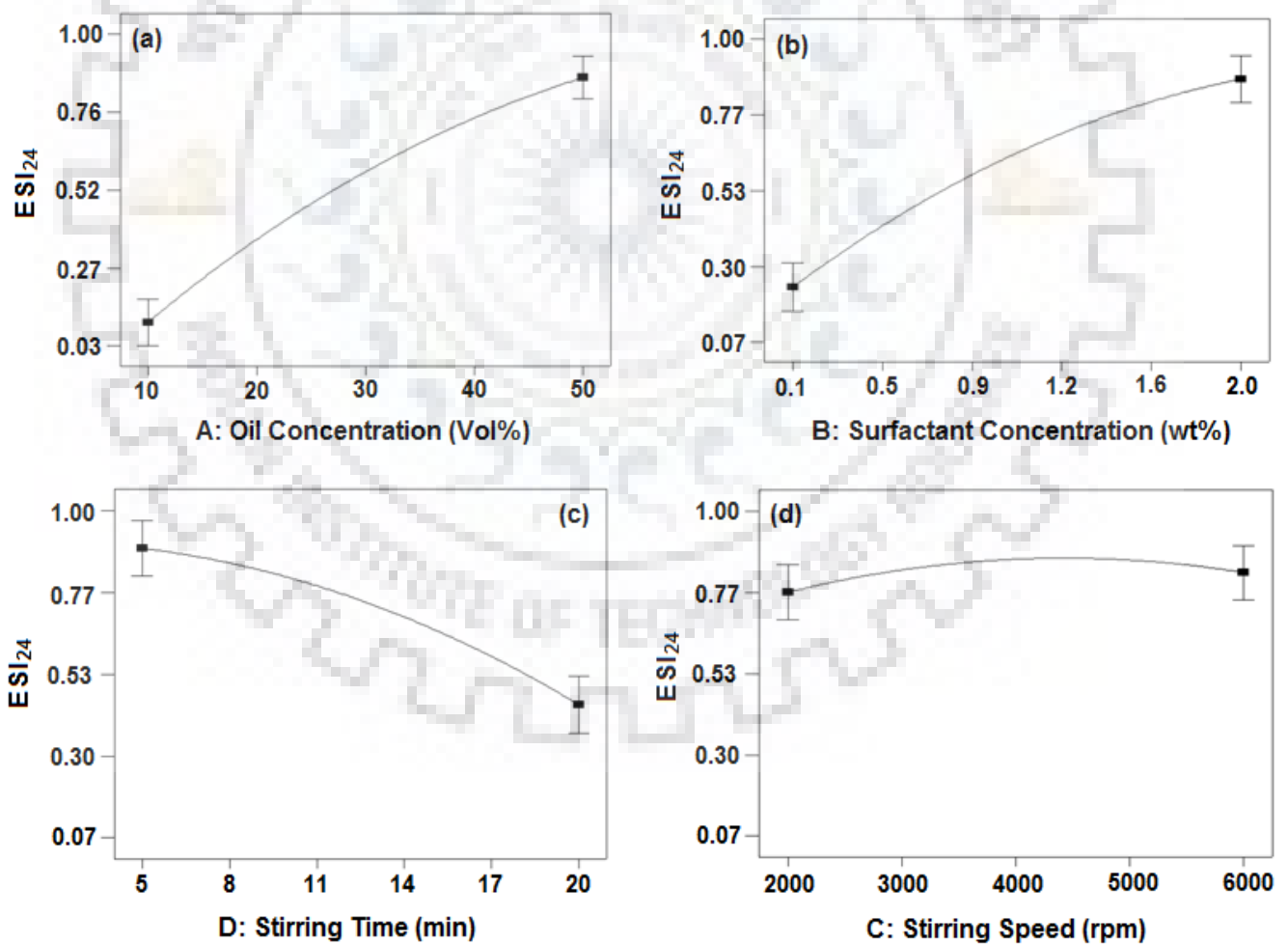


Fig. 4.7: Single factor plot showing the effect of (a) oil concentration; (b) surfactant concentration; (c) stirring time; and (d) stirring speed on emulsion stability (ESI_{24}).

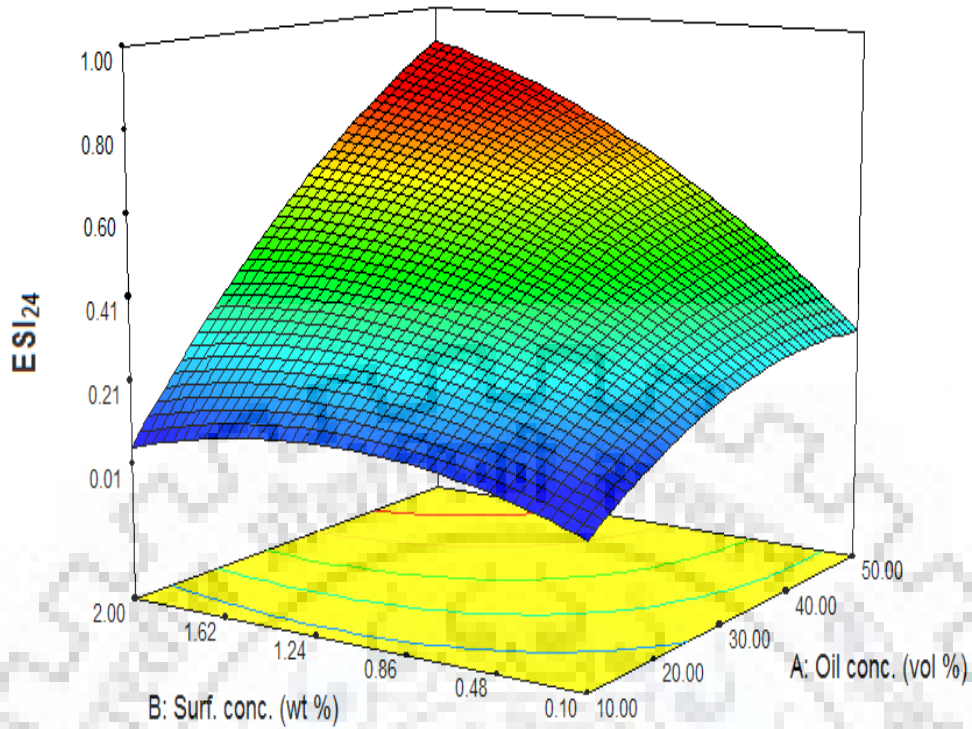


Fig. 4.8: 3D response surface plot showing the effect of oil concentration and surfactant concentration on emulsion stability index (ESI_{24}).

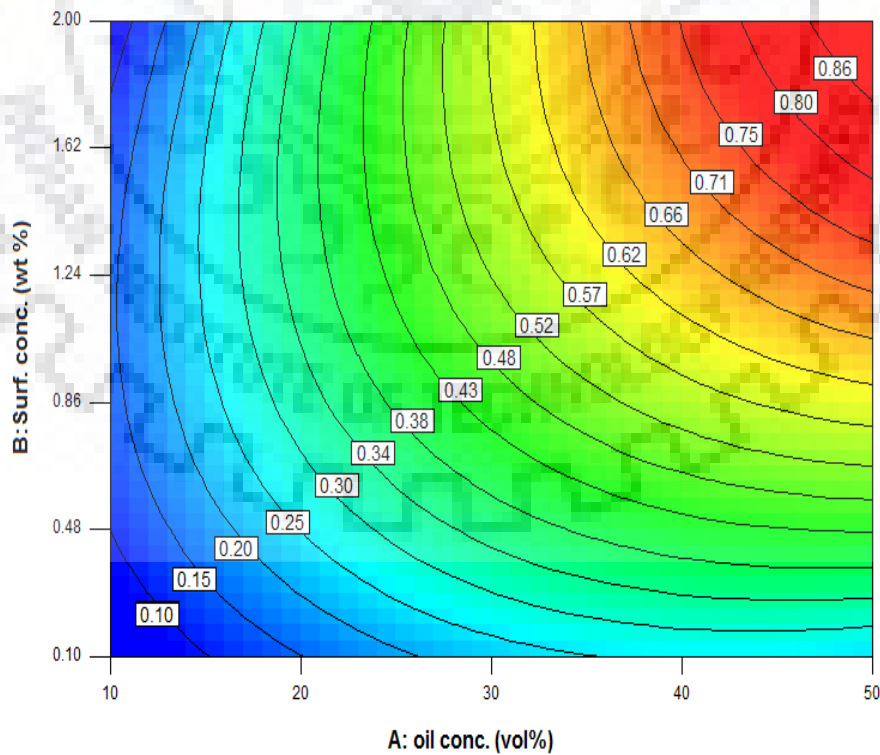


Fig. 4.9: 2D contour plot showing the variation of emulsion stability index (ESI_{24}) with oil concentration and surfactant concentration.

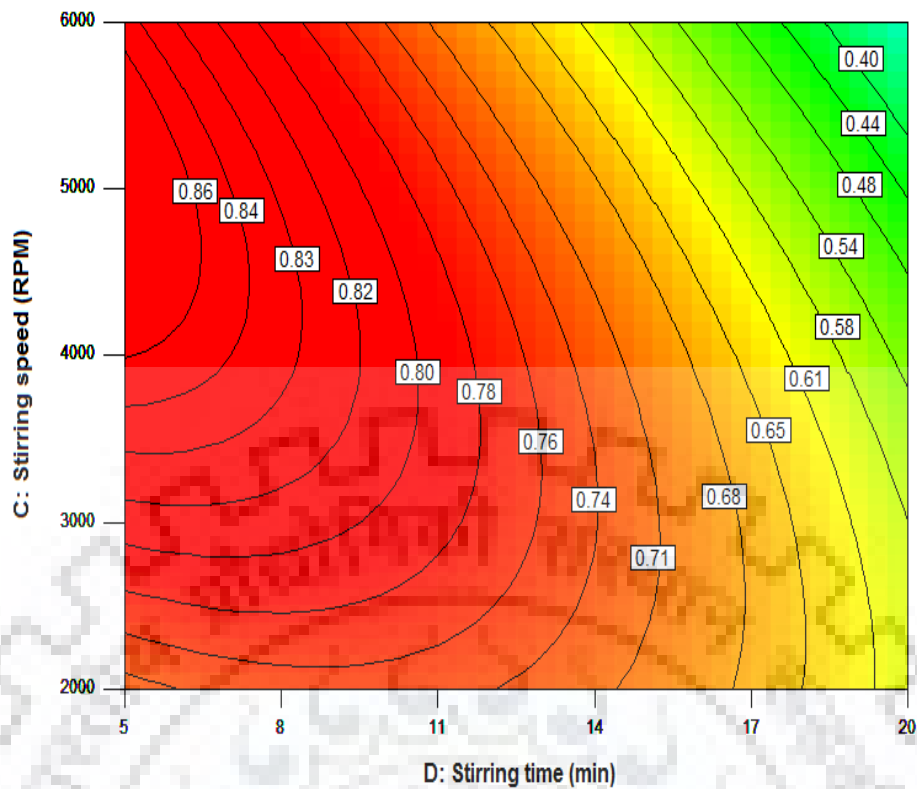


Fig. 4.10: 2D contour plot showing the combine effect of stirring time and stirring speed on emulsion stability index (ESI_{24}).

Fig. 4.11-4.12 shows the mutual interactions of stirring time and oil concentration on emulsion stability. As the stirring time becomes longer, the oil-water interface is severely disturbed and the surfactant drops out from the interface, which lead to a decrease in the emulsion stability. From Fig. 4.10(a, b), it can be seen that the ESI_{24} increases with an increase in oil concentration and stirring time. At low oil concentration ($< 20\%$ (v/v)), stirring time has no effect on emulsion stability. Emulsion stability increases significantly ($ESI_{24} > 0.5$) for oil concentration > 30 vol% and stirring time ~ 5 -11 min. For higher oil concentrations (40-50% (v/v)), very stable emulsions were obtained ($ESI_{24} > 0.7$) upto stirring time of 12 min. Beyond 12 min, the emulsion stability decreases progressively mainly because of the dropping out effect of surfactant from the oil-water interface.

4.1.5 Validation of Hybrid GA and RSM-BBD Models

The optimum combinations of emulsion stability process parameters obtained by the developed hybrid GA and RSM models (Table 4.7) were validated by performing confirmatory experiments at predicted optimized conditions. The confirmatory experiments were performed in triplicate, and the averaged values are shown in Table 4.7. The deviation between the hybrid GA and RSM-BBD model predicted results with the experimental data are in the percentage error range of $\sim \pm 5\%$. This showed that the model predictions were satisfactory. Hence, the adequacy of hybrid GA and RSM models on emulsion stability was confirmed.

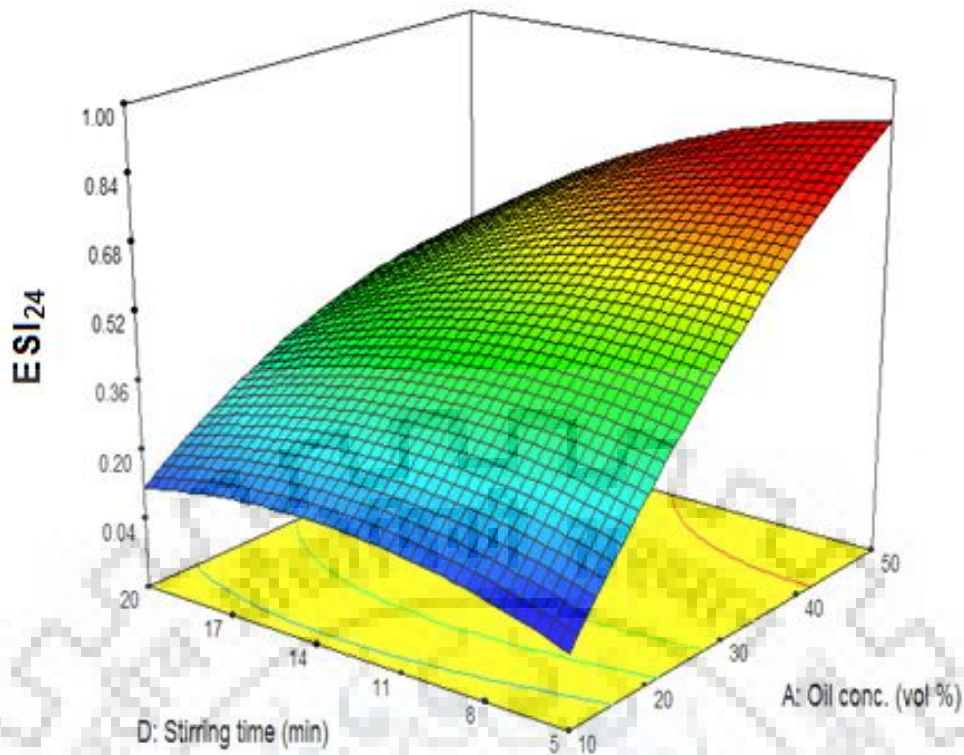


Fig. 4.11: 3D response surface plot showing the effect of oil concentration and stirring time on emulsion stability index (ESI_{24}).

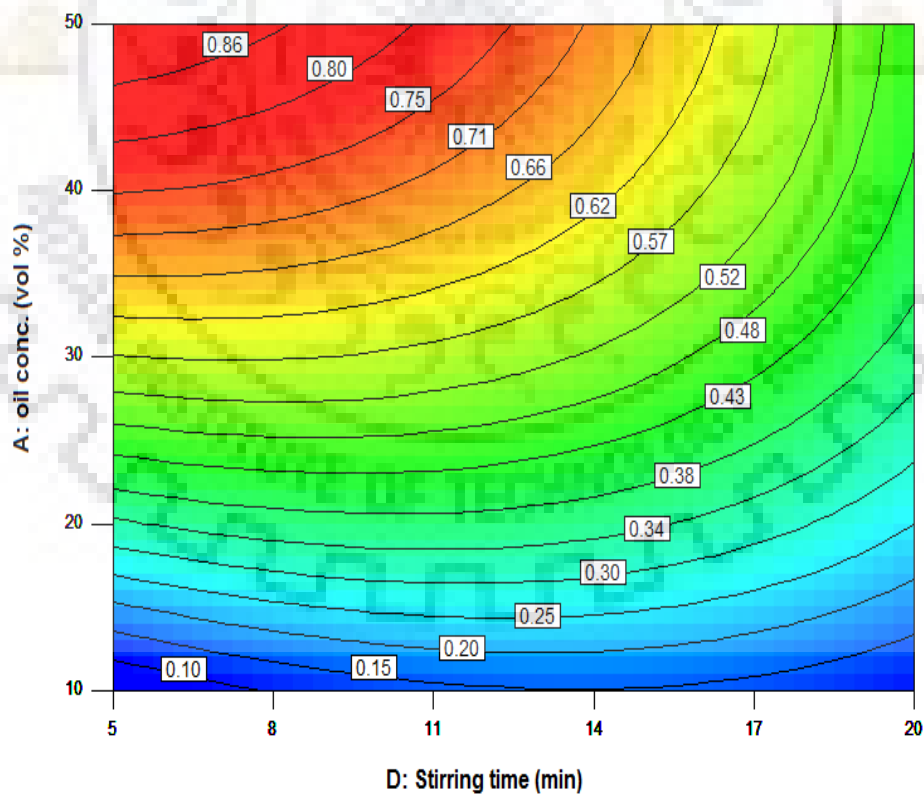


Fig. 4.12: 2D contour plot showing the combined effect of stirring time and oil concentration on emulsion stability index (ESI_{24}).

Table 4.7: Comparative results of confirmatory experiments for model validation.

Models Process Parameters	RSM-BBD model				Hybrid GA model	
	Solution criterion 1*		Solution criterion 2#		Optimized values	Experimental values
	Optimized values	Experimental values	Optimized values	Experimental values		
A: Oil Concentration (vol %)	49.13	49	50	50	50	50
B: Surfactant Concentration (wt %)	1.88	1.88	1.05	1	2	2
C: Stirring Speed (rpm)	4962.60	4950	2000.73	2000	5691.33	5700
D: Stirring Time (min)	7.1	7	5.0	5	5.0	5
Response (Y): ESI_{24} (vol. fraction)	0.866	0.826	0.546	0.584	0.913	0.872
Error (%)	4.84		6.50		4.70	

Criterion 1*: A, B, C, D are in range and ESI_{24} (response) maximize.

Criterion 2#: A is in range; B, C, D are minimize and ESI_{24} (response) maximize.

4.2 EMULSION STABILITY

4.2.1 Effect of Volume Fraction on Emulsion Stability

The emulsion stability was assessed by CI and EI, and is shown in Fig. 4.13(a-b) as a function of storage time. Both CI and EI provided indirect information about the extent of droplet aggregation and coalescence in an emulsion. Higher CI indicates higher aggregation. Larger the droplets, faster the creaming (Perrechil and Cunha, 2010; Lovaglio et al., 2011). Higher EI indicates higher stability of the emulsion.

From Fig. 4.13(a-b) it can be seen that the dilute o/w emulsions i.e., set 1 and set 2 emulsions, are flocculating in nature. Specially set 1 emulsion was highly flocculated, having a CI of ~85% and EI of ~15%. For these emulsions, the creaming process was much more pronounced. During the storage time, a turbid serum phase was separated at the bottom and a gel cream layer moved upward and settled at the top of the separating funnel. For set 1 emulsion, the creaming process was very fast and continued for 15 min. Thereafter, the creaming process became slow and the creamed emulsion layer became stable for about 3 days, without separating into oil and water phases individually. In comparison to set 1, set 2 and set 3 emulsions had lower CI, i.e. ~60% and 35 %, respectively, and EI, i.e. ~40% and 65 %, respectively. The highly concentrated o/w emulsions, i.e. set 4 and set 5 emulsions, showed a very low creaming tendency. As the dispersed phase concentration increases, the creaming tendency of the emulsions decreases. As a result, the concentrated emulsion was formed with high EI (> 90%). Actually, for highly concentrated o/w emulsion (set 5), the CI and EI were ~2% and ~98%, respectively, which indicated no creaming. Thus, the highly concentrated emulsions were highly stable for a longer period of time. Photomicrographs of all sets of o/w emulsions were shown in Fig. 4.14.

4.2.1.1 Droplet size distribution (DSD) of emulsions

DSD as determined by the zetasizer is shown in Fig. 4.15. It was observed that the average size of the emulsion droplets gradually decreases from 1.72 to 0.712 μm with an increase in the oil concentration from 10% to 80% (v/v). For the set 4 and set 5 emulsions the droplet size distributions were within a narrow band. The distribution curve becomes broader and wider as the oil concentration decreases (set 3, set 2, set 1). DLS measurements showed a uni-modal droplet size distribution of emulsions with average droplets size increasing from 0.71 μm (set 5) to 1.72 μm (set 1).

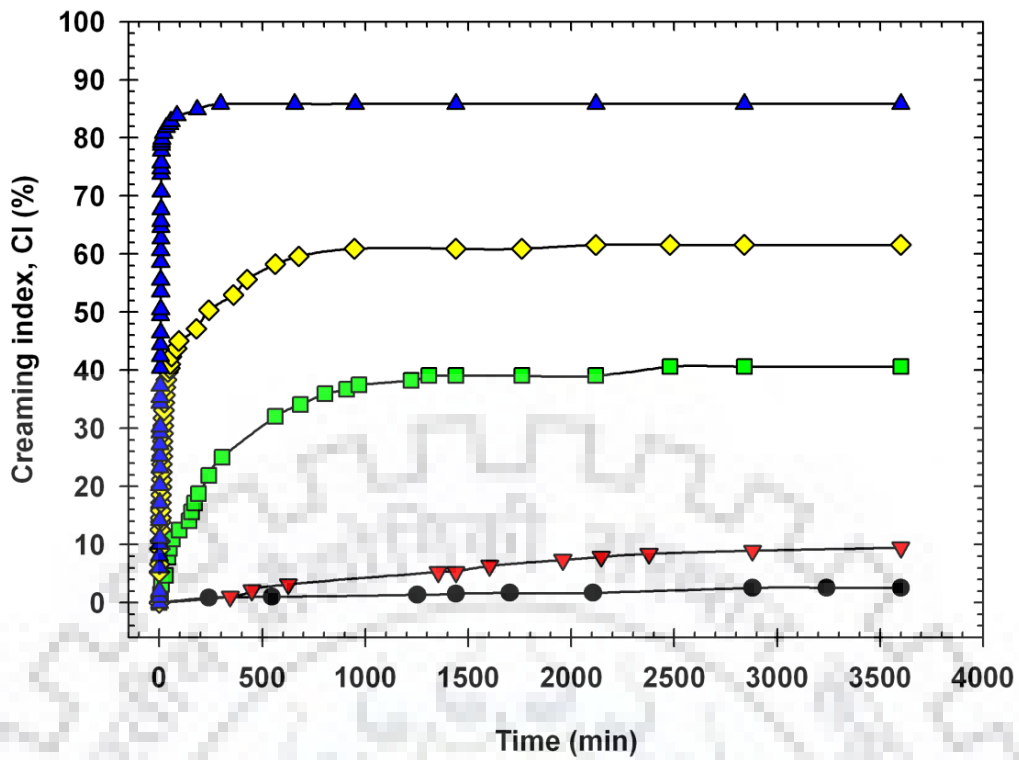


Fig. 4.13(a): Variation of creaming index (CI) with time for different o/w emulsions.

Set 5 (—●—); set 4(—▼—); set 3(—■—); set 2(—◆—); set 1(—▲—).

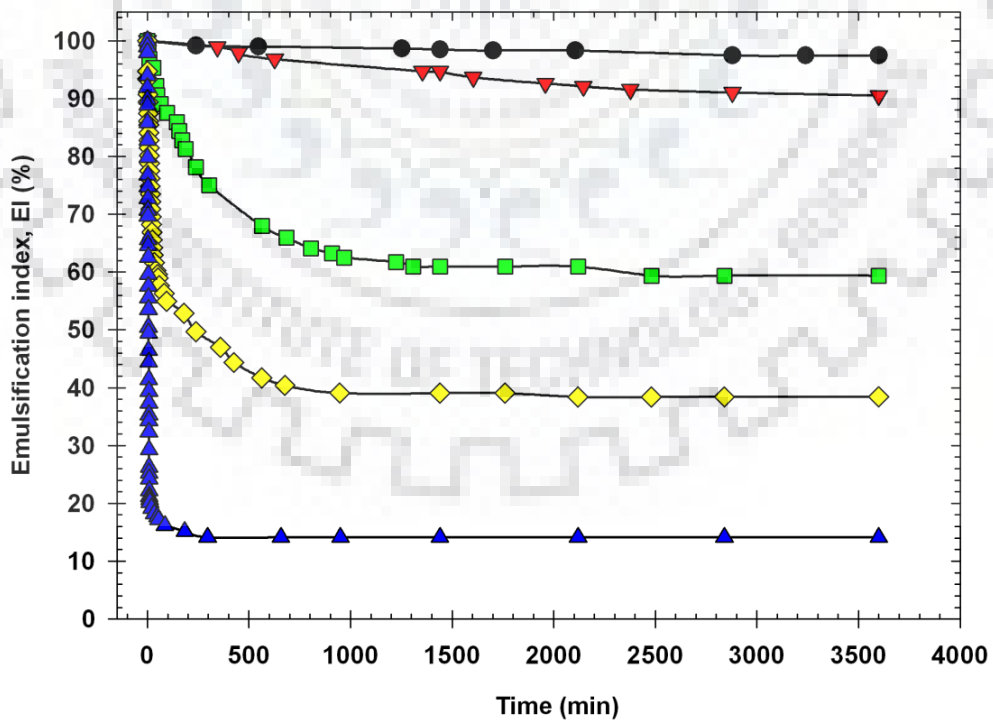


Fig. 4.13(b): Variation of emulsification index (EI) with time for different o/w emulsions.

Set 5 (—●—); set 4(—▼—); set 3(—■—); set 2(—◆—); set 1(—▲—).

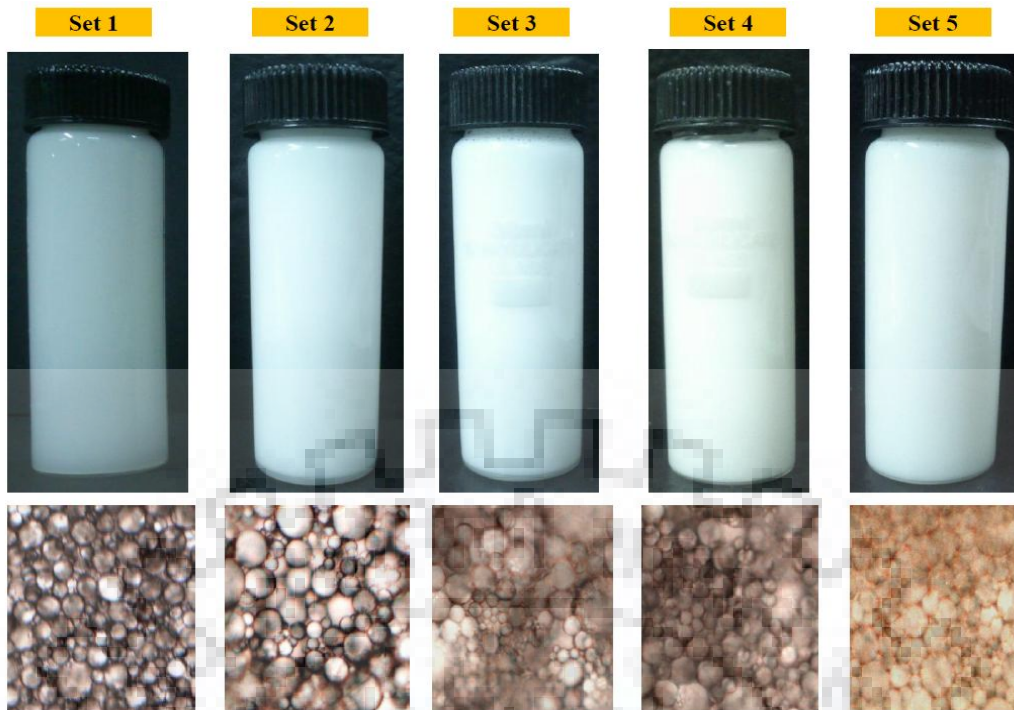


Fig. 4.14: Photomicrographs of freshly prepared oil-in-water emulsions at 40X.

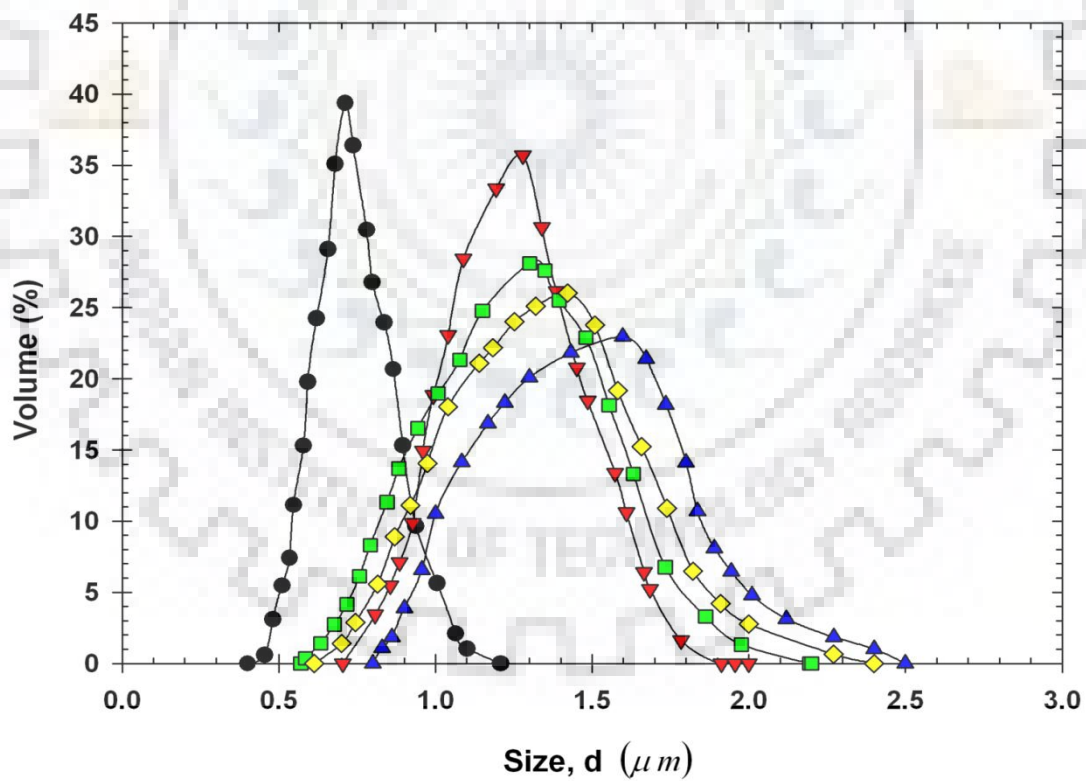


Fig. 4.15: Droplet size distribution of o/w emulsions.

Set 5 (—●—); set 4(—▼—); set 3(—■—); set 2(—◆—); set 1(—▲—).

4.2.1.2 Electrophoretic characteristics of emulsions

Zeta potential and electrophoretic mobility of different sets of emulsions are shown in Fig. 4.16. All the emulsions showed a characteristic stabilized behavior with an anionic surfactant. Both zeta potential and electrophoretic mobility progressively increased with an increase in the oil volume fraction (Fig. 4.16). This suggests that more and more oil droplets get attached to the interface and increase the stability of emulsions. For set 1 emulsion, the magnitude of zeta potential was smaller (52.87 mV) than that of set 5 emulsion (88.67 mV). This may be because of the fact that at lower zeta potential the steric repulsion between the dispersed oil droplets may not be high enough to overcome the attractive interaction between the droplets (i.e. van der Waals and hydrophobic attraction forces) and the energy barrier (Zee et al., 2012; Kundu et al., 2013). As a result, the emulsion becomes flocculating in nature and prone to aggregation of droplets which enhances the creaming rate. On the other hand, the emulsion with higher zeta potential, i.e. set 5 and set 4 emulsions, (>70 mV) possess strong steric repulsive forces, which prevent coalescence of droplets (higher electrophoretic mobility). Thus, the emulsion becomes highly stable for a longer period of time, having a very low creaming rate.

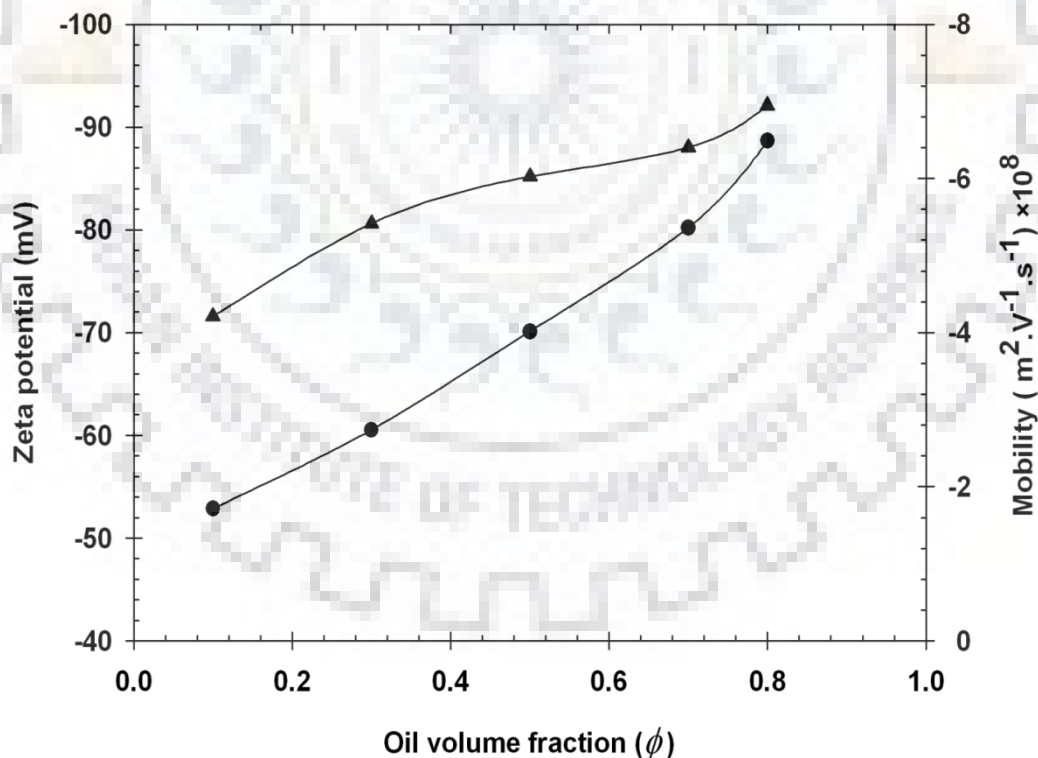


Fig. 4.16: Zeta potential and electrophoretic mobility of emulsions with oil volume fraction.

Zeta potential –●–; Mobility –▲–.

4.2.1.3 Surface tension of emulsions

The variation of surface tension (SFT) of emulsions is shown in Fig. 4.17 along with two extreme cases, i.e. the SFT of pure deionized water ($\phi = 1.0$) and pure oil ($\phi = 0$). The SFT of emulsions gradually decreases as the oil volume fraction increases. From $\phi = 0.5$ onwards, there is a sharp decrease in SFT, forming highly concentrated o/w emulsion. As the oil volume fraction increases (at a fixed surfactant concentration, 1 w/v %) successively larger number of oil droplets get attached onto the oil water interface. This increases the interfacial adsorption, reduces the SFT of oil and water phases and results in the formation of more stable emulsions with the large interfacial area and film strength. These results are also in agreement with those of Wang et al. (2000).

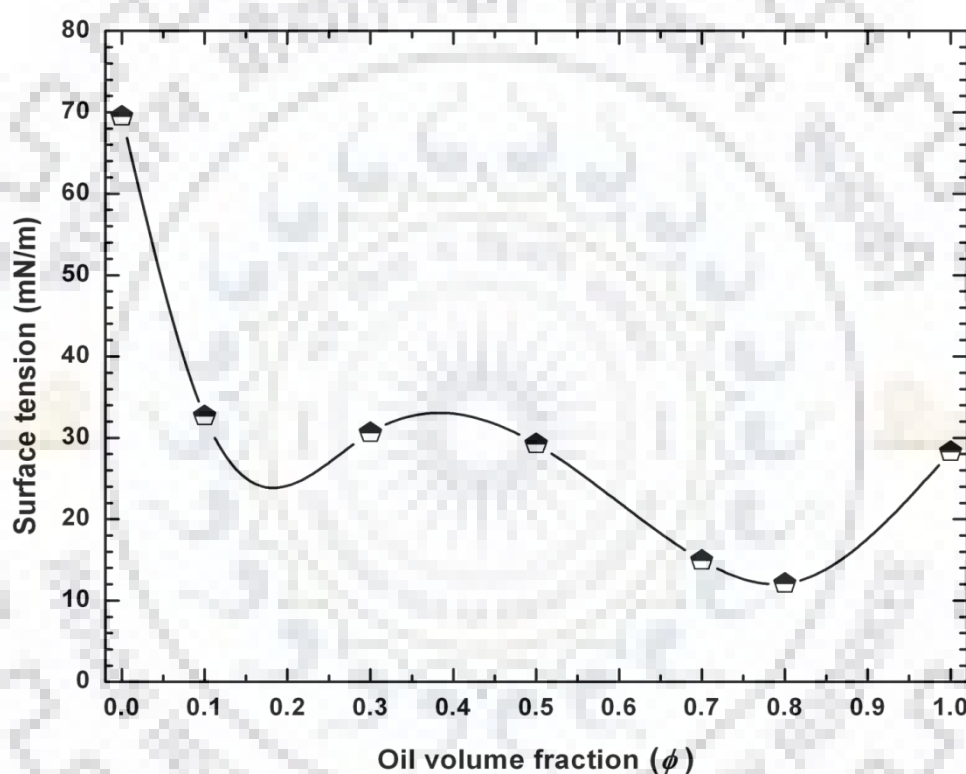


Fig. 4.17: Variation of surface tension of emulsions with oil volume fraction.

4.2.2 Effect of pH on Emulsion Stability

The emulsification index (EI) and the creaming index (CI) of the emulsions as functions of storage time are shown in Fig. 4.18(a)-4.18(b). From this figure, it can be seen that all the sets of o/w emulsions are flocculating in nature. The creaming process is found to be dominating. During storage, a turbid serum phase separates at the bottom and a gel creamy layer moves upward and settles at the top of the fluid column in the separating funnel. The relative volume of emulsion phase changes with time logarithmically. The degree of flocculation is found to increase as the pH of the emulsion decreases. The emulsion at pH 2 was highly flocculated having a high CI of $\sim 78\%$ and an EI of $\sim 22.4\%$ (after 24 h) as compared to pH 12 (CI -61 % and EI $\sim 39\%$, after 24 h). The

EI and *CI* values of all other emulsions at different pH ($\text{pH} = 10, 8, 8, 4$) lie in between. It is observed that for the first 20s, the creaming rate is rapid and, thereafter, it gradually slows down with time and becomes eventually steady after 500 s. After this times, the creaming process slows down and the creamy emulsion layer become stable for a long period of time without separating into oil and water phase individually except at the emulsion pH 2.

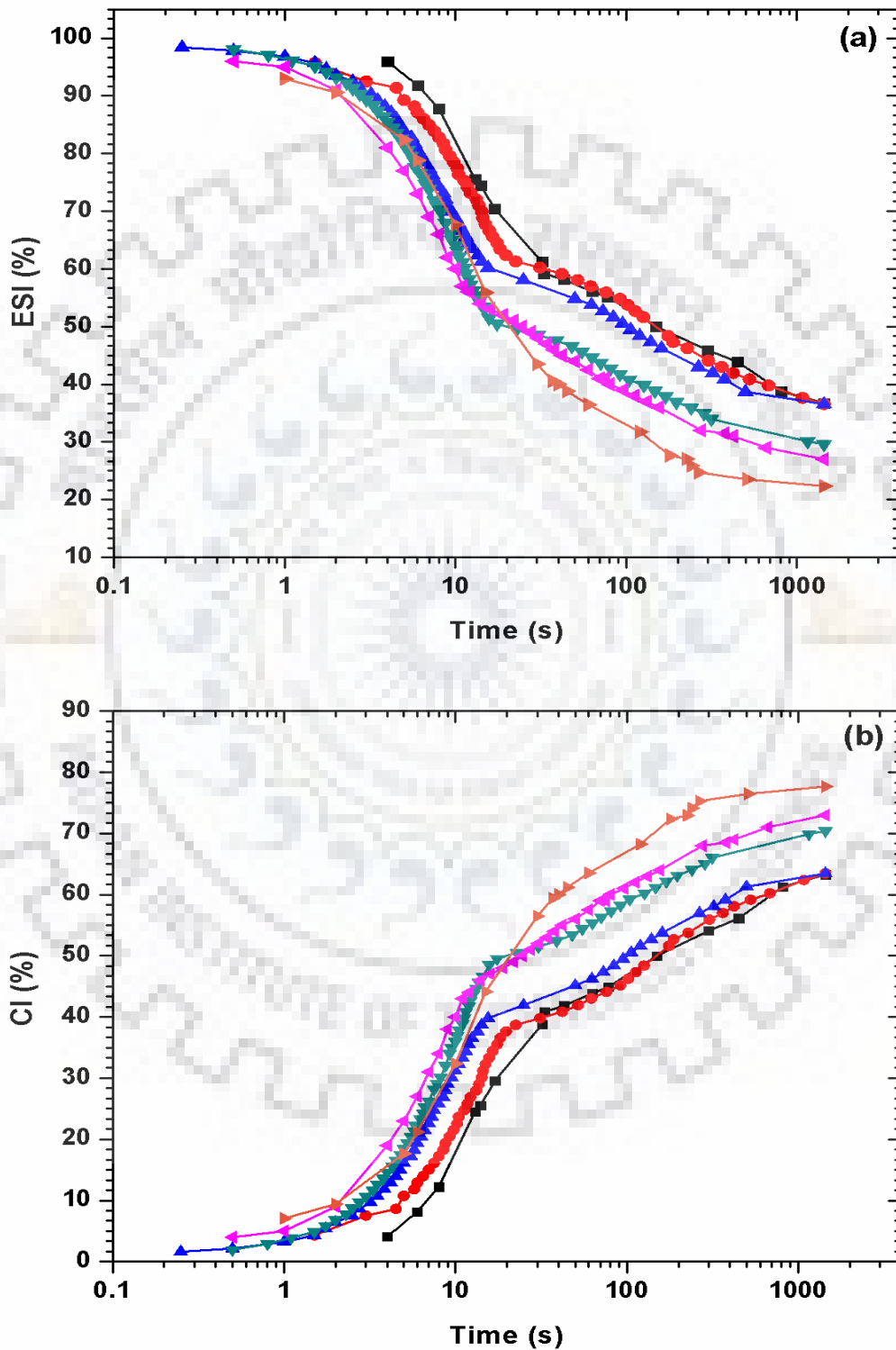


Fig. 4.18: Influence of pH on o/w emulsion stability (a) Emulsification stability index (EI) plot (b) Creaming index (CI) plot. pH: 12 –■–; 10 –●–; 8 –▲–; 6 –▴–; 4 –▾–; 2 –▴–.

4.2.2.1 Droplets size distributions (DSD) of emulsions

Droplets size distribution (DSD) of o/w emulsions for different pH is shown in Fig. 4.19. It is observed that the DSD for pH 12, 10 and 8 (i.e. basic emulsion) shows a monomodal shape. But for pH 6, 4 and 2 (i.e. acidic emulsion), the DSD shows a bimodal shape with the secondary maximum at a relatively high values of the droplet diameter and wider distribution with higher mean sizes. The DSD profiles for all emulsions get spreader and move to the right for the higher sizes as the pH of the emulsion decreases. The wide and bimodal DSD profile can be explained by the fact that the disruption of emulsion droplets is followed by a coalescence process as the pH of the emulsion decreases due to the charge neutralizations at the interface. The reverse will happen with an increase in pH favoring droplet-droplet collision and preventing coalescence. The average droplet size, expressed as d_{43} , is an important structural parameter that dictates the flow behavior of emulsions (Otsubo and Prudhomme, 1994), and is also related to linear viscoelasticity parameters (Princen and Kiss, 1989; Partal et al., 1998; Romero et al., 2002).

Under a steady macroscopic flow, the droplets of emulsions are subjected to two opposing effects: (i) a viscous stress of magnitude $(\eta_c \dot{\gamma})$, that tends to elongate the droplet, and (ii) a interfacial stress of magnitude (σ/R) that tends to minimize the surface energy and hence tends to maintain the droplet in a spherical shape. Therefore the realized morphology of a drop is determined by the ratio of these forces expressed through a non-dimensional scaling term referred to as capillary number (N_{Ca}). In the present study, modified capillary number ($N_{Ca,m}$) has been used by replacing viscosity of continuous phase (η_c) with viscosity of emulsion (η_{em}) (mean field viscosity) for generalizing the rheological data and expressed as (Derkach et al., 2009):

$$N_{Ca,m} = \frac{\eta_{em} \dot{\gamma}}{\sigma/R} \quad (4.4)$$

where $\dot{\gamma}$ is the shear rate, σ the interfacial tension and R is the mean droplet radius. This approach provided a possibility to present all experimental values of drop anisotropy as a function of shear rate for emulsions of different pH as a unique function of the $N_{Ca,m}$.

The significance of deformation of the droplets under shear flow can be determined by the equation proposed by Torza et al. (1972), and is expressed by:

$$D_m = \frac{5(19\eta_r + 16)}{4(\eta_r + 1) \left[(20/Ca_m)^2 + (19\eta_r)^2 \right]^{1/2}} \quad (4.5)$$

where, η_r is the relative viscosity (i.e. η_{em}/η_c)

Droplet size distribution of all freshly prepared emulsions were measured before commencing the rheological test. Droplet size measurement also performed at the end of each

rheological test to check the change in droplet size distribution of emulsion samples. Eventually no significant change in droplet size distribution was observed. The capillary number ($N_{Ca,m}$) and the deformation (D_m) for the emulsions of different pH at three different shear rate (i.e. $\dot{\gamma}=10^{-02},10^0,10^3 s^{-1}$) are summarized in Table 4.8. It was observed that both $N_{Ca,m}$ and D_m are small for o/w emulsions, where small dispersed droplets are suspended in a continuous aqueous phase. At low and high share rate, i.e. ($10^{-02} \leq \dot{\gamma} \leq 10^3$), $N_{Ca,m}$ and D_m are very small ($N_{Ca,m} \rightarrow 0; D_m \rightarrow 0$) for all sets of emulsions. This indicates that the deformation of droplets is indeed negligible. Therefore, droplets can be treated as spherical and assume to behave as rigid spheres under shear flow (Pal, 2001; Berli et al., 2002). In this case, droplets may form tight clusters and cannot be broken under low shear, which exhibit higher viscosity.

The viscosity ratio (η_r) along with capillary number ($N_{Ca,m}$) completely determines the dynamics of viscous drop (Stone, 1994). Further, at a fixed shear rate there is a certain value of viscosity ratio above which it is difficult to break a viscoelastic drop (Varanasi et al., (1994)]. Also droplets, at a viscosity ratio of 3.4 or more, cannot be fragmented as a result of deformation in a steady shear flow (Ha and Leal, 2001). In the present study, η_r for all sets of emulsions is found to be greater than 5 (i.e. $\eta_r > 5$), even at high shear rate. Emulsion drops in viscoelastic matrix remain bounded at low capillary numbers where surface tension overpowers viscous stretching and at high viscosity ratios where motion inside the drop approaches a rigid body motion hindering stretching.

Table 4.8: Effect of pH on modified capillary number ($N_{Ca,m}$) and drops deformation (D_m) in the emulsions.

pH	IFT (mN/m)	d_{av} (μm)	$(N_{Ca,m})_{\dot{\gamma}=10^{-02}}$	$(N_{Ca,m})_{\dot{\gamma}=10^0}$	$(N_{Ca,m})_{\dot{\gamma}=10^3}$	$(D_m)_{\dot{\gamma}=10^{-02}}$	$(D_m)_{\dot{\gamma}=10^0}$	$(D_m)_{\dot{\gamma}=10^3}$
			$\times 10^6$	$\times 10^5$	$\times 10^3$	$\times 10^6$	$\times 10^5$	$\times 10^3$
2	5.648	5.51	0.109	0.561	1.531	0.129	0.658	1.749
4	5.056	5.30	0.787	2.307	3.261	0.933	2.730	3.787
6	3.443	1.69	1.423	2.258	3.117	1.690	2.677	3.656
8	2.593	1.71	4.091	5.939	4.916	4.857	7.046	5.766
10	1.526	1.77	17.45	23.18	11.59	20.69	27.41	13.34
12	1.143	1.27	34.11	48.57	14.90	39.73	53.45	16.44

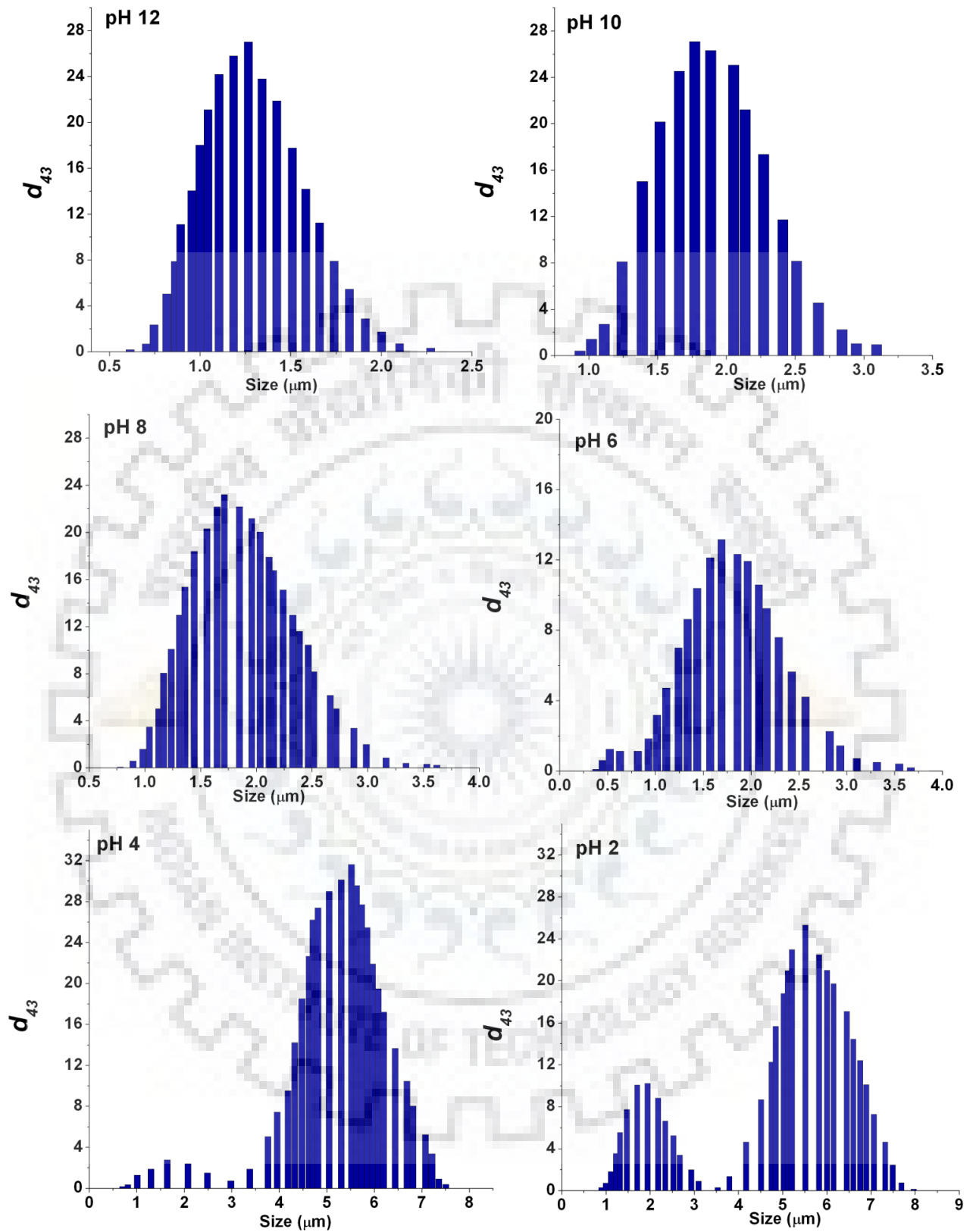


Fig. 4.19: Evolution of droplet size distribution (DSD) of o/w emulsions with pH.

4.2.2.2 Electrophoretic characteristics of emulsions

Fig. 4.20, shows the Zeta potential and the electrophoretic mobility of o/w emulsions. It is seen that both the zeta potential and the electrophoretic mobility progressively increase with an increase in the pH of the emulsion. This suggests that the electrostatic repulsion among the charged droplets progressively increased with an increase in pH. This behaviour enhances the stability of the emulsions at higher pH (pH 12; $\zeta = -64$ mV).

The magnitude and sign of the electrical charge on an emulsion droplet depends on the type of emulsifier, the concentration of the emulsifier and the prevailing medium conditions. All the droplets in an emulsions are usually stabilized by the same type of emulsifier and therefore have the same electrical charge. The electrostatic interaction between similarly charged droplets is repulsive in nature, and so electrostatic interactions play a significant role in preventing droplets from coming close enough together to aggregate. The concentration of counter-ions near a charged surface is always greater than the concentration of co-ions, and so a charged surface can be considered to be surrounded by a cloud of counter-ions (Hiemenz and Rajagopalan, 1997; Hunter, 2001). The distribution of ions close to a charged droplet surface is referred as the "electrical double layer". The characteristic Debye length (κ^{-1}) is a measure of the thickness of the electrostatic double layer and it is related to the properties of the electrolyte solution. The characteristic Debye length is given by Hunter (1992):

$$\kappa^{-1} = \left[\frac{N_A e^2}{\epsilon_0 k_B T (1 - \phi_{oil})} \sum z_i^2 c_i^\infty \right]^{-0.5} \quad (4.6)$$

where, N_A is Avogadro's number, e is the charge of an electron, ϵ is the dielectric constant of the medium, ϵ_0 is the permittivity of the free space, and z_i and c_i are valence and molar concentration of the electrolyte, respectively, in the bulk solution. The factor $(1 - \phi_{oil})$ accounts for the reduced volume available to electrolyte due to the presence of the oil phase. In the present study NaCl was used as an electrolyte of 0.061(M) concentration. Therefore, the characteristic Debye length for the o/w system was calculated as 1.03 nm. This corresponds to the distance from the charged droplet surface where the electrical potential has fallen to 1/e of its value at the droplet surface. Thus, the electrostatic interactions has an important consequences for the stability and rheology of an emulsion systems.

When ionic surfactant molecules are adsorbed at the oil-water interface, the electrostatic double layer can extend up to a few tens of nanometers. Emulsion droplets constitute as a 'kinetic unit' which moves when the interface is set into motion. As the interface (surfactant monolayer) begins to move, this imparts a force on the counter-ions of the double layer and induces motion. The motion of the counter-ions gives rise to a body force on the liquid in the double layer, and setting it in motion. The presence of the electrostatic double layer at the liquid-liquid interface makes the

interface appear to have an enhanced viscosity (Banik and Ghose, 2013). In addition, the distortion of electrostatic double layer by the application of shear leads to energy dissipation, and the net effect of this phenomenon is an increase in the viscosity of the dispersion, due to the primary electro-viscous effect (Hiemenz and Rajagopalan, 1977).

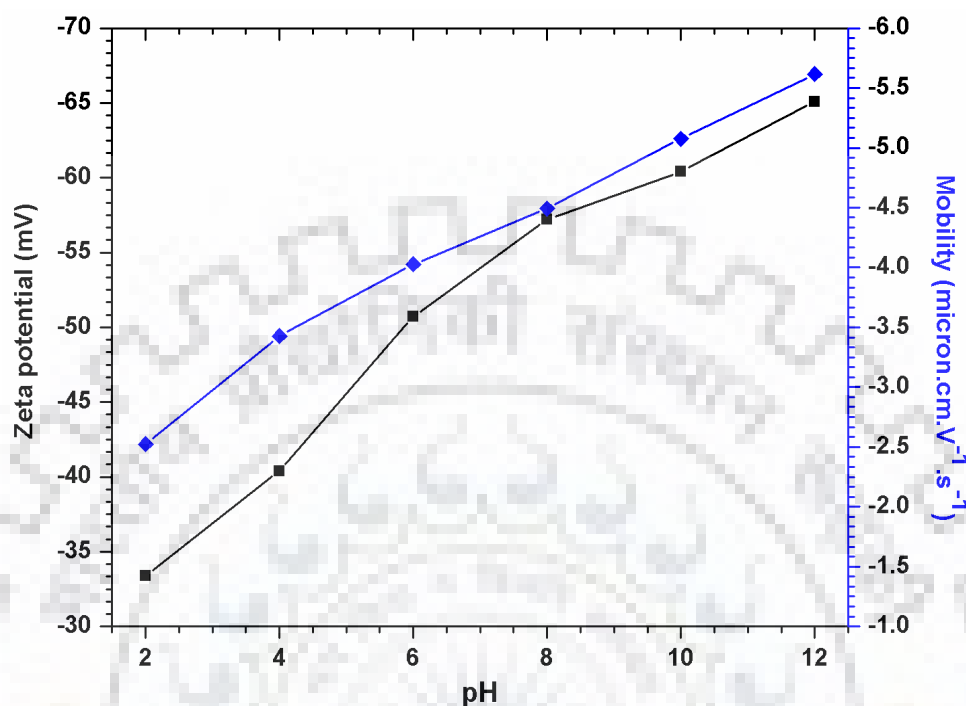


Fig. 4.20: Zeta potential and electrophoretic mobility of o/w emulsions with different system pH.

4.3 RHEOLOGICAL BEHAVIOR OF O/W EMULSION

In the present work, the effect of internal phase (oil) concentration, pH, temperature and an anionic surfactant concentration on the rheological properties and flow characteristics of dilute to highly concentrated o/w emulsions were investigated.

4.3.1 Steady Shear Rate Analysis

Typical shear flow (shear rate versus shear stress) and viscosity curves of emulsions at different temperatures are shown in Fig. 4.21(a-b). It can be seen that all the five sets of emulsions exhibit non-Newtonian behavior. All sets of emulsions showed the characteristic shear-thinning/ pseudo-plastic non-Newtonian behavior. The viscosity of emulsions decreases with an increase in the shear rate. The shear rate versus shear stress profile is in good agreement with the typical shear-thinning plot. A decrease in the viscosity of emulsion with an increase in shear rate (shear stress) occurred due to continuous rupture of microstructure, i.e., aggregation of oil droplets (Pal, 1997). The rate of viscosity change decreases non-linearly with an increase in the shear rate up to a certain shear rate ($< 60 \text{ s}^{-1}$) and becomes constant at high shear rate ($> 60 \text{ s}^{-1}$). Non-linearity of rheograms for sets 5-3 are much more pronounced than sets 2 and 1.

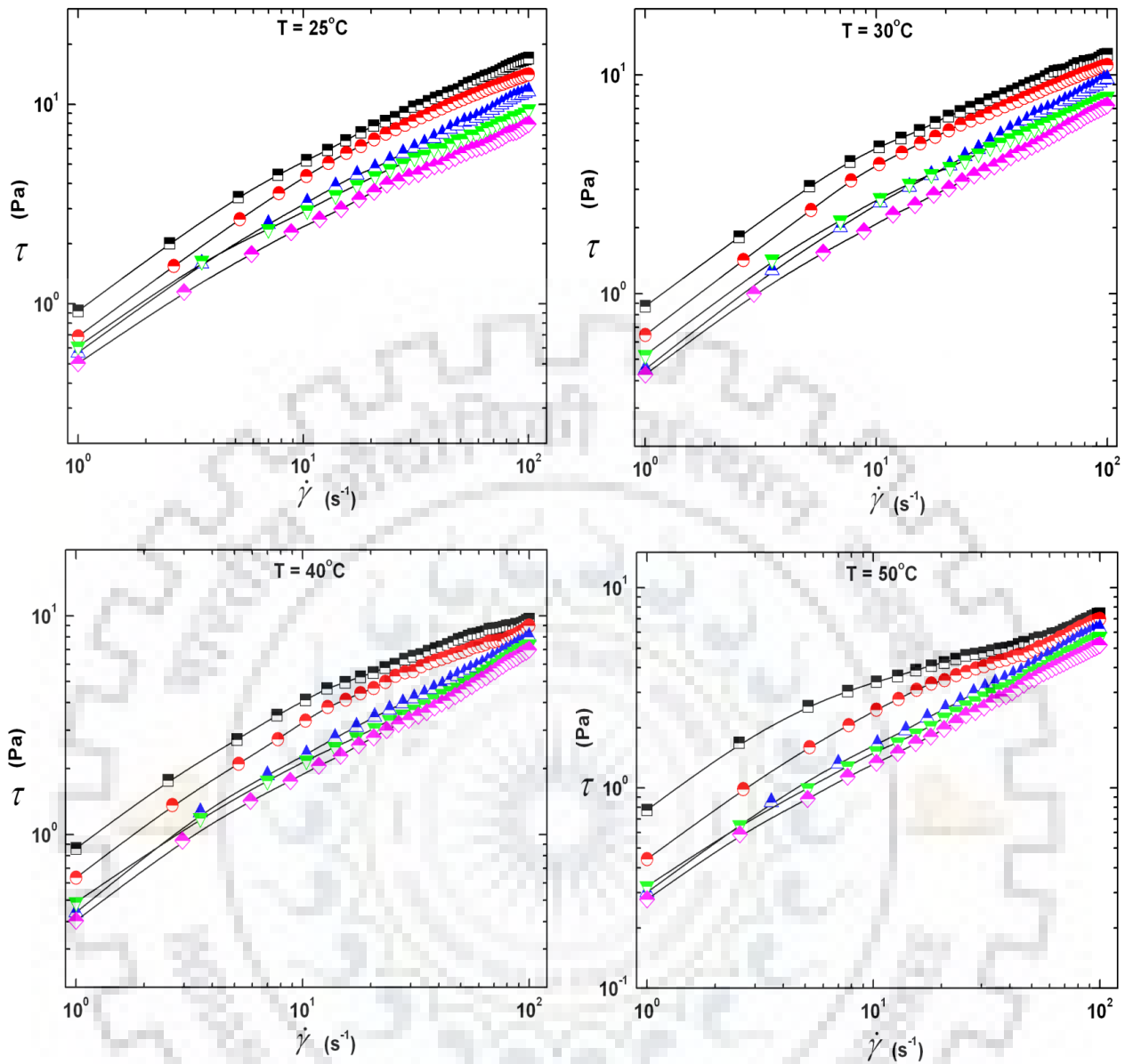


Fig. 4.21(a): Rheograms (shear rate vs shear stress plots) of different o/w emulsions.

Set 5 (—■—); set 4(—●—); set 3(—▲—); set 2(—▼—); set 1(—◆—).

4.3.2 Modeling of Emulsion Flow Behavior

It can be seen from Fig. 4.21(a-b), that all sets of emulsions exhibit non-Newtonian flow behavior in the shear rate range ($1-100 \text{ s}^{-1}$). Thus, non-Newtonian models (Ostwald-de-waele power law, Casson and Herschel-Bulkley) were evaluated to represent the emulsion rheological experimental data.

The power law model (Eq. 4.7) is two parameter model containing flow consistency index (K) and the flow behavior index (n). The non-linear flow behavior of an emulsion can be described by

the Herschel-Bulkley (HB) model and Casson model (Eqs. 4.8 and 4.9). These models combine the characteristics of both power law and Bingham plastic models (Pedersen and Rønningsen, 2000).

$$\text{Ostwald-de-waele power law: } \tau = K\dot{\gamma}^n \quad (4.7)$$

$$\text{HB model: } \tau = \tau_y + K_{HB} \dot{\gamma}^n \quad (4.8)$$

$$\text{Cason model: } \sqrt{\tau} = \sqrt{\tau_y} + \sqrt{K_c} \sqrt{\dot{\gamma}} \quad (4.9)$$

When the yield stress (τ_y) = 0, both Eq. (4.8) and Eq. (4.9) reduce to the power law Newton's law, respectively. When $n = 1$, Eq. (4.8) reduces to the Bingham model. The different models were fitted to the experimental data through regression analysis. It was found that the power law fit is the best amongst the three models. The power law fit is shown in Table 4.9, the fits for HB and Casson models are given in Table 4.10 and Table 4.11 respectively.

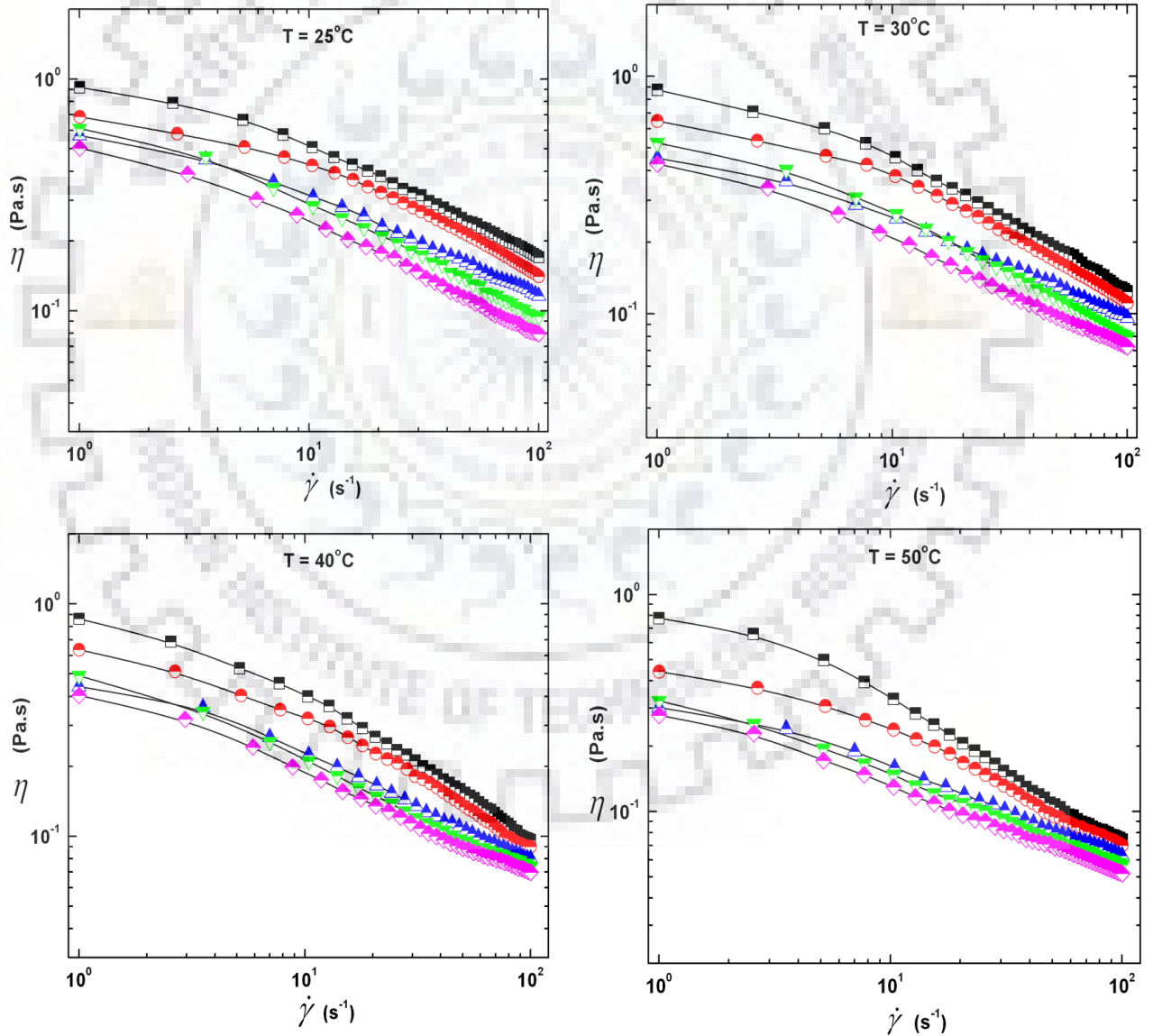


Fig. 4.21(b): Shear rate vs apparent viscosity of different o/w emulsions.

Set 5 (—■—); set 4(—●—); set 3(—▲—); set 2(—▼—); set 1(—◆—).

Table 4.9: Power law model fitting parameters for o/w emulsions at different temperature.

Emulsions set/ Temperature(°C)	K (Pa.s ⁿ)	n	R^2	Adj R^2	SEE	PRESS
Set 5 (80 %)						
25	1.6192±0.0346	0.5036±0.0052	0.9980	0.9980	0.1973	1.6307
30	1.6870±0.0526	0.4375±0.0076	0.9938	0.9937	0.2394	2.4426
40	1.7390 ±0.0729	0.3770±0.0103	0.9844	0.9840	0.2810	3.4231
50	1.3662±0.0513	0.3609±0.0092	0.9854	0.9850	0.1894	1.5441
Set 4 (70 %)						
25	1.4476±0.0542	0.5068±0.0090	0.9937	0.9935	0.2962	3.7248
30	1.3364±0.0424	0.4647±0.0077	0.9945	0.9944	0.2083	1.8515
40	1.2991±0.0554	0.4184±0.0104	0.9874	0.9870	0.2388	2.4350
50	0.7924±0.0287	0.4706±0.0088	0.9929	0.9927	0.1434	0.8635
Set 3 (50%)						
25	0.8567±0.0176	0.5677±0.0049	0.9989	0.9989	0.1022	0.3287
30	0.6867±0.0150	0.5740±0.0052	0.9988	0.9988	0.0889	0.2457
40	0.6486±0.0130	0.5420±0.0048	0.9989	0.9988	0.0694	0.1550
50	0.4020±0.0079	0.5967±0.0047	0.9991	0.9991	0.0499	0.0778
Set 2 (30%)						
25	0.9640 ±0.0259	0.5042±0.0065	0.9975	0.9974	0.1201	0.4598
30	0.8875±0.0205	0.4777±0.0056	0.9980	0.9979	0.0907	0.2619
40	0.5361±0.0174	0.5678±0.5678	0.9973	0.9972	0.1008	0.3277
50	0.3705±0.0048	0.5936±0.0031	0.9995	0.9995	0.0346	0.0497
Set 1 (10%)						
25	0.7708±0.0173	0.5144±0.0054	0.9980	0.9998	0.0897	0.2973
30	0.5526±0.0091	0.5585±0.0040	0.9991	0.9991	0.0556	0.1137
40	0.4487±0.0131	0.5937±0.0070	0.9977	0.9976	0.0888	0.2921
50	0.3243±0.0042	0.6036±0.0031	0.9995	0.9995	0.0315	0.0415

Table 4.10: Casson model fitting parameters for o/w emulsions at different temperatures.

Emulsion set / Temperature(°C)	τ_y (Pa)	K_c (Pa.s ⁿ)	R^2	Adj R^2	SEE	PRESS
Set 5 (80 %)						
25	1.1221±0.0695	0.5519±0.0098	0.9619	0.9609	0.1511	1.0951
30	1.1490±0.0714	0.4870±0.0101	0.9356	0.9339	0.1552	1.1601
40	1.1625±0.0720	0.4375±0.0102	0.9030	0.9005	0.1564	1.1689
50	1.1206±0.0511	0.3894±0.0072	0.9206	0.9185	0.1110	0.6117
Set 4 (70 %)						
25	1.0734±0.0765	0.5303±0.1080	0.9468	0.9454	0.1659	1.3003
30	1.0725±0.0686	0.4850±0.0097	0.9394	0.9378	0.1487	1.0611
40	1.0722±0.0667	0.4414±0.0094	0.9191	0.9170	0.1445	0.9894
50	0.9610±0.0479	0.4239±0.0068	0.9489	0.9475	0.1038	0.5235
Set 3 (50%)						
25	0.9491±0.0568	0.5126±0.0080	0.9745	0.9736	0.1080	0.4530
30	0.8910±0.0517	0.4913±0.0073	0.9750	0.9741	0.0983	0.3711
40	0.9021±0.0466	0.4560±0.0066	0.9727	0.9717	0.0885	0.0885
50	0.7899±0.0355	0.4416±0.0050	0.9819	0.9812	0.0674	0.1793
Set 2 (30%)						
25	0.9946±0.0596	0.4664±0.0084	0.9597	0.9582	0.1133	0.4940
30	0.9755±0.0581	0.4452±0.0082	0.9541	0.9524	0.1105	0.4768
40	0.8793±0.0339	0.4473±0.0048	0.9842	0.9836	0.0645	0.1679
50	0.7850±0.0250	0.4283±0.0035	0.9861	0.9857	0.0543	0.1426
Set 1 (10%)						
25	0.9444±0.0478	0.4484±0.0068	0.9640	0.9629	0.0976	0.4118
30	0.8741±0.0354	0.4474±0.0050	0.9798	0.9792	0.0722	0.2317
40	0.8366±0.2850	0.4461±0.0040	0.9866	0.9862	0.0583	0.1525
50	0.7517±0.0238	0.4221±0.0034	0.9866	0.9862	0.0518	0.1287

Table 4.11: Herschel-Bulkley (HB) model fitting parameters for o/w emulsions at different temperatures.

Emulsion set / Temperature (°C)	τ_0 (Pa)	m' (Pa.s ⁿ)	n'	R^2	Adj R^2	SEE	PRESS
Set 5 (80 %)							
25	0.921	1.2027±0.0471	0.5682±0.0094	0.9949	0.9948	0.3152	4.0987
30	0.876	1.2244±0.0615	0.4928±0.0121	0.9884	0.9881	0.3282	4.5161
40	0.864	1.2245±0.0781	0.4344±0.0155	0.9854	0.9848	0.3522	5.2947
50	0.778	0.8732±0.0477	0.4353±0.0133	0.9811	0.9806	0.2155	1.9685
Set 4 (70 %)							
25	0.688	1.1349±0.0609	0.5441±0.0129	0.9896	0.9893	0.3790	6.0247
30	0.648	1.0139±0.0496	0.5130±0.0118	0.9900	0.9897	0.2809	3.3109
40	0.636	0.9509±0.0590	0.4712±0.0150	0.9806	0.9801	0.2958	3.6887
50	0.442	0.5717±0.0282	0.5287±0.0119	0.9903	0.9900	0.1676	1.1659
Set 3 (50%)							
25	0.571	0.6353±0.0249	0.6232±0.0093	0.9970	0.9969	0.1718	0.9077
30	0.452	0.5149±0.0215	0.6278±0.0099	0.9967	0.9966	0.1500	0.6883
40	0.441	0.4651±0.0169	0.6033±0.0087	0.9972	0.9971	0.1094	0.3643
50	0.302	0.2932±0.0096	0.6560±0.0077	0.9982	0.9981	0.0731	0.1617
Set 2 (30%)							
25	0.612	0.6802±0.0340	0.5557±0.0120	0.9937	0.9935	0.1899	1.1255
30	0.524	0.6342±0.0295	0.5375±0.0112	0.9941	0.9939	0.1562	0.7583
40	0.491	0.3465±0.0128	0.6499±0.0088	0.9975	0.9975	0.0964	0.2847
50	0.324	0.2547±0.0066	0.6642±0.0061	0.9984	0.998	0.0597	0.1439
Set 1 (10%)							
25	0.504	0.5427±0.0229	0.5678±0.0101	0.9949	0.9947	0.1432	0.7396
30	0.427	0.3833±0.0111	0.6267±0.0069	0.9981	0.9980	0.0833	0.2438
40	0.404	0.3024±0.0096	0.6684±0.0075	0.9980	0.9979	0.0822	0.2408
50	0.278	0.2280±0.0066	0.6700±0.0069	0.9981	0.9981	0.0610	0.1523

All sets of o/w emulsions were found to exhibit pseudoplastic behavior with the flow behavior index (n) within the range of $0.44 \leq n \leq 0.55$. The pseudoplastic (shear-thinning) behavior may be because of the droplet aggregation and structural breakdown of emulsions during shearing. The pseudoplasticity of the emulsions is affected by temperature, as shown in Fig. 4.22. With an increase in temperature, the flow behavior index (n) for sets 5 and 4 decreases, with an increase in the pseudoplasticity, i.e. shear thinning behavior, of the o/w emulsions. Set 1 and set 2 emulsions have higher flow behavior index (n) than set 4 and set 5. For these emulsions, the flow behavior index (n) increases with an increase in temperature, and the emulsion behavior approaches the Newtonian behaviour. The flow behavior index of emulsion set 3 is not affected much with temperature, and showed $n = 0.57$. The flow consistency index (K) of emulsions decreases with increase in temperature, as shown in Fig. 4.23.

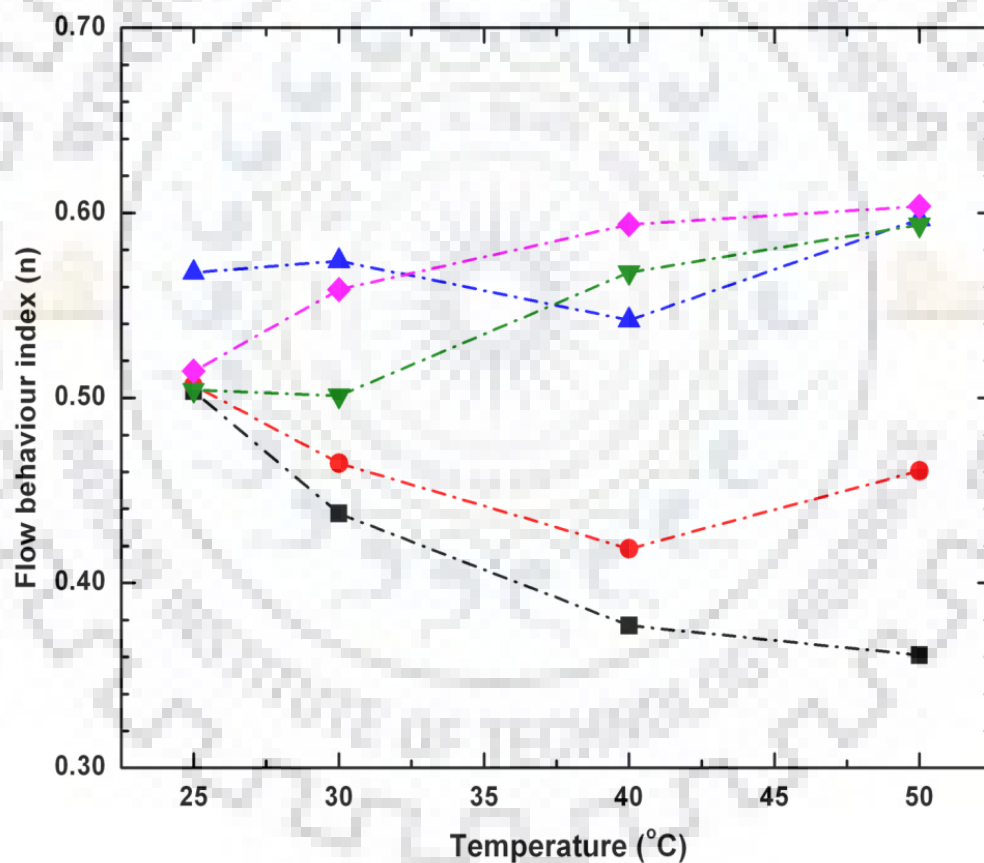


Fig 4.22: Effect of temperature on flow behavior index (n) of o/w emulsions.

Set 5 (—■—); set 4(—●—); set 3(—▲—); set 2(—▼—); set 1(—◆—).

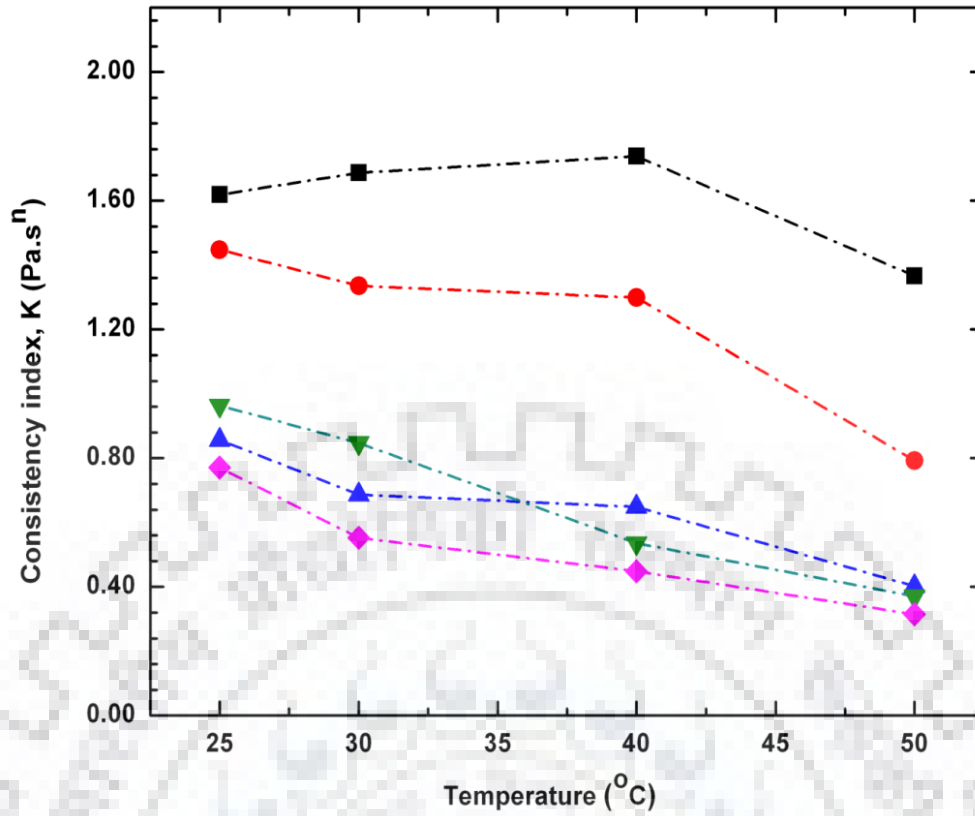


Fig 4.23: Effect of temperature on flow consistency index (K) of o/w emulsions.

Set 5 (—■—); set 4(—●—); set 3(—▲—); set 2(—▼—); set 1(—◆—).

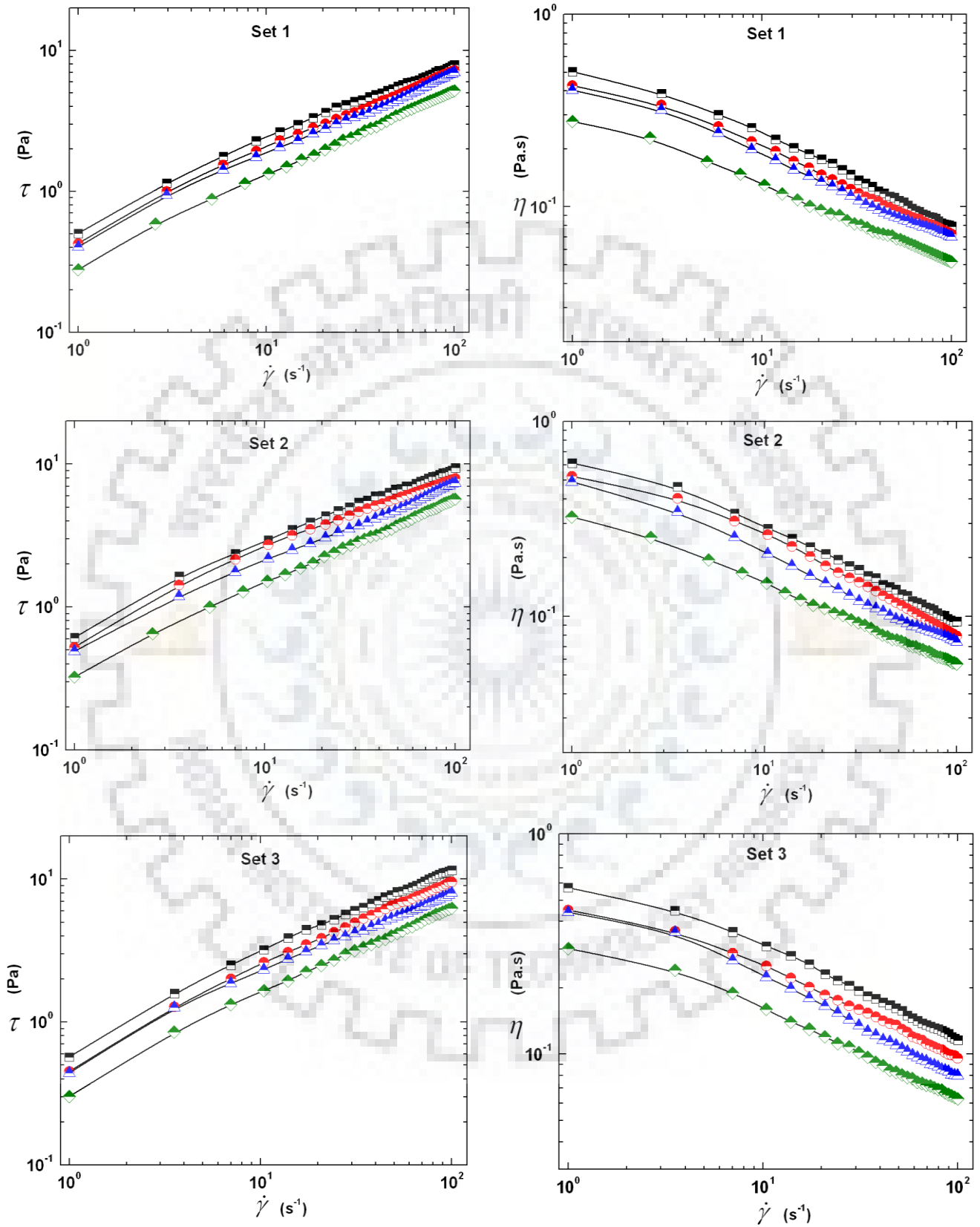
4.3.3 Effect of Temperature on Emulsion Rheology

Temperature plays an important role on the rheological characteristics of emulsions. The effect of temperature is shown in Fig 4.24. From the rheograms, it can be seen that the viscosity of emulsions decreases with an increase in temperature. The effect of temperature on the apparent viscosity of emulsions at a specified shear rate of 50 s^{-1} was also investigated.

The Arrhenius model was used to study the effect of temperature on apparent viscosity, which is given by

$$\eta = A \exp\left(\frac{-E_{\eta}}{RT}\right) \quad (4.10)$$

The Arrhenius plot ($\ln \eta$ versus $1/T$) for all five sets of emulsions is shown in Fig. 4.25. It was observed that the apparent viscosity of all the emulsions decreases with increase in temperature. The parameters obtained from Arrhenius model by curve fitting are reported in Table 4.5.



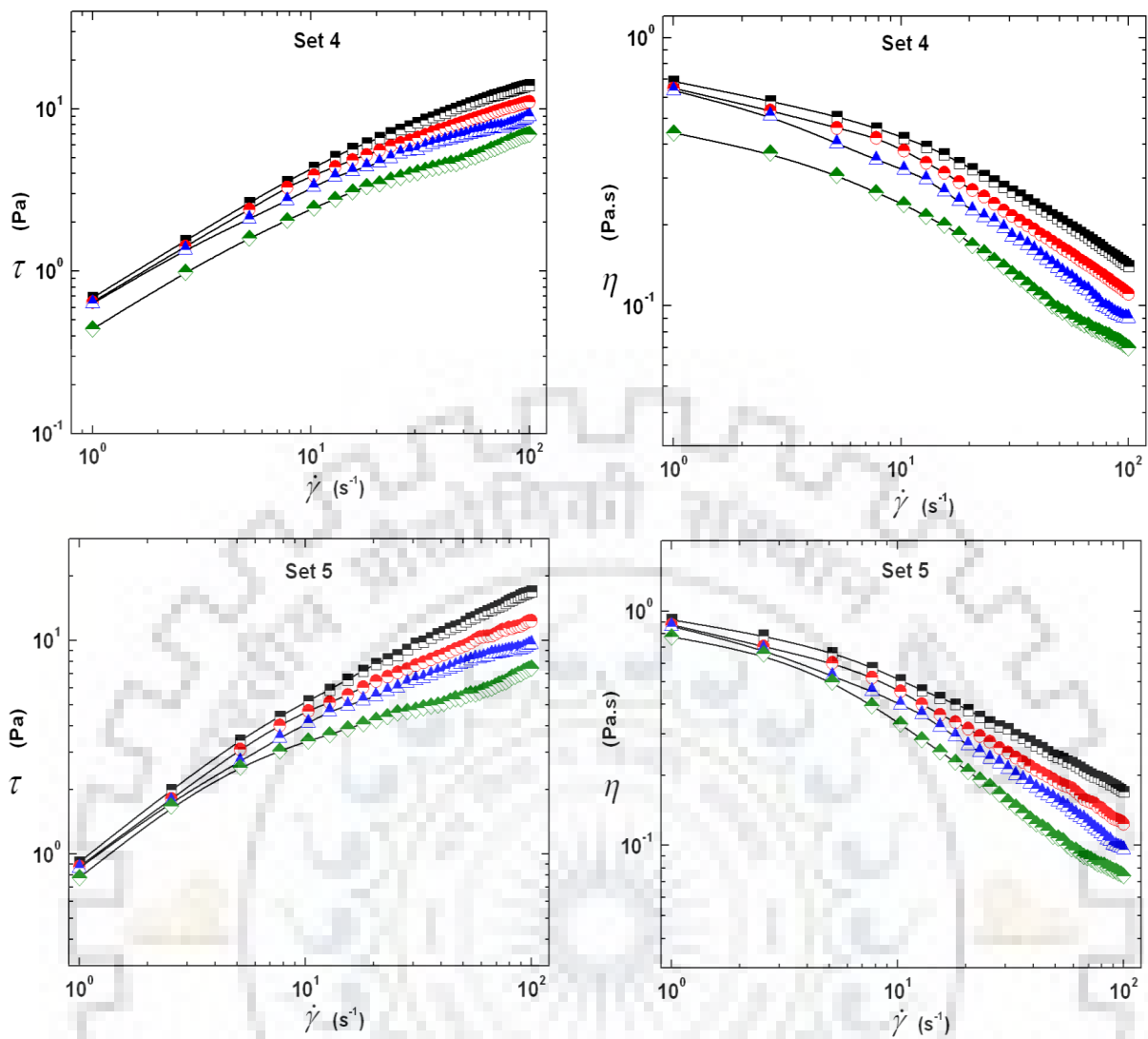


Fig. 4.24: Effect of temperature on the rheograms of o/w emulsion.

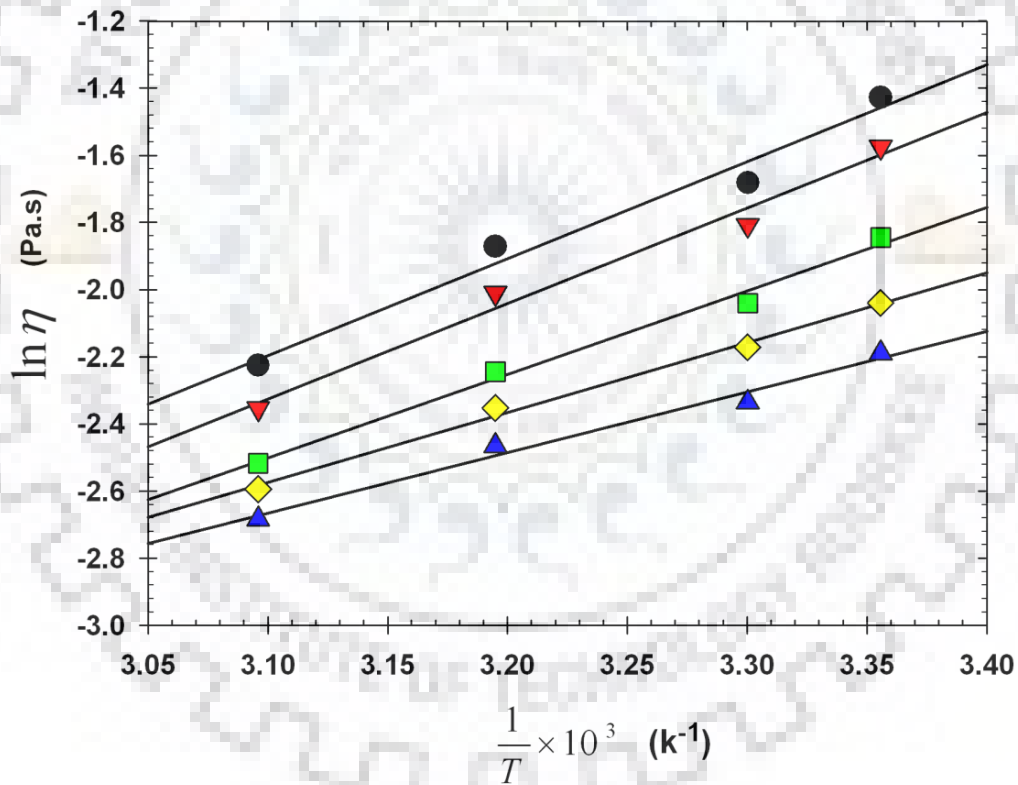
25 °C (—■—); 30 °C (—●—); 40 °C (—▲—); 50 °C (—◆—).

It can be seen that the apparent viscosity data of all sets of emulsions are adequately and satisfactorily represented by Eq. (4.10). The R^2 values for the emulsions of sets 1-4 were greater than 0.98, while for set 5, the R^2 value was 0.9763, which may be due to increased shear thinning behavior of the emulsion.

Table 4.12 shows that the activation energy increases with an increase in the oil concentration of the emulsion (i.e. from set 1 to set 5). The emulsions of sets 4, 5 (highly concentrated) and 3 (moderately concentrated) exhibited higher viscous activation energy (E_η) as compared to emulsions of sets 1 and 2 (dilute and semi-dilute emulsions), which indicated relatively higher sensitivity of temperature on the apparent viscosity of concentrated emulsions as compared to dilute o/w emulsions.

Table 4.12: Arrhenius model parameters for temperature dependency on apparent viscosity of different sets of o/w emulsions.

Emulsion set	A (Pa.s)	ΔE_η (kJ/mol)	R^2	adj. R^2	SEE	PRESS
Set 5	1.45×10^{-05}	23.9910	0.9763	0.9645	0.0634	0.0264
Set 4	1.46×10^{-05}	23.6282	0.9828	0.9741	0.0531	0.0188
Set 3	3.68×10^{-05}	20.6698	0.9909	0.9863	0.0336	0.0073
Set 2	1.21×10^{-04}	17.2842	0.9944	0.9916	0.0220	0.0041
Set 1	2.56×10^{-04}	15.0287	0.9836	0.9755	0.0329	0.0073

**Fig. 4.25:** Arrhenius plot for apparent viscosity of different o/w emulsions.

Set 5 (—●—); set 4(—▼—); set 3(—■—); set 2(—◆—); set 1(—▲—).

4.3.4 Modelling of Temperature Dependency on Emulsion Rheology

In order to give an overall picture of the flow behavior of different types of o/w emulsions with temperature, the master-curve technique was used to model the rheological behavior of the emulsions for the entire range of temperature and shear rate. This technique is useful for reporting the rheological behavior of emulsions with respect to any temperature, and hence allows convenient comparison of o/w emulsions of different volume fractions. The master-curve was developed through the determination of shift factor (a_T) at a reference temperature of 30 °C. The results of the modified power law model fitting of the master-curve data displaying modified consistency coefficient (K'') and flow behavior index (n'') is shown in Table 4.13. The shift factor (a_T) was calculated as given below (Ferry, 1980):

$$\ln a_T = \frac{E}{R} \left(\frac{1}{T} - \frac{1}{T_{ref}} \right) \quad (4.11)$$

Eq. (4.11) is similar to the Arrhenius equation. Shift factor for five different sets of emulsions were plotted at different temperatures as shown in Fig. 4.26. The master-curve was plotted using original shear rate versus reduced shear stress obtained by dividing the actual shear stress with the dimensionless shift factor. The shifting of data causes the data to overlap on a single curve. Master curves for reduced shear stress and reduced viscosity are shown in Figs. 4.27(a-b). Finally the master-curves for all five sets of emulsions at various oil concentrations and temperatures are represented in a single plot and are fitted to the original power law equation to present a single description of flow behavior in terms of K'' and n'' .

Multiple regression analysis indicated that the Master-Curve presents a good agreement for o/w emulsions at all oil concentrations, with $R^2 > 0.98$. The value of n'' decreases with concentration, thus confirming the earlier analysis suggesting that all the five sets of emulsions are pseudoplastic in nature, and that the pseudoplasticity increases with an increase in oil volume fraction.

Table 4.13: Parameters from master-curve for power law equation fitting into master curve at various temperatures (°C).

Emulsion sets	K'' (Pa.s ⁿ)	n''	R^2	Adj R^2	PRESS
Set 5	2.3582 ± 0.0987	0.3869 ± 0.0102	0.9844	0.9840	6.2640
Set 4	1.4163 ± 0.0512	0.4711 ± 0.0088	0.9929	0.9927	2.7585
Set 3	0.8431 ± 0.0168	0.5425 ± 0.0048	0.9989	0.9988	0.2618
Set 2	0.6674 ± 0.0216	0.5680 ± 0.0078	0.9973	0.9972	0.5080
Set 1	0.5429 ± 0.0158	0.5940 ± 0.0070	0.9977	0.9976	0.4275

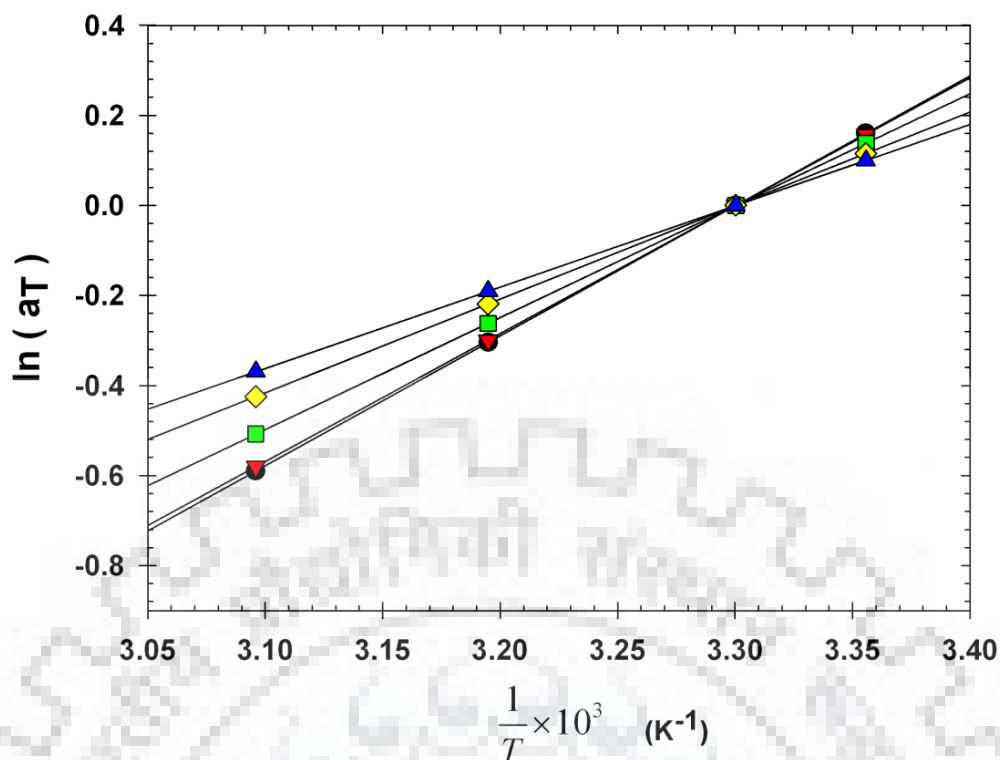


Fig. 4.26: Shift factor plot for master curve for different o/w emulsions.

Set 5 (—●—); set 4(—▼—); set 3(—■—); set 2(—◆—); set 1(—▲—).

4.3.5 Effect of Volume Fraction on O/W Emulsion Rheology

In order to observe the effect of volume fraction on emulsion viscosity, the apparent viscosity of emulsions at four shear rates (20 s^{-1} , 40 s^{-1} , 80 s^{-1} and 100 s^{-1}) was plotted against volume fraction of the oil in Fig. 4.28. It was observed that the apparent viscosity of the emulsion increases with a gradual increase in the volume fraction of oil, and the maximum apparent viscosity was obtained at an oil volume fraction of 0.8.

The apparent viscosity of highly concentrated emulsions (set 5 and set 4) is much higher in comparison to that of the dilute o/w emulsions (set 1 and set 2). From the previous rheograms, it can be seen that the highly concentrated (set 5 and set 4) emulsions tend to be more shear-thinning in comparison to dilute (set 2, and set 1) emulsions, at different temperatures and different shear rates, especially at low temperature ($25 \text{ }^\circ\text{C}$). The increase in viscosity and shear-thinning property with an increase in volume fraction of the dispersed phase (oil) was attributed to the size reduction of the droplets and an increase in the droplet-droplet interactions, which causes the aggregation/flocculation of the droplets (Schramm, 1983). As the volume fraction of the dispersed phase increases, the size of droplets decreases and the number density of droplets (number of droplets per unit volume of emulsions at a given dispersed phase volume fraction) increases. As a consequence, the mean distance of separation between the droplets decreases where London-van der Waals forces of attraction between the droplets are dominant.

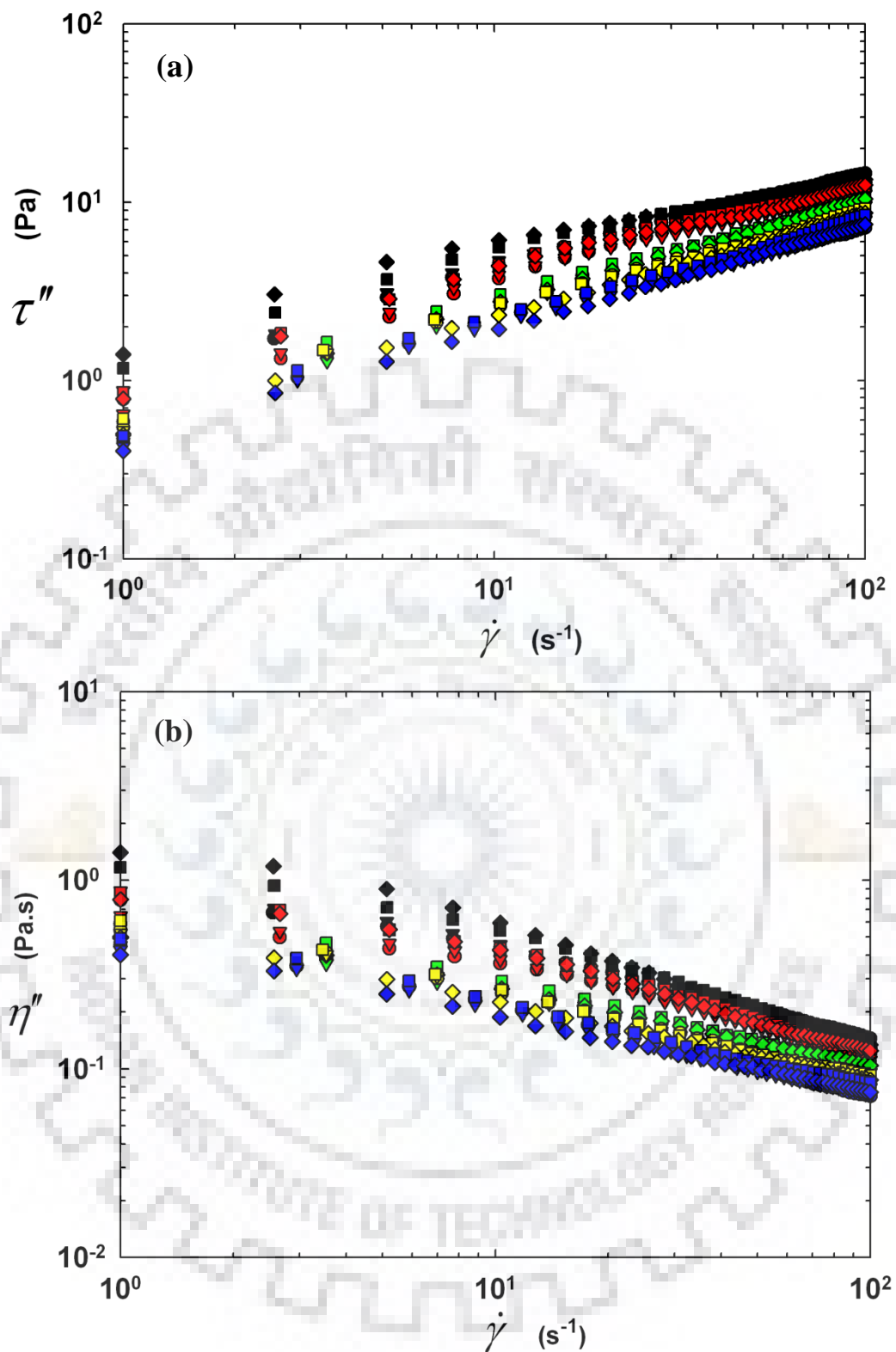


Fig.4.27: Master-curve showing superimposition on (a) shear stress–temperature (b) emulsion apparent viscosity–temperature with shear rate for different o/w emulsions at different temperature ($T_{\text{ref}} = 30\text{ }^{\circ}\text{C}$).

Set 5 (—●—); set 4(—▼—); set 3(—■—); set 2(—◆—); set 1(—▲—).

This facilitates the droplet–droplet collisions and flocculation of emulsion droplets. The flocculated droplets immobilize a significant amount of the continuous phase within them. As the shear rate (or shear stress) increases the size of the flocs decreases releasing some amount of the continuous phase, that was originally immobilized within the flocculated droplets. As a result, the effective dispersed-phase concentration decreases, which causes a decrease in the viscosity, and the shear-thinning effect (Pal and Rhodes, 1985, 1997).

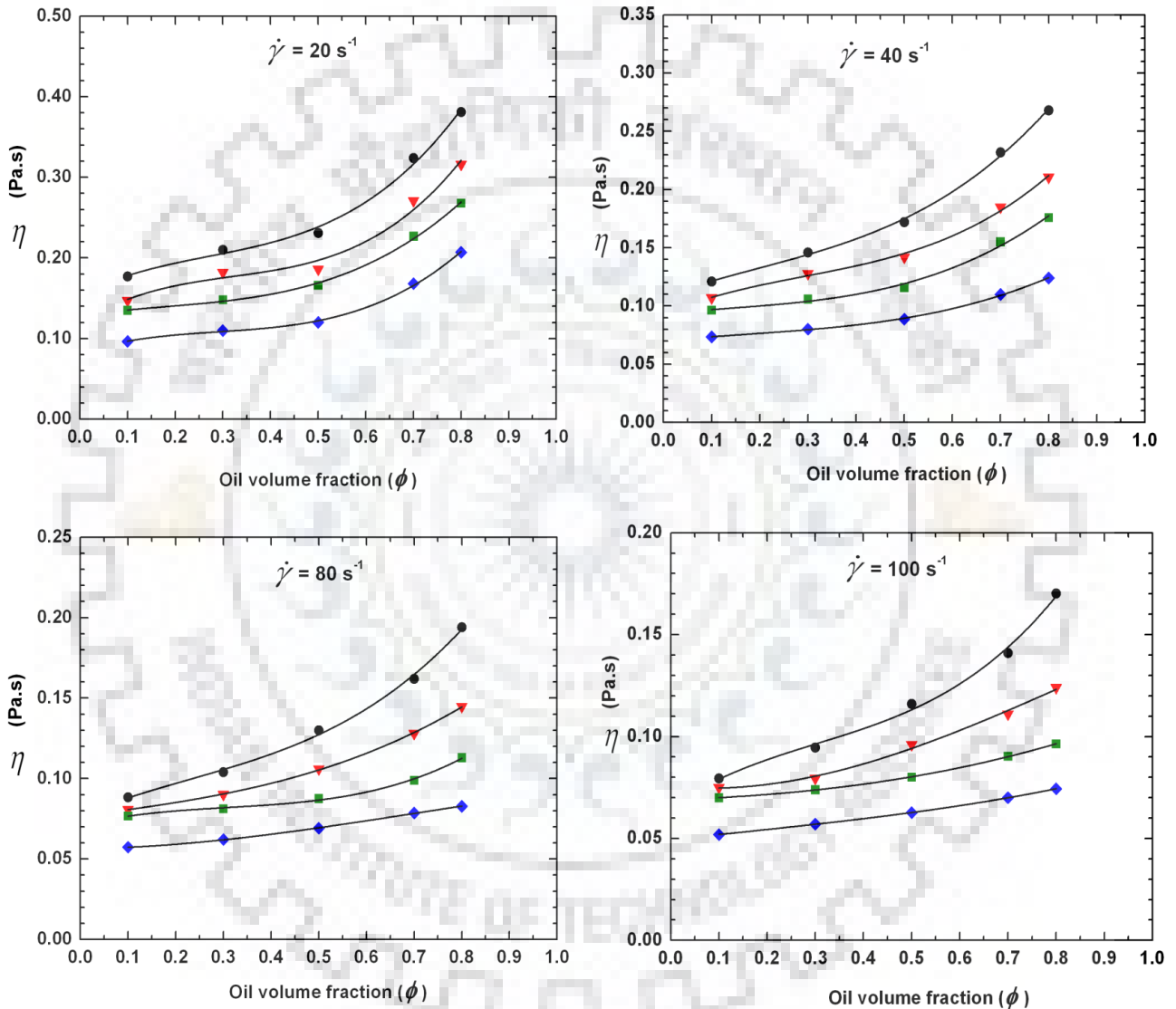


Fig. 4.28: Variation of emulsions apparent viscosity with internal phase (oil) volume fraction with temperature as a parameter at different shear rates.

25 °C (—●—); 30 °C (—▼—); 40 °C (—■—); 50 °C (—◆—).

In order to provide a general correlation between the apparent viscosity and the volume fraction of oil in the emulsion at a particular temperature, an exponential model and a polynomial model were proposed, as follows:

$$\text{Exponential model: } \eta_a = Y_M + K_V \exp(K_p \phi) \quad (4.12)$$

$$\text{Polynomial model: } \eta_a = \Lambda + (C_1 \phi + C_2 \phi^2 + C_3 \phi^3) \quad (4.13)$$

These two models were fitted to the experimental data using nonlinear regression analysis and the plots are shown in Fig. 4.29. In the above models the coefficients $\Lambda, K_M, K_V, K_p, C_1, C_2, C_3$ are model constants, which are functions of shear rate and volume fraction. The values of the model constants are reported in the Appendix B (Table B2 and Table B3). The thermal effect on the apparent viscosity of emulsions can be described by an equation of the type:

$$\eta_a = E_0 + E_1 \exp(-A_p T) \quad (4.14)$$

The combined effect of temperature and dispersed phase volume fraction on the apparent viscosity of emulsions can be illustrated by combining the Eqs. (4.12) and (4.14), as follows:

$$\begin{aligned} \eta_a &= f(\phi, T) \\ \ln(\eta_a) &= p_1 + p_2 \phi + p_3 T + p_4 \phi T \end{aligned} \quad (4.15)$$

Eq. (4.15) was used to fit the experimental data as shown in Fig. 4.29. It was observed that the proposed correlation represents the experimental data significantly well with $R^2 = 0.9739$ and a mean deviation of ± 0.116 .

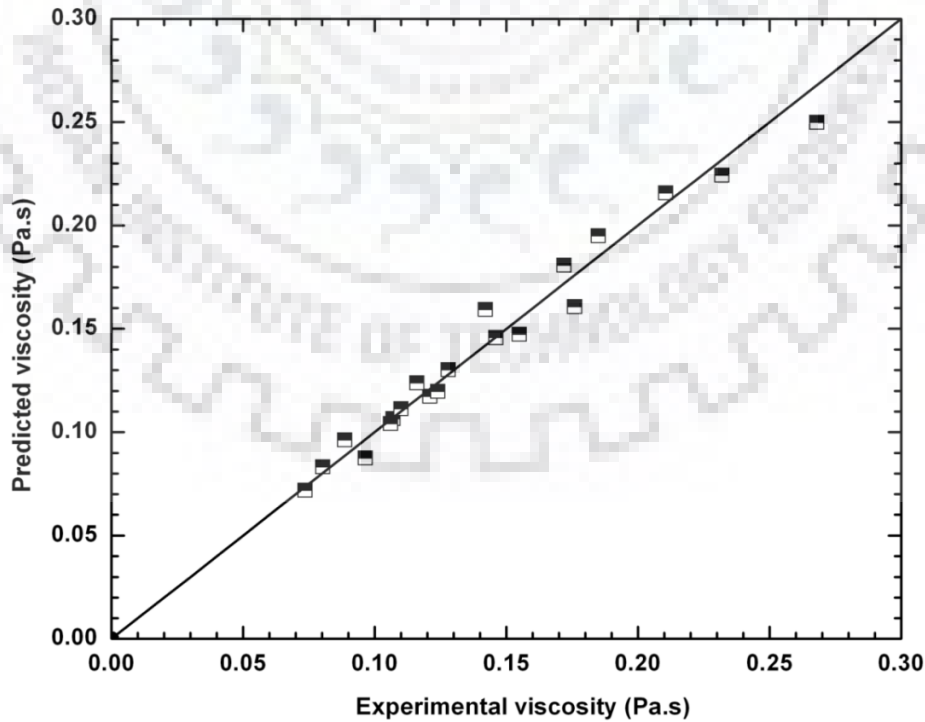


Fig. 4.29: Parity Plot of predicted viscosity with experimental viscosity of o/w emulsions at

$$\dot{\gamma} = 40 \text{ s}^{-1} .$$

4.3.6 Effect of Surfactant Concentration on O/W Emulsion Rheology

The effect of surfactant concentration on the rheology of o/w emulsions is shown in Fig. 4.30. The emulsion viscosity increases with an increase in the surfactant concentration in the range of 0.5 - 2 % (w/v). The plots of apparent viscosity versus shear rate for emulsions having different surfactant concentrations indicates a decrease in viscosity (η_a) with an increase in shear rate ($\dot{\gamma}$). Emulsions (o/w) at different surfactant concentrations exhibited non-Newtonian behavior, i.e. the shear thinning pseudoplastic behavior. This may be because of the progressive breakdown of the emulsion flocculated microstructure with an increase in shear rate. At high values of $\dot{\gamma}$, the emulsion becomes relatively unflocculated. The emulsion with a low surfactant concentration (0.5 wt %) exhibited a linear behavior with an insignificant low yield stress value and described well by Power law model. At surfactant concentration higher than 1% and highly concentrated (70 % o/w, (v/v)) emulsion the rheological data exhibited appreciable amount of yield stress. The yield stress may be attributed to the formation of interconnected network structure between the flocculated emulsion droplets (Pal, 1997). The yield stress depends upon the number of the dispersed droplets and the degree of flocculation of these droplets, and increases with an increase in the degree of flocculation and the number of droplets, for high surfactant (> 1% w/v) and the dispersed phase (oil) concentrations (> 50 % v/v). A plateau region was observed for moderately concentrated (50%, v/v) and highly concentrated (70%, v/v) emulsions having higher SDBS concentration (2 % w/v) on the rheogram. This may be due to the flocculating nature of emulsions and “slip flow” phenomena (Dzuy and Boger, 1983; Barnes, 1995; Pal, 2000).

To account for the non-Newtonian behavior and yield stress in the emulsions, experimental data was fitted with the well-known Ostwald-de-Waele power law, HB and Casson models. The values of the model parameters for the present experimental data are given in Table 4.14. It was observed that the HB model represents the emulsion rheological behavior for 2 % (w/v) surfactant concentration well ($R^2 \sim 0.99$) as compared to power law and Casson model.

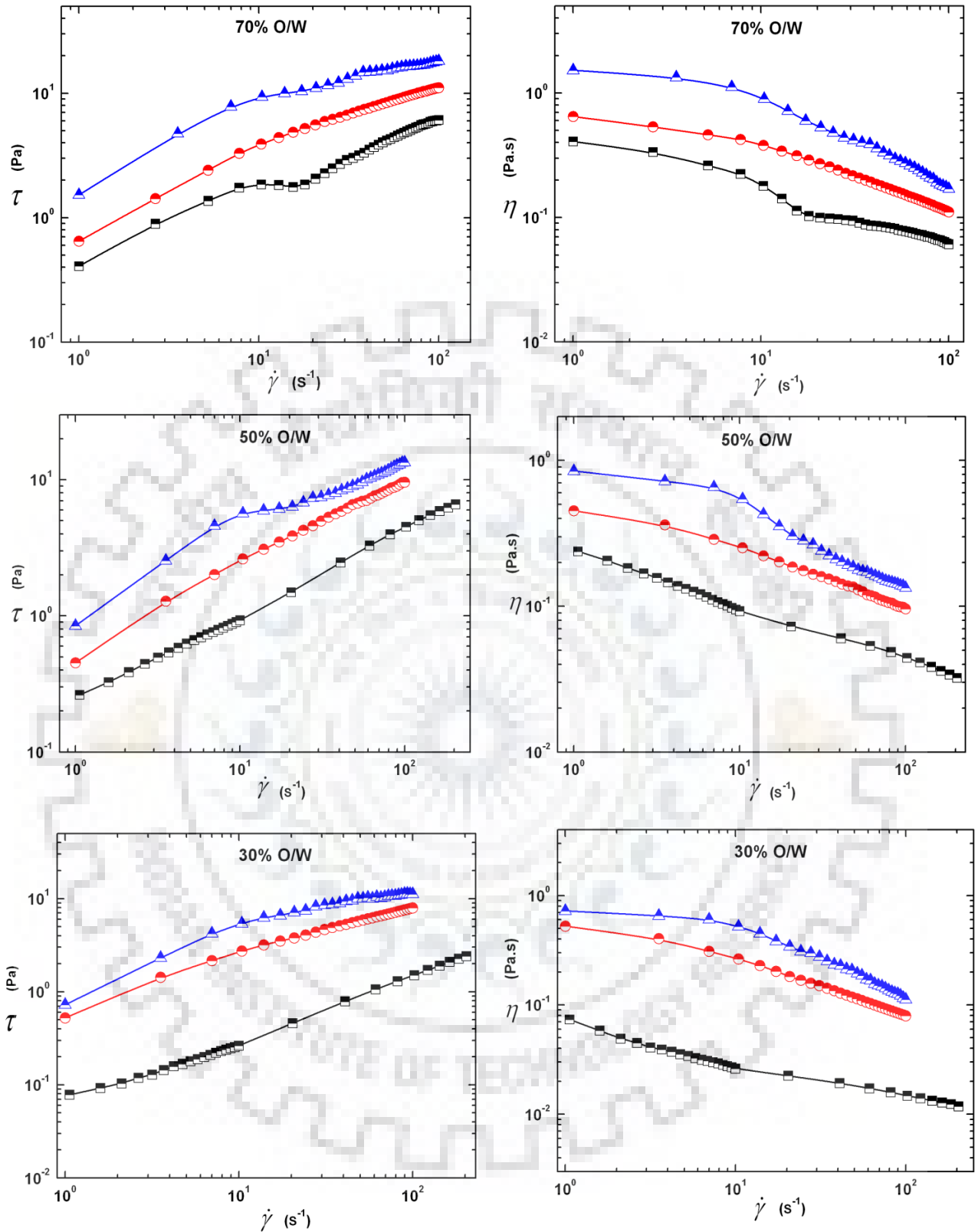


Fig. 4.30: Effect of surfactant concentration on the rheograms of o/w emulsions.

Surfactant concentration (wt %): 0.5% (—■—); 1% (—●—); 2% (—▲—).

Table 4.14: Various model fitting parameters of o/w emulsions at different surfactant concentrations.

Surfactant concentration (% w/v)	τ_0 (Pa)	m' (Pa.s ⁿ)	n'	R^2	Adj R^2	SEE	PRESS
Power law model							
O/W (70%)							
2	-	1.8845 ± 0.0838	0.3618 ± 0.0225	0.9300	0.9275	0.1764	1.2295
1	-	1.3364 ± 0.0424	0.4647 ± 0.0077	0.9945	0.9944	0.2083	1.8515
0.5	-	0.6267 ± 0.0195	0.5986 ± 0.0154	0.9831	0.9831	0.0613	0.1650
O/W (50%)							
2	-	1.2356 ± 0.0416	0.4671 ± 0.0169	0.9760	0.9751	0.0979	0.3542
1	-	0.6867 ± 0.0150	0.5740 ± 0.0058	0.9988	0.9988	0.0889	0.2457
0.5	-	0.4774 ± 0.0049	0.6392 ± 0.0047	0.9988	0.9988	0.0240	0.0183
O/W (30%)							
2	-	1.3773 ± 0.0684	0.4084 ± 0.0250	0.9347	0.9323	0.1511	0.8698
1	-	0.8875 ± 0.0205	0.4777 ± 0.0056	0.9980	0.9979	0.0907	0.2619
0.5	-	0.2352 ± 0.0027	0.7124 ± 0.0051	0.9990	0.9989	0.0138	0.0056
Herschel-Bulkley model							
O/W (70%)							
2	1.526	30.3506 ± 8.5221	0.1542 ± 0.0237	0.9928	0.9923	0.3575	5.1549
1 %	0.648	1.0139 ± 0.0496	0.5130 ± 0.0118	0.9900	0.9897	0.2809	3.3109
0.5	0.408	0.2196 ± 0.0388	0.7162 ± 0.0352	0.9920	0.9915	0.1525	1.0923
O/W (50%)							
2	0.847	1.4927 ± 0.3790	0.4691 ± 0.0459	0.9847	0.9837	0.4073	8.8790
1	0.452	0.5149 ± 0.0215	0.6278 ± 0.0099	0.9967	0.9966	0.1500	0.6883
0.5	0.238	0.2883 ± 0.0260	0.5958 ± 0.0163	0.9988	0.9987	0.0752	0.2076
O/W (30%)							
2	0.725	26.5192 ± 11.3116	0.0775 ± 0.0271	0.9905	0.9898	0.2760	8.4875
1	0.524	0.6342 ± 0.0295	0.5375 ± 0.0112	0.9941	0.9939	0.1562	0.7583
0.5	-	0.0587 ± 0.0082	0.7014 ± 0.0096	0.9996	0.9996	0.0149	0.0082
Casson model							
	τ_y (Pa)	K_c (Pa.s ⁿ)	R^2	Adj R^2	SEE	PRESS	
O/W (70%)							
2	4.328±0.1507	0.0561±0.0213	0.8155	0.8090	0.2864	3.1880	
1	1.072±0.0686	0.4850±0.0097	0.9394	0.9378	0.1487	1.0611	
0.5	0.412±0.0265	0.0363±0.0037	0.9855	0.9852	0.5750	0.1548	
O/W (50%)							
2	1.752±0.0825	0.0580 ± 0.0117	0.9384	0.9362	0.1568	0.9971	
1	0.891±0.0517	0.4913±0.0073	0.9750	0.9741	0.0983	0.3711	
0.5	0.201±0.0190	0.0251±0.0020	0.9915	0.9912	0.0642	0.1349	
O/W (30%)							
2	2.265±0.1277	0.0450±0.0180	0.8314	0.8254	0.2428	2.2601	
1	0.975±0.0581	0.4452±0.0082	0.9541	0.9524	0.1105	0.4768	
0.5	0.039±0.0077	0.0098±0.0012	0.9964	0.9962	0.0231	0.0222	

4.3.7 Effect of pH on Rheological Behavior Under Steady Shear Flow

Fig. 4.19 shows that the emulsions exhibit a shear-thinning behavior, with a clear tendency of both a zero-shear rate-limiting viscosity (η_0), at low shear rates and a high-shear rate-limiting viscosity (η_∞), at high shear rates. This kind of flow behavior is observed in flocculated emulsions due to droplet-droplet deflocculation mechanism (Otsubo and Prudhomme, 1994; Franco *et al.*, 1998). A hump is observed at the low shear rate ($\dot{\gamma} \sim 10^{-3} \text{ s}^{-1}$) for pH 12 and pH 10. At a shear rate of 0.002 s^{-1} , a yield point is observed and thereafter, shear-thinning behavior is seen. The shear-thinning behavior is manifested because of the gradual break-up of inter-particle fluid structure (flocculated droplets) (Lee *et al.*, 1997). For pH 12 and pH 10, the dilatant behaviour is observed at $\dot{\gamma} < 0.002 \text{ s}^{-1}$. This shear rate of $\dot{\gamma}_c = 0.002 \text{ s}^{-1}$ may be seen as the critical shear rate below which no structural deformation occurred due to very low applied shear stress against the strong flocculation force. As the pH decreases (pH < 10), the yield point gets diminished and no hump is observed in the low shear rate region. From Fig. 4.7, it is seen that the DSD profile shifts right toward the larger droplet size as the pH of the emulsion decreases, and the mean d_{43} also increases. Thus the droplet size of the emulsion is large as compared to that for pH 12 and 10. Therefore, the structural deformation of the emulsions occurred continuously from flocculated to a deflocculated state under applied shear rate even at lower values overcoming the weak flocculation force.

Fig. 4.31 (a-b) shows that the o/w emulsions at different pH exhibit non-Newtonian flow behavior within the measured range of shear rate ($10^{-3} - 10^3 \text{ s}^{-1}$). The emulsion flow spectra showed three distinct flow regimes, i.e. low shear rate, intermediate and high shear rate regime. Various non-Newtonian rheological model: (Ostwald-de Waele, Cross, Carreau, and Sisko) are, therefore, used to evaluate their applicability to satisfactorily represent the non-Newtonian behavior of the o/w emulsion.

Sisko model:
$$\eta_a = \eta_\infty + K\dot{\gamma}^{n-1} \quad (4.16)$$

Cross model:
$$\frac{\eta_a - \eta_\infty}{\eta_0 - \eta_\infty} = \left[1 + \left(\frac{\dot{\gamma}}{\dot{\gamma}_c} \right)^m \right]^{-1} \quad (4.17)$$

Carreau model:
$$\frac{\eta_a - \eta_\infty}{\eta_0 - \eta_\infty} = \left[1 + \left(\frac{\dot{\gamma}}{\dot{\gamma}_c} \right)^2 \right]^{-N} \quad (4.18)$$

The power law model given in Eq. (4.7), is frequently used to describe the time-independent shear rate- shear stress relationship for non-Newtonian fluids. It is a two parameter model containing flow consistency index (K) and flow behavior index (n). The Sisko model (Eq. 4.16) is a

three parameter model including the parameter η_{∞} . The Sisko model is used to describe the emulsion flow in the upper shear rate regions.

The rheograms for emulsions at pH 12 and pH 10 show a complex behaviour. Fig. 4.31 clearly shows that the power law model cannot represent the shear stress-shear rate data over the entire range of shear rate. At low shear rate region ($\dot{\gamma} < 0.1 \text{ s}^{-1}$), the power law model did not fit well. However, the power law model is satisfactory for the intermediate shear rate region ($10^{-1} \text{ s} \leq \dot{\gamma} \leq 10^3 \text{ s}^{-1}$), for all the sets of o/w emulsions ($2 \leq \text{pH} \leq 12$). The Results of regression analysis are shown in Table 4.15. It is observed that the average flow behavior index (n) for all o/w emulsions lies in between 0.55 and 0.89, which exhibit the shear-thinning pseudoplastic nature of the emulsion. These may be due to the droplet aggregation and the structural breakdown of the emulsions for the hydrodynamic force generation during shearing. It is also seen that the flow behavior index (n) decreases, with an increase in pH of the emulsions. Thus, the pseudoplasticity of o/w emulsions increases with an increase in pH and becomes more shear thinning in nature. The flow consistency index (K) of emulsions also increases with an increase in pH.

The Sisko model does not exactly represent the experimental data in the low shear rate region with a lower value of correlation coefficient than that of the power law model. However, both the Power law model and Sisko model cannot describe the overall rheological behavior of o/w emulsion within the shear rate range of 10^{-2} - 10^3 s^{-1} studied for all emulsions. Therefore, the rheological data encompassing the upper and lower shear rate regimes coupled with an intermediate power law regime, were described by following four parameter complex rheological models.

Table 4.15: Flow parameters of o/w emulsions determined by power law and Sisko model.

Power law model (Two parameter)					
pH	η_{∞} (Pa. s)	K (Pa.sⁿ)	n	χ^2	R^2
pH12	-	0.8832 ± 0.0155	0.5483 ± 0.0115	4.54×10^{-4}	0.9923
pH 10	-	0.3991 ± 0.0145	0.5631 ± 0.0059	3.67×10^{-2}	0.9988
pH 8	-	0.2064 ± 0.0104	0.6301 ± 0.0077	6.99×10^{-4}	0.9979
pH 6	-	0.0935 ± 0.0006	0.7267 ± 0.0011	6.59×10^{-4}	0.9999
pH 4	-	0.0456 ± 0.0029	0.7190 ± 0.0098	1.27×10^{-2}	0.9975
pH 2	-	0.0068 ± 0.0002	0.8880 ± 0.0049	5.57×10^{-4}	0.9995
Sisko model (Three parameter)					
pH12	0.0269	0.8689 ± 0.0217	0.5074 ± 0.0177	8.24×10^{-4}	0.9860
pH 10	0.02	0.4284 ± 0.0090	0.4963 ± 0.0166	1.66×10^{-4}	0.9882
pH 8	0.0149	0.1746 ± 0.0025	0.5072 ± 0.0084	1.15×10^{-5}	0.9904
pH 6	0.0127	0.0883 ± 0.0024	0.5314 ± 0.0145	1.07×10^{-5}	0.9676
pH 4	0.00622	0.0396 ± 0.0008	0.5564 ± 0.0107	1.27×10^{-5}	0.9831
pH 2	0.00314	0.0099 ± 0.0004	0.5540 ± 0.0200	3.03×10^{-5}	0.9317

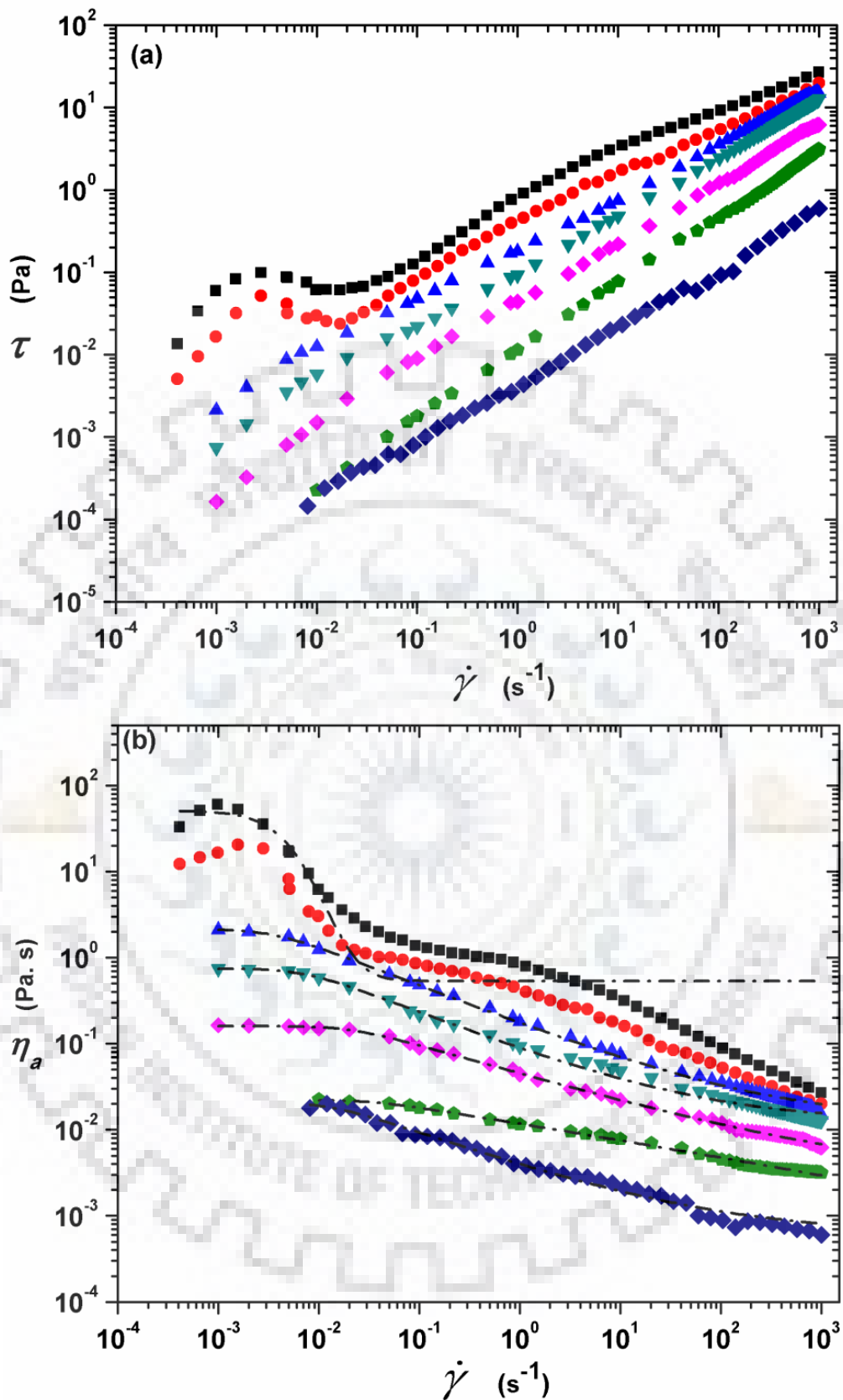


Fig. 4.31: Evolution of steady-state rheograms of o/w emulsion for different pH.

(a) Shear stress-shear rate plot (b) Apparent viscosity-shear rate plot.

pH: 12 —■—; 10 —●—; 8 —▲—; 6 —▼—; 4 —◆—; 2 —◆—; surf 1 wt% —◆—.

Table 4.16: Flow parameters of o/w emulsions determined by Cross and Carreau model.

Cross model (Four parameter)						
pH	η_0 (Pa. s)	η_∞ (Pa. s)	$\dot{\gamma}_c$ (s ⁻¹)	m	χ^2	R^2
pH 12	49.3922±1.9041	0.8322±0.5153	0.0042±0.0003	2.9271±0.5291	10.6	0.9486
pH 10	16.5244±0.5704	0.4974±0.1830	0.0049±0.0002	4.9049±1.4526	1.37	0.9460
pH 8	2.7545±0.0980	0.0241±0.0044	0.0083±0.0011	0.6324±0.0232	9.02×10^{-4}	0.9958
pH 6	0.8409±0.0217	0.0191±0.0021	0.0267±0.0028	0.7378±0.0330	2.10×10^{-4}	0.9937
pH 4	0.1788±0.0029	0.0074±0.0006	0.1246±0.0102	0.5978±0.0219	7.58×10^{-6}	0.9968
pH 2	0.02947±0.0012	0.0017±0.0002	0.2356±0.0575	0.3584±0.0191	7.03×10^{-8}	0.9973
Carreau model (Four parameter)						
pH	η_0 (Pa. s)	η_∞ (Pa. s)	$\dot{\gamma}_c$ (s ⁻¹)	N	χ^2	R^2
pH 12	50.6595±2.041	0.7338±0.5543	0.0059±0.0027	1.7669±1.1352	11.778	0.9462
pH 10	16.8304±0.7189	0.4088±0.2142	0.0153±0.0220	6.2948±16.494	1.8111	0.9331
pH 8	2.1540±0.0140	0.0128±0.0025	0.0035±0.0001	0.2270±0.0033	2.0×10^{-4}	0.9990
pH 6	0.7461±0.0044	0.0122±0.0011	0.0072±0.0003	0.2279±0.0040	3.81×10^{-5}	0.9989
pH 4	0.1604±0.0008	0.0028±0.0005	0.0216±0.0011	0.1707±0.0040	2.41×10^{-6}	0.9990
pH 2	0.0221±0.0002	0.0031±0.0003	0.0359±0.0033	0.0927±0.0035	5.49×10^{-8}	0.9980

Both the Cross model (Eq. 4.17) and Carreau model (Eq. 4.18) takes account the two limiting viscosities, zero shear viscosity, η_0 and infinite shear viscosity, η_∞ over the entire range of shear rate studied. The characteristic parameters of the Cross and Carreau models from their fit to experimental data are shown in Table 4.16. The experimental rheological data well describe by both this model with the average R^2 value of 0.99 for ($2 \leq pH \leq 8$). But the rheological behaviour of the emulsions at pH 10, and pH 12 are very complex to model due to high non-linearity in the rheograms. For pH 10 and pH 12, two shear thinning regimes are observed: one at low shear rate zone ($3 \times 10^{-3} - 4 \times 10^{-2} \text{ s}^{-1}$), and the other at a relatively higher shear rate zone ($10^0 - 10^3 \text{ s}^{-1}$). In between these two zones, a plateau region is observed, which gets diminished at lower pH.

It can be observed from the Fig. 4, that for pH of 8 and below the curves reach a zero-shear plateau with a steadily increasing zero-shear viscosity. However we see a departure of this for pH 10 and 12 with a sudden jump to a larger value. This is an indication of a liquid-solid (sol-gel transition) due to the electrostatic repulsion which enhances the stability of the emulsion and may even form a weak crystalline solid. These shear induced phenomena also termed as Shear banding (SB) which observed in variety of other complex fluids, such as lamellar surfactant phases (Roux et al., 1993; Salmon et al., 2003), wormlike micelles (Mair and Callaghan, 1997; Miller and Rothstein, 2007; Helgeson et al., 2009), suspensions (Ragouilliaux et al., 2006) and polymeric solutions (Ravindranath et al., 2008; Boukany and Wang, 2009). SB phenomena is the stratification of the

flow into regions of high and low shear rate, $\dot{\gamma}$, connected by an “interface” of sharp $\dot{\gamma}$ change in which this homogeneous velocity gradient profile becomes unstable to heterogeneous perturbations and splits into high and low shear rate bands that coexist in the cell, so that the local shear rate varies spatially $\dot{\gamma} = \dot{\gamma}(y)$. Thus a characteristic stress plateau was observed in the flow curve at low shear rate regime. It occurs in homogeneously sheared systems when there is a range of shear rates where the stress apparently decreases with increasing shear rate, before it resumes its ascent (Huseby, 1966). The molecular origin of this double-valuedness in the constitutive behavior is usually the existence of at least two separate relaxation mechanisms, each being prevalent at a disparate region of the $\dot{\gamma}$ spectrum (Tsenoglou and Voyiatzis, 2008).

4.3.8 Scaling Analysis of Rheological Response of Emulsions

The apparent viscosity of emulsions is a function of following ten variables: such as, shear rate ($\dot{\gamma}$), time (t), continuous-phase viscosity (η_c), dispersed-phase viscosity (η_d), continuous-phase density (ρ_c), dispersed-phase density (ρ_d), droplet radius (R), concentration of droplets (θ), interfacial tension (σ) and thermal energy (kT).

$$\eta \equiv f(\dot{\gamma}, t, \eta_c, \eta_d, \rho_c, \rho_d, R, \theta, \sigma, kT) \quad (4.19)$$

According to degree of freedom analysis non-dimensional relative viscosity of emulsions is represented as a function of 7 dimensionless groups. Therefore,

$$\eta_r \equiv f(\rho_r, \tau_r, \mu_r, \phi, N_{Pe}, N_{Ca}, N_{Re,p}) \quad (4.20)$$

where, η_r is relative viscosity ($=\eta/\eta_c$), ρ_r is relative density ($=\rho_d/\rho_c$), τ_r is reduced time ($=t/(\eta_c R^3/kT)$), μ_r is viscosity ratio ($=\eta_d/\eta_c$), ϕ is volume fraction, N_{Pe} is Peclet number ($=\eta_c \dot{\gamma} R^3/kT$), N_{Ca} is capillary number ($=\eta_c \dot{\gamma} R/\sigma$), and $N_{Re,p}$ is particle Reynolds number ($=\rho_c \dot{\gamma} R^2/\eta_c$).

As average emulsion droplets quite large ($>1 \mu\text{m}$), the Brownian motion has little significance, i.e., the effect of the Peclet number can be neglected. Under steady-state ($\tau_r \rightarrow \infty$). The capillary number for oil-in-water emulsions is also very small ($N_{Ca} \rightarrow 0$) and can be neglected (Table 4.8). It should be noted further that the presence of surfactant at the surface of the dispersed particles inhibits internal circulation (Sherman, 1983). Thus the effect of internal circulation is neglected. Therefore, the relative viscosity of oil-in-water emulsions can be expressed as:

$$\eta_r = f(\phi, N_{Re,p}) \quad (4.21)$$

Hence, rheological data of all sets of emulsions for different pH can be scaled in terms of $N_{Re,p}$, which includes emulsion droplets size shown in Fig. 4.32(a). However, master curve cannot be

obtained due to variation of droplet size with different pH. Master curve was constructed by superposition method using a dimensionless viscosity and shear rate by using an empirically calculated shift factor. Values of the shift factors for the different emulsions studied, as a function of pH, are shown in Fig. 4.32(b). A dimensionless viscosity, including both the zero-shear rate and the high-shear rate-limiting viscosities, obtained from the fitting of the Carreau model, was used. Thus, $\eta'_{red} \equiv \alpha_{pH} \cdot \eta_{red}$ vs. $\dot{\gamma}$ leads to an empirical master curve that describes the flow behavior of these emulsions in the range of pH studied, where α_{pH} is the empirical shift factor (Fig. 4.32), which is equal to 1 for the reference flow curve (pH = 12) and $\eta_{red} = (\eta - \eta_{\infty}) / (\eta_0 - \eta_{\infty})$. However, pH dependence of the shift factor must provide information about the influence of emulsion pH on viscous behavior. This parameter gives information about the resistance of the emulsion microstructure to a shear induced breakdown process in the shear-thinning region.

4.3.9 Electro-viscous effect on emulsion rheology

The behavior of colloidal dispersions/emulsions depends to a large extent on the surface charge of the suspended colloidal particles, which are surrounded by a diffuse electrical double layer and contains a net charge per unit volume. Therefore, the fluid in double layer can be considered as an electrically charged fluid, which is subject to an electric field generated by the surface potential of the particles. When the dispersions or emulsions are subjected to flow, a coupling arises between the hydrodynamic flow field, and the electro-kinetics arising from the flow of a charged fluid relative to a charged surface (M van de Ven, 2001).

Electroviscous phenomena significantly influence the emulsion rheology as the dispersed phase volume fraction is determining emulsions viscosity. The viscosity of the emulsion is directly related to the magnitude of the repulsive forces. The influences of charge and repulsion on the interaction between droplets in an emulsion are sometimes referred to as electro-viscous effects. Due to the presence of electrical charge on the colloidal dispersions, three kinds of contribution may affect the viscosity behavior (Masliyah and Bhattacharjee, 2006). The primary effect refers to enhanced energy dissipation caused by electrostatic forces that oppose the distortion of the diffuse double layer of counter-ions around the molecule during the flow. The secondary effect is an enhancement of energy dissipation during flow that arises from inter-molecular repulsion between double layers and mutual repulsion of charged particles (Conway, 1960). The 'tertiary effect' that may arise if the inter-molecular repulsion affects the shape of macromolecule. These three are collectively known as the 'electro-viscous effects'.

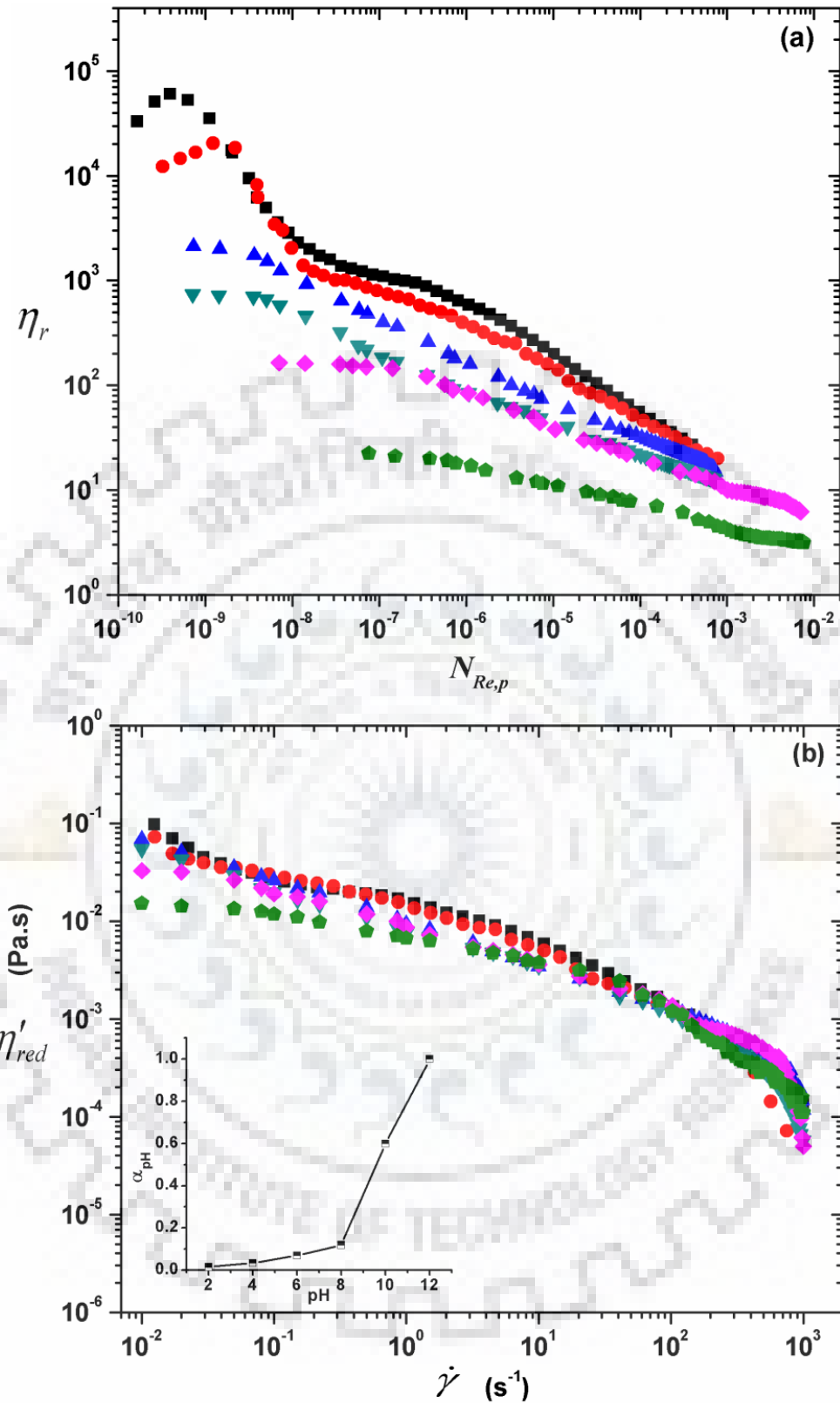


Fig. 4.32: (a) Relative viscosity (η_r) as a function of particle Reynolds number ($N_{Re,p}$) and (b) pH-Reduced master flow curve and evolution of the shift factor for 30% (v/v) oil-in-water emulsions with 1 wt% surfactant concentration.

pH: 12 —■—; 10 —●—; 8 —▲—; 6 —▼—; 4 —◆—; 2 —◆—.

The increase in effective viscosity of dispersions is due to the electro-viscous effect and is expressed by a modified Einstein's model as expressed below:

$$\eta = \eta_0 \left\{ 1 + \frac{5}{2} \phi [1 + \mathfrak{R}(\zeta, \kappa a)] \right\} \quad (4.22)$$

Waiterson and White (1981) theoretically derived the electro-viscous coefficient $\mathfrak{R}(\zeta, \kappa a)$, as a function of the zeta potential ζ of the suspension, as follows:

$$\mathfrak{R}(\zeta, \kappa a) \approx \frac{3\epsilon k_B T}{10\pi\eta_0 e^2} \left\{ \frac{\sum_{i=1}^N n_i^\infty z_i^2 \lambda_i}{\sum_{i=1}^N n_i^\infty z_i^2} \right\} L(\kappa a) \left(\frac{e\zeta}{k_B T} \right)^2 \quad (4.23)$$

where η is the effective viscosity of a suspension, ϕ is the volume of the suspension, κa is the dimensionless Debye inverse length, η_0 is the viscosity of the pure dispersions medium, ζ is the zeta potential, n_i^∞ , Z_i and λ_i are the properties of the electrolyte ions (viz. bulk number density, the electronic charge, hydrodynamic drag coefficient of an ion of type i , respectively), ϵ is the permittivity of the medium, k_B is the Boltzman constant and T is the absolute temperature. This suggests that the electro-viscous effect play a significant role in increasing the viscosity of emulsions. The magnitude of the electro-viscous effect is proportional to ζ^2 . Thus, this effect can cause a large increase in the viscosity of emulsions mainly for the case of pH 12 and 10.

Droplet agglomeration/flocculation also increases the emulsion viscosity, which is attributed to retardation of flow of continuous phase fluid entrapped in the interstices of cluster of droplets (Sherman, 1968). The extent of agglomeration/flocculation is a function of the shear rate of measurement and the balance of attractive and repulsive inter-particle forces. At higher pH emulsions are more flocculated in nature having relatively higher viscosity and agglomeration gradually decreases with a decrease in emulsion viscosity due to charge neutralization leading to coalescence of dispersed droplets. The observed behavior suggests that the viscosity should increase with an increase in pH due to the additional resistance to flow offered by the electro-viscous effects.

The chemical nature of the emulsifier has an effect on the relative viscosity. The nature of the emulsifier, in particular its solubility and distribution in both phases, also has a significant effect on the rheology of the system. The emulsifier molecules adsorb at the oil–water interface and reduce the interfacial tension, thereby favoring emulsification and forming a protective barrier around the oil droplets. This charge is also responsible for columbic interaction forces between different particles and between particles and continuous phase electrolytes. These forces lead to electro-viscous effects, which increase the emulsion viscosity above the viscosity normally obtained in uncharged, concentrated dispersions where only hydrodynamic interactions are present (Conway,

1960). This induces a reduction of droplet size that increase inter droplet interactions and provides enhanced stability against coalescence. An extensive flocculation of droplets to form a weak gel-like particulate network, depending on the nature and concentration of the emulsifier (Dickinson, 1989). The extensive flocculation process provides enhanced stability to the emulsion because the creaming rate is significantly decreased due to immobilization of the continuous phase (Franco et al., 1995). This also facilitate the electro-viscous effect and increase the emulsion viscosity.

The increase in pH with an increase in NaOH concentration results in ionization of more charged ions, and the effective surfactant concentration in the emulsion increases. As a result, interfacial tension is reduced and particle size decreases (Table 4.8). At the same time, there is an increase in the surface charge densities of the dispersed emulsion droplets, which intern increase the strength of electro-viscous effect in the vicinity of charged droplets. The decrease in particle diameter and the increase in surface charge density contribute to the increase in emulsion viscosity. The increase in zeta potential and electrophoretic mobility with an increase in emulsion pH support this fact (Fig. 4.20).

4.4 VISCOELASTIC BEHAVIOUR OF EMULSIONS

Rheological measurements (steady state, controlled stress and oscillatory measurements) provide information on physical stability and micro-structure of the emulsions. Dynamic (oscillatory) measurements are used to investigate the viscosity of the emulsions. In oscillatory measurements, the response in stress of a viscoelastic material (emulsions) subjected to a sinusoidally varying strain is monitored as a function of the amplitude and frequency of the strain (Tadros,1993). The phase angle shift (δ) between stress and strain, is given by

$$\delta = \Delta t \omega \quad (4.24)$$

where, ω is the frequency (rad. s^{-1}) ($\omega = 2\pi\nu$, where ν is the frequency (s^{-1})). From the measurement of the angular deflection (using a transducer) and the resulting torque on the detector shaft used for monitoring the stress, the phase angle shift and stress and strain amplitudes are determined, so that the rheological parameters- the storage modulus (G'), the loss modulus (G''), the complex modulus (G^*) and the complex viscosity (η^*) can be determined. The modulus G' is the measure of the energy stored elastically in the system, whereas G'' is a measure of the energy dissipated as viscous flow (Barnes, 1994; Bui et al., 2012). The viscoelasticity originates from the energy stored at the o/w interface of droplets. At lower volume fractions, the sphericity of droplets controlled and ensured by interfacial tension. But at higher packing densities (high volume fractions) droplets shape deformation occurred due to the volumetric constraints force which causing an increase in surface area and resulting in energy storage (elastic energy) (Lacasse et

al.,1996). The viscoelastic properties of the emulsions depend on the state of flocculation. Un-flocculated or weakly flocculated emulsions show a crossover point between G' and G'' , which signifies the characteristic relaxation time for the specific emulsion system (Tadros, 1993).

4.4.1 Rheological Behavior of O/W Emulsion Under Dynamic Oscillatory Shear Flow

The viscoelastic behavior of o/w emulsions were assessed by dynamic oscillatory measurement in terms of dynamic moduli G' and G'' as a function of frequency. The G' assesses the energy stored, and recovered per cycle of deformation reflecting the elastic part of the emulsion. The loss modulus is a measure of the energy lost per cycle and reflects the liquid-like component of the emulsions.

The linear viscoelastic region of o/w emulsions was established by an amplitude sweep (AS) test. Thereafter, the frequency sweep (FS) tests were performed for all emulsions at a constant stress (0.5 Pa) in the linear viscoelastic region. Oscillatory rheological measurements of storage modulus and loss modulus indicate that the emulsion system is associated strongly or weakly. The evolution of the storage modulus (G'), loss modulus (G''), complex viscosity (η^*) and loss tangent ($\tan \delta$) with frequency (ω) for all emulsions at different pH are shown in Fig. 4.33. From this figure, it can be seen that G' and G'' increase with an increase in frequency. Both G' and G'' are functionally dependent on frequency, which indicates that the o/w emulsions are flocculating in nature. It is observed that in the lower frequency regime ($\omega \leq 40 \text{ s}^{-1}$), G'' is greater than G' and attains a certain characteristic frequency (ω^*), which is referred to as the cross-over frequency. At the cross-over frequency (ω^*), G' equals G'' . Above this frequency, G'' decreases and G' becomes greater than G'' . This kind of behaviour was observed for the emulsion system (Tadros, 1994). This also shows that the emulsion behaves more like an elastic fluid.

Below the cross-over frequency (ω^*), in the lower frequency regime ($\omega < 40$), $G'' > G'$ and the o/w emulsions show more viscous behavior than elastic behavior. At the lower frequency regime, the emulsion behaves like the systems intermediate between cross linked gels and physically entangled systems, showing a decrease in G' at lower frequencies (Ross-Murphy and McEvoy, 1986). At the higher frequency ($\omega > \omega^*$), the emulsion behaviour is predominantly elastic. This means that in the linear viscoelastic range (LVR), under relatively slow deformation, the emulsion is more viscous, whereas it is elastic during relatively fast deformation. Elastic response is basically because of the presence of the weak macromolecular network structure between dispersed phase droplets.

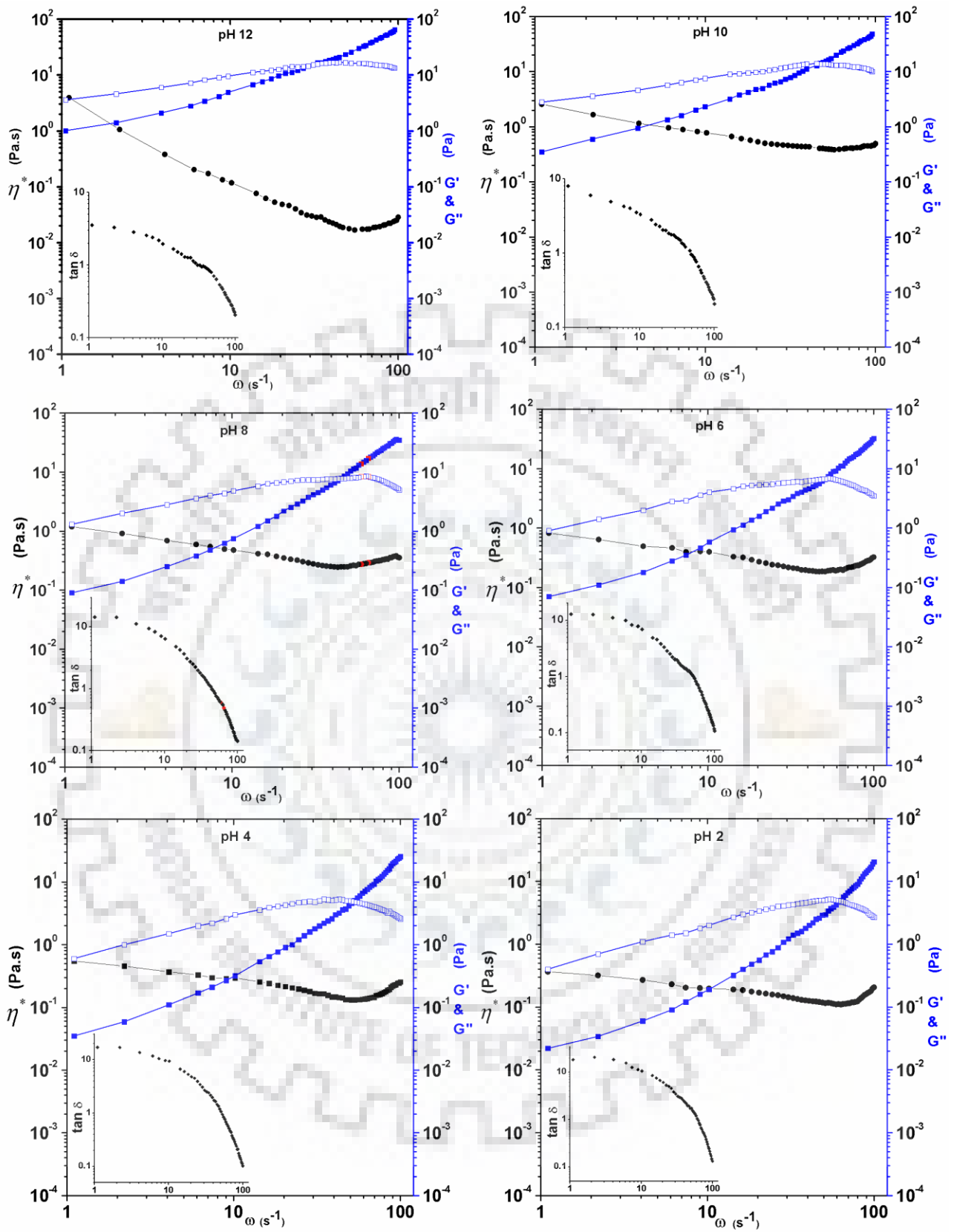


Fig. 4.33: The dynamic oscillation spectra of o/w emulsions at different emulsion pH.

G'' -□; G' -■; η^* -●.

The pH plays a prominent role in the changing flow behaviour of the emulsions. With a decrease in the pH, the emulsion stability decreases with the consequent decreases in G' , and the emulsion behaves more like a viscous fluid than an elastic fluid. The emulsion is more stable at pH 12 than that at pH 2 (Figs. 4.18 and 4.20). The presence of repulsive force among the charged droplets at the water (high dielectric fluid) and oil (low dielectric fluid) interface helps stabilize the emulsion. This arises because of an asymmetric distribution of counter-ions at the interface, creating a dipole normal to the fluid/fluid interface (Aveyard et al., 2000). This prevents the droplet-droplet coalescence. As the pH increases, zeta potential of the emulsion increases, enhancing the repulsive force at the interface (Fig. 4.18). At a higher pH (pH 12), the surfactant produces a thin viscoelastic film at the o/w interface. This hinders coalescence of droplets, and the emulsion droplets behave like hard spheres. As a consequence, the emulsion shows elastic behaviour (Saiki et al., 2008). As the pH decreases, the charges at the interface get gradually neutralized and the surfactant separates out from the o/w interface, causing the film drainage and a gradual decrease in emulsion stability. Thus, the emulsion shows an increasing viscous behavior with a decrease in the pH of the emulsion. From Fig. 4.33, it is observed that G' decreases with a decrease in the emulsion pH. The gap between G' and G'' also increases with a gradual shift in ω^* to the higher side.

The loss tangent ($\tan \delta$) is also an important parameter to describe the viscoelastic behaviour of the emulsions. The loss tangent in the range of $0.1 < \tan \delta < 1$, indicates a weak gel-like behaviour (Lapasin et al., 2001), whereas, at $\tan \delta > 1$, the emulsion shows a liquid-like behaviour (Madsen et al., 1998; Pereira et al., 2008). The inset of Fig. 4.33 shows the mechanical spectra of $\tan \delta$ for different emulsions. It is observed that the viscous behaviour of the emulsions gets enhanced with a decrease in the pH of the emulsions accompanied by the dampening of the elastic behaviour. The overall viscoelastic response of the emulsions can be obtained from the phase angle (θ) spectra as shown in Fig. 4.34. For an o/w emulsion system, the phase angle lies in the range of $0 < \theta < 90^\circ$. For the purely elastic networks, θ is zero, whereas for purely viscous liquids, $\theta = 90^\circ$. As discussed earlier, the influence of pH has significant influence on the viscoelastic properties of the emulsions.

4.4.2 Modeling the Dynamic Viscoelastic behavior of O/W Emulsions

The dynamic rheological data (frequency versus G' and G'') of different emulsions can be described by a power-law type model as shown below:

$$G' = K'(\omega)^{n'} \quad (4.25)$$

$$G'' = K''(\omega)^{n''} \quad (4.26)$$

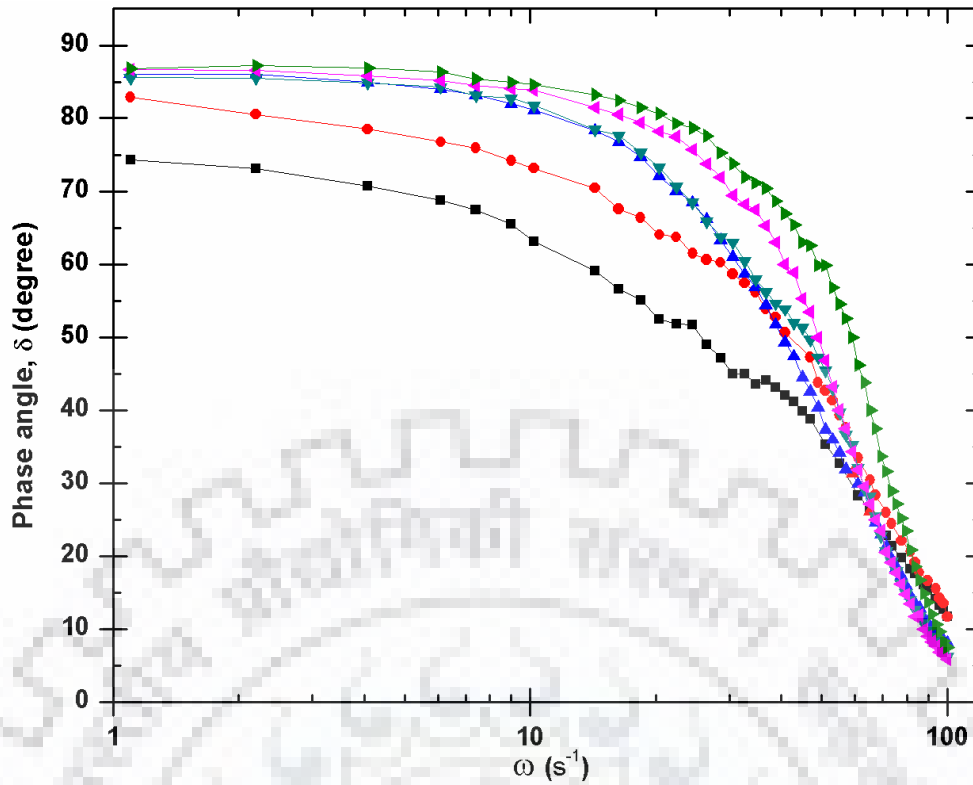


Fig. 4.34: Evolution of phase angle ($\tan\delta$) as a function of angular frequency at different pH.

pH: 12 —■—; 10 —●—; 8 —▲—; 6 —▼—; 4 —▶—; 2 —◀—.

where K' , K'' , n' and n'' are estimated from the rigorous non-linear regression of Eq. 4.24-4.25. The model parameters are shown in Table 4.17. The loss modulus shows a shear-thinning behavior ($n'' < 1$) due to shear induced structural breakdown of the viscous emulsions. Mechanical spectra of the elastic moduli show highly non-linear behaviour and exhibit shear-thickening behaviour ($n' > 1$) due to the macro-molecular aggregation. It is found that G' is a strong function of frequency, and the ($G' - G''$) crossover frequency leads to the inference that the emulsion behaves like a weak gel (Gunasekaran and Mehmet Ak, 2000).

The mechanical spectra of the dynamic moduli (Fig. 4.33), shows the variation of G' and G'' with frequency. In the experimental frequency range, a plateau region is observed. This may be ascribed to the extensive flocculation of the surfactant molecules at the o/w interface under shear (Dickinson, 1989). In the plateau region $\tan \delta$ passes through a minimum which can be characterized by the plateau modulus (G_p^0). The plateau modulus is a viscoelastic parameter which is obtained by the extrapolation of the entanglement contribution to G' at higher frequencies (Baumgaertel et al., 1992). G_p^0 can be estimated by the following relation:

$$G_p^0 = [G']_{\tan \delta \rightarrow \text{minimum}} \quad (4.27)$$

The cross over frequency is also characterized by the cross over moduli (G_C) which is defined as

$$G_C = [G_{\omega}]_{G' = G''} \quad (4.28)$$

The variation in the value of G_p^0 and G_C with the pH of the emulsion is shown in Fig. 4.35. It is found that both these moduli increase logarithmically with an increase in the emulsion pH as the viscoelasticity of the emulsion increases. The steady-state apparent viscosity at zero shear ($\eta_{a,0}$) is less reliable than the value at the low shear ($\dot{\gamma} = 0.01s^{-1}$). The low-shear apparent viscosity is given as:

$$\eta_{a(0.01)} = |\eta_a|_{\dot{\gamma}=0.01} \quad (4.29)$$

The evolution of low-shear steady-state viscosity $\eta_{a(0.01)}$ with emulsion pH is also shown in Fig. 4.35. $\eta_{a(0.01)}$ increase logarithmically with an increase in the emulsion pH. A similar tendency is found for linear viscoelasticity functions, G_p^0 and G_C of these emulsions.

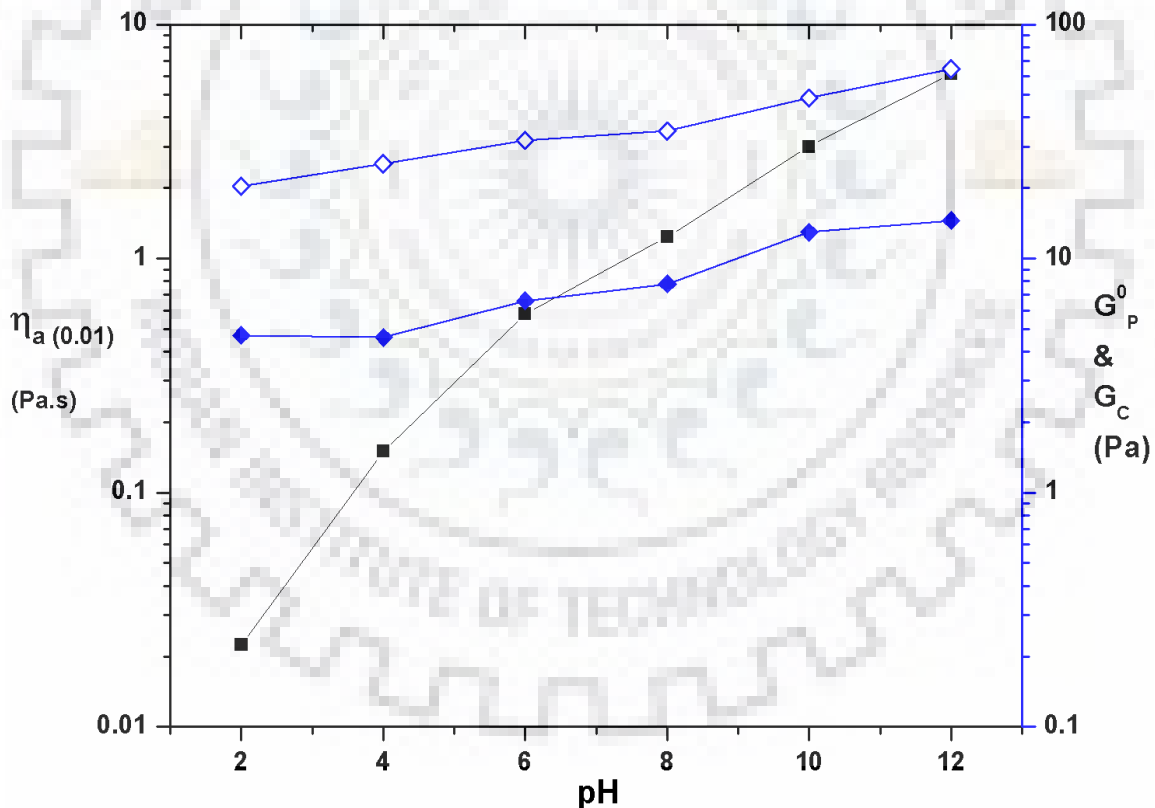


Fig. 4.35: Influence of pH on the steady-state viscosity at $0.01 s^{-1}$, the plateau modulus (G_p^0) and with cross over moduli (G_C) of o/w emulsion.

$$\eta_{a(0.01)} - \blacksquare; G_p^0 - \blacklozenge; G_C - \diamond.$$

Table 4.17: Dynamic shear parameters of power-law functions describing storage and loss moduli of o/w emulsions at different pH and temperature.

pH	$G' = K'(\omega)^{n'}$				$G'' = K''(\omega)^{n''}$			
	K' (Pa.s ^{n'})	n'	χ^2	R^2	K'' (Pa.s ^{n''})	n''	χ^2	R^2
pH12	0.1500±0.0177	1.3029±0.0271	2.4938	0.9932	6.4463±0.6978	0.2092±0.0279	3.8366	0.6921
pH 10	0.0279±0.0031	1.6070±0.0249	0.7406	0.9963	5.0429 ± 0.6061	0.2161±0.0308	2.9723	0.6617
pH 8	0.0063±0.0007	1.8879±0.0248	0.3906	0.9972	3.6451±0.5037	0.1633±0.0353	1.7035	0.4080
pH 6	0.0011±0.0002	2.2177±0.0324	0.3165	0.9963	3.0696 ± 0.5053	0.1378±0.0422	1.5458	0.2593
pH 4	0.0002±0.0001	2.5720±0.0352	0.1745	0.9969	2.5140 ± 0.4445	0.1170±0.0456	1.1010	0.2078
pH 2	$2.946 \times 10^{-5} \pm$ 7.468×10^{-6}	2.9081±0.0567	0.1981	0.9938	1.6640 ± 0.3233	0.2185±0.0489	0.8934	0.4226
Temperature (°C)								
20	0.3900±0.0260	1.1320±0.0155	1.7819	0.9963	8.3635 ± 0.8658	0.2143±0.0261	6.1548	0.6906
30	0.1500±0.0177	1.3029±0.0271	2.4938	0.9932	6.4463 ± 0.6978	0.2092±0.0279	3.8366	0.6921
40	0.1153±0.0073	1.2774±0.0145	0.4162	0.9974	4.9845 ± 0.5082	0.2063±0.0257	2.0459	0.6785
50	0.0354±0.0031	1.4863±0.0203	0.3698	0.9964	4.0324 ± 0.4859	0.2032±0.0304	1.8436	0.5974

From the droplet size evolution (Fig. 4.19), it is observed that the mean droplet diameter decreases with an increase in the emulsion pH. This explains the increase in viscous and viscoelastic functions. The droplet size distribution (DSD) is an important structural parameter which influences the emulsion rheology significantly (Otsubo and Prudhomme, 1994). Specially, in the structured macromolecule-stabilized systems (at higher pH), in which inter-droplet interactions may play a key role.

4.4.3 Cox–Merz Rule

The dynamic and steady shear rheological properties of emulsions are correlated by Cox-Merz empirical relationship at equal values of angular frequency (ω , s^{-1}) and shear rate ($\dot{\gamma}$, s^{-1}) (Cox and Merz, 1958; Snijkers and Vlassopoulos, 2014):

$$|\eta^*(\omega)| \equiv \eta_a(\dot{\gamma})_{\omega=\dot{\gamma}} \quad (4.30)$$

The applicability of the Cox-Merz rule on o/w emulsions were verified by plotting apparent viscosity (η_a) and complex viscosity (η^*) of o/w emulsion against shear rate ($\dot{\gamma}$) and angular frequency (ω) in a single plot. Fig. 4.36 shows the Cox-Merz plot for o/w emulsions at different values of pH. It is observed that the magnitude of $|\eta^*|$ are higher than the $|\eta_a|$ value for all emulsions. It is also observed that the difference between η_a and η^* increases as the pH of the emulsion decreases. This indicates that the o/w emulsion does not obey the Cox-Merz rule over the range of $\dot{\gamma}$ and ω studied. The deviation may be explained due to the weak-gel like structure of emulsions (Ndjouenkeu et al., 1995). The emulsion structural decay depends on the extent of the applied strain (Rochefort and Middleman, 1987). For a small-amplitude oscillatory shear (SAOS) measurement, the applied strain is low in the linear viscoelastic region (LVR). But it is relatively high enough for the breakdown of the structured inter and intermolecular droplet aggregation in steady shear measurement (Gunasekaran and Mehmet Ak, 2000; Karaman et al., 2011). In the present study, it is found that the emulsion pH has significant influence on the droplet aggregation, as the degree of flocculation increases with a decrease in pH. Thus the deviations from the Cox–Merz rule imply that the o/w emulsion exhibits a weak gel viscoelastic structure which is sensitive to system pH.

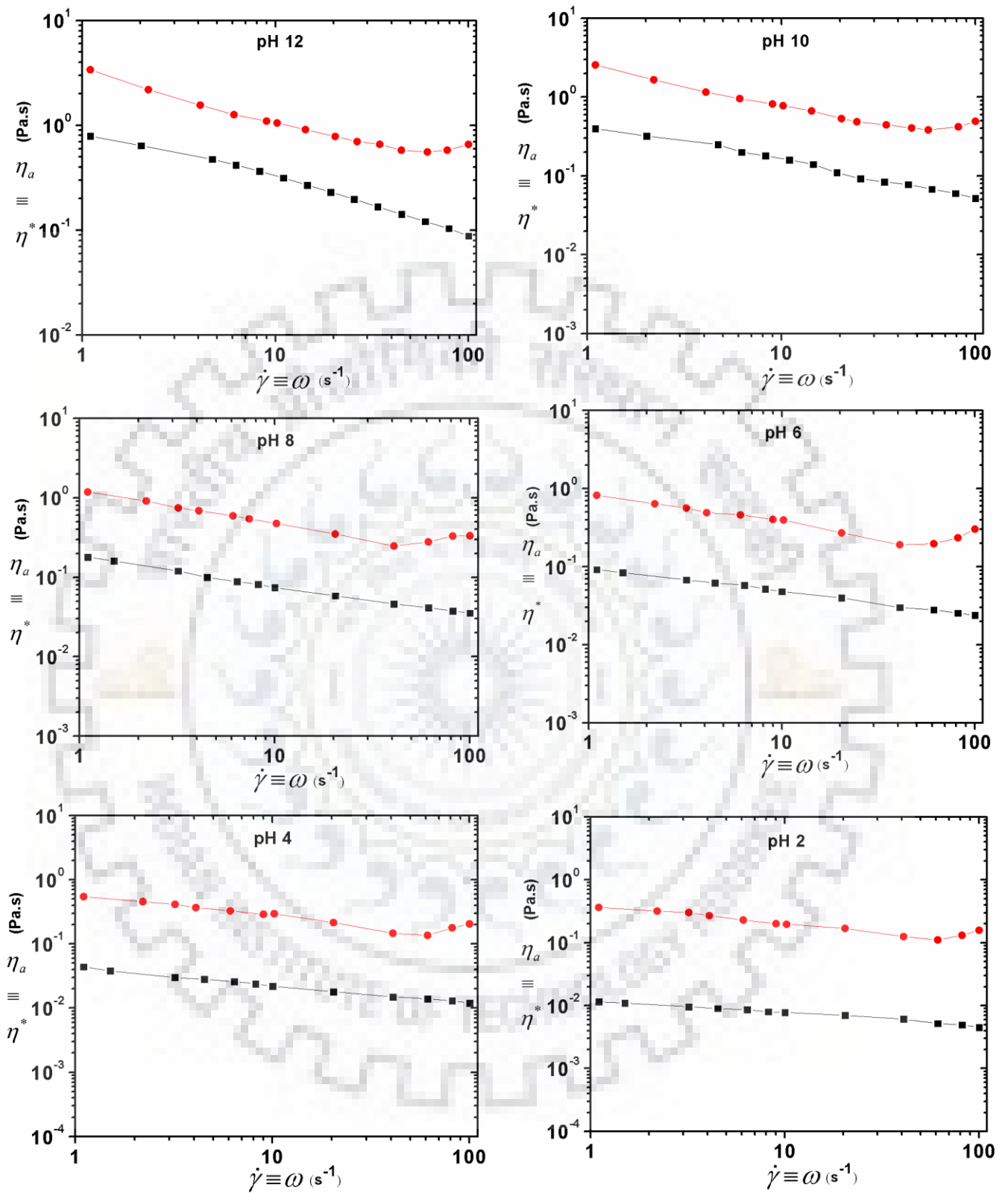


Fig. 4.36: Comparison of dynamic oscillatory and steady-state shear viscosities (Cox–Merz rule) of all the o/w emulsions at different pH. η_a —■—; η^* —●—.

4.4.4 Time-Dependent Flow Behavior of O/W Emulsions

The time dependency and the structure recovery of o/w emulsions are shown in Fig. 4.37. The time-dependency of o/w emulsions was tested in three intervals under controlled shear rate (CSR). The performed tests are simulated using the following shear conditions: rest (pre-shear)-high shearing (structure decomposition)-rest (structure regeneration/recovery).

In the first interval a constant, but low shear rate (1 s^{-1}) was applied to the emulsion for 50 s. In the second interval, a constant but high shear rate (100 s^{-1}) was imposed for 50 s on the emulsion which caused the internal structural decomposition of the emulsions. Thereafter, the imposed high shear rate was withdrawn and the emulsions were allowed to recover their structure under constant low shear rate (10^0 s^{-1}) for a long period of time of about 300 s. During the whole shearing period, the resulting change of emulsion apparent viscosity was observed with time as shown in Fig. 4.37. It was observed that the emulsions exhibit viscoelastic behaviour confirming the earlier observations. The effect of emulsion pH in changing the viscoelastic nature of emulsions is significant. The $\eta - t$ curve (Fig. 4.37) shows that the emulsion with different pH exhibit thixotropic behaviour.

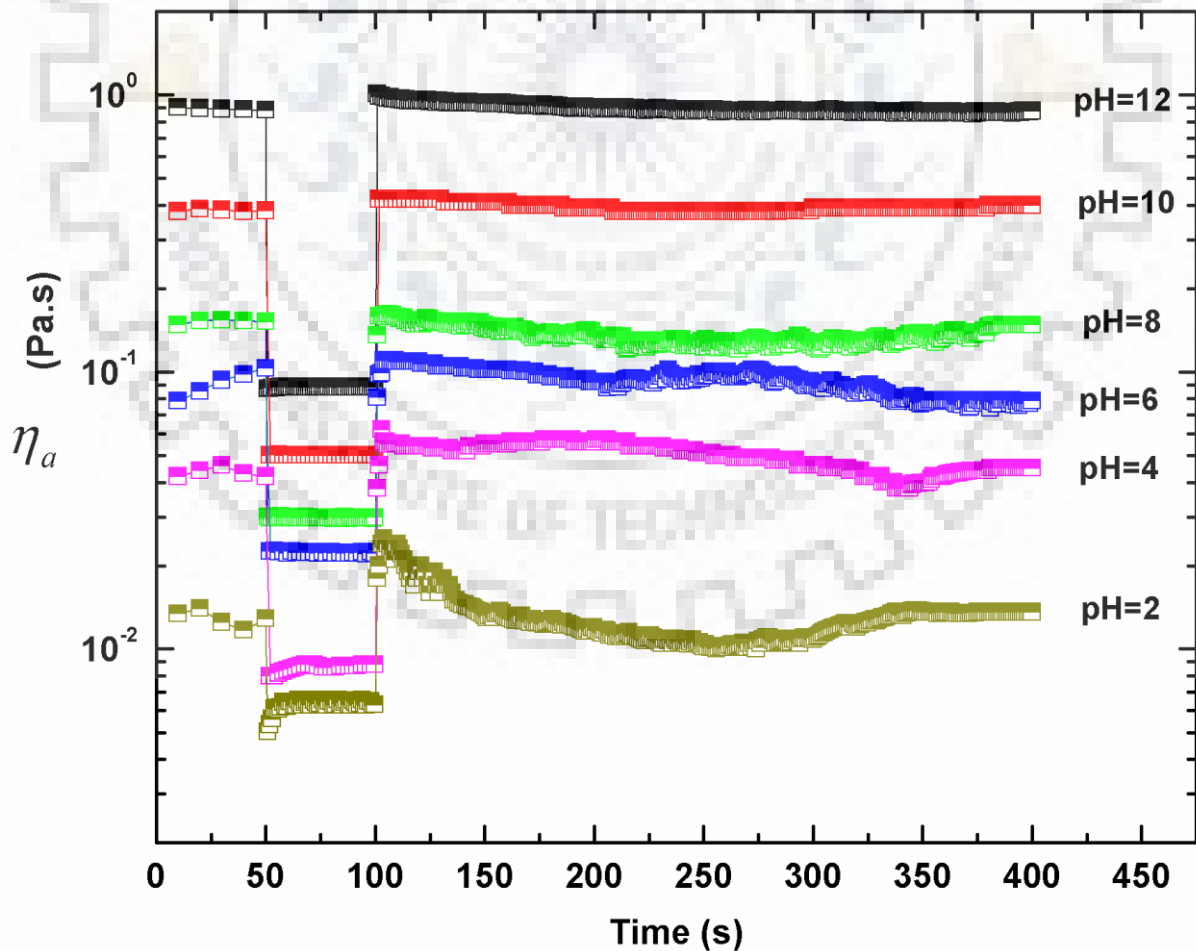


Fig. 4.37: Time dependent behavior ($\eta - t$ plot) of o/w emulsions at different pH.

Emulsions having pH 12 and pH 10 exhibit very good regeneration of the complete structure which decomposed during the high shearing process. As the pH decreases, the structure regeneration tendency of the emulsions also decreases. This indicates that the viscoelasticity of the emulsions decreases with a decrease in its pH. For the emulsion having pH 8 and pH 6, the decomposed structure regenerates very slowly. For the emulsions having pH 4 and pH 2, the viscosity data showed a wide scatter over the regeneration period. For these emulsions, a transient or unsteady state behavior was observed during the regeneration period. Thus, it can be inferred that the emulsions with pH 4 and pH 2 exhibit poor structure recovery and are not able to regenerate their internal structure over a prolonged regeneration period.

4.4.5 Effect of Temperature on Steady and Dynamic (Viscoelastic) Rheological Behavior of O/W Emulsions

The effect of temperature on the rheological behaviour of the emulsions (pH = 12, 30 % v/v o/w emulsion) is shown in Fig. 4.38. It is found that the o/w emulsion exhibited temperature-dependent viscous behaviour. The apparent viscosity of the emulsions decreases with an increase in temperature. It was observed that the viscous behaviour becomes highly non-linear at lower shear rates.

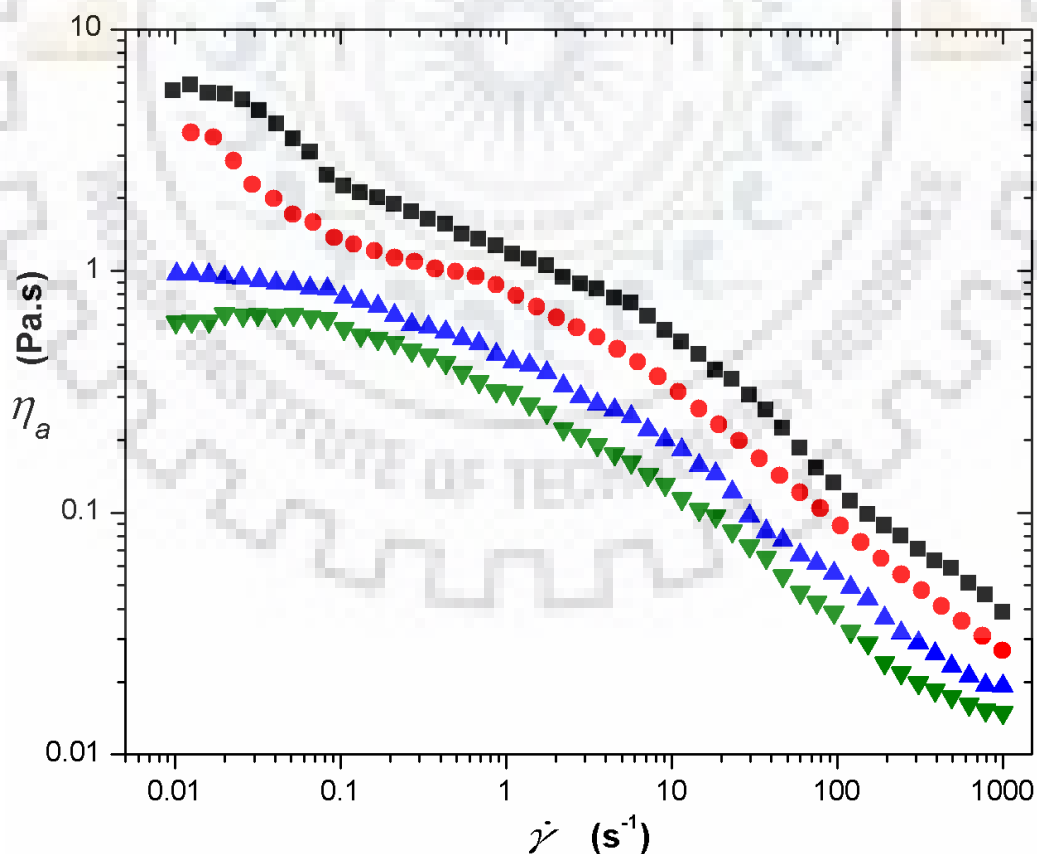


Fig. 4.38: Rheogram of o/w emulsions at different temperature.

20 °C —■—; 30 °C —●—; 40 °C —▲—; 50 °C —▼—.

The emulsions exhibited the characteristics of non-Newtonian, shear-thinning (pseudoplastic) fluids over the studied temperature range (20-50°C). Various non-Newtonian viscosity models are fitted with the experimental data (Table B4 and Table B5). The non-Newtonian behaviour increases strongly with a decrease in temperature. From the power law model, it was observed that the flow behaviour index, $n < 1$, and that it decreases with an increase in temperature. This shows inferred that the shear thinning behaviour of o/w emulsion increases with a decrease in temperature as also the pseudoplasticity of the emulsions. Evolution of droplet size distribution (DSD) of o/w emulsions at different temperatures is shown in Fig. 4.39. All DSD curves show a uni-modal distribution characteristic. It is observed that as the temperature increases, the DSD curve shifts towards the higher droplet size range with an increase in average droplet size. As the in-situ temperature of the o/w emulsion increases, the disruption of emulsion droplets gets enhanced, and facilitating the droplet coalescence process. This results in the evolution of comparatively larger droplets with a wider DSD spectrum.

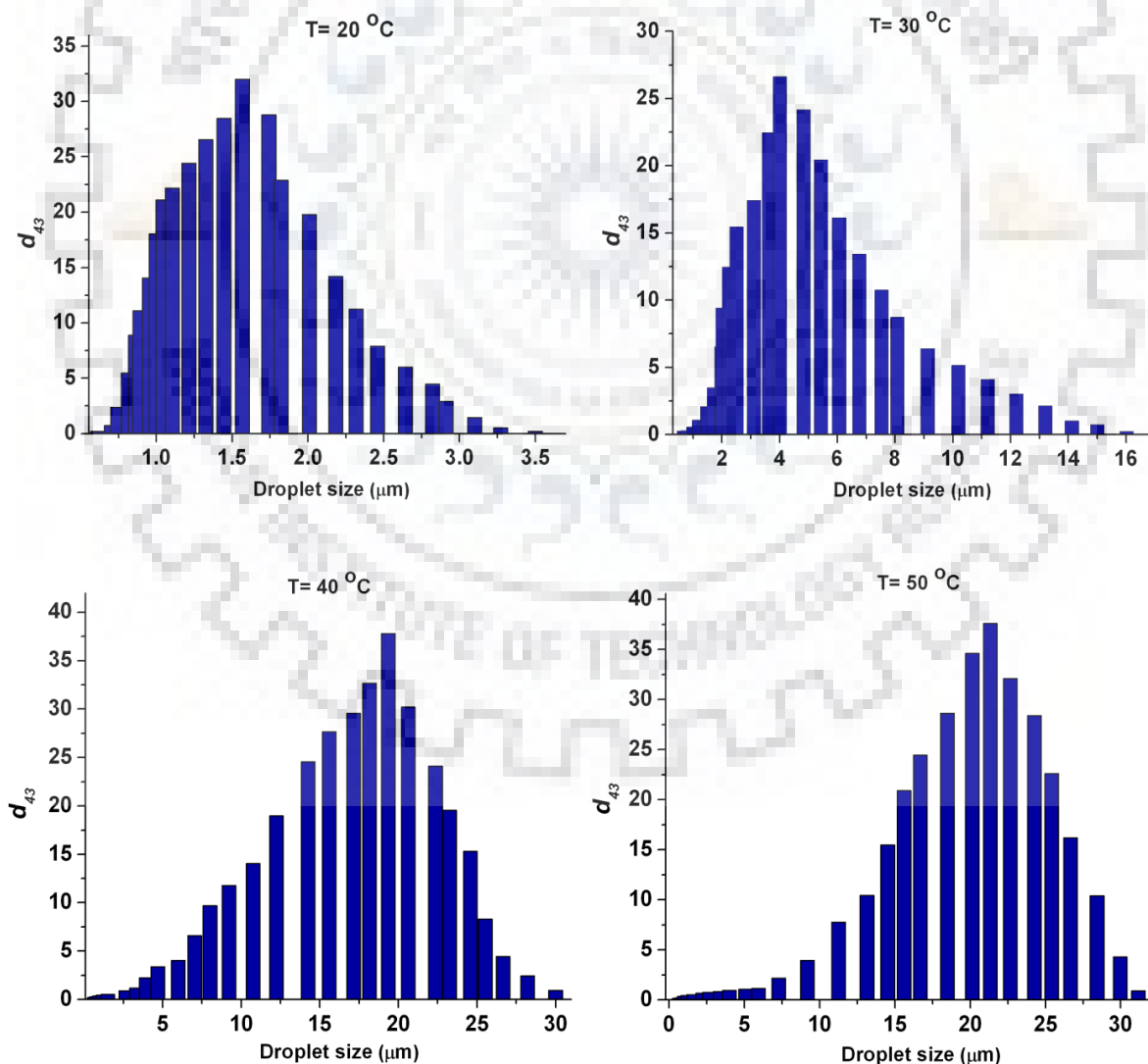


Fig. 4.39: Effect of temperature on evolution of droplet size distribution (DSD) of o/w emulsions.

From the rheogram (Fig. 4.38), it is observed that the o/w emulsion exhibits two limiting viscosities over the range of studied: the zero shear viscosity (η_0) at low shear rate and the infinite shear viscosity (η_∞) at high shear rate. It is very difficult to model the overall rheological behavior of the emulsions over a wide range of shear rate. In addition to power law model, the rheological data were also fitted to four different viscosity models. The model fitted parameters are shown in Tables B4 and B5. The Carreau model represents the rheological behavior of the o/w emulsion very well over the entire range of shear rate as compared to Cross and Sisko models, with high R^2 value and low error.

The effect of temperature on viscoelastic properties (G' , G'' and η^*) of the emulsions in the whole range of applied frequency is shown in Fig. 4.40. From the mechanical spectra of o/w emulsions at different temperatures, it is found that the viscoelastic parameters are temperature dependent. G' , G'' and η^* decrease with an increase in temperature. It is also found that $G'' > G'$ at lower frequency (below $\omega \sim 30 \text{ s}^{-1}$) and $G' > G''$ at higher frequency range (above $\omega \sim 50 \text{ s}^{-1}$) with a characteristic crossover frequency (ω_c). The mechanical spectra showed a viscous response of the emulsion at lower frequency and an elastic response at a higher frequency. As the temperature of the emulsion increases, the ω_c shift towards the higher frequency and the emulsion shows viscous behavior at the higher frequency. A power-law type model (Eq. 4.25-4.26) describes well the variation of viscoelastic parameters with temperature (Table 4.17). All the o/w emulsions at different temperatures can be characterized as a weak gel like viscoelastic fluid as the slope (n' and n'') of G' and G'' spectra were positive (Ross-Murphy and McEvoy 1986; Karaman et al. 2011). The viscoelasticity of the emulsion decreases with an increase in temperature as both K' (0.390-0.0354 Pa.sⁿ) and K'' (8.3635-4.0324 Pa.sⁿ) decrease with an increase in temperature (20-50 °C). Furthermore, the exponent of G' and G'' varied as $n' = 1.1320$ -1.14863 and $n'' = 0.2143$ -0.2032, (Table 4.17). From these results, one can infer that the o/w emulsion behaves like a structured liquid over the studied temperature range (20-50 °C) (Sanchez et al., 2002). The temperature dependency of η_a and η^* can be described by an Arrhenius-type relationship, as given below:

$$\eta_a = A \exp\left(\frac{-E_\eta}{RT}\right) \quad (4.31)$$

$$\eta^* = A^* \exp\left(\frac{-E_{\eta^*}}{RT}\right) \quad (4.32)$$

Steady state and dynamic rheological data for $\dot{\gamma} = 10 \text{ s}^{-1}$ were fitted to Eqs. (4.31-4.32) and the best-fit model parameters are shown in Table 4.18. It is observed that the complex viscosity (η^*) is always greater than the steady state shear viscosity (η_a) over the temperature range (20-50°C). Both η_a and η^* decrease with an increase in temperature from 20 to 50 °C due to an increase in the intermolecular distances for thermal expansion. The magnitude of viscous activation energy, $E_\eta > E_{\eta^*}$, implies that the steady-state shear viscosity of o/w emulsion samples are more sensitive to temperature than the complex viscosity. Therefore, the viscosity of emulsions decreases with an increase in temperature accompanied by an increase in mean droplet diameter.

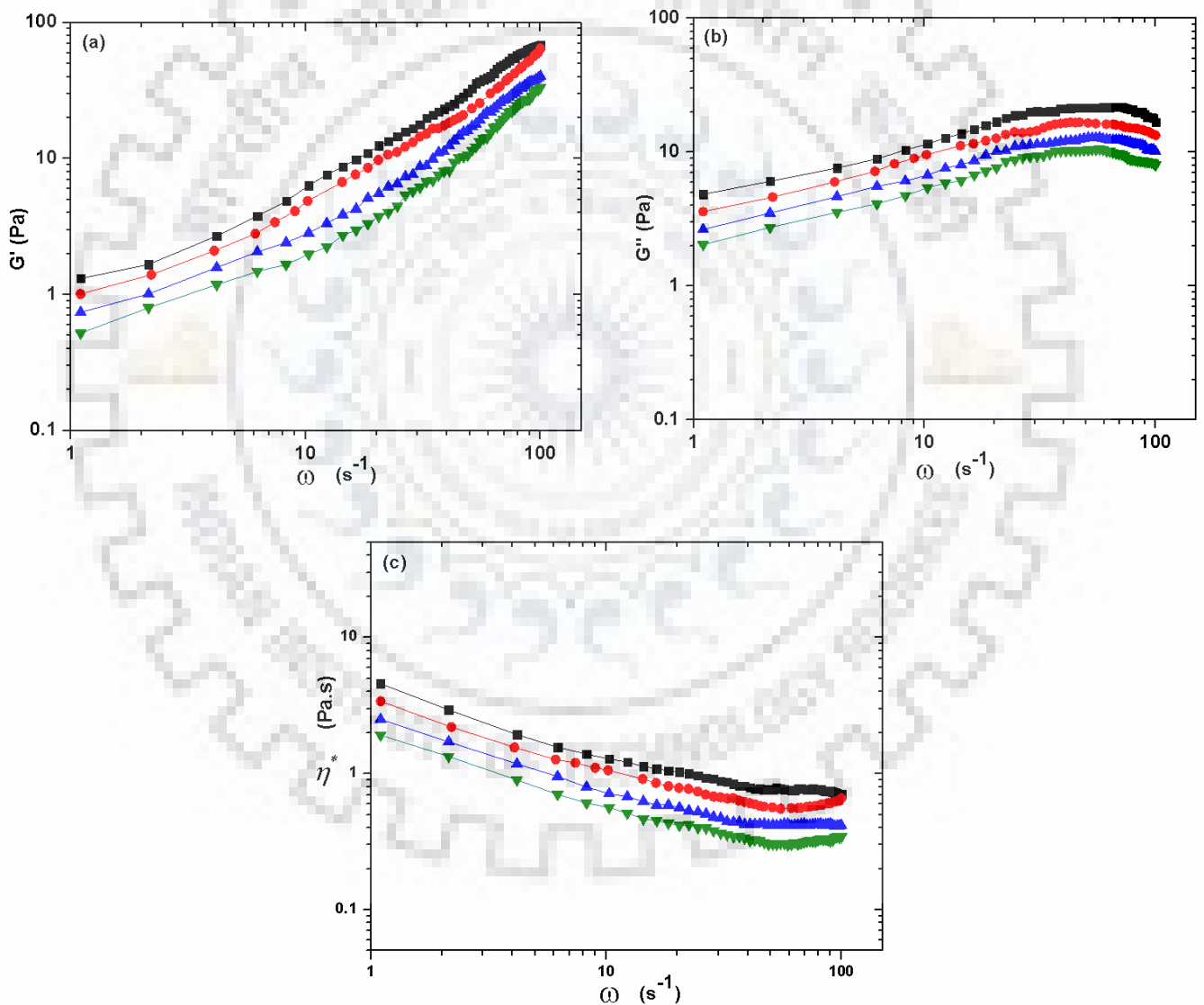


Fig. 4.40: Influence of temperature on the dynamic oscillatory mechanical spectra of o/w emulsions. (a) G' versus ω plot ; (b) G'' versus ω plot ; (c) η^* versus ω plot.

20 °C –■–; 30 °C –●–; 40 °C –▲–; 50 °C –▼–.

Table 4.18 :Arrhenius model temperature dependency parameters of o/w emulsions.

Temperature (°C)	$\eta_a = A \exp\left(\frac{-E_\eta}{RT}\right)$				$\eta^* = A^* \exp\left(\frac{-E_{\eta^*}}{RT}\right)$			
	η (Pa.s)	A (Pa.s ⁿ)	E_η (kJ/mol)	R^2	η^* (Pa.s)	A*(Pa.s ⁿ)	E_{η^*} (kJ/mol)	R^2
20	0.568				1.28			
30	0.320	7.4349×10^{-08}	38.5545	0.9978	1.06	1.270×10^{-04}	22.5435	0.9680
40	0.20	± 0.4089			0.71	± 0.9210		
50	0.130				0.562			

CHAPTER 5

FLUID FLOW THROUGH POROUS MEDIA

In the process oil fields both Darcy and non-Darcy flow regimes estimation of is often a critical issue. Flow regime estimation is a key parameter for understanding the behavior of petroleum reservoirs and also in the prediction of production performance. In this chapter, at first the pressure drop evolution in the various flow regimes, viz. from pre-Darcy to Darcy and inertial non-Darcy regimes including transitional flow domain in different types of porous media for Newtonian fluid was investigated and discussed in section 5.1. A new set of data for different types of porous media is presented which were obtained from rigorous steady flow experiments. The flow behavior and the localization of the transition from one flow regime to the next regime are also discussed. Thereafter the emulsion flow through different type of porous media (packed bed with different size of particle diameter and sand pack core holder packed with different mesh of sand particles) was studied. Effect of emulsion volume fraction, flow rate and number of PV injected on bed pressure drop and permeability reduction for different types of porous media have also been studied and discussed in section 5.3.

5.1 NEWTONIAN FLUID FLOW THROUGH POROUS MEDIA

5.1.1 Pressure Drop-Velocity Relationship

The relationships between the pressure gradient and the average velocity in the porous bed with different particle sizes have been investigated. It can be seen from Fig. 5.1 that the pressure gradient increases nonlinearly with the average velocity over the entire velocity range studied. It was observed that the pressure drop across the bed increases with a decrease in the particle size. The bed becomes denser as the particle size decreases, and offer large resistance to the flow due to reduction in flow passages in the bed. The pressure loss-velocity relationships are found to be nonlinear in nature, deviating from the linear relationship as predicted by Darcy's law (Eq. 5.1). The characteristics of the pressure drop-velocity plot for porous media were evaluated by fitting the experimental data to various model equations (cubic, quadratic and power law model):

$$-\frac{d\langle \bar{P} \rangle}{dL} = \left(\frac{\mu}{K} \right) \langle \bar{u}_D \rangle \quad (5.1)$$

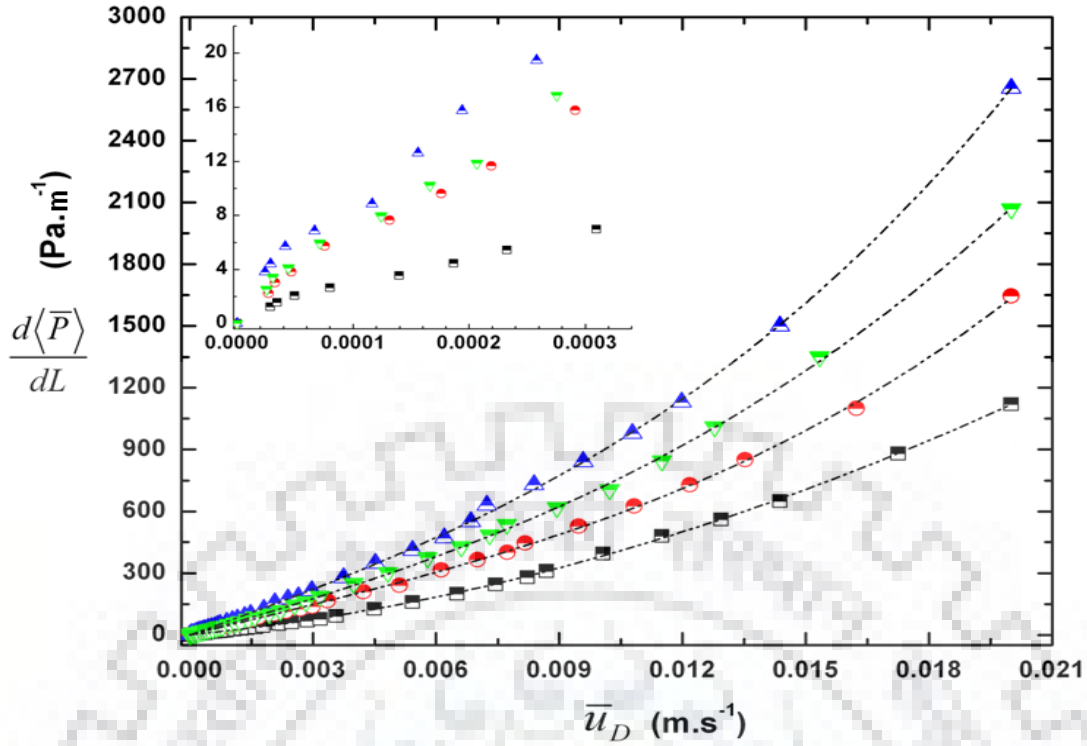


Fig. 5.1: Relationship between the Pressure gradient per unit length versus average velocity across the porous bed with different particle sizes.

Porous media (d_p (mm))= 2.5 \blacktriangle ; 3.2 \bullet ; 5 \blacksquare ; Mix \blacktriangledown

The Darcy's law is valid for flow with sufficiently small velocity. As the velocity gradually increases non-Darcy effects will appear. Increased flow velocity, pore irregularities, and excessive momentum transfer perturb the Darcy flow. It is, therefore desirable to introduce some corrections to Darcy's law and further propose a general relation that can be used to include non-Darcy effects. The relation consists of two terms: a viscous loss term and an inertial loss term, which are shown below (Coulaud et al. 1988; Rojas and koplik, 1998; Zimmerman et al., 2004; Lage et al., 1997; Chai et al., 2010).

Type-I: Quadratic Forchheimer equation:

$$-\frac{d\langle\bar{P}\rangle}{dL} = \left(\frac{\mu}{K}\right)\langle\bar{u}_D\rangle + (\beta\rho)\langle\bar{u}_D\rangle^2 \quad (5.2)$$

Type-II: Cubic equation:

$$-\frac{d\langle\bar{P}\rangle}{dL} = \left(\frac{\mu}{K}\right)\langle\bar{u}_D\rangle + \left(\frac{\alpha_2\rho^2}{\mu}\right)\langle\bar{u}_D\rangle^3 \quad (5.3)$$

Type-III: Cubic equation with quadratic term:

$$-\frac{d\langle\bar{P}\rangle}{dL} = \left(\frac{\mu}{K}\right)\langle\bar{u}_D\rangle + (\alpha_1\rho)\langle\bar{u}_D\rangle^2 + \left(\frac{\alpha_2\rho^2}{\mu}\right)\langle\bar{u}_D\rangle^3 \quad (5.4)$$

Type-IV: Power law equation:

$$-\frac{d\langle\bar{P}\rangle}{dL} = \Lambda \langle\bar{u}_D\rangle^m \quad (5.5)$$

It can be seen from Fig. 5.1 that the pressure gradient across the porous bed increases with an increase in velocity and exhibit better quadratic relationships, when compared to power law model equation for different particle sizes. More specifically, the pressure gradient-velocity plots for different particle sizes are best represented by Type-I, Type-II and III flow model equations ($R^2 \sim 0.999$). Type-I and Type-IV model equations describe the non-Darcy flow with strong inertial effect. In this regime, the inertial effect is more significant than viscous effect, and the flow behavior is mainly governed by the inertial force. Type-II and III model equation represent the transitional inertial regime. The non-linear effects arise from the inertia-viscous cross effect resulting from the streamline deformation (Panfilov and Fourar, 2006). In this regime, the inertial force is comparable to viscous force and its effect becomes more pronounced with an increase in fluid velocity. Boundary layers begin to develop near solid boundaries inside the porous medium and they become pronounced, and an inertial core appears (Dybbbs and Edwards, 1984). Thus the experimental results reveal that the flow within the porous media does not confirm to purely viscous fluid flow (Darcian flow) and that the inertial effect exists simultaneously.

The coefficients of different model equations are listed in Table 5.1. It can be seen that the medium permeability and the inertial resistance factor are affected significantly by the particle size. Permeability of the porous media can be defined as the ability of the media to transmit the fluid (i.e. how easily fluid can flow through a porous media). It was found that the permeability of porous media increases with an increase in the particle size. As the particle size gradually decreases, the fluid passage path becomes more and more constricted and complex, offering more resistance to the flow. In the experiment, the relation of the inertial resistance factor B with the particle size D_p reflected more clearly than that of the permeability \bar{K} . From Fig. 5.1, it is evident that as the particle diameter decreases, the pressure gradient-velocity plot becomes more asymptotic in nature. Thus, it is necessary to correlate the bed permeability and the inertial resistance with particle size in terms of a particle characteristic coefficient.

The pressure drop in porous media can be represented in terms of bed porosity, particle diameter and velocity as (Nield and Bejan, 1999; Zhang et al. 2013):

$$-\frac{d\langle\bar{P}\rangle}{dL} = \left[\frac{\Omega\mu(1-\phi)^2}{d_p^2\phi^3} \right] \langle\bar{u}_D\rangle + \left[\frac{\omega\rho(1-\phi)}{d_p\phi^3} \right] \langle\bar{u}_D\rangle^2 \quad (5.6)$$

Table 5.1: Coefficient of different types of flow correlation equations between the pressure gradient and velocity in porous bed with various particle diameters

Model equations			Type-I			Type-II			Type-III				Type-IV		
Porous media	Mean Particle Size, d_p (mm)	Porosity ϕ	$\bar{K} \times 10^{08}$ (m ²)	β (m ⁻¹)	R^2	$\bar{K} \times 10^{08}$ (m ²)	α_2	R^2	$\bar{K} \times 10^{08}$ (m ²)	α_1	α_2	R^2	$\Lambda \times 10^{-04}$	m	R^2
	PM1	2.5	0.4174	1.879	3842	0.9981	3.284	0.067	0.9977	5.077	1862.4	0.0025	0.9998	38.796	1.499
PM2	3.5	0.3696	2.819	2194.4	0.9973	1.353	0.147	0.9996	1.400	447.41	0.1306	0.9997	71.694	1.441	0.9936
PM3	5.0	0.3478	4.990	1799.1	0.9998	1.662	0.110	0.9994	1.799	798.63	0.0801	0.9995	49.811	1.411	0.9950
PM4	3.25	0.3913	2.253	2873	0.9986	2.115	0.086	0.9996	2.024	370.70	0.0994	0.9996	36.833	1.398	0.9928

On comparing Eq. (5.2) and Eq. (5.6), the permeability (\bar{K}) and inertial resistance factor (β) can be expressed as follows:

$$\bar{K} = \frac{d_p^2}{\Omega} \cdot \frac{\phi^3}{(1-\phi)^2} \quad (5.7)$$

$$\beta = \frac{\omega}{d_p} \cdot \frac{(1-\phi)}{\phi^3} \quad (5.8)$$

where Ω and ω are the characteristic coefficients of the particles in the porous bed and can be evaluated from Eqs. (5.7) and (5.8) and are listed in Table 3.6 in Chapter 3.

5.1.2 Various Flow Regimes in the Porous Media

In the previous section, it was confirmed that the non-Darcy type flow was observed during the passage of fluid through porous media over the studied range of flow rate. The various flow regimes encountered during the flow through porous media were identified and characterized by extended Darcy-Forchheimer equation (also known as the Hazen-Dupuit-Darcy equation) (Eq. 5.9) modifying the Darcian velocity when the pressure drop-velocity relationship deviates from linearity and enters the inertial regime through transition regimes (Oun and Kennedy, 2014; Boomsma and Poulikakos, 2001; Dukhan and Minjeur, 2011; Bagci et al., 2014):

$$-\frac{d\langle \bar{P} \rangle}{dL} = \left(\frac{\mu}{\bar{K}} \right) \cdot \langle \bar{u}_D \rangle + \left(\frac{\rho F_D}{\sqrt{\bar{K}}} \right) \cdot \langle \bar{u}_D \rangle^2 \quad (5.9)$$

$$\left. \begin{aligned} -\frac{d\langle \bar{P} \rangle}{dL} \cdot \frac{1}{\langle \bar{u}_D \rangle} &= \left(\frac{\mu}{\bar{K}} \right) + \left(\frac{\rho F_D}{\sqrt{\bar{K}}} \right) \cdot \langle \bar{u}_D \rangle \\ \frac{\Delta P}{L \cdot \langle u_D \rangle} &= A + B \cdot \langle \bar{u}_D \rangle \end{aligned} \right\} \quad (5.10)$$

The left side of Eq. (5.9) is the reduced pressure drop. Graphical demarcation of the pore flow regimes can be done by observing the change in slope of the reduced pressure drop-velocity (*RPD*) plot. If *RPD* plot yields a constant gradient horizontal line to x- abscissa of $\left(\frac{\Delta y}{\Delta x} \right) = 0$ will ensure typical Darcy flow regime and plot having positive slope, $\left(\frac{\Delta y}{\Delta x} \right) > 0$ characterize the non-Darcy Forchheimer inertial regimes. The *RPD* plot for different sized particles is shown in Fig. 5.2.

From *RPD* flow map plot, four different pore flow regimes were identified as: (i) pre-Darcy regime, (ii) transition to Darcy regimes, (iii) Darcy regimes, and (iv) Forchheimer inertial regimes.

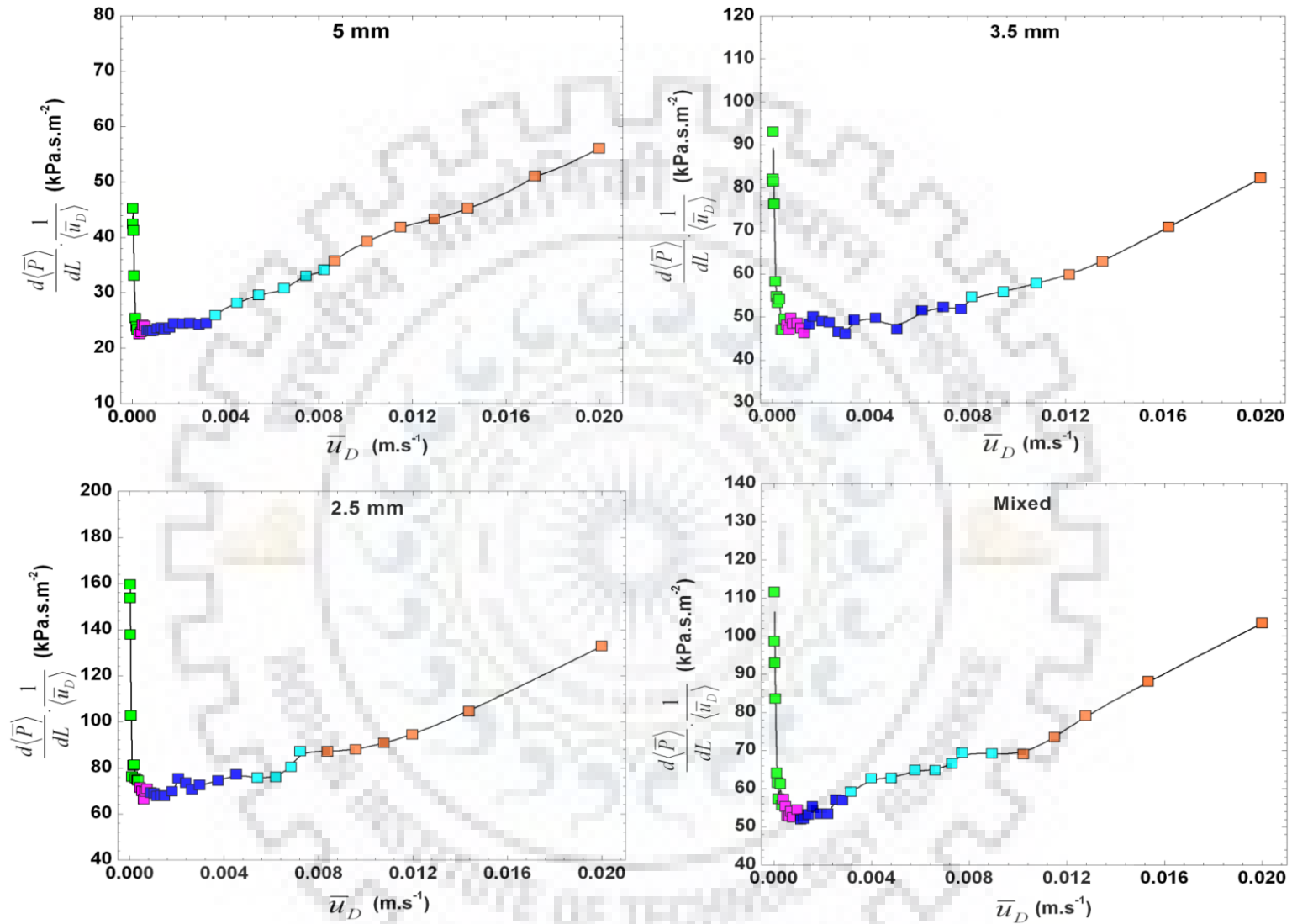


Fig. 5.2: Reduced pressure drop (RPD) plot for flow regime demarcation of different types of porous media. pre-Darcy (■); transition to Darcy (■); Darcy (■); weak inertia (■); non-Darcy Forchheimer regime (■).

(i) Pre-Darcy regime: A pre-Darcy regime was observed at very low velocity for three different sized particles and mixed particles system. In pre-Darcy regimes the slope of RPD plot $\left(\frac{\Delta y}{\Delta x}\right)$ being negative. The pre-Darcy regime exists only for velocities in the range of $2.88 \times 10^{-05} \leq \bar{u}_D \leq 1.90 \times 10^{-04} \text{ m. s}^{-1}$. Very limited information is available regarding the pre-Darcy regime (Fand et al. 1987; Kececioglu and Jiang, 1994; Bagci et al. 2014). The magnitude of the reduced pressure gradient in this regime was relatively very high as compared to preceding flow regimes. In this regime, the pressure drop increases nonlinearly with velocity, and the fluid shows non-Newtonian flow behaviour. Pressure drop across the porous bed varies inversely to the Reynolds number (Kececioglu and Jiang, 1994). This may be attributed due to the electro-osmotic and capillary-osmotic forces acting on porous media. The streaming potential generated due to these hydrodynamic forces produces small counter currents along the pore walls in a direction opposite to the main flow direction (Fand et al. 1987; Bagci et al. 2014). The effect of hydrodynamic forces became more pronounced as the particle size decreased. It was observed that the pre-Darcy effect increases with a decrease in particle size (Fig. 5.2). For mixed particles, the pre-Darcy effect is higher than the isotropic porous media ($D_p = 3.5$ and 5 mm).

(ii) Transition to Darcy regime: There is a transition regime between the pre-Darcy regime and the next Darcy regime. This regime is short and transient with scattered reduced pressure drop data points having relatively less $(\Delta P / L\bar{u}_D)$ values.

(iii) Darcy regime: The Darcy regime persists for steady slow creeping flow. The viscous drag solely contributes to the pressure drop because of low velocity and low momentum fluid stream masked over the solid surface without formation of any wakes and inertial cores like fluid structure. The purely viscous Darcy regime was identified by the horizontal line with a constant $(\Delta P / L\bar{u}_D)$ value. In Darcy regime, the second term on the right hand side of Eq. (5.9-5.10) becomes zero. Thus, for purely viscous fluid Eq. (5.9 and 5.10) becomes:

$$\left. \begin{aligned} -\frac{d\langle \bar{P} \rangle}{dL} \cdot \frac{1}{\langle \bar{u}_D \rangle} &= \left(\frac{\mu}{\bar{K}} \right) \\ \frac{\Delta P}{L \cdot \langle \bar{u}_D \rangle} &= \left(\frac{\mu}{\bar{K}} \right) \end{aligned} \right\} \quad (5.11)$$

where \bar{K} is the permeability of the porous media which characterized the internal morphology of the porous media. The onset of Darcy flow regime depends on the particle size. Details of Darcian velocity (\bar{u}_D) range for different sized particles are shown in Table 5.2.

(iv) Forchheimer inertial regimes: As the velocity gradually increases, deviation starts from Darcian relationship. It should be mentioned that the flow within the porous media remains steady and laminar. Kinetic energy degradation begins due to the pore constrictions and changes in flow direction around the solid phase. Hence, the flow energy dissipation becomes the sum of the viscous and inertial drags. The contribution of the inertial drag can be captured by a second-order velocity dependent term in the Darcy equation (Eq. 5.9). From RPD plot it was observed that the inertial regime starts from $\bar{u}_D > 0.05 \text{ m.s}^{-1}$ for uniform isotropic particles, but for mixed particles, the inertial regime starts early from $\bar{u}_D \geq 0.03 \text{ m.s}^{-1}$. This indicates that the flow resistance offered by the mixed anisotropic particles is more as compared to uniform isotropic particles. Panfilov and Fourar (2006) suggested that the non-Darcy flow behaviour in the porous media arises due to inertial-viscous and purely inertial effects. At the beginning of the Forchheimer regime inertia-viscous cross effect plays significant role in the deformation of the streamlines, thereby creating non-Darcy flow regime. As the velocity gradually increases to higher values, this effect becomes more and more pronounced with purely inertial effect dominating the flow. For mixed particles, the inertial-viscous cross effects substantially altered the flow regime to non-Darcian flow due to pore blockage, internal pore size heterogeneity and highly tortuous flow path.

5.1.3 Pressure Gradient-Flow Rate Behaviour

The pressure gradient-flow rate behaviour along the porous bed as a function of particle size and porosity can be described by following non-dimensional relationship:

Kozney-Carman correlation:

$$\left(\frac{d\langle \bar{P} \rangle}{dL} \right) \left(\frac{d_p}{\rho \bar{u}_s^2} \right) \left(\frac{\phi^3}{(1-\phi)^2} \right) = \frac{180}{\text{Re}_p} \quad (5.12)$$

$$f_{K-C} = \frac{180}{\text{Re}_p}$$

Ergun relation:

$$\left(\frac{d\langle \bar{P} \rangle}{dL} \right) \left(\frac{d_p}{\rho \bar{u}_s^2} \right) \left(\frac{\phi^3}{(1-\phi)} \right) = \frac{150}{\text{Re}'_p} + 1.75 \quad (5.13)$$

$$f_{Er} = \frac{150}{\text{Re}'_p} + 1.75$$

Table 5.2: Flow regimes boundaries of different porous media for incompressible Newtonian fluid

Flow regime	Pre-Darcy			Darcy			Non-Darcy Forchheimer		
	$Re_{\sqrt{k}}$	Re_D	Re_p	$Re_{\sqrt{k}}$	Re_D	Re_p	$Re_{\sqrt{k}}$	Re_D	Re_p
Kececioglu and Jiang (1994) 3mm	-	-	-	$0.013 < Re_{\sqrt{k}} < 0.025$	-	-	$0.07 < Re_{\sqrt{k}} < 0.48$	-	-
Fand et al. (1987) 3mm	-	-	-	-	$Re_D < 2.3$	-	-	$5 < Re_D < 80$	-
Bagci et al., (2014) 3mm	$Re_{\sqrt{k}} < 0.02$	$Re_D < 0.72$	-	$0.02 < Re_{\sqrt{k}} < 0.59$	$0.92 < Re_D < 22.45$	-	$1.81 < Re_{\sqrt{k}} < 6.21$	$68.0 < Re_D < 232.5$	-
Bagci et al., (2014) 1mm	$Re_{\sqrt{k}} < 0.25$	$Re_D < 9.65$	-	$0.29 < Re_{\sqrt{k}} < 0.77$	$11.0 < Re_D < 29.3$	-	$1.28 < Re_{\sqrt{k}}$	$48.7 < Re_D$	-
Present study									
2.5 mm $\phi = 0.4174$	$Re_{\sqrt{k}} < 0.01$	$Re_D \leq 0.485$	$Re_p \leq 0.202$	$0.01 \leq Re_{\sqrt{k}} \leq 0.5$	$2.0 \leq Re_D \leq 18.1$	$0.8 \leq Re_p \leq 7.15$	$Re_{\sqrt{k}} \geq 0.7$	$Re_D \geq 20$	$Re_p \geq 7.55$
3.5 mm $\phi = 0.3696$	$Re_{\sqrt{k}} < 0.02$	$Re_D \leq 1.48$	$Re_p \leq 0.55$	$0.02 \leq Re_{\sqrt{k}} \leq 0.7$	$5.28 \leq Re_D \leq 27.07$	$2.0 \leq Re_p \leq 10$	$Re_{\sqrt{k}} \geq 0.8$	$Re_D \geq 28.6$	$Re_p \geq 12.25$
5 mm $\phi = 0.3478$	$Re_{\sqrt{k}} < 0.005$	$Re_D \leq 2.37$	$Re_p \leq 0.54$	$0.006 \leq Re_{\sqrt{k}} \leq 0.2$	$4.86 \leq Re_D \leq 27.34$	$1.27 \leq Re_p \leq 6.21$	$Re_{\sqrt{k}} \geq 0.3$	$Re_D \geq 28$	$Re_p \geq 7.82$
Mixed $\phi = 0.3913$	$Re_{\sqrt{k}} < 0.02$	$Re_D \leq 1.01$	$Re_p \leq 0.40$	$0.02 \leq Re_{\sqrt{k}} \leq 0.3$	$2.7 \leq Re_D \leq 11.63$	$1.14 \leq Re_p \leq 5.0$	$Re_{\sqrt{k}} \geq 0.4$	$Re_D \geq 14.67$	$Re_p \geq 5.74$

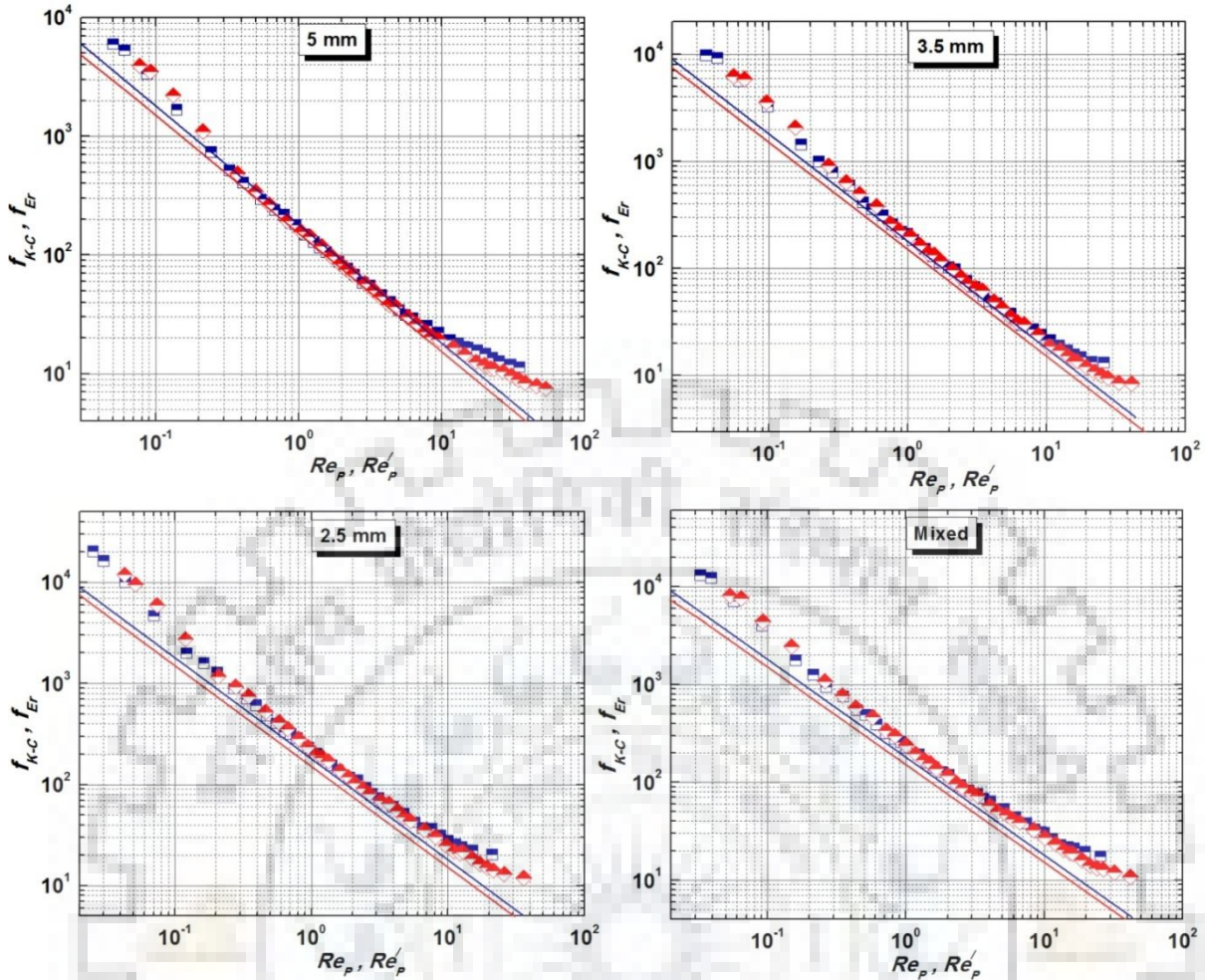


Fig 5.3: Friction factor-Reynolds number plots for Newtonian fluid flow through different types of porous media. Kozney-Carman (---); Ergun (---) equation.

According to Dupuit–Forchheimer equation (Nield and Bejan, 1999), the superficial or seepage velocity in the porous media can be expressed as follows:

$$\bar{u}_s = \phi \cdot \langle \bar{u}_D \rangle \quad (5.14)$$

Fig. 5.3 shows the friction factor versus Reynolds number plot, of the experimental data, for four different sets of porous media. A total of 148 experimental runs has been represented by this plots.

Experimental data show a typical friction factor-Reynolds number pattern according to Eq. (5.12-5.13). In general, for isotropic porous media, the pressure drop data agreed well with the Kozney-Carman equation than that with the Ergun equation. The experimental data generally lie above the Ergun prediction. The flow regimes are also identified from these plots. For isotropic porous media, a deviation from linearity was observed at very low Reynolds number, $Re_p < 0.2$, which is characterized by the pre-Darcy regime. The next deviation occurred at $Re_p > 8$ which is characterized as the non-Darcy Forchheimer regime.

In the Reynolds number range of $0.2 < \text{Re}_p < 8$, better agreement with the Kozney-Carman and Ergun equations was observed. This regime is characterized as the Darcy regime. The flow regime demarcation obtained using the friction factor plot were compared with those obtained using the RPD plots of Fig. 5.2, and were found to be consistent. However, a transition regime before the Darcy regime was identified from the RPD plot which cannot be traced from friction factor-Reynolds number plot. Similar pattern was observed for mixed particles, however, the non-Darcy Forchheimer regime is found to begin at $\text{Re}_p > 5$, i.e. earlier than the isotropic porous media. The flow regime demarcation obtained using the friction factor-Reynolds number plot were contrasted with those obtained using the RPD plot of Fig. 5.2 and were found to be consistent.

Further, pressure drop variation in the porous media was analyzed through the modified friction factor and modified Reynolds number which includes permeability (\bar{K}) as porous media characteristic length scale (Beavers and Sparrow, 1969; Venkataraman and Rao, 1980; Papathanasiou et al., 2001). The Forchheimer equation (Eq. 5.10) can be rewritten and expressed as:

$$\left. \begin{aligned} \left(\frac{d\langle \bar{P} \rangle}{dL} \right) \left(\frac{\sqrt{\bar{K}}}{\rho \bar{u}_s^2} \right) &= \frac{1}{\text{Re}_{\sqrt{\bar{K}}}} + F_D \\ f_{\sqrt{\bar{K}}} &= \frac{1}{\text{Re}_{\sqrt{\bar{K}}}} + F_D \end{aligned} \right\} \quad (5.15)$$

where F_D in Eq. (5.15) represents the influence of inertial force in the porous media. Permeability of the porous media changes in different flow regimes. According to Dybbs and Edwards (1984) in the purely viscous Darcy regime, the exact nature of the flow field was determined by the local internal structure of the porous medium. In the non-Darcy inertial regimes, the actual internal structure of the porous medium is masked by various effects such as boundary layers on solid surfaces, inertial cores, and wake formations (Bagci et al., 2014). Thus, the permeability obtained in the Darcy regime represents the actual internal structure of the porous medium most accurately (Kececioğlu and Jiang, 1994). Therefore, the permeability obtained from the Darcy flow regime was used in the Forchheimer equation (Eq. 5.15). Permeability and Forchheimer coefficient for different porous media are given in Table 5.3. From Fig. 5.4 it can be seen that $f_{\sqrt{\bar{K}}}$ varies inversely with $\text{Re}_{\sqrt{\bar{K}}}$.

Three distinct zones can be seen from Fig. 5.4 by comparing the experimental data with the projected $1/\text{Re}_{\sqrt{\bar{K}}}$ plot. A deviation from $1/\text{Re}_{\sqrt{\bar{K}}}$ was observed at a lower $\text{Re}_{\sqrt{\bar{K}}}$ ($\text{Re}_{\sqrt{\bar{K}}} < 0.01$) which is classified as the pre-Darcy regime. Another deviation was observed

at $Re_{\sqrt{K}} > 0.04$, which is classified as non-Darcy Forchheimer regime. In between, where experimental data depart from the $1/Re_{\sqrt{K}}$ plot, signifies the end of the Darcy regime. Darcy regime exists within the range of $0.01 < Re_{\sqrt{K}} < 0.5$. The demarcation, $Re_{\sqrt{K}}$, range for different flow regimes varies with the particle size and the type of porous media. A comprehensive flow regime range based on $Re_{\sqrt{K}}$ for different types of porous media is given in Table 5.2.

Table 5.3. Parameters of Forchheimer equation for different porous media.

Porous media	Type of porous media	Mean Particle Size, d_p (mm)	Porosity, ϕ	Permeability, $\bar{K} \times 10^8$ (m ²)	Forchheimer coefficient, F_D
PM 1	Uniform isotropic	2.5	0.4174	5.488	0.902
PM 2	Uniform isotropic	3.5	0.3696	7.202	0.964
PM 3	Uniform isotropic	5.0	0.3478	1.417	0.594
PM 4	Mixed non-isotropic	3.25	0.3913	6.775	1.346

5.2.4 Variation of Medium Permeability at Different Pore Flow Regimes

Medium permeability has a significant influence on the fluid percolation through the porous media. Fluid percolation through porous media is the result of physical interaction between the solid structure and the fluid. The relation between the medium permeability and the Reynolds number has been derived from Eq. (5.2) and Eq. (5.4) for Darcy and non-Darcy flow regimes. The medium permeability is represented as the reciprocal of the normalized permeability (*RNP*).

Viscous Darcy regime:

$$-\frac{d_p^2}{\mu \bar{u}_s} \frac{d\langle \bar{P} \rangle}{dL} = \frac{d_p^2}{K_e} = \frac{d_p^2}{K} = Const \quad (5.16)$$

Weak transitional non-Darcy regime:

$$\frac{d_p^2}{K_e} = b_1 Re_p^2 + b_2 Re_p + \frac{d_p^2}{K} \quad (5.17)$$

Quadratic Forchheimer regime:

$$\frac{d_p^2}{K_e} = A Re_p + \frac{d_p^2}{K} \quad (5.18)$$

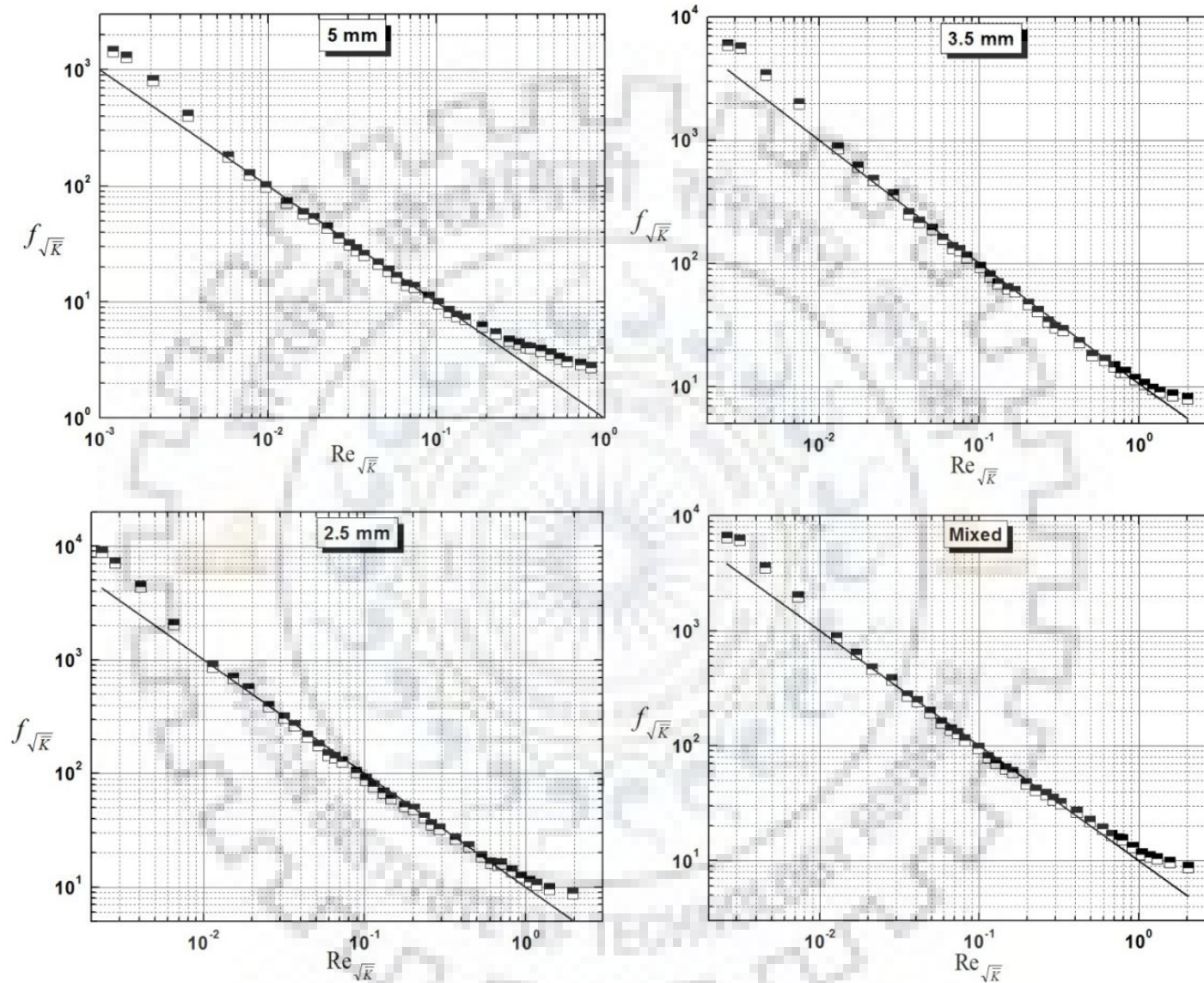


Fig. 5.4: Permeability based modified friction factor versus Reynolds number plot for different porous media.

In the Darcy regime, the RNP of the porous media remains constant with Re_P whereas in the non-Darcy Forchheimer regime, the RNP increases with an increase in the Re_P . The RNP plots for different porous media are shown in Fig. 5.5. It was found that the experimental results were well correlated by Eq. 5.16 at low Re_P ($Re_P < 5$), i.e. in the Darcy regime, this was also identified in the previous section. In this regime, the viscous force dominates over the inertial force, and RNP becomes independent of Re_P . Thus only the local geometry or pore structure influences the flow behavior. The extended Darcy regime covers the range of $0.5 < Re_P < 5$. As the Re_P gradually increases ($Re_P > 5$) permeability becomes a function of Re_P , and RNP increases with an increase in Re_P . Under the same pressure gradient, the larger the increase in flow velocity, the more easily fluid percolates through the porous media. This signifies the end of the Darcy regime and the beginning of non-Darcy flow regime. At $Re_P > 5$, the curve is characterized by a typical inflexion towards x-axis. In the range of $5 < Re_P < 10$, a transition regime was seen where a small change in permeability with Re_P was found. This regime is characterized by a weak inertial regime where the inter play of both the viscous and inertial effects is seen. With a further increase in Re_P ($Re_P > 10$), RNP increases steadily.

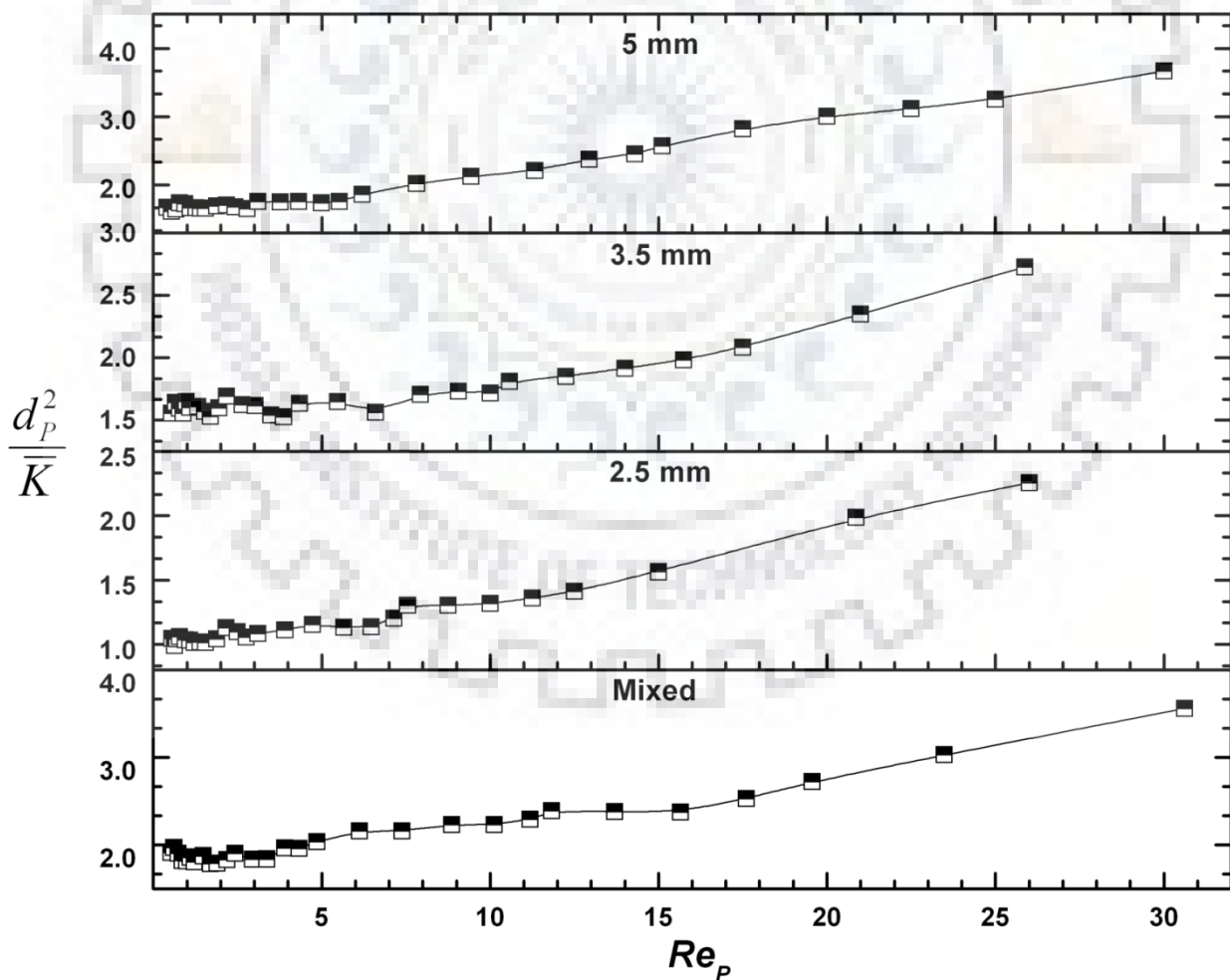


Fig. 5.5: Variation of reciprocal of normalized permeability of different porous media with Re_P .

This is the region of transition from weak inertial regime to quadratic Forchheimer regime. The flow in porous media in this regime is than governed by the Forchheimer equation unlike flow in the Darcy regime, and hence by the inertial force. An anomalous behaviour was observed in the pre-Darcy regime, where RNP value was quite high and was a function of Re_p . Therefore, the variation of permeability in pre-Darcy regime ($Re_p < 0.5$) was not considered here.

5.2 FLOW OF EMULSIONS THROUGH POROUS MEDIA

5.2.1 Emulsion Flow Modeling

The capillary tube bundle approach together with the mean hydraulic diameter concept has been extended for modeling emulsion flow through porous media. According to generalized capillary flow model the porous media or granular bed of solid particles consists of irregularly shaped channels provided by the space between the particles in the bed. These channels are considered as large numbers of capillary tubes running parallel to the direction of flow. The laminar flow of a fluid was considered flowing through a bed of solid particles contained in a cylindrical column of diameter D_t , bed length L and particle diameter d_p . The tortuous path of the channel is l_e , traversed by the fluid elements, and it is more than the bed length, L . For porous media flow parameters used were as follows:

$$\text{Average velocity, } \bar{u} = \frac{u_s}{\phi} \quad (5.19)$$

$$\text{Tortuosity factor, } C_t = \frac{l_e}{l} \quad (5.20)$$

$$\text{Hydraulic radius, } R_h = \left(\frac{\phi}{1-\phi} \right) \frac{d_p}{6} \quad (5.21)$$

Typically, an emulsion behaves like non-Newtonian fluid. The general form of constitutive power-law equation for non-Newtonian fluid is given as follows:

$$\tau = K \left(\frac{du}{dy} \right)^n = k \dot{\gamma}^n \quad (5.22)$$

The momentum flux or shear stress was obtained by momentum balance over cylindrical fluid element in a capillary of radius r as follows:

$$\begin{aligned} \tau &= \left(\frac{P_0 - P_L}{2L} \right) r \\ &= \left(\frac{\Delta P}{2L} \right) r \end{aligned} \quad (5.23)$$

The fluid velocity become zero (i.e., $V_{r=R} = 0$) at the tube wall and at the particle surface.

Thus, shear stress becomes

$$\tau_w = \left(\frac{\Delta P}{2L} \right) R_H \quad (5.24)$$

$$\frac{r}{R_h} = \frac{\tau}{\tau_w} \quad (5.25)$$

The average velocity through the capillary is written as:

$$\langle \bar{u} \rangle = \frac{\int_0^{R_H} 2\pi r u dr}{\pi R^2} \quad (5.26)$$

The volumetric flow rate through capillary is expressed as:

$$q = \langle \bar{u} \rangle \cdot (\pi R^2) = 2\pi \int_0^{R_h} u \cdot r dr \quad (5.27)$$

On integrating Eq. (5.27), we have

$$q = -\pi \int_0^{R_h} \left(\frac{du}{dr} \right) r^2 dr \quad (5.28)$$

Rearranging Eq. (6) and Eq. (7) in Eq.(10), we get

$$\frac{q \tau_w^3}{\pi R_h^2} = \int_0^{\tau_w} \left(-\frac{du}{dr} \right) \cdot r^2 d\tau \quad (5.29)$$

For non-Newtonian fluid

$$\left(-\frac{du}{dr} \right) = \left(\frac{\tau}{K} \right)^{-n} \quad (5.30)$$

Eq. (5.29) becomes,

$$\frac{q \tau_w^3}{\pi R_h^2} = \int_0^{\tau_w} \left(\frac{\tau}{K} \right)^{-n} \cdot r^2 d\tau \quad (5.31)$$

After integration and rearranging, we have

$$\tau_w = K \left(\frac{u_s}{R_h} \right)^n \left(\frac{3n+1}{n} \right)^n \quad (5.32)$$

or

$$\tau_w = K \left(\frac{8u_s}{D_h} \right)^n \left(\frac{3n+1}{4n} \right)^n \quad (5.33)$$

The effective viscosity is defined as

$$\mu_{eff} = \frac{\tau_w}{\dot{\gamma}} = \frac{\tau_w}{\left(\frac{8u_s}{D_h} \right)} \quad (5.34)$$

Therefore, substituting Eq. (5.32 or 5.33) in Eq. (5.34), yields the expression of 'effective viscosity' for emulsions behaves as a non-Newtonian fluid.

$$\mu_{eff} = K \left(\frac{8u_s}{D_h} \right)^{n-1} \left(\frac{3n+1}{4n} \right)^n \quad (5.35)$$

5.2.2 Pressure Drop in Packed Bed of Different Porous Media for o/w Emulsion Flow

Pressure drop data $(d\langle \bar{P} \rangle / dL vs \bar{u}_D)$ of all o/w emulsions at different volume fraction (10-80% v/v) were obtained for different porous bed at ambient conditions (30°C). The observed pressure data are represented in Fig. 5.6. It was observed that, with an increase in average velocity (Darcy velocity), there was an increase in the pressure drop. The observed pressure drop increases with an increase in emulsion volume fraction at the same velocity, which could be due to increase in consistency index (K) and emulsion viscosity. It was also observed that the emulsion volume fraction significantly influence the porous bed pressure drop. As the emulsion volume fraction gradually increases, viscosity of emulsions increases and emulsion become more pseudoplastic ($n < 1$) with a decrease in flow behaviour index (n) and an increase in consistency index (K). The increase in emulsion pseudoplasticity contribute the enhancement of bed pressure drop. Similar pressure drop trend was observed with porous bed of different particle diameter (d_p). Pressure drop across the bed increases with a decrease in d_p as the pore space becomes constricted and free area available for fluid propagation gradually reduced.

5.2.3 Modified Friction Factor-Reynolds Number Relation in porous media flow

For non-Newtonian power-law fluids, Darcy-Forchheimer can be written as follows (Shenoy, 1993):

$$\nabla P = \left[\frac{\mu^* \langle u \rangle^{n-1}}{K^*} + \frac{C \rho \langle u \rangle}{\sqrt{K}} \right] \langle u \rangle \quad (5.36)$$

Eq. (5.36) become non-dimensional by multiplying with $\left[\frac{d\varepsilon}{\rho \langle u \rangle^2 (1-\varepsilon)} \right]$

$$f_m^* = \frac{A'}{\text{Re}_p^*} + B' \quad (5.37)$$

where

$$\text{Re}_p^* = \frac{\rho \langle u \rangle / \varepsilon}{\mu^*} \left(\frac{d_p \varepsilon}{1-\varepsilon} \right)^n \quad \text{and} \quad f_m^* = \left(-\frac{dP}{dL} \right) \frac{1}{\rho \langle u \rangle / \varepsilon} \left(\frac{d_p \varepsilon}{1-\varepsilon} \right)$$

$$A' = 2C_i [(3n+1)/n]^n 3^{n+1}$$

and

$$B' = 1.75$$

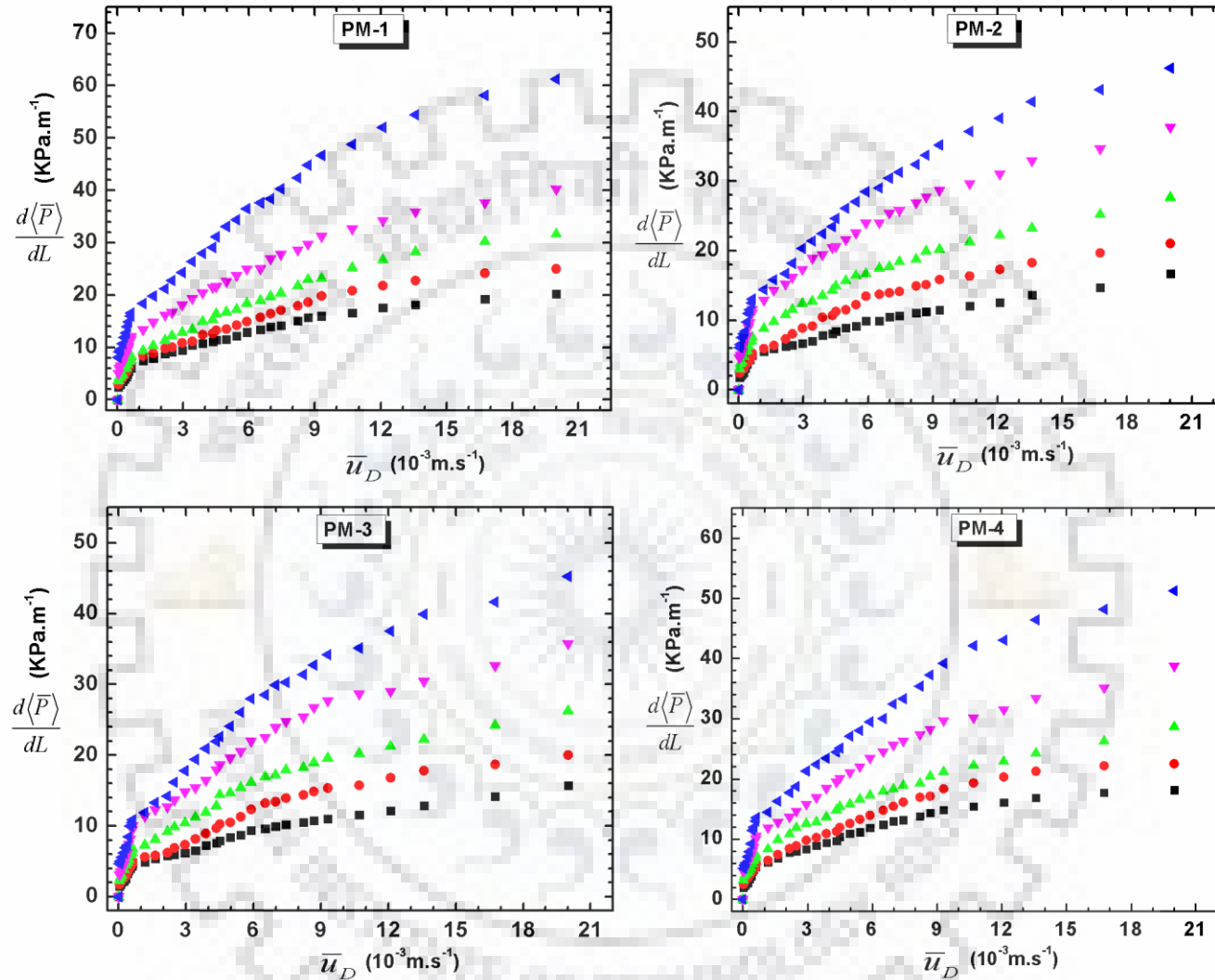


Fig. 5.6: Relationship between the Pressure gradient per unit length versus average velocity across the porous bed for different emulsion volume fraction. Emulsion vol. fr. (v/v) = 10% ●, 30% ■; 50% ▲; 70% ▼; 80% ◀.

For laminar flow the second term in Eq. (5.37) is neglected. Therefore, the modified friction factor and modified Reynolds number can be expressed as:

$$f_m^* = \frac{A'}{\text{Re}_p^*} \quad (5.38)$$

The tortuosity factor, C_t , has been defined differently by various authors as follows:

Christopher and Middleman (1965) and Mishra et al. (1975) :

$$C_t = \frac{25}{12} \quad (5.39)$$

Kemblowski and Michniewicz (1979):

$$C_t = 2.5^n 2^{(1-n)/2} \quad (5.40)$$

Pascal (1983):

$$C_t = \left(\frac{25}{12}\right)^{(n+1)/2} \quad (5.41)$$

Dharmadhikari and Kale (1985):

$$C_t = \frac{2}{3} \left(\frac{8n'}{9n'+3}\right)^{n'} \left(\frac{10n'-3}{6n'+1}\right) \left(\frac{75}{16}\right)^{3(10n'-3)/(10n'+11)} \quad (5.42)$$

$$n' = n + 0.3(1-n)$$

Table 5.4: Variation of C_t given by Eq. (5.39-5.42) for different emulsion volume fraction.

Volume Fraction (% v/v)	n	Christopher and Middleman (1965) and Mishra et al. (1975)	Kemblowski and Michniewicz (1979)	Pascal (1983)	Dharmadhikari and Kale (1985)
10	0.559	2.083	1.945	1.772	0.979
30	0.4977	2.083	1.878	1.733	0.847
50	0.504	2.083	1.885	1.737	0.860
70	0.4647	2.083	1.843	1.712	0.778
80	0.4375	2.083	1.815	1.695	0.822

The variation of C_t with emulsion volume fraction estimated by Eq.(5.39-5.42) is shown in Table 5.4. Experimental pressure drop results for different porous media were compared with Eq. (5.38) using C_t as predicted by Eq. (5.39-5.42), and shown in Fig. 5.7. Experimental results showed good agreement with the other models. The deviation was observed at Reynolds number $\text{Re}_p^* \geq 10^{-03}$ but better agreement was observed at $\text{Re}_p^* \leq 10^{-03}$. It was observed that as the oil volume fraction increases the deviation at higher Reynolds number

gradually decreases. Experimental pressure drop data for 50-70% v/v emulsion showed overall good agreement with the model predictions as compared to other emulsions. A comparison between the experimental results and predicted values were presented in terms of M.R.Q.E and are shown in Table 5.5. It was observed that Pascal (1983) and Dharmadhikari and Kale (1985) model reasonably fit the pressure drop data for the entire range of emulsion volume fraction and Re_p^* . Christopher and Middleman (1965), Mishra et al. (1975) and Kembrowski and Michniewicz (1979) model over predicted the experimental data at $Re_p^* \geq 10^{-03}$.

Furthermore, experimental pressure drop results were compared with other model equation proposed by various researches is given in Table 5.6. On comparing the M.R.Q.Es the model predicted by Hayes et al. (1996) and Dharmadhikari and Kale (1985) best fit the emulsion pressure drop data among others.

The modified friction factor (f_m^*) and modified Reynolds number (Re_p^*) was calculated according to Eq. (5.22). Fig. 5.8 represents the $f_m^* - Re_p^*$ plot for emulsion with different volume fractions flowing through porous bed. It was observed that for all sets of emulsions, the f_m^* decreases with an increase in Re_p^* . Further it was observed that all data points for different emulsion volume fraction superimposed in a single curve at $Re_p^* \geq 10^{-03}$. However, at $Re_p^* \leq 10^{-03}$ volume fraction alter the f_m^* with Re_p^* .

Effect of particle diameter on $f_m^* - Re_p^*$ plot is shown in Fig. 5.9. Variation of f_m^* with particle diameter (d_p) was observed at $Re_p^* \geq 3 \times 10^{-04}$. Modified friction factor increases with an increase in particle diameter varying from 2.5 to 5 mm, where friction factor for mixed particles lies among them. But at $Re_p^* \leq 3 \times 10^{-04}$ no significant effect of d_p on $f_m^* - Re_p^*$ plot was observed.

5.2.4 Rheological Behavior of Emulsions Flow through Porous Media

The rheological properties of emulsions flowing through a porous media were studied on the basis of shear stress versus shear rate relationship. The shear stress ($\bar{\tau}_w$) versus shear rate ($8u_s/R_h$) curves for different emulsions quality in porous bed of different particles is shown in Fig. 10. It was observed that the shear stress increases with an increase in shear rate during percolation of emulsions through the bed. The bed shear stress progressively increases with an increase in emulsion volume fraction. Similar trend was observed for different particle diameters.

The effective viscosity of emulsions have been calculated from the derived model (Eq. 5.35) and is shown in Fig. 5.11, as a function of shear rate for porous bed of different particle sizes. The effective viscosity of emulsions is decreases with shear rate as flowing through the porous bed. It was also found that the effective viscosity of emulsions increases with an increase in oil volume fraction in the o/w emulsion when flowing through a porous media at a specified shear rate.

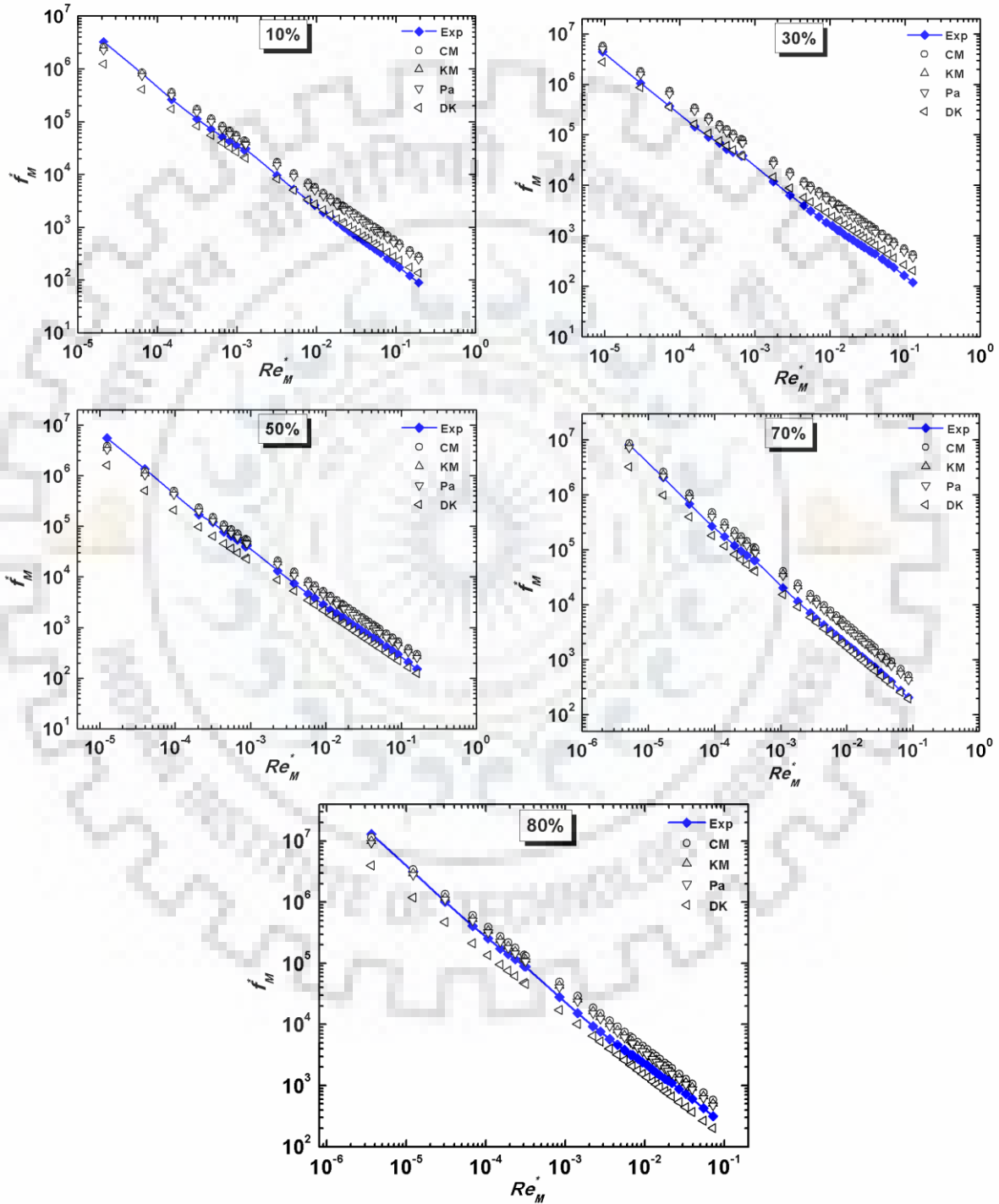


Fig. 5.7: Modified friction factor-Reynolds number plot and model compression for o/w emulsion flowing through PM-1 at different volume fraction.

Table 5.5: Statistical comparison (MRQE) of various model predictions (Eq. 5.39-5.42) and experimental results.

Porous media	Christopher and Middleman (1965)	Kemblowski and michniewicz (1979)	Pascal (1983)	Dharmadhikari and Kale (1985)
PM-1				
10%	1.346	1.198	1.015	0.285
30%	1.971	1.776	1.535	0.450
50%	0.723	0.571	0.461	0.335
70%	1.161	0.919	0.788	0.242
80%	0.758	0.542	0.447	0.406
PM-2				
10%	1.545	1.384	1.183	0.342
30%	1.631	1.376	1.197	0.176
50%	0.572	0.439	0.346	0.395
70%	0.895	0.684	0.571	0.319
80%	0.853	0.622	0.520	0.370
PM-3				
10%	0.830	0.720	0.587	0.281
30%	0.945	0.759	0.628	0.241
50%	0.203	0.148	0.149	0.532
70%	0.473	0.313	0.229	0.453
80%	0.426	0.255	0.185	0.508
PM-4				
10%	1.055	0.926	0.769	0.239
30%	1.648	1.475	1.259	0.298
50%	0.508	0.382	0.294	0.411
70%	0.903	0.691	0.576	0.312
80%	0.739	0.521	0.425	0.399

Table 5.6: Statistical comparison (MRQE) of various model predictions for o/w emulsions as test fluid.

Porous media	Kumar and Upadhyay (1981)	Al Fariss (1990)	Hayes et al. (1996)	Sabiri and Comiti (1997)
PM-1				
10 %	1.131	2.465	0.969	0.745
30 %	1.318	1.779	1.048	0.715
50 %	0.554	0.915	0.395	0.807
70 %	0.925	0.976	0.667	0.761
80 %	0.562	0.440	0.337	0.804
PM-2				
10 %	1.314	2.852	1.113	0.733
30 %	1.361	1.869	1.061	0.716
50 %	0.428	0.794	0.286	0.830
70 %	0.693	0.779	0.456	0.795
80 %	0.648	0.525	0.390	0.800
PM-3				
10 %	0.674	0.776	0.535	0.803
30 %	0.747	0.318	0.525	0.785
50 %	0.146	0.300	0.175	0.867
70 %	0.320	0.310	0.148	0.835
80 %	0.274	0.434	0.113	0.841
PM-4				
10 %	0.869	1.997	0.729	0.775
30 %	1.067	1.431	0.825	0.745
50 %	0.369	0.662	0.246	0.832
70 %	0.697	0.709	0.471	0.789
80 %	0.543	0.367	0.311	0.806

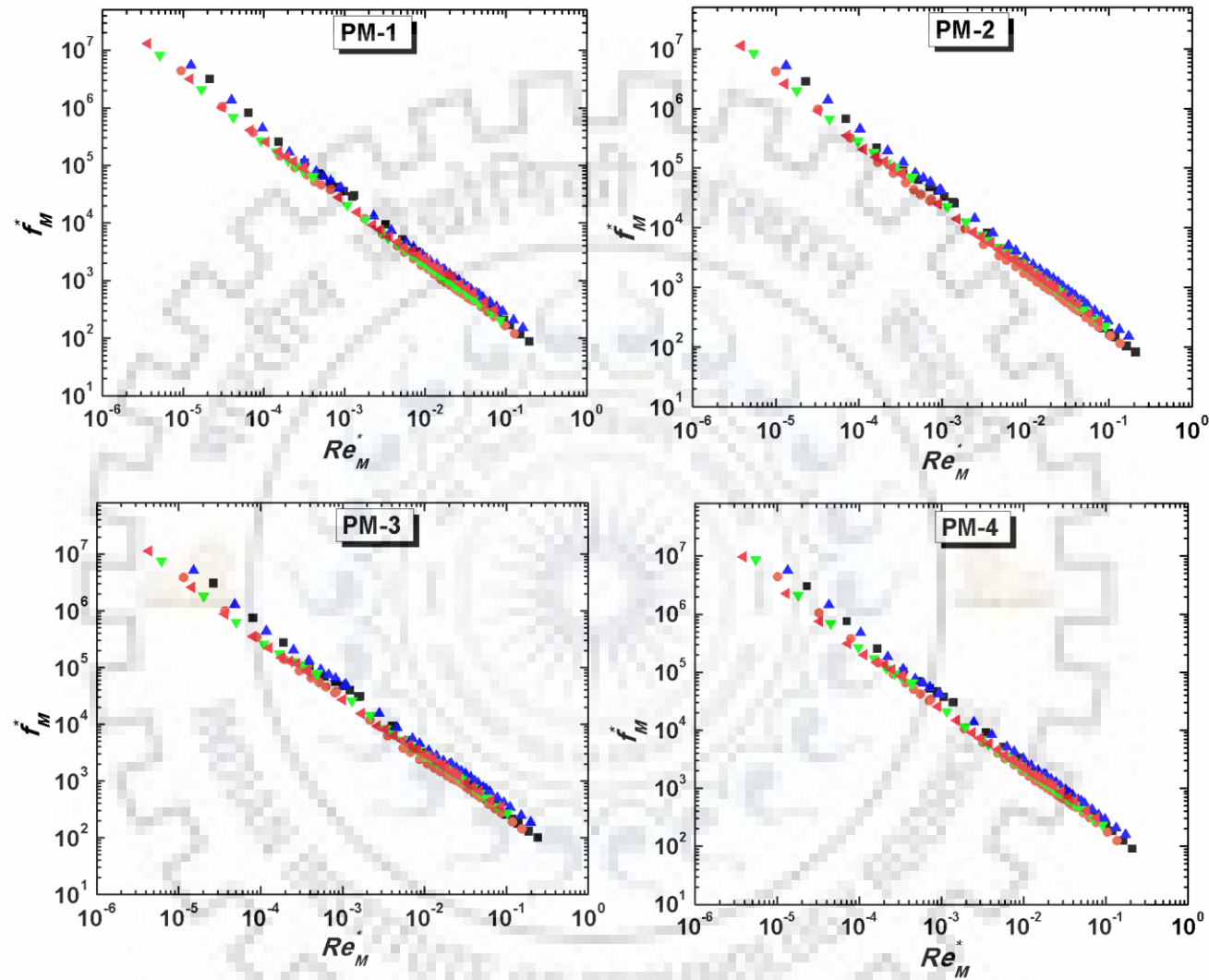


Fig. 5.8: Modified friction factor-Reynolds number plot different emulsion volume fraction.

Emulsion vol. fr. (v/v) = 10% ●, 30% ■ ; 50% ◀; 70% ▶ ; 80% ▼ .

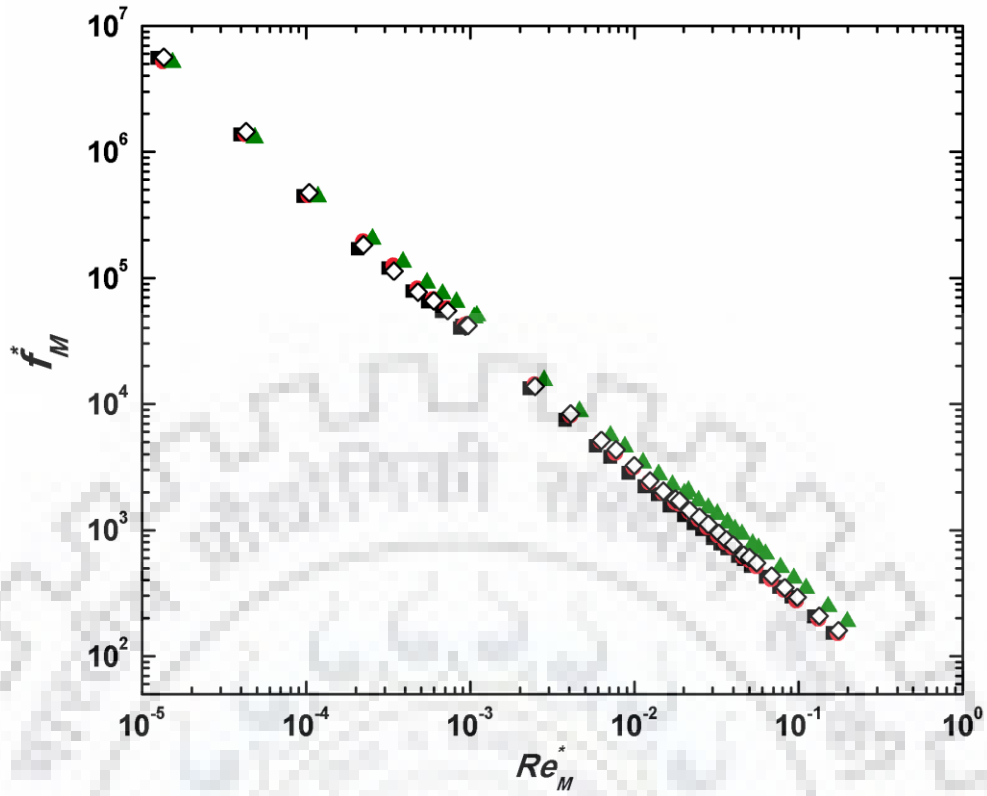


Fig. 5.9: f_m^* Vs Re_M^* plot for different particle diameter (50% o/w emulsion).

PM ■ ; PM2 ● ; PM3 ▲ ; PM4 ◇

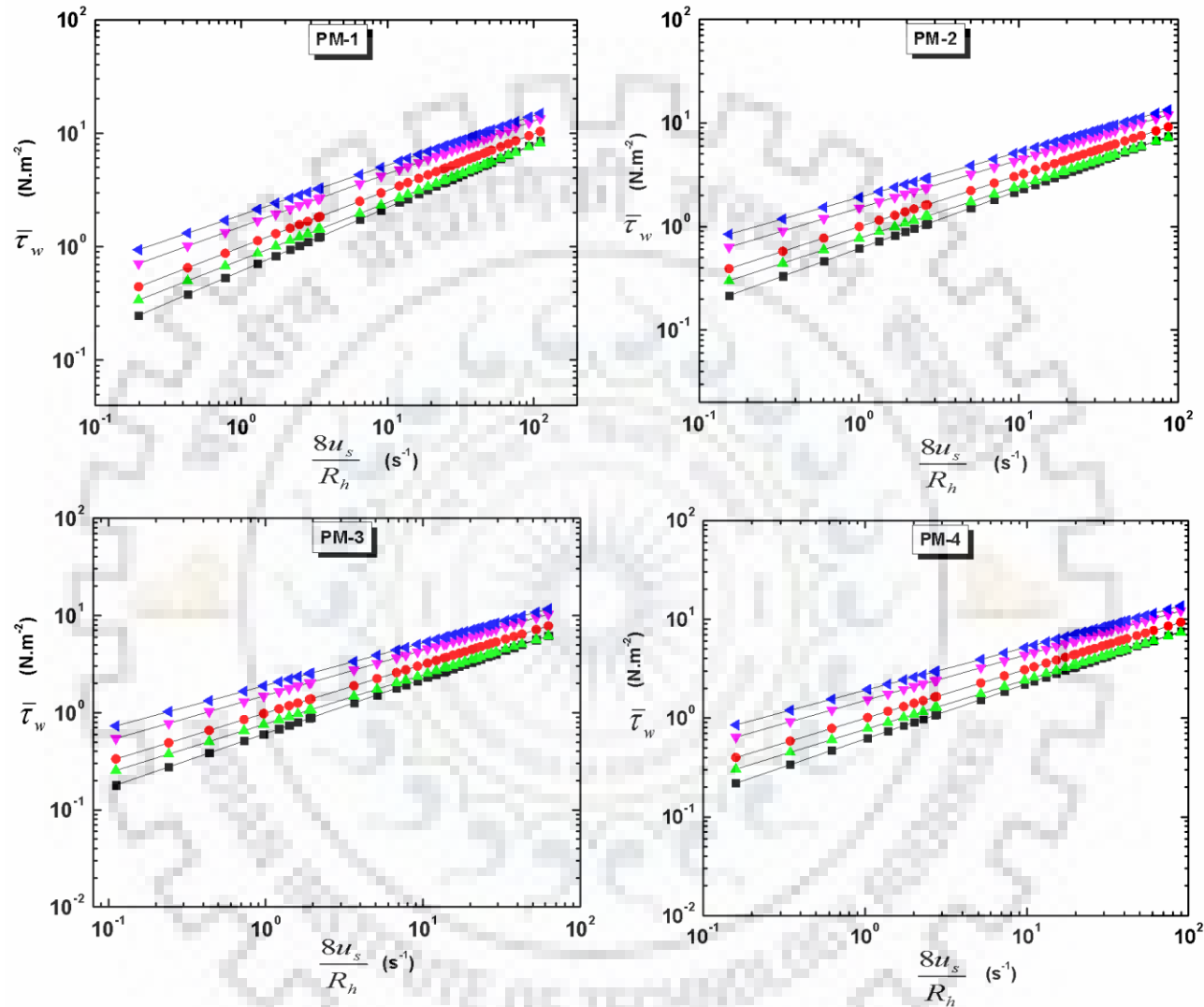


Fig. 5.10: Rheological behavior of emulsions in different type of porous media.
 Emulsion vol. fr. (v/v)= 10% ■; 30% ●; 50% ▲; 70% ▼; 80% ◀.

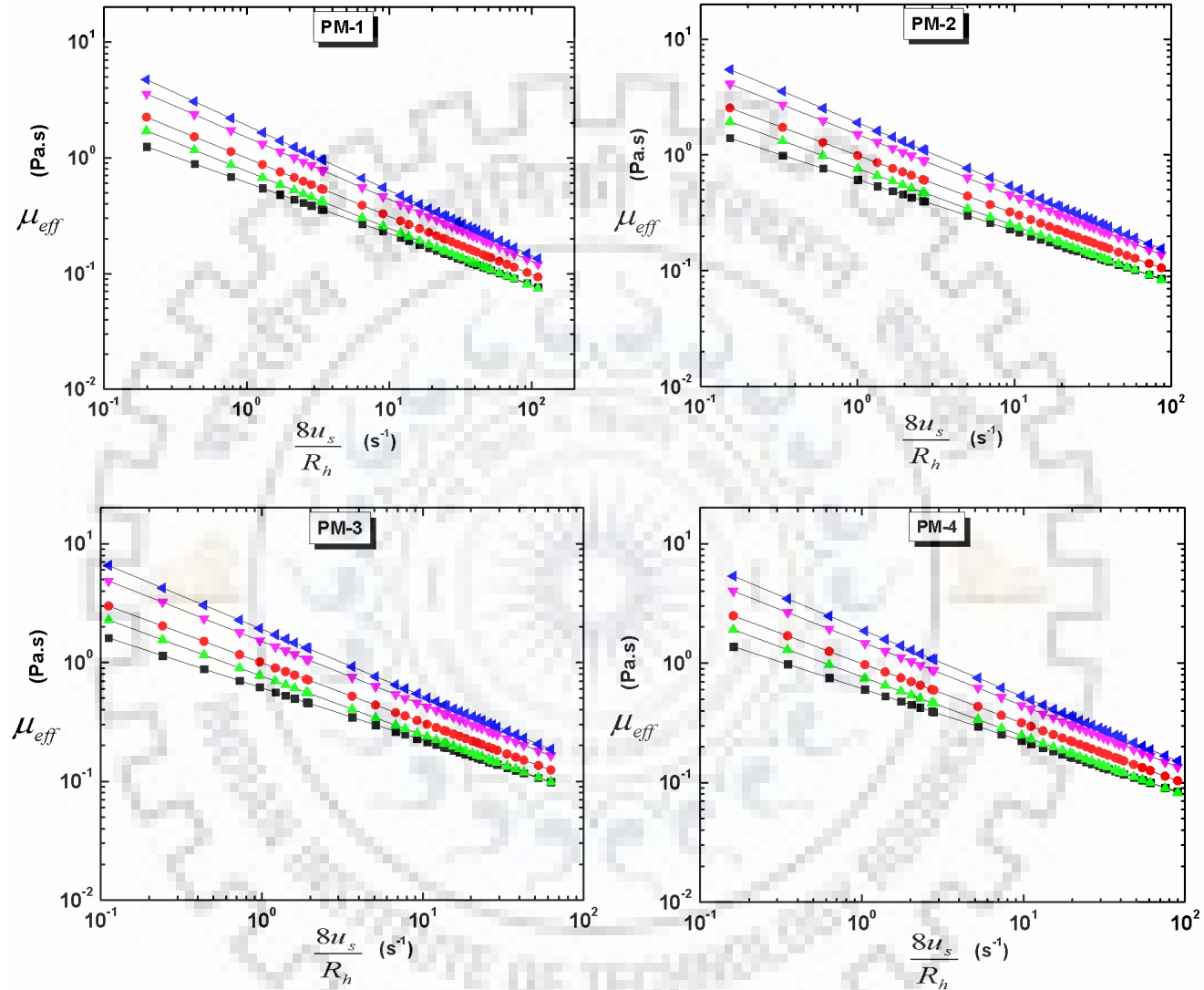


Fig. 5.11: Effective viscosity of emulsions with volume fraction at different shear rates in porous media.
 Emulsion vol. fr. (v/v) = 10% ■; 30% ●; 50% ▲; 70% ▼; 80% ◀.

5.2.5 Quantification of Emulsion Flow Resistance Factor in Porous Media

The flow resistance or flow restriction in porous media due to passage of emulsion was evaluated by introducing resistance factor (RF). The RF is a measure of mobility reduction in porous media due to fluid seepage, and it is expressed as follows:

$$RF = \left(\frac{\Delta P_{emulsion}}{\Delta P_{water}} \right)_{at\ same\ flowrate} \quad (5.43)$$

Fig. 5.12 shows the variation of RF with volumetric flow rate of emulsion injected at different oil volume fraction. Initially, when the emulsion was injected, it percolate through high permeability zones due to low resistance in the flow. It was observed that RF decreases with an increase in flow rate. It varies exponentially. The interaction between emulsion and grains particles leads to altering the RF profile. As the oil volume fraction increases viscosity of emulsions gradually increases and consequently RF increases. Fig. 5.13 shows the variation of RF with emulsion volume fraction for different porous media. It was observed that the RF increases exponentially with emulsion volume fraction. It was also observed that, as the porosity of bed decreases RF increases. The low porous media offered much more resistance to flow as compared to relatively high porous media, which was observed from Fig. 5.13. Further, Fig. 5.13 also depict that PM3 shows high RF variation with emulsion volume fraction as compared to PM1. The RF profile of PM4 (bed of mixed particle) lies between profile of PM1 and PM2, respectively. Thus, the porous bed characteristics and emulsion volume fraction significantly affect the mobility reduction or RF of porous media.

5.2.6 Emulsion Flow through Sand Pack Core Holder

5.2.6.1 Pressure drop-flow rate relation of emulsion flow

Variation of pressure drop along the three different sand pack core holders (S-A, S-B, and S-C) with emulsion volume fraction is shown in Fig. 5.14. The details of core holder and packing materials were tabulated in Table 3.7 in Chapter 3. The emulsion quality/volume fraction significantly influence the pressure drop along the core. It was observed that pressure drop across the core holder increases with emulsion injection flow rate for all three core holders. Pressure drop also increases with an increase in emulsion volume fraction due to an increase in emulsion viscosity. Pressure drop for water flow through the core holders are shown in Fig. 5.15, which follow linear relationship with flow rate. As the emulsion volume fraction gradually increases flow curve deviates from linearity.

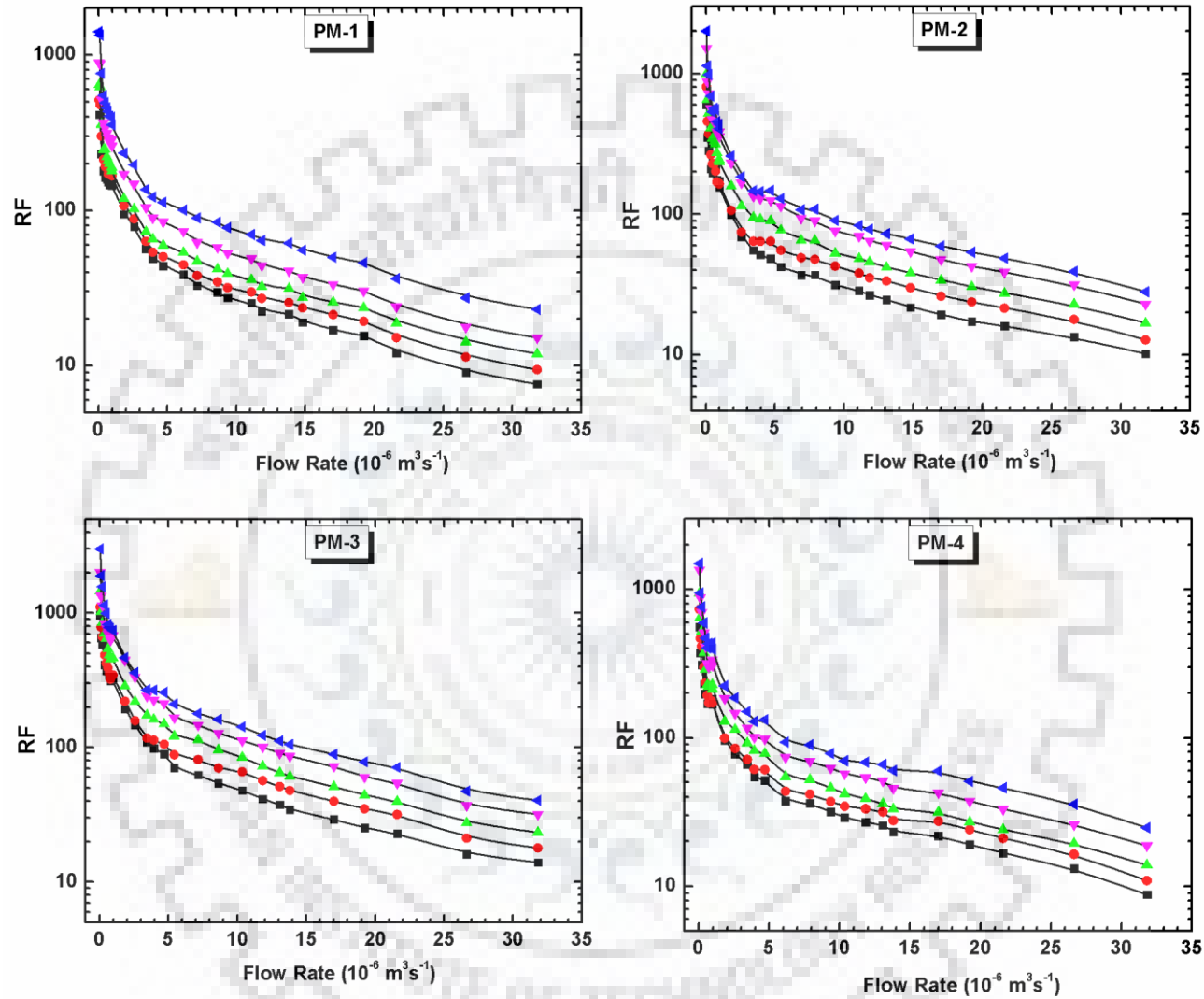


Fig. 5.12: RF versus injected flow rate of emulsion with different volume fraction in porous media. Emulsion vol. fr. (v/v)= 10% ■; 30% ●; 50% ▲; 70% ▼; 80% ◀.

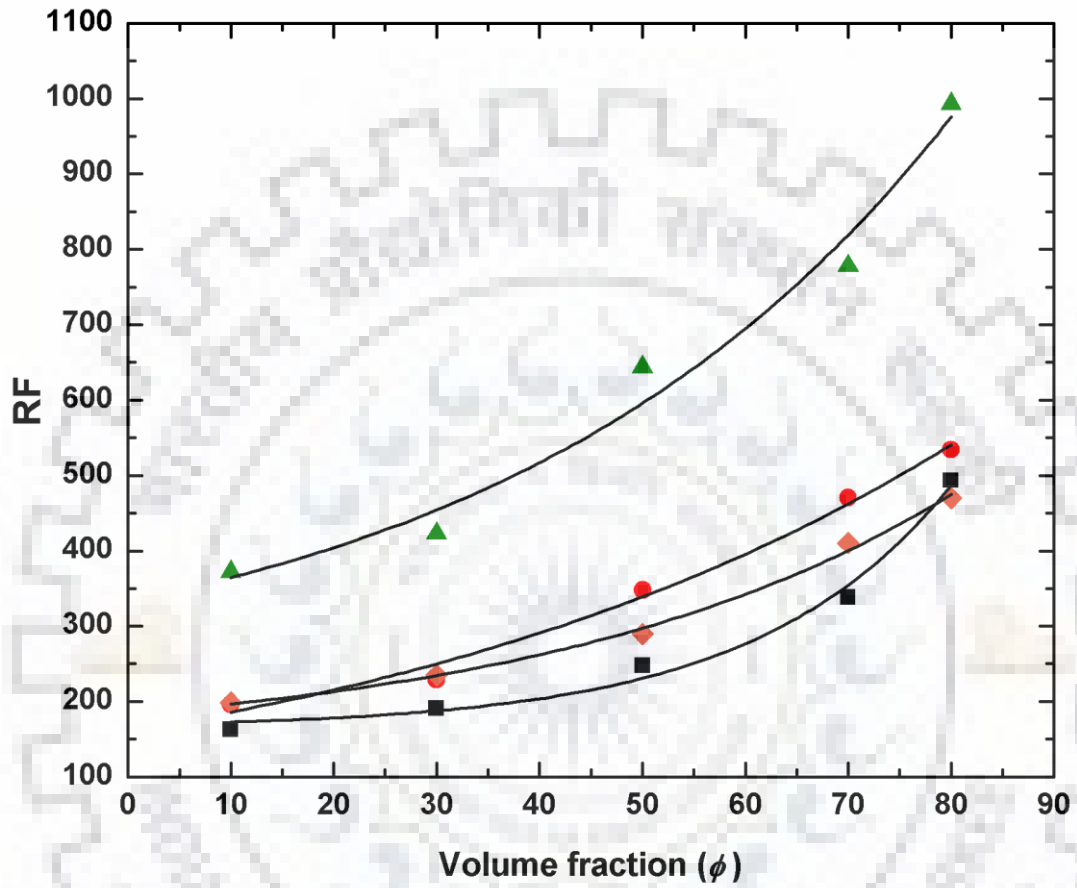


Fig. 5.13: Effect of emulsion volume fraction on the RF for different porous media

(Emulsion flow rate $5 \times 10^{-6} \text{ m}^3/\text{s}$).

PM1 ■ ; PM2 ● ; PM3 ▲ , PM ◆

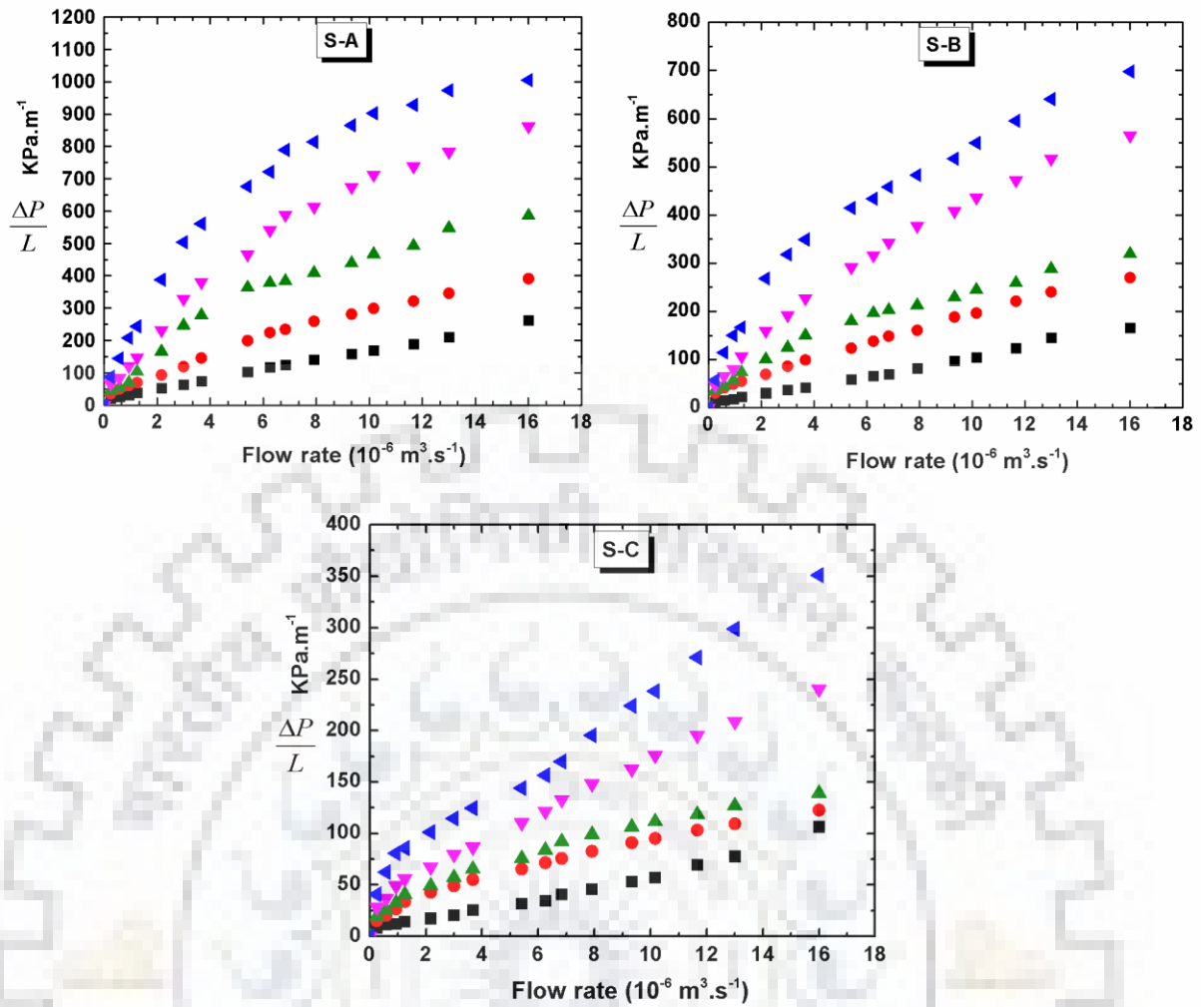


Fig. 5.14: Relationship between the Pressure gradient per unit length versus injection flow rate across the sand pack core holder for o/w emulsions and water.

Emulsion vol. fr. (v/v)= 10% ●; 30% ▲; 50% ▼; 70% ◀; water ■

The effect of sand particle size on the flow rate versus pressure drop traces for 30 % v/v o/w emulsion is shown Fig. 5.15. It was observed that the pressure drop for small particle (S-A) is more as compared to large particle (S-B and S-C). Pore space becomes constricted and pore space becomes more tortuous and effective flow area decreases with decrease in sand particle size, which in turns reduced the permeability of the porous media. As a consequence, for the same flow rate the higher pressure drop was observed.

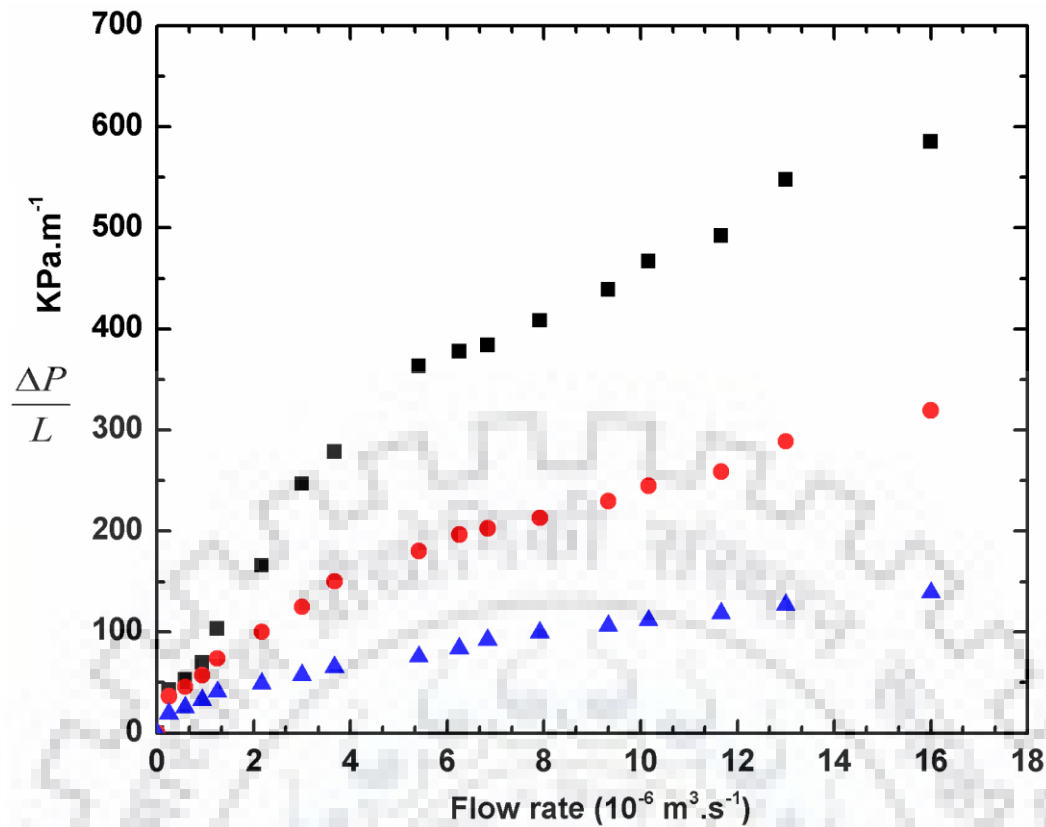


Fig. 5.15: Plot of pressure gradient per unit length versus injection flow rate for 30 % O/W emulsions. Porous media: S-1 ■; S-B ●; S-C ▲

5.2.6.2 Permeability reduction

The Permeability reduction behaviour of porous media was investigated by observing the change in pressure drop across the core holder as a function of number of pore volume of emulsion injected. The Permeability reduction across the porous bed was quantified as the reduced permeability or permeability ratio (K/K_0), which is defined as the ratio of transient permeability to initial permeability of porous media. The reduced permeability plot versus number of pore volume (PV) of emulsion injected in water saturated porous media is shown in Fig. 5.16. It was observed that the permeability ratio across the core holder decreases with an increase in PV of emulsion injected. A similar trend was observed for three different porous media. For the porous media S-A and S-B at 10% emulsions, a comparatively small reduction was observed, and suggested the free flow of emulsion through the porous media. Moreover for 30%, 50% and 70% emulsions large permeability reductions was observed. For porous media S-C large permeability reduction was observed for all set of emulsions. It was observed that for a sharp change in permeability, the change was observed within 5 pore volumes for all three types of porous media as well as for different emulsion qualities. Thereafter, a smooth change in permeability ration was observed. Initially free pore space are occupied vary quickly by the emulsion droplets which causes sharp change in permeability of

media. Further, emulsion moves to saturation with gradual change in permeability and become constant.

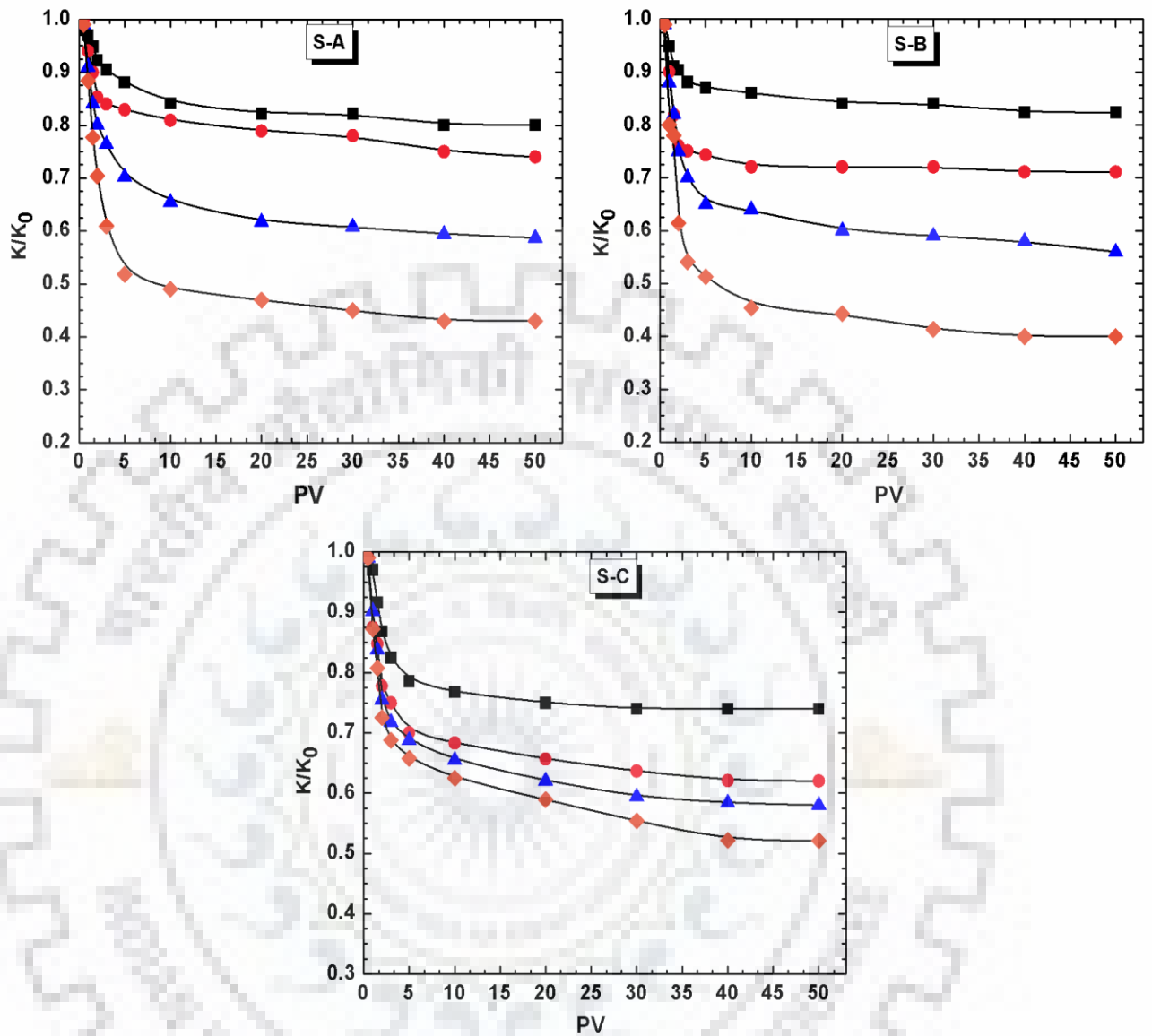


Fig. 5.16: Permeability reduction of different porous media versus number of pore volume of emulsion injected at different emulsion quality (Flow rate= 15 ml/min).

Emulsion Vol. fr. (v/v): 10% ■; 30% ●; 30% ▲; 50% ◆

Emulsion volume fraction and number of PV injected significantly alter the medium permeability. As the emulsion volume fraction increases pore plugging occurs more rapidly and consequently the change in permeability ratio decreases more rapidly which can be seen from Fig. 5.17. It can also be seen that the variation of permeability decline for emulsion fractions at different number of pore volumes injected in porous media. It was observed that, the permeability ratio decreases with an increase in the number of pore volumes injected.

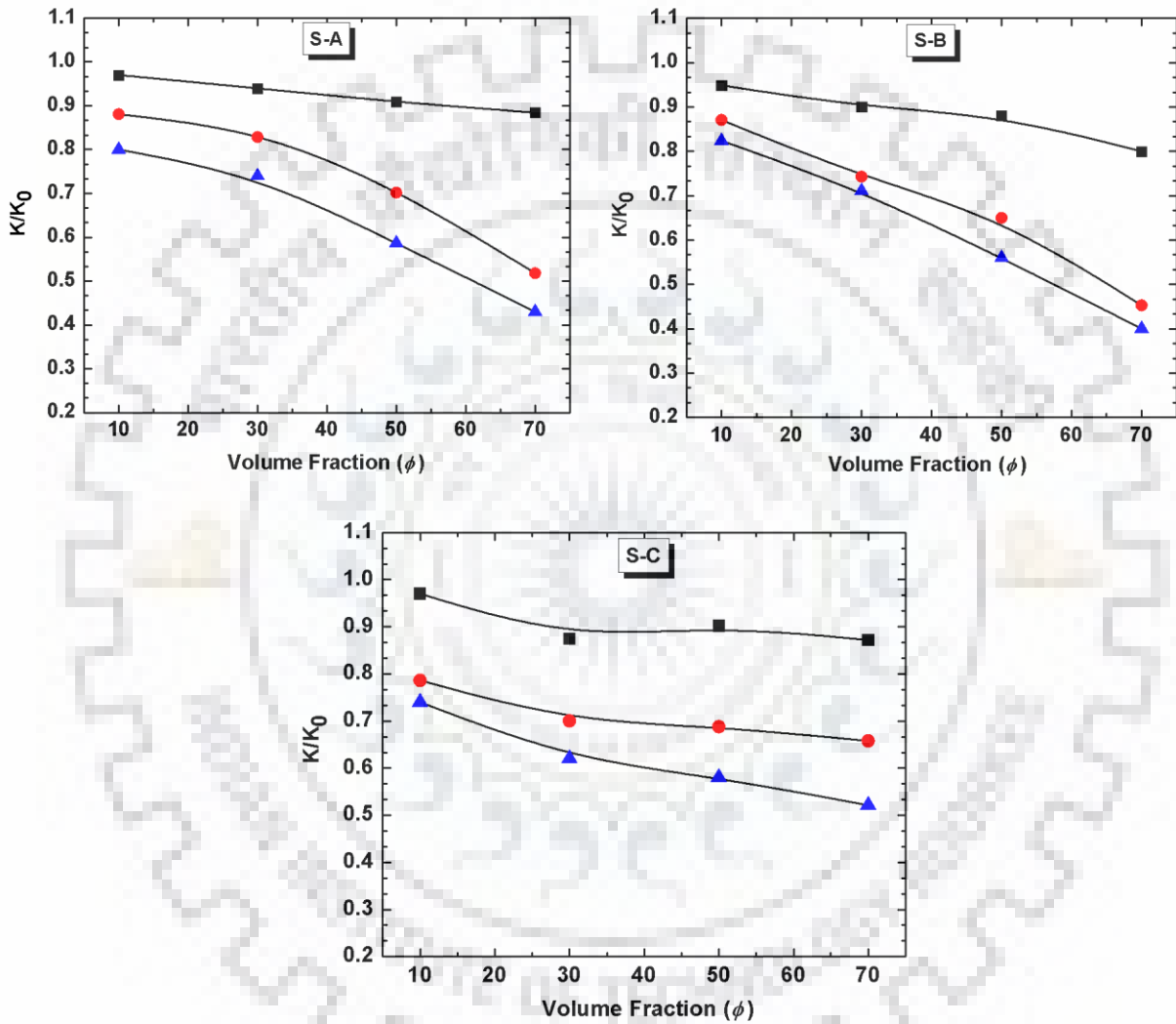


Fig. 5.17: Variation of emulsion volume fraction on permeability reduction of porous media as a function of different pore volume of emulsion injected.

No. of PV injected: PV-1 ■; PV-5 ●; PV-50 ▲

CHAPTER 6

MODELING OF FLUID FLOW THROUGH ISOTROPIC POROUS MEDIA

6.1 GENERAL

The flow through porous media is encountered in many areas of engineering such as chemical, mechanical, geophysical, environmental, hydraulics, etc. In all cases, the understanding of flow interaction with the intrinsic structures of the porous medium and the momentum transfer across the porous matrix are very important. In most of the engineering applications, a wide range of porosity and flow rates (or Reynolds numbers) are encountered in the porous materials, e.g. Darcy/Stokes type flows are observed in ground water flows while turbulent flows are found in applications such as heat exchangers, nuclear reactors, catalytic convertors, petroleum reservoirs, etc. (Kaviany, 1991; Kinjal et al., 2013). In case of ground water flows and oil reservoirs, generally fluid flows through a tortuous interconnected pores with very little geometric information, and hence pose challenges in pore scale modeling with full geometric information. The geometric complexity of such complex structural configurations causes problems in simulating the detailed flow field inside each individual porous structure. The common practice is, therefore, to smooth-out the local complexity of the actual phenomena by concentrating on the mass and momentum conservation principles while treating the porous medium as a continuum. This approach allows one to define fluid quantities at every point, irrespective of whether it corresponds to the fluid or the solid phase.

In this chapter, the flow and turbulent characteristics of flow through a structured porous media has been studied assuming a porous media as a *representative elementary volume (REV)*. It is assumed that the result is independent of the size of the representative elementary volume. The length scale of the *REV* is much larger than the pore scale, but considerably smaller than the length scale of the macroscopic flow domain. The fluid flow and turbulence characteristics have been predicted in a *REV* assuming it as an array of square or circular cylinders. Both porous media porosity and Reynolds number, based on particle, were varied over a wide range. For porous media comprising of square cylinders the flow and turbulence characteristics were modeled using low *Re* $k-\varepsilon$ turbulence, standard $k-\varepsilon$ turbulence and pseudo-direct numerical simulations, while in case of porous media comprising of circular

cylinders flow and turbulence behavior was modeled using laminar, standard $k-\varepsilon$ turbulence and large eddy simulation (LES) approaches.

6.2 GOVERNING EQUATIONS FOR POROUS MEDIA FLOW MODELING

Fluid flows are described by homogeneous volume-average mass and momentum balance equations within representative elementary volumes (*REV*) in case of turbulent flow. The steady state flows are often encountered in porous media flow as the forces that drive the flow change very slow with time. The flow is assumed to be steady state, incompressible and isothermal with no chemical reaction are described in following sections.

6.2.1. Laminar Flow Model

For laminar stokes flow simulations, the continuity and N-S equations are numerically solved in the *REV* for different porosities:

Mass conservation (continuity) equation:

$$\frac{\partial u_i}{\partial x_i} = 0 \quad (6.1)$$

Momentum conservation equation:

$$\frac{\partial}{\partial x_j} (\rho u_i u_j) = -\frac{\partial p}{\partial x_i} + \frac{\partial}{\partial x_j} \left[\mu \left(\frac{\partial u_i}{\partial x_j} + \frac{\partial u_j}{\partial x_i} - \frac{2}{3} \delta_{ij} \frac{\partial u_l}{\partial x_l} \right) \right] \quad (6.2)$$

6.2.2. Turbulence models

6.2.2.1. Reynolds averaged Navier–Stokes (RANS) turbulence models

The continuity and Reynolds-averaged N-S (RANS) equations for the turbulent flow of an incompressible viscous fluid are given as follows:

Continuity equation:

$$\frac{\partial \rho}{\partial t} + \frac{\partial}{\partial x_i} (\rho \bar{u}_i) = 0 \quad (6.3)$$

RANS equation:

$$\frac{\partial}{\partial t} (\rho \bar{u}_i) + \frac{\partial}{\partial x_j} (\rho \bar{u}_i \bar{u}_j) = -\frac{\partial \bar{p}}{\partial x_i} + \frac{\partial}{\partial x_j} \left[\mu \left(\frac{\partial \bar{u}_i}{\partial x_j} + \frac{\partial \bar{u}_j}{\partial x_i} - \frac{2}{3} \delta_{ij} \frac{\partial \bar{u}_l}{\partial x_l} \right) + \frac{\partial}{\partial x_j} (-\rho \bar{u}'_i \bar{u}'_j) \right] \quad (6.4)$$

6.2.2.2. The standard $k-\varepsilon$ turbulence model

k equation:

$$\frac{\partial}{\partial t} (\rho k) + \frac{\partial}{\partial x_i} (\rho k \bar{u}_i) = \frac{\partial}{\partial x_j} \left[\left(\mu + \frac{\mu_t}{\sigma_k} \right) \frac{\partial k}{\partial x_j} \right] + G_k - \rho \varepsilon \quad (6.5)$$

ε equation:

$$\frac{\partial}{\partial t}(\rho\varepsilon) + \frac{\partial}{\partial x_i}(\rho\bar{u}_i\varepsilon) = \frac{\partial}{\partial x_j} \left[\left(\mu + \frac{\mu_t}{\sigma_\varepsilon} \right) \frac{\partial \varepsilon}{\partial x_j} \right] + C_{1\varepsilon} \frac{\varepsilon}{k} G_k - C_{2\varepsilon} \rho \frac{\varepsilon^2}{k} \quad (6.6)$$

In equations (3) and (4), G_k represents the generation of turbulence kinetic energy due to the mean velocity gradients, and is defined as follows:

$$G_k = \mu_t S^2 \quad (6.7)$$

where S is the modulus of the mean rate-of-strain tensor and is defined as

$$S \equiv \sqrt{2\bar{S}_{ij}\bar{S}_{ij}} \quad (6.8)$$

$$\bar{S}_{ij} = \frac{1}{2} \left(\frac{\partial \bar{u}_i}{\partial x_j} + \frac{\partial \bar{u}_j}{\partial x_i} \right) \quad (6.9)$$

$C_{1\varepsilon}$, $C_{2\varepsilon}$, $C_{3\varepsilon}$ are constants, and σ_k and σ_ε are turbulent Prandtl numbers for k and ε respectively. The turbulent (or eddy) viscosity, μ_t is computed by combining k and ε as follows:

$$\mu_t = \rho C_\mu \frac{k^2}{\varepsilon} \quad (6.10)$$

6.2.2.3. The Low Re - k - ε turbulence model

Near-wall treatment is very important in wall-bounded flows. The standard k - ε model is modified to extend its applicability to the low-Reynolds number flows. This allows calculations right up to the wall. In the present study, low Re k - ε model with Yang-Shih algorithm was used which incorporates the modified damping function. The modification improves the model prediction capability of the low Re k - ε model for near-wall flow and effectively captures the non-linear wall effects.

$$k \text{ equation: } \frac{\partial}{\partial x_i}(\rho\bar{u}_i k) = \frac{\partial}{\partial x_j} \left[\left(\mu + \frac{\mu_t}{\sigma_k} \right) \frac{\partial k}{\partial x_j} \right] + P_k - \rho\varepsilon \quad (6.11)$$

$$\varepsilon \text{ equation: } \frac{\partial}{\partial x_i}(\rho\bar{u}_i \varepsilon) = \frac{\partial}{\partial x_j} \left[\left(\mu + \frac{\mu_t}{\sigma_\varepsilon} \right) \frac{\partial \varepsilon}{\partial x_j} \right] + (C_{1\varepsilon} f_1 P_k - C_{2\varepsilon} f_2 \rho\varepsilon) \frac{\varepsilon}{k} \quad (6.12)$$

$$\text{where, } P_k = -\rho\bar{u}_i \bar{u}'_j \frac{\partial \bar{u}_j}{\partial x_i}$$

By adopting the Boussinesq approximations for the eddy viscosity, the Reynolds stresses are expressed as:

$$-\rho\bar{u}_i \bar{u}'_j = \mu_t \left[\frac{\partial \bar{u}_j}{\partial x_i} + \left(\frac{\partial \bar{u}_j}{\partial x_i} \right)^T \right] - \frac{2}{3} \rho \delta_{ij} k \quad (6.13)$$

where the turbulent viscosity is defined as

$$\mu_t = \rho C_\mu f_\mu \frac{k^2}{\varepsilon} \quad (6.14)$$

where f_1 , f_2 and f_μ are the low Re k - ε (Yang-Shih) damping functions. The damping functions account for the low Reynolds number and the enhanced wall effects and are given as follows (Yang and Shih, 1993):

$$f_1 = f_2 = \frac{1}{1 + \frac{c_k}{\sqrt{R_T}}} \quad (6.15)$$

$$f_\mu = \left[1 - \exp\left(-1.5 \times 10^{-4} R_y - 5.0 \times 10^{-7} R_y^3 - 1.0 \times 10^{-10} R_y^5\right) \right]^{1/2} \quad (6.16)$$

The values of the model constants used for the numerical simulation are taken as follows:

$$C_{1\varepsilon} = 1.44, C_{2\varepsilon} = 1.92, C_\mu = 0.09, C_k = 1, \sigma_k = 1.0, \sigma_\varepsilon = 1.3$$

6.2.3. Large Eddy Simulation (LES) Modeling Approach

LES is based upon the application of a spatial filtering operation (denoted by a bar) to three dimensional (3D) unsteady N-S equations (Adam et al., 2011). The governing equations employed for LES are obtained by filtering the time-dependent N-S equations in either Fourier (wave-number) space or configuration (physical) space (Tajallipour et al., 2009, 2013; Xu et al., 2010). The filtering process effectively filters out eddies whose scales are smaller than the filter width or grid spacing used in the computations. The resulting equations thus govern the dynamics of large eddies.

A filtered variable by the finite-volume discretization method is defined as:

$$\bar{\Phi}(x) = \frac{1}{V} \int_V \Phi(x') \Pi(x, x') dx', \quad x' \in v \quad (6.17)$$

where V is the volume of a computational cell. The filter function, $\Pi(x, x')$ is given as

$$\Pi(x, x') = \begin{cases} 1/V, & x' \in v \\ 0, & x' \text{ otherwise} \end{cases} \quad (6.18)$$

Therefore, the filtered N-S equation is:

$$\frac{\partial}{\partial t} (\rho \bar{u}_i) + \frac{\partial}{\partial x_j} (\rho \bar{u}_i \bar{u}_j) = \frac{\partial}{\partial x_j} \left(\mu \frac{\partial \sigma_{ij}}{\partial x_j} \right) - \frac{\partial \bar{p}}{\partial x_i} - \frac{\partial \tau_{ij}}{\partial x_j} \quad (6.19)$$

where σ_{ij} is the stress tensor, defined as

$$\sigma_{ij} = \left[\mu \left(\frac{\partial \bar{u}_i}{\partial x_j} + \frac{\partial \bar{u}_j}{\partial x_i} \right) \right] - \frac{2}{3} \mu \frac{\partial \bar{u}_l}{\partial x_l} \delta_{ij} \quad (6.20)$$

and τ_{ij} is the sub-grid-scale stress and is defined as

$$\tau_{ij} \equiv \overbrace{\rho u_i u_j} - \rho \bar{u}_i \bar{u}_j \quad (6.21)$$

Based on the Boussinesq's hypothesis and the Smagorinsky model (Smagorinsky, 1963), the sub-grid-scale turbulent stresses are expressed as

$$\tau_{ij} - \frac{1}{3} \tau_{kk} \delta_{ij} = -2\mu_t \bar{S}_{ij} \quad (6.22)$$

where, μ_t is the subgrid-scale eddy viscosity. \bar{S}_{ij} is the filtered strain rate tensor for the resolved scale defined by

$$\bar{S}_{ij} \equiv \frac{1}{2} \left(\frac{\partial \bar{u}_i}{\partial x_j} + \frac{\partial \bar{u}_j}{\partial x_i} \right) \quad (6.23)$$

The subgrid-scale eddy viscosity, μ_t can be estimated by the Smagorinsky model as follows:

$$\mu_t = \rho (C_s \Delta)^2 (2\bar{S}_{ij} \bar{S}_{ij})^{0.5} \quad (6.24)$$

where, C_s is the Smagorinsky coefficient, and Δ is the characteristic sub-grid length scale given by (Tutar and Oguz, 2002):

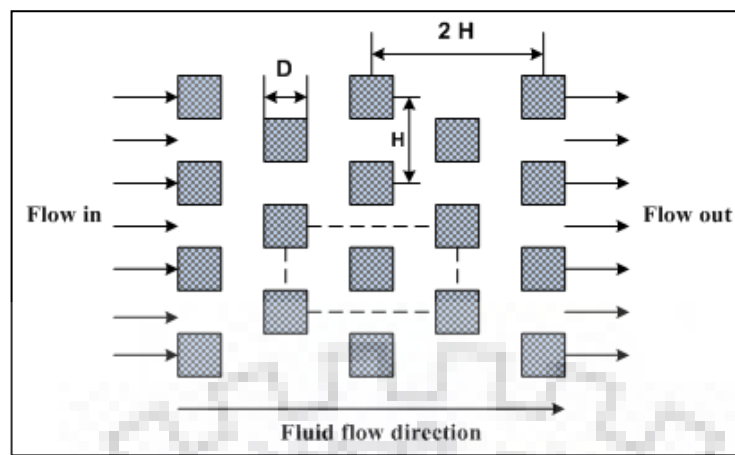
$$\Delta = (\Delta_x \Delta_y \Delta_z)^{1/3} \quad (6.25)$$

The Smagorinsky constant ensures the accounting of the near-wall behaviour of the turbulent viscosity, which does not include wall damping functions.

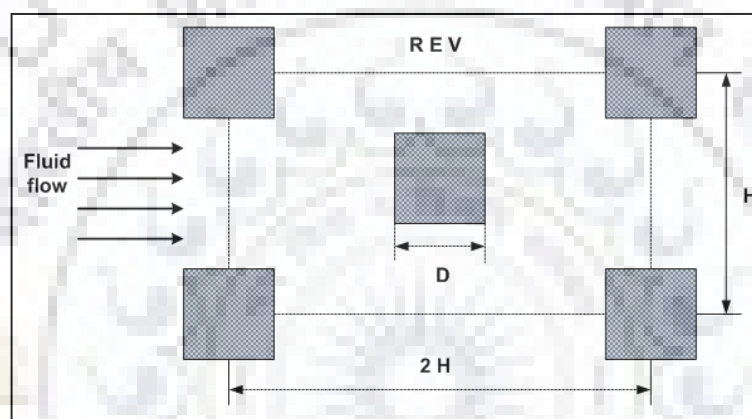
6.3 SIMULATION FRAMEWORK AND GRID TOPOLOGY

6.3.1 Computational Domain

In the present study, the porous media is considered to be formed by an infinite periodic array of square or circular cylinders (D_p) arranged in a regular pattern (center to center distance between the particles being H). The physical model for the porous medium is shown in Figs. 6.1 and 6.2. Fig. 6.1(b) shows the schematic representation of a 2D square representative elementary volume (REV) consisting of a fixed solid phase saturated with a continuous fluid phase. Therefore the solid phase does not change randomly if different ensembles are considered. The volume of the REV is constant (no space dependence) and is equal to the sum of the fluid and the solid volumes inside. Only one structural unit is chosen for the calculation domain, and along its boundaries, the periodicity of the flow is assumed. Therefore, the flow is solved only through the domain as shown in Fig. 6.1(b).



(a)



(b)

Fig. 6.1: Conceptual porous media flow domain for numerical computations (a) periodic array of square cylinder, and (b) representative elementary volume (REV) for array of square cylinders.

Computations were carried out by using the transport equations based on the absolute value of the Darcian velocity and the longitudinal center-to-center distance $2H$ as reference scales. For carrying out a series of numerical calculations, it may be convenient to use the Reynolds number based on pore diameter (D). The Reynolds number $Re_H = u_D H / \nu$ based on the center-to-center distance H (H is set equal to unity), is converted to a Reynolds number based on D i.e., $Re_D = Re_H \times D / H$. Re_D is varied between 100 and 40000. The value of D was varied between 0.4 and 0.84 (i.e., $D = 0.4, 0.6, 0.71$. and 0.84). In case of porous media comprising array of square cylinders, the porosity of the domain, $\phi = [1 - (D/H)^2]$, was varied between 0.84 and 0.3 (i.e. 0.3, 0.5, 0.64 and 0.84).

The physical model of the porous medium comprising 3D periodic array of circular cylinders is shown in Fig. 6.2(a). The fully developed macroscopic turbulent flow

(incompressible Newtonian fluid) was assumed to be uniform and parallel to the x -direction. Due to symmetry (in y and z directions) and periodicity (in x direction) of the model, only one structural array cell (representative elementary volume, REV) with dimensions of $2H \times 1H \times 0.5H$ was chosen as the computational domain (Fig. 6.2 (b)). Fluid is flowing along the x -axis and perpendicular to the y -axis of the flow domain (REV_{1234}) (Fig. 6.2b). A symmetry boundary condition was considered along the z -axis of the REV_{1234} . In order to reduce the computational effort and, thereby, the cost, the width of the REV_{1234} was taken as $0.5H$ instead of H . The microscopic turbulent flow inside the REV was considered to be fully developed. Therefore, the flow problem was solved only through the domain as shown in Fig. 6.2(b). The Reynolds number based on the tube diameter (D), i.e., $Re_D = (u_D \times D)/\nu$ was varied from 100 to 40000. In case of porous media comprising array of circular cylinders the

porosity of the domain, $\phi = \left[1 - \frac{\pi}{4} \left(\frac{D}{H} \right)^2 \right]$, was varied between 0.3 and 0.8 (i.e., $D = 0.94, 0.87, 0.80, 0.71$ and 0.51).

Laminar and RANS simulations were carried out with two-dimensional while LES simulations were carried out with three-dimensional domains. All simulations have been carried out using same methodology using Re_D .

6.3.2 Grid Topology

The 2D computational domain for array of square cylinders was constructed of non-uniformly spaced staggered mesh system consisting of 88418 hybrid quadrilateral cells while array of circular cylinder was having 1,60786 (i.e. 16,588 nodes) hybrid quadrilateral cells (Figs. 6.3 and 6.4). A very fine mesh was considered near the walls. For LES modeling and simulation, the computational domain was constructed of non-uniformly spaced staggered mesh system consisting of 1083700 nodes and 1035950 hexahedral cells. The 3D grid topology is shown in Fig. 6.2(b). Very fine mesh resolution is used in the vicinity of the curved wall. Boundary layers were imposed near the wall surface, with the aim of enhancing resolution on the complex geometrical boundary so as to achieve a better solution in the near-wall region.

Computations were carried out using structured grid systems, which ensured that the grid spacing close to the wall is small enough to satisfy the Kolmogorov length scale (Eq. 6.26). Quality of the grid size for the computational cell was examined by comparing with the Kolmogorov scale, i.e.

$$\frac{\Delta V^{1/3}}{\kappa} < 10$$

$$\kappa = \left(\frac{\nu^3}{\varepsilon} \right)^{1/4} \quad (6.26)$$

The cell volume to Kolmogorov scale ratio was always kept below 10 for all simulations. This is valid for all cells in the computational domain.

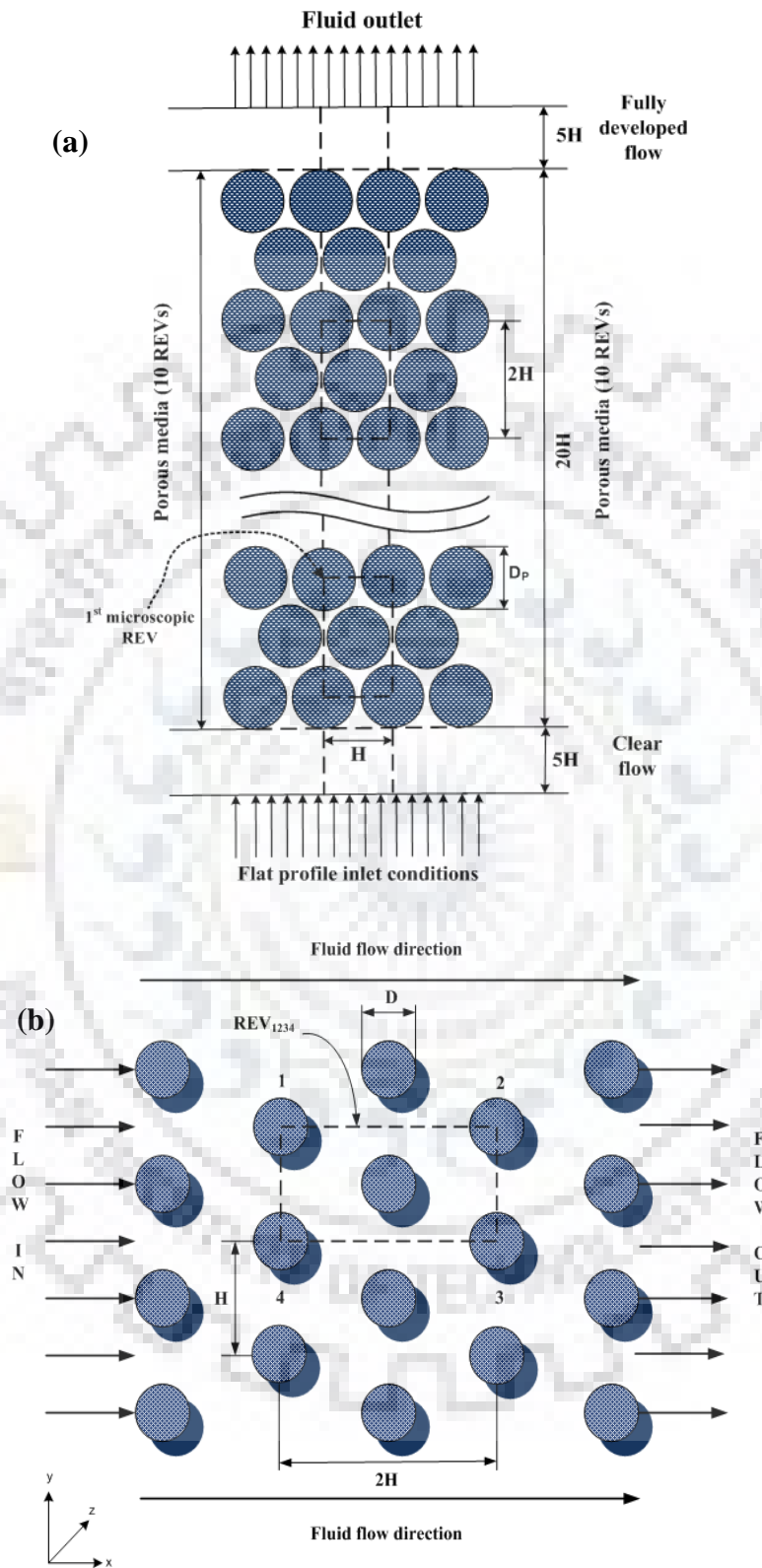


Fig. 6.2: Conceptual porous media flow domain for numerical computations (a) periodic array of circular cylinder, and (b) representative elementary volume (REV) for array of circular cylinders.

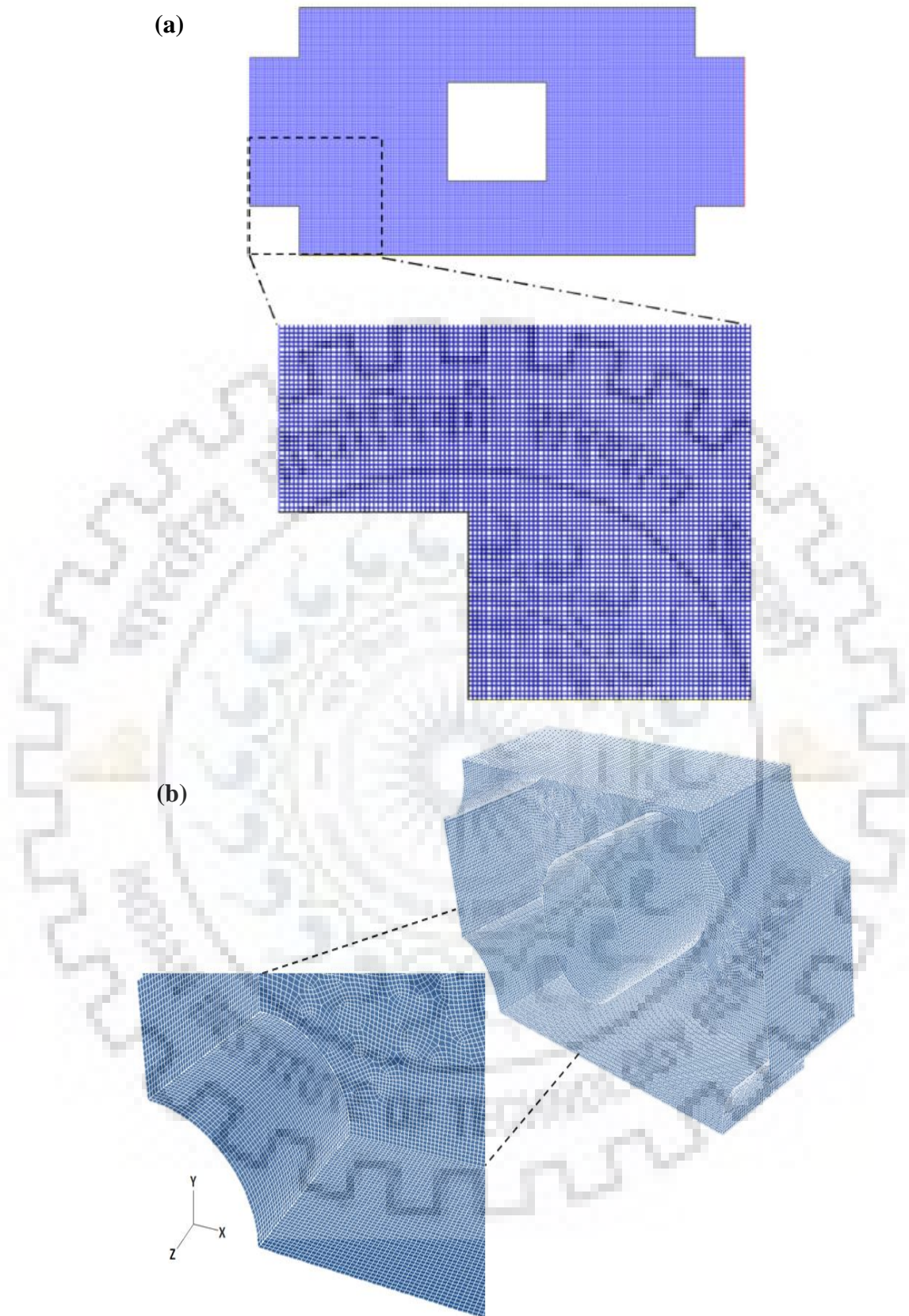


Fig. 6.3 (a) Grid topology of REV of array of (a) square cylinders, and (b) 3D porous representative elementary volume (REV) of circular cylinders.

6.4. NUMERICAL APPROACH AND BOUNDARY CONDITIONS

6.4.1 Numerical Approach

The control volume finite difference method (CVFDM) was used for all simulation runs. The flow characteristics were obtained by solving the governing flow equations using ANSYS® 14. Four different approaches were used to compute the porous flow field: laminar fluid flow, steady RANS formulation with two distinct turbulence models (i.e. standard $k-\varepsilon$ and low Re $k-\varepsilon$ models) and the unsteady LES approach. The flow governing equations on the computational domain were discretized using second-order finite-volume schemes. For the time integration, a central second-order implicit differencing scheme was employed. The pressure and velocity field coupling was done by the SIMPLE algorithm. The RANS flow calculations were performed with $k-\varepsilon$ turbulence model using enhanced wall functions and with low Re- $k-\varepsilon$ formulation. Unsteady LES calculations were performed using the Smagorinsky–Lilly SGS model (Smagorinsky, 1963; Lilly, 1966).

All simulations were performed with a pressure-based solver and a specified mass flow rate. The time step for the LES approach was estimated by Courant–Friedrichs–Lewy (CFL) condition (Pope, 2005). The time step was set small enough to satisfy the CFL condition as follows:

$$CFL = \frac{|\bar{u}|\Delta t}{\Delta V^{1/3}} \leq 1 \quad (6.27)$$

where $V^{1/3}$ is the characteristic length of the mesh volume. The time-step used for all the simulation runs was ($\Delta t =$) 10^{-4} s. Simulations were initialized with an isotropic turbulent flow field to set the fully developed flow within the computational domain. After attaining the fully developed flow, the turbulent statistics were collected over a period of time until the solutions became stable. The convergence criterion was set to 10^{-4} for all simulations. The relaxation parameters for all variables (\bar{u} , p , k , ε) were kept equal to 0.8.

6.4.2 Boundary Conditions For The Computational Domain

6.4.2.1 Array of square cylinders

In case of structured porous media comprised of array of square cylinders, with an assumption of macroscopic fully developed uni-dimensional flow, the following boundary conditions for the periodic cells were adopted:

At the solid walls no slip boundary condition was applied:

$$\bar{u} = 0, \quad k = 0, \quad \text{and} \quad \varepsilon = \nu \frac{\partial^2 k}{\partial n^2} \quad (6.28)$$

Periodic boundary conditions were considered at $x = 0$ and $x = 2H$:

$$\left. \begin{aligned} \bar{u}|_{x=0} &= \bar{u}|_{x=2H}, \bar{v}|_{x=0} = \bar{v}|_{x=2H} \\ \bar{k}|_{x=0} &= \bar{k}|_{x=2H}, \bar{\varepsilon}|_{x=0} = \bar{\varepsilon}|_{x=2H} \end{aligned} \right\} \quad (6.29)$$

Symmetry boundary conditions were considered at $y = 0$ and $y = H$:

$$\frac{\partial \bar{u}}{\partial y} = \frac{\partial \bar{v}}{\partial y} = \frac{\partial \bar{k}}{\partial y} = \frac{\partial \bar{\varepsilon}}{\partial y} = 0 \quad (6.30)$$

6.4.2.2 Array of circular cylinders

The periodic boundary conditions were applied over REV_{1234} for relevant variables. These conditions were adopted to achieve the fully developed flow regime without the involvement of the entrance region. The periodic boundary conditions for the REV_{1234} are as follows:

$$\left. \begin{aligned} \bar{u}(y)|_{x=0} &= \bar{u}(y)|_{x=2H} & \bar{v}(y)|_{x=0} &= \bar{v}(y)|_{x=2H} \\ \bar{u}(x)|_{y=0} &= \bar{u}(x)|_{y=H} & \bar{v}(x)|_{y=0} &= \bar{v}(x)|_{y=H} \end{aligned} \right\} \quad (6.31)$$

$$\left. \begin{aligned} \bar{k}(y)|_{x=0} &= \bar{k}(y)|_{x=2H} & \bar{\varepsilon}(y)|_{x=0} &= \bar{\varepsilon}(y)|_{x=2H} \\ \bar{k}(x)|_{y=0} &= \bar{k}(x)|_{y=H} & \bar{\varepsilon}(x)|_{y=0} &= \bar{\varepsilon}(x)|_{y=H} \end{aligned} \right\} \quad (6.32)$$

$$\left. \begin{aligned} \bar{p}(y)|_{x=0} &= \bar{p}(y)|_{x=2H} - \Delta P \\ \bar{p}(x)|_{y=0} &= \bar{p}(x)|_{y=H} \end{aligned} \right\} \quad (6.33)$$

Thus the components of the velocity vectors and the turbulence quantity were set to be periodic as shown in Eqs. 6.31-6.32. In that case, the pressure function, $P(x, y)$, behaves in a periodic manner, as shown in Eq. 6.33. The resulting pressure field is the sum of a flow-direction-dependent function (the macroscopic pressure drop) and a periodic function $[P(x + 2H, y) = P(x, y)]$. $\Delta P/L$ is the driving force or pressure gradient that is responsible for the motion of the fluid resulting in a corresponding Re_D .

In the present study, a given fixed mass flow rate (or fixed Re) is considered, and hence the pressure-drop through the REV has been calculated as part of the solution. This matter is resolved by considering a fixed pressure-drop (ΔP) in the x-direction as indicated in Eq. (6.33). A constraint of constant mass flow rate provides an additional equation needed to calculate the pressure-drop (ΔP). The quantity ΔP must take a value such that the non-

dimensional streamwise velocity averaged over the fluid inlet section is equal to unity (a normalized value), which can be expressed as:

$$\int_{inlet} \frac{\partial}{\partial y} (\bar{u}_x) = 1 \quad (6.34)$$

The equation (6.34) was solved for ΔP together with the x-momentum equation ensuring that the mass flow rate was fixed at each time step. The implementation of the periodic boundary conditions on the top and bottom faces of the REV_{1234} is relatively simple since no net pressure gradient exists in the vertical direction.

The symmetry boundary conditions were applied at the front and back surfaces of the REV_{1234} along the z-axis which are the mirror images of each other and the predicted flow fields have mirror symmetry. Since the LES required relatively high CPU time as compared to RANS calculations in 3D porous computational domain, the symmetric boundary conditions reduce the computational effort and time. Symmetry boundary conditions were considered at $z = 0$ and $z = H/2$:

$$\frac{\partial \bar{u}}{\partial z} = \frac{\partial \bar{v}}{\partial z} = \frac{\partial k}{\partial y} = \frac{\partial \varepsilon}{\partial y} = 0, \quad \bar{w} = 0 \quad (6.35)$$

Stationary wall (no-slip) boundary conditions were used for the arc-shaped corner boundary and the center cylinder (particle) walls:

$$\bar{u} = \bar{v} = \bar{w} = 0, \quad k = 0, \quad \text{and} \quad \varepsilon = \nu \frac{\partial^2 k}{\partial n^2} \quad (6.36)$$

All fluid properties, including density and viscosity, are assumed constant for all simulations.

6.5 MICROSCOPIC LAMINAR PORE SCALE FLOW SIMULATION

The simulation results were compared with the experimental pressure drop data as also with the three different correlations, namely Kozney-Carman, Ergun and Zhavoronkov et al. (1949). The pressure drop simulation results were represented in the form of dimensionless pressure gradient (DPG) given as follows:

$$\Psi = \frac{180}{\text{Re}_p} \frac{(1-\phi)^2}{\phi^3} \quad (6.37)$$

$$\Psi = \frac{150}{\text{Re}_p} \frac{(1-\phi)^2}{\phi^3} + 1.75 \frac{(1-\phi)}{\phi^3} \quad (6.38)$$

$$\Psi = \frac{165.35 A_w^2}{\text{Re}_p} \frac{(1-\phi)^2}{\phi^3} + 1.2 B_w \frac{(1-\phi)}{\phi^3} \quad (6.39)$$

$$\Psi = -\frac{d\langle P \rangle}{dL} \frac{D_p}{\rho \bar{u}_s} \quad (6.40)$$

It can be seen from Fig. 6.4 that the simulation results agree well with the results obtained from the correlations, but were somehow underestimated. Numerically predicted DPG for flow in the modeled porous media agreed very well with Kozney-Carman, Ergun and Zhavoronkov as well as with the experimental results for lower porosity ($\phi = 0.3478$). Deviations were observed with an increase in the porosity. The experimental results lie above the simulation results due to the fact that the viscous effect was more prominent in the real randomly arranged particles than the simulation model of simulated packing with specially ordered particle arrangement. In real porous media the particles are actually touching each other and the fluid propagation pathways becomes much more tortuous in nature. Therefore, the viscous dissipation plays more direct role in the real porous media (Coulaud et al., 1988).

To further understand the nonlinear effect, numerical simulations were also performed to visualize micro-flow phenomena confined in the pore space. At low Reynolds number, inertia forces are negligible as compared to the viscous forces, and the streamlines follow the solid particle in the porous matrix. The streamline for the porosity of 0.3478 ($D_p = 5\text{mm}$) is shown in Fig. 6.5. The flow around the particles is perfectly symmetrical and this flow corresponds to Darcy's regime.

As discussed in the previous section, for $Re_p < 5$, the fluid flow behavior is characterized by pure Darcy flow, i.e. the momentum transport through porous media is governed by the viscous force only. With an increase in Re_p , the inertial forces are no longer negligible compared to viscous forces and the flow becomes asymmetric. Solid–fluid interaction comes into the play and the countercurrent flow occurred close to the solid. As a consequence smaller eddies formation should take place which will lead to the reduction of the flow section and a modification of velocity fields may be necessary. For $Re_p = 9.44$, a pair of smaller eddies are formed at the downstream of the particle surface and the streamlines are more concentrated at the pore-throat section. This flow corresponds to the transient flow regime with weak inertia which is characterized at $Re_p > 5$ in the earlier section. As the Re_p gradually increases ($Re_p > 10$), the size of the eddies in the upstream and downstream face of the particles also increases (in Fig. 6.5 $Re_p = 15$). Eddies become elongated, coalesce and occupy the whole porous region. Thus, the flow-section is considerably reduced and detached from the solid surface. For $Re_p = 30$, the streamlines are more homogeneous in the y -direction, and more complex around the particles; vortices appear behind the particles due to an increase of the inertial effect and traverse down through the porous matrix. This flow corresponds to the strong inertial regime (non-Darcy). From the analysis presented above, we

can see that the deviation from Darcy law is attributed to microscopic inertial effect, which is also responsible for different flow regimes encountered during flow through the porous media.

The contours of the velocity fields within the porous matrix are shown in Fig. 6.6. It can be seen that the average velocity magnitude (relative high shear flow zone) in the near particle surface and pore constriction (converging-diverging section) was higher than the center region of porous medium. Near the wall and at the contact points, fluid flow is less than other points in the particle. Fluid layers close to the wall tend to move faster resulting in a flattened velocity profile.

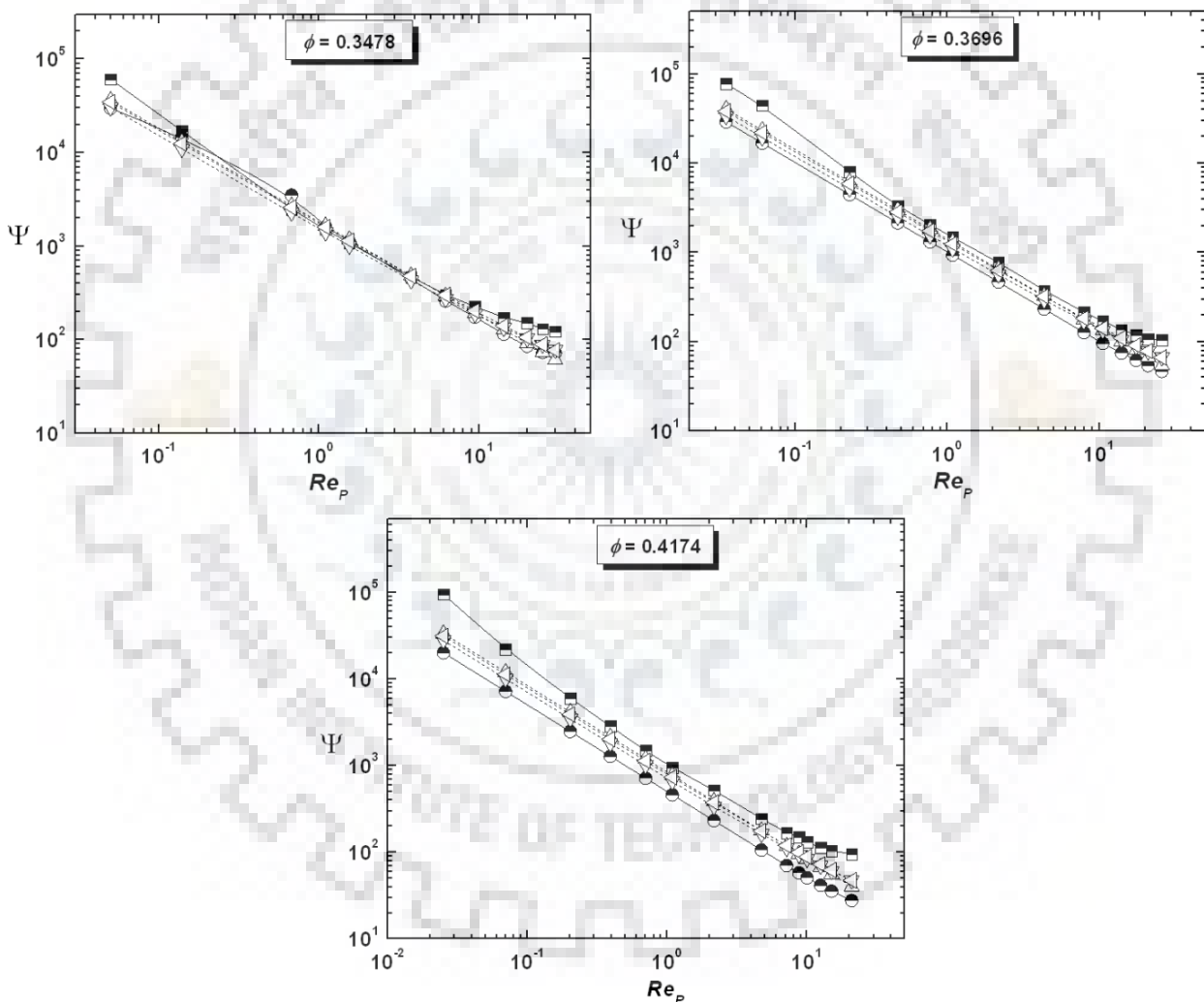


Fig. 6.4: Plot of dimensionless pressure gradient (DPG) versus Re_p for different isotropic porous media (Experimental (-■-); Simulation (-●-); Kozney-Carman (Δ); Ergun (∇); Zhavoronkov (\triangleleft)).

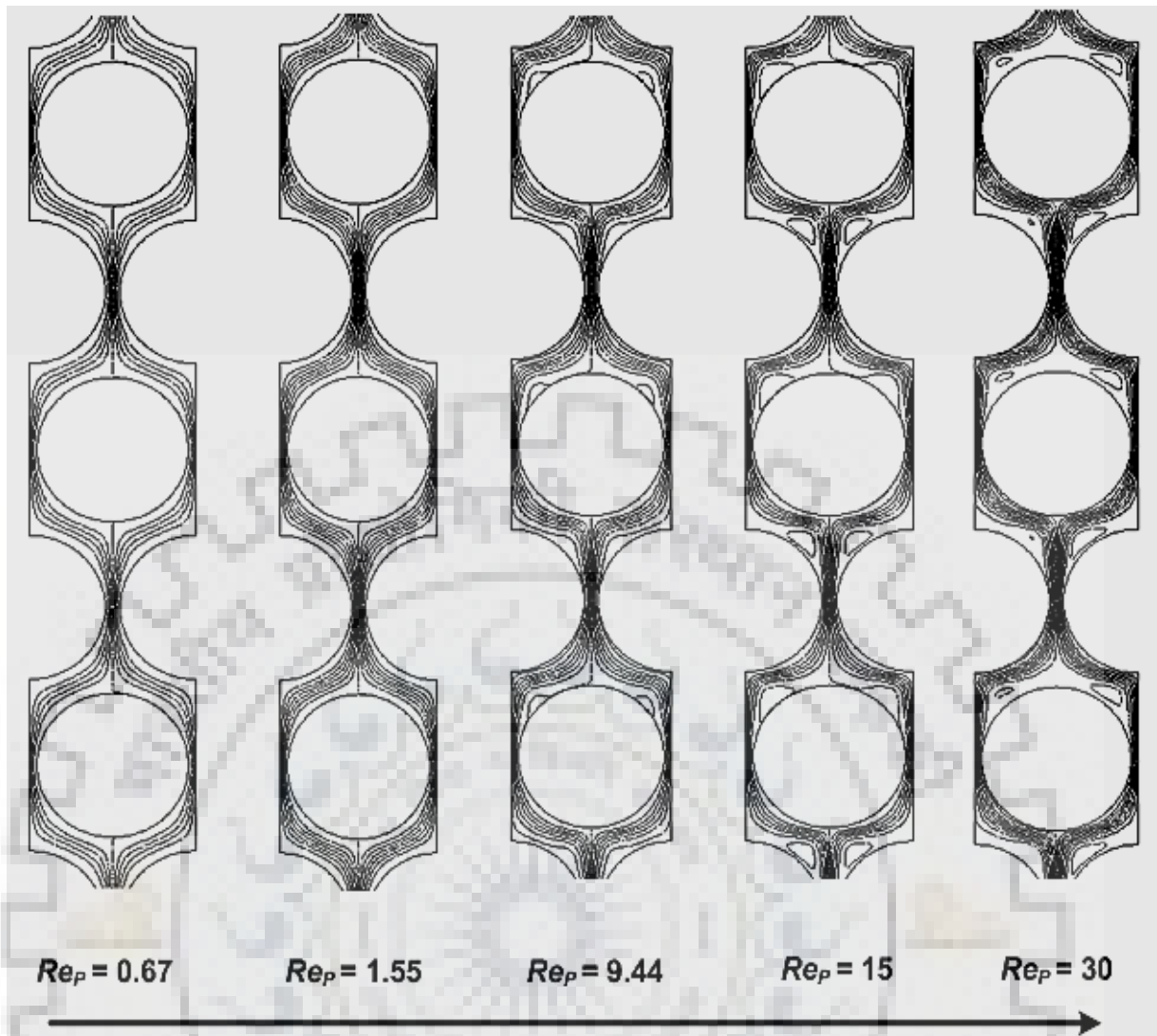


Fig. 6.5: Evolution of Streamlines for the case (three *REV*) of $\phi = 0.3478$ with different Re_p .

As Re_p increases the more homogeneous and concentrated velocity spectra developed in the porous matrix. The recirculation zone increases gradually at the front and back face of the particles with an increase in Re_p due to increasing inertial effects (Fig. 6.6). This signifies that the pore flow transition occurred gradually from the creeping Darcy flow regime to inertial non Darcy regime. The high-shear flows and recirculation zones are dissipative in nature and are responsible for the development of the non-Darcy flow (nonlinear inertial effects) (Cheng et al. 2008). The change in the flow structure and a transition from linear to non-linear regime occurs mainly because of the inertial effects which can be seen from the simulated micro-flow phenomena.

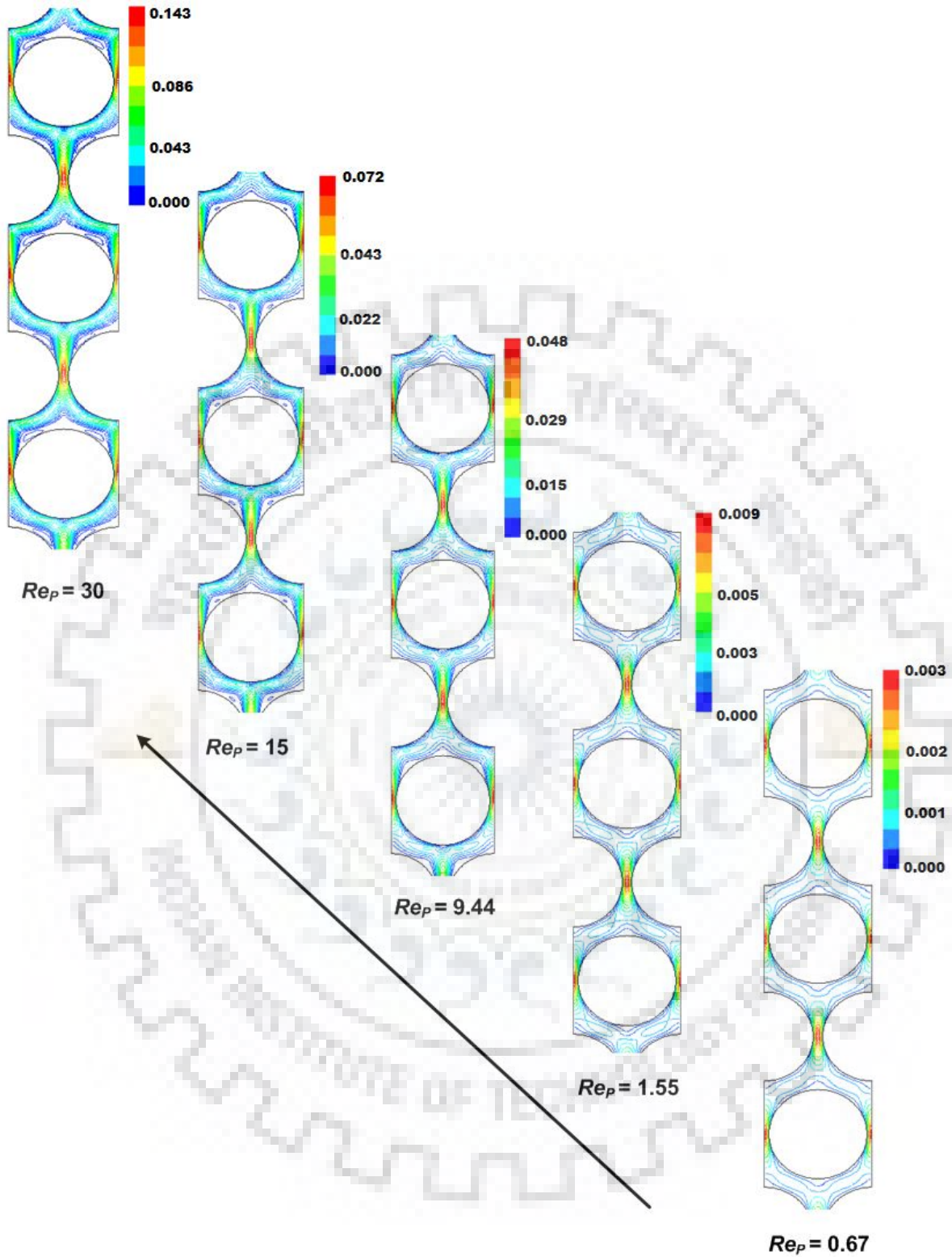


Fig. 6.6: Contours of velocity magnitude for the case (three *REV*) of $\phi = 0.3478$ with different Re_p .

6.6 TURBULENT FLOW MODELING IN POROUS MEDIA

6.6.1 Microscopic Streamlines and Velocity Field

The simulated results of streamlines for different porosity and Re_D values are shown in Fig. 6.7(a)-6.7(b). The steady periodic nature of flow is observed across the square cylinder. The flow accelerates in the upper and lower passages around the square cylinder and separates at the downstream section. As a consequence, wake appears in the downstream of the square cylinder. As expected, a larger wake region is formed at the front of the square cylinder. At low Re_D ($Re_D = 100$), the intensity of wake formation is low due to the smooth fluid flows over the square cylinder. The turbulence increases with increase in Re_D , in the downstream of the square cylinder, and the intensity of large wake region is generated in the form of eddies. Complete flow separation at the downstream section and two upstream corner sections were observed at higher Re_D ($Re_D = 40000$). Eventually larger eddy formation takes place in these sections. For porosity, $\phi = 0.84$ and 0.64 , a small recirculation zone is generated at the upper and lower face of the square cylinder which ultimately traverses down to the downstream with vortices separated from the square cylinder at higher Re_D ($Re_D > 10000$). From the computed streamline contours in the vicinity of the square cylinder, it was observed that the size of the vortex in the downstream of the cylinder gets compressed gradually with decrease in porosity, as the passage for fluid flow narrows down.

Fig. 6.8(a)-6.8(b) shows the computed velocity vector contours in the vicinity of the square cylinder with different Re_D and porosity values. For a particular porosity value, it was observed that the velocity magnitude was maximum at the centre of the upstream section and diverged to the upper and lower section of the square cylinder, as the fluid approached the surface of the cylinder. A stagnation point was formed at the centre of the upstream face of the cylinder. It was observed that the flow separation occurred mainly at the corner of the upstream face of the cylinder and at the downstream corner section of the wall where the velocity magnitude was very high. Due to flow separation, wake region was created with eddies in front of the square cylinder. This phenomenon gets more and more pronounced at high Re_D ($Re_D > 10000$).

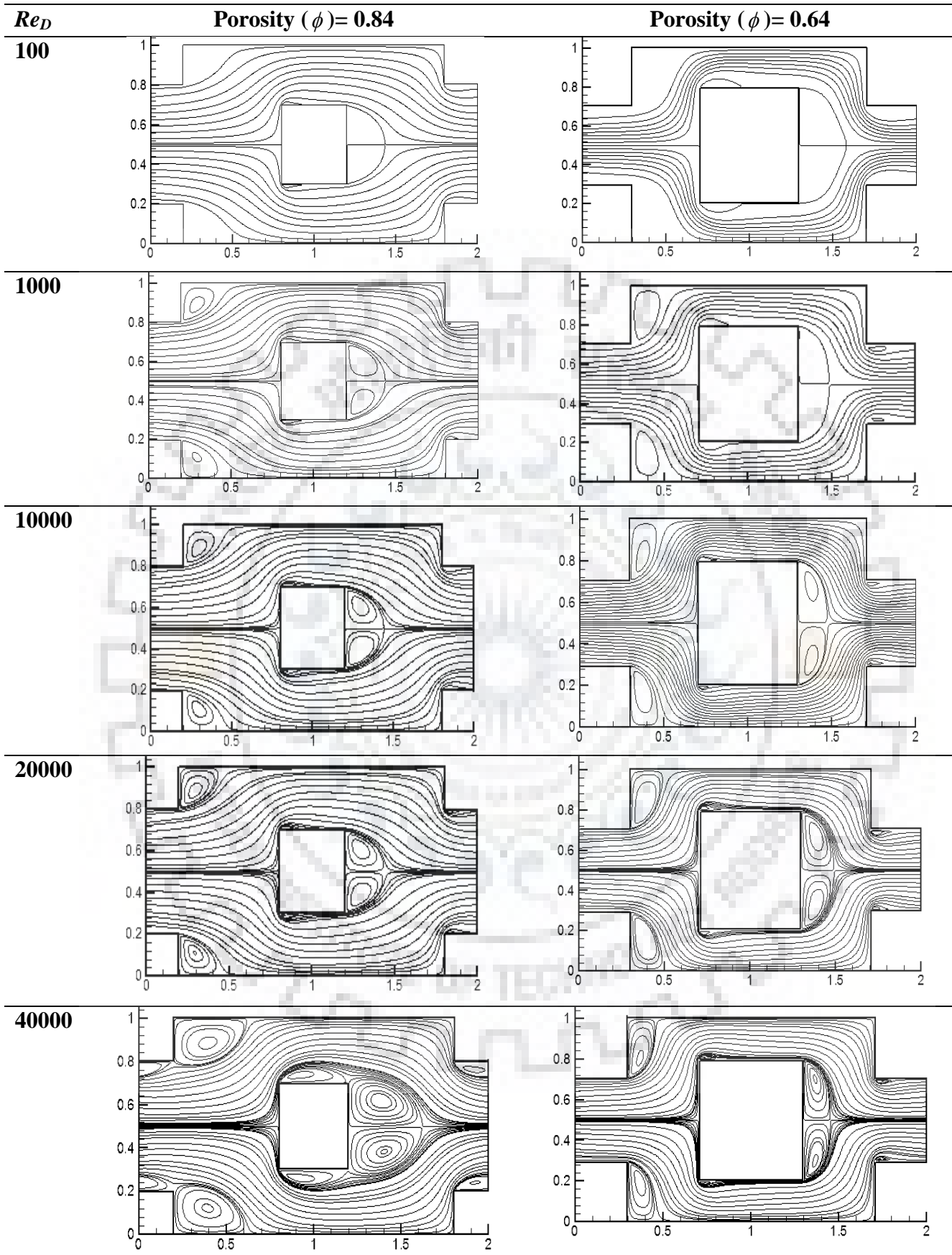


Fig. 6.7(a): Streamline contours in porous media at porosity (ϕ) = 0.84 and 0.64.

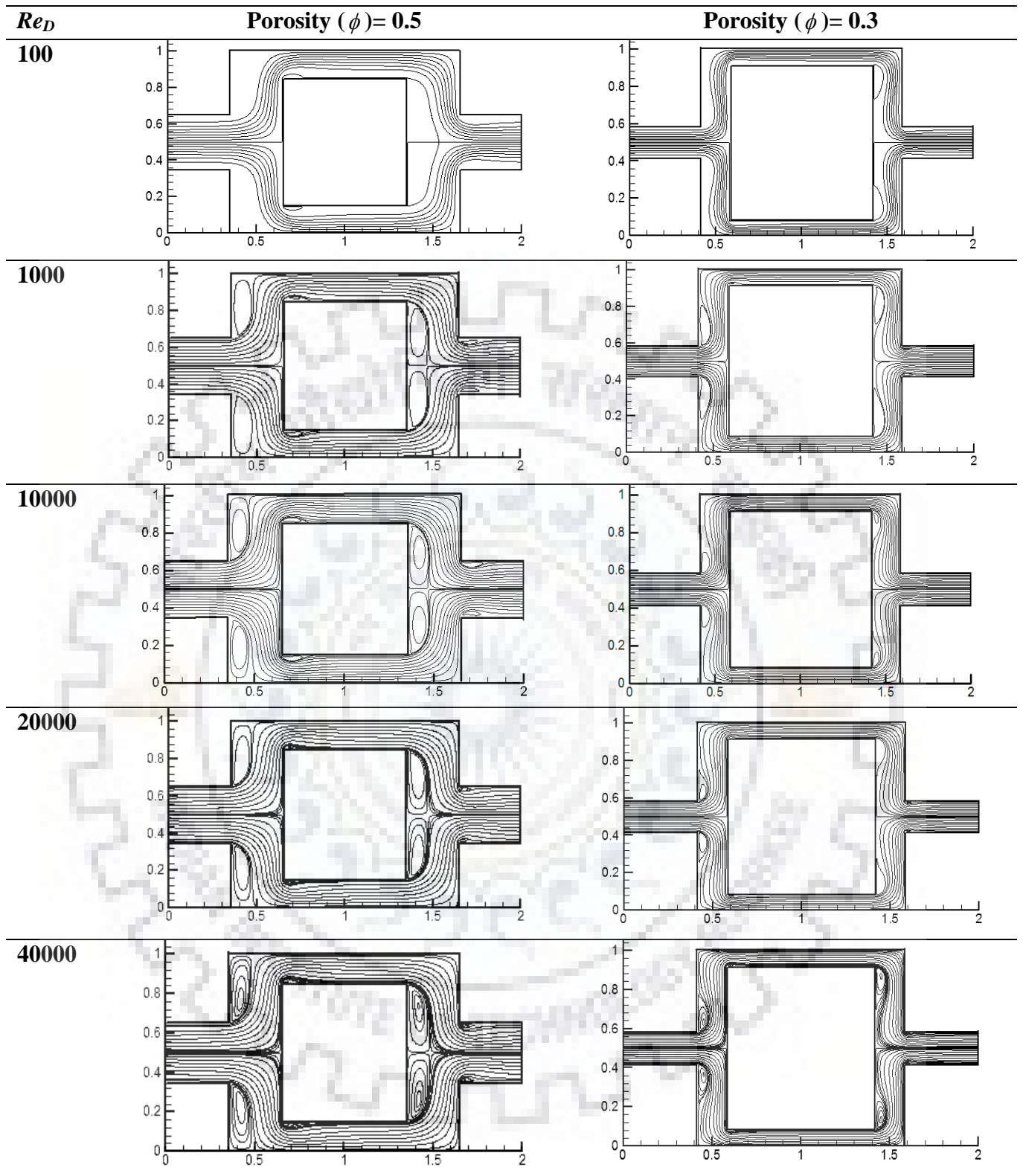


Fig. 6.7(b): Streamline contours in porous media at porosity (ϕ) = 0.5 and 0.3.

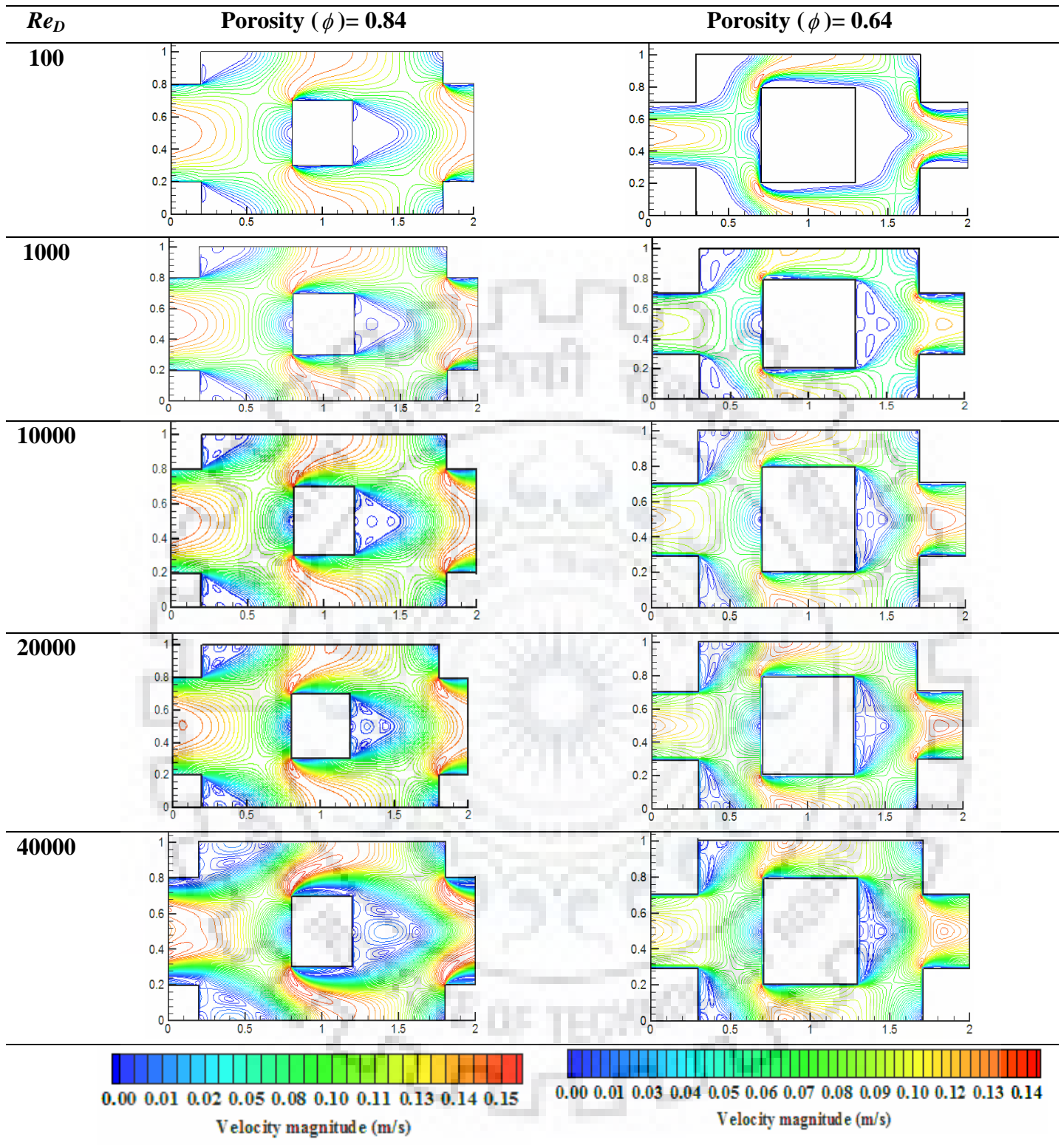


Fig. 6.8(a): Velocity contours in porous media at porosity (ϕ) = 0.84 and 0.64.

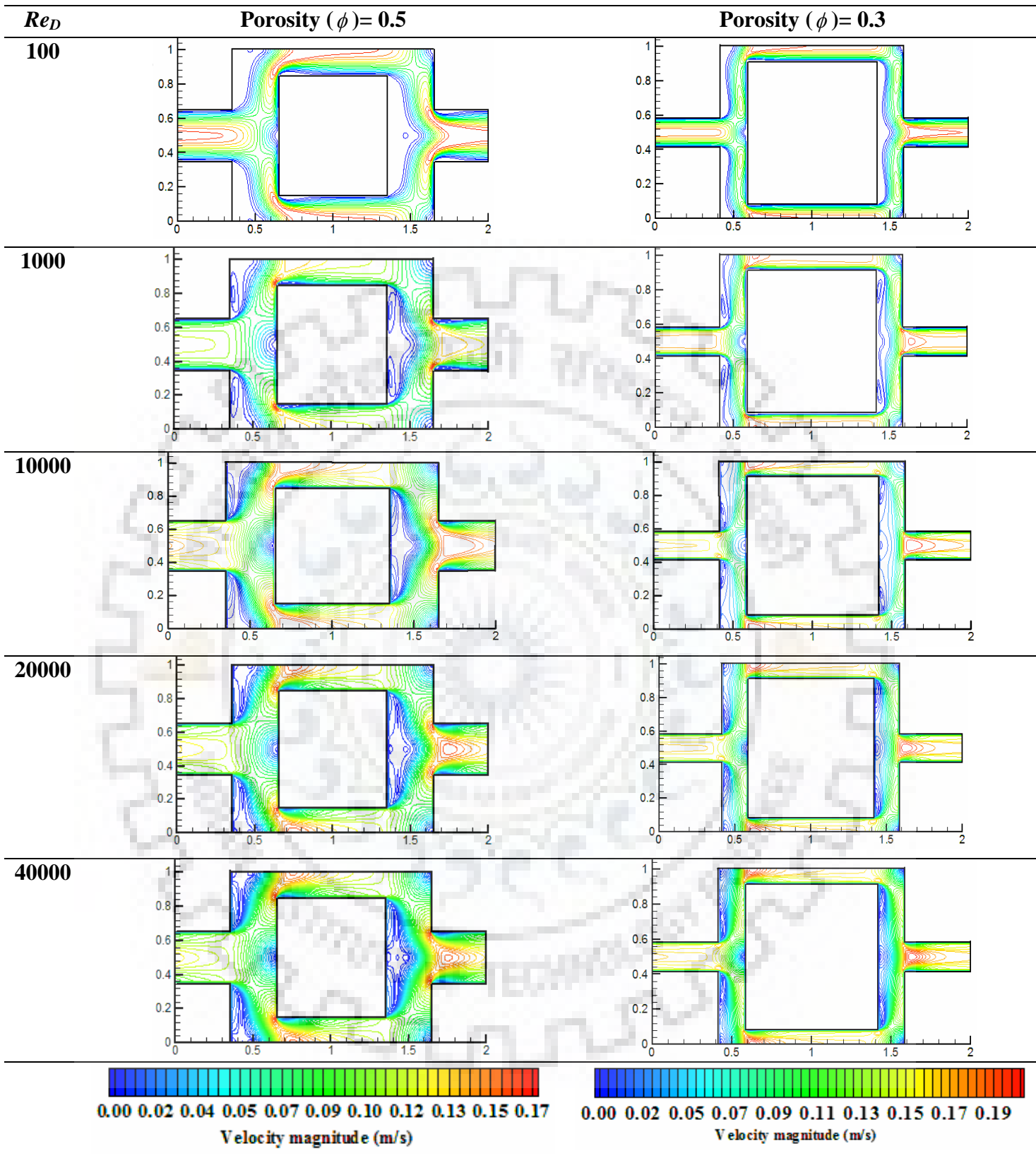


Fig. 6.8(b): Velocity contours in porous media at porosity (ϕ) = 0.5 and 0.3.

6.6.2 Macroscopic Turbulent Kinetic Energy and Dissipation Rate

A series of computations were performed for different values of porosity and Reynolds numbers and the results are presented in terms of the normalized macroscopic turbulent kinetic energy. The normalized macroscopic turbulent kinetic energy was obtained by dividing the macroscopic turbulent kinetic energy by the square of Darcian velocity ($\langle k \rangle^f / u_D^2$).

The normalized macroscopic turbulent kinetic energy and the dissipation rate against Re_D with porosity as a parameter is shown in Figs. 6.9 and 6.10, respectively. It was found that the normalized $\langle k \rangle^f$ increases with Re_D , upto $Re_D = 1000$, and stays constant thereafter for large Re_D ($Re_D > 1000$). The normalized $\langle k \rangle^f$ decreases gradually with an increase in porosity. As the porosity decreases at a given Re_D , the fluid flow passage reduced, which lead to an increase in the local fluid velocity gradient. The velocity gradient actually dictates the rate at which the mean flow mechanical energy transferred into turbulent energy, which causes the larger production rates of k within the fluid and as a result $\langle k \rangle^f$ increases. It was also found that turbulence may appear at a comparatively low Reynolds number, especially for low porosity. The Darcian velocity, $u_D^2 = (\phi \langle u \rangle^f)^2$, is small and the normalized $\langle k \rangle^f$ exceeds unity for comparatively low porosity (Kuwahara et al., 2006).

The simulated contours of turbulent kinetic energy and dissipation rate in the flow domain for different porosity and Reynolds number are shown in Fig. 6.11 (a–d). It was observed that, the spectra of turbulent kinetic energy and dissipation rate are concentrated near the wall of the square cylinder. Kuwahara et al. (2006) also observed that, the turbulent kinetic energy is produced exclusively with in the shear layer above and at the lateral surface of the cylinder, where the mean strain rate is quite high, due to flow separation. For higher porosity ($\phi = 0.84, 0.64$) values, the gradient of turbulent kinetic energy is high at the upper and the lower faces of the cylinder and at the downstream corner walls. Consequently, the dissipation rate grows gradually from the square cylinder wall and the downstream corner walls. Further it can be seen that with decrease in porosity, the magnitude of turbulence gradient increases.

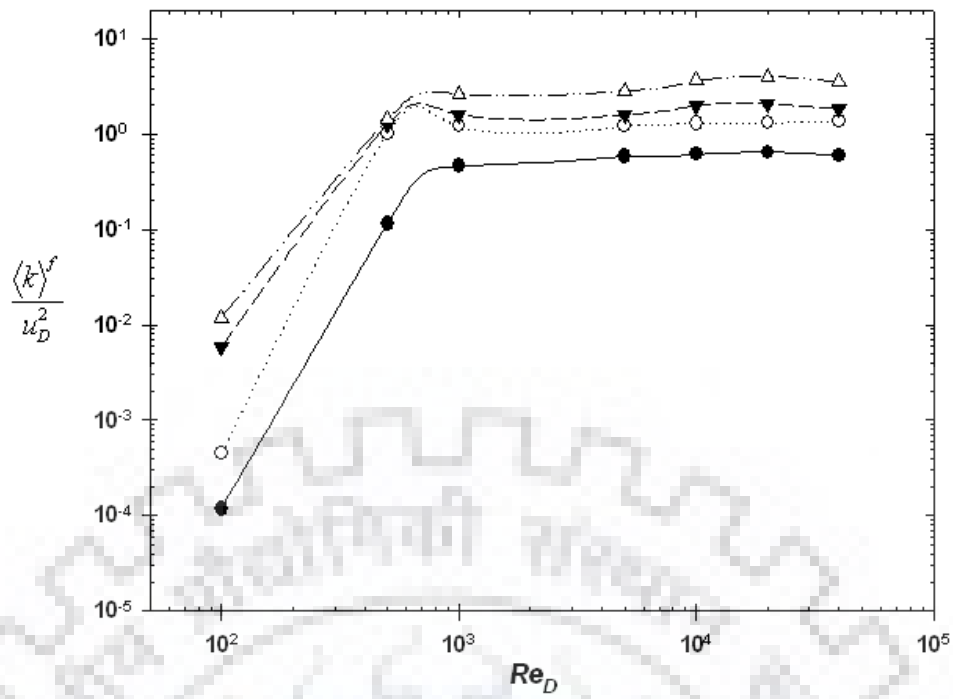


Fig. 6.9: Variation in normalized $\langle k \rangle^f$ with Re_D for different porosities (ϕ): 0.84 —●—; 0.64 ···○···, 0.5 ---▼---; 0.3 -·△-·.

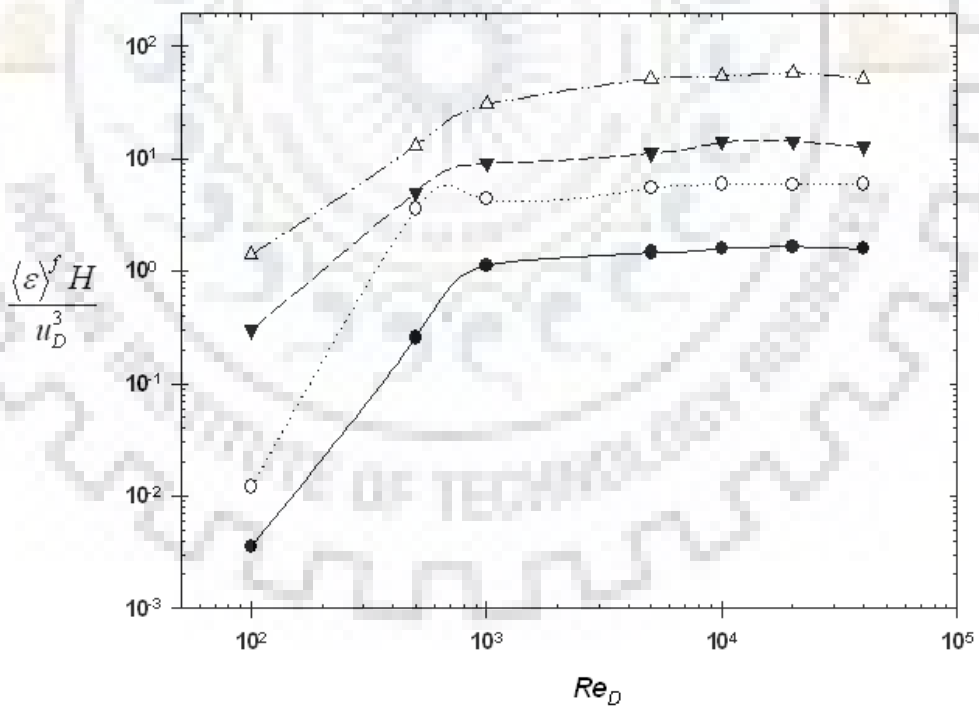


Fig. 6.10: Variation in normalized $\langle \varepsilon \rangle^f$ with Re_D for different porosities (ϕ): 0.84 —●—; 0.64 ···○···; 0.5 ---▼---; 0.3 -·△-·.

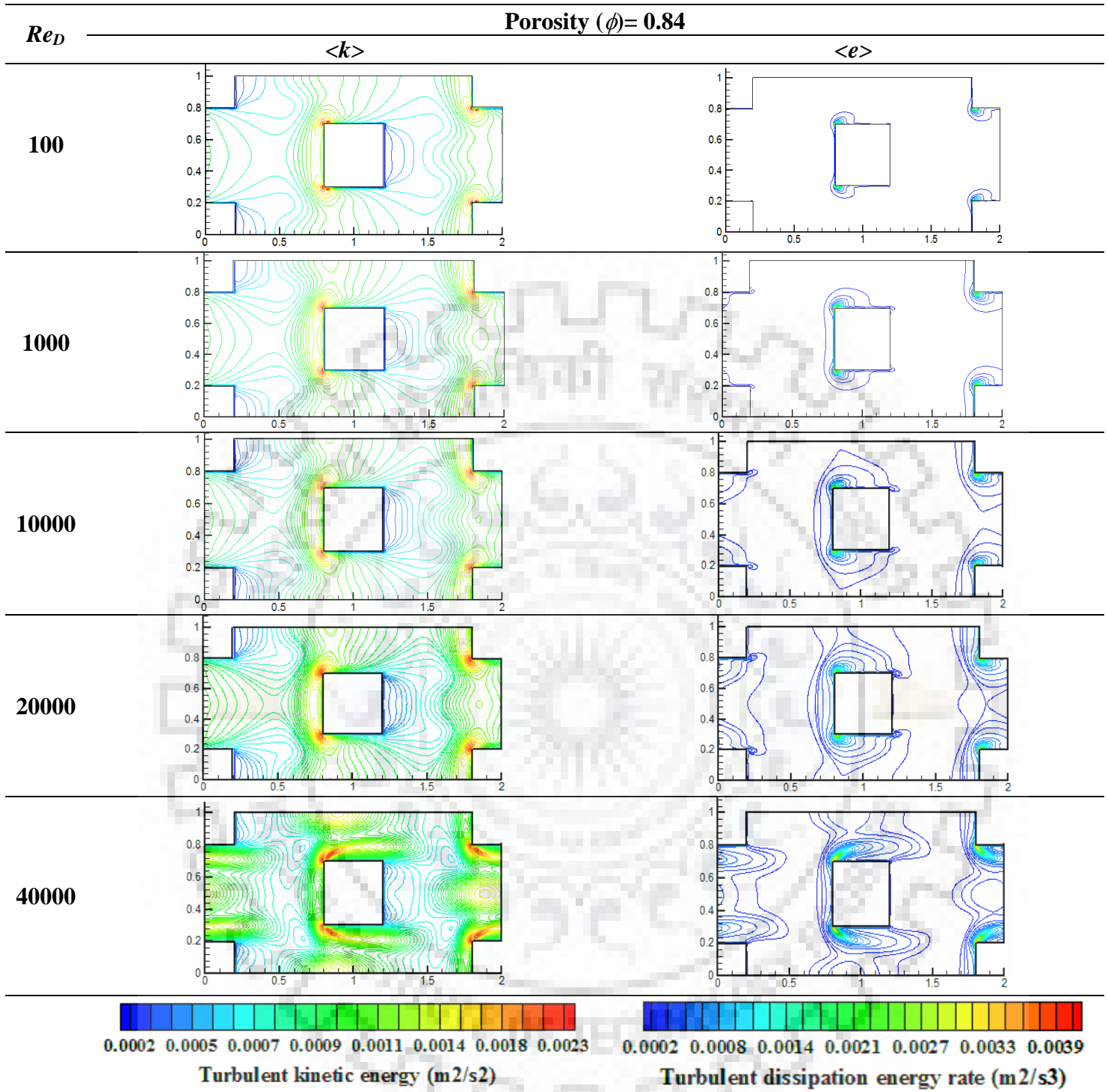


Fig. 6.11(a): Turbulent kinetic energy and dissipation rate contours in porous media at porosity (ϕ) = 0.84.

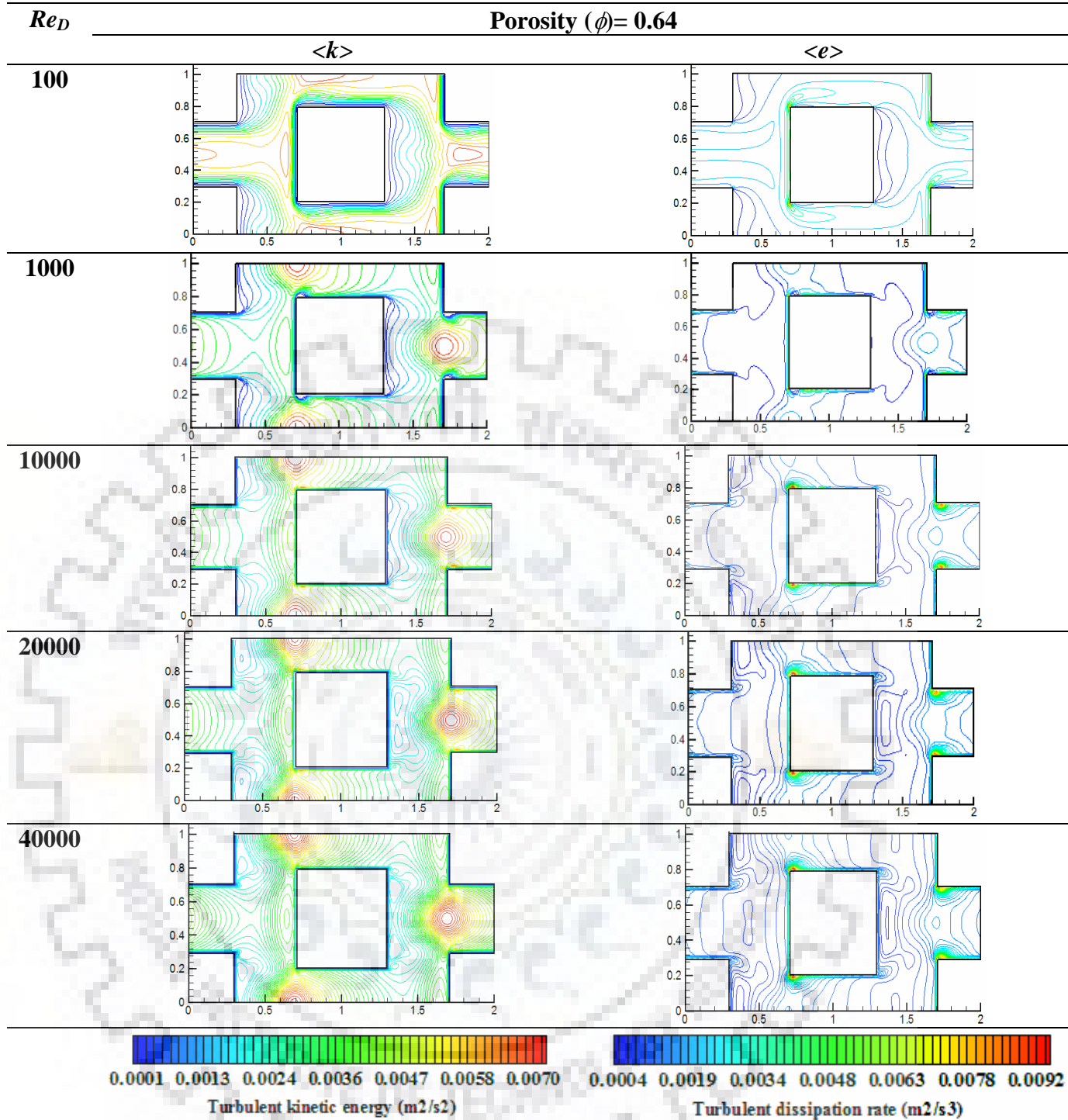


Fig. 6.11(b): Turbulent kinetic energy and dissipation rate contours in porous media at porosity (ϕ) = 0.64

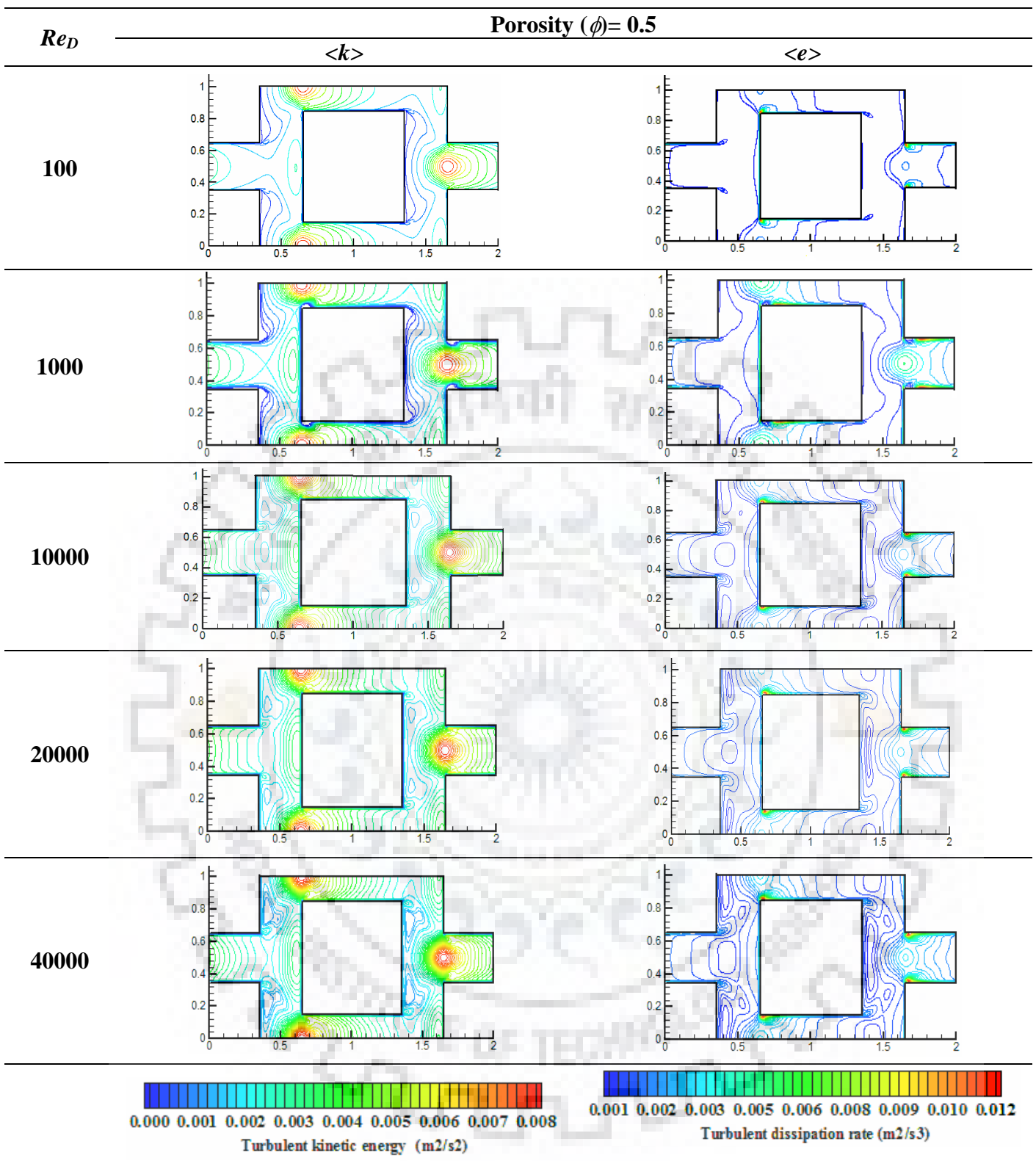


Fig.6.11(c): Turbulent kinetic energy and dissipation rate contours in porous media at porosity (ϕ) = 0.5.

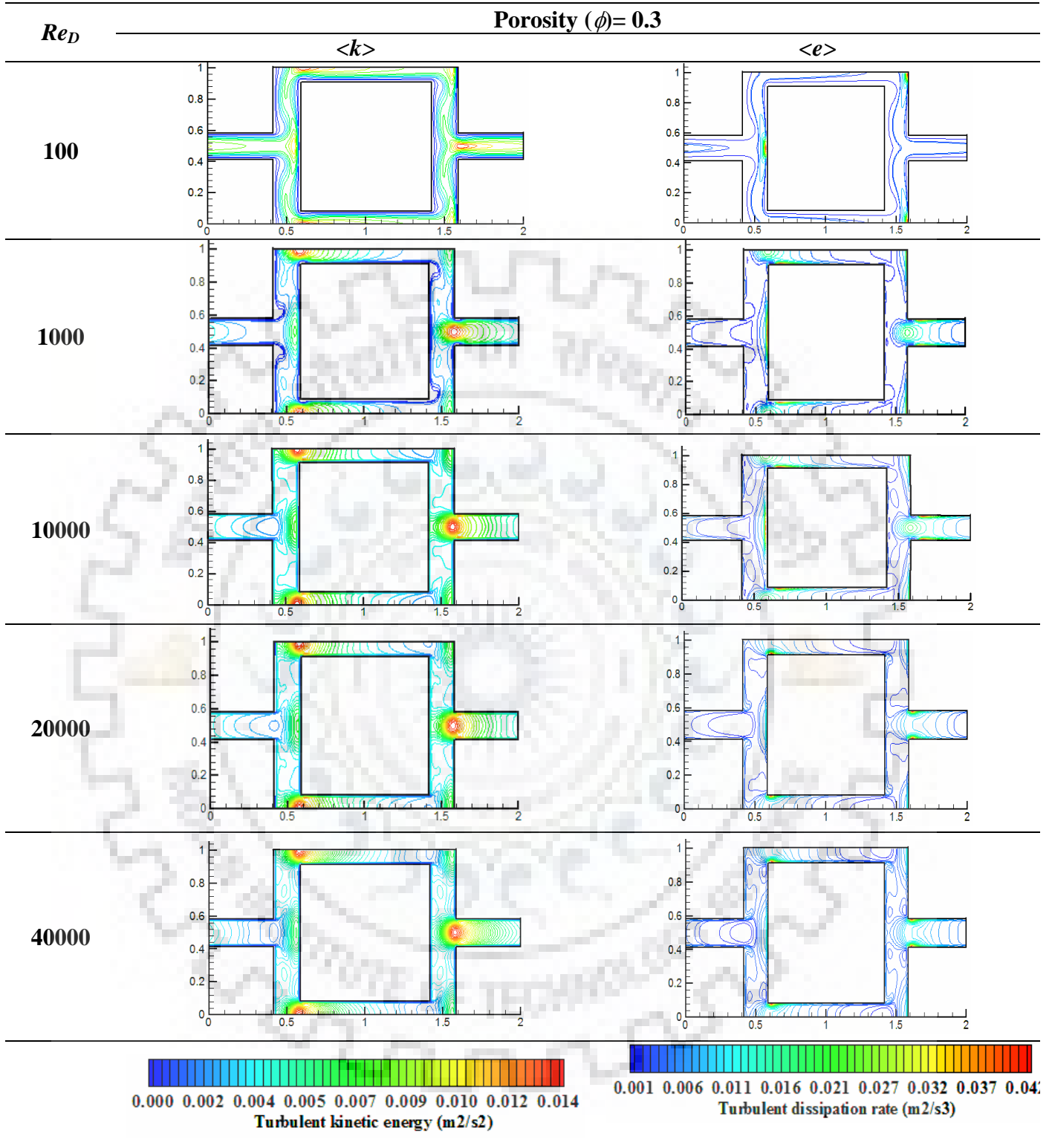


Fig. 6.11(d): Turbulent kinetic energy and dissipation rate contours in porous media at porosity (ϕ) = 0.3.

6.6.3 Comparison of Turbulence Model

The normalized macroscopic turbulent kinetic energy data for the present low Re k - ε model are compared with the results obtained using LES model (large eddy simulation model) (Kuwahara et al., 2006) and $v2f$ model (Kazerooni and Hannani, 2009). The model comparisons are shown in Figs. 6.9 for different porosities (0.84, 0.64, 0.5, and 0.3). The low Re k - ε model shows a good logarithmic pattern similar to that given by the LES model. For higher porosity (0.84 and 0.64), the normalized $\langle k \rangle^f$ values lie between the LES and $v2f$ models. However, for lower porosity values (0.5 and 0.3), in the high Re_D range (i.e., $Re_D > 1000$), the normalized $\langle k \rangle^f$ values are somewhat greater than that obtained from the LES and $v2f$ models. This is because of the overestimation of the k production term. At high Re_D , the decelerating flow around the front stagnation point is large, yielding an extremely high production rate of k (Kuwahara et al., 2006). Qualitatively, the present low Re k - ε model shows the normalized $\langle k \rangle^f$ data reasonably well compared to $v2f$ model. From Figs. 6.12-6.15, all the three models are found to show a constant value of normalized $\langle k \rangle^f$ at large Re_D . For $Re_D < 1000$, the present low Re k - ε model shows better predictions as compared to LES model than to $v2f$ model. The deviations occur because these models incorporate different turbulent model constants exhibiting appreciable non-uniformity in the low Reynolds number range ($Re_D < 1000$) (Hannani and Stanislas, 1999, 2000).

Fig. 6.16 shows the normalized macroscopic turbulent kinetic energy as a function of $(1-\phi)/\phi^{1/2}$ for the three models. The present low Re k - ε shows a reasonably close correspondence with the LES and $v2f$ models, although closer to the LES model at $\phi < 0.5$. For high porosity ($\phi > 0.5$), the simulated data from low Re k - ε model seemed to be greater than both the models. The deviation arises due to the overestimation of the turbulent k production term near the stagnation point which is inherent in the k - ε model.

The normalized dissipation rate of macroscopic turbulent kinetic energy for different porosities considered in the present study is shown in Fig. 6.17. The simulated data of the present low Re k - ε model are compared with the LES and $v2f$ model. The normalized dissipation rates of macroscopic turbulent kinetic energy of the present low Re k - ε model was in good agreement with the simulated results of the other two models.

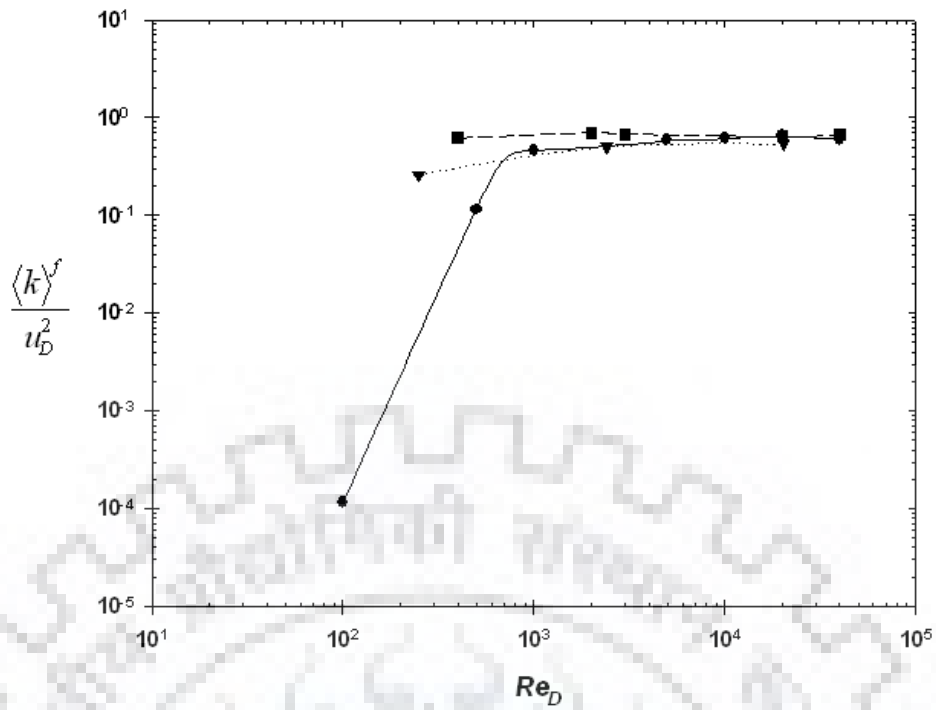


Fig. 6.12: Variation of normalized macroscopic turbulent kinetic energy with Re_D at porosity, $(\phi) = 0.84$: Low-Re k - ε -LB model (present work) —●—; LES (Kuwahara et al., 2006) $\cdots \blacktriangledown \cdots$; v2f (Kazerooni and Hannani, 2009) —■--.

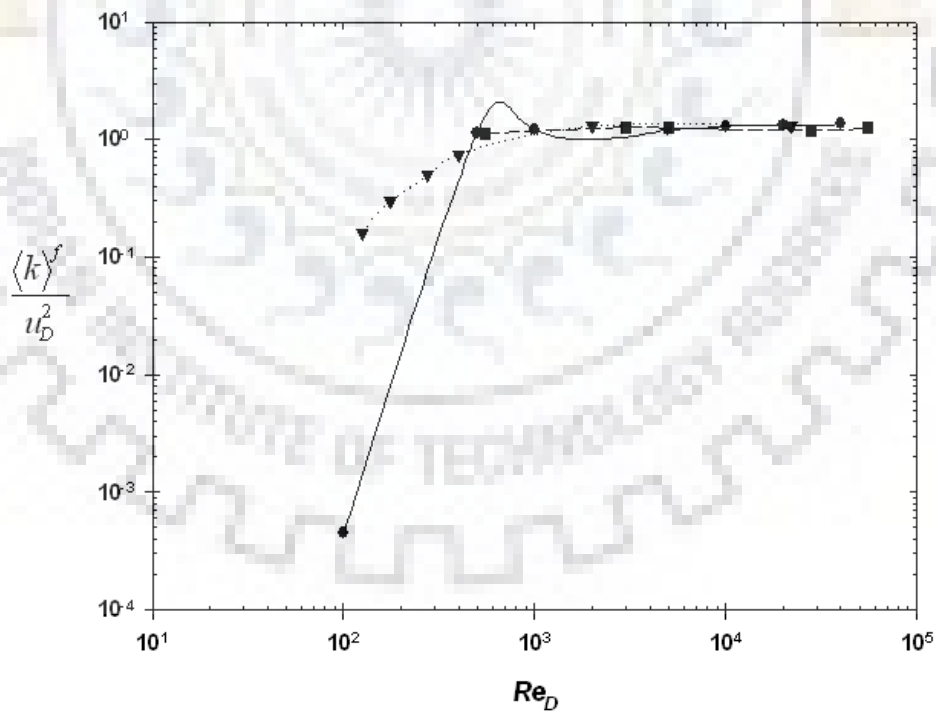


Fig. 6.13: Variation of normalized macroscopic turbulent kinetic energy with Re_D at porosity, $(\phi) = 0.64$: Low-Re k - ε -LB model (present work) —●—; LES (Kuwahara et al., 2006) $\cdots \blacktriangledown \cdots$; v2f (Kazerooni and Hannani, 2009) —■--.

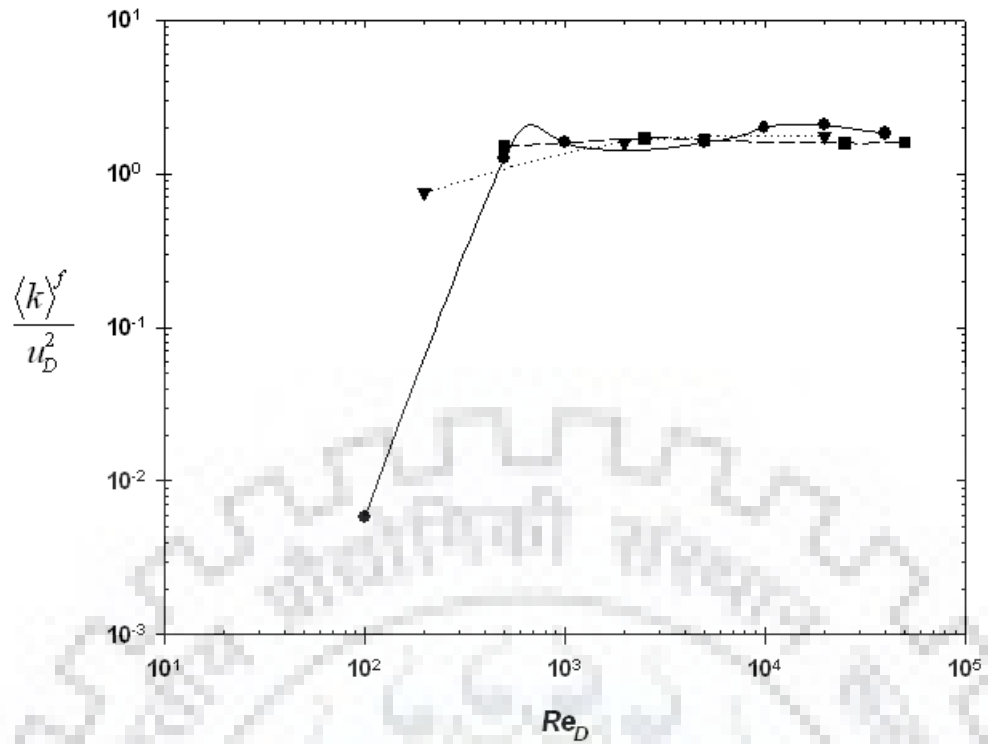


Fig. 6.14: Variation of normalized macroscopic turbulent kinetic energy with Re_D at porosity, $(\phi) = 0.5$: Low-Re $k-\varepsilon$ -LB model (present work) —●—; LES (Kuwahara et al., 2006) ···▼···; v2f (Kazerooni and Hannani, 2009) --■--.

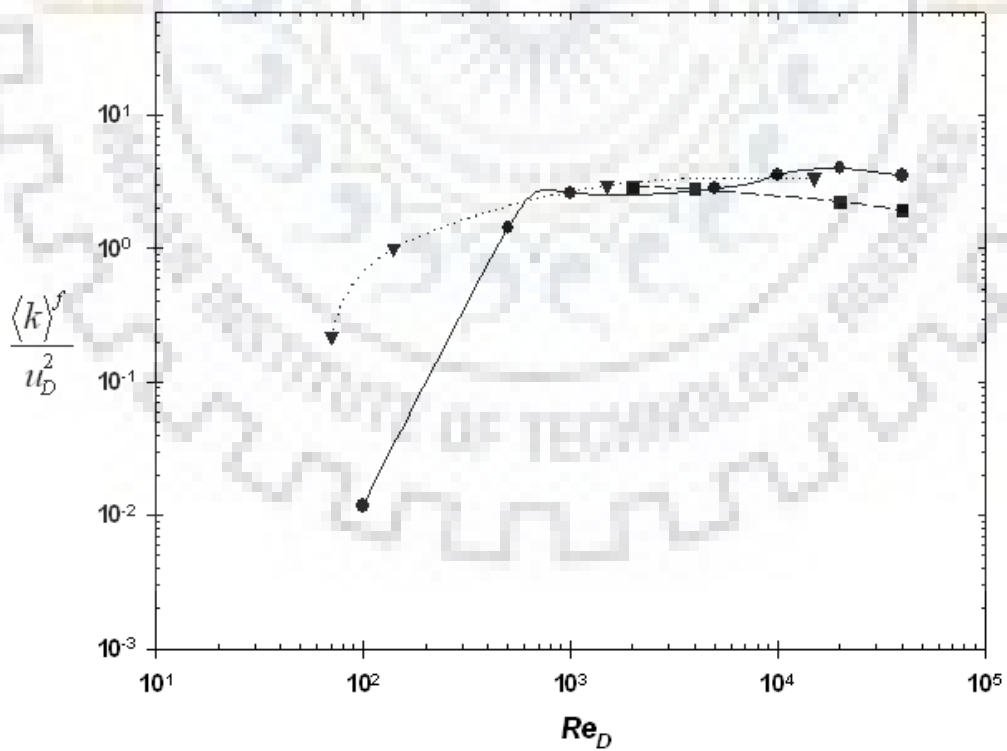


Fig. 6.15: Variation of normalized macroscopic turbulent kinetic energy with Re_D at porosity, $(\phi) = 0.3$: Low-Re $k-\varepsilon$ -LB model (present work) —●—; LES (Kuwahara et al., 2006) ···▼···; v2f (Kazerooni and Hannani, 2009) --■--.

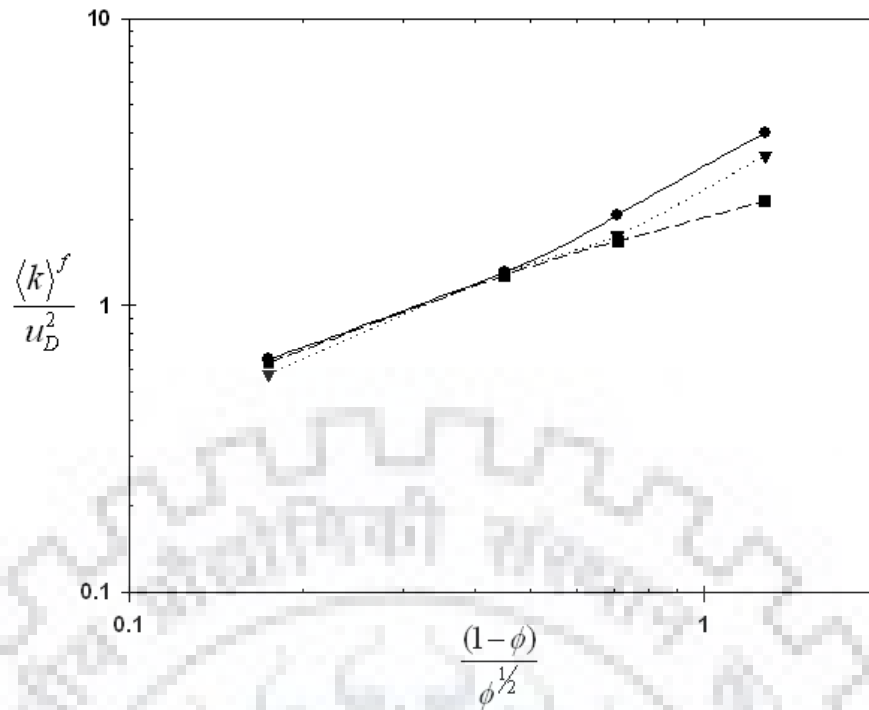


Fig 6.16: Normalized macroscopic turbulent kinetic energy versus $(1 - \phi)/\phi^{1/2}$ (Low- Re k - ε - LB model (present work) —●—; LES (Kuwahara et al., 2006) $\cdots \blacktriangledown \cdots$; v2f (Kazerooni and Hannani, 2009) —■—).

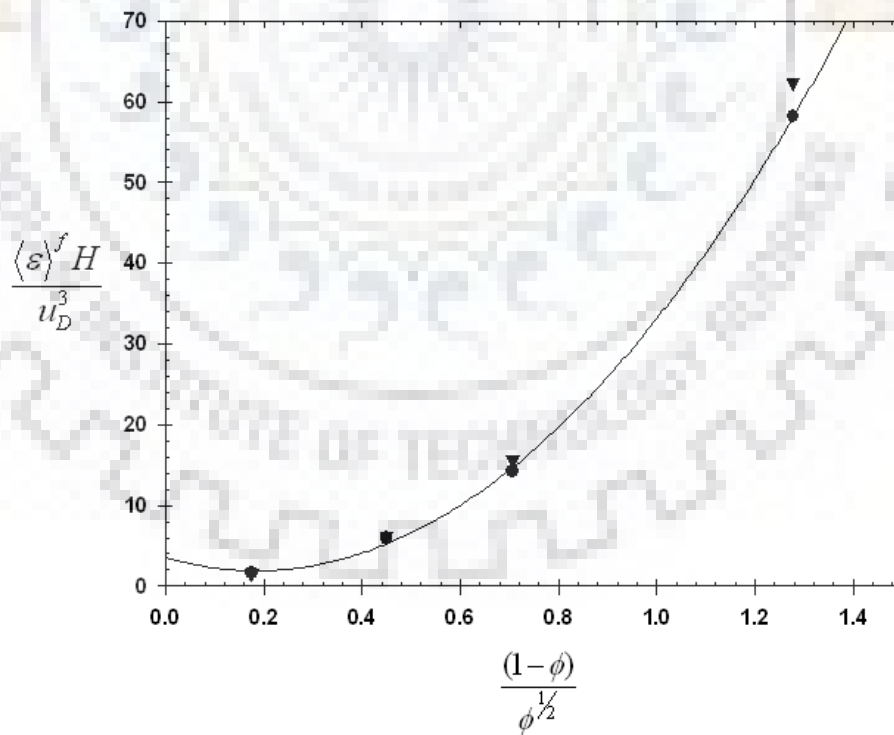


Fig. 6.17: Normalized macroscopic dissipation rate versus $(1 - \phi)/\phi^{1/2}$ (Low- Re k - ε - LB model (present work) ●; v2f (Kazerooni and Hannani, 2009) ▼).

6.6.4 Direct Numerical Simulations (DNS)

The direct numerical simulations (DNS) require large memory usage and CPU time. DNS Computational cost also very high compared to RANS and it is limited for the Reynolds numbers, less than 10,000 (Lai and Yang, 1997). From Fig. 6.12– 6.15 it can be seen that at low Re_D (< 500) the numerical predictions of low Re $k-\varepsilon$ deviate from both v2f and LES results. Therefore following the referee’s suggestions we have carried out simulations using direct numerical simulations (DNS) at $Re_D=100$ for different porosities ($\phi = 0.3, 0.5, 0.64,$ and 0.84). The normalized kinetic energy predictions using DNS, LES and low Re $k-\varepsilon$ model are shown in Fig. 6.18, which is also included in the modified manuscript.

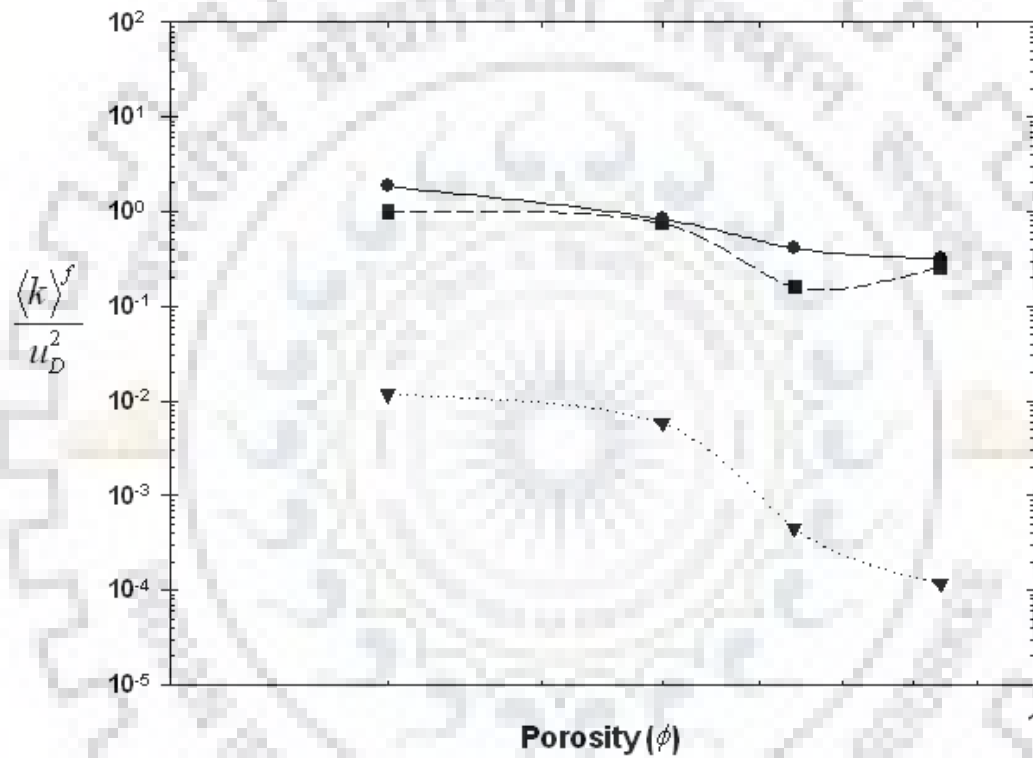


Fig. 6.18: Comparison of different turbulence model at $Re_D=100$ (Low- Re $k-\varepsilon$ -LB model (present work) $\cdots \blacktriangledown \cdots$; DNS (present work) $\text{---} \bullet \text{---}$; LES (Kuwahara et al., 2006) $\text{---} \blacksquare \text{---}$.)

From Fig. 6.18 it can be seen that, DNS and LES results fitted close well. Both DNS and low Re $k-\varepsilon$ results show a consistent and smooth pattern. Fig. 6.19 also shows that the normalized kinetic energy decreases linearly with porosity, however the LES results of Kuwahara et al. (2006) fluctuates at different porosities. In DNS and LES the REV is three-dimensional which is inconsistent with the low Re $k-\varepsilon$ predictions, where the simulations were carried out on 2D assumption. The complex three dimensionality of flow domain (REV) effectively capture the flow characteristics and velocity distribution as compared to 2D simulations at the onset of turbulence ($Re_D=100$). Thus the 2D simulations (low Re $k-\varepsilon$

model) results differs from those 3D DNS and LES results at low Re_D . However, the numerical prediction from the low Re $k-\varepsilon$ model shows a very good agreement with the LES results at higher Re_D ($Re_D \geq 500$). Therefore from the present analysis it can be concluded that the low Re $k-\varepsilon$ model does not give accurate results for very low Reynolds numbers (i.e. $Re_D \leq 100$). This has been an advantage in understanding the turbulence modeling in porous media over a wide range of porosity and Re_D .

6.6.5 Computation of Macroscopic Pressure Gradient

Fig. 6.19 represents the pressure distribution in the simulation domain. In the previous section, it was observed that the flow accelerates in the upper and lower passages around the square cylinder and separates at the upstream face. A larger wake region was formed at the front of square cylinder which may contributed the larger pressure drop for the same mass flow rate through the porous media. It was also observed that the pressure increases at the front of square cylinder and decreases at the upper and lower faces. In the present work, the simulated macroscopic pressure gradient over the flow domain is represented in terms of dimensionless pressure gradient.

The effect of Re_D on dimensionless macroscopic pressure gradient is shown in Fig. 6.20. It was observed that the pressure drop across the flow domain increases linearly with Re_D and increases with decrease in porosity. As the porosity decreases, the passage for flow is reduced and the seepage velocity increases significantly. However, the size of the wake region is gradually reduced. As a consequence, the overall pressure drop increases with decrease in porosity.

At $Re_D > 10$ Darcy law is no longer valid, and non-Darcy flow may occur. As the inertial effect dominates the flow field in comparison to viscous effect (Teitel, 2011), accurate prediction of pressure drop cannot be made by the Darcy equation. In order to account for this high velocity inertial effects at pore scale level, an inertial term is included which represents the kinetic energy of the fluid in the Darcy equation. The modified Darcy law for $Re_D > 10$ is known as the Forchheimer equation:

$$-\frac{d\langle p \rangle^f}{dx} \left[\frac{D}{\rho u_D^2} \right] = \frac{150(1-\phi)^2}{\phi} + 1.75 \frac{1-\phi}{\phi^3} \quad (6.41)$$

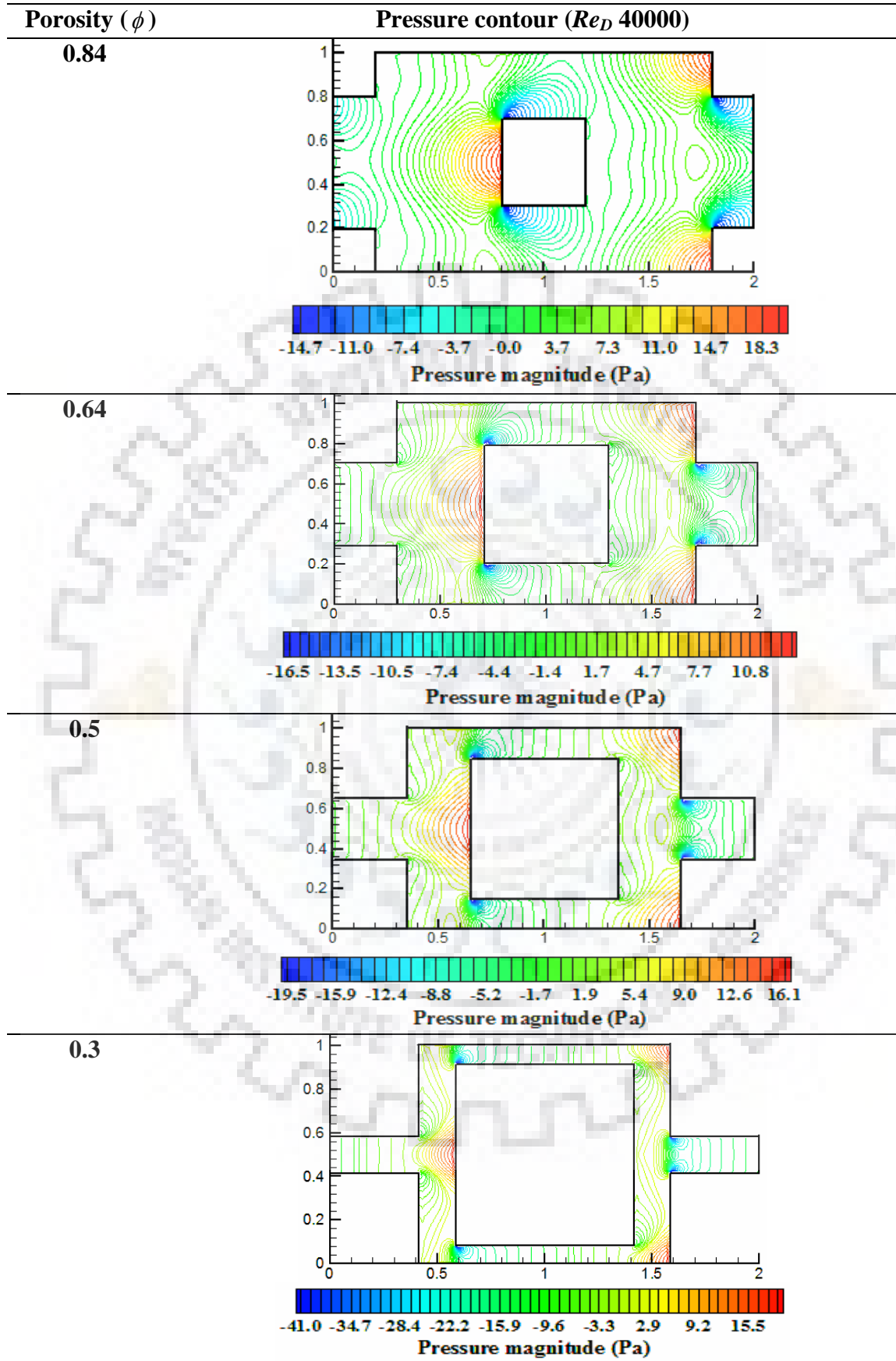


Fig. 6.19: Pressure contour in porous media at $Re_D = 40000$.

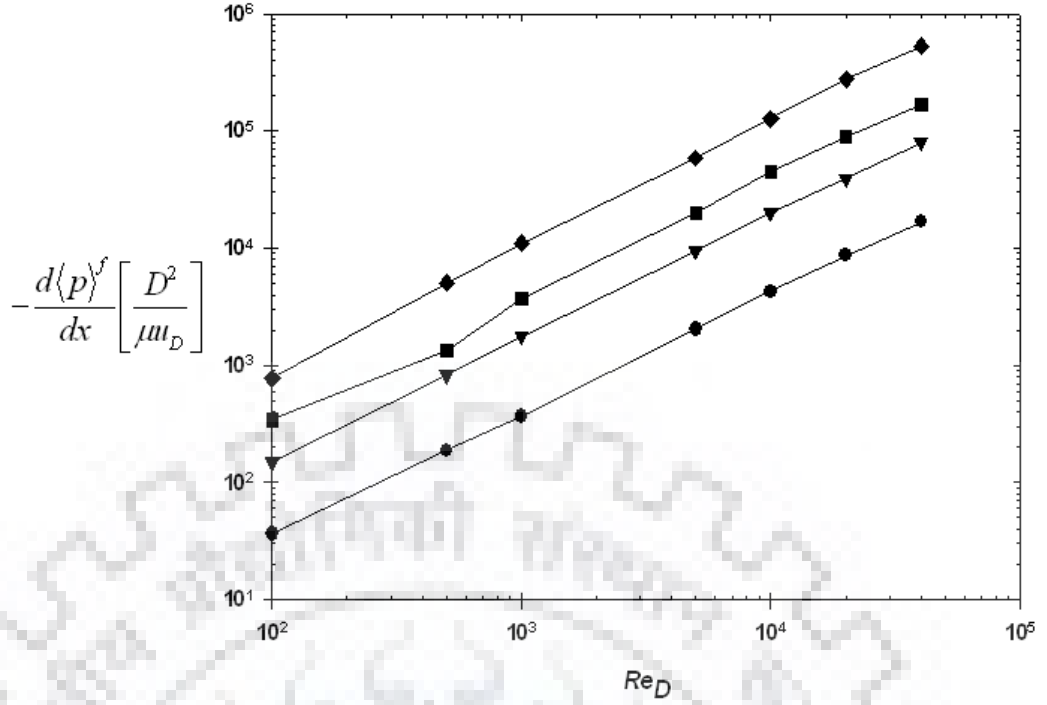


Fig. 6.20: Macroscopic pressure gradient versus Re_D for different porosities ($\phi = 0.84$ —●—; 0.64 —▼—; 0.5 —■—; 0.3 —◆—).

The second term in the above equation (Eq. 6.41) represent the form drag (Forchheimer drag), which arises due to fluid inertial effects. For fully turbulent flow, form drag predominates over the Darcian term. Hence, at higher Reynolds number ($Re_D > 3000$), Eq. (6.41) reduces to following form:

$$-\frac{d\langle p \rangle^f}{dx} \left[\frac{D}{\rho u_D^2} \right] = 1.75 \frac{1-\phi}{\phi^3} \quad (6.42)$$

In order to investigate the above relationship, the dimensionless pressure gradient is plotted against porosity $(1-\phi)/\phi^3$. Fig. 6.21 shows the functional relationship of the Forchheimer drag with porosity. As expected, non-dimensional pressure gradient varies linearly with porosity. The non-dimensional pressure gradient results as obtained from the low Re $k-\varepsilon$ model are found to be in good agreement with the results obtained from the LES and v2f turbulence models. In order to validate the reduced Forchheimer equation (Eq. 6.42), the dimensionless pressure gradient is plotted against porosity $(1-\phi)/\phi^3$. From Fig. 6.22 it can be seen that the non-dimensional pressure gradient predictions, as obtained from the low Re $k-\varepsilon$ model, shows good agreement with the results obtained from the LES and v2f models in the porosity range $0.9 \geq \phi \geq 0.5$. For the considered porosity range the present numerical predictions shows a good linearity ($R^2=0.97$) with a coefficient of 1.50 which is approximately equals to empirical value, i.e. 1.75. As the porosity decreases, $\phi \leq 0.5$, the

numerical predictions deviate from linearity. It may be due to the fact that at lower porosities the friction factor grows very slowly as compared to the high porosities (Teruel and Rizwanuddin, 2009). As a result drag and pressure drop across the porous media does not varies linearly. Therefore a correlation (Eq. 6.43) for Forchheimer drag with porosity has been proposed which justifies the present simulation results for the porous media approximation (Fig. 6.23).

$$F_D = -\frac{d\langle p \rangle^f}{dx} \left[\frac{D}{\rho u_D^2} \right] = 5.185 \left(\frac{1-\phi}{\phi} \right)^{1.349} \quad (6.43)$$

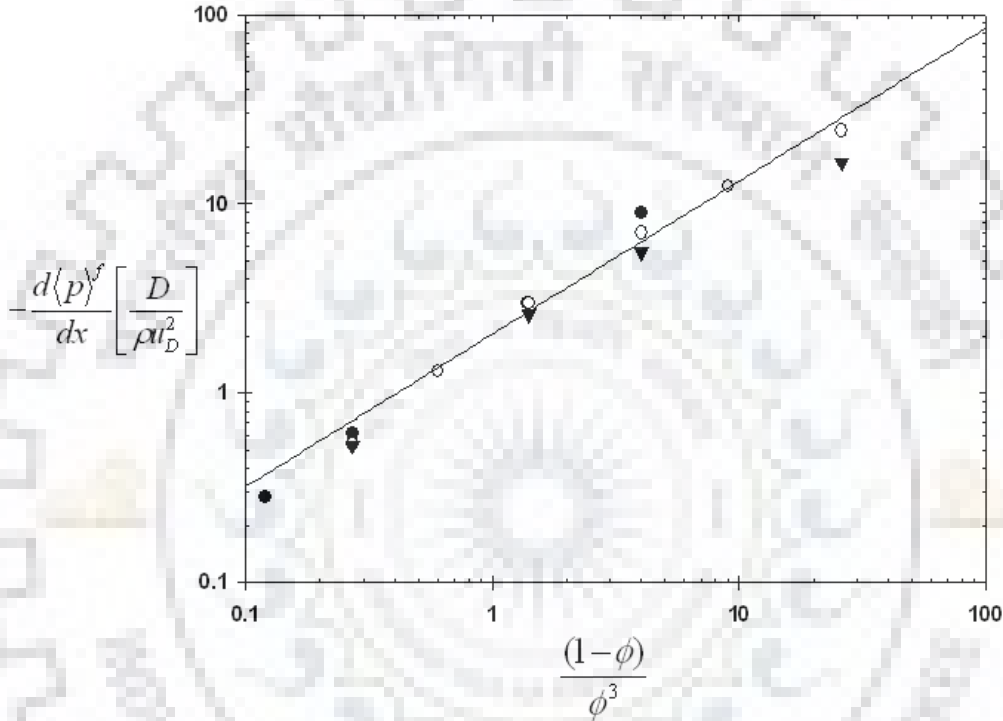


Fig. 6.21: Macroscopic pressure gradient versus $(1 - \phi)/\phi^3$ for Forchheimer drag (—) (Low-Re $k-\varepsilon$ -LB model (present work) —▼—; LES (Kuwahara et al., 2006) —●—; v2f (Kazerooni and Hannani, 2009) —○—.)

Pressure gradient across the porous media is represented in terms of *friction factor* (f) and $Re_{D_{eq}}$, and is shown in Fig. 6.23. The friction factor was computed in the transition zone from laminar flow regime ($Re_{D_{eq}} = 1$) to fully turbulent flow regime ($Re_{D_{eq}} = 80000$) and the effect of porosity and Reynolds number with in REV was investigated. The computed *friction factor* (f) was plotted with $Re_{D_{eq}}$, which is shown in Fig. 6.23. It was observed that the *friction factor* strongly depend on the medium porosity. As porosity of the porous media decreases the *friction factor* increases, which is also in good agreement with the work of Teitel, (2011). It was found that, for a fixed porosity friction factor of the media was

significantly high at laminar flow regimes ($Re_{D_{eq}} < 20$) and then exponentially decreases with $Re_{D_{eq}}$ and become almost constant in fully turbulent regimes ($Re_{D_{eq}} > 1000$). It may be concluded that, at laminar flow regimes friction factor strongly depends on $Re_{D_{eq}}$ and become independent in turbulent flow regimes.

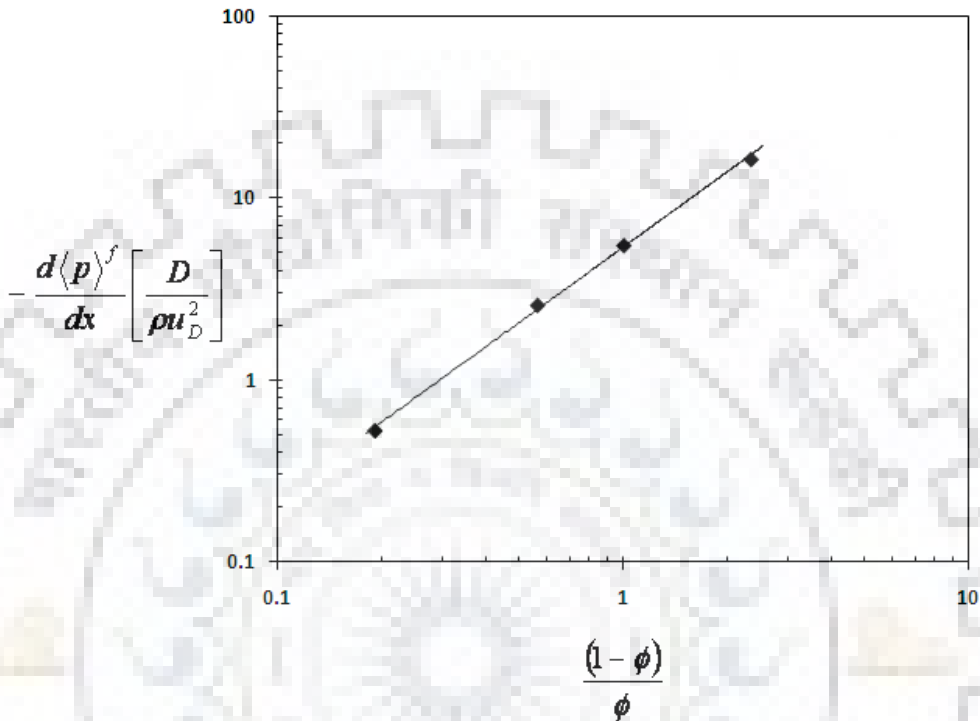


Fig. 6.22: Dimensionless macroscopic pressure gradient versus $(1 - \phi)/\phi$ fitted with Eq. 6.43.

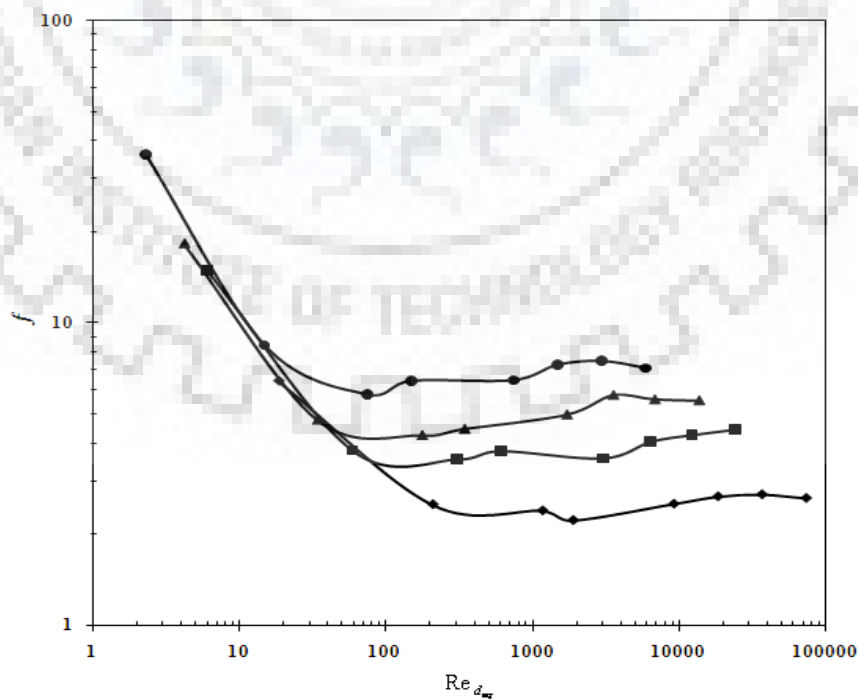


Fig. 6.23: Friction factor (f) versus $Re_{d_{eq}}$ for different porosity (ϕ)

$$(\phi = 0.84 \text{ --}\blacklozenge\text{--}; 0.64 \text{ --}\blacksquare\text{--}; 0.5 \text{ --}\blacktriangle\text{--}; 0.3 \text{ --}\bullet\text{--}).$$

6.6.6 Macroscopic Turbulence Modeling

In the present study the methodology reported by Pedras and Lemos (2001) was adopted for macroscopic modeling of fluid flow through the isotropic homogeneous porous bed. A volume averaging procedure is applied to couple the turbulence modeling with porous approximation. According to Dupuit-Forchheimer relationship turbulent transport equations (k and ε equation) are modified and proposed.

k equation:

$$\frac{\partial}{\partial x_i} (\rho \bar{u}_D \langle k \rangle^f) = \frac{\partial}{\partial x_j} \left[\left(\mu + \frac{\mu_t \phi}{\sigma_k} \right) \frac{\partial}{\partial x_j} (\phi \langle k \rangle^f) \right] + P_k + c_k \rho \frac{\bar{u}_D \langle k \rangle^f}{\sqrt{K}} - \rho \phi \langle \varepsilon \rangle^f \quad (6.44)$$

ε equation:

$$\begin{aligned} \frac{\partial}{\partial x_i} (\rho \bar{u}_D \langle \varepsilon \rangle^f) = & \frac{\partial}{\partial x_j} \left[\left(\mu + \frac{\mu_t \phi}{\sigma_k} \right) \frac{\partial}{\partial x_j} (\phi \langle \varepsilon \rangle^f) \right] + C_{1\varepsilon} f_1 P_k \frac{\langle \varepsilon \rangle^f}{\langle k \rangle^f} + C_{2\varepsilon} f_2 \rho \phi \left[c_k \frac{\bar{u}_D \langle \varepsilon \rangle^f}{\sqrt{K}} \right] \\ & - C_{2\varepsilon} f_2 \rho \phi \frac{\langle \varepsilon \rangle^{f^2}}{\langle k \rangle^f} \end{aligned} \quad (6.45)$$

where, $P_k = -\rho \phi \langle \bar{u}'_i \bar{u}'_j \rangle^f \frac{\partial}{\partial x_i} (\phi \langle \bar{u} \rangle^f)$

$$-\rho \phi \langle \bar{u}'_i \bar{u}'_j \rangle^f = \mu_t \left[\frac{\partial}{\partial x_i} (\phi \langle \bar{u} \rangle^f) + \left(\frac{\partial \bar{u}_D}{\partial x_i} \right)^T \right] - \frac{2}{3} \rho \delta_{ij} \phi \langle k \rangle^f \quad (6.46)$$

In above equations a generation terms (third term on the right side) were introduced for production of $\langle k \rangle^f$ inside the bed due to the presence of porous matrix. The generation term contains a constant, c_k where c_k is a characteristic and unique constant for the macroscopic model of a homogeneous isotropic porous matrix. The value of the constant c_k is determined by using the limiting condition ($\phi \rightarrow 1$; $K \rightarrow \infty$). Under this limiting condition Eq. (6.44) and Eq. (6.45) reduced to Eq. (6.47), where the turbulence production and dissipation rate becomes equal.

$$\frac{\varepsilon_\phi \sqrt{K}}{\bar{u}_D^3} = c_k \frac{k_\phi}{\bar{u}_D^2} \quad (6.47)$$

The simulated volume average results of the macroscopic solutions are fitted to Eq. 6.47 for the calculation of constant, c_k . In Fig. 6.24 the numerical prediction of $\varepsilon_\phi \sqrt{K} / \bar{u}_D^3$ are Plotted with k_ϕ / \bar{u}_D^2 for different porosity and Re_D . From Fig. 6.24 the values of c_k were found to be 0.292 which is close to the value 0.28 as reported by Pedras and Lemos, (2001)

for circular cylinder. The present simulation results showed a good agreement and provide a generalized methodology for porous media modeling.

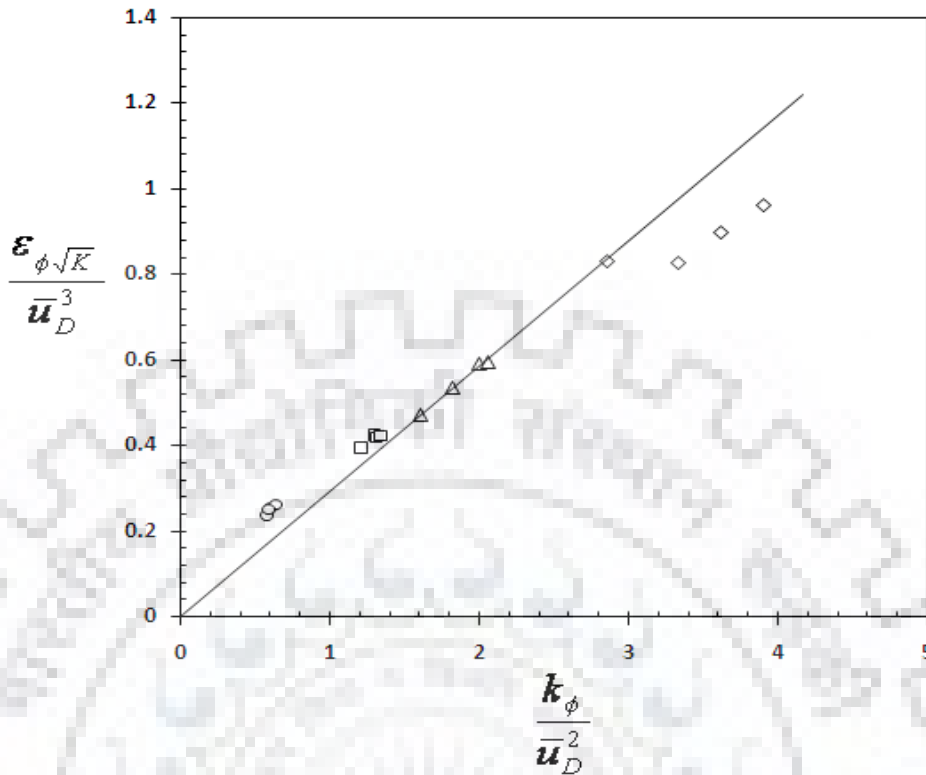


Fig. 6.24: Plot for the determination of constant c_k using simulation data for different porosity and Re_D ($\phi = 0.84$ –○–; 0.64 –□–; 0.5 –△–; 0.3 –◇–).

6.7 FLOW THROUGH ISOTROPIC ARRAY OF CIRCULAR CYLINDERS

6.7.1. Spanwise Microscopic Turbulent Flow Fields

The simulated results of spanwise velocity, pressure and turbulent kinetic energy contours for different ϕ (0.3 and 0.8) and Re_D values are shown in Figs. 6.25(a-d), in the computed REV. The fluid passes through the upper and lower surfaces of the cylinder having higher velocity, and flow separation takes place at the downstream region behind the cylinder. A larger wake region is formed at the front face of the circular cylinder. The vortex or eddy formation is also observed at the corner circular surface in the upstream direction, where flow separation also takes place. The size of the vortex increases with an increase in Re_D and the vortex is dissipated upon travelling through downstream. At low Re_D ($Re_D=100$), the intensity of wake formation is low due to the fluid flowing smoothly over the entire circular cylinder. Turbulence increases with an increase in Re_D at the downstream region of the cylinder. Consequently, an intense wake region is generated with the formation of eddies. At higher Reynolds number ($Re_D=40,000$), complete flow separation takes place in the downstream section and at the front face of the cylinder. The size of the vortex at the front face of the

circular cylinder in the downstream gets compressed gradually with a decrease in porosity, as the passage for the fluid flow narrows down.

Fig. 6.25 shows that the maximum velocity magnitude is observed at the centre of the upstream section and the upper and lower faces of the circular cylinder at a fixed value of ϕ . However, the flow is separated from the back of the circular cylinder. A pair of stagnation points was formed at the centre of the upstream and the downstream face of the circular cylinder. A larger wake region is formed at the front of the circular cylinder which will contribute to a larger pressure drop for the same mass flow rate through the porous media. In the remaining fields, it is observed that the pressure increases at the front of the circular cylinder and decreases at the upper and lower faces.

The RANS simulations showed the excessively smooth turbulent structures within the *REV*, near the wall and around the cylindrical surface. The turbulent structures (vortex shape and eddy structure) are overestimated. LES captures the turbulent flow features significantly well especially the near-wall turbulent characteristics. The velocity and turbulent spectra are fluctuating in nature. From LES results, the spectra of instantaneous streamwise velocities shows that a large region of low velocity is detached from the surface of the cylinder into the wake and transported towards the stagnation point. The high magnitude velocity blobs occasionally entered this region. These eddies are largely affected by the pore diameter and the curvature of the wall.

It seems that the turbulent kinetic energy is produced exclusively within the shear layers above the lateral surfaces of the cylinder, where the mean strain rate was quite high. This is in contrast with the result of the RANS model. This is because of the fact that the conventional $k-\varepsilon$ model involves a k production term (P_k) (Eq. 6.12), which is coupled with the effective viscosity formulation. For a decelerating flow around the front stagnation point, an extremely high production rate of k is observed, which leads to over-estimation of the level of turbulent kinetic energy (Pedras and de Lemos, 2001). This limitation can be overcome by the LES approach which provides a reasonable turbulent kinetic energy distribution within the *REV*.

The improvement is brought about by the significant reduction of the turbulent kinetic energy produced in the back surface of the cylinder, as can be seen from the k -contours of LES computations given in Fig. 6.25(b). The excessive kinetic energy in the back surface of the cylinder was also absent in the LES results which indicate strong turbulence generation in the separated shear layer. More kinetic spectra were observed at the upper and lower surfaces of the cylinder. As a consequence, the LES computations exhibit more turbulence sweeping around the cylinder. The RANS and LES computations for 3D simulations at $Re_D=10000$

were carried out for the visualization of pore flow hydrodynamics in the modeled porous matrix which can be seen in the animation file.

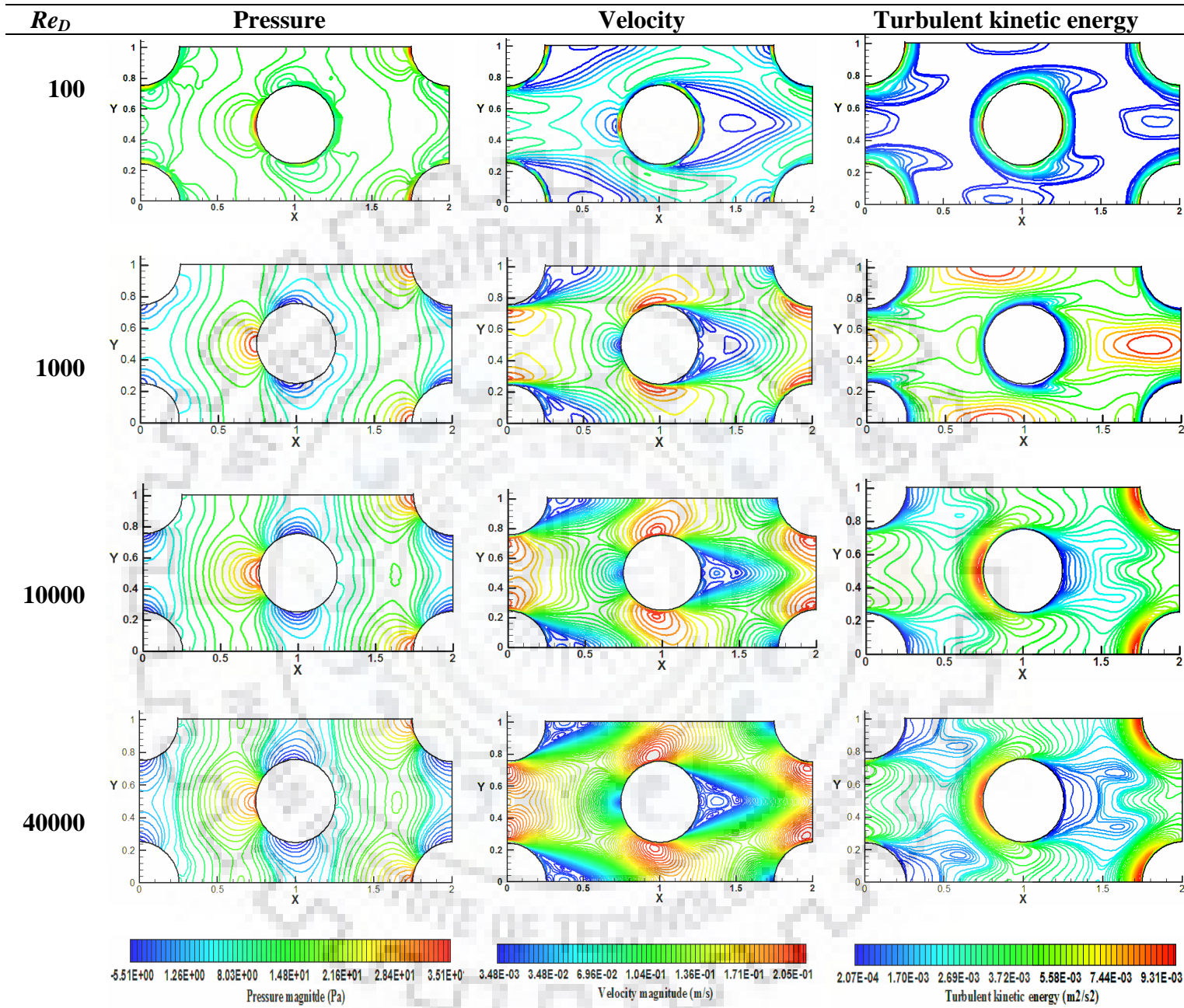


Fig. 6.25 (a): Contours of pressure, velocity and turbulent kinetic energy from RANS simulations at $\phi = 0.8$.

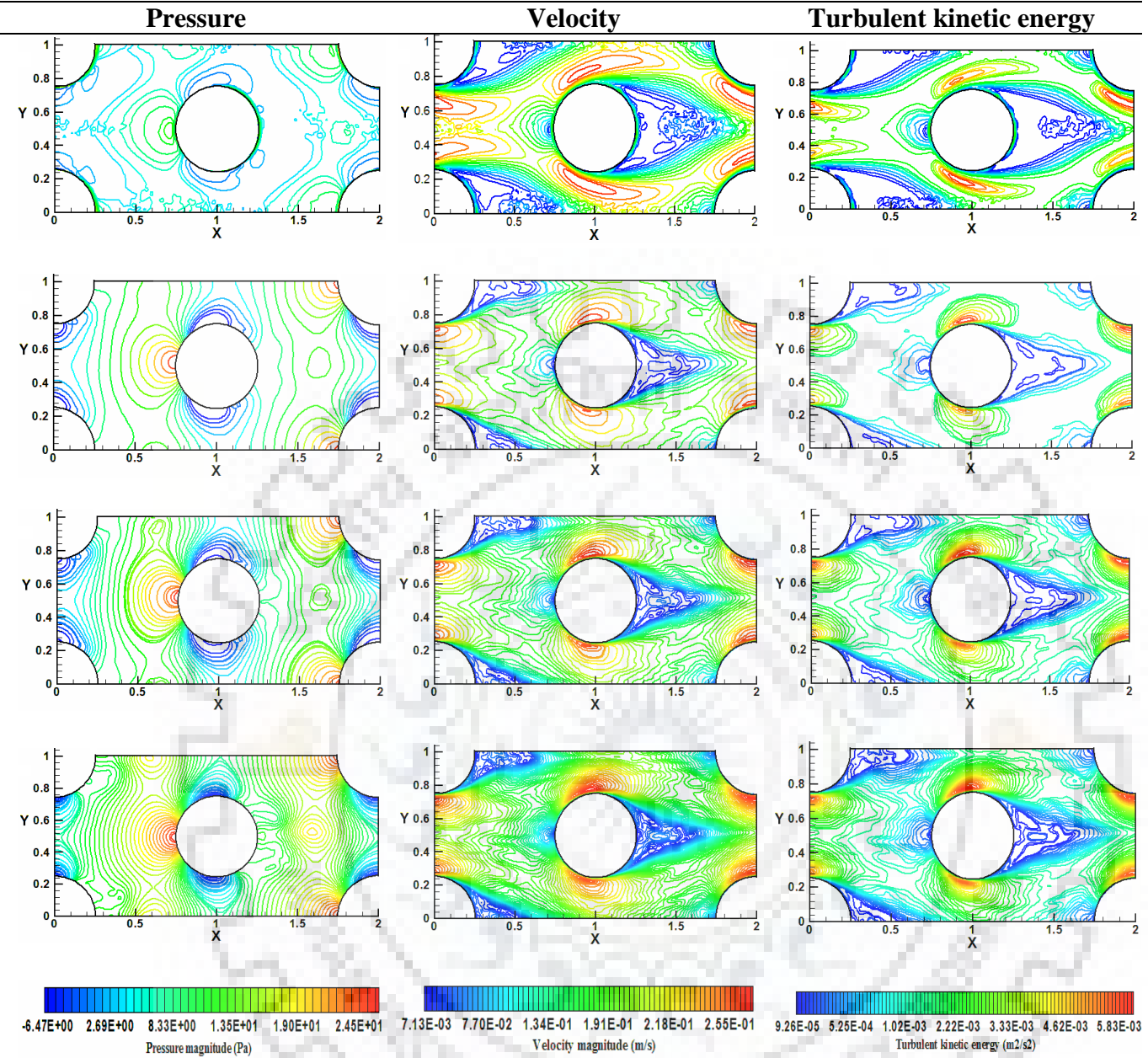


Fig. 6.25(b): Contours of pressure, velocity and turbulent kinetic energy from LES computations at $\phi = 0.8$.

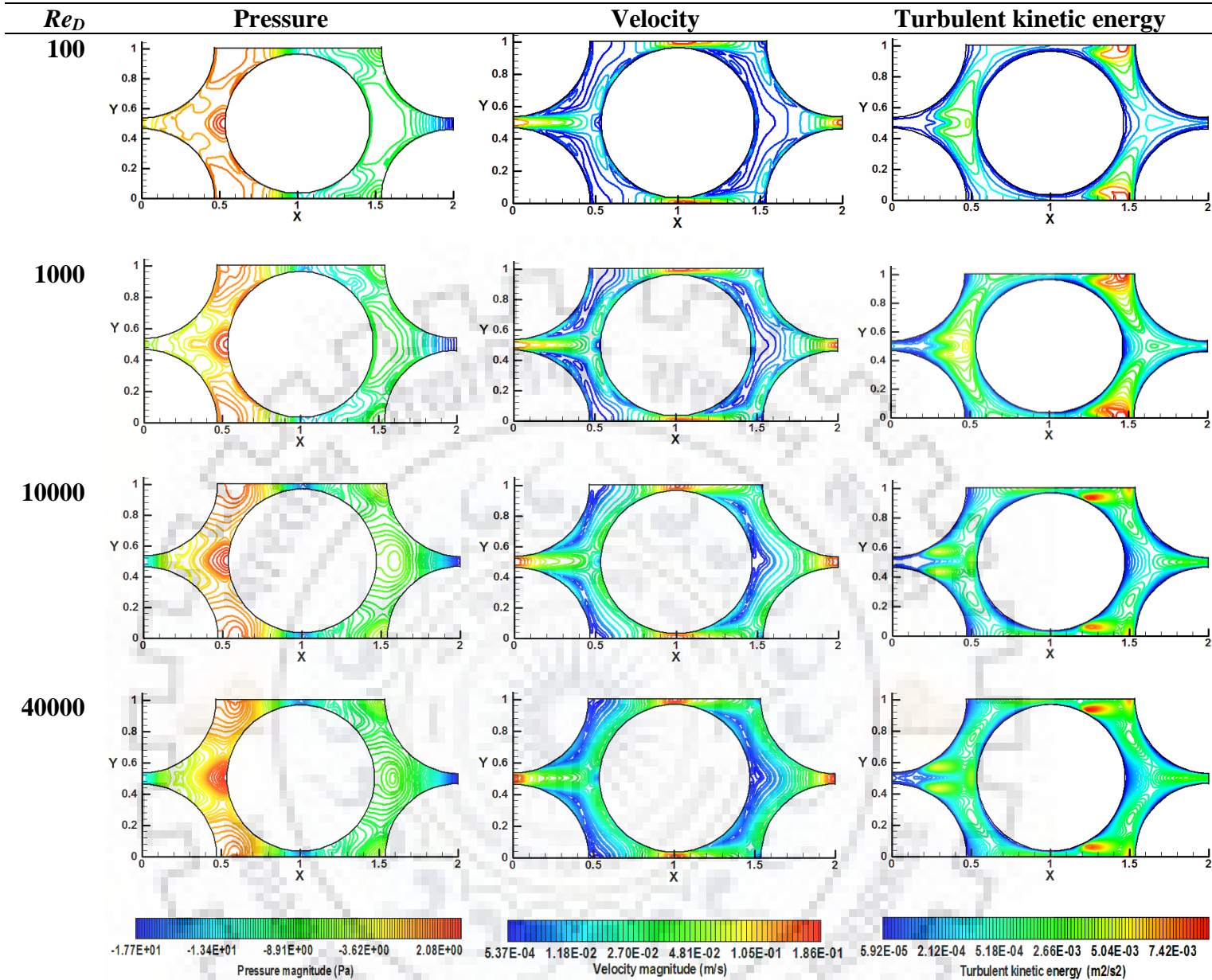


Fig. 6.25(c): Contours of pressure, velocity and turbulent kinetic energy from RANS simulations at $\phi = 0.3$.

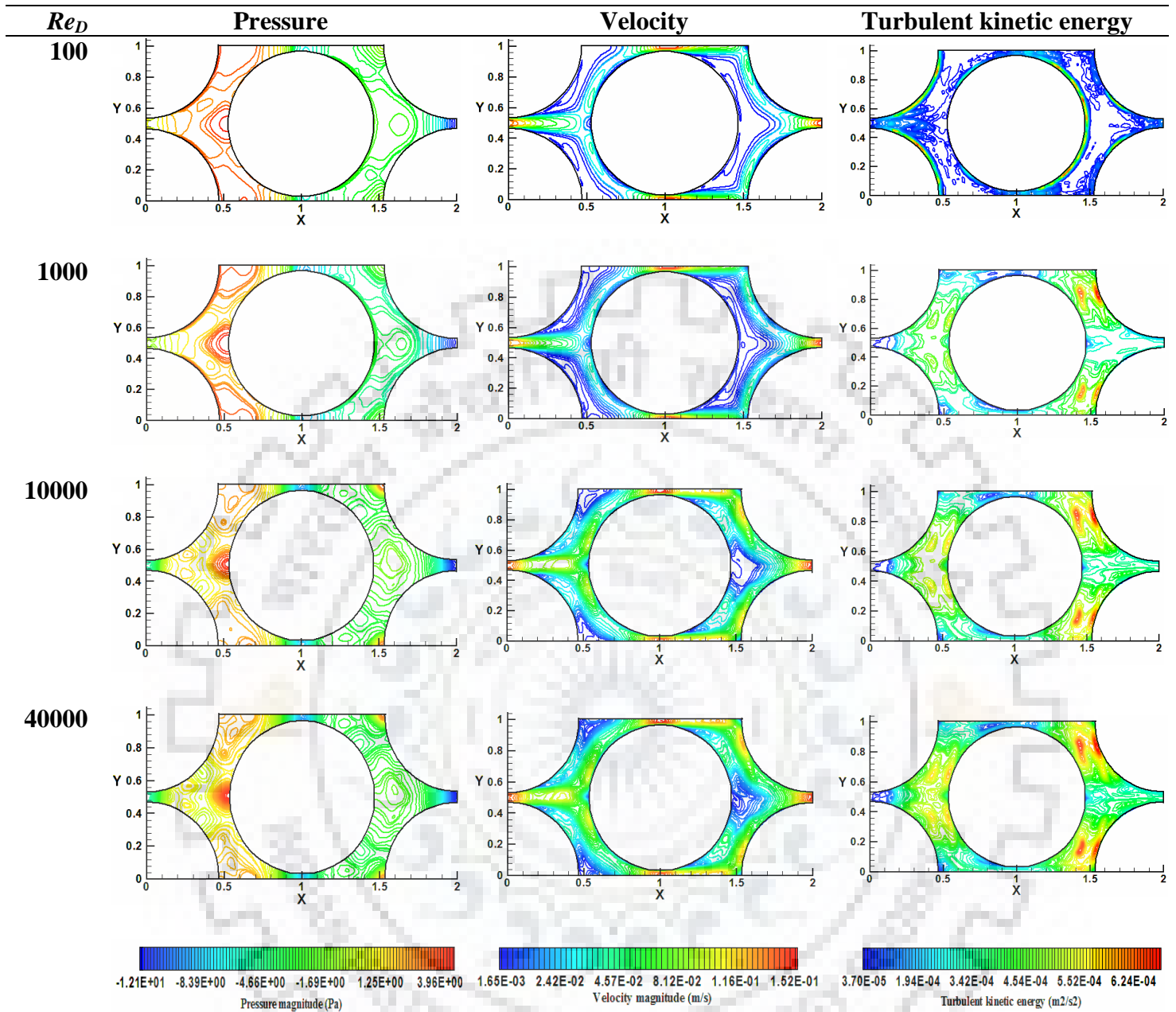


Fig. 6.25(d): Contours of pressure, velocity and turbulent kinetic energy from LES computations at $\phi = 0.3$.

6.7.2. Solid fluid interactions and 3D flow structures

Turbulent flow is inherently three-dimensional, therefore it is interesting to investigate the coherent fluid structure generated in the porous matrix due to solid surface-fluid interactions. The iso-contours and iso-surfaces of the velocity vector field are presented to illustrate the fluid flow structures and the three dimensionality of the flow field. The perspective view of computed 3D flow field of different porosities for RANS and LES calculations are shown in Fig. 6.26.

The flow field is divided into the two regions, which show the most important physical phenomena, such as the flow separation at the upstream of the cylinder, the reattachment at the downstream of the cylinder and the formation-evolution of eddies within the separated region. The RANS computations show steady and smooth iso-contours (Fig. 6.26a). Flow separation occurs behind the cylinder, leading to a separation region at the downstream region. The evolution of the wake region transition from attached to separated wake and leading to flow separation was determined by monitoring the stagnation points around the cross-section of the cylinder.

A single upstream stagnation together with a single downstream stagnation indicates fully attached boundary layers around the cylinder surface. The recirculation zone is clearly visible downstream of the cylinder cross-section, and the flow field is steady. The generation of eddies and flow structure at the separation region were not captured well. The RANS models over-predicted the extent of the separation region at the corner and frontal regions of the cylinder. The coherent flow structures were captured more realistically by LES computed iso-contours and the flow was fully axisymmetric (Fig. 6.26b). The recirculation region continuously contained several streamwise structures and, in addition, vortex loops were also observed. The circumferential variation occurred within the recirculation region. These structures constantly impinged on the shear layer and thereby generated turbulence. The turbulence experienced amplification in the streamwise direction, which, most probably, resulted in the generation of additional structures. A significant azimuthal modulation of the fluid structure could be observed at the upper and lower surfaces of the cylinder, which pushed the fluid toward the shear layer through induction of radial velocity. The resolution of large-scale unsteady motions in LES calculations seemed to produce the correct effect, while RANS calculations do not account such effects, explaining possibly the over prediction of the separation region.

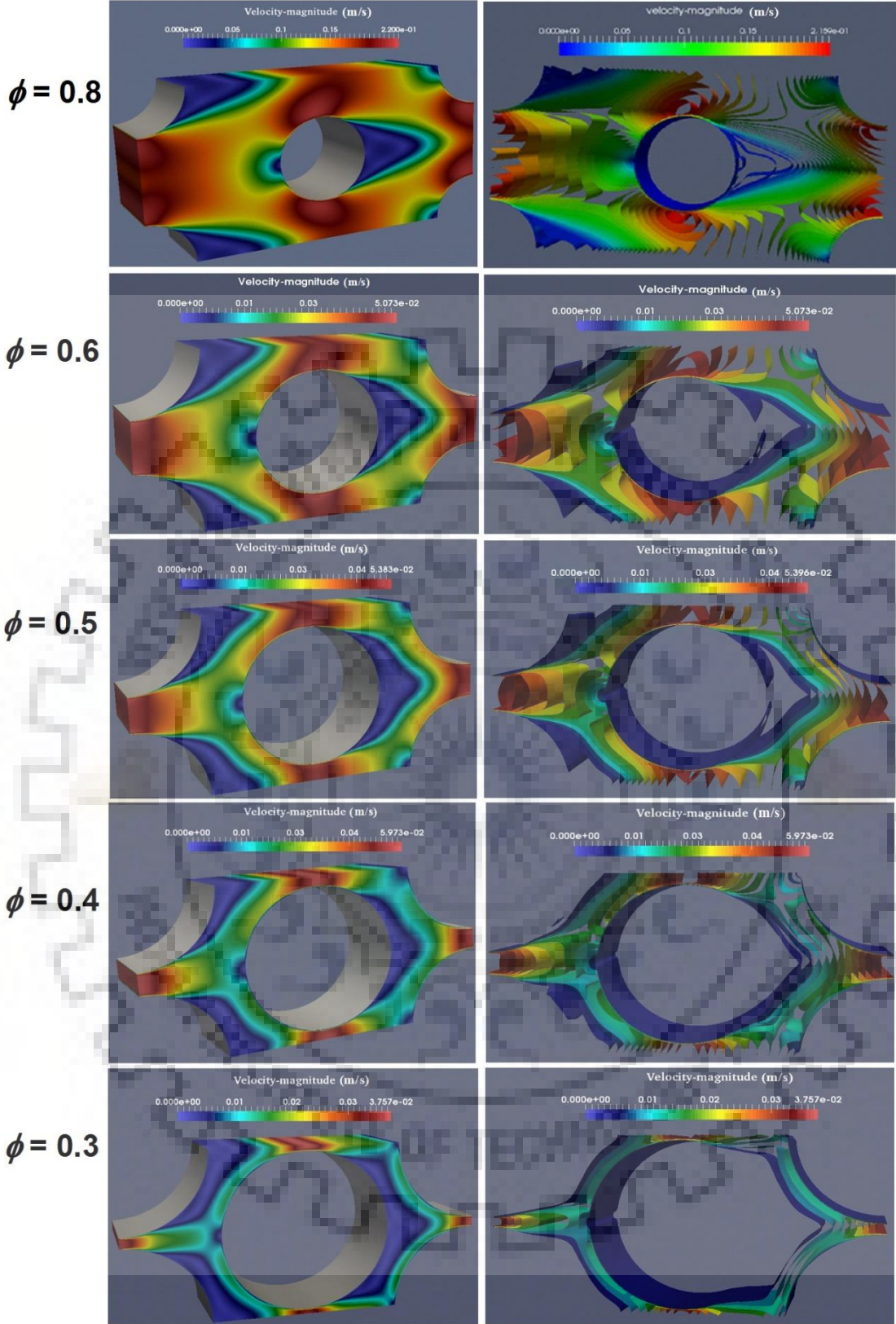


Fig. 6.26(a): 3D pore flow iso-contours of RANS computed velocity magnitude for different porosities at $Re_D=10000$.

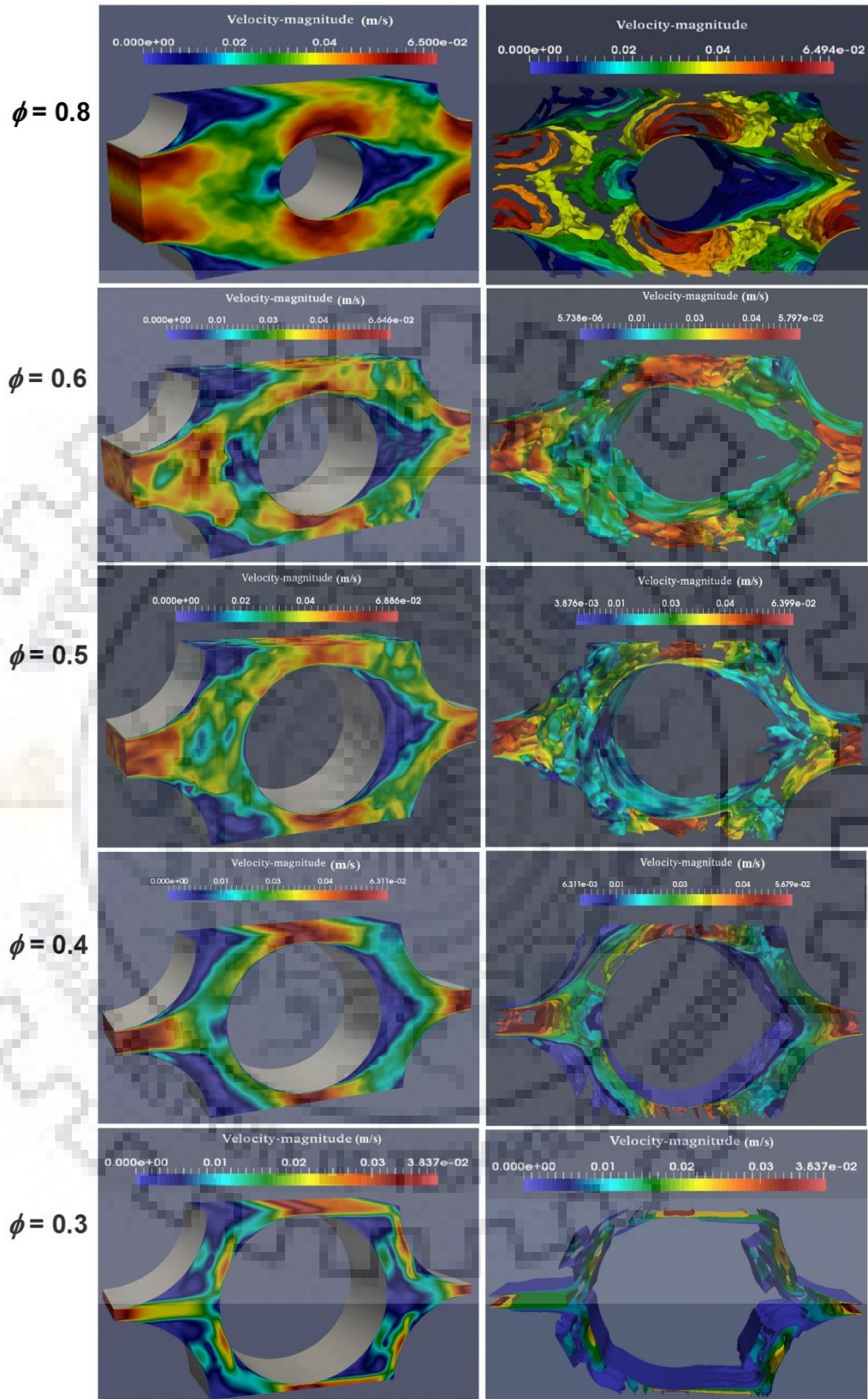


Fig. 6.26(b): 3D pore flow iso-contours of LES computed velocity magnitude for different porosities at $Re_D=10000$.

Fig. 6.27 presents the instantaneous iso-surfaces for different idealized pore geometry to show the three dimensionality of the flow field, the formation of eddies within the separated region and also the evolution of the random vortical structures. The complex behaviour of the pore flow hydrodynamics were well captured by the LES calculations. Strong solid-fluid interactions were observed at the front and back surfaces of cylinder and the corner region. As the fluid propagated across the REV, the breakdown of the fluid volume, rapid stretching and initiation of small scale structure were observed. Fluid structure became constricted as the porosity decreased.

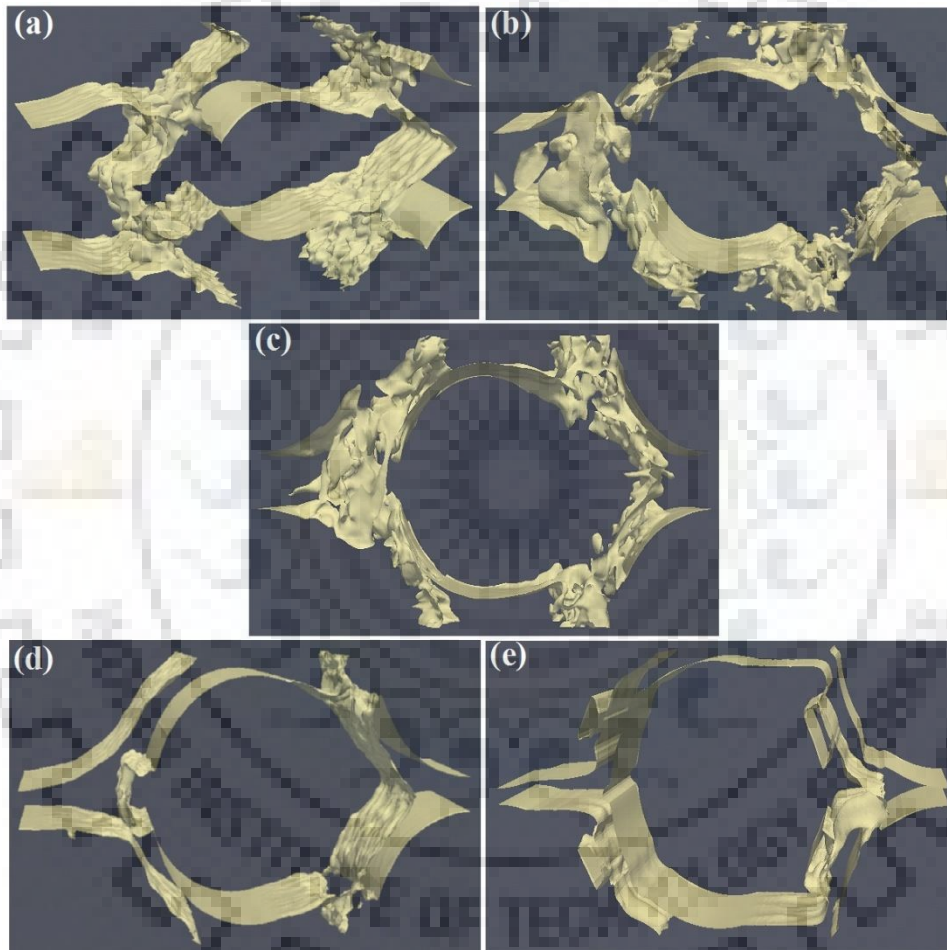


Fig. 6.27: 3D perspective view of mean velocity iso-surfaces of different porous enclosures for LES computations at $Re_D=10000$ (ϕ : (a) 0.8; (b) 0.6; (c) 0.5; (d) 0.4; (e) 0.3).

Fig. 6.27 also reveals a significantly larger number of small-scale structures generated at the corner region where solid fluid interactions were intense. The perspective view of the iso-surface at the wake region (front and back surfaces of the cylinders) shows the break-down of the streamwise structure and the formation of small vortex structures. A cloud or mushroom-shaped fluid structure can be observed in the wake region due to the presence of the streamwise vortices within the shear layer. As the porosity gradually decreased, the available

flow path became narrower, pore space mostly occupied by the solid surfaces. Thus fluid volume within the porous matrix decreased and the size and volume of the cloud structure got reduced.

6.7.3. Mean flow statistics

The velocity distributions predicted by the LES and RANS models are compared in Fig. 6.25 at the selected x-center ($x = 1.5$) and y-center ($y = 0.5$) locations. The spanwise mean velocities were normalized by the approaching free stream velocity (U_∞) and are shown in Fig. 6.28. The distribution of the streamwise component of the mean velocity along the wake center line provides information about the recovery of the streamwise mean velocity in the REV downstream section as well as the wake zone generated at the front face of the cylindrical particles. The simulation results showed that the LES and RANS low Re $k-\varepsilon$ models predict similar mean velocity profiles at both the specified locations. The standard $k-\varepsilon$ model predictions of mean velocity are underestimated and cannot capture the structure of the wake region in front of the cylinder as compared to low Re $k-\varepsilon$ and LES predictions. The discrepancy might be attributed to the insensitivity of the standard $k-\varepsilon$ model to streamline curvature.

The flow field obtained from LES is not smooth and exhibits random fluctuations as compared to RANS flow fields (Fig. 6.25(a-d)) and low Re - $k-\varepsilon$ model damps the normal turbulent fluctuations which are over-estimated. Both these models show excessively smooth fluid structures near the wall. The high frequency oscillations, which are characteristics of turbulent flows field at solid surface due to solid-fluid interactions, were being well captured by LES simulations. The streamwise mean velocity profile obtained from LES calculations were oscillatory in nature as compared to RANS calculations. The contours of velocity and mean velocity profile (Fig. 6.29) reveal this fact. There was a good agreement between the predictions of RANS and LES in the streamwise velocity profile, specifically at the upstream surface of the cylinder at higher porosity ($\phi = 0.8, 0.6, 0.5$) and the deviation was observed at the downstream of the cylinder where velocity fluctuations were more prominent due to formation of eddies. The turbulent flow oscillations at the downstream of the cylinder increased with an increase in the porosity due to significant solid-fluid interactions with an increase in the porous space.

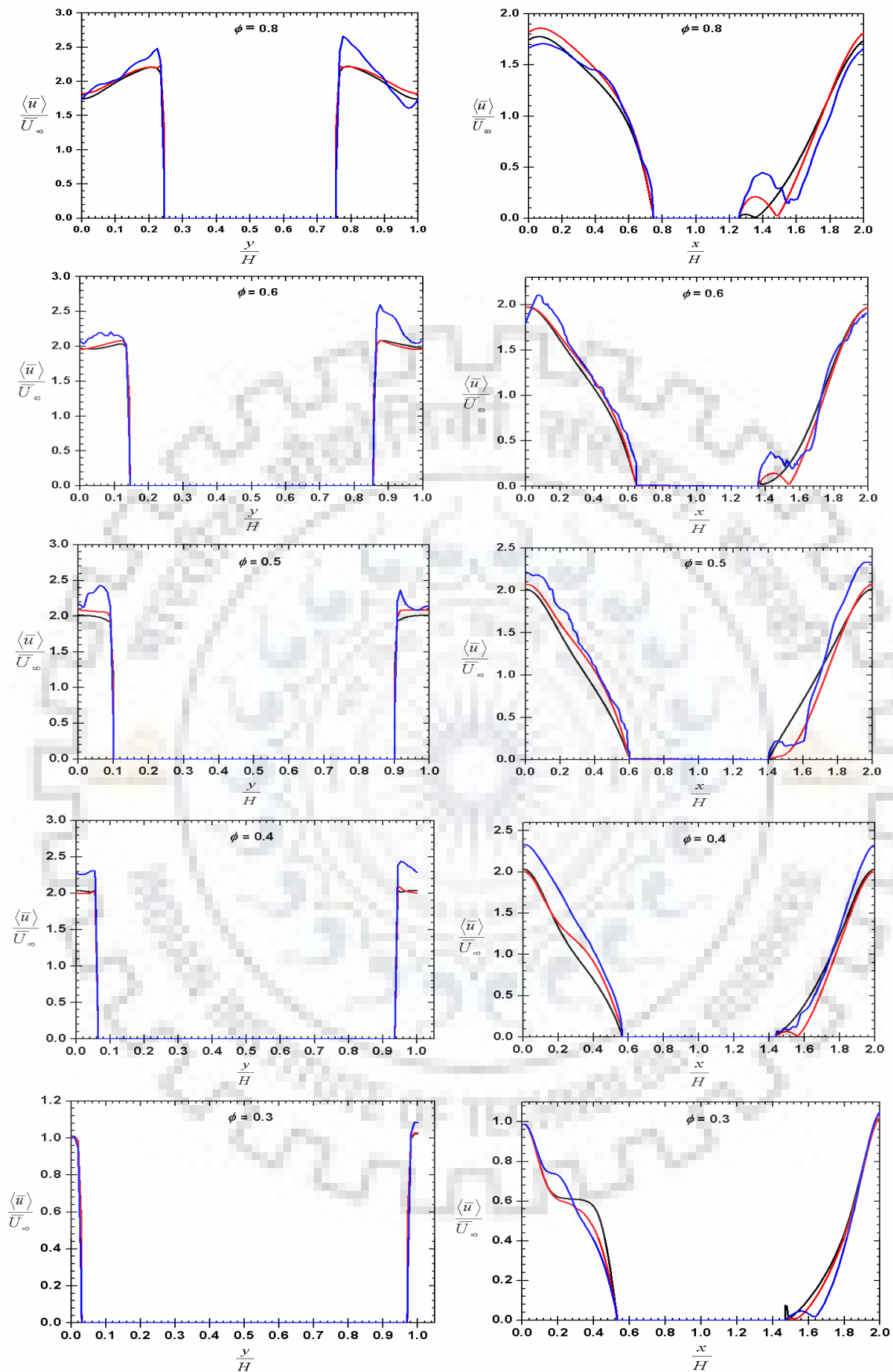


Fig. 6.28: Comparison of normalized streamwise mean velocity profiles predicted using different turbulence models at centerlines in x- and y- directions, respectively.

LES (—); low Re - k - ϵ (---); Std. k - ϵ (—).

The profiles of the mean velocity are found to be affected by the medium porosity. The LES predictions showed that most of the fluctuations were due to an oscillation of the flow around the cylinder caused by the generation of small scale eddies near the solid surface. The overall agreement of the mean velocity between the low Re k - ε , and the LES seemed to be satisfactory over the entire range of ϕ , which further validated the simulation results.

6.7.4. Computation of macroscopic turbulent kinetic energy and dissipation rate

LES and RANS simulated results are shown in Fig. 6.29 for different values of ϕ . It is found that the normalized $\langle k \rangle^f$ increases with an increase in Re_D and a decrease in ϕ . For $\phi < 0.6$, the increment is greater than unity even at a lower Re_D . As the porosity decreases at a certain Re_D , the fluid flow passage gets reduced leading to an increase in the local fluid velocity gradient. This dictates the rate at which the mean flow mechanical energy transferred into the turbulent kinetic energy. This causes the larger production rate of k within the REV. As a consequence, the normalized kinetic energy ($\langle k \rangle^f$) increases. It is also found that the turbulence gets intensified at a comparatively low Re_D , especially for low porosity.

It is observed that the LES and low Re k - ε models show similar logarithmic patterns as compared to standard k - ε model, which shows a flat increment with Re_D . The relative deviation of low Re k - ε and standard k - ε model predictions with respect to LES predictions are presented in Fig. 6.29. The low Re k - ε , and the LES predictions agreed reasonably well as the mean relative deviation ($\delta x \approx 0.15$) was less than that of standard k - ε model predictions ($\delta x \approx 0.30$). The deviation seemed to be significantly reduced ($\delta x < 0.09$) at higher Re_D ($Re_D > 10^3$) between low Re k - ε and LES predictions. But the standard k - ε model under predicted the normalized $\langle k \rangle^f$ for all values of ϕ . The normalized $\langle k \rangle^f$ for LES and low Re - k - ε model agreed significantly well in the higher Re_D region ($> 10^3$).

The variation of turbulent kinetic energy with medium porosity is shown in Fig. 6.30(a). The simulated normalized $\langle k \rangle^f$ predicted by LES and low Re k - ε model showed good agreement for $\phi < 0.8$. However, the results deviated from each other at lower porosity ($\phi=0.8$). The normalized dissipation rate $\langle \varepsilon \rangle^f$ for different porosities is shown in Fig. 6.30(b). At higher values of ϕ ($\phi = 0.6$ and 0.8) the predicted values of normalized $\langle \varepsilon \rangle^f$ by all the three different models followed similar trends. However, the results deviated at lower porosity ($\phi \leq 0.5$). Even at lower porosity, the low Re - k - ε results were closer to LES results.

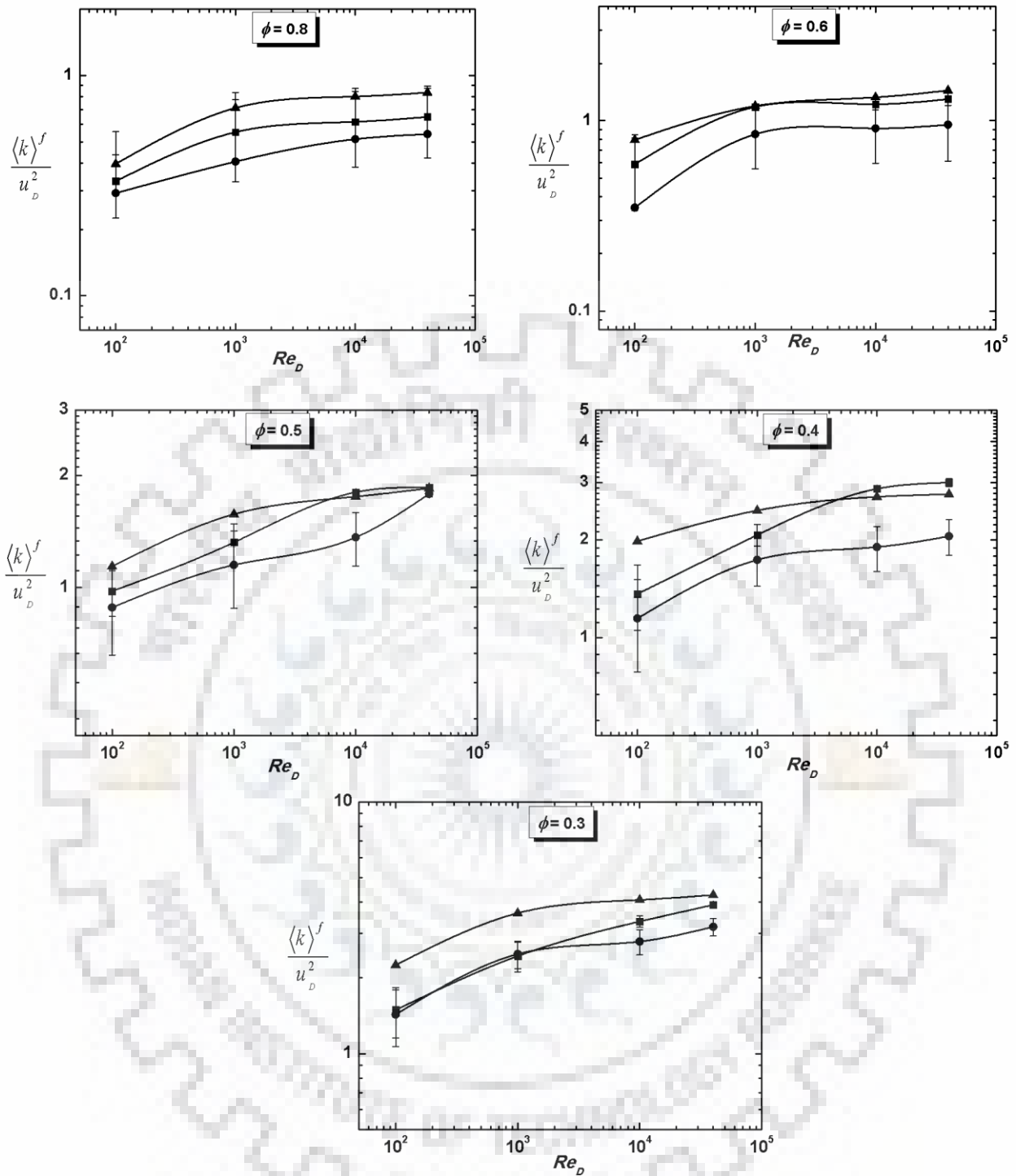


Fig. 6.29: Normalized turbulent kinetic energy versus Re_D at different porosities ($\phi = 0.3, 0.4, 0.5, 0.6,$ and 0.8) using various turbulence models.

LES (—▲—); Low Re $k-\varepsilon$ (—■—); Std $k-\varepsilon$ (—●—).

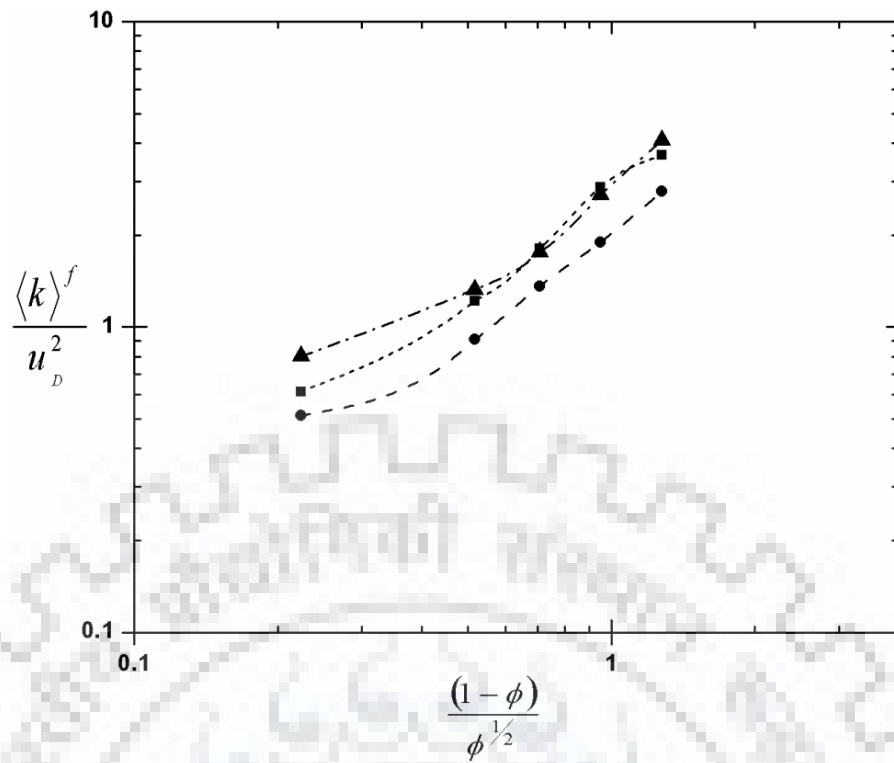


Fig. 6.30(a): Normalized turbulent kinetic energy versus $(1-\phi)/\phi^{1/2}$ using different turbulence models. LES (\blacktriangle); Low Re $k-\varepsilon$ (\blacksquare); Std $k-\varepsilon$ (\bullet).

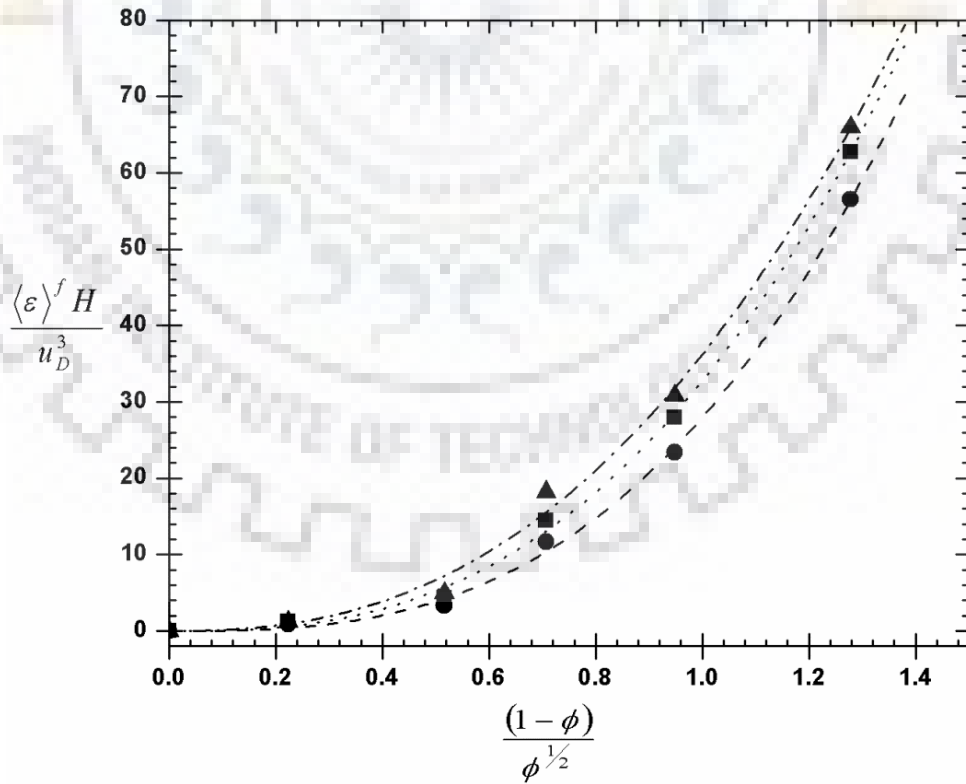


Fig. 6.30(b): Normalized energy dissipation versus $(1-\phi)/\phi^{1/2}$ using different turbulence models. LES (\blacktriangle); Low Re $k-\varepsilon$ (\blacksquare); Std $k-\varepsilon$ (\bullet).

6.7.5. Computation of pressure drop across the REV

The pressure distribution within the porous matrix is significantly influenced by the pore diameter. The pressure contours predicted by LES and RANS low Re $k-\varepsilon$ model are shown in Figs. 6.25(a-d). It is observed that the pressure magnitude is high at the upstream face of the cylinder near to the stagnation point and at the downstream corner section. The macroscopic pressure gradient across the porous media as calculated using RANS low Re $k-\varepsilon$, and LES methods are non-dimensionalized and are presented as a function of Re_D and ϕ in Fig. 6.31(a-b). It is seen that the dimensionless pressure gradient (DPG) increases with an increase in Re_D and a decrease in ϕ . As ϕ decreases, the effective flow area within the porous media decreases, and the free fluid flow passage gets constricted, thereby causing an increase in DPG. The variation of DPG with Re_D for $\phi = 0.8$ is shown in Fig. 6.31(a). The RANS and LES results show good agreement with each other at higher Re_D ($\geq 10^3$). However, the results show deviation at lower Re_D ($Re_D = 100$).

The pressure drop across the porous REV can be estimated by the Ergun's equation. The Ergun's equation including the Forchheimer drag in the porous matrix with pore diameter being D_p , is given as:

$$-\frac{d\langle p \rangle^f}{dx} \left[\frac{D_p}{\rho u_D^2} \right] = \frac{150(1-\phi)^2}{\phi} \left(\frac{\nu}{u_D D_p} \right) + 1.75 \frac{1-\phi}{\phi^3} \quad (6.48)$$

The first term of the right hand side of Eq. (6.48) accounts for low velocity situations (creeping flow) and the second term accounts for the effect of turbulence and/or inertia, which depends on the property of porous media. At higher Re_D , the viscous term becomes insignificant and the fluid inertial effect dominates. Therefore, at $Re_D > 3000$, Eq. (6.48) is reduced to

$$-\frac{d\langle p \rangle^f}{dx} \left[\frac{D_p}{\rho u_D^2} \right] = 1.75 \left(\frac{1-\phi}{\phi^3} \right) \quad (6.49)$$

The variation of DPG with porosity, ϕ is shown as a linear relationship in Fig. 6.31(b). The best-fit value of the coefficient is found to be 2.2, instead of 1.75, as envisaged in Eq. (6.49). The numerical results of the LES and RANS models agree well with the extended Forchheimer-Darcy's law within the porosity range, $0.8 \leq \phi \leq 0.5$, but at lower porosity, large deviations are observed.

The DPG relevant to the present porous media configuration can be fairly described by a power-law formulation. A correlation for DPG with medium porosity is proposed by re-scaling the porosity as $(1-\phi)/\phi$, as follows:

$$-\frac{d\langle p \rangle^f}{dx} \left[\frac{D_p}{\rho u_D^2} \right] = 4.662 \left(\frac{1-\phi}{\phi} \right)^{2.254} \quad (6.50)$$

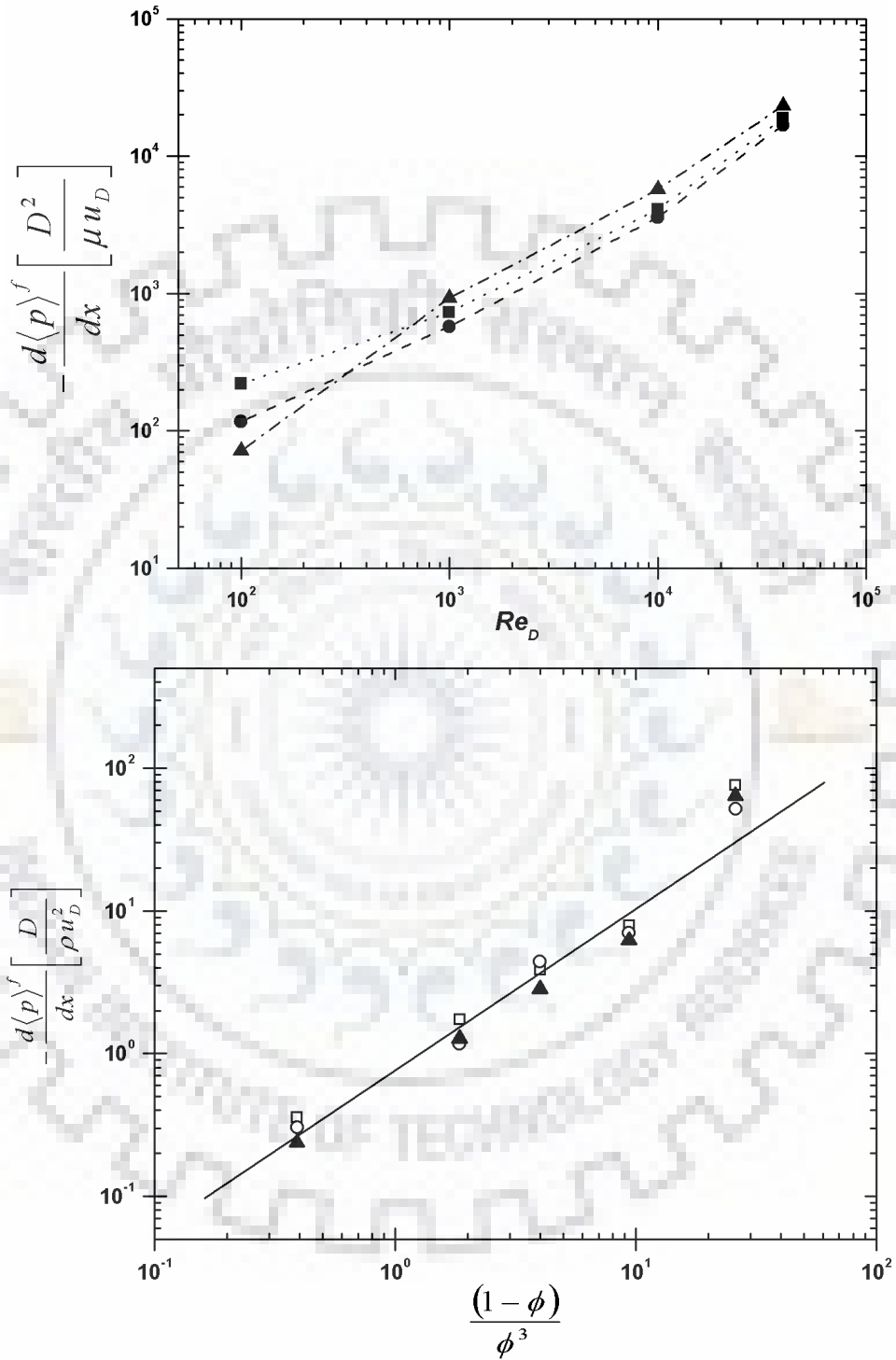


Fig. 6.31: Dimensionless macroscopic pressure gradient versus (a) Re_D , (LES (—▲—); Low Re $k-\epsilon$ (—□—); Std $k-\epsilon$ (—○—)) and (b) $(1-\phi)/\phi^3$ (LES (—▲—); Low Re $k-\epsilon$ (—□—); Std $k-\epsilon$ (—○—)).

6.7.6. Computation of permeability and Darcy-Forchheimer co-relation for porous REV

The permeability appearing in the porous *REV* was estimated at low Re_D ($Re_D = 10$) in the Darcy flow regime. Flow streamlines for different porosities at $Re_D=10$ are shown in Fig. 6.32. A fully developed steady laminar flow was observed within the *REV*. The streamlines are seen to start from the inlet section, travel as a continuum across the *REV* and finish at the outlet section. The flow is found to be symmetric about the center x-axis with no eddies or recirculation zone being observed. This signifies that the flow is fully developed steady laminar flow.

For permeability calculation, the N-S equation was solved inside the *REV* to determine the microscopic flow quantities (Darcy velocity and pressure gradient). The microscopic results are converted into macroscopic quantities using the volume average operator within the *REV*:

$$\begin{aligned} \nabla \langle P \rangle^f &= \nabla \left[\frac{1}{V_f} \int_{V_f} P dV \right] \\ &= \frac{1}{\nabla V_f} \int_{V_f} [P(x + 2H, y) - P(x, y)] dV \end{aligned} \quad (6.50)$$

$$\begin{aligned} u_D &= \phi \langle \bar{u} \rangle^f \\ \langle \bar{u} \rangle^f &= \frac{1}{V_f} \int_{V_f} u dV \end{aligned} \quad (6.51)$$

The permeability within the *REV* is calculated using the Darcy's law as given below.

$$-\frac{\nabla \langle P \rangle^f}{L} = \frac{u_D \mu}{K} \quad (6.52)$$

The estimated permeability is compared with the permeability as calculated using the equation proposed by Kuwahara et al. (1998):

$$K = \frac{\phi^3}{144(1 - \phi)^2} D^2 \quad (6.53)$$

The permeability as estimated for different values of ϕ are shown in Table 6.1. It is seen that the permeability of the porous *REV* decreases with a decrease in the medium porosity. The estimated values agree well with the values calculated using Eq. (6.52), however, the estimated values deviate from the calculated results at lower porosities ($\phi \leq 0.4$).

Table 6.1: Computed permeability, K for different porosity at $Re_D = 10$.

Particle size, D_p (m)	Porosity, ϕ	$K_{Simulated}$ (m^2)	$K_{estimated}$ (Eq. 36) (m^2)
0.51	0.8	2.51×10^{-2}	2.31×10^{-2}
0.71	0.6	4.49×10^{-3}	4.73×10^{-3}
0.80	0.5	1.26×10^{-3}	2.22×10^{-3}
0.87	0.4	4.16×10^{-4}	9.34×10^{-4}
0.94	0.3	1.41×10^{-4}	3.38×10^{-4}

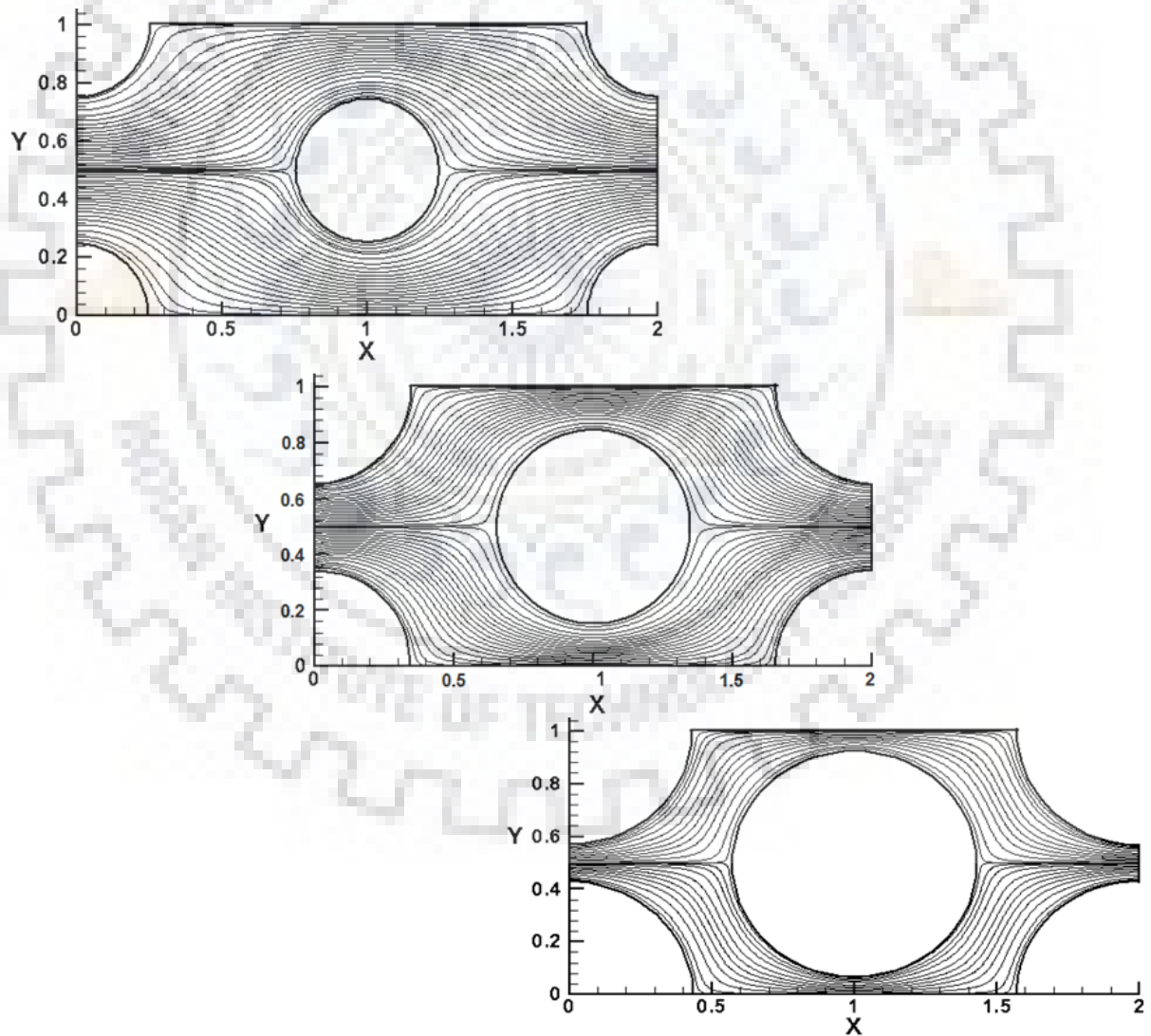


Fig. 6.32: Streamlines in porous REV at $Re_D = 10$ at different porosities ($\phi = 0.8, 0.6$ and 0.4 from top to bottom diagonally).

The porous matrix is characterized by the permeability and porosity. There is no general correlation relating permeability with porosity. A relation can, however, be obtained using Kozney-Carman equation and the Darcy's law for the REV as given below :

$$\frac{K}{H^2} = \frac{1}{141.3} \frac{\phi^3}{(1-\phi)} \quad (6.54)$$

The dimensionless permeability is plotted against $\phi^3/(1-\phi)$, as shown in Fig. 6.33(a). The best-fit value of the Kozney constant using Eq. (6.54) with the experimental data is 111.11, which is lower than 141.3. This disagreement is ascribed to the fact that the Kozney constant in Kozney-Carman equation is porosity-dependent (Kaviany, 1991). Therefore, the simulated permeability results are plotted as a function of ϕ , as shown in Fig. 6.33(b). The functional dependency of the medium permeability with porosity for the present REV can be represented by the following equation:

$$\frac{K}{H^2} = 0.097 \phi^{6.057} \quad (6.55)$$

The best numerical fit ($R^2 = 0.999$) of the simulated data with Eq. (6.55) represents the permeability over the entire range of porosity.

At high Re_D , the fluid inertial effects become significant. In order to capture the influence of inertia during the flow through porous media, the Darcy's law can be extended with a power law term, which is termed as Darcy-Forchheimer equation. The Darcy-Forchheimer equation for the flow through isotropic and homogeneous porous media is given as follows (Papathanasiou et al., 2001):

$$-\frac{K}{\mu} \cdot \frac{\nabla \langle P \rangle^f}{L} = \bar{u}_D + \beta \bar{u}_D^m \quad (6.56)$$

This equation models the viscous and inertial behaviour of flow through porous media describing the macroscopic pressure gradient along the REV. The first term on the right hand side is for viscous behaviour and the second term is for Forchheimer correction for inertial effect. Eq. (6.56) is non-dimensionalized with the square root of permeability and the square of Darcy velocity. Hence, the empirical Darcy-Forchheimer equation can be expressed in the form of a non-dimensional modified friction factor ($f_{\sqrt{K}}$), and a modified Reynolds number ($Re_{\sqrt{K}}$) as shown below:

$$\left. \begin{aligned} f_{\sqrt{K}} &\equiv -\left(\frac{\sqrt{K}}{\rho \bar{u}_D^2}\right) \frac{\nabla \langle P \rangle^f}{L} = \frac{\nu}{\bar{u}_D \sqrt{K}} + \frac{\beta \nu}{\sqrt{K}} \\ f_{\sqrt{K}} &= \frac{1}{\text{Re}_{\sqrt{K}}} + F \end{aligned} \right\} \quad (6.57)$$

$$\text{where, } \text{Re}_{\sqrt{K}} = \frac{\bar{u}_D \sqrt{K}}{\nu} \quad \text{and } F = \frac{\beta \nu}{\sqrt{K}}$$

The numerically determined medium permeability from macroscopic simulation results have been used to calculate the $f_{\sqrt{K}}$ and $\text{Re}_{\sqrt{K}}$. The friction factor is computed for both laminar flow ($\text{Re}_{\sqrt{K}} = 0.7$) and the fully developed turbulent flow ($\text{Re}_{\sqrt{K}} = 5 \times 10^3$), within the REV. The Darcy-Forchheimer plot for different turbulence models is shown in Fig. 6.34. All the three turbulence models show asymptotic behaviour. The modified friction factor decreases gradually with an increase in the modified Reynolds number. A linear variation of friction factor with modified $\text{Re}_{\sqrt{K}}$, up to $\text{Re}_{\sqrt{K}} \leq 10^1$, is observed within the Darcy flow regime. Thereafter, $f_{\sqrt{K}}$ shows a non-linear relation with $\text{Re}_{\sqrt{K}}$. This indicates the existence of inertial effect. The results of the LES and low Re k - ε show a similar trend for the variation of the friction factor with $\text{Re}_{\sqrt{K}}$ as compared to the standard k - ε model. However, the results of the low Re k - ε model are marginally higher than those obtained from the LES predictions. In general, it may be concluded that the present simulation results showed very good agreement with the Darcy-Forchheimer relationship.

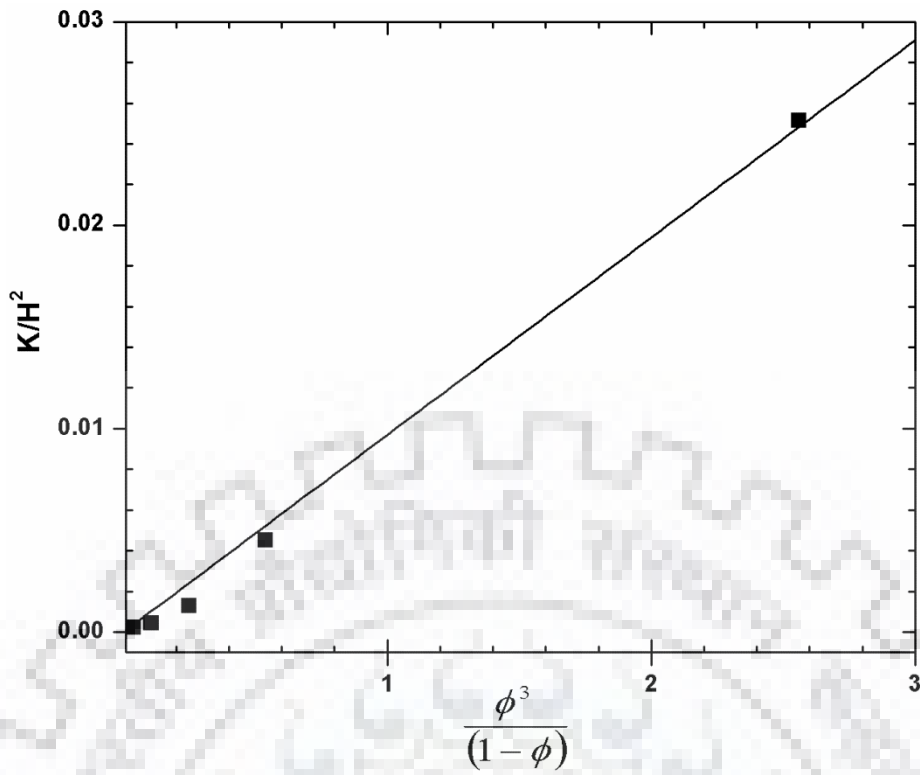


Fig. 6.33(a): Numerically computed permeability for the porous REV fitted to Kozney-Carmen equation.

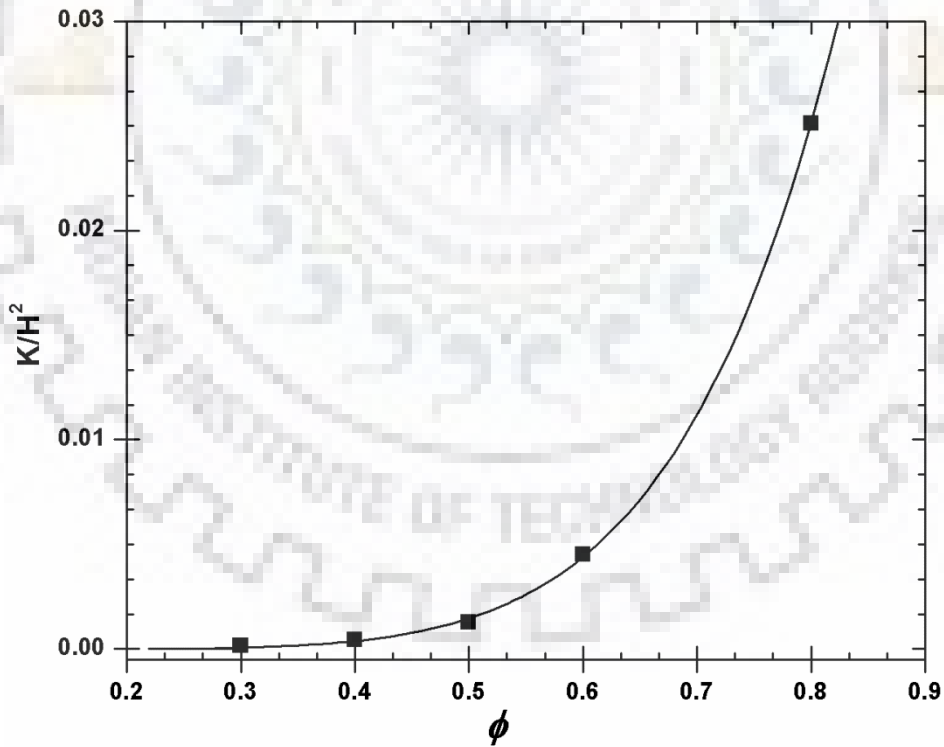


Fig. 6.33(b): Numerically computed permeability as a function of porosity fitted to the proposed correlation (Eq. 42).

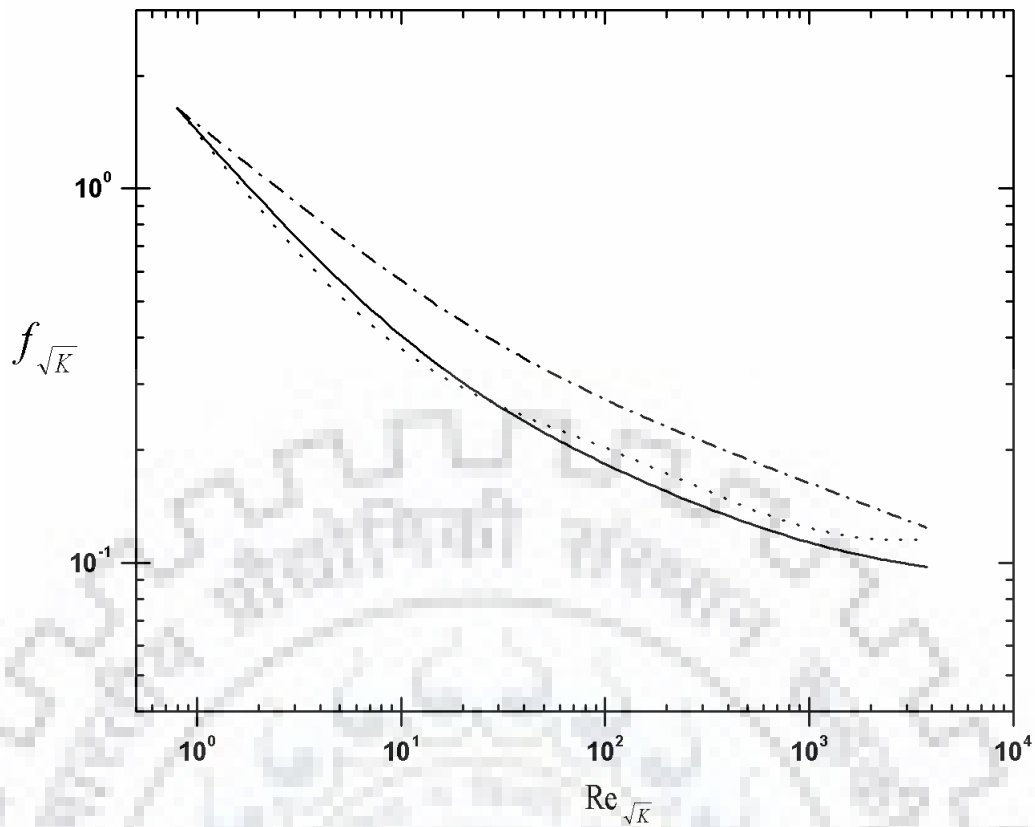


Fig. 6.34: Darcy-Forchheimer plot in terms of modified friction factor and $Re_{\sqrt{K}}$ for different turbulence models. LES (—); Low Re $k-\varepsilon$ (-·-·-); Std. $k-\varepsilon$ (·····).

6.7.7. Effect of Medium Morphology on Porous Media Flow

The morphology of the medium plays an important role in the modeling of flow through porous media. In the present study, a morphology-based closer was used for mathematical modeling of flow through porous media by resolving the microscopic flow equations within the computational domain, regardless of the porous structure. For that, a characterization of the medium topology is necessary in order to reveal the microscopic flow field. In a previous study (array of square cylinder), the porous media was modeled as a specially periodic array of square cylinders. In the present study, the porous media is modeled as a periodic array of circular cylinders. The computations of flow behavior for the two types of porous structures are compared in Fig.6.35.

From the Fig. 6.36, it is observed that the shape of the porous media significantly alters the flow pattern inside the porous matrix. The difference in the flow pattern becomes prominent in the computed streamline spectra and the velocity contour of the two different porous matrices (Fig. 6.35). The flow separates at the front surface and corner walls of the square cylinder. A large separation region develops behind the square cylinder which interacts with the vortex. Some predominant wake regions with vortex are traced at the downstream face and the top and bottom surfaces of the square cylinder. The flow field for

circular cylinders are different. Fluid propagates smoothly across the circular cylinder. Flow separation is observed behind the cylinder with the formation of relatively small wake region. The separation region behind the square media is wider and spread than the circular media. The size of the vortices are relatively small as compared to square media. A similar difference is observed for the case of velocity contours. There is a similarity between the isobar spectra for both kinds of porous media- one of square cylinders and the other of circular cylinders. Pressure gradient also varies in a similar fashion across both the *REV*s. But the turbulent kinetic energy spectra are different for the two *REV*s. For the square media, the kinetic energy is exclusively generated at the corner wall and the upper and lower surfaces of the cylinder. In the case of circular media, the kinetic energy spectra are produced at the front surface and the downstream corner surface of the cylinders. The turbulence swept around the front and the upper and lower surfaces of the square media is more than that for the circular media, leading to a longer flow separation region behind the cylinder.

Morphology of the porous media can be characterized by evaluating a characteristic macroscopic model constant, C_k . For macroscopic fully developed flow in isotropic porous media, C_k is expressed by the following non-dimensional relationship as shown in Eq. (6.47). The k_ϕ - ε_ϕ plot was constructed by calculating the corresponding limiting values of k_ϕ and ε_ϕ for different porosities and Re_D used in this study, and is shown in Fig. 6.36. The value of C_k was found to be 0.32 from the slope of the best-fitted line ($R^2 = 0.971$) for the 3D porous matrix comprising circular cylinders. It should be noted that the value of C_k is unique for a particular shape of the porous media. The macroscopic turbulent quantities of our earlier simulation results for 2D square media are compared with the simulation results of the present 3D circular media. For square media, the C_k value was 0.29 as compared to 0.32 obtained for 3D circular cylindrical media. Thus, the morphology of the porous media significantly influences the macroscopic model constant.

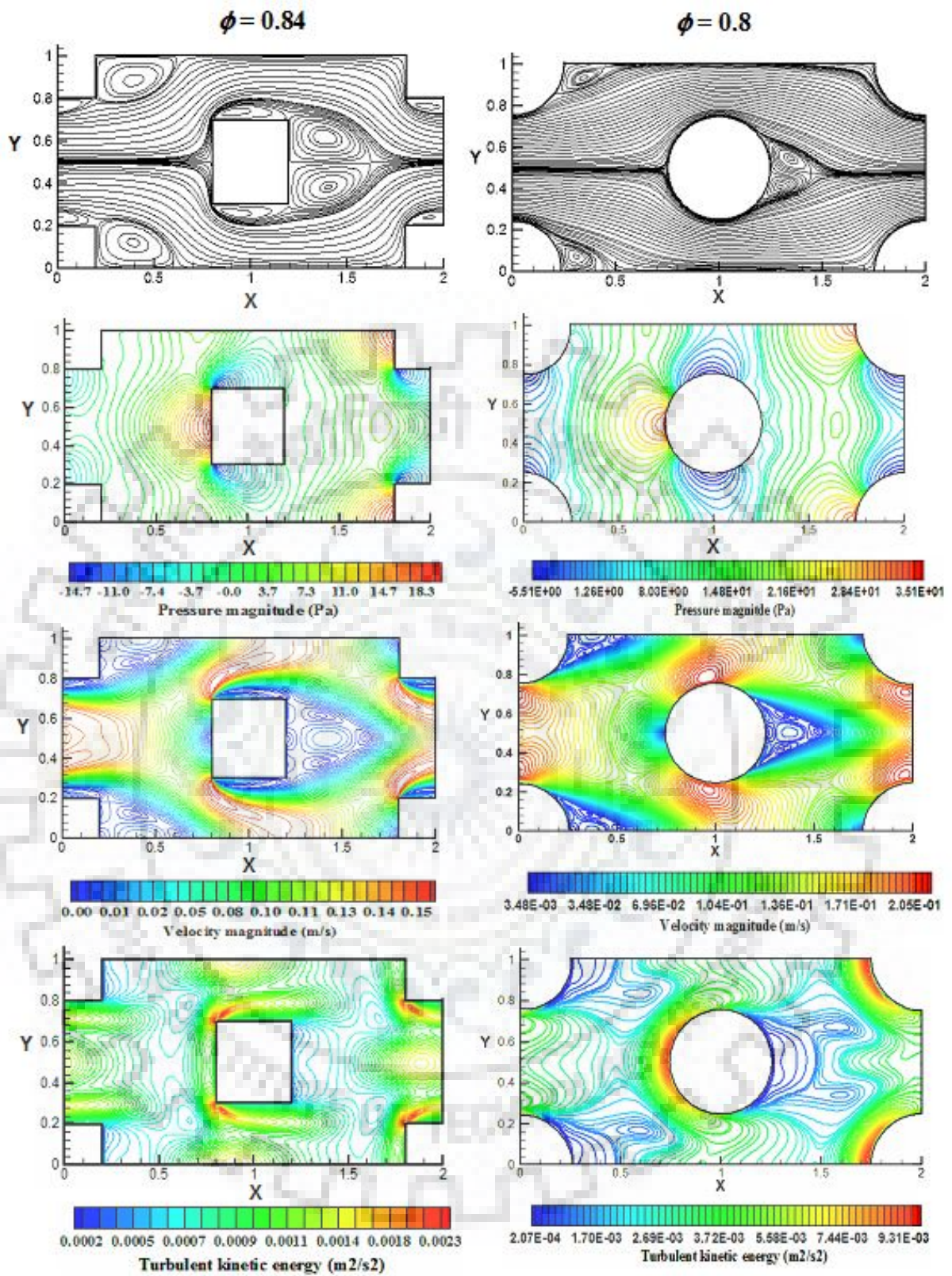


Fig. 6.35: Simulated microscopic results of different porous matrix at $Re_D = 40000$.

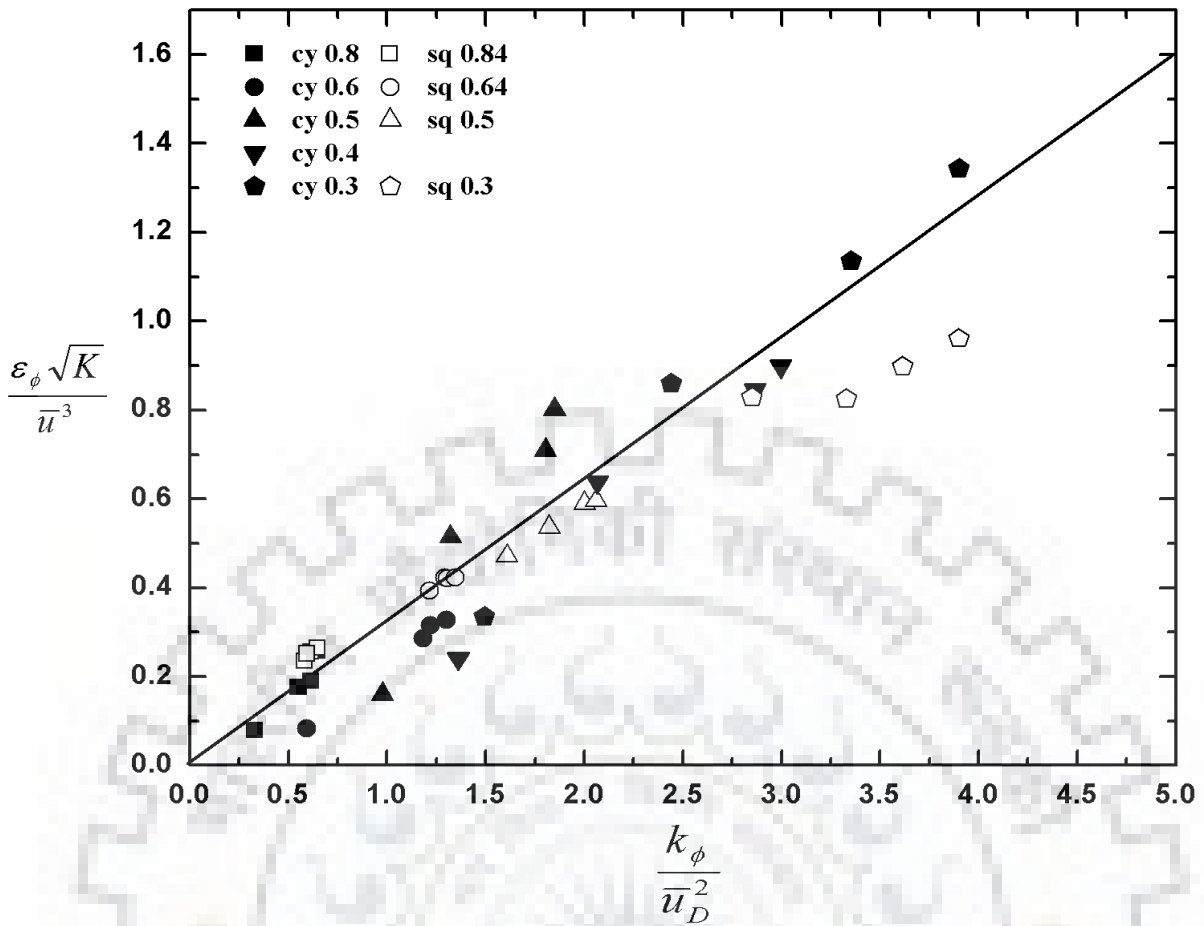


Fig. 6.36: Normalized k_ϕ - ϵ_ϕ plot for different media morphology.

(Filled legend: 3D circular cylinder; Unfilled legend: 2D square cylinder.)

CHAPTER 7

CONCLUSIONS AND RECOMMENDATIONS

7.1 CONCLUSIONS

On the basis of work carried out in this thesis for the preparation and characterization, in terms of stability and rheology, of emulsions and Newtonian and emulsion flow through porous media, following conclusions were made:

7.1.1 Emulsion Formation, Stability and Characterizations

A statistical modelling and optimization of process parameters for emulsification and characterization was carried out using an integrated modelling approach of GA–BPANN coupled with RSM–BBD model. BBD model was developed by using data of 29 experimental runs and a hybrid GA (GA-BPANN coupled with RSM-BBD) model was developed by using a set of 120 experimental data sets. The emulsion stability was assessed by creaming (CI) and emulsification (EI) indexes. Response surface plots provided an efficient way of visualizing the parametric interactions with emulsion stability and the resulting model explained the effects of process parameters on the emulsion stability. Surface plots suggested that the oil and surfactant concentration and stirring time influenced the emulsion stability significantly. The following conclusions were made:

- The optimized conditions for maximum emulsion stability ($ESI_{24} = 0.866$) predicted by the hybrid ANN-GA model coupled with RSM-BBD were: oil concentration – 50% (v/v), surfactant concentration – 2% (w/v), stirring speed – 5700 rpm and stirring time – 5 min. The percentage error between the model predictions and the experimental values was found to be approximately $\pm 5\%$, thereby showing the advantage of the multi objective hybrid ANN-GA technique over other optimization methods.
- The stability of an o/w emulsion increases with an increase in oil volume fraction (10-80% v/v).
- The average size of the emulsion droplets gradually decreases from 1.72 to 0.712 μm with an increase in the oil concentration from 10% to 80% (v/v).
- Both zeta potential as well as electrophoretic mobility increases with an increase in
 - oil volume fraction, and suggested that more and more oil droplets get attached to the interface and enhance the emulsion stability.
 - pH of the medium, and prevent coalescence phenomena

- The interfacial tension of o/w emulsions gradually decreases as the oil volume fraction increases.
- Stability of o/w emulsion increases with an increase in pH of the bulk medium and with decrease in droplet size.

7.1.2. Effect of Oil Volume Fraction, Surfactant Concentration, pH and Temperature on Emulsion Rheology

The rheological behaviour of five sets of o/w emulsions having varying dispersed phase (oil) volume fractions (10–80%) at different temperatures (25–50 °C), surfactant (SDBS) concentrations (0.5–2%, w/v) and four shear rates (20 s⁻¹, 40 s⁻¹, 80 s⁻¹ and 100 s⁻¹) was studied. The oil volume fraction and temperature dependency of rheological characteristics were determined for different types of o/w emulsions (dilute, semi-dilute, concentrated and highly concentrated). The rheological behaviour of emulsions was modeled using a master-curve approach. The effect of temperature on emulsion rheology was described by using the Arrhenius model, on the apparent viscosity at a constant shear rate. It was concluded that:

- The emulsion viscosity decreases with an increase in temperature, and the pseudoplasticity increases with an increase in oil volume fraction.
- The emulsion viscosity and pseudoplasticity increases with an increase in oil volume fraction of the emulsions with 1% (w/v) SDBS.
- The power law model indicated that all five sets of emulsions have pseudoplastic ($n < 1$) characteristics. The analysis of the apparent viscosity curve for highly concentrated o/w emulsions (set 4 and set 5) showed highly shear thinning behaviour, due to the high oil concentration (internal phase) in the emulsions contributing to the lubricating effect between the oil droplets.
- The magnitude of activation energy increases with an increase in oil volume fraction. Highly concentrated o/w emulsions were more sensitive to temperature due to high shear thinning characteristics as compared to other sets of emulsions.
- A correlation was proposed to describe the combined effects of temperature and oil volume fraction of emulsions which fitted well to the experimental data ($R^2 \sim 0.9739$).
- As the surfactant concentrations increases, the apparent viscosity of the emulsions also increases, with a yield stress at higher oil fractions. Herschel-Bulkley model fitted the rheological data for 2% (w/v) surfactant concentration very well as compared to Casson model.
- The rheological behaviour of o/w emulsions (different pH and temperature at fixed oil volume fraction 30% v/v) was tested by Ostwald-de Waele, Sisko Cross and Carreau models. The four parameter Cross and Carreau model described the emulsion

behaviour reasonably well over the entire shear rate range (10^{-3} – 10^3 s^{-1}) as compared to other two models.

- The electro-viscous effect plays a significant role in increasing the viscosity of emulsions. The magnitude of the electro-viscous effect is proportional to ξ^2 . Thus, this effect can cause a large increase in the viscosity of emulsions mainly for the case of pH 12 and 10 as compared to emulsion with pH8 to pH2.
- The shear thinning property and the pseudoplasticity of the emulsions decreased with a decrease in pH and an increase in temperature with a corresponding larger average droplet size and a wider DSD.
- The dynamic moduli (G' and G'') decreased with an increase in temperature and a decrease in pH.
- The steady shear viscosity of o/w emulsions is more sensitive to temperature than the complex viscosity ($E_\eta > E_{\eta^*}$).
- The viscoelastic properties (G' , G'' , η^* and $\tan\delta$) were found to be a strong function of angular frequency and exhibited a characteristic cross over frequency (ω_c). For $\omega < \omega_c$, the viscous response is predominating ($G'' > G'$) and for $\omega > \omega_c$, the elastic response ($G' > G''$) is predominating. Thus o/w emulsion can be characterized as a flocculated structured liquid or weak gel.
- The values of the oscillatory shear parameters and the steady shear parameters revealed that the o/w emulsions do not obey the Cox–Merz rule as $\eta^* > \eta_\alpha$ over the range of steady shear rate ($10^{-04} \leq \dot{\gamma} \leq 10^{03}$) and angular frequency ($10^0 \leq \omega \leq 10^2$) studied.

7.1.3 Newtonian Fluid Flow through Porous Media

Experimental investigated the rise in nonlinearity in Darcy law to describe the evolution of inertial effects in a porous medium. The present study highlights the demarcation limit of the various flow regimes (pre-Darcy, Darcy, transition and non-Darcy) which enable accurate determination of the permeability (K) and form drag coefficient (F_D) for different types of porous media. It was concluded that:

- The first pre-Darcy's flow regime represents the surface-interactive flow which is strongly dependent on the porous media and the flowing fluid.
- The Darcy regime was characterized by purely viscous effect and governed by local pore structure.
- The weak transition and inertial regimes were characterized by the fact that inertial effects are not negligible compared to viscous effects.
- The inertial effects lead to the formation of eddies in the pore constrictions depending on the Reynolds number. The presence of these eddies reduces the actual flow area

with an increase in total viscous dissipation. The maximum of energy dissipation occurs in the regions of small flow section (pore constrictions) and mainly due to the friction of solid-fluid interactions at the solid walls.

- The flow changes from weak inertial regime to quadratic Forchheimer regime at critical Re in between 5 to 10.
- The microscopic inertial effect is the governing factor which leads to the transition from the Darcy to non-Darcy flow regimes in porous media.
- The detailed microscopic pore hydrodynamics in the form of flow streamlines and velocity contours were reported over the Darcy and non-Darcy flow regimes, i.e. $0.02 \leq Re_D \leq 30$.
- The flow structure evolution significantly captures well which correspond to Darcy's regime, the transition regime (weak inertia) and the strong inertia non-Darcy regime.

7.1.4 Emulsion Flow through Porous Media

Emulsion (o/w) flow behaviour was investigated with different oil volume fraction (10-80% v/v) for different porous media, such as packed bed with four different sizes of glass beads (PM1, PM2, PM3 and PM4). The rheological properties of emulsions flowing through the porous media were studied on the basis of shear stress ($\bar{\tau}_w$) versus shear rate ($\delta u_s/R_h$) relationship. The Permeability reduction behaviour of porous media was investigated by observing the change in pressure drop across the core holder as a function of no of pore volume of emulsion injected. Following conclusions were made:

- Emulsion volume fraction significantly influences the porous bed pressure drop. Pressure drop data ($d\langle\bar{P}\rangle/dL$) across the porous bed for all sets of o/w emulsions increases with increase in emulsion volume fraction, increases with decrease in particle diameter (glass beads) and an increase in medium porosity.
- Modified friction factor for emulsion with different volume fraction decrease with an increase in modified Reynolds number for different porous media.
- The shear stress increases with an increase in shear rate and volume fraction during percolation of emulsions through the porous bed.
- The effective viscosity of the emulsion for porous bed of different particle diameter decreases with an increase in shear rate.
- Resistance factor (RF) for different porous bed increases with an increase in emulsion volume fraction and decreases with an increase in emulsion injection rate.
- The emulsion quality/volume fraction significantly influences the pressure drop along the sand pack core holder.

- The pressure drop across the core holder increases with emulsion injection flow rate for all three different sand pack core holders (S-A, S-B, and S-C) studied in the present work. Pressure drop also increases with an increase in emulsion volume fraction due to the increase in emulsion viscosity.
- The pressure drop for small particle (S-A) is more as compared to large particles (S-B and S-C).
- The permeability ratio across the core holder decreases with an increase in pore volume (PV) of emulsion injected.
- Emulsion volume fraction and number of PV injected significantly alter the medium permeability.
- The Permeability reduction across the core holder decreases largely with an increase in emulsion volume fraction and also with an increase in the number of PV injected.

7.1.5 Modeling of Fluid Flow through an Isotropic Porous Media

Porous media was modeled by *representative element volume* (REV) approach using an infinite spatial periodic array of both square and circular cylinders. A detailed numerical study was performed for different porosities ($0.3 \leq \phi \leq 0.8$) and particle Reynolds numbers ($10 \leq Re_D \leq 40000$) on pore hydrodynamics, pressure gradient across the modelled porous media and turbulence statistics. It was concluded that:

7.1.5.1 Array of square cylinder:

- The macroscopic turbulent kinetic energy and dissipation rate increases with a decrease in porosity.
- The present low Re k - ϵ turbulence model and DNS predictions (square cylinder) were compared with the simulation results obtained from v2f (Kazerooni and Hannani, 2009) and LES turbulent models (Kuwahara et al., 2006). The numerical predictions of low Re - k - ϵ turbulence model from present work was in good agreement with the results of LES models available in the literature.
- The simulation results satisfactorily visualized the flow field, pressure variation and distribution of turbulent kinetic energy within the porous media.

7.1.5.2 Array of circular cylinder

- A series of computations in Darcy flow regime were performed at $Re_D = 10$ for different porosity ($0.3 \leq \phi \leq 0.8$) and a steady streamline flow was observed within the computational REV without any trace of eddy formation.
- At higher porosity values the numerical predictions agreed well with the semi-empirical equations of Kozney-Carman and Kuwahara et al. (1998). However, a deviation was observed at lower porosity ($\phi \leq 0.4$) values.

- A correlation was proposed for permeability of porous media as a function of porosity, which describe the simulation results significantly well over the entire range of porosity ($0.3 \leq \phi \leq 0.8$).
- The predicted flow-fields and TKE were strongly influenced by porosity and Re_D .
- Flow over the circular cylinder undergoes strong attenuation and enhancement of turbulence and leads to flow separation and vortex formation.
- The pressure fields predicted by both RANS and LES were in good agreement. However, there was deviation in velocity and TKE fields.
- The anisotropic turbulent flow physics was not predicted by RANS simulation because of the unsteady nature of wakes formed within the REV, however, unsteadiness was effectively captured using LES technique. The low Re $k-\varepsilon$ results agreed well with the LES predictions.
- The Darcy-Forchheimer relationship was tested with simulation results obtained by LES and RANS models. The RANS model predictions were somewhat over predicted the friction factor values as compared to LES predictions.

7.2 RECOMMENDATIONS

On the basis of the present study, the following recommendations can be made for the future study:

- The rheological behaviour of water-in-oil (w/o) emulsion with different water volume fraction and surfactant concentration.
- Flow behaviour of w/o emulsion having different volume fractions through porous media.
- The thermal effect on emulsion flow behaviour in porous media.
- Flow behaviour of o/w emulsion stabilized with different type surfactants such as cationic, non-ionic and zwitterionic surfactants through porous media.
- Effect of pH and ionic strength on permeability reduction of porous media.
- Rheological and flow behaviour of emulsions stabilized with fine solid particles through porous media.
- The existing experimental set-up need to scale-up and upgraded which mimic the actual process condition.
- A detailed understanding of actual flow physics occurring in real porous media using advance X-ray topographic techniques.

REFERENCES

- Adams JF, Fairweather WM, Yao J. Modelling and simulation of particle re-suspension in a turbulent square duct flow. *Comput. Chem. Eng.* 2011; 35: 893-900.
- Ahmad K, Ho CC, Fong WK, Toji D. Properties of palm oil-in water emulsions stabilized by nonionic surfactants. *J. Colloid Interf. Sci.* 1996; 181, 595-604.
- Ahuja A, Singh A. Slip velocity of concentrated suspension in Couette flow. *J. Rheol.* 2009; 53: 1461-1485.
- Aomari N, Gaudu R, Cabioch F, Omari A. Rheology of water in crude oil emulsions. *Colloids Surf. A.* 1998; 139: 13-20.
- Al-Fariss TF, Pinder KL. Flow through porous media of shear-thinning liquid with yield stress. *Can. J. Chem. Eng.* 1987; 65(3): 391-406.
- Al-Fariss TF. A new correlation for non-Newtonian flow through porous media. *Comput. Chem. Eng.* 1989; 13: 475-482.
- Al-Fariss, T. Flow of polymer solution through porous media. *Ind. Eng. Chem. Res.* 1990; 29; 2150–2151
- Al-Fariss TF, Jang LK, Ozbelge HO, Ghassem NM. A new correlation for the viscosity of waxy oils. *J. Petrol. Sci. Eng.* 1993; 9: 139-144.
- Al-Fariss TF, Fakeeha, Al-Odan MA. Flow of oil emulsion through porous media. *J. King Saud Univ. Eng. Sci.* 1994; 6(1): 1-16.
- Allen DM. The relationship between variable selection and data augmentation and a method for prediction. *Technometrics.* 1974; 16: 125–127.
- Al-Yaari M, Al-Sarkhi A, Hussein IA, Abu Sharkh B. Effect of drag reducing polymers on surfactant-stabilized water-oil emulsions flow. *Exp. Therm. Fluid Sci.* 2013; 51: 319-331.
- Al-Yaari M, Al-Sarkhi A, Hussein IA, Chang F, Abbad M. Flow characteristics of surfactant stabilized water-in-oil emulsions. *Chem. Eng. Res. Des.* 2014; 92(3): 405-412.
- Al-Yaari M, Hussein IA, Al-Sarkhi A, Abbad M, Chang F. Effect of water salinity on surfactant-stabilized water-oil emulsions flow characteristics. *Exp. Therm. Fluid Sci.* 2015; 64: 54–61.
- Antohe BV, Lage JL. A general two-equation macroscopic turbulence model for incompressible flow in porous media. *Int. J. Heat Mass Transfer.* 1997; 40: 3013–3024.

- Aomari N, Gaudu R, Cabioc'h F, Omari A. Rheology of water in crude oil emulsions. *Colloids Surf. A*. 1998; 139: 13-20.
- Ash M, Ash I. Handbook of Food Additives. 3rd Edition, Edited by, Synapse Information Resources, Inc., 2008.
- Arhuoma M, Dong M, Yang D, Idem R. Determination of water-in-oil emulsion viscosity in porous media. *Ind. Eng. Chem. Res.* 2009, 48 (15), pp 7092–7102
- Aveyard R, Clint JH, Nees D, Paunov V N. Compression and structure of monolayers of charged latex particles at air/water and octane/water interfaces. *Langmuir*. 2000; 16: 1969–1979.
- Avranas A, Stalidis G, Ritzoulis G,. Demulsification rate and zeta potential of o/w emulsions. *Colloid Polym. Sci.* 1988; 266: 937-940.
- Bachmat Y, Bear J. Macroscopic modelling of transport phenomena in porous media. *Trans Porous Media*. 1986; 1: 241-269.
- Bagcı Ö, Dukhan N, Özdemir M. Flow regimes in packed beds of spheres from pre-Darcy to turbulent. *Trans. Porous Media*. 2014; 104: 501–520.
- Balakhrisna T, Ghosh S, Das G, Das PK. Oil–water flows through sudden contraction and expansion in a horizontal pipe–Phase distribution and pressure drop. *Int. J. Multi. Flow*. 2010; 36(1): 13–24.
- Baldygin A, Nobes DS, Mitra SK. New laboratory core flooding experimental system, *Ind. Eng. Chem. Res.* 2014, 53, 13497–13505.
- Bancroft WD. The theory of emulsification I. *J Phy Chem*. 1912; 16: 177 - 233.
- Banik M, Ghosh P. The electroviscous effect at fluid–fluid interfaces. *Ind. Eng. Chem. Res.* 2013; 52: 1581–1590.
- Barnes HA. Rheology of emulsions – a review. *Colloid. Surf. A*. 1994; 91: 89-95.
- Barnes, HA. A review of the slip (wall depletion) of polymer solutions, emulsions and particle suspensions in viscometers: its cause, character and cure. *J. Non-Newtonian Fluid. Mech.* 1995; 56: 221–251.
- Basu S, Nandakumar K, Masliyah JH. A study on daughter droplets formation in bitumen/glass/water contact line displacement due to instability. *Fuel*. 2000; 79(7): 837–841.
- Basu S, Shravan S. Preparation and characterization of petroleum sulfonate directly from crude. *Pet. Sci. Technol.* 2008; 26(13): 1559-1570.

- Basu S. Wall effect in laminar flow of non-Newtonian fluid through a packed bed. *Chem. Eng. J.* 2001; 81(1): 323-329.
- Basu, S, Nandakumar K, Masliyah JH. A study on oil displacement on model surfaces. *J. Colloid Interface Sci.* 1996; 182: 82-94.
- Baumgaertel M, De Rosa ME, Machado J, Masse M, Winter HH. The relaxation time spectrum of nearly monodisperse polybutadiene melts. *Rheol. Acta.* 1992; 31: 75–82.
- Bear J. Dynamics of fluids in porous media. American Elsevier, New York, 1972.
- Beavers GS, Sparrow EM. Non-Darcy flow through fibrous porous media. *J. Appl. Mech.* 1969; 36: 711–714.
- Becher P. Emulsions and practice. 2nd ed. Reinhold Pub. Corp. New York, 1965.
- Becher P. Emulsions: theory and practice, 3rd Ed., Washington, D.C., American Chemical Society, Oxford; New York, Oxford University Press, 2001.
- Benhamadouche S, Laurence D. LES, coarse LES, and transient RANS comparisons on the flow across a tube bundle. *Int. J. Heat Fluid Flow.* 2003; 24: 470-479.
- Berli CLA, Quemada D, Parker A. Modelling the viscosity of depletion flocculated emulsions. *Colloids Surf. A: Physicochemical and Eng. Aspects* 203 (2002) 11–20.
- Berryman JG. Random close packing of hard spheres and disks. *Phys. Rev. A.* 1983; 27: 1053-1061.
- Bey O, Eigenberger G. Fluid flow through catalyst filled tubes. *Chem Eng Sci.* 1997; 52(8): 1365-1376.
- Boomsma K, Poulikakos D. The effects of compression and pore size variations on the liquid flow characteristics in metal foams. *J. Fluids Eng.* 2002; 124: 263-272.
- Borwankar RP, Lobo LA, Wasan DT. Emulsion stability-kinetics of flocculation and coalescence. *Colloids and Surf.* 1992; 69: 135-146.
- Boukany PE, Wang SQ. Shear banding or not in entangled DNA solutions depending on the level of entanglement, *J. Rheol.* 2009; 53(1): 73– 83.
- Bower C, Gallegos C, Mackley MR, Madiedo JM. The rheological and microstructural characterisation of the non-linear flow behaviour of concentrated oil-in-water emulsions, *Rheol Acta* 38: 145-159 (1999)
- Box GEP, Hunter JS. Multi-factor experimental designs for exploring response surfaces. *Ann. Math. Stat.* 1957; 28: 195-241.
- Box GEP, Behnken DW. 1960, Some new three level designs for the study of quantitative variables. *Technometrics.* 1960; 2: 455-475.

- Brinkman H. The viscosity of concentrated suspensions and solutions. *J. Chem. Phys.* 1952; 20 (4): 571–584.
- Brooks BW, Richmond HN, Zerfa M. Phase inversion and drop formation in agitated liquid-liquid dispersions in the presence of nonionic surfactant, in *Modern Aspect of Emulsion Science*. Binks, B.P. Editor, Ch-6, The Royal Society of Chemistry, UK, 1998.
- Bui B, Saasen A, Maxey J, Ozbayoglu E, Miska SZ, Yu M, Takach NE. Viscoelastic properties of oil-based drilling fluids. *Ann. Trans. Nordic Rheo. Soc.* 2012; 20: 33-47.
- Burke SP, Plummer WB. Gas flow through packed column. *Ind. Eng. Chem. Res.* 1928; 20: 1196-1200.
- Carman PC. Fluid flow through granular beds. *Trans. Ins. Chem. Eng.* 1937; 12: 150-166.
- Chai Z, Shi B, Lu J, Guo Z. Non-Darcy flow in disordered porous media: A lattice Boltzmann study. *Computers & Fluids.* 2010; 39: 2069–2077.
- Chakrabarti D. P, Ghoshal P. Das G. Behavior of pressure gradient and transient pressure signals during liquid-liquid two-phase flow. *Chem. Eng. & Technol.* 2006; 29: (10) 1183–1195.
- Craig FF. The reservoir engineering aspect of water flooding. Society of Petroleum Engineers: Richardson, TX, 1971.
- Chauveteau G, Thirriot CR. Regimes d'écoulement en milieu poreux et limite de la loi de Darcy. *La Houille Blanche.* 1967; 1(22): 1–8.
- Cheng NS, Hao Z, Tan S K. Comparison of quadratic and power law for nonlinear flow through porous media. *Exp. Therm. Fluid Sci.* 2008; 32: 1538–1547.
- Chhabra RP, Comiti J, Macháč I. Flow of non-Newtonian fluids in fixed and fluidised beds. *Chem. Eng. Sci.* 2001; 56 (1): 1-27.
- Chhabra RP, Richardson JF. Non-Newtonian flow in process industries. Butterworth-Heinemann, London, 1999.
- Chhabra RP, Srinivas BK. Non-newtonian (purely viscous) fluid flow through packed beds: Effect of particle shape. *Powder Technol.* 1991; 67(1): 15-19.
- Choi SJ, Schowalter WR. Rheological properties of non-dilute suspensions of deformable particles. *Phys. Fluids.* 1975; 18: 420–427.

- Choi HW, Paraschivoiu M. Adaptive domain decomposition for the bound method: application to the incompressible navier-stokes and energy equations in three space dimensions. *Comput. Method Appl. M.* 2007; 196(8): 1484-1497.
- Christopher RH, Middleman S. Power-law flow through a packed tube. *Ind. Eeng. Chem. Funda.* 1965; 4: 422-426.
- Chung K, Lee KS, Kim WS. Modified macroscopic turbulence modeling for the tube with channel geometry in porous media. *Numer. Heat Transfer Part A.* 2003; 43: 659–668.
- Cloete M, Smit GJ, Maritz MF. External boundary effects on the velocity profile for generalized Newtonian fluid flow inside a homogeneous porous medium. *J. Non-Newton. Fluid.* 2015; 215: 40–52.
- Comiti J, Sabiri NE, Montillet A. Experimental characterization of flow regimes in various porous media-III: limit of Darcy's or creeping flow regime for Newtonian and purely viscous non-Newtonian fluids. *Chem. Eng. Sci.* 2000; 55: 3057-3061.
- Coulaud O, Morel P, Caltagirone JP. Numerical modelling of nonlinear effects in laminar flow through a porous medium. *J. Fluid Mech.* 1988; 190: 393–407.
- Cox W, Merz E. Correlation of dynamic and steady flow viscosities. *J. Polym. Sci.* 1958; 28 (118): 619–622.
- Craig FF. The reservoir engineering aspect of water flooding. *Soc. Petro. Eng.: Richardson, TX*, 1971.
- Dagréou S, Mendiboure B, Allal A, Marin G, Lachaise J, Marchal P, Choplin L. Modeling of the linear viscoelastic properties of oil-in-water emulsions. *J. Colloid. Inter. Sci.* 2005; 282: 202–211.
- Dan D, Jing G. Apparent viscosity prediction of non-Newtonian water-in-crude oil emulsions. *J. Petrol. Sci. Eng.* 2006; 53: 113–122.
- Darcy HPG. Les fontaines publiques de la ville de Dijon. Victor Dalmont, Paris, 1856.
- De B, Mandal TK, Das G. The rivulet flow pattern during oil–water horizontal flow through a 12 mm pipe. *Exp. Therm. Fluid Sci.* 2010; 34(5): 625–632.
- de Boer JH. The influence of van der Waals forces and primary bonds on binding energy, strength and orientation, with special reference to some artificial resins. *Trans Faraday Soc.* 1936; 32: 10-37.
- Derkach SR, Rheology of emulsions. *Adv. Colloid Inter. Sci.* 2009; 151: 1–23.

- Deshiikana SR, Eschenazia E, Papadopoulos K D. Transport of colloids through porous beds in the presence of natural organic matter. *Colloid Surf. A*. 1998; 145(1–3): 93–100.
- Devereux OF. Emulsion flow in porous solids II. Experiments with a crude oil-in-water emulsion in porous sandstone. *Chem. Eng. J*. 1974; 7: 129-136.
- Dharmadhikari RV, Kale DD. Flow of non-Newtonian fluids through porous media. *Chem. Eng. Sci*. 1985; 40: 527-529.
- Dickinson E. Food Colloids—An Overview. *Colloids Surf. A*. 1989; 42: 191–204.
- Dickinson E. Hydrocolloids and emulsion stability. Chapter 2, in: Handbook of Hydrocolloids (Second Edition) (2009), Edited by G. O. Phillips and P. A. Williams, CRC Press.
- Dimitrios H, Hojat M, Arne S. Polymer flow through water- and oil-wet porous media, *J. Hydrodynamics*, 2015; 27(5):748-762.
- Dokic PP, Dakovic LM, Radivojevic PP, Sovilj VJ, Sefer IB. Dynamics of emulsion formation. *J. Disp Sci*. 1990; 20 (1–2): 215–234.
- Dolejs V, Cakl J, Siska B, Dolecek P. Creeping flow of viscoelastic fluid through fixed beds of particles, *Chem. Eng. Proc*. 2002; 41: 173–178
- Drouin M, Grégoire O, Simonin O. A consistent methodology for the derivation and calibration of a macroscopic turbulence model for flows in porous media. *Int. J. Heat Mass Transfer*. 2013; 63: 401–413.
- du Noüy PL. An interfacial tensiometer for universal use. *J. Gen. Physiol*. 1925; 7(5): 625–633.
- Durst F, Haas R, Interthal W. The nature of flows through porous media. *J. Non-Newtonian Fluid Mech*. 1987; 22(2):169–189.
- Du Plessis JP, Masliyah JH. Mathematical modelling of flow through consolidated isotropic porous media. *Trans. Porous Media*. 1988; 3:145–161.
- Du Plessis JP, Masliyah JH. Flow through isotropic granular porous media. *Trans. Porous Media*. 1991; 6: 207–221.
- Duan G, Chen B, Large Eddy Simulation by particle method coupled with Sub-Particle-Scale model and application to mixing layer flow. *Appl. Math. Modell*. 2015; 39: 3135–3149.
- Dukhan N, Minjeur II C. A two-permeability approach for assessing flow properties in metal foam. *J. Porous Mater*. 2011; 18, 417–424.

- Dullien FAL, El-Sayed MS, Batra VK. Rate of capillary rise in porous media with non uniform pores', *J. Colloid. Interface. Sci.* 1976; 60: 497-506.
- Durst F, Haas R, Interthal W. The nature of flows through porous media. *J. Non-Newtonian Fluid Mech.* 1987; 22(2):169–189.
- Dybbs A, Edwards RV. A new look at porous media fluid mechanism-Darcy to turbulent. In *Fundamentals of Transport Phenomena in Porous Media*, ed. J. Bear and V. Corapcioglu. Martinus Nijhoff. The Netherlands, 1984.
- Dzuy NQ, Boger DV. Yield stress measurement for concentrated suspensions. *J. Rheol.* 1983; 27: 321-249.
- Eastoe J. Surfactant aggregation and adsorption at interfaces. Chap. 4, in: *Colloid Science: Principles, Methods and Applications*, Edited by Terence Cosgrove, Blackwell Publishing Ltd., 2005.
- Einstein A. Eineneue bestuimmung der molecular dimensionen. *Ann. Phys.* 1906; 9: 289–306.
- Ergun S. Fluid flow through packed columns. *Chem. Eng. Prog. (AIChE)*. 1952; 48: 89-94.
- Fand RM, Kim BYK, Lam ACC, Phan RT. Resistance to the flow of fluids through simple and complex porous media whose matrices are composed of randomly packed spheres. *J. Fluids Eng. AIME Trans.* 1987; 109: 268-274.
- Farah MA, Oliveira RC, Caldas JN, Rajagopal K. Viscosity of water-in-oil emulsions: variation with temperature and water volume fraction. *J. Petrol. Sci. Eng.* 2005; 48: 169–184.
- Ferry JD. *Viscoelastic Properties of Polymers*. 3rd ed. John Wiley & Sons, New York, 1980.
- Finkle P, Draper HD, Hildebrand JH. The theory of emulsification. *J. Amec. Chem. Soc.* 1923; 45: 2780 - 2788.
- Flew S, Sellin RHJ. Non-Newtonian flow in porous media-a laboratory study of polyacrylamide solutions, *J. Non-Newtonian Fluid Mechanics*. 1993; 47: 169-210.
- Fogel. D. B., 1994. An introduction to simulated evolutionary optimization. *IEEE Trans. Neural Networks*. 5(1), 3-14.
- Fourar M, Radilla G, Lenormand R, Moyne C. On the non-linear behavior of a laminar single-phase flow through two and three-dimensional porous media. *Adv. Water Res.* 2004; 27: 669–677.

- Fourar M, Lenormand R, Karimi-Fard M, Horne R. Inertia effects in high-rate flow through heterogeneous porous media. *Trans. Porous Media*. 2005; 60(3): 353-370.
- Francisco J, Valdes-Parada J, Ochoa-Tapia A, Alvarez-Ramirez J. Validity of the permeability Carman–Kozeny equation: A volume averaging approach. *Physica A*. 2009; 388: 789-798.
- Franco JM, Raymundo A, Sousa I, Gallegos C. Influence of processing variables on the rheological and textural properties of lupin protein-stabilized emulsions. *J. Agric. Food Chem*. 1998; 46: 3109–3115.
- Franco JM, Guerrero A, Gallegos C. Rheology and processing of salad dressing emulsions, *Rheol. Acta*. 1995; 34: 13–524.
- Friedrich R, Huttl TJ, Manhart M, Wagner C. Direct numerical simulation of incompressible turbulent flows. *Comp. & Fluids*. 2001; 30: 555-579.
- Gaonkar AG, Borwankar RP. Adsorption behaviour of monoglycerides at vegetable oil/water interface. *J. Colloid Interface Sci*. 1991; 146: 525-532.
- Getachew D, Minkowycz WJ, Lage JL. A modified form of the k– ϵ model for turbulent flows of an incompressible fluid in porous media. *Int. J. Heat Mass Transfer*. 2000; 43: 2909–2915.
- Ghosh S, Pradhan M, Patel T, Haj-shafiei S, Rousseau D. Long-term stability of crystal-stabilized water-in-oil emulsions, *J. Colloid and Interface Sci.*, 2015; 460: 247–257.
- Godwin JW. Emulsions and microemulsions, Chapter 7, in: *Colloids and Interfaces with Surfactants and Polymers - An Introduction* (2004), John Wiley and Sons, Ltd.
- Goldberg DE. Genetic algorithms in search, optimization, and machine learning. Addison-Wesley, New York, 1989.
- Graillat C, Lepais-Masmejean M, Pichot C. Stabilization optimization of aqueous monomer solutions in oil emulsions using the cohesive energy ratio concept *J. Dispers. Sci. Technol*. 1990; 11: 455–477.
- Griffin WC. Classification of surface-active agents by HLB. *J. Soc. Cosmet. Chem*. 1949; 1: 311 - 326.
- Guillen VR, Carvalho M S, Alvarado V. Pore scale and macroscopic displacement mechanisms in emulsion flooding. *Transp. Porous Med*. 2012; 94:197–206.
- Gullapalli RP, Sheth BB. Influence of an optimized non-ionic emulsifier blend on properties of oil-in-water emulsions. *Eur. J. Pharm. Biopharm*. 1999; 48: 233- 238.

- Gunasekaran S, Mehmet AM. Dynamic oscillatory shear testing of foods selected applications. *Trends Food Sci. Technol.* 2000; 11: 115-127.
- Guth E, Simha R. Investigations of viscosity of suspensions and solutions: part 3. The viscosity of spherical suspensions. *Kolloid Z.* 1936; 74: 266-275.
- Hagan MT, Menhaj M. Training feed forward networks with the Marquardt algorithm. *IEEE Trans. Neural Networks.* 1994; 5: 989–993.
- Haj-shafiei S, Ghosh S, Rousseau D. Kinetic stability and rheology of wax-stabilized water-in-oil emulsions at different water cuts, *J. Colloid Interface Sci.* 2013; 410: 11–20.
- Hamaker HC. The London-Van der Waals attraction between spherical particles. *Physica.* 1937; 4: 1058-1072.
- Hannani SK, Stanislas M. Finite element simulation of turbulent Couette-Poiseuille flows using a low Reynolds $k-\epsilon$ model. *Int. J. Num. Methods Fluids.* 1999; 30: 83-103.
- Hannani S. K, Stanislas M. Incompressible turbulent flow simulation using a Galerkin/least-squares formulation and a low Reynolds $k-\epsilon$ model. *Comput Meth Appl Mech Eng.* 2000; 181: 107-116.
- Hayes RE, Afacan A, Boulanger B. An equation of motion for an incompressible Newtonian fluid in a packed bed. *Trans. Porous Media.* 1995; 18: 185-198.
- Hayes RE, Afacan A, Boulanger B, Shenoy AV. Modelling the flow of power law fluids in a packed bed using a volume-averaged equation of motion. *Trans. Porous Media.* 1996; 23: 175-196.
- Helgeson ME, Vasquez PA, Kaler EW, Wagner NJ. Rheology and spatially resolved structure of cetyltrimethylammonium bromide wormlike micelles through the shear banding transition. *J. Rheol.* 2009; 53(3): 727–756 (2009).
- Helmreich A, Vorwerk J, Steger R, Mdler M, Brunn PO. Non-viscous effects in the flow of xanthan gum a packed bed of spheres, *The Chem. Eng. J.* 1995; 59: 111–119,
- Hempoonsert, J., Tansel, B., Laha, S., 2010. Effect of temperature and pH on droplet aggregation and phase separation characteristics of flocs formed in oil–water emulsions after coagulation. *Colloids Surf., A.* 353, 37–42.
- Hiemenz, P.C., and R. Rajagopalan, "Principles of Colloid and Surface Chemistry", New York: Marcel Dekker (1997).
- Hlushkou D, Tallarek U. Transition from creeping via viscous-inertial to turbulent flow in fixed beds. *J. Chromatogr.* 2006; 1126: 70–85.

- Hofman JAMH, Stein HN. Permeability reaction of porous media on transport of emulsions through them, *Colloids and Surfaces*, 1931; 61: 317-329.
- Hrenya CM, Bolio EJ, Chakrabarti D, Sinclair JL. Comparison of low Reynolds number $k-\epsilon$ turbulence models in predicting fully developed pipe flow. *Chem. Eng. Sci.* 1995; 50: 1923-1941.
- Hunter RJ. Foundations of Colloid Science, Oxford University Press, 1989.
- Hunter RJ. Foundations of colloid science, 2nd ed. Oxford, New York, Oxford University Press, 2001.
- Izadifar M, Zolghadri JM. Application of genetic algorithm for optimization of vegetable oil hydrogenation process. *J. Food Eng.* 2007; 78(1): 1-8.
- Jafari P, Zamankhan SM, Mousavi K, Pietarinen K. Modeling and CFD simulation of flow behavior and dispersivity, through randomly packed bed reactors. *Chem. Eng. J.* 2008; 144: 476-482.
- Jansen KMB, Agterof WGM, Mellema J. Viscosity of surfactant stabilized emulsions. *J. Rheol.* 2001; 45: 1359-1371.
- Kabalnov A. Thermodynamic and theoretical aspects of emulsions and their stability. *Curr. Opin. Colloid Interface Sci.* 1998; 3: 270-275.
- Kabalnov AS, Shchukin ED. Ostwald ripening theory: applications to fluorocarbon emulsion stability. *Adv. Colloid Interface Sci.* 1992; 38: 69-97.
- Karaman S, Yilmaz MT, Dogan M, Yetim H, Kayacier A. Dynamic oscillatory shear properties of o/w model system meat emulsions: Linear viscoelastic analysis for effect of temperature and oil concentration on protein network formation. *J. Food Eng.* 2011; 107: 241-252.
- Karbaschi M, Orr R, Bastani D, Javadi A, Lotfi M, Miller R. A novel technique to semi-quantitatively study the stability of emulsions and the kinetics of the coalescence under different dynamic conditions *Colloids and Surfaces A: Physicochemical and Engineering Aspects.* 460, 2014, 327-332.
- Kaur N, Singh R, Wanchoo R. K. Flow of Newtonian and Non-Newtonian Fluids Through Packed Beds: An Experimental Study, *Transp. Porous Med.* 2011; 90: 655-671.
- Kaushik VVR, Ghosh S, Das G, Das P K. CFD simulation of core annular flow through sudden contraction and expansion. *J. Pet. Sci. Eng.* 2012; 86-87: 153-164.
- Kaviany M. Principles of Heat Transfer in Porous Media. Springer-Verlag, 1991.

- Kazerooni RB, Hannani SK. Simulation of turbulent flow through porous media employing a v_2f model. *Transaction B: Mech Eng.* 2009; 16: 159-167.
- Kececioglu I, Jiang Y. Flow through porous media of packed spheres saturated with water. *J. Fluids Eng.* 1994; 116: 164–170.
- Kemblowski Z, Michniewicz MA. New look at the laminar flow of power-law fluids through granular beds. *Rheol. Acta.* 1979; 18: 730-739.
- Khasanov MM, Bulgakova, GT, Telin AG, Akhmetov AT. Non-equilibrium and nonlinear effect in water-in-oil emulsion flows in porous media. *Energy Fuel* 2011; 25: 1173-1181.
- Kim J, Moin P, Moser R. Turbulence statistics in fully developed channel flow at low Reynolds number. *J. Fluid Mechanics.* 1987; 177: 133-166.
- Kinjal R, Patel M, Mehta N, Patel TR. A mathematical model of imbibition phenomenon in heterogeneous porous media during secondary oil recovery process. *Appl. Math. Modell.* 2013; 37: 2933–2942.
- Kokal SL, Najman J, Sayegh SG, George AE. Measurement and correlation of asphaltene precipitation from heavy oils by gas injection, *J. Can. Petrol. Technol.*, 1992; 31: 24-30.
- Korać R, Krajišnik D, Savić S, Pantelić I, Jovančić P, Cekić N, Milić J. A new class of emulsion systems – fast inverted o/w emulsions: formulation approach, physical stability and colloidal structure, *Colloids and Surfaces A: Physicochemical and Engineering Aspects.* 2014; 461: 267–278.
- Kozeny J. On capillary movement of water in soil in German. *Sitzber Akad Wiss Wien.* 1927; 136 (Abt. IIa): 271-306.
- Krieger IM, Dougherty TJ. A mechanism for non-Newtonian flow in suspensions of rigid spheres. *Trans. Soc. Rheol.* 1959; 3: 137–152.
- Krishnamoorthy CP, Deshpande AP, Pushpavanam S. Immiscible fluid Displacement in porous media: experiments and simulations. *J. Porous Media.* 2011; 14(5): 423-435.
- Kulyakhtin O, Muskulus SM. Numerical simulation of droplet impingement and flow around a cylinder using RANS and LES models. *J. Fluids Structures.* 2014; 48: 280-294.
- Kumar S, Upadhyay S.N. Mass and momentum transfer to Newtonian and non-Newtonian fluids in fixed and fluidized beds. *Ind. Eng. Chem. Fundam.* 1981; 20: 186–195.

- Kundu P, Agrawal A, Mateen H, Mishra IM. Stability of oil-in-water macro-emulsion with anionic surfactant: Effect of Electrolytes and Temperature. *Chem. Eng. Sci.* 2013; 102: 176-185.
- Kundu P, Mishra IM. Treatment of Surfactant Stabilised Oily Wastewater Using Coalescing Bed of Bagasse Fly Ash (BFA) As a Low Cost Filter Medium: Modeling and Optimization of Process Parameters, *Desalination and Water Treatment*, 2015; 1: 1-14.
- Kuwahara F, Kameyama Y, Yamashita S, Nakayama A. Numerical modelling of turbulent flow in porous media using a spatially periodic array. *J. Porous media.* 1998; 1: 47-55.
- Kuwahara F, Yamane T, Nakayama A. Large eddy simulation of turbulent flow in porous media. *Int. Commun. Heat Mass Transfer.* 2006; 33: 411-418.
- Lacasse MD, Grest GS, Levine D, Mason TG, Weitz DA. Model for the elasticity of compressed emulsions. *Phys. Rev. Lett.* 1996; 76: 3448-3451.
- Lage JL, Antohe BV, Nield DA. Two types of nonlinear pressure-drop versus flow-rate relation observed for saturated porous media. *Trans. ASME J. Fluid Eng.* 1997; 119: 700-706.
- Lai JCS, Yang CY. Numerical simulation of turbulence suppression: Comparisons of the performance of four k- ϵ turbulence models. *Int. J. Heat Fluid Flow.* 1997; 18: 575-584.
- Lam CKG, Bremhorst K. A modified form of the k- ϵ model for predicting wall turbulence. *J. Fluids Eng. ASME.* 1981; 103: 456-460.
- Langevin D, Poteau S, Hénaut I, Argillier JF Crude oil emulsion properties and their application to heavy oil transportation. *Oil & Gas Sci. Technol.* 2004; 59: 511-521.
- Lapasin R, Grassi M, Cocean N. Effect of polymer addition on the rheology of o/w emulsions. *Rheol. Acta.* 2001; 40: 185-192.
- Launder BE, Sharma BI. Application of the energy dissipation model of turbulence to the calculation of flow near a spinning disc. *Letts. Heat Mass Transfer.* 1974; 1: 131-138.
- Lee HM, Lee JW, Park OO. Rheology and dynamics of water-in-oil emulsions under steady and dynamic shear flow. *J. Colloid Inter. Sci.* 1997; 185: 297-305.
- Lee K, Howell JR. Forced convective and radiative transfer within a highly porous layer exposed to a turbulent external flow field. *Proc 2nd ASME/JSME Therm Eng. Joint Conf.* 1987; 2: 377 - 386.

- Leonardi GR, Perrechil FA, Silveira LP, Brunca HO, Friberg SE. Silicone/vegetable oil Janus emulsion: Topological stability versus interfacial tensions and relative oil volumes, *J. Colloid and Interface Science*, 2015; 449: 31–37.
- Li L, Ma. Experimental study on the effective particle diameter of a packed bed with non-spherical particles. *Trans. Porous Media*. 2011; 89(1): 35-48.
- Lifshitz EM. The theory of molecular attractive forces between solids. *Zh. Eksper. Teorer. Fiz.*, 1955; 29: 94-110.
- Lilly DK. On the application of the eddy viscosity concept in the inertial subrange of turbulence. *NCAR Manuscript*. 1966; 123: 1-19.
- Liu AJ, Ramaswamy S, Mason TG, Gang H, Weitz DA. Anomalous viscous loss in emulsions, *Phys. Rev. Lett.* 1996; 76(16): 3017-3020.
- Liu C, Li M, Han R, Li J, Liu C. Rheology of water-in-oil emulsions with different drop sizes, *J. Disper. Sci. Tech.* 37:333–344, 2016.
- Liu S, Afacan A, Masliyah J. Steady incompressible laminar flow in porous. *Chem. Eng. Sci.* 1994; 49(21): 3565–3586.
- Liu S, Masliyah J. Single fluid flow in porous media. *Chem. Eng. Comm.* 1996; 148: 653-732.
- Liu S, Masliyah J. On non-Newtonian fluid flow in ducts and porous media. *Chem. Eng. Sci.* 1998; 53(6): 1175–1201.
- Lovaglio RB, Santos FJ, Junior MJ, Contiero J. Rhamnolipid emulsifying activity and emulsion stability: pH rules. *Colloid Surf. B*. 2011; 85: 301–305.
- Lucassen-Reynders E.H. P. Becher (Ed.), *Encyclopedia of Emulsion Technology*, Marcel Dekker, New York (1996).
- Lundgren TS. Slow flow through stationary random beds and suspensions of spheres. *J Fluid Mech.* 1972; 51: 273–299.
- M van de Ven TG. Electroviscous phenomena in colloidal dispersions. *Chem Eng Sci* 2001; 56(9): 2947–2955.
- Ma H, Ruth DW. The microscopic analysis of high forchheimer number flow in porous media. *Trans. Porous Media*. 1993; 13: 139-160.
- Macdonald IF, El-Sayed MS, Mow K, Dullien FAL. Flow through porous media-Ergun equation revisited. *Ind. Eng. Chem. Fundam.* 1979; 18: 199-208.

- MacDonald MJ, Chao-Feng C, Guilloit PP, Ng KM. A generalized Blake-Kozeny equation for Multi sized Spherical Particle. *AIChE J.* 1991; 37: 1583-1588.
- Macini P, Mesini E, Viola R. Laboratory measurements of non-Darcy flow coefficients in natural and artificial unconsolidated porous media. *J. Petrol. Sci. Eng.* 2011; 77: 365–374.
- Madsen F, Eberth K, Smart JD. A rheological examination of the mucoadhesive/mucus interaction: the effect of mucoadhesive type and concentration. *J. Control Release.* 1998; 50: 167–178.
- Mahesh K, Constantinescu G, Apte S, Iaccarino G, Ham F, Moin P. Large-eddy simulation of reacting turbulent flows in complex geometries. *ASME J. App. Mech.* 2006; 73: 374-381.
- Maier, H. R., Dandy, G. C., 1998. Understanding the behavior and optimizing the performance of back-propagation neural networks: an empirical study. *Environ. Modell. Softw.* 13, 179-191.
- Mair RW, Callaghan PT. Shear flow of wormlike micelles in pipe and cylindrical Couette geometries as studied by nuclear magnetic resonance microscopy. *J. Rheol.* 1997; 41: 901–924.
- Mandal A, Bera A. Modeling of flow of oil-in-water emulsions through porous media. *Pet. Sci.* 2015; 12(2): 273-281.
- Mandal A, Samanta A, Bera A, Ojha K. Characterization of oil–water emulsion and its use in enhanced oil recovery. *Ind. Eng. Chem. Res.* 2010; 49(24): 12756-12761.
- Marrucci G. A theory of coalescence. *Chem. Eng. Sci.* 1969; 24: 975 - 985.
- Masliyah JH, Bhattacharjee S. *Electrokinetic and Colloid Transport Phenomena*, John Wiley & Sons, 2006.
- Mason TG. New fundamental concepts in emulsion rheology. *Curr. Opin. Colloid Interface Sci.* 1999; 4: 231–238.
- Mason TG, Bibette J, Weitz DA. Elasticity of compressed emulsions. *Phys. Rev. Lett.* 1995; 75(10): 2051-2054.
- Mason TG, Bibette J, Weitz DA. Yielding and flow of monodisperse emulsions. *J Colloid Interface Sci.* 1996; 179 (2): 439-448.
- Masoodi R, Pillai KM. Darcy’s law-based model for wicking in paper–like swelling porous media. *AIChE J.* 2010; 56(9): 2257-2267.

- Masuoka T, Takatsu Y. Turbulence model for flow through porous media. *Int. J. Heat Mass Transfer*. 1996; 39: 2803–2809.
- McAuliffe CD. Oil-in-water emulsion and their flow properties in porous media. *J. Pet. Tech*. 1973; 727-733.
- McClements DJ. Food Emulsions-Principles, Practices, and Techniques - 2nd Edition, Edited, CRC Press, 2004.
- McFarland JD, Dranchuk PM. Visualization of the transition to turbulent flow in porous media. *J. Can. Petrol. Technol*. 1976; 15: 71-78.
- Medhi B J, Kumar A, Singh A. Apparent wall slip velocity measurements in free surface flow of concentrated suspensions. *Int. J. Multiphase Flow*. 2011; 37: 609-619.
- Meyer R, Krause FF. Experimental evidence for permeability minima at low velocity gas flow through naturally formed porous media. *J. Porous Media*. 1998; 1: 93–106.
- Miller E, Rothstein JP, Transient evolution of shear-banding wormlike micellar solutions. *J. Non-Newtonian Fluid Mech*. 2007; 143(1): 22–37.
- Mishra P, Singh D, Mishra IM, Momentum transfer to Newtonian and non-Newtonian fluids flowing through packed and fluidized beds. *Chem. Eng. Sci*. 1975; 30: 397-405.
- Mohammadpoura R, Ghanian AA, Azamathulla HM. Numerical modeling of 3-D flow on porous broad crested weirs. *Appl. Math. Modell*. 2013; 37(22): 9324–9337.
- Mohanty KK, Davis HT, Scriven LE. Physics of oil entrapment in water-wet rock. *SPE Reservoir Eng*. 1987; 113-128.
- Montgomery D C. Design and Analysis of Experiments. Vth ed., Wiley 2004, Singapore.
- Mooney MJ. The viscosity of a concentrated suspensions of spherical particles. *J. Colloid Sci*. 1951; 6: 162–170.
- Moradi M, Kazempour M, French J T, Alvarado V. Dynamic flow response of crude oil-in-water emulsion during flow through porous media, *Fuel* 2014; 135: 38–45.
- Morais JM, Rocha-Filho PA, Burgess DJ. Influence of phase inversion on the formation and stability of one-step multiple emulsions. *Langmuir*. 2009; 25: 7954–7961.
- Moutsopoulos KN, Tsihrintzis VA. Approximate analytical solutions of the Forchheimer equation. *J. Hydrol*. 2005; 309(1–4): 93–103.
- Moutsopoulos KN, Papaspyros JNE, Tsihrintzis VA. Experimental investigation of inertial flow processes in porous media. *J. Hydrol*. 2009; 374: 242–254.

- Myers D. Surfactants and Science Technology, 3rd edition, John Wiley & Sons Inc., New Jersey, 2006.
- Nagano Y, Tagawa M, Niimi M. An improvement of the k- ϵ turbulence model (the limiting behavior of wall and free turbulence and the effect of adverse pressure gradient). *JSME*. 1989; B55: 1008-1015.
- Nagano Y, Tagawa M. An improved k- ϵ model for boundary layer flows. *J. Fluids Eng.* 1990; 112: 33-39.
- Nakayama A, Kuwahara F. A macroscopic turbulence model for flow in a porous medium. *J. Fluids Eng.* 1999; 121: 427-433.
- Ndjouenkeu R, Akingbala J, Richardson R, Morris E, Weak gel properties of klan flour from *Belshmiedia* sp. a traditional food thickener from tropical West Africa. *Food Hydrocoll.* 1995; 9 (3): 165-172.
- Nield DA, Bejan A. Convection in Porous Media, second ed., Springer-Verlag, New York, 1999.
- Nield DA, Bejan A. Convection in Porous Media. Springer, 2006.
- Nogueira GL, Carvalho MS, Alvarado V. Dynamic network model of mobility control in emulsion flow through porous media. *Transp. Porous Med.* 2013; 98:427-441
- Noor El-Din MR, El-Gamal IM, El-Hamouly SH, Mohameda HM, Mishrifa MR, Ragab AM. Rheological behavior of water-in-diesel fuel nanoemulsions stabilized by mixed surfactants. *Colloids Surf. A.* 2013; 436: 318- 324.
- Orafidiya L. O., Oladimeji, F. A., 2002. Determination of the required HLB values of some essential oils. *Int. J. Pharm.* 237, 241-249.
- Otsubo Y, Prudhomme RK. Rheology of oil-in-water emulsions. *Rheol. Acta.* 1994; 33: 29-37.
- Oun H, Kennedy A. Experimental investigation of pressure-drop characteristics across multi-layer porous metal structures. *J Porous Mater.* 2014; 21: 1133-1141.
- Pal R, Rhodes E. A novel viscosity correlation for non Newtonian concentrated emulsions. *J Colloid Interface Sci.* 1985; 107: 301-307.
- Pal R, Rhodes EJ. Viscosity/concentration relationships for emulsions. *J. Rheol.* 1989; 33: 1021-1045.
- Pal R, Masliyah J. Rheology of oil in water emulsion with added solids. *Can. J. Chem. Eng.* 1990; 68: 24-28.

- Pal R. Rheological behaviour of concentrated surfactant solutions and emulsions. *Colloids Surf. A*. 1992; 64: 207-215.
- Pal R. Rheological behaviour of surfactant-flocculated water-in-oil emulsions, *Colloids Surf. A*. 1993; 71: 173-185.
- Pal R. Scaling of relative viscosity of emulsions. *J. Rheol.* 1997; 4: 141-150.
- Pal R. Viscosity and storage/loss moduli for mixtures of fine and coarse emulsions. *Chem. Eng. J.* 1997; 44: 37-44.
- Pal R. A novel method to correlate emulsion viscosity data. *Colloids Surf. A*. 1998; 137: 275-286.
- Pal R. Slippage during the flow of emulsions in rheometers. *Colloids Surf. A*. 2000; 162: 55 - 66.
- Pal R. Evaluation of theoretical viscosity models for concentrated emulsions at low capillary numbers. *Chem. Eng. J.* 2001; 8: 15-21.
- Pamuk MT, Özdemir M. Friction factor, permeability and inertial coefficient of oscillating flow through porous media of packed balls. *Exp. Therm. Fluid Sci.* 2012; 38: 134-139.
- Panfilov M, Fourar M. Physical splitting of nonlinear effects in high-velocity stable flow through porous media. *Adv. Water Resour.* 2006; 29(1): 30-41.
- Pareek VK, Brungs MP, Adesina AA, Sharma R.. Artificial neural network modeling of a multiphase photo degradation system. *J. Photochem. Photobiol. A*. 2002; 149: 139-146.
- Pan T, Wang Z, Xu J, Wu Z, Qi H. Stripping of nonionic surfactants from the coacervate phase of cloud point system for lipase separation by Winsor II microemulsion extraction with the direct addition of alcohols. *Process bio-chemistry*. 2010; 5 (5), 771-776.
- Papathanasiou TD, Markicevic B, Dendy ED. A computational evaluation of the Ergun and Forchheimer equations for fibrous porous media. *Phys. Fluids*. 2001; 13: 2795-2804.
- Partal P, Guerrero Gallegos AC. Linear viscoelastic properties of sucrose ester-stabilized oil-in-water emulsions. *J. Rheol.* 1998; 42: 1375-1388.
- Pascal H. Nonsteady flow of non-Newtonian fluids through a porous medium. *Int. J. Eng. Sci.* 1983; 21: 199-210.
- Patankar SV. Numerical Heat Transfer and Fluid Flow. Hemisphere, New York, 1980.

- Pedersen KS, Rønningsen HP. Effect of precipitated wax on viscosity a model for predicting non-Newtonian viscosity of crude oils. *Energy & Fuels*. 2000; 14: 43-51.
- Pedras MHJ, de Lemos MJS. Macroscopic turbulence modeling for incompressible flow through undeformable porous media. *Int. J. Heat. Mass. Transfer*. 2001; 44: 1081–1093.
- Pedras MHJ, de Lemos MJS. Simulation of turbulent flow in porous media using a spatially periodic array and a low Re two-equation closure. *Num. Heat. Transfer. Part A*. 2001; 39: 35-39.
- Pereira EA, Brandão EM, Borges SV, Maia MCA Influence of concentration on the steady and oscillatory shear behavior of umbu pulp. *Rev. Bras. Eng. Agríc. Ambient*. 2008; 2: 87-90.
- Perrechil FA, Cunha RL. Oil-in-water emulsions stabilized by sodium caseinate: Influence of pH, high-pressure homogenization and locust bean gum addition. *J. Food. Eng.* 2010; 97(4): 441-448.
- Perrin R, Braza M, Cid E, Cazin S, Moradei F, Barthet A, Sevrain A, Hoarau Y. Near-wake turbulence properties in the high reynolds number incompressible flow around a circular cylinder measured by two- and three-component piv. *Flow. Turb. Combust.* 2006; 77: 185–204.
- Phan-Thien N, Pham DC. Differential multiphase models for poly-dispersed suspensions and particulate solids. *J. Non-Newton Fluid. Mech.* 1997; 72: 305–318.
- Pinson F, Gregoire O, Simonin O. $K-\epsilon$ Macro-scale modeling of turbulence based on a two scale analysis in porous media. *Int. J. Heat Fluid Flow*. 2006; 27: 955–966.
- Pope SB. *Turbulent Flows*. Cambridge University Press. Cambridge, 2005.
- Princen HM, Kiss AD. Rheology of Foams and Highly Concentrated Emulsions. *J. Colloid. Inter. Sci.* 1986; 112: 427–444.
- Paul BK, Moulik SP. Use and application of microemulsion, *Current Sci.* 2001; 80: 990-1001.
- Pichot R, Spyropoulos F, Norton IT. O/W emulsions stabilised by both low molecular weight surfactants and colloidal particles: The effect of surfactant type and concentration. *J. Colloid. Inter. Sci.* 2010; 352: 128 - 135.
- Pichot R, Spyropoulos F, Norton IT. Competitive adsorption of surfactants and hydrophilic silica particles at the oil-water interface: Interfacial tension and contact angle studies. *J. Colloid. Interface. Sci.* 2012; 377, 396-405.

- Pinfield VJ, Dickinson E, Povey MJW. Modeling of Combined Creaming and Flocculation in Emulsions. *J. Colloid. Interface. Sci.* 1997; 186: 80-89.
- Ragouilliaux A, Herzhaft B, Bertrand F, Coussot P. Flow instability and shear localization in a drilling mud. *Rheol. Acta.* 2006; 46: 261–271.
- Rao PT, Chhabra RP. Viscous non-Newtonian flow in packed beds: effects of column walls and particle size distribution. *Powder Technology.* 1993; 77: 171-176.
- Ravindranath S, Wan SQ, Olechnowicz M, Quirk RP. Banding in simple steady shear of entangled polymer solutions. *Macromolecules.* 2008; 41(7): 2663–2670.
- Reiner M. The rheology of concrete, in Eirich, F. R., ed., *Rheology: Theory and applications*, v. 3: New York, Academic Press, 1960.
- Richardson EG. The flow of emulsions. II. *J. Colloid Sci.* 1953; 8(3): 367-373.
- Richardson EG. The formation and flow of emulsion. *J. Colloid Sci.* 1950; 5: 404-413.
- Robins MM. Emulsions-creaming phenomena. *Curr Opin Colloid Interface Sci.* 2000; 5: 265-272.
- Rochefort WE, Middleman S. Rheology of Xanthan Gum: Salt, Temperature and Strain Effects in Oscillatory and Steady Shear Experiments. *J. Rheol.* 1987; 31: 337-369.
- Rodney C, Schmidt AR, Kerstein SW, Vebjorn N. Near-wall LES closure based on one-dimensional turbulence modeling. *J. Comput. Phys.* 2003; 186: 317-355.
- Rodriguez S, Romero C, Sargenti ML, Mtiller AJ, Saez AE, Odell JA. Flow of polymer solutions through porous media. *J. Non-Newtonian Fluid Mech.* 1993; 49: 3-85.
- Rojas S, Koplik J. Nonlinear flow in porous media. *Phys Rev E.* 1998; 58: 4476–782.
- Romero N, Ca´rdenas A, Henri´quez M, Rivas H. Viscoelastic properties and stability of highly concentrated bitumen in water emulsions. *Colloid. Surf. A.* 2002; 204: 271–284.
- Romero N, Cardenas A, Henriquez M, Rivas H. Viscoelastic properties and stability of highly concentrated bitumen in water emulsions. *Colloid. Surf A.* 2002; 204: 271–284.
- Ronningsen HP. Correlations for predicting viscosity of w/o emulsions based on North Sea crude oils. *Proc SPE Int Symp. Oil Field Chem. SPE 28968.* Houston, Texas, 1995.
- Ross-Murphy SB, McEvoy H, Fundamentals of hydrogels and gelation. *Br Polym J.* 1986; 18: 2–7.
- Roux D, Nallet F, Diat O. Rheology of lyotropic lamellar phases. *Europhys. Lett.* 1993; 24: 53–59.
- Rybczynski W. About the progressive movement of a liquid sphere in a tenacious medium. *Bull Acad Sci Cracovie Ser A.* 1911; 1: 40-46.

- Sabiri NE, Comiti J, pressure drop in non-newtonian purely viscous fluid flow through porous media, *Chem. Eng. Sci.* 1995; 50 (7): 1193-1201.
- Sabiri NE, Comiti J. Experimental validation of a model allowing pressure gradient determination for non-Newtonian purely viscous fluid-flow through packed beds. *Chem. Eng. Sci.* 1997; 52(20): 3589-3592.
- Sahimi M, Stauffer D. Efficient simulation of flow and transport in porous media. *Chem Eng Sci.* 1991; 46: 2225-2233.
- Saiki Y, Horn RG, Prestidge CA. Droplet structure instability in concentrated emulsions. *J Colloid Inter Sci.* 2008; 320: 569–574.
- Salager JL, Briceno MI, Brancho CL Heavy hydrocarbon emulsions. In: Sjöblom, J. (Ed.), *Encyclopedic Handbook of Emulsion Technology*. Marcel Dekker, New York, 2001; pp.455–495.
- Salmon, J.B, Manneville S, Colin A. Shear banding in a lyotropic lamellar phase. I. Time-averaged velocity profiles. *Phys. Rev. E.* 2003; 68: 1-10 .
- Samanta A, Ojha K, Mandal A, Interactions between acidic crude oil and alkali and their effects on enhanced oil recovery. *Energy & Fuels.* 2011; 25(4): 1642-1649.
- Samanta A, Ojha K, Mandal A, The characterization of natural surfactant and polymer and their use in enhanced recovery of oil. *Pet Sci Technol.* 2011; 29(7): 765-777.
- Sanatkar N, Masalova I, Malkin AY. Effect of surfactant on interfacial film and stability of highly concentrated emulsions stabilized by various binary surfactant mixtures. *Colloid. Surf. A.* 2014; 461: 85–91.
- Sanchez C, Renard D, Robert P, Schmitt C, Lefebvre J. Structure and rheological properties of acacia gum dispersions. *Food Hydrocoll.* 2002; 16: 257-267.
- Sanchez MC, Berjano M, Guerrero A, Brito E, Gallegos C. Evolution of the microstructure and rheology of o/w emulsions during the emulsification process. *Can J Chem Eng.* 1998; 76: 479–485.
- Sandberg RD, Fasel HF. Direct numerical simulations of transitional supersonic base flows. *AIAA J.* 2006; 44(4): 848-858.
- Sanfeld A, Steinchen A. Emulsions stability, from dilute to dense emulsions - Role of drops deformation. *Adv Colloid Interface Sci.* 2008; 140: 1-65.
- Santos RG, Bannwart AC, Loh W. Physico-chemical properties of heavy crude oil-in-water emulsions stabilized by mixtures of ionic and non-ionic ethoxylated nonylphenol surfactants and medium chain alcohols. *Chem. Eng Res Des.* 2011; 89: 957–967.

- Sarkar T, Sayer PG, Fraser SM. Flow simulation past axisymmetric bodies using four different turbulence models. *Appl. Math. Modell.* 1997; 21: 783-792.
- Schmidts T, Dobler D, Guldán AC, Paulus N, Runkel F. Multiple W/O/W emulsions—Using the required HLB for emulsifier evaluation. *Colloid. Surf., A* 2010; 372: 48–54.
- Schmidts T, Dobler D, Nissing C, Runkel FJ. Influence of hydrophilic surfactants on the properties of multiple W/O/W emulsions. *J. Colloid. Interface. Sci.* 2009; 338: 184–192.
- Schramm LL. Emulsions fundamentals and applications in the petroleum industry, Advances in Applications in Petroleum Industry, In: Advances in Chemistry Series, vol. 231, American Chemical Society, 1992.
- Schramm P. In: Becher, P. (Ed.), Encyclopedia of Emulsion Technology, In Marel Dekker, Inc., New York, 1983; 421–422.
- Schubert H, Engel R. Product and formulation engineering of emulsions. *Chem. Eng. Res. Des.* 2004; 82 (A9): 1137–1143.
- Schulz EN, Ambrusi RE, Miraglia DB, Schulz EP, García SG, Rodríguez JL, Schulz PC. Evaluation of oil-in-water emulsions with cationic–anionic surfactants mixtures for potential use in the oil industry. *Colloid. Surf. A.* 2016; 490: 145–154.
- Sedghi-Asl M, Rahimi H, Salehi R. Non-Darcy Flow of Water Through a Packed Column Test. *Trans. Porous Media.* 2014; 101: 215–227.
- Seguin D, Montillet A, Comiti J. Experimental characterization of flow regimes in various porous media-I: Limit of laminar flow regime. *Chem Eng Sci.* 1998; 53(21): 3751-3761.
- Seguin D, Montillet A, Comiti J, Huet F. Experimental characterization of flow regimes in various porous media-II: Transition to turbulent regime. *Chem Eng Sci.* 1998; 53(22): 3897-3909.
- Selvaraju N, Pushpavanam S. Adsorption characteristics on sand and brick beds. *Chem. Eng. J.* 2009; 147(2-3): 130-138.
- Setoodeh P, Jahanmiri A, Eslamloueyan R. Hybrid neural modeling framework for simulation and optimization of diauxie-involved fed-batch fermentative succinate production. *Chem. Eng. Sci.* 2012; 81: 57–76.
- Sheng JJ. Modern Chemical Enhanced Oil Recovery (Theory and Practice), Elsevier Inc, USA. 2011.

- Shenoy AV. Darcy-Forchheimer natural, forced and mixed convection heat transfer in non-Newtonian power-law fluid-saturated porous media. *Trans. Porous Media*. 1993; 11: 219-241.
- Sherman P. Emulsion Science, Ed, Academic Press, London, 1968.
- Sherman P. Industrial Rheology with Particular Reference to Foods, Pharmaceuticals and Cosmetics, Academic Press, London, 1970.
- Shields M, Ellis R, Saunders BR. A creaming study of weakly flocculated and depletion flocculated oil-in-water emulsions. *Colloid. Surf., A*. 2001; 178: 265-276.
- Shinde V, Marcel T, Hoarau Y, Deloze T, Harran G, Baj F, Cardolaccia J, Magnaud JP, Longatte E, Braza M. Numerical simulation of the fluid–structure interaction in a tube array under crossflow at moderate and high Reynolds number. *J. Fluids Structures*. 2014; 47: 99–113.
- Shinoda K, Saito H, The Stability of O/W Type Emulsions as Functions of Temperature and the HLB of Emulsifiers: The Emulsification by PIT- method. *J. Colloid. Interface. Sci*. 1969; 30: 258-263.
- Shiran BS, Skauge A. Enhanced Oil Recovery (EOR) by Combined Low Salinity Water/Polymer Flooding. *Energy Fuel*, 2013; 27 (3): 1223–1235.
- Shu R, Sun W, Wang T, Wang C, Liu X, Tong Z. Linear and nonlinear viscoelasticity of water-in-oil emulsions: Effect of droplet elasticity, *Colloid. Surf. A*. 2013; 434: 220–228.
- Sidiropoulou MG, Moutsopoulos KN, Tsihrintzis VA. Determination of Forchheimer equation coefficients a and b. *Hydrol. Process*. 2007; 21(4): 534–554.
- Singh A. Dynamics of suspension of spherical doublets in simple shear and pressure driven flow. *Chem Eng Sci*. 2013; 104: 17-24.
- Skjetne E, Auriault JL. New insights on steady, non-linear flow in porous media. *Eur. J. mech. B/Fluids*. 1999; 18(1): 131-1458.
- Slattery JC. Single-phase flow through porous media. *AIChE Journal*. 1969; 15: 866–872.
- Smagorinsky J. General Circulation Experiments with the Primitive Equations. I. The Basic Experiment. *Month. Wea. Rev*. 1963; 91: 99-164.
- Snijkers F, Vlassopoulos D. Appraisal of the Cox-Merz rule for well-characterized entangled linear and branched polymers. *Rheol Acta*. 2014; 53: 935–946 .

- Solans C, Izquierdo P, Nolla J, Azemar N, Garcia-Celma MJ. Nano-emulsions. *Curr. Opin. Colloid Inter. Sci.* 2005; 10: 102–110.
- Soleimani R, Shoushtari NA, Mirza B, Salahi. Experimental investigation, modeling and optimization of membrane separation using artificial neural network and multi-objective optimization using genetic algorithm. *Chem. Eng. Res. Des.* 2013; 91(5): 883–903.
- Soma J, Papadopoulos KD. Flow of dilute, sub-micron emulsions in granular porous media: effects of pH and ionic strength. *Colloid. Surf. A.* 1995; 101: 51-61.
- Soma J, Papadopoulos, KD. Deposition of oil-in-water emulsions in sand beds in the presence of cetyltrimethylammonium bromide. *Environ. Sci. Technol.* 1997; 31(4): 1040-1045.
- Song MG, Jho SH, Kim JY, Kim JD. Rapid Evaluation of Water-in-Oil (w/o) Emulsion Stability by Turbidity Ratio Measurements. *J. Colloid. Interf. Sci.* 2000; 230: 213–215.
- Soni JP, Islam N, Basak P. An experimental evaluation of non-Darcian flow in porous media. *J. Hydrology.* 1978; 38: 231–241.
- Soo H, Radke CJ. The Flow Mechanism of Dilute, stable emulsion in porous media. *Ind. Eng. Chem. Fundam.* 1984; 23: 342-347.
- Srinivas BK, Chhabra RP. Effect of particle to bed diameter ratio on pressure drop for power law fluid flow in packed beds. *Int. J. Eng. Fluid Mecha.* 1992; 5(3): 309-327.
- Sriram S, Deshpande AP, Pushpavanam S. Characterization of viscoelastic fluid flow in a periodically driven cavity: Flow structure, frequency response, and phase lag. *Poly. Eng. Sci.* 2008; 48(9): 1693-1706.
- Stalidis G, Avranas A, Jannakoudakis D. 1990. Interfacial Properties and Stability of Oil-in-Water Emulsions Stabilized with Binary Mixtures of Surfactants. *J. Colloid. Interf. Sci.* 135, 313-324.
- Stoesser T, Salvador GP, Rodi W, Diplas P. Large Eddy Simulation of turbulent flow through submerged vegetation. *Trans. Porous Media.* 2009; 78: 347–365.
- Stokes GG. On the effect of the internal friction of fluid on the motion of pendulums. *Philos Mag.* 1851; 1: 337-339.
- Stone HA. Dynamics of drop deformation and breakup in viscous fluids. *Annu. Rev. Fluid Mech.* 26, 65–102 (1994).

- Strand S, Austad T, Puntervold T, Aksulu H, Haaland B, Doust AR. Impact of Plagioclase on the Low Salinity EOR-Effect in Sandstone. *Energy & Fuels*. 2014; 28: 2378–2383.
- Sun G, Zhang J, Li H. Structural Behaviors of Waxy Crude Oil Emulsion Gels. *Energy Fuel*. 2014; 28: 3718–3729.
- Swernath S, Benny M, Pushpavanam S. Effect of Korteweg stress on viscous fingering of solute plugs in a porous medium. *Chem Eng Sci*. 2010; 65(7): 2284-2291.
- Tadros TF. Fundamental principles of emulsion rheology and their applications. *First World Congress on Emulsions*. 1993; 4: 237-265.
- Tadros T, Izquierdo P, Esquena J, Solans C. Formation and stability of nano-emulsions. *Adv. Colloid. Interf. Sci*. 2004; 108–109: 303–318.
- Tadros TF. Fundamental principles of emulsion rheology and their applications. *Colloid. Surf. A*. 1994; 91: 39-55.
- Tajallipour N, Kumar V, Paraschivoiu M. Large-eddy simulation of a compressible free jet flow on unstructured elements. *Int. J. Numer. Meth. Heat Fluid Flow*. 2013; 23: 336-354.
- Tajallipour N, Owlam BB, Paraschivoiu M. A Self-Adaptive Upwinding Method for Large Eddy Simulation of Turbulent Flows on Unstructured Elements. *J. Aircraft*. 2009; 46(3): 915-926.
- Tarpey T. A Note on the Prediction Sum of Squares Statistic for Restricted Least Squares. *Am. Stat*. 2000; 54(2): 116–118.
- Taylor G. The viscosity of a fluid containing small drops of another fluid. *Proc. R. Soc. Lond*. 1932; 138: 42–48.
- Taylor P. Ostwald ripening in emulsions. *Colloid Surf. A*. 1995; 99: 175 - 185.
- Tcholakova S, Denkov ND, Danner T. Role of surfactant type and concentration for the mean drop size during emulsification in turbulent flow. *Langmuir*, 2004; 20: 7444–7458.
- Teitel M. On the applicability of the Forchheimer equation in simulating flow through woven screens. *Biosystems Eng*. 2011; 109: 130-139.
- Teruel FE, Rizwan-uddin. A new turbulence model for porous media flows. Part I: Constitutive equations and model closure. *Int. J. Heat. Mass. Transfer*. 2009; 52: 4264–4272.
- Teruel FE, Rizwan-uddin. Characterization of a porous medium employing numerical tools: Permeability and pressure-drop from Darcy to turbulence. *Int. J. Heat. Mass Transfer*. 2009; 52: 5878–5888.

- Thirupathi G, Krishnamoorthy CP, Pushpavanam S. Adsorption characteristics of inorganic salts and detergents on sand beds. *Chem. Eng. J.* 2007; 125(3): 177-186.
- Thomas S, Farouq Ali SM. Flow of emulsion in porous media and potential for enhanced oil recovery. *J. Petrol. Sci. Eng.* 1989; 3: 121-136.
- Tiu C, Zhou JZQ, Nicolae G, Fang TN, Chhabra RP. Flow of Viscoelastic Polymer Solutions in Mixed Beds of Particles. *Can. J. Chem Eng.* 1997; 75(5): 843-850.
- Torres LG, Iturbe R, Snowden MJ, Chowdhry BZ, Leharne S A. Preparation of o/w emulsions stabilized by solid particles and their characterization by oscillatory rheology. *Colloid Surf. A.* 2007; 302: 439-448.
- Travkin VS, Catton I, Gratton L. Single phase turbulent transport in prescribed non-isotropic and stochastic porous media. *ASME HTD.* 1993; 240: 43-48.
- Tsenoglou C, Voyiatzis E. Steady shear banding in complex fluids. *J. Non-Newtonian Fluid Mech.* 2008; 151(1-3): 119-128.
- Tsotsas E. Transport phenomena in packed-beds—history, state-of-the-art, and research outlook. *Chemie Ingenieur Technik.* 1992; 64(4): 313-322.
- Tung Mapaulson AT. Rheological concepts for probing ingredient interactions in food systems, in *Ingredient Interactions: Effecting Food Quality*. Gaonkar, A, Bd., Marcel Dekker. New York, 1995
- Tutar M, Oguz G. Large eddy simulation of wind flow around parallel buildings with varying configurations. *Fluid. Dyn. Res.* 2002; 31: 289-315.
- Vafai K, Tien CL. Boundary and inertia effects on flow and heat transfer in porous media. *Int. J. Heat Mass Transfer.* 1981; 24: 195-203.
- van den Tempel M. Mechanical properties of plastic-disperse systems at very small deformations. *J. Colloid Sci.* 1961; 16: 284 - 296.
- Varanasi PP, Ryan ME, Stroeve P. Experimental-study on the breakup of model viscoelastic drops in uniform shear-flow. *Ind. Eng. Chem. Res.* 33, 1994:1858-1866 ().
- Velev OD, Gurkov TD, Chakarova SvK, Dimitrova VI, Ivanov IB, Borwankar RP., Experimental investigations on model emulsion systems stabilized with non-ionic surfactant blends. *Colloids Surf. A.* 1994; 83: 43-55.
- Venkataraman P, Rao PRM. Darcian, transitional and turbulent flow through porous media. *J. Hydraul. Eng.* 1998; 124: 840-846.
- Vergue P, Kamel M, Querry M. Behavior of coldrolling oil-in-water emulsions: a rheological approach. *Trans. ASME (J. Tribol.)*. 1997; 119: 250-258.
- Vinckier I, Minale M, Mewis J, Moldenaers P. Rheology of semi-dilute emulsions: viscoelastic effects caused by the interfacial tension. *Colloid Surf A.* 1999; 150: 217-228.
- Vorwerk J, Brunn PO. Shearing effects for the flow of surfactant and polymer solutions through a packed bed of spheres. *J. Non-Newtonian Fluid Mech.* 1994; 51: 79-95.
- Walstra P. Principles of emulsion formation. *Chem Eng Sci.* 1993; 48: 333-349.

- Walstra P. Physical Chemistry of Foods. Marcel Dekker, Inc., 2003.
- Wang W, Zhou Z, Nandakumar K, Xu Z, Masliyah, JH. Effect of charged colloidal particles on adsorption of surfactants at oil-water interface. *J. Colloid Inter Sci.* 2004; 274: 625-630.
- Wangli, K, Yi L, Baoyan Q, Guangzhi L, Zhenyu Y, Jichun H. Interactions between alkali/surfactant/polymer and their effects on emulsion stability. *Colloids Surf A.* 2000; 175: 243–247.
- Wen X, Afacan A, Nandakumar K, Chuang KT. A generalized approach to pressure drop predictions in packed beds based on detailed geometry of the packing. *J. Ins. Eng. Singapore. Chem. Eng.* 2003; 43: 6-13.
- Whitaker S. The equations of motion in porous media. *Chem. Eng. Sci.* 1966; 21: 291-300.
- Whitaker S. The Forchheimer equation: a theoretical development. *Trans. Porous media.* 1996; 25(1): 27–61.
- Whitaker S. The Method of Volume Averaging. Kluwer, 1999.
- Wilcox D C. Turbulence Modeling for CFD. DCW Industries, La Canada, CA, 1993.
- Wilson WRD, Sakaguchi Y, Schmid SRA. A dynamic concentration model for lubrication with oil-in-water emulsions. *Wear.* 1993; 161: 207–212.
- Winsor PA. Hydrotrophy solubilisation and related emulsification processes. *Trans Faraday Soc.* 1948; 44: 376–398.
- Xu T, Sullivan P, Paraschivoiu M. Fast Large Eddy Simulation of Low Reynolds Number Flows over a NACA0025. *J. Aircraft.* 2010; 47(1): 328-333.
- Yang Z, Shih TH. New time scale based k- ϵ model for near-wall turbulence. *AIAA J.* 1993; 31(7): 1191 – 1198.
- Yilmaz N, Bakhtiyarov A S, Ibragimov RN. Experimental investigation of Newtonian and non-Newtonian fluid flows in porous media. *Mech. Res. Commu.* 2009; 36: 638–641.
- Zee B, Gibis M, Fischer L, Weiss J. Cross linking of interfacial layers in multilayered oil-in-water emulsions using laccase: Characterization and pH-stability. *Food Hydrocoll.* 2012; 27: 126-136.
- Zhang M, Lai Y, Li D, Chen W, Tong G. Experimental study on ventilation characteristics of a concrete-sphere layer and a crushed-rock layer. *Int. J. Heat Mass Transfer.* 2013; 59: 407–413.
- Zhang YP, Sayegh SG, Huang S. The Role of Effective Interfacial Tension in Alkaline/Surfactant/Polymer Flooding. *Can. Int. Petroleum Conference Paper-022.* 2005.
- Zhavoronkov NM, Aerov ME, Umnik NN. Hydraulic resistance and density of packing of a granular bed. *J. Phys. Chem.* 1949; 23: 342-361.
- Zimmerman RW, Al-Yaarubi A, Pain CC, Grattoni CA. Non-linear regimes of fluid flow in rock fractures. *Int. J. Rock Mech. Min. Sci.* 2004; 41: 163–169.

APPENDIX A

ASTM Standards for Characterization of Petroleum Oil

A.1 Kinematic Viscosity (ASTM D88)

This test method covers the standard procedures for determining the kinematic viscosities of petroleum products at specified temperatures between 21 and 99°C (70 and 210°F). The efflux time in seconds of 60 ml of sample, flowing through a calibrated orifice, is measured under carefully controlled conditions. This time is corrected by an orifice factor and reported as the viscosity of the sample at that temperature. A cork stopper was inserted, having a cord attached for its easy removal, into the chamber at the bottom of the viscometer. About 60 ml of sample was poured into the viscometer until the level is above the overflow rim. The sample was stirred in the viscometer with the appropriate viscosity thermometer equipped with the thermometer support. A circular motion was used at 30 to 50 rpm in a horizontal plane. The sample was heated in its original container to about 50°C (122°F), with stirring. When the sample temperature remains constant within 0.03°C (0.05°F) of the test temperature during 1 min of continuous stirring, the thermometer was removed. Immediately, the tip of the withdrawal tube is placed in the gallery at one point, and applied suction to remove oil until its level in the gallery is below the overflow rim. It was checked that the receiving flask is in proper position; then snapped the cork from the viscometer using the attached cord, and started the timer at the same instant. The timer was stopped when the bottom of the oil meniscus reaches the graduation mark on the receiving flask. The efflux time recorded in seconds.

A.2 Dynamic viscosity (ASTM D1298)

This test method covers the determination, of the density, relative density (specific gravity), or API gravity of crude petroleum, petroleum products using a glass hydrometer. The sample was transferred to the clean, temperature stabilized hydrometer cylinder without splashing, to avoid the formation of air bubbles, and minimize evaporation of the lower boiling constituents of more volatile samples. Any air bubbles formed on the surface of the test portion was removed by touching them with a piece of clean filter paper before inserting the hydrometer. The cylinder

containing test portion was placed in a vertical position in a location free from air currents and where the temperature of the surrounding medium does not change more than 2°C during the time taken to complete the test. The appropriate thermometer or temperature measurement device was inserted and stirred the test portion with a stirring rod, using a combination of vertical and rotational motions to ensure uniform temperature and density throughout the hydrometer cylinder. Recorded the temperature of the sample to the nearest 0.1°C and removed the thermometer/temperature measuring device and stirring rod from the hydrometer cylinder. Lowered the appropriate hydrometer into the liquid and released when in a position of equilibrium, taking care to avoid wetting the stem above the level at which it floats freely.

The hydrometer was allowed to settle slowly into the liquid. Sufficient time was taken for the hydrometer to come to rest, and for all air bubbles to come to the surface. Recorded the hydrometer reading as the point on the hydrometer scale at which the principal surface of the liquid cuts the scale by placing the eye slightly below the level of the liquid and slowly raising it until the surface, first seen as a distorted ellipse, appears to become a straight line cutting the hydrometer scale. Immediately after recording the hydrometer scale reading, carefully lifted the hydrometer out of the liquid, and inserted the thermometer or temperature measurement device and stir the test portion vertically with the stirring rod. The temperature of the test portion was recorded to the nearest 0.1°C.

A.3 Water content (ASTM D95)

This test method covers the determination of water in the range from 0 to 25 % volume in petroleum products. 100 ml of sample to an accuracy of $\pm 1\%$ measured in a graduated cylinder and transferred to the properly dried still. Glass beads or boiling chips were added to reduce bumping. The components of the apparatus and trapping was assembled and making all connections vapor and liquid tight. The condenser tube and trap were cleaned with acetone to ensure free drainage of water into the bottom of the trap. A loose cotton plug was inserted in the top of the condenser to prevent condensation of atmospheric moisture inside it. Cold water was circulated through the jacket of the condenser. Apply heating to the still, adjusting the rate of boiling so that condensed distillate discharges from the condenser at the rate of two to five drops per second. Distillation continued until no water is visible in any part of the apparatus except in

the trap and the volume of water in the trap remains constant for 5 min. When the evolution of water was completed, the trap and contents were allowed to cool to room temperature. Any residual drops of water adhering to the sides of the trap was dislodged with a glass or polytetrafluoroethylene (PTFE) rod or other suitable means and transferred them to the water layer. The volume of the water in the trap read to the nearest scale division. The water content in the sample was calculated, volume percent, as follows:

$$\text{Water, \% (V/V)} = \frac{(\text{Volume in water trap, ml}) - (\text{Water in solvent blank, ml})}{\text{Volume in test sample, ml}} \times 100 \quad (\text{A.1})$$

A.4 Cloud Point (ASTM D2500)

The sample was poured into the test jar to the level mark. The test jar was closed tightly by the cork carrying the test thermometer (a cloud thermometer). Adjusted the position of the cork and the thermometer so that the cork fits tightly, the thermometer and the jar were coaxial, and the thermometer bulb was resting on the bottom of the jar. The disk, gasket, and the inside of the jacket were checked for clean and dry. The disk was placed in the bottom of the jacket. The disk and jacket was placed in the cooling medium a minimum of 10 min before the test jar is inserted. The use of a jacket cover while the empty jacket is cooling is permitted. The gasket was placed around the test jar, 25 mm from the bottom. The test jar was inserted in the jacket. The temperature of cooling bath was maintained at $-18 \pm 1.5^\circ\text{C}$. At each test thermometer reading, i.e. a multiple of 1°C , the test jar was removed from the jacket quickly but without disturbing the specimen, inspected for cloud, and replaced in the jacket. This complete operation required not more than 3 s. The cloud point was report, to the nearest 1°C , at which any cloud is observed at the bottom.

A.5 Pour point (ASTM D97)

Similarly for pour point measurement the sample was poured into the test jar to the level mark. The test jar was closed with the cork carrying the thermometer. After the sample was cooled to allow the formation of paraffin wax crystals, care was taken not to disturb the mass of specimen nor permit the thermometer to shift in the sample, any disturbance of the spongy network of wax crystals will lead to low and erroneous results. Pour points are expressed in

integers that are positive or negative multiples of 3°C. At each test thermometer reading, i.e. a multiple of 3°C below the starting temperature, the test jar from the jacket was removed. To remove condensed moisture that limits visibility wipe the surface with a clean cloth moistened in alcohol (ethanol or methanol). The test jar was tilted just enough to ascertain whether there is a movement of the specimen in the test jar. If movement of sample in the test jar is noted, then replace the test jar immediately in the jacket and repeat a test for flow at the next temperature, 3°C lower. Typically, the complete operation of removal, wiping, and replacement required not more than 3 s. If the sample in the jar does not show movement when tilted, hold the jar in a horizontal position for 5 s, as noted by stopwatch, and the sample was observed carefully. If the sample shows any sign of movement before 5 s has passed, replace the test jar immediately in the jacket and repeat a test for flow at the next temperature, 3°C lower. Continued in this manner until a point was reached at which the sample shows no movement when the test jar is held in a horizontal position for 5 s and recorded the observed reading of the test thermometer.

A.6 Flash point (ASTM D93)

This flash point test method is a dynamic test method which depends on specified rates of heating to be able to meet the precision of the test method. The Pensky-Martens test cup was filled with the sample to the filling mark inside of the test cup.

The test cover was placed on the test cup and the assembly was placed into the apparatus. The temperature measuring device (thermometer) was inserted into its holder. Lighted the test flame, and adjusted it to a diameter of 3.2 mm to 4.8 mm (0.126 in. to 0.189 in.), or switched on the electric igniter and adjusted the intensity. The heat was applied at such a rate that the temperature, as indicated by the temperature measuring device, increased 5 °C to 6 °C (9 °F to 11 °F) /min. The stirring device turned at 90 r /min to 120 r /min, and stirring in a downward direction. The ignition source was applied when the temperature of the sample close to the expected flash point and each time thereafter at a temperature reading that is a multiple of 1 °C or 2 °F. The stirring of the sample was discontinued and applied the ignition source by operating the mechanism on the test cover which controls the shutter so that the ignition source is lowered into the vapor space of the test cup in 0.5 s, left in its lowered position for 1 s, and quickly raised to its upward position. The observed flash point was recorded as the reading on the temperature

measuring device at the time ignition source application causes a distinct flash in the interior of the test cup. The sample was deemed to have flashed when a large flame appears and instantaneously propagates itself over the entire surface of the test specimen. The apparatus was cooled down to a safe handling temperature, less than 55 °C (130 °F), the test cover was removed and both the test cup and apparatus was cleaned.

A.7 Fire point (ASTM D92)

The sample was filled in the test cup (Cleveland open cup) exactly at the filling mark, and the test cup was placed on the center of the heater. The test flame was lighted and adjust mounted on the apparatus. Heat initially applied at such a rate that the temperature as indicated by the temperature measuring device increased 14 to 17°C (25 to 30°F)/min. When the sample temperature was $\approx 56^{\circ}\text{C}$ (100°F) below the expected flash point, the heat was decreased so that the rate of temperature rise during the last 28°C (50°F) before the flash point was 5 to 6°C (9 to 11°F)/min. The test flame was applied when the temperature of the test specimen was $\approx 28^{\circ}\text{C}$ below the expected flash point and each time thereafter at a temperature reading that is a multiple of 2°C. The test flame was passed across the center of the test cup at right angles to the diameter, which passes through the temperature measuring device. With a smooth, continuous motion, the test flame was applied either in a straight line or along the circumference. The observed flash point was recorded as the reading on the temperature measuring device at the time the test flame causes a distinct flash in the interior of the test cup. When a flash point was detected on the first application of the test flame, the test was discontinued, and the test was repeated with a fresh test sample.

A.8 Aniline point (ASTM D611)

The Aniline Point apparatus was cleaned and dried. 10 ml of Aniline and 10 ml of sample were added into the test tube fitted with stirrer and thermometer. The thermometer was centered in the test tube so that the immersion mark is at the liquid level, making sure that the thermometer bulb does not touch the side of the tube. The mixture was stirred rapidly using a 50-mm (2-in.) stroke, avoiding the introduction of air bubbles. The aniline-sample mixture is not miscible at room temperature, applying the heat directly to the jacket tube so that the temperature

rises at a rate of 1 to 3°C (2 to 5°F)/min by removing or reducing the heat source until complete miscibility is obtained. Continued stirring and allowed the mixture to cool at a rate of 0.5 to 1.0°C (1.0 to 1.8°F)/min. Cooling was continued to a temperature of 1 to 2°C (2.0 to 3.5°F) below the first appearance of turbidity, and recorded as the aniline point the temperature at which the mixture suddenly becomes cloudy throughout. The observation of aniline point temperature was repeated by heating and cooling continuously for accuracy.

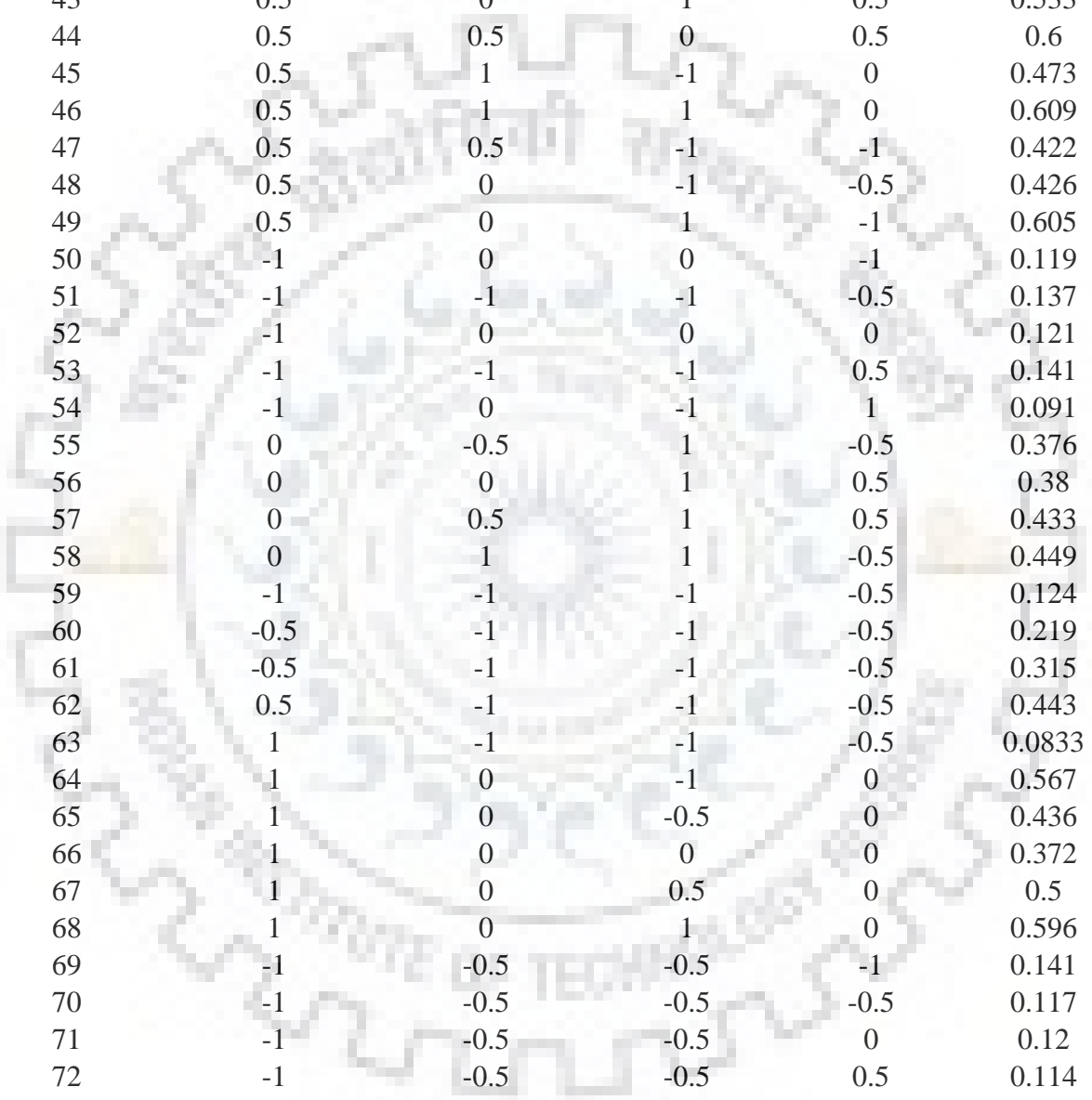


Appendix B

Table B1: Experimental data sets used for generating BP-ANN and hybrid GA model.

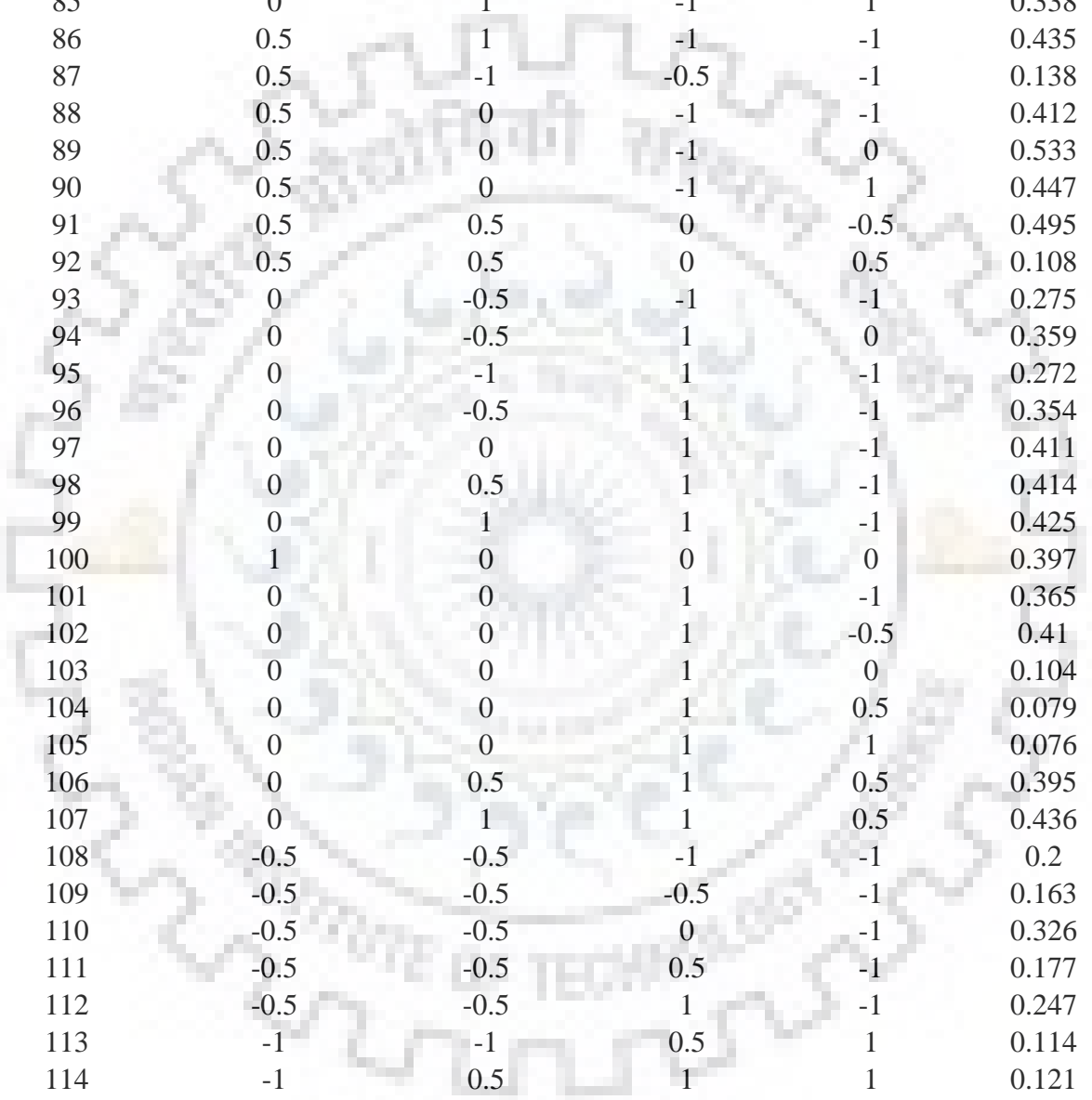
Experimental run no.	A: Oil concentration (vol %)	B: Surfactant concentration (wt %)	C: Stirring intensity (rpm)	D: Stirring time (min)	ESI_{24}
1	-1	0	0	1	0.18
2	0	1	0	-1	0.525
3	1	0	0	-1	0.714
4	0	0	-1	1	0.48
5	0	0	-1	-1	0.386
6	0	1	1	0	0.464
7	0	0	0	0	0.495
8	0	-1	0	-1	0.177
9	0	0	0	0	0.48
10	-1	1	0	0	0.209
11	1	1	0	0	0.788
12	-1	-1	0	0	0.131
13	0	-1	-1	0	0.174
14	0	-1	0	1	0.18
15	0	0	1	-1	0.396
16	-1	0	-1	0	0.155
17	1	0	-1	0	0.582
18	0	1	0	1	0.502
19	1	-1	0	0	0.08
20	0	1	-1	0	0.489
21	-1	0	0	-1	0.13
22	0	0	0	0	0.489
23	0	0	0	0	0.503
24	0	0	1	1	0.076
25	1	0	0	1	0.248
26	0	-1	1	0	0.143
27	1	0	1	0	0.517
28	-1	0	1	0	0.187
29	0	0	0	0	0.482
30	-0.5	-1	-1	0	0.212
31	-0.5	0	-1	0	0.257
32	-0.5	1	-1	0	0.221
33	-0.5	-0.5	-1	0	0.244
34	-0.5	0.5	-1	0	0.274
35	-0.5	0	-1	1	0.26
36	-0.5	0	0	1	0.257
37	-0.5	0	1	1	0.286

APPENDIX B



38	-0.5	0	-0.5	1	0.244
39	-0.5	0	0.5	1	0.258
40	0.5	-0.5	0	-1	0.453
41	0.5	-0.5	0	0	0.467
42	0.5	0	0	1	0.523
43	0.5	0	1	0.5	0.533
44	0.5	0.5	0	0.5	0.6
45	0.5	1	-1	0	0.473
46	0.5	1	1	0	0.609
47	0.5	0.5	-1	-1	0.422
48	0.5	0	-1	-0.5	0.426
49	0.5	0	1	-1	0.605
50	-1	0	0	-1	0.119
51	-1	-1	-1	-0.5	0.137
52	-1	0	0	0	0.121
53	-1	-1	-1	0.5	0.141
54	-1	0	-1	1	0.091
55	0	-0.5	1	-0.5	0.376
56	0	0	1	0.5	0.38
57	0	0.5	1	0.5	0.433
58	0	1	1	-0.5	0.449
59	-1	-1	-1	-0.5	0.124
60	-0.5	-1	-1	-0.5	0.219
61	-0.5	-1	-1	-0.5	0.315
62	0.5	-1	-1	-0.5	0.443
63	1	-1	-1	-0.5	0.0833
64	1	0	-1	0	0.567
65	1	0	-0.5	0	0.436
66	1	0	0	0	0.372
67	1	0	0.5	0	0.5
68	1	0	1	0	0.596
69	-1	-0.5	-0.5	-1	0.141
70	-1	-0.5	-0.5	-0.5	0.117
71	-1	-0.5	-0.5	0	0.12
72	-1	-0.5	-0.5	0.5	0.114
73	-1	0.5	-0.5	1	0.108
74	-0.5	0.5	-1	0.5	0.187
75	-0.5	0.5	-0.5	0.5	0.215
76	-0.5	0.5	0	0.5	0.236
77	-0.5	0.5	0.5	0.5	0.261
78	-0.5	0.5	1	0.5	0.356

APPENDIX B



79	0	1	-0.5	-0.5	0.473
80	0	1	0	-1	0.389
81	0	1	-0.5	-0.5	0.409
82	0	1	0	-1	0.365
83	0	1	0.5	0	0.33
84	0	1	-1	-1	0.275
85	0	1	-1	1	0.338
86	0.5	1	-1	-1	0.435
87	0.5	-1	-0.5	-1	0.138
88	0.5	0	-1	-1	0.412
89	0.5	0	-1	0	0.533
90	0.5	0	-1	1	0.447
91	0.5	0.5	0	-0.5	0.495
92	0.5	0.5	0	0.5	0.108
93	0	-0.5	-1	-1	0.275
94	0	-0.5	1	0	0.359
95	0	-1	1	-1	0.272
96	0	-0.5	1	-1	0.354
97	0	0	1	-1	0.411
98	0	0.5	1	-1	0.414
99	0	1	1	-1	0.425
100	1	0	0	0	0.397
101	0	0	1	-1	0.365
102	0	0	1	-0.5	0.41
103	0	0	1	0	0.104
104	0	0	1	0.5	0.079
105	0	0	1	1	0.076
106	0	0.5	1	0.5	0.395
107	0	1	1	0.5	0.436
108	-0.5	-0.5	-1	-1	0.2
109	-0.5	-0.5	-0.5	-1	0.163
110	-0.5	-0.5	0	-1	0.326
111	-0.5	-0.5	0.5	-1	0.177
112	-0.5	-0.5	1	-1	0.247
113	-1	-1	0.5	1	0.114
114	-1	0.5	1	1	0.121
115	-1	0.5	-1	1	0.108
116	-1	1	0	1	0.144
117	1	-0.5	-0.5	1	0.074
118	1	0.5	0	0	0.595
119	1	0.5	0.5	-0.5	0.723
120	1	1	1	-1	0.733

Table B2. Proposed polynomial model fitting parameters for apparent viscosity of o/w emulsions at different temperatures.

Shear rate (SR)/ Temperature (°C)	Λ	C_1	C_2	C_3	R^2	adj R^2	SEE	PRESS
SR- 40 s⁻¹								
25	0.1084 ± 0.0131	0.1459 ± 0.1315	(-)0.1824 ± 0.3431	0.3145 ± 0.2547	0.9984	0.9937	0.0048	0.0036
30	0.0930 ± 0.0138	0.1728 ± 0.1389	(-)0.3147 ± 0.3624	0.3560 ± 0.2691	0.9964	0.9854	0.0051	0.0040
40	0.0935 ± 0.0140	0.0399 ± 0.1409	(-)0.0740 ± 0.3676	0.1942 ± 0.2729	0.9942	0.9767	0.0052	0.0041
50	0.0702 ± 0.0038	0.0393 ± 0.0377	(-)0.0623 ± 0.0983	0.1223 ± 0.0730	0.9989	0.9957	0.0014	0.0003
SR- 20 s⁻¹								
25	0.1543 ± 0.0327	0.2959 ± 0.3277	(-)0.6615 ± 0.8552	0.8141 ± 0.6349	0.9949	0.9798	0.0121	0.0221
30	0.1190 ± 0.0483	0.3793 ± 0.4845	(-)0.9255 ± 1.2642	0.9590 ± 0.9385	0.9838	0.9354	0.0179	0.0484
40	0.1284 ± 0.0135	0.0884 ± 0.1358	(-)0.2201 ± 0.3545	0.4125 ± 0.2632	0.9980	0.9922	0.0050	0.0038
50	0.0825 ± 0.0094	0.1891 ± 0.0941	(-)0.5183 ± 0.2457	0.5975 ± 0.1824	0.9986	0.9943	0.0035	0.0018
SR- 80 s⁻¹								
25	0.0772 ± 0.0116	0.1222 ± 0.1165	(-)0.1632 ± 0.3041	0.2389 ± 0.2258	0.9975	0.9900	0.0043	0.0028
30	0.0767 ± 0.0028	0.0395 ± 0.0283	0.0007 ± 0.0738	0.0698 ± 0.0548	0.9996	0.9984	0.0010	0.0002
40	0.0710 ± 0.0043	0.0720 ± 0.0430	(-)0.1760 ± 0.0021	0.1885 ± 0.0832	0.9971	0.9882	0.0016	0.0004
50	0.0565 ± 0.0010	0.0019 ± 0.0105	0.0626 ± 0.0274	(-)0.0298 ± 0.0203	0.9997	0.9987	0.0004	0.000023
SR- 100 s⁻¹								
25	0.0659 ± 0.0124	0.1566 ± 0.1248	(-)0.2729 ± 0.3256	0.2977 ± 0.2417	0.9960	0.9839	0.0046	0.0032
30	0.0756 ± 0.0079	-0.0225 ± 0.0792	0.1477 ± 0.2067	(-)0.0565 ± 0.1535	0.9950	0.9801	0.0029	0.0013
40	0.0690 ± 0.0008	0.0082 ± 0.0079	0.0225 ± 0.0207	0.0129 ± 0.0154	0.9998	0.9993	0.0003	0.000013
50	0.0494 ± 0.0001	0.0260 ± 0.0013	(-)0.0072 ± 0.0033	0.0173 ± 0.0024	0.9999	0.9999	0.000046	3.2e-07

Table B3. Proposed exponential model fitting parameters for apparent viscosity of o/w emulsions at different temperatures.

Shear rate (SR)/ Temperature (°C)	Y_M	K_V	K_P	R^2	adj R^2	SEE	PRESS
SR-20 s⁻¹							
25	0.1599 ± 0.0206	0.0147 ± 0.0106	3.3974 ± 0.8191	0.9925	0.9849	0.0104	0.0012
30	0.1383 ± 0.0274	0.0100 ± 0.0130	3.6114 ± 1.4941	0.9765	0.9530	0.0152	0.0025
40	0.1255 ± 0.0072	0.0064 ± 0.0031	3.8884 ± 0.5586	0.9969	0.9937	0.0045	0.0004
50	0.0934 ± 0.0057	0.0032 ± 0.0019	4.4510 ± 0.6971	0.9957	0.9914	0.0043	0.0002
SR-40 s⁻¹							
25	0.0905 ± 0.0136	0.0248 ± 0.0095	2.4645 ± 0.3970	0.9978	0.9957	0.0040	0.0002
30	0.0877 ± 0.0160	0.0167 ± 0.0110	2.4970 ± 0.6892	0.9935	0.9871	0.0048	0.0003
40	0.0888 ± 0.0078	0.0054 ± 0.0039	3.4927 ± 0.8145	0.9927	0.9854	0.0041	0.0003
50	0.0671 ± 0.0027	0.0049 ± 0.0016	3.0832 ± 0.3598	0.9984	0.9969	0.0012	1.85e-05
SR-80 s⁻¹							
25	0.0643 ± 0.0121	0.0196 ± 0.0087	2.3449 ± 0.4551	0.9971	0.9942	0.0033	0.0002
30	0.0630 ± 0.0028	0.0142 ± 0.0021	2.1806 ± 0.1450	0.9997	0.9994	0.0007	5.76e-06
40	0.0753 ± 0.0024	0.0016 ± 0.0010	3.9175 ± 0.7372	0.9946	0.9891	0.0015	6.99e-05
50	0.0371 ± 0.0078	0.0177 ± 0.0071	1.1941 ± 0.2999	0.9985	0.9969	0.0006	7.93e-06
SR-100 s⁻¹							
25	0.0592 ± 0.0158	0.0171 ± 0.0114	2.3101 ± 0.6789	0.9935	0.9870	0.0041	0.0004
30	0.0580 ± 0.0120	0.0131 ± 0.0093	2.0204 ± 0.6889	0.9929	0.9859	0.0025	7.92e-05
40	0.0623 ± 0.0014	0.0061 ± 0.0011	2.1496 ± 0.1704	0.9996	0.9991	0.0003	2.17e-05
50	0.0306 ± 0.0029	0.0193 ± 0.0027	1.0238 ± 0.0951	0.9998	0.9997	0.0002	6.86e-07

Table B4: Flow parameters of o/w emulsions at different temperature determined by power law and Sisko model.

Power law model (Two parameter)					
Temperature (oC)	η_{∞} (Pa. s)	K (Pa.s ⁿ)	n	χ^2	R^2
20	-	1.6497 ± 0.0704	0.4573 ± 0.0071	0.4653	0.9955
30	-	1.0459 ± 0.0223	0.4681 ± 0.0035	0.0423	0.9991
40	-	0.4596 ± 0.0277	0.5276 ± 0.0098	0.1211	0.9939
50	-	0.2355 ± 0.0206	0.5879 ± 0.0141	0.1097	0.9903
Sisko model (Three parameter)					
20	0.0387	1.1141 ± 0.0445	0.6233 ± 0.0110	0.0515	0.9828
30	0.0269	0.6170 ± 0.0330	0.6030 ± 0.0154	0.0226	0.9749
40	0.0192	0.3760 ± 0.0150	0.7560 ± 0.0120	0.0066	0.9426
50	0.0149	0.2698 ± 0.0138	0.7643 ± 0.0154	0.0057	0.9046

Table B5. Flow parameters of o/w emulsions at different temperature determined by Cross and Carreau model.

Cross model						
Temperature (oC)	η_0 (Pa. s)	η_∞ (Pa. s)	$\dot{\gamma}_c$ (s ⁻¹)	m	χ^2	R^2
20	5.88 ± 0.01	0.0387 ± 0.01	0.1098 ± 0.01	0.7736 ± 0.0530	0.1447	0.9517
30	3.73 ± 0.011	0.0269 ± 0.01	0.0782 ± 0.0104	0.6271 ± 0.0547	0.0716	0.9204
40	1.0936 ± 0.0189	0.0192 ± 0.01	0.4710 ± 0.0333	0.57963 ± 0.0134	2.4617 × 10 ⁻⁰⁴	0.9979
50	0.6999 ± 0.01301	0.0149 ± 0.01	0.7713 ± 0.0662	0.7077 ± 0.0293	4.0136 × 10 ⁻⁰⁴	0.9934
Carreau model						
Temperature (oC)	η_0 (Pa. s)	η_∞ (Pa. s)	$\dot{\gamma}_c$ (s ⁻¹)	N	χ^2	R_2
20	6.5279 ± 0.3116	0.0881 ± 0.0613	0.0135 ± 0.0028	0.2200 ± 0.01445	0.0367	0.9883
30	3.730 ± 0.01	0.0269 ± 0.010	0.0115 ± 0.0016	0.1978 ± 0.0120	0.0338	0.9624
40	0.9706 ± 0.001	0.0192 ± 0.001	0.0801 ± 0.006	0.1809 ± 0.0060	9.1912 × 10 ⁻⁰⁴	0.9920
50	0.662 ± 0.001	0.0149 ± 0.001	0.1363 ± 0.0091	0.2098 ± 0.0069	3.5770 × 10 ⁻⁰⁴	0.9939

BIO-DATA

Name : **Partha Kundu**
Date of Birth : 4th April 1984
Nationality : Indian

Educational qualification:

- ❖ B. Sc, Chemistry Honours (2006), Scottish Church College, University of Calcutta.
- ❖ B. Tech, Chemical Engineering, (2009), UCST, University of Calcutta.
- ❖ M. Tech, Chemical Engineering, (2011), Indian Institute of Technology, Roorkee, Roorkee, India.

PUBLICATIONS FROM THE THESIS

International Journals

1. **P. Kundu**, V. Kumar, I. M. Mishra, Modeling the steady shear rheological behavior of dilute to highly concentrated oil-in-water (o/w) emulsions: Effect of temperature, oil volume fraction and anionic surfactant concentration, *Journal of Petroleum Science and Engineering* 129 (2015) 189-204.
2. **P. Kundu**, V. Paul, V. Kumar, I. M. Mishra, Formulation development, Modeling and optimization of emulsification process using evolving RSM coupled hybrid ANN-GA framework, *Chemical Engineering Research and Design* 104 (2015) 773-790.
3. **P. Kundu**, V. Kumar, I. M. Mishra, Numerical modeling of turbulent flow through isotropic porous media, *International Journal of Heat and Mass Transfer* 75 (2014) 40-57.
4. **P. Kundu**, V. Paul, V. Kumar, I. M. Mishra, An Adaptive Modeling of Petroleum Emulsion Formation and Stability By A Heuristic Multi-Objective Artificial Neural Network-Genetic Algorithm, *Petroleum Science and Technology* (2015) (Accepted).
5. **P. Kundu**, V. Kumar, I. M. Mishra, Synergistic influence of pH and temperature on viscoelastic behaviour of surfactant stabilized oil-in-water emulsions, *Journal of Rheology*, (2015), (Revision submitted).
6. **P. Kundu**, V. Kumar, I. M. Mishra, Numerical simulation and analysis of fluid flow hydrodynamics through porous media using Reynolds averaged Navier-Stokes and Large Eddy Simulation approach, *Applied Mathematical Modelling*, (2015), (Under revision).

7. **P. Kundu**, V. Kumar, I. M. Mishra, Investigation of Fluid Flow Hydrodynamics in Porous Media: Characterization of Darcy and non-Darcy Flow Regimes, *Powder Technology* (2015), (Under review).

International Conferences

1. **P. Kundu**, V. Kumar, I. M. Mishra, "Numerical modeling and simulation of turbulent flow of newtonian fluids through porous media using rans and les approach", Eleventh International Conference on CFD in the Minerals and Process Industries CSIRO, Melbourne, Australia 7-9 December 2015.
2. **P. Kundu**, V. Kumar, I. M. Mishra, "Experimental study of oil-in-water (o/w) emulsion flow through porous Media" CHEMCON 2014, Conference proceedings of 67th Annual session of Indian Institute of Chemical Engineers organized by IChE & Punjab University, Chandigarh. December 27-30, 2014.
3. **P. Kundu**, V. Kumar, I. M. Mishra "Numerical Simulation of Fluid Flows through Porous Media using Low-Re Turbulence Model", Conference proceedings of International Conference on Advances in Chemical Engineering (ACE) 2013, February 22-24, 2013, IIT Roorkee, India.
4. **P. Kundu**, V. Kumar, I. M. Mishra, "Simulation of Turbulent Flows through Porous Media by k- ϵ Turbulent Model", CHEMCON 2012, Conference proceedings of 65th Annual session of Indian Institute of Chemical Engineers organized by IChE & NIT Jalandhar. December 27-30, 2012.